

FUNDAMENTAL STUDIES ON SURFACE CHEMISTRY AND INTERFACIAL
INTERACTIONS OF NANOSCALE HETEROSTRUCTURES FOR CHEMICAL SENSING,
PHOTOCATALYSIS, AND THERMAL TRANSPORT MANAGEMENT

by

YUAN LI

NITIN CHOPRA, COMMITTEE CHAIR

RAMANA G. REDDY

JINHUI SONG

SAMIT ROY

UDAY VAIDYA

A DISSERTATION

Submitted in partial fulfillment of the requirements
for the degree of Doctor of Philosophy
in the Department of Metallurgical and Materials Engineering
in the Graduate School of
The University of Alabama

TUSCALOOSA, ALABAMA

2015

Copyright Yuan Li 2015
ALL RIGHTS RESERVED

ABSTRACT

By combining carbon nanostructures (e.g., graphene, CNTs) with noble metal nanoparticles and further integration them with semiconducting nanowires or quantum dots, it is possible to achieve unique multifunctional hybrid nanoscale heterostructures. The heterostructures are anticipated to exhibit novel thermal, chemical, mechanical, electrical and optical performances. This dissertation mainly focused on fundamentally understanding of the processing, structure-property relationships and novel physical phenomenon related noble metal-carbon nano-systems and their heterostructuring with semiconducting nanowires or quantum dots. This leads to the generation of fundamental knowledge and effective control of their structure, morphology, surface and interface properties with novel processing methods, and thus further allows for modulating their electric, optical, chemical, thermal and mechanical performances.

The main content of this dissertation was summarized as follows. (1) Carbon-base surface chemistry: fabrication (Chemical Vapor Deposition or CVD) and controlled patterning of graphene encapsulated gold nanoparticles (referred as graphene nanoparticles or GNPs) on silicon substrate and their surface functionalization with DNA, external nanoparticles, or semiconducting quantum dots; (2) metal oxide heterostructures for photocatalysis and electrocatalysis: cobalt oxide (Co_3O_4) nanowires were grown on the cobalt foil using a water vapor-assisted thermal oxidation method. These Co_3O_4 nanowires were further decorated with tungsten oxide nanostructure for the fabrication of p-n junction heterostructures with improved light-driven organic degradation efficiency; (3) Surface-enhanced Raman Spectroscopy (SERS): Vapor-Liquid-Solid (VLS) growth of silicon (Si) nanowires and their surface decoration with noble metal nanoparticles or graphene nanoparticles (GNPs) for precise and controlled Raman sensing of trace-amount organics; (4)

thermal management on carbon nanomaterials: Design of thermal conductivity measurement set-up based on the Raman spectroscopy. The thermal conductivity of carbon nanotube films (pristine and/or after plasma/acid treatment) was measured using the self-designed Raman set-up. A multilayer CNT/polymer nanocomposite film with gradient thermal transport property was designed and fabricated. Their isotropic thermal conduction was further studied and simulated.

DEDICATION

This thesis is dedicated to everyone who helped me and guided me through the trials and tribulations of creating this manuscript. In particular, my family and close friends who stood by me throughout the time taken to complete this masterpiece.

LIST OF ABBREVIATIONS AND SYMBOLS

a	Absorbance coefficient
A	A constant related to the Tauc equation
$h\nu$	The energy of light
n	Constant depending on the nature of the electron transition
Q_{ext}	The extinction efficiency factor
Q_{sca}	The scattering efficiency factor
Q_{abs}	The absorbance factor
λ	The wavelength of light
k	Equals to $2\pi/\lambda$
R	The radius of the particles
$F(m)$	Function of the refractive index (m).
$E(m)$	The function of the refractive index relying on a non-zero imaginary part
t	The degradation time
C_0	The initial phenol concentration in water
C	The phenol concentration at specific t .
R_s	Solution resistance
R_f	Film resistance
R_t	Electron transfer resistances
s	A constant related to the Warburg impedance
ω	The angular frequency

Q	The capacity parameter with unit of $S\text{ cm}^{-2}\text{ s}^n$ ($0 < n < 1$),
j	Equals to $(-1)^{1/2}$
n	The deviation from the ideal behavior
R	The reflectance
v	The scan rate of the potential perturbation (v , mV/s),
D	The diffusion coefficient of ions in the solution (cm^2/s)
C^*	The concentration of the probe molecule in the bulk solution (mol/cm^3)
I_P	The peak current of the $\text{Fe}(\text{CN})_6^{3-/4-}$ redox couple.
a_0	The Tafel intercept obtained from OriginLab
ϕ	The equilibrium electrode potential corresponding to the oxygen evolution reaction
R	The outside radius of the core/shell structure
H	The photoelectron emission depth and was assumed to be 8 nm
r	The radius of the metallic gold core
x	The thickness of gold silicide shell, ($x = R - r$)
erf	The Gauss error function
T	The temperature
D_0	Pre-exponential factor
I_{SERS}	Raman intensity obtained on the nanostructures decorated substrate
I_{bulk}	Raman intensity obtained on the bulk MB solution
N_{SERS}	The number of molecules used for the generation of Raman signal
I_{bulk}	The number of molecules in the bulk MB solution
q'''	The incident heat flux per unit volume generated by Raman laser
r_0	The radius of laser spot

- q'' The maximum absorbed laser power per unit area at the center of the spot
- K Thermal conductivity
- $Ei(x)$ The exponential integral
- T_0 The edge temperature
- T_m Equals to $T(r) - T(R)$
- T_T Temperatures at the top surface of the nanocomposites
- T_B Temperatures at the bottom surface of the nanocomposites
- K_e Effective thermal conductivity of the nanocomposite
- K_C Thermal conductivity of MWCNTs
- K_m Thermal conductivity of polystyrene
- f The volume fraction of MWCNTs in polymer
- $c, b, \text{ and } T_0'$ The constants depending on the Joule heating and the effective thermal conductivity of the nanocomposite
- c' and T_0'' The constants depending on the Joule heating and the effective thermal conductivity of a specific MWCNT film within the nanocomposite

ACKNOWLEDGMENTS

I am pleased to have this opportunity to thank the many colleagues, friends, and faculty members who have helped me with this research project. I am most indebted to Nitin Chopra, the chairman of this dissertation, for sharing his research expertise and wisdom regarding motivational theory. I would also like to thank all of my committee members, Ramana G. Reddy, Jinhui Song, Samit Roy, and Uday Vaidya for their invaluable input, inspiring questions, and support of both the dissertation and my academic progress. I would like to thank all of my group members who helped me at every step of my graduate research, with special thanks to Wenwu Shi (graduate student), Junchi Wu (graduate student), Lyndon Smith Jr. (graduate student), John Dykes (NSF-REU), Todd Gilliam (NSR-REH), Aditya Gupta (NSR-REH), Kelly Burnham (NSF-REU), and Michael Gamble (NSF-REU) for their help in experimental processing.

Thanks to the Central Analytical Facility (CAF) staff including Rich Martens, Johnny Goodwin and Rob Holler for providing training and assistance. I also thank staff from Metallurgical and Materials Engineering (MTE) department and Center for Materials for Information Technology (MINT), Jan Creitz, Susan Noble, Kim Walker, Bob Fanning, Casey McDow, Jamie Crawford, Gary Mankey, Patrick LeClair, John Hawkins, and Jason Foster. I am grateful for the financial support from MINT GSS scholarship (2013-2014), University of Alabama's Office of Sponsored Programs, Research Grant Committee (RGC) Award, NSF EPSCOR award, and Chinese Scholarship Council (CSC).

Finally, I would like to thank my family and friends with all encouragements and supports.

CONTENTS

ABSTRACT.....	ii
DEDICATION.....	iv
LIST OF ABBREVIATIONS AND SYMBOLS	v
ACKNOWLEDGMENTS	viii
LIST OF TABLES.....	xvii
LIST OF FIGURES	xviii
CHAPTER 1. INTRODUCTION	1
1.1. Complex carbon nanoscale architecture	2
1.1.1. Basic carbon nanostructures	2
1.1.2. Hybridization of carbon nanostructures.....	3
1.2. Potential applications of hybridized carbon nanostructures	5
1.2.1. Chemical sensing	5
1.2.2. Solar energy harvesting.....	7
1.2.3. Bio-chemical applications.....	8
1.3. Nanoscale heterostructures for SERS	9
1.3.1. Surface-enhanced Raman Spectroscopy (SERS).....	9
1.3.2. Silicon nanowire based SERS substrate	10
1.4. Carbon nanostructures for thermal management	12
1.5. Challenges and major goals	15

PART I.....	20
CHAPTER 2. PLASMA OXIDATION OF GRAPHENE-ENCAPSULATED GOLD NANOPARTICLES AND FURTHER BIO-FUNCTIONALIZATION	21
Abstract.....	22
2.1. Introduction.....	23
2.2. Experimental details.....	26
2.3. Results and disucssion	29
2.3.1. Growth of graphene shells on gold nanoparticles.....	29
2.3.2. Oxygen plasma treatment to GNPs.....	31
2.3.3. Heterostructuring of GNPs for SERS	38
2.3.4. Immobilization of DNA on GNPs	45
2.4. Conclusions.....	48
CHAPTER 3. PLASMON-ENHANCED PHOTOCATALYTIC DEGRADATION USING NANOSCALE HETEROSTRUCTURES COMPRISED OF GRAPHENE- ENCAPSULATED GOLD NANOPARTICLES AND SEMICONDUCTING QUANTUM DOTS	49
3.1. Introduction.....	51
3.2. Experimental section.....	54
3.3. Results and discussion	57
3.3.1. Synthesis and chemical modification of GNPs.....	59
3.3.2. Fabrication of GNP-QD heterostructures	66
3.3.3. Optical properties of GNPs and GNP-QD heterostructures	71
3.3.4. Plasmonic-enhanced photodegradation of phenol	77

3.4. Conclusions.....	82
CHAPTER 4. GOLD NANOPARTICLE MODIFIED BY CARBON AND QUANTUM DOTS: SYNTHESIS AND OPTICAL PROPERTIES.....	83
Abstract.....	84
4.1. Introduction.....	85
4.2. Experimental section.....	86
4.3. Results and Discussion	89
4.4. Conclusions.....	102
CHAPTER 5. GRAPHENE ENCAPSULATED GOLD NANOPARTICLE – QUANTUM DOTS HYBRIDS DECORATED SILICON ELECTRODE.....	103
Abstract.....	104
5.1. Introduction.....	105
5.2. Experimental section.....	106
5.3. Results and discussion	108
5.3. Conclusions.....	118
CHAPTER 6. FABRICATION AND OPTICAL PROPERTIES OF GRAPHENE SHELLS ENCAPSULATE GOLD NANOPARTICLE – CARBON NANOTUBE HETEROSTRUCTURES.....	119
Abstract.....	120
6.1. Introduction.....	121
6.2. Experimental section.....	122
6.3. Results and discussion	125
6.3.1. Fabrication of GNP-QD heterostructures	126

6.3.2. Discrete Dipole Approximation modeling.....	131
6.4. Conclusions.....	137
PART II.....	138
CHAPTER 7. WATER VAPOR-ASSISTED SINGLE-STEP THERMAL GROWTH OF FREE-STANDING COBALT OXIDE NANOWIRES	139
Abstract.....	140
7.1. Introduction.....	141
7.2. Experimental details.....	143
7.3. Results and discussion	144
7.3.1 Thermodynamic analysis	144
7.3.2. Morphology and structure of final Co_3O_4 nanowires	148
7.3.3. Parameter study for the growth of Co_3O_4 nanowires.....	150
7.3.4. Analysis of parameter study results	164
7.4. Conclusions.....	171
CHAPTER 8. FABRICATION AND ELECTROCHEMICAL PROPERTIES OF COPPER OXIDE NANOWIRE-COBALT OXIDE NANOPARTICLE HETEROSTRUCTURES FOR OXYGEN EVOLUTION REACTION	172
Abstract.....	173
8.1. Introduction.....	174
8.2. Experimental Section.....	175
8.3. Results and discussion	177
8.3.1. Growth of CuO nanowire- Co_3O_4 nanoparticle heterostructures.....	177

8.3.2. Effective surface area and electron transfer resistance	178
8.3.3. Oxygen evolution reaction on the heterostructures	185
8.4. Conclusions.....	188
CHAPTER 9. NOVEL MULTI-COMPONENT P-N JUNCTION COBALT OXIDE- TUNGSTEN OXIDE NANOWIRE HETEROSTRUCTURES FOR EFFICIENT ORGANIC PHOTODEGRADATION	189
Abstract	191
9.1. Introduction.....	192
9.2. Experimental section.....	194
9.3. Results and discussion	197
9.4. Conclusions.....	209
PART III	210
CHAPTER 10. CONTROLLED GROWTH OF SILICON NANOWIRES AND THEIR FURTHER DECORATION WITH GOLD NANOPARTICLE FOR SURFACE- ENHANCED RAMAN SENSING	211
Abstract	212
10.1. Introduction.....	213
10.2. Experimental details.....	216
10.3. Results and discussion	219
10.3.1 Silane-based CVD growth of Si nanowires	219
10.3.2. Surface decoration of Si nanowires	231
10.3.3. Surface-enhanced Raman Spectroscopy.....	234
10.4. Conclusions.....	241

CHAPTER 11. THERMAL TREATMENT OF SILICON NANOWIRE – GOLD NANOPARTICLE HETEROSTRUCTURES FOR SURFACE-ENHANCED RAMAN SCATTERING SENSING	242
11.1. Introduction.....	243
11.2. Experimental section.....	245
11.3. Results and discussion	249
11.3.1. Growth of Si nanowires and their surface decoration with Au nanoparticles	250
11.3.2. Annealing of Si nanowire-Au nanoparticle heterostructures	252
11.3.3. XPS study for the formation of gold silicide	261
11.3.4. Kinetics for the formation of gold silicide.....	265
11.3.5. SERS-based chemical sensing	266
11.4. Conclusions.....	270
CHAPTER 12. HIGHLY-ORDERED GRAPHENNE-ENCAPSULATED GOLD NANOPARTICLES FOR SERS SENSING.....	271
Abstract.....	272
12.1. Introduction.....	273
12.2. Experimental section.....	274
12.3. Results and discussion	276
12.3.1. Fabrication and patterning of Au nanoparticles and GNPs on the silicon substrate.....	276
12.3.2. SERS sensing on the patterned substrate	284
12.3.3. Evaluation of selectivity and enhancement factor	288
12.4. Conclusions.....	291

CHAPTER 13. GROWTH AND DECORATION OF SILICON NANOWIRES WITH GRAPHENE-ENCAPSULATED GOLD NANOPARTICLES FOR SURFACE-ENHANCED RAMAN SENSING	292
Abstract.....	293
13.1 Introduction.....	294
13.2 Experimental section.....	296
13.3 Results and discussion	299
13.3.1. Silane-based CVD growth of Si nanowires	299
13.3.2. Surface decoration of Si nanowire with Au nanoparticles and GNPs	307
13.3.3. SERS sensing on the Si nanowire-GNP heterostructures.....	312
13.3.4. Discrete Dipole Approximation modeling.....	313
13.4 Conclusions.....	316
PART IV	317
CHAPTER 14. CHEMICALLY MODIFIED AND DOPED CARBON NANOTUBE-BASED COMPOSITES WITH TUNABLE THERMAL CONDUCTIVITY GRADIENT.....	318
Abstract.....	319
14.1. Introduction.....	320
14.2. Experimental details.....	322
14.3. Results and discussion	327
14.3.1 Synthesis and surface modification of doped and un-doped MWCNTs.....	327
14.3.2 Thermal conductivity analysis for MWCNT films	333
14.3.3 Temperature distribution profiles for MWCNT films	341

14.3.4 MWCNT-polystyrene nanocomposites and their thermal behavior	345
14.4. Conclusions.....	353
CHAPTER 15. CONCLUSIONS AND FUTURE PROSPECTS	354
REFERENCES	359

LIST OF TABLES

2.1. Various experimental parameters designed for the plasma treatment of GNPs.	27
5.1. Impedance parameters of the blank Si electrode, Au nanoparticles, GNPs, and GNP-QD heterostructures obtained using the EEC (Fig. 4d). <i>Note: R_s, R_f, and R_t are the solution, film, and electron transfer resistances, respectively.</i>	116
7.1. Detailed experimental parameters for the optimization of Co_3O_4 nanowire growth on the cobalt substrate using the direct oxidation approach.....	151
7.2. Band gap of cobalt oxide nanostructures formed on the surface of cobalt foil. The samples were obtained at various experimental conditions as listed in Table 7.1. These band gap energies were based on the Tauc plot generated from the Uv-vis reflectance spectra for various Co_3O_4 nanostructure samples.	166
8.1. Equivalent Electrical Circuit (EEC) parameters obtained from simulation results as shown in the impedance spectra in Figure 8.6.	183
10.1. Experimental parameters showing the optimization and control of Silicon nanowire growth on gold-sputtering substrates	221
11.1. Detailed experimental parameters for the annealing of Si nanowire-Au nanoparticle heterostructures. <i>Note: Sample #2, #6 are the baseline samples (bold and italics) and were repeated in each set (shaded).</i>	248
12.1. Labeling of various samples in this study according to different galvanic deposition time for preparation of Au film.	277
13.1. Experimental parameters showing the optimization and control of Silicon nanowire growth on substrates prepared by galvanic deposition.....	301
14.1. Average diameters for pristine and acid- or plasma- treated MWCNTs and the corresponding sample #.....	324
14.2. Various nanocomposites prepared by stacking films of doped and/or un-doped MWCNTs (with/without acid/plasma treatment). These stacked MWCNTs layers were impregnated within polystyrene to result in various samples (#1 - #5).	326

LIST OF FIGURES

1.1. Graphene is a 2-D building material for carbon materials of all other dimensionalities. It can be wrapped up into 0-D buckyballs, rolled into 1-D nanotubes or stacked into 3-D graphite. Reproduced with permission. ⁴ copyright 2010 Nature Publishing Group.	3
1.2. (A-D) In-suit growth of graphene shells on the surface of Co (A), Co-Fe (B), Cu (C), and Au nanoparticles (D). Reproduced with permission from ref. 17. Copyright 2010, Royal Society of Chemistry. (E-G) In suit synthesis of SnO ₂ nanoparticles (E), non-covalent attachment of inorganic nanoparticles (F), and covalent bonding of Au nanoparticles on the surface of CNTs. (H) In-suit synthesis of Ag nanoparticle on graphene sheet. Reproduced from ref. 5 with copyright permission (Wiley).	6
1.3. (A) FET bio-sensor made from the CNTs heterostructures. (B) Graphene encapsulated Au nanoparticles sensor for the detection of cancer makers. (C-D) electron transfer principle and of energy level for the graphene/CdS quantum dots sensitized solar cell (QDSSC). (E) Graphene-metal oxide composites in the application of photocatalysis. Reprinted with permission from ref. 8. Copyright 2010, American Chemical Society.	7
1.4. (A-B) Surface plasmonic resonance of Au nanoparticles. (C-D) Silicon nanowires and their surface decoration with nanoparticles for SERS sensing. (E-H) Surface plasmonic resonance and morphology of GNPs for SERS sensing. Reprinted with permission from ref. 20. Copyright 2013 American Chemical Society.	11
1.5. (A) Application of CNTs as heat dissipater in CPU. (B-C) Atomic structure and morphology of N-doped CNTs. (D-F) Thermal conductivity measurement of graphene using the Raman based technique. Reprinted with permission from ref. 25. Copyright 2010 American Chemical Society.	14
1.6. Schematic showing the overview structure of proposed dissertation. The basic contents of this dissertation include materials fabrication, characterization, simulation and applications.	19
2.1. (a) Schematic showing the growth of graphene shell on gold nanoparticles. (b-d) TEM images and (e) FFT corresponding to (d) showing the as-produced graphene-encapsulated gold nanoparticles (GNPs).	30
2.2. (a-l) TEM images showing the influence of plasma treatment on the structure of GNPs: (a-d) duration of 5 s, 15 s, 60 s, and 90 s; (e-h) power of 30 W, 60 W, 90 W, and 120 W; (i-l) pressure of 200 mTorr, 250 mTorr, 400 mTorr, and 600 mTorr. (m) Schematic illustration of the GNP structure at various conditions. (n-p) Variation of graphene shell thickness according to treatment time (n), power (o), and pressure (p).	33

2.3. Raman spectra (a, c and e) and corresponding I_D/I_G (b, d and f) of GNPs before and after plasma treatment at (a,b) different time, (c,d) different power, and (e,f) different pressure.	34
2.4. (a) Variation of -COOH and -COH fraction in the graphene shells before and after plasma treatment at different duration (top), different power (middle), different oxygen pressure (bottom). (b-g) Deconvoluted XPS spectra of C 1s for various samples marked in Figure 2.4a.	36
2.5. Hydrophilicity test of GNP substrate before and after plasma treatment. (a) Blank silicon wafer, (b) as-produced GNP substrate, (c) plasma treated GNP substrate under the optimum conditions (time 15 s, power 120 W, and pressure 300 mTorr). (d) Schematic showing the principle of the interactions between water and the GNP substrates.....	38
2.6. Schematic showing the carbodiimide chemistry used for functionalizing extraneous gold nanoparticle and λ -DNA onto the plasma-treated GNPs.	39
2.7. (a-c) TEM images extraneous gold nanoparticles functionalized GNPs (GNP-Au nanoparticle heterostructures). Note: Inset in Figure 2.7a illustrates the structure of the heterostructures, and the arrows show the graphene shells after plasma oxidation. (d) HRTEM image showing the lattice and interface between GNPs and the extraneous gold nanoparticles.....	41
2.9. (a) Schematic for the GNP-Au nanoparticle heterostructures used for the plasmonic modeling. (b) Extinction spectra of (1) plasma-treated GNPs and (2) GNP-Au nanoparticle heterostructures. (c) Normalized electric field across the heterostructures in the incident direction. (d) Distribution of electromagnetic field near the surface of the plasma-treated GNPs (left, incident 518 nm) and the GNP-Au nanoparticle heterostructures (right, incident 540 nm).	44
2.10. (a) Schematic showing the Hind III technique for cleaving λ -DNA into fragments. (b) FTIR spectra of (1) as-produced GNPs, (2) plasma-treated GNPs, (3) covalently-linked GNP-DNA architectures, and (4) Pristine λ -DNA segments.	46
2.11. SEM images (a,b) and HRTEM images (c,d) of the covalently-linked GNP-DNA architectures. (e,f) AFM images of the GNP-DNA architectures before (e) and after (f) spin stretching with 1 mM $MgCl_2$	47
Scheme 3.1. Schematic representation of GNP-QD heterostructure fabrication on Si substrate.	58
3.1. SEM images for the as-produced and uniformly-patterned Au nanoparticles (a) and GNPs (b). The insets show high-resolution SEM images (scale bar: 25 nm). TEM images of the	

as-produced GNPs (c and d), GNPs after plasma treatment (e) and acid treatment (f). The insets show corresponding FFT images indicating diffraction of carbon and gold.60

3.2. (a) Raman spectra of the as-produced GNPs, GNPs after plasma, and GNPs after acid treatment. (b-d) Deconvoluted XPS spectra (C 1s) for as-produced GNPs (b) and GNPs after plasma treatment (c) and acid treatment (d). (e) Surface chemical groups (-COH, -COOH, and C-C) for GNPs before and after plasma/acid treatment estimated using C 1s peaks observed in XPS results. *NOTE: The scatters in (b-d) show the XPS results and the solid lines show the fitted data.*64

3.3. (a) Schematic of the GNP-QD heterostructures and the necessary amide bonds formed between GNPs and quantum dots. (b) FTIR spectra of (1) as-produced GNPs, (2) GNPs after plasma treatment, (3) GNPs after acid treatment, (4) GNP(plasma-treated)-QD heterostructures, and (5) GNP(acid-treated)-QD heterostructures. SEM images of the GNP-QD heterostructures fabricated using (c) plasma- and (d) acid- treated GNPs. (e) Control sample that used as-produced GNPs with no -COOH surface derivatization for physically binding with quantum dots. (d-f) Fluorescence images corresponding to samples (c-e).....68

3.4. (a, b) TEM images of the GNP-QD heterostructures formed on the plasma-treated GNPs. (c) FFT image corresponding to (b). (d and e) Representative STEM mode spot EDS analysis and (f and g) STEM mode EDS line profile analysis of the GNP-QD heterostructures. *Note: The dotted circles in (b) indicate quantum dots and the red spot and line in (e) and (g), respectively, shows the analysis spot and line for EDS profiling.*70

3.5. (a) UV-vis spectra for Au nanoparticles, as-produced GNPs, and GNPs after plasma and acid treatment. (b) UV-vis spectra of pristine quantum dots, GNP-QD heterostructures, and physically mixed GNPs and quantum dots. *Note: The insets showing digital images of (0) dispersed pristine quantum dots, (1) Au nanoparticles, (2) as-produced GNPs, (3) plasma-treated GNPs, (4) acid-treated GNPs, (5) physically mixed GNPs with quantum dots, and (6) GNP-QD heterostructures.*72

3.6. Targets: (a, e) Au nanoparticle, (b, f) GNP, (c, g) plasma-treated GNP, and (d, h) GNP-QD heterostructure. (i) Simulated extinction spectra for Au nanoparticles (1), GNPs (2), plasma-treated GNPs (3) and GNP-QD heterostructures (4). (j-m) Normalized electrical field distribution ($|E/E_0|$) near the surface of (j) Au nanoparticle (incident wavelength ~ 538 nm), (k) as-produced GNPs (shell thickness ~ 3.8 nm, incident wavelength ~ 562 nm), (l) plasma-treated GNPs (shell thickness ~ 0.8 nm, incident wavelength ~ 540 nm), and (m) GNP-QD heterostructure (incident wavelength ~ 543 nm). (n) $|E/E_0|$ vs. position along the center of the targets across the incident direction for target 1-4 in (i). *Note: Schematic in (i) shows the target and incident wavevector (k). Schematic in (n) shows ideal GNP-QD heterostructure and various positions plotted in (n)*.....76

3.7. (a) Tauc plots obtained from the UV-vis spectra (Figure 3.5b) indicating band gap energies and tailings for various samples. (b) I-V curves for various samples (all samples

were on the Si substrate). The inset DC image shows the digital image of the device. (c) Experimental photodegradation of phenol under UV irradiation (8 W lamp) in presence of sacrificial agent (H_2O_2) and different samples as photocatalyst. (d) First order fit of various phenol degradation processes indicated in (C). *Note: The legend in (d) is as shown in (c).*78

3.8. (a) Schematic of the GNP-QD heterostructures under illumination. (b) Excited electron transfer at the positive charge accumulated side of the heterostructures. (c) Derived band gap energy and relative band edge locations for GNP-QD heterostructures. *The electron transfer as well as degradation reaction under illumination are indicated by arrows.*81

4.1. (A-C) SEM images of GNPs with different size that were uniformly patterned onto silicon substrate. (D-F) TEM images of GNPs corresponding to (A-C). (G) Histogram showing the distribution of GNP diameter for various GNP samples. (H) Histogram of GNP diameters and inter-particle spacing for various GNP samples.91

4.2. TEM images of the GNP-QD heterostructures corresponding to (A) GNP_45, (B, D) GNP_90, and (C, E) GNP_120. *Note: (D) and (E) show the high resolution TEM for attached quantum dots on GNPs as shown in (B) and (C). The blue dotted lines indicate the regions observed at higher resolution.*.....93

4.3. UV-vis absorbance spectra for GNP samples (A) and corresponding GNP-QD heterostructures (B). (C) Tauc plots or $(ah\nu)^2$ vs. $h\nu$ plots used for the band gap energies estimation of the as-purchased quantum dots and GNP-QD heterostructures. (D) Fluorescence spectra of the as-purchased quantum dots and GNP-QD heterostructures.95

4.4. 3-D targets for various GNP samples (A-F) and GNP-QD heterostructure (G-K) samples developed by the 3ds Max software (A-C, G-I) and the LiteBil software (D-E, J-K). *Note: The LiteBil images were used for the chemical configuration identification. GNP samples (A-C) were named as Target#1-#3 and the GNP-QD samples (G-I) were named as Target #4-#6.*.....98

4.5. Simulated extinction spectra as a function of wavelength for the GNP targets (A-C: Target#1-#3) and the GNP-QD heterostructure targets (D-F: Target#4-#6) showing in Figure 4.4. *Note: These extinction spectra were further deconvoluted into absorbance and scattering spectra.*99

4.6. (A) Simulated extinction spectra of the GNP and GNP-QD targets. (B) Normalized electric field intensity (E/E_0) vs. positions along the center of the targets across the incident direction for the GNP and GNP-QD targets. (C-H) Normalized electric field distributions near/around the GNPs (C-E: Target#1-#3) and GNP-QD heterostructures (D-F: Target#4-#6).101

5.1. (a) SEM image of the Au film obtained through galvanic deposition on the Si substrate. (b) SEM image of the Au nanoparticles after annealing of Au film in (a). (c) SEM image of the as-produced GNPs. (d) SEM image of the GNP-QD heterostructures on the Si substrate. (e) HRTEM image of the as-produced GNPs. (f-h) Schematic and TEM/HRTEM images of the GNP-QD heterostructures.	109
5.2. Deconvoluted XPS spectra of C 1s (a), Au 4f (b), Cd 3d (c) and S 2p (d) obtained on the GNP-QD heterostructures decorated Si substrate.	110
5.3. I-V curves obtained on the as-received Si substrate, on the Au nanoparticles, as-produced GNPs, and GNP-QD heterostructures decorated Si electrode.	112
5.4. (a) Digital images of electrodes comprised of various samples: (1) blank Si substrate, (2) Au nanoparticles, (3) as-produced GNPs, (4) GNP-QD heterostructures. (b) CV diagrams and (c) EIS for Au nanoparticles, as-produced GNPs, and GNP-QD heterostructures. (d) EEC used for the simulation of EIS data in the ZSimpWin software. <i>NOTE: Scatters in (c) show the experimental data and the solid fitted lines correspond to simulated data.</i>	115
6.1. Schematic showing the preparation of multilayer graphene shells encapsulated gold nanoparticles (GNPs) and further plasma treatment for the covalent linking of single-walled carbon nanotube (SWCNT) by combining the EDC/NHS and biotin/streptavidin chemistry.	125
6.2. Schematic showing the principle of carbodiimide chemistry and biotin-streptavidin chemistry for the fabrication of the GNP-CNT heterostructures.	126
6.3. SEM images showing the as-produced Au nanoparticles (A), GNPs (B) and the GNP-CNT heterostructures (C and D). <i>NOTE: The insets in (A and B) show high-resolution SEM images (scale bar: 20 nm).</i> (E) Histogram showing the variation of particle diameter and inter-particle spacing of the Au nanoparticles, GNPs and GNP-CNT heterostructures.	127
6.4. (A, B) TEM/HRTEM images of the as-produced GNPs. (C) HRTEM image of the GNPs after plasma treatment. (D-F) TEM/HRTEM images of the GNP-CNT heterostructures. ...	128
6.5. (A-C) Fluorescence images obtained from (A) the pristine GNPs and (B, C) GNP-CNT heterostructures. (D) Raman spectra of the pristine GNPs, plasma-treated GNPs and GNP-CNT heterostructures. (E) FTIR spectra of the plasma-treated GNPs, SWCNT/streptavidin, and GNP-CNT heterostructures.	130
6.6. (A) 3-D image of the GNP-CNT heterostructures developed by 3ds Max software for DDSCAT-based plasmonic modeling. (B, C) Corresponding 3-D images developed by LiteBil software showing the chemical composition of the heterostructures. (D, E) 3-D	

images of the target composed of two GNP-CNT heterostructure with inter-particle spacing of 0 nm.	132
6.7. Simulated extinction, absorbance and scattering plots as a function of wavelength for a single GNP-CNT heterostructure target (A), Two GNP-CNT heterostructure target with inter-particle spacing of 0 nm (B), 5 nm (C) and 10 nm (D).	134
6.8. Normalized electric field distributions of a single GNP-CNT heterostructure target (A), Two GNP-CNT heterostructure target with inter-particle spacing of 0 nm (B), 5 nm (C) and 10 nm (D). The corresponding wavelength was 530 nm, 540 nm, 550 nm and 540 nm, respectively.....	135
6.9. (A) Simulated extinction of single GNP-CNT heterostructure target, Two GNP-CNT heterostructure target with inter-particle spacing of 0 nm, 5 nm and 10 nm. (B) Normalized electric field intensity (E/E_0) vs. position in the incident direction for the targets corresponding to (A).....	136
7.1. Scheme showing the set-up for growth of Co_3O_4 nanowires: (A) water vapor and air flowed simultaneously, (B) water vapor and air flowed separately.	145
7.2. (A, B) Thermodynamics calculation of Co oxidation reaction in the absence and presence of water vapor: (A) approach 1, (B) approach 2. (B) Schematic showing the growth mechanism of Co_3O_4 nanowires in the presence of water vapor and stress.....	147
7.3. SEM (A-B) and TEM (C-D) images showing the cobalt oxide nanostructures produced by the thermal oxidation of Co foil.	148
7.4. SEM image and EDS spectra showing the morphology and chemical content of Co_3O_4 nanowires (A-B), Co_3O_4 film (C-D) and CoO film (E-F). (G-H) EDS mapping showing the distribution of oxygen in the cobalt oxide film.	149
7.5. Influence of growth environment on the structure and density of Co_3O_4 nanowires (A-C) in air, (D-F) in water vapor, (G-I) in air and water vapor.	153
7.6. Influence of substrate treatment on the growth of Co_3O_4 nanowires (A-C) Polished, (D-F) Blended, (G-I) Scratched, (J-L) Penetrated, (M-O) Pressed with sand paper.	153
7.7. Influence of additives on the growth of Co_3O_4 nanostructures (A-C) KI, (D-F) NH_4F , (G-I) continuous water droplet.....	154
7.8. Sand blaster treated Co foils as substrate (A) 15 s, (B) 30 s, (C) 1 min, (D) 1.5 min, (D) 2 min.....	154

7.9. Sputtered Co film on Si wafer as substrate: (A) 5 nm, (B) 50 nm, (C) 100 nm, (D) 300 nm, (E) 500 nm.....	155
7.10. Co powder (300 mesh) as the growth substrate: (A-C) in air, (D-F) in water vapor, (G-I) in water vapor and air.	155
7.11. Influence of water vapor flow rate on the structure and density of Co ₃ O ₄ nanowires: (A-C) 6 ml/h, (D-F) 9 ml/h, (G-I) 12 ml/h, (J-L) 15 ml/h, (M-O) 18 ml/h.....	156
7.12. (A) Raman spectra of Co ₃ O ₄ nanowires obtained at different water vapor feeding rate; (B) XRD characterization of Co ₃ O ₄ nanowires (water vapor set). (C) UV-vis Absorbance spectra of Co ₃ O ₄ nanowires with different structures. (D) Band gap of Co ₃ O ₄ nanowires based on the UV-vis reflection spectra.....	157
7.13. Influence of the flow rate oxygen source on the structure and density of Co ₃ O ₄ nanowires: (A-C) air 0.1 SLM, (D-F) air 0.8 SLM, (G-I) air 1.2 SLM, (J-L) air 1.6 SLM, (M-O) 5% O ₂ /Ar 1.2 SLM.	158
7.14. (A) Raman spectra of Co ₃ O ₄ nanowires obtained at different oxygen source feeding rate; (B) XRD characterization of Co ₃ O ₄ nanowires. (C) UV-vis Absorbance spectra of Co ₃ O ₄ nanowires with different structures. (D) Band gap of Co ₃ O ₄ nanowires based on the UV-vis reflection spectra.....	159
7.15. Influence of temperature on the structure and density of Co ₃ O ₄ nanowires: (A-C) 375 °C, (D-F) 425 °C, (G-I) 475 °C, (J-L) 575 °C, (M-O) 625 °C, (P-R) 725 °C.	160
7.16. (A) Raman spectra of Co ₃ O ₄ nanowires obtained at different temperature; (B) XRD characterization of Co ₃ O ₄ nanowires. (C) UV-vis Absorbance spectra of Co ₃ O ₄ nanowires with different structures. (D) Band gap of Co ₃ O ₄ nanowires based on the UV-vis reflection spectra.	161
7.17. Influence of growth duration on the structure and density of Co ₃ O ₄ nanowires: (A-C) 10 min, (D-F) 30 min, (G-I) 1 h, (J-L) 5 h, (M-O) 20 h, (P-R) 30 h.....	162
7.18. (A) Raman spectra of Co ₃ O ₄ nanowires obtained at different growth time; (B) XRD characterization of Co ₃ O ₄ nanowires. (C) UV-vis Absorbance spectra of Co ₃ O ₄ nanowires with different structures. (D) Band gap of Co ₃ O ₄ nanowires based on the UV-vis reflection spectra.	163
7.19. TEM characterization of Co ₃ O ₄ nanowires obtained in air (A-C), nanorods (D-F), nanowires obtained in 5% O ₂ /Ar (G-I) and nanowalls (J-L).....	165

7.20. Influence of growth parameter on the density of nanowires: (A) water feeding rate, (B) oxygen source flow rate, (C) temperature, (D) growth duration.....	167
7.21. Influence of growth parameter on the length and diameter of nanowires: (A) water feeding rate, (B) oxygen source flow rate, (C) temperature, (D) growth duration.....	168
7.22. Influence of growth parameter on the thickness of under layer CoO and Co ₃ O ₄ film: (A) water feeding rate, (B) oxygen source flow rate, (C) temperature, (D) growth duration.....	169
7.23. Schematic showing the influence of growth conditions on the structure of cobalt oxide nanowires.....	170
8.1. SEM images of (A) standing CuO nanowires and (B) CuO nanowire-Co ₃ O ₄ nanoparticle heterostructures grown on the copper foil. TEM images of (C and D) CuO nanowires and (E and F) CuO nanowire-Co ₃ O ₄ nanoparticle heterostructures. <i>Note: Insets in (D) and (F) show the corresponding FFT images with indexed diffraction spots. Dotted circles in (F) indicate Co₃O₄ nanoparticles on CuO nanowire.</i>	179
8.2. XRD patterns of the CuO nanowires (1) and CuO nanowire-Co ₃ O ₄ nanoparticle heterostructures (2) and corresponding indexing of planes.....	180
8.3. CV diagram of the CuO electrode and CuO-Co ₃ O ₄ electrode obtained in 1.0 mM Fe(CN) ₆ ^{3-/4-} and 0.1 M KCl aqueous solution.	181
8.4. Peak current vs. scanning rate for the determination of effective surface area of the (A) CuO electrode and (B) CuO-Co ₃ O ₄ electrode.....	182
8.5. (A) EIS spectra of the CuO-Co ₃ O ₄ electrode and corresponding impedance contributing regions. (B) Equivalent electric circuit (EEC) for impedance spectra shown in (A).	184
8.6. Experimental and simulated impedance spectra of (A) CuO electrode and (B) CuO-Co ₃ O ₄ electrode.	184
8.7. CVs for the CuO electrode and CuO-Co ₃ O ₄ electrode obtained in 1 M KOH aqueous solution.	185
8.8. Tafel plots for oxygen evolution reaction for (A) CuO electrode and (B) CuO-Co ₃ O ₄ electrode. The polarization was conducted in 1 M KOH aqueous solution.	186
9.1. (A, B) SEM images showing the cross-section and top view of the pristine Co ₃ O ₄ nanowires produced by water vapor-assisted thermal oxidation. (C) Top view of the as-sputtered Co ₃ O ₄ -WO ₃ nanowire heterostructures. (D-G) TEM/HRTEM images showing	

the structure and lattice of the Co_3O_4 nanowires (D and E) and the as-sputtered Co_3O_4 - WO_3 nanowire heterostructures (F and G).....	199
9.2. (A) SEM images of the annealed Co_3O_4 - WO_3 nanowire heterostructures. (B-E) TEM/HRTEM images showing the structure and lattice of the annealed heterostructures. (F) FFT image generated from E. (G and H) STEM images of the Co_3O_4 - WO_3 nanowire heterostructures before (G) and after (H) annealing. (I, J) EDS line profiles cross the nanowire heterostructures corresponding to G and H, respectively.....	200
9.3. (A) XRD patterns of the Co_3O_4 nanowires, Co_3O_4 - WO_3 nanowire heterostructures before and after annealing. (B) Detailed XRD spectra for the typical (311) peak of Co_3O_4 in (A). (C) Raman spectra of the Co_3O_4 nanowires, Co_3O_4 - WO_3 nanowire heterostructures before and after annealing. (D, E) Detailed Raman spectra for (D) the E_g band of Co_3O_4 and (E) representative $\nu(\text{O}-\text{W}^{6+}-\text{O})$ band of WO_3 in (C). <i>Note: The as-produced Co_3O_4 nanowires were referred as (CNs), the as-sputtered Co_3O_4-WO_3 nanowire heterostructures are referred as (CWNHs) and the annealed nanowire heterostructures were referred as (ACWNHs) as shown in Figure 9.3C.</i>	202
9.4. Deconvoluted XPS spectra corresponding to Co 2p (A, C and E) and W 4f (B, D and F) of the Co_3O_4 nanowires (A, B), Co_3O_4 - WO_3 nanowire heterostructures before (C, D) and after (E, F) annealing.....	205
9.5. (A) Tura plots based on the UV-vis reflectance spectra showing the band gap of the Co_3O_4 nanowires (CNs) and the annealed Co_3O_4 - WO_3 nanowire heterostructures (ACWNHs). (B) Photocatalytic degradation of phenol with various nanostructures under UV or visible light. (C) Kinetics study for the photodegradation of phenol. (4) Schematic illustration of band gap energies of the annealed Co_3O_4 - WO_3 nanowire heterostructures and possible charge transfer and separation mechanism.....	207
Scheme 10.1. Schematic showing the growth of silicon nanowires and synthesis of silicon nanowire-gold heterostructures for SERS detection	220
10.1. SEM showing the as-sputtered gold film (A) and dewetted gold nanoparticle catalysts after annealing (B).....	222
10.2. Silicon nanowire arrays grown on the gold-sputtered substrate by contralling different feeding rate of SiH_4 : (A) 10 sccm (Sample#1A); (B-C) 20 sccm (Sample#2A); (D-E) 30 sccm (Sample#3A). (F) Schematic showing the growth process of SNWA on gold-sputtering substrate. (G-J) TEM demonstration of as-grown SNWA corresponding to (D-E). (Baseline conditions: growth temperature 625 °C; carrier gas: 100 sccm 5% H_2/Ar ; growth duration: 1 min; gold sputtering 60 s.).....	225
10.3. Silicon nanowires with high aspect ratio grown on the gold-sputtered substrate by controlling different grow time: (A-B) 2 min (Sample#4A); (C) 5 min (Sample#5A); (D-	

E) 10 min (Sample#6A); (F) Schematic showing the growth of long-aspect ratio Si NWs from nanowire arrays; (G-J) TEM demonstration of as-grown SNWA corresponding to (D). (Baseline conditions: growth temperature 625 °C; carrier gas: 100 sccm 5% H ₂ /Ar; flow rate: 20 sccm; sputtering time: 60 s.)	226
10.4. Branched silicon nanowires obtained at different growth temperature: (A-B) 675°C (Sample#7A); (C-D) 725 °C (Sample#8A); (E) Schematic showing the influence of growth temperature on the structure of silicon nanowires. (Baseline conditions: carrier gas: 100 sccm 5% H ₂ /Ar; flow rate: 20 sccm; grow time: 2 min; grow time 60 s.).....	228
10.5. Influence of gold sputtering time on the configuration of silicon nanowires and their ability in Raman enhancement: (A) 15 s (Sample#9A); (B) 30 s (Sample#10A); (C) 45 s (Sample#11A); (D) Schematic showing the influence of growth temperature on the structure of silicon nanowires. (Baseline conditions: growth temperature 625 °C; carrier gas: 100 sccm 5% H ₂ /Ar; flow rate: 20 sccm; grow time: 2 min.).....	229
10.6. Influence of growth conditions on the diameter of silicon nanowires: (A) flow rate set, (B) grow time set, (C) sputtering time set, (D) temperature set.....	230
10.7. Galvanic deposition of gold film on preferred silicon nanowires selected from each set: (A) Sample#4A, (B) Sample#8A, (C) Sample#11A. (D) Schematic showing the galvanic deposition of gold shell on silicon nanowires.	231
10.8. Si NWs-Au NPs heterostructures obtained by annealing above Si-Au core-shell nanowires (Sample#11A) at different temperatures: (A) 700 °C (Sample#11a), (B-D) 625 °C (Sample#11b); (C) 500 °C (Sample#11c), and at different environments: (A-C) in Ar, (D) in air (Sample#11d). (E) Schematic showing the influence of annealing on the structure of heterostructures.	232
10.9. TEM images of Si NW-Au heterostructures after (A-C) galvanic deposition (sample#11B) and further annealing in (D-F) Ar and (G-I) air environment, respectively.	233
10.11. (A) Schematic showing the Surface Enhanced Raman Scattering (SERS) effect of pristine Si NW arrays. (B-E) Raman spectra of R6G obtained on silicon nanowires grown at different conditions: (A) flow rate set, (B) grow time set, (C) temperature set, and (D) gold sputtering time set. (<i>Note: Spectra (1-11) in B-E corresponds to the sample # in Table 10.1.</i>).....	237
10.12. (A) Schematic showing the Surface Enhanced Raman Scattering (SERS) effect of Si NWs-Au NPs heterostructures. (B-C) Raman spectra of R6G obtained on Si-Au core-shell nanowires (B) and Si NWs-Au NPs heterostructures. (<i>Note: Spectra (A'~C') in B correspond to samples in Figure. 6, and spectra (A~D) in C correspond to samples in Figure. 7.</i>).....	238

10.13. Raman mapping on Si NW array and Si nanowire-Au NPs heterostructures: (A) Optical images showing the Raman measurement, (B-C) distribution of Raman signal of R6G at 1360 cm ⁻¹ for (B) Si nanowire arrays (Sample#11A) and (C) Si nanowire-Au nanoparticle heterostructures(Sample#11C).	239
10.14. Detection limit of (A) pristine nanowire and (B) nanowire-gold nanoparticle heterostructures; (C) Variation of Raman peak (at 1360 cm ⁻¹) intensity according to the concentration of target R6G solution.	240
11.1. Schematic representation of the process for fabricating Si nanowire-Au nanoparticle heterostructures and their application for SERS sensing. (1) CVD growth of Si nanowires, (2) direct and wet-chemical nucleation of Au nanoparticles on Si nanowires, (3) dispersion of the heterostructures on substrate, (4) thermal annealing, and (5) SERS-based organic dye detection.	249
11.2. (A and B) SEM images of the as-produced Si nanowires. (C) The diameter distribution (~172.44 ± 90 nm) of Si nanowires. (D) TEM image of the as-produced Si nanowires. (E) HRTEM image indicating the lattice structure of the Si nanowire (marked as “1” in D). (F) HRTEM image indicating the lattice structure of the Au nanoparticle (catalyst/seed) at the tip of the Si nanowire (marked as “2” in D). <i>Note: The inset in (F) show the corresponding FFT image for diffraction spots for silicon and gold.</i>	251
11.3. (A-C) TEM images of the as-produced Si nanowire-Au nanoparticle heterostructures (before annealing). (D) XRD spectra of the as-produced Si nanowires and the Si nanowire-Au nanoparticle heterostructures before annealing. (E) Size and inter-particle spacing of the Au nanoparticle on Si nanowires.	252
11.4. TEM images and lattice structure of the Si nanowire-Au nanoparticle heterostructures after annealing for (A, E) 15 min, (B, F) 45 min, (C, G) 75 min, and (D, H) 120 min. (I) Average diameter and inter-particle spacing of Au nanoparticles on Si nanowires after annealing for different durations. Contour graphs showing the distribution of Au nanoparticle (J) diameter and (K) spatial density as a function of the Si nanowire diameter and the annealing duration.	255
11.5. TEM images and lattice structure of the Si nanowire-Au nanoparticle heterostructures after annealing at (A, E) 300 °C, (B, F) 500 °C, (C, G) 700 °C, and (D, H) 800 °C. (I) Average diameter and inter-particle spacing of Au nanoparticles on Si nanowires after annealing for different temperatures. Contour graphs showing the distribution of Au nanoparticle (J) diameter and (K) spatial density as a function of Si nanowire diameter and the annealing temperature. <i>Note: Baseline annealing conditions were 45 min duration and in Ar environment.</i>	257
11.6. TEM images and lattice structure of the Si nanowire-Au nanoparticle heterostructures after annealing in various environments including (A, E) 5%O ₂ /Ar, (B, F) 10%H ₂ /Ar, (C,	

G) N ₂ , and (D, H) vacuum. (I) Average diameter and inter-particle spacing of Au nanoparticles on Si nanowires after annealing for different environments. Contour graphs showing the distribution of Au nanoparticle (J) diameter and (K) spatial density as a function of Si nanowire diameter and the annealing environment.....	259
12.1. (a) Schematic showing the procedures for the fabrication of assembly of multilayer graphene shells encapsulated on gold (Au) nanoparticles for Surface-enhanced Raman Spectroscopy (SERS): (1) galvanic deposition, (2) annealing, (3) chemical vapor deposition (CVD) of multilayer graphene shells, (4) oxygen plasma treatment. (b-d) Schematic showing the basic principle of (b) galvanic deposition, (c) CVD, (d) molecule detection using SERS.	277
12.2. SEM images of Au film prepared by galvanic deposition at various deposition times: (A) 0.5 min, (B) 1 min, (C) 3 min, (D) 5 min, and (E) 7 min.	278
12.3. (A) XRD patterns for the as-deposited Au films corresponding to Figure 12.2. (B) Au film thickness calculated according the density and size of Au nanoparticle in Figure 12.4.....	279
12.4. SEM images of Au nanoparticles obtained by annealing various Au films corresponding to 12.1: (A) 0.5 min, (B) 1 min, (C) 3 min, (D) 5 min, (E) 7 min. SEM images of multilayer graphene shells encapsulated Au nanoparticles (GNPs) with different size corresponding to Figure 12.3: (F) 0.5 min, (G) 1 min, (H) 3 min, (I) 5 min, (J) 7 min. <i>Note: The insets in (B) and (E) show the representative SEM images for a single GNP (inset scale bar: 20 nm).</i>	281
12.5. TEM images of the as-produced (A-E) GNPs and (F-J) plasma-treated GNPs. These samples are corresponding to various galvanic deposition time: (A,F) 0.5 min, (B,G) 1 min, (C,H) 3 min, (D,I) 5 min, (E,J) 7 min.	282
12.6. (A-C) Variation of particle size (A), inter-particle spacing (B), and particle density (C) for the Au nanoparticles and GNPs according to the galvanic deposition time. (D) Variation of thickness of the multilayer graphene shells before and after oxygen plasma treatment.....	284
12.7. (A, B) SERS spectra of R6G (A) and MB (B) on the Au nanoparticle samples corresponding to various galvanic deposition time. (C, D) SERS spectra of R6G (C) and MB (D) on the GNP samples corresponding to various galvanic deposition time. (E) Average Raman intensity of R6G and MB corresponding to A and B. (F) Average Raman intensity of R6G and MB corresponding to C and D. <i>Note: The peak locations (cm⁻¹) were mark on the top of these spectra. The Raman intensity of R6G was estimated to the peak centered at ~1360 cm⁻¹ and that of MB was estimated using the peak centered at 1390 cm⁻¹.</i>	286

12.8. (A,B) SERS spectra of MB. These spectra correspond to the Au nanoparticle (A) and GNP (B) samples immersed in MB solution with various concentration. The peak locations (cm^{-1}) were mark on the top of these spectra. (C) Average Raman intensity MB corresponding to A and B. <i>Note: The Raman intensity of MB was estimated using the peak centered at 1390 cm^{-1}.</i>	287
12.9. (A) SERS spectra of MB and R6G obtained on Au nanoparticles and GNPs immersed in a mixture of 10^{-6} M R6G and 10^{-6} M MB. (B) Average Raman intensity MB and R6G corresponding to A. The inset further shows the intensity ration of MB and R6G.....	288
12.10. (A) Digital image showing (1) pristine MB solution (10^{-6} M), (2) MB solution after immerse Au nanoparticle sample (B3) for 10 h, and (3) MB solution after immerse GNPs sample (D3) for 10 h. (B) UV-vis spectra of MB solution corresponding to (A). (C) Representative Raman spectra of 10^{-6} M MB in DI-water. (D) Calculated enhancement factor for Au nanoparticles (B3) and GNPs (D3).....	290
13.1. Schematic showing the galvanic deposition of gold film on Si substrate and CVD growth of silicon nanowires.....	300
13.2. Au film and corresponding Au nanoparticles prepared by galvanic deposition under different times: (A, F) 0.5 min, (B, G) 1 min, (C, H) 3 min, (D, I) 5 min, (E, J) 7 min. (K) XRD pattern of Au films. (L-M) Variation of particle size according to the galvanic deposition time.	302
13.3. (A-C) SEM images showing the Si nanostructures obtained on different Au nanoparticles catalysts. (D-F) HRTEM images showing the morphology of gold tip (E) and branches (F). (G) Schematic showing the CVD products obtained on different substrates.	303
13.4. (A-B) Silicon nanowire arrays obtained at different temperatures: (A) $675 \text{ }^\circ\text{C}$, (B) $775 \text{ }^\circ\text{C}$. (C-E) TEM image corresponding to (A). (F) Schematic showing the structure of Si nanowires obtained at different temperature.	304
13.5. (A-C) Silicon nanowires obtained at different growth times: (A) 1 min, (B) 15 min, (C) 60 min. (D-E) HRTEM image showing the gold tip-silicon nanowire-silica shell interface and branch structure. (I) Schematic showing the Si nanowires obtained at different growth times.	306
13.6. (A-C) Silicon nanowires obtained at different SiH_4 flow rates: (A) 20 sccm, (B) 40 sccm, (C) 50 sccm. (D) TEM image corresponding to (A). (E) TEM image corresponding to (B). (I-J) HRTEM and FET image showing the silicon branch structure. (K) Schematic showing the Si nanowires obtained at different SiH_4 feed rates.	307

13.7. (A) Schematic showing the surface decoration of Si nanowires with Au nanoparticles and GNPs. (B) Representative low-resolution SEM image of the Si nanowire based heterostructure substrate for SERS sensing. (C) Schematic showing the SERS sensing on the molecule attached Si nanowire-GNP heterostructures.	308
13.8. (A-C) Si nanowire-Au core-shell structures obtained by galvanic deposition of gold film on silicon nanowires: (A) sample 6B, (B-C) sample 13B. (D-F) Si nanowire-Au nanoparticle heterostructures obtained by annealing the core-shell structure: (D) sample 6C and (E-F) sample 13C. (G) Representative TEM image corresponding to (A). (H-I) HRTEM and FET images corresponding to (G). (J) Representative TEM image corresponding to (D). (K-L) HRTEM and FET images corresponding to (J). (<i>Note: Galvanic deposition solution: 1mM KAuCl₄ + 1% HF, deposition time: 2 min, temperature: 25 °C, annealing temperature: 625 °C, time: 10 min, environment: air.</i>).....	310
13.9. Growth of graphene on the gold nanoparticles decorated on the silicon nanowires: (A-D) TEM/HRTEM images of the Si nanowire-GNP heterostructures. (E-F) Raman spectra obtained on the as-produced Si nanowires and the Si nanowire-GNP heterostructures.	311
13.10. (A) Raman spectra of R6G (1×10^{-6} M) obtained on different substrates: (a) Annealed Au nanoparticle catalysts, (b) pristine Si nanowire arrays (Sample 6A), (c-d) Si nanowire-Au nanoparticle heterostructures (sample 6C, 11C). (B) Raman spectra obtain on the Si nanowire-GNP heterostructure with or without R6G.....	312
13.11. Schematics showing (A) two directions of incident lights (X: radial to nanowire, Y: axial to nanowire), (B) Si nanowire, (C) Si nanowire-Au nanoparticles, (D) a section of Si nanowire-Au nanoparticles, (E) a section of Si nanowire coated with GNPs (shell ~2 nm thickness), (F) and (G) comparison of extinction spectra for two directions for k vectors (X and Y) and peak locations.	314
13.12. Distribution of normalized electric field in X direction for (A) Si nanowire, (B) Si nanowire-Au nanoparticles, (C) a section of (B), (D) Si nanowire-GNP heterostructures and in Y direction for (E) Si nanowire, (F) Si nanowire-Au nanoparticles, (G) a section of (F), (H) Si nanowire-GNP heterostructures.	315
14.1. (A-C) SEM images showing the morphology and dispersion of pristine MWCNT films (sample #a1, #b1, #c1) comprised of (A) un-doped MWCNTs, (B) 2.6%N-MWCNTs, and (C) 5%N-MWCNTs. (D) A representative SEM image of the cross-section of drop-casted MWCNT film (pristine and un-doped) on the oxidized Si wafer. <i>Note: The sample # are detailed in Table 14.1</i>	329
14.2. TEM images of the un-doped and N-doped MWCNTs before and after acid or plasma treatment. (A-D) Un-doped MWCNTs, (E-H) 2.6%N-MWCNTs, and (I-L) 5%N-MWCNTs. <i>Note: Insets show the lattice or inter-wall spacing for MWCNTs. The dotted rings indicate the defects and stress marks while arrows indicate amorphous carbon.</i>	330

14.3. Surface groups on the MWCNTs and their percentage (mol%). (A) -COOH and (B) N-containing groups on the MWCNTs before and after acid or plasma treatments. <i>Note: The sample # and the corresponding treatments are detailed in Table 14.1.</i>	332
14.4. (A) Raman spectra of pristine un-doped and doped MWCNTs (sample #a1, b1, c1). (B) Digital image and (C) schematic representation of the sample-heater geometry for the thermal conductivity measurement. (D) Histogram showing the thermal conductivities for un-doped and N-doped MWCNTs before and after acid or plasma treatment.....	336
14.5. Theoretical estimation of temperature distribution profiles for the MWCNT films (sample #a1). (A) Representative profile for the pristine and un-doped MWCNT film as a function of Q. (B) Detailed thermal map for the pristine and un-doped MWCNT film at 1 mW and (C) corresponding to different Q.	343
14.6. (A) Calculated peak temperatures at the center of Raman laser spot on the MWCNT films corresponding to laser power of 1 mW and 10 mW. (B-E) SEM images of 2.6%N-MWCNT film (sample #b1) after exposure to Raman laser with Q fixed at (B, C) 25 mW and (D, E) 50 mW.	344
14.7. (A) Schematic of stacked multi-layered MWCNT films impregnated within polystyrene matrix (sample details in Table 14.2). (B) Digital image and (C, D) SEM image of a nanocomposite (sample #1). (E) Hot wire measurement set-up for nanocomposites showing the MWCNT film thickness (y -axis, F) and thermocouple locations (x -axis, F). Hot wire is located at $x = 0$ and $y = 0$. (G-K) Temperature distribution profiles on the top and bottom surface of the multi-layer nanocomposites (sample #1-#5, Table 14.2).	351
14.8. Temperature distribution profiles or thermal maps for various nanocomposites (sample #1-#5, Table 14.2). (A) Sample #1, (B) Sample #2, (C) Sample #3, (D) Sample #4, and (E) Sample #5. <i>Note: Color bar unit: °C and each figure shows expanded temperature distribution profile for distances less than 2.1 mm.</i>	352

CHAPTER 1

INTRODUCTION

Materials in nanoscale have been intensively studied in the past 20 years due to its superior intrinsic properties such as surface effect, small-size effect, quantum effect and macro quantum tunnel effect. The possible application of nanomaterials were considered to extend to energy conversion/storage, catalysis, chemical sensor, bio-science and so on.^{1,2} According to the difference in structure and morphology, nanomaterials can be basically divided into zero dimension (nanoparticles, quantum dots, etc.), one dimension (nanowires, nanotubes, etc.), two dimensions (nano-film/sheet, etc.), and three dimensions (nano-trees/flowers, .etc). So far the studies were mainly focused on the exploration of synthesis approaches and properties characterization. The further refinements on their stability, low production cost, large-scale yield and industrial feasibility are still the major challenge. Heterostructures by combining two or more materials exhibit complementary and collaborative features as compared with individual material, and thus provide a large opportunity to improve the stability, lower the production cost and increase the application feasibility. Here we present a comprehensive introduction on the studies and progress on the nanoscale heterostructures composed of gold nanoparticles (Au nanoparticles), silicon nanowires (Si nanowires), and graphene/carbon nanotubes (CNTs) in chemical sensing, energy conversion, and thermal management.

1.1. Complex carbon nanoscale architecture

1.1.1. Basic carbon nanostructures

Carbon nanostructures such as graphene, CNTs, fullerene and so on have drawn intensive attentions recent years.³ An ideal graphene is a monatomic layer/sheet of carbon atoms arranged on a honeycomb lattice through sp^2 bonding. Therefore, graphene is a perfect two-dimensional (2D) material. However, such ideal two-dimensional crystals at free-state are unstable at finite temperature. As a result, a perfect graphene is tending to evolve into other types of structures with enhanced stability, such as fullerene, CNTs, and graphite (Figure 1.1). Graphite is formed through layering of a large number of graphene layers via van der Waals force, and therefore, from physics point of view, it falls into the category of three-dimensional (3D) systems. Under appropriate conditions, a single-layer graphene (SLG) or multiple layer graphene (MLG) can also roll up along certain directions to form tubular structure – CNTs. The CNTs, which can be in the form of single-walled, double-walled, and multiple-walled structures, are considered as one-dimensional (1D) objects. With the introduction of pentagons, the graphene can also be wrapped up to form zero-dimensional (0D) fullerenes. Although ideal graphene is unstable, it may become stable through the introduction of local curvatures or support formed by foreign materials. Macroscopic SLG was successfully isolated from graphite through mechanical exfoliation in 2004, which was found to be stable on a foreign substrate, highly crystalline, and chemically inert under ambient conditions, albeit with local roughness and ripples.⁴

Several potential applications for these carbon nanostructures are under development, and many more have been proposed. These include lightweight, thin, flexible, yet durable display screens, electric circuits, and solar cells, as well as various medical, chemical and industrial processes enhanced or enabled by the use of new graphene materials, of which the most interesting approach

is to hybridize these nanostructures with nanoparticles, nanowires for the fabrication of high-performance nanoscale heterostructures.

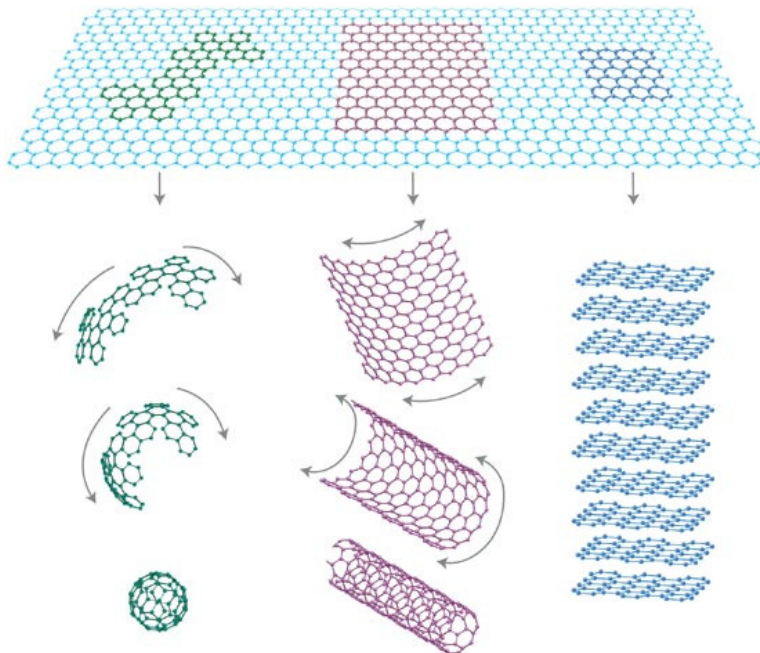


Figure 1.1. Graphene is a 2-D building material for carbon materials of all other dimensionalities. It can be wrapped up into 0-D buckyballs, rolled into 1-D nanotubes or stacked into 3-D graphite. Reproduced with permission from Ref 4, copyright 2010 Nature Publishing Group.

1.1.2. Hybridization of carbon nanostructures

The major challenge in making these hybrid architectures is to control the fraction, formalization, and precise spatial positioning of the foreign hybridizing nanostructures on the supporting materials since the strong distance dependence of charge separation and energy transfer between the electron donors and acceptors. As summarized in Figure 2, strategies for combination include either covalent⁵ (formation of discrete chemical bonds) or non-covalent⁶ (physical absorption) methods. Moreover, in situ synthesis such as chemical reduction, electrostatic-force-directed assembly, and electrodeposition have been proposed to prepare the carbon-based nanoscale

conjugates. Two approaches for the in-suit synthesis strategy can be summarized. On one hand, the carbon nanostructures were first dispersed in synthesis solution, nanocrystals such as nanoparticles, quantum dots will attached on carbon surface through a heterogeneous nucleation process during. The key disadvantage of the in suit synthesis of QDs on the surface of these nanostructures is the difficulty in defining and controlling the spatial coverage and distribution of nanocrystals. On the other hand, complex architectures were synthesized by directly growth of carbon structures on foreign nanostructures. A representative example in CVD growth of graphene shells on the surface of Au, Ni, Cu nanoparticles. These metal-carbon composite present novel advantages such as improved chemical stability, largely expanded surface functionalization ability with the maintenance of the electric and optical properties of these nanostructures. The heterostructures based on the non-covalent reaction (e.g. π - π stacking) is attractive in that it can preserve the intrinsic properties of carbon materials. However, the associated presence of polymer shell will largely shield even distort the inherent properties of carbon materials or diminish the effective charge transfer between carbon and hybridizing materials. As a result, covalent strategies have become the most preferable and promising approach in synthesizing such complex heterostructures. The basic advantages of this approach are as follows: (I) the shape and size of hybridizing can be tailored by the sophisticated synthesis before connect to the nanostructures, (II) reliable and robust chemical bonds formed between the carbon and hybridizing nanostructures, which can even stand for sonication or extensive washing, (III) the spatial coverage and exact positions of extraneous materials can be precisely controlled by the specific functionalities on the surface of nanostructures.

1.2. Potential applications of hybridized carbon nanostructures

As mentioned above, based on the nature of nanocrystals, there are basically three type of carbon nanostructure hybrid systems, including carbon-metal nanoparticles, carbon-QDs, and carbon-metal oxide nanoparticles. In the best possible case, therefore, conjugation of these nanocrystals with carbon template will uniquely combine properties of both components in one systems and thus gift the heterostructures with significantly enhanced optoelectronic, mechanical, optical, thermal and chemical properties. The potential here is that one can create a tailorable, nanoscale heterostructure with novel and potentially unforeseen properties. So far these complex carbon architectures have been involved in the application of chemical sensors, solar energy conversion/storage, bio-electronics, photocatalysis and so on Potential applications of these carbon hybrids was summarized in Figure 1.3.

1.2.1. Chemical sensing

Chemical sensing typically relies on strong interactions between a sensor material and its target molecules. Adsorption interactions generally result in a degree of charge transfer between molecules and the interacting carbon materials, causing a dramatic change in conductivity that can be subsequently detected.⁷ Hence, electron donating and withdrawing molecules will either transfer electrons to or attract electrons from SWNTs, thereby providing for either additional charge carriers or holes that are reflected in their measured conductance. However, not all molecules (such as methane with its poor electron accepting/donating properties), that are nevertheless of high interest to environmental monitoring, industrial chemical processes, as well as agricultural and biomedical applications, can be probed in such a manner. In this regard, chemical decoration of SWNTs with metal nanoparticle has often been an important route forward

towards resolving this issue and enhancing detection. In fact, theory predicts that CNTs-Al system, for instance, facilitate the adsorption of both ammonia and CO, and that Ru-decorated SWNTs enhance the detection of CO.⁸

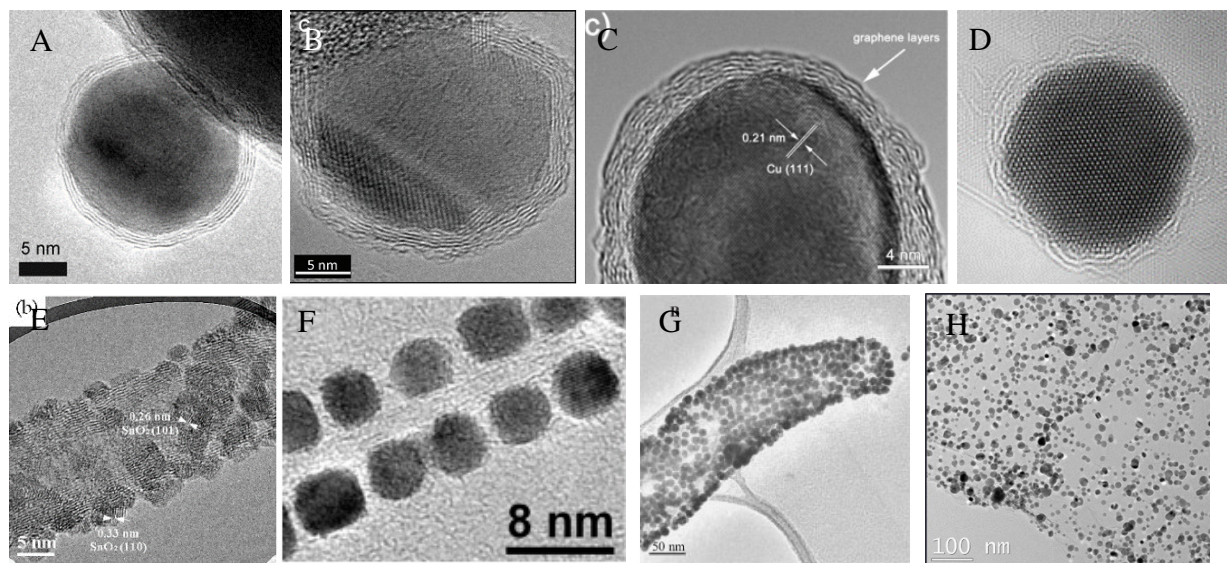


Figure 1.2. (A-D) In-suit growth of graphene shells on the surface of Co (A), Co-Fe (B), Cu (C), and Au nanoparticles (D). Reproduced with permission from ref. 17. Copyright 2010, Royal Society of Chemistry. (E-G) In suit synthesis of SnO₂ nanoparticles (E), non-covalent attachment of inorganic nanoparticles (F), and covalent bonding of Au nanoparticles on the surface of CNTs. (H) In-suit synthesis of Ag nanoparticle on graphene sheet. Reproduced from ref. 5 with copyright permission (Wiley).

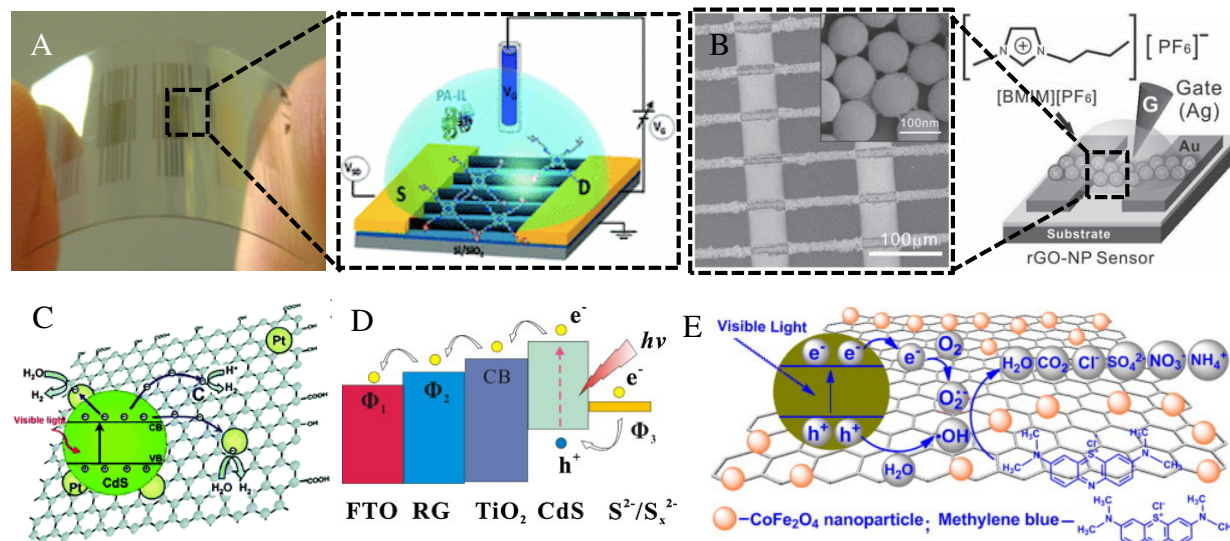


Figure 1.3. (A) FET bio-sensor made from the CNTs heterostructures. (B) Graphene encapsulated Au nanoparticles sensor for the detection of cancer makers. (C-D) electron transfer principle and of energy level for the graphene/CdS quantum dots sensitized solar cell (QDSSC). (E) Graphene-metal oxide composites in the application of photocatalysis. Reprinted with permission from ref. 8. Copyright 2010, American Chemical Society.

1.2.2. Solar energy harvesting

Quantum dots with size-dependent tunable absorption properties enable in principle to design a carbon nanostructures-QDs system to match the absorption spectrum to the solar spectrum. Moreover, an intriguing recent discovery is that of multiple exciton generation in QDs which effectively converts a photon into more than one electron-hole pair allowing for more efficient use of solar energy and a potential for quantum efficiencies greater than 100%. At the same time, carbon nanostructures can act as an efficient electron acceptor over relatively large distances, That is, in these complex systems, the charge collection efficiency might be enhanced due to enhanced charge transport. In general though, one individual nanoscale component will have some but not all of the desired properties needed for enhanced overall solar energy utilization. For example, while QDs can lead to higher quantum efficiency, an isolated dot must have the excitations

removed and charges separated to be useful. Hence, there has been a strong interest in developing hybrids of CNTs and semiconducting QDs in recent years.

1.2.3. Bio-chemical applications

Approaches to the functionalization of carbon nanostructures with biomolecules on their external surface have been reported for potential bio-applications such as drug delivery. For instance, CNTs, graphene that non-covalently bound to proteins or genes mediated by phospholipids were internalized into cells through endocytosis. These carbon materials can also be covalently functionalized with small molecules linked to the carboxylic sites localized at their ends, defect sites, or sidewalls. Thus, amine-terminated molecules can be effectively transported into different types of living cells *via* appropriately functionalized carbon nanostructures. Nonetheless, in order to track such conjugates in a living system, a fluorescent is commonly used as a tagging label. However, the disadvantage of this approach is the low quantum yield and short lifetime of dye molecules upon interaction with these species. For this reason, quantum dots have often been used to replace organic dyes and to visualize various molecules in bio-systems both under *in vitro* and *in vivo* conditions. Not surprisingly, QDs⁹ and iron oxide nanoparticles¹⁰ have recently been attached to CNT/graphene to form bio-imaging agents that can then be readily visualized using fluorescence microscopy or magnetic resonance/near IR fluorescence techniques.

1.3. Nanoscale heterostructures for SERS

1.3.1. Surface-enhanced Raman Spectroscopy (SERS)

Surface-enhanced Raman Spectroscopy (SERS) is a Raman Spectroscopic technique that provides greatly enhanced Raman signal from Raman-active analyte molecules that have been adsorbed onto certain specially prepared metal surfaces. Increases in the intensity of Raman signal have been regularly observed on the order of 10^4 - 10^6 , and can be as high as 10^8 and 10^{14} for some systems. The major feature of SERS lies in its surface selectivity and high sensitivity as compared with normal Raman spectroscopy. Raman spectroscopy is ineffective for surface studies because the photons of the incident laser light simply propagate through the bulk and the signal from the bulk overwhelms any Raman signal from the analytes at the surface. SERS selectivity of surface signal results from the presence of surface enhancement mechanisms only at the surface.

There are two primary mechanisms of enhancement described in the literature: an electromagnetic and a chemical enhancement. The electromagnetic effect is dominant, the chemical effect contributing enhancement only on the order of an order or two of magnitude. The electromagnetic enhancement is dependent on the presence of the metal surface's roughness features, while the chemical enhancement involves changes to the adsorbate electronic states due to chemisorption of the analytes. The importance of SERS is that the surface selectivity and sensitivity extends normal Raman spectroscopy utility to a wide variety of interfacial systems previously inaccessible because it was not surface sensitive. The structural and molecular identification power of SERS can be used for numerous interfacial systems, including electrochemical, modeled and actual biological systems, catalytic, in-situ and ambient analyses and other adsorbate-surface interactions.

Coinage metals such as gold, silver, and copper were usually used as the preferred SERS substrate in the form of rough surface and nanoscale structures.^{11, 12} The enhancement of Raman signal is believed to be originated from the interaction between metallic substrate and absorbed target molecules under the electromagnetic field generated by Raman laser, which is normally called Localized Surface Plasmon Resonance (LSPR).¹³ LSPR can be simply tuned by controlling the size, shape, and distribution of nanoparticles,¹⁴ as well as using effective supporting substrate. Directly dispersing these nanostructures on flat medium such as silicon wafer has been initially studied¹⁵. However, the further developed is thought to be confined by the limited maximum particle density, uncontrollable aggregation, and non-uniform distribution of Raman signal.¹⁶ Consequently, heterostructures by combining these Raman sensitive nanoparticles with one-dimensional nanowire as supporting medium¹⁷ were further explored. Silicon nanowire supported nanoparticles, for instance, were reported as the preferred SERS heterostructures. The application of these nanomaterials as sensitive SERS substrate was summarized in Figure 1.4.

1.3.2. Silicon nanowire based SERS substrate

Silicon nanowire has been studied for several decades due to their excellent electronic/ mechanical properties, convenient surface tailorability and industrial compatibility, which make it a promising material in field-effect transistors, solar cells, and sensors.^{18, 19} Among these applications, using silicon nanowires as chemical sensors are of particularly important due to their biocompatibility, vast surface-to-bulk ratio, fast response, good reversibility and oxide-coated or H-terminated surface.²⁰ However, it is now widely accepted that as-produced pristine silicon nanowires only exhibit moderate sensitivity in chemical detection. As a result, appropriate surface modification is definitely needed and well developed. We can find papers that showing the

decoration/functionalization of silicon nanowires with platinum nanoparticles²¹, boron and magnesium²², alkyl and nanotrees²³, diamond-like carbon (DLC)²⁴ and polymers²⁵.

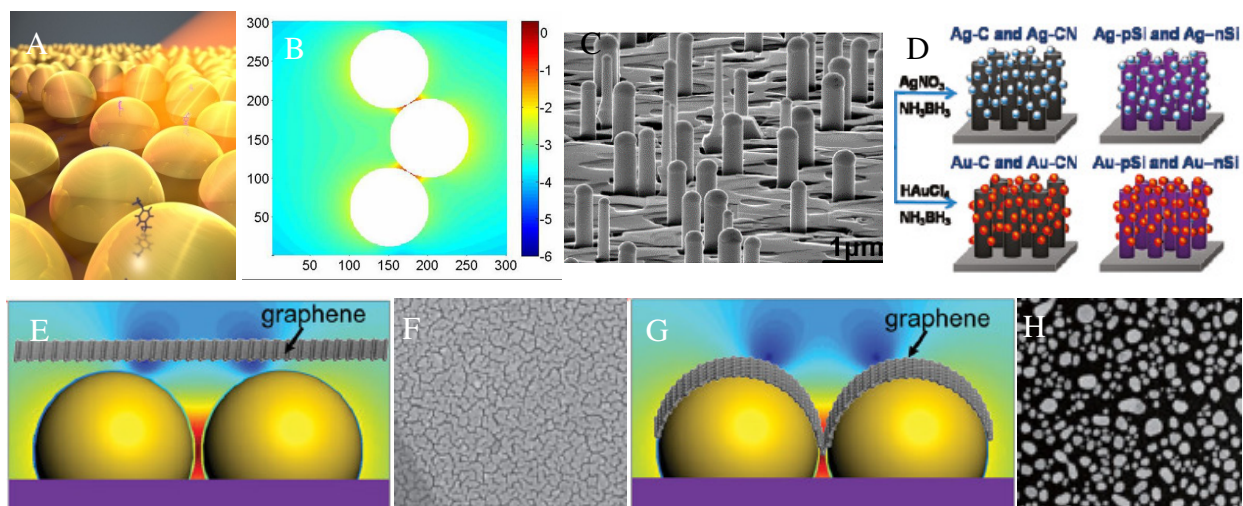


Figure 1.4. (A-B) Surface plasmonic resonance of Au nanoparticles. (C-D) Silicon nanowires and their surface decoration with nanoparticles for SERS sensing. (E-H) Surface plasmonic resonance and morphology of GNPs for SERS sensing. Reprinted with permission from ref. 20. Copyright 2013 American Chemical Society.

However, in the approaches for Raman-based chemical sensors, silicon nanowires were exclusively surface-decorated with silver nanoparticles²⁶ or gold nanoparticles. The significant enhancement on silicon nanowire based heterostructures was attributed to (1) the enlargement of specific substrate area, which is capable to absorb more target molecule per unit area, and (2) the appropriate distribution of nanoparticles on the nanowire, which is able to generate more hot-spots for Raman detection. For instance, silver nanostructures decorated silicon nanowires have been intensively studied as ultrasensitive SERS substrate in the detection of R6G²⁷, CV²⁸, DNA²⁹, as well as amoxicillin³⁰. It is found that the detection limit can reach as low as 10^{-14} M.³¹ Compared with silver-based substrate, gold nanoparticles are considered to be increasingly important due to its chemical stability, low-temperature processibility (low melting point, especially for nanoparticle), and excellent bio-compatibility. Based on these super properties, gold nanoparticle

based heterostructures are of particularly promising in the up-coming bio-chemical and life science. The concept of SERS based on gold nanostructure supported on silicon nanowires has been previously confirm by the well-defined Tip Enhanced Raman Scattering (TERS) technique³²,³³. It is found that the Raman scattering signal, compared that generated on single nano-tip, will be significantly enlarged when two or more gold tips combined together. As a result, the capability for the detection of infinite low-concentration molecules will be largely increased. However, the decoration of silicon nanowire with extraneous gold nanoparticles severing as SERS substrate is really coming new. For instance, Sun et al.³⁴ studied the charge-selective ability of silver/gold nanoparticles supported on silicon-carbon core-shell nanowires. Chen et al.³⁵ reported the Raman scattering enhancement of gold nanoparticle decorated silicon nanowire and demonstrated its Raman photodetection ability.

1.4. Carbon nanostructures for thermal management

Carbon nanotubes (CNTs) have been considered to be one of the ideal materials for various engineering applications due to their remarkable electrical, mechanical, and thermal properties.^{36,37} Especially, thermal management based on CNT materials has been considered as one of the hottest topic.³⁸ Experimental and theoretical studies show that individual CNT present thermal conductivity as high as 2000 W/m-K to 6000 W/m-K,³⁹ which is nearly 10 times higher than normally used thermal conducting materials such as copper and silver. Among the multiple applications of CNTs, of particular interest is the random network of CNTs for integrated circuits and display drivers on flexible or transparent substrate.⁴⁰ In practice, CNT film, mats, buckypaper, and vertically aligned arrays, attract more and more attentions due to their outstanding

performance in the field of gas and bio-sensing, optoelectronics, and thermal interface layers for heat dissipation.⁴¹ However, when it comes to such kind of bulk films, the thermal conductivity was estimated to be significantly decreased due to the presence of amorphous carbon, defects, impurities and thermal intertube junction resistance. It is reported that the thermal conductivity value is around 10-220 W/m-K.⁴² Thus, the studies on the thermal transport properties of CNT film/network become of great importance (Figure 1.5A).

Chemical and structure modifications of CNTs mainly include elemental doping and surface modifications are frequently applied to the pristine CNTs in the practical application.⁴³ CNTs doped with nitrogen were reported to exhibit significantly enhanced electric conductivity, capacity and electrocatalytic properties (Figure 1.5B-C), which endow them with promising applications in micro/nano electric device, energy storage and catalysis.⁴⁴ Surface modifications such as acid treatment⁴⁵ and gas plasma treatment⁴⁶ have been reported to take a significant role in enhancing the applicability of CNTs. Strong acid treatment can effectively purify CNTs by removing metal catalyst and amorphous carbon from the CVD process and also create plenty of functionalized carboxylic group on the surface, which significantly increase its compatibility in biosensing application. Gas-phase plasma oxidation, as another strategy for CNT surface modification, has been considered to be solvent-free, time-efficient, flexible and able to provide a wide range of functional groups depending on the plasma parameters. However, the practical thermal management based on such chemically modified CNTs is still limited by the lack of understanding the influence of these modifications on the thermal transport properties of CNTs.

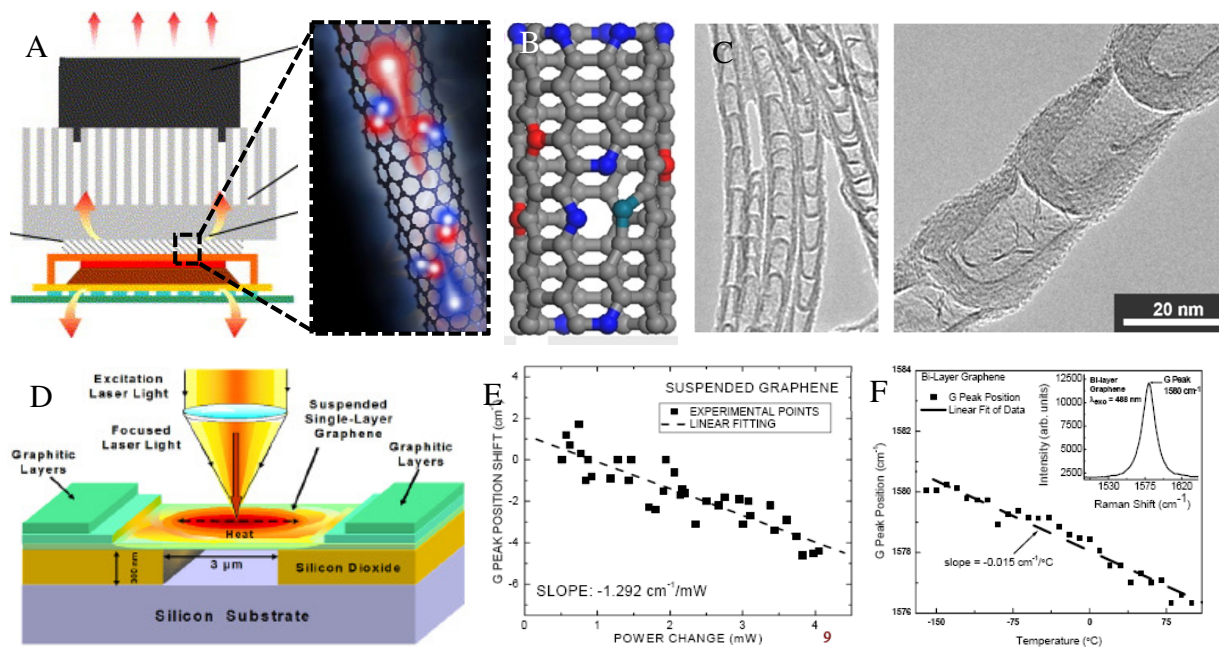


Figure 1.5. (A) Application of CNTs as heat dissipater in CPU. (B-C) Atomic structure and morphology of N-doped CNTs. (D-F) Thermal conductivity measurement of graphene using the Raman based technique. Reprinted with permission from ref. 25. Copyright 2010 American Chemical Society.

Another promising application of such novel CNTs is as filler in polymer matrix to produce nanocomposites with enhanced electric, mechanical, and thermal properties.⁴⁷ For the respect of thermal properties, due to their intrinsic anisotropic physical properties along the nanotube and in the radial direction, such composites normally present anisotropic thermal conductivity, which is preferred to be used in producing anisotropic thermal conductor/spreader. Anisotropic heat conductor is commonly defined as a material with significantly different thermal conductivity in the in-plane direction and through-thickness direction. Compared with conventional isotropic heat conductors such as Cu, Al, W-Cu, etc., anisotropic thermal conductors have been paid increasing attention since they can be used to, for instance, significantly enhance the performance and reliability of microelectronics and solid-state light-emitting diodes by eliminating the overheat, or

design one-direction heat transfer pipes with negligible radial heat dissipation, or act as the effective heat exchange interface. The advantage is mainly reflected that a very low through-thickness thermal conductivity enables the heat spreader to serve as a thermal insulator in the through-thickness direction, thus avoiding heat flow to nearby components in the electronic package or other heat transfer system. Normally, flexible graphite and continuous carbon fiber polymer matrix composite have been used as such kinds of heat spreaders. However, these anisotropic thermal conduction materials are in essence based on the difference of intrinsic thermal conductivity of CNTs, and thus the effective management of heat transfer flux at specific direction still represents a big challenge.

1.5. Challenges and major goals

The major hypothesis of this dissertation is that by combining carbon/graphene coating with noble metal system and further integration them with semiconducting nanowires, it is possible to achieve unique multifunctional nanoscale hybrid heterostructures. The heterostructures are anticipated to exhibit novel thermal, chemical, mechanical, electrical and optical performance. The proposed goals include fundamentally understanding of the processing, structure-property relationships and novel physical phenomenon related to graphene shell encapsulated gold nanoparticles and their heterostructures with nanowires. The specific purpose was focused on theoretical understanding of the surface and interface interactions and effective control of the nanostructure performance with novel processing methods. This will further allow for the modulation of the electric, optical, chemical, thermal and mechanical properties of GNPs as well as their heterostructures with external nanoparticles, bio-molecules, and semiconducting quantum dots and nanowires.

Therefore, as schematically shown in Figure 1.6, the major contents of this dissertation include materials fabrication, characterization, simulation and applications, of which the specific aims were demonstrated as follows.

(1) Fabrication and patterning of noble metal nanoparticles, GNPs Si nanowires and their complex heterostructures

(a) Highly ordered assembly of noble metal nanoparticles on the Si substrate via a galvanic deposition – annealing approach

(b) Xylene-based Chemical vapor deposition (CVD) to grow graphene shells on the patterned Au nanoparticles.

(c) Silane-based CVD process for the growth of Si nanowires *via* the VLS mechanism.

(d) Fabrication of nanowire heterostructures through the surface decoration of Si nanowires.

(2) Surface and interface process for the hybridization of heterostructures

(a) Anchoring of amine-terminated Au nanoparticles, quantum dots, and DNA on the surface-oxidized GNPs *via* the well-defined carbodiimide (EDC/NHS) chemistry.

(b) Generation of fluorescent properties on GNPs through the biotin-streptavidin chemistry.

(c) Chemical nucleation/galvanic deposition of Au nanostructure on Si nanowires.

(d) Surface migration behaviors of Au nanoparticles on Si nanowires during the high-temperature annealing.

(3) Photocatalysis on GNP hybrids and ceramic complex heterostructures

(a) Fabricated GNP-QD heterostructures for plasmon-enhanced photocatalytic organic degradation.

(b) Designed and optimized the water-vapor assisted thermal oxidation furnace for the direct growth of free-standing Co_3O_4 nanowires on the Co substrate.

- (c) Fabricated CuO/Co₃O₄ nanowire heterostructures for Oxygen Evolution Reaction (OER) in photocatalytic water splitting process.
 - (d) Studied the growth of Co₃O₄ nanowires and further exploration of Co₃O₄/WO₃/CoWO₄ nanowire heterostructures for photocatalytic organic degradation.
- (4) Thermal conductivity and thermal transport control of CNT/polymer nanocomposites
- (a) Developed the Raman-based technique for thermal conductivity measurement of CNT network, CNT-based composite film.
 - (b) Studied the influence of surface modifications on the thermal conductivity of (N-doped) carbon nanotubes (CNTs)
 - (c) Designed and fabricated CNT/polymer nanocomposites for gradient thermal conductors, studied and modulated their thermal transport behaviors.
- (5) Materials characterizations
- (a) Morphology and structure analysis of Au nanoparticles, GNPs, Si nanowires and the heterostructures (SEM, TEM, XRD).
 - (b) XPS technique to evaluate the activation efficiency of surface function groups on graphene, CNTs through plasma, acid treatment and to study the surface migration kinetics of Au nanoparticles on Si nanowires during the high-temperature annealing.
 - (c) Raman, FTIR were used to characterize the variation of functional groups on GNPs during the plasma/acid treatment and the formation of covalent bonds in the combining chemistry.
 - (d) Surface-enhanced Raman Spectroscopy (SERS) was used for molecule detection on Au nanoparticles, GNPs, Si nanowires and their heterostructures.
 - (e) Raman technique was used to thermal conductivity of various CNT films.

(f) UV-VIS-NIR spectroscopy was used to study the optical properties and further evaluate the band gap of semiconducting nanostructures.

(4) Simulation and modeling

(a) Simulation of heat transfer CNT films and CNT/polymer composites (MATLAB solution of Second Order Partial Differential Equation).

(b) Discrete Dipole Scattering (DDSCAT) modeling of the surface plasmonic properties (light scattering and absorption) of Au nanoparticles, GNPs, Si nanowires and combined heterostructures.

(5) Application approaches

(a) Surface-functionalized GNPs, Si nanowire-GNP heterostructures for the anchoring and detection of DNA, biotin-streptavidin.

(b) Fabrication of GNP-QD architectures with modulated energy gap for efficiency electron transfer application in solar energy harvesting and plasmon-enhanced photocatalysis.

(c) Highly-ordered Au nanoparticles, GNPs, Si nanowires and their heterostructures for highly sensitive and selective SERS chemical sensing.

(d) Variable thermal conductivity of chemically modified CNTs and their application in Gradient Thermal Conductor (GTC).

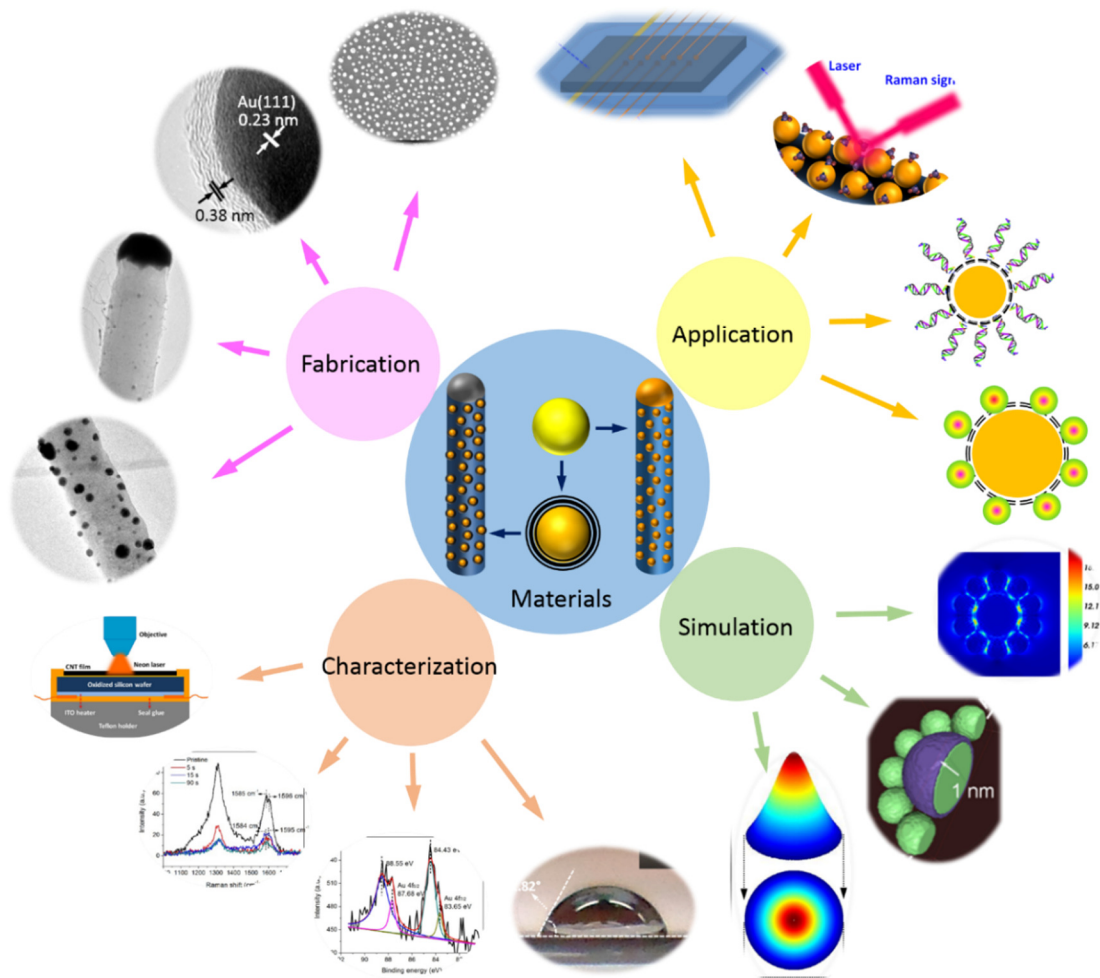


Figure 1.6. Schematic showing the overview structure of proposed dissertation. The basic contents of this dissertation include materials fabrication, characterization, simulation and applications.

PART I

**CARBON SURFACE CHEMISTRY ON MULTILAYER GRAPHENE SHELL
ENCAPSULATED GOLD NANOPARTICLES**

CHAPTER 2

PLASMA OXIDATION OF GRAPHENE-ENCAPSULATED GOLD NANOPARTICLES AND FURTHER BIO-FUNCTIONALIZATION

Yuan Li,¹ Wenwu Shi,¹ Junchi Wu,¹ Nitin Chopra^{,1,2}*

¹Metallurgical and Materials Engineering Department, Center for Materials for Information Technology (MINT), The University of Alabama, Tuscaloosa, AL 35487, U.S.A.

²Department of Biological Sciences, The University of Alabama, Tuscaloosa, AL 35487, U.S.A.

***Corresponding Author**

E-mail: nchopra@eng.ua.edu

Tel: [205-348-4153](tel:205-348-4153)

Abstract

Graphene-based hybrids heterostructures has been considered as a promising substitute material in electronic devices, bio-compatible sensors and other biopolymer molecular analysis. In this paper, we reported the facile production of graphene shells-encapsulated gold nanoparticles (GNPs) and their further plasma treatment and bio-functionalization for highly sensitive SERS sensing and DNA immobilization. GNPs were grown *via* a xylene-based chemical vapor deposition process, and their subsequent structure modification was achieved by oxygen plasma treatment. The optimized nanostructure presents bio-chemical properties and were further used for heterostructuring with extraneous gold nanoparticles or λ -DNA segments. The resulting gold nanoparticles-attached GNPs heterostructures exhibit excellent SERS ability on molecule detection. Highly-ordered assembly of GNP-DNA architectures were also obtained with this manner. Such combination will be of importance in future DNA detection/recognition and bio-device applications.

Keywords: multilayer graphene shell encapsulated gold nanoparticles, Surface-enhanced Raman Spectroscopy (SERS), DNA immobilization

2.1. Introduction

Sensitive, selective, rapid, and cost-effective analysis of biomolecules has become of importance due to an increasing demand for lab-on-chip-type analytical devices.⁴⁸ Deoxyribonucleic acid (DNA) can be potentially used as a building block for the assembly of nanoscale electronic devices, clinical testing, environmental monitoring, and food safety.⁴⁹ However, DNA purification and yield remains a major limitation for such applications. In addition, high cost, low efficiency, and poor repeatability of DNA binding substrates or detection devices is a challenge. These necessitates detailed study of immobilization of DNA on sensitive and selective substrates. Chemical absorption, covalent binding, electrostatic attraction, copolymerization, and streptavidin-biotin affinity systems are frequently reported methods for DNA immobilization and detection.⁵⁰

The applications of gold nanoparticles in DNA-based architectures and other chemical sensors are also interesting and promising, allowing the programmability, molecular recognition, and catalytic property of biopolymers to couple to the unique optical, thermal, electric and catalytic property of gold nanoparticles.⁵¹ Numerous practices have since been made including the preparation of ordered nanostructures,⁵² gene and drug delivery⁵³ and biosensing⁵⁴. For instance, DNA has been used as a rigid spacer between gold nanoparticles to prepare ordered architectures with distance-dependent optical⁵⁵ and physical properties⁵⁶ in terms of heat, electron, and energy transfer. In ref. 55, the authors reported the preparation of highly uniform DNA-tailorable gold nanoparticle architectures with 1 nm inter-particle gap. Such controllable interior nanogaps highly strengthened the near-field electromagnetic field induced by the Localized Surface Plasmon Resonance (LSPR) of gold nanoparticles, and resulted in significant amplification of Raman signals (enhancement factor up to $\sim 5 \times 10^9$). These studies open new insights and reliable approaches to the development

of bio-nano sensing devices and other bio-technologies due the well-established thiol-chemistry, bio-compatibility and chemical stability of gold nanoparticles.⁵⁷

Optical and sensing performances of gold nanoparticles can be significantly improved through their surface-functionalization or heterostructuring.⁵⁸ Thiol-chemistry was the most used approach to combine gold nanoparticles to other nanostructures or thiolated bio-components. However, this also limited or complicated the widening hybridization of gold nanoparticles with other thiol-absent materials since additional thiolating step has to be involved in the hybridization process. For instance, a thiolated tip was normally attached at the end of DNA stretch so that they can be covalently combined with gold nanoparticles.⁵⁹ This not only brought extra demand of raw DNA materials and complicated the process, but also increased the toxicity of final composite product due to the low-compatibility of the thiol items in a lot of bio-systems. Thus, development of thiol-free approaches for heterostructuring or functionalization of gold nanoparticles are feasibly demand and promising.

Carbon nanotubes (CNTs) and graphene, the representative fundamental carbon-based low-dimensional nanostructures, have been also widely used as the backbone for DNA immobilization⁶⁰ due to their interesting properties and surface chemistries. Recently, the authors reported a facile and scalable chemical vapor deposition (CVD) approach to produce and pattern graphene-encapsulated gold nanoparticle (graphene nanoparticles, GNPs) on silicon substrate, resulting in uniform coverage of gold nanoparticles with sub-2 nm thin and non-turbostratic multi-layered graphene shells.⁶¹ Such GNPs preserved/improved the unique optical properties of gold nanoparticle,⁶² and at the same time they also presented the excellent surface chemical properties of carbon nanostructures,⁶³ thus is of promise for future chemical sensor and bio-medicine applications. Nevertheless, for the as-produced GNPs, the graphene surface is highly hydrophobic

due to the presence of amorphous carbon (a normal by-product from CVD) and lack of surface functionalities such as carboxyl (-COOH) and hydroxyl (-COH) groups.⁶⁴ Meanwhile, the as-produced graphene shells are thick (~10-15 layers), which may have a slight shadow effect on the optical gold nanoparticles core.⁶² Thus, further structure modification to the graphene shells are necessary to remove the extra amorphous carbon, introduce surface chemical functionalities (-COOH and -COH) and finally obtain GNPs with controlled shell thickness.

With respect to these purposes, in this paper, we conducted an oxygen plasma treatment to the as-produced GNPs. Various experimental conditions were used to evaluate their influence on the graphene shell structure, thickness and content of surface functionalities. The plasma-treated GNPs under the optimum conditions were further used to anchor extraneous gold nanoparticles (referred as GNP-Au nanoparticle heterostructures in the following) as a SERS substrate or used as a uniform substrate for the immobilization of λ -DNA. The optical properties of the GNP-Au nanoparticle heterostructures were simulated by the Discrete Dipole Approximation method and their SERS sensitivity was characterized by detection the trace amount of rhodamine 6G (R6G) and methylene blue (MB) molecules containing in water. The GNP-DNA architectures immobilized on the silicon substrate were characterized by SEM, TEM, AFM and FTIR. Such orderly patterned GNP-DNA architectures will be important and useful in the development of hybrid bio-nano electronic devices and biosensors.

2.2. Experimental details

Materials and methods: Silicon wafers (100), n-type, were purchased from IWS (Colfax, CA). Gold colloid was purchased from Sigma-Aldrich (St. Louis, MO). 1-ethyl-3-(3-dimethylaminopropyl) carbodiimide (EDC), N-hydroxysuccinimide (NHS), and 2-(N-morpholino)ethanesulfonic acid (MES) were purchased from THERMO scientific (Rockford, IL). TrackIt™ λ -DNA/Hind III Fragments were purchased from Invitrogen (Grand Island, NY). DI water (18.1 M Ω -cm) was obtained using a Barnstead International DI water system (E-pure D4641). All chemicals were used without further purification. Graphene growth were carried out in GSL-1100X Tube Furnace (MTI Corporation) with a quartz tube from ChemGlass (Vineland, NJ). H₂ (UHP grade, 40% balanced with Ar) and Ar (UHP grade) gas cylinders were purchased from Airgas South (Tuscaloosa, AL). Oxygen plasma treatment was performed in a Nordson March Jupiter III Reactive Ion Etcher (Concord, CA).

Growth and plasma treatment of GNPs: N-type (100) silicon substrate was first treated in Piranha solution (H₂SO₄:H₂O₂ = 4:1) at 100 °C for 30 min to create surface -OH groups. Then the siloxane functionalization was carried out in 2 mM MPTMS/ethanol by shaking for 12 h. The samples were rinsed with ethanol and dry in N₂. This was followed by putting the samples were placed in vacuum oven at 80 °C for 1 h to complete Si-O bond formation. Commercial gold colloid was diluted by 10 times with ethanol, then the S-ended Si substrate was put into the diluted gold colloid solution and slightly stirred overnight for gold nanoparticles patterning. As a next step, the gold nanoparticles were oxidized under oxygen plasma for 15 min to produce a surface gold oxide layer (plasma power 160 W and oxygen pressure 600 mTorr). Finally the graphene growth was carried out *via* the xylene CVD process we reported before.^{61,63} Briefly, Xylene was used as the carbon source with a feeding rate of 10 mL/h. A mixture of 10% H₂/Ar with a total flow rate of 1.15 SLM

was used as the carrier gas. The growth process was continued for 1 h at 675 °C. The as-produced GNPs were further treated with oxygen plasma at various conditions for structure modification and surface functionalization. Detailed experimental parameters for the plasma treatment were listed in Table 2.1.

Table 2.1. Various experimental parameters designed for the plasma treatment of GNPs.

Sample #	Duration (s)	Plasma power (W)	Oxygen Pressure (mTorr)
1	5	150	300
2	15	150	300
3	30	150	300
4	60	150	300
5	90	150	300
6	120	150	300
7	15	30	300
8	15	60	300
9	15	90	300
10	15	120	300
2	15	150	300
11	15	120	200
12	15	120	250
10	15	120	300
13	15	120	400
14	15	120	500
15	15	120	600
16	15	120	700

Anchoring extraneous gold nanoparticles on GNPs: The plasma-treated GNPs on silicon substrate were put into 50 mM MES buffer (pH = 4.7) containing 2 mM EDC and stirred for 10 min to form *o*-acylisourea ester, then 4 mM of NHS was added into the solution and continuously stirred for 1 h to form stable amine-reactive NHS ester. After slightly washed with MES buffer and ethanol, the sample was immersed in diluted gold colloid/ethanol solution for 36 h to finally form amide-bonded GNPs-extraneous gold nanoparticles heterostructures. Surface-enhanced Raman Scattering (SERS) effect on these substrate was characterized by detection of trace amount dyes in the aqueous solution.

DNA immobilization with GNPs: Covalent binding of GNPs and λ -DNA fragments was achieved via the well-defined carbodiimide chemistry.⁶⁵ Briefly, plasma-treated GNPs on silicon substrate were first put into 50 mM MES buffer (pH = 4.7) with 2 mM EDC and stirred for 10 min, then 4 mM NHS was added into the solution and further stirred for 1 h. The sample was then rinsed with MES buffer and PBS buffer (pH=7.4). 5 mL PBS buffer with 4 mM λ -DNA, 1 mM EDC, and 2 mM NHS was used for DNA immobilization. The sample was immersed in this solution and slightly stirred overnight. The obtained GNP-DNA architectures were washed with DI-water and dried in N₂.

Characterizations: Transmission Electron Microscopy (TEM, Tecnai F-20) was used to observe the morphology and structure of GNPs before and after plasma treatment. Scanning Electron Microscopy (SEM, JOEL-7000) and Atomic Force Microscopy (AFM) were used to characterize the morphology of GNP-DNA architectures. A Bruker Senterra Raman system was used to identify the quality of graphene shells and collect signal of dyes on SERS substrates. The chemical composition of GNPs before and after plasma treatment was analyzed *via* X-ray Photoelectron

Spectra (XPS, Kratos Axis 165). Fourier Transform Infrared spectroscopy (FTIR, JASCO 4100) was used to characterize the surface functionalities and covalent bonds.

2.3. Results and discussion

2.3.1. Growth of graphene shells on gold nanoparticles

The growth of graphene shells on gold nanoparticles was achieved *via* a xylene-based chemical vapor deposition process. Commercial gold nanoparticles was patterned on the surface-oxidized silicon substrate through the MPTMS-functionalization as described before.⁶⁶ Gold oxide was further created on the surface of gold nanoparticles *via* the oxygen plasma treatment. This oxide layer has been found to be of importance for the catalytic growth of initial graphene layers on the gold nanoparticles (Figure 2.1a) and the detailed mechanism was reported in our previous studies.⁶¹ The following growth was completed by continuous decomposition of CH₄ in a H₂/Ar environment and further deposition of carbon atoms on the initial graphene shells. TEM image in Figure 2.1b shows the as-production graphene-encapsulated gold nanoparticles (GNPs) dispersed on the lacy carbon grid. The average diameter of GNPs was increased to 25.4 ± 3.9 nm as compared with the pristine commercial gold nanoparticles (~10 nm) due to their inevitable aggregation at high temperature. Representative high-resolution TEM images in Figure 2.1c and d illustrate that the as-produced graphene shells are $\sim 3.2 \pm 0.6$ nm thick, with an inter-lattice spacing of $\sim 0.40 \pm 0.03$ nm. This value is slightly larger than the natural c-axis spacing of graphite (~ 0.34 nm) due to the arching strain induced by the curved graphene layers. The TEM image in Figure 2.1d was converted by Fast Fourier transform (FFT) and the resulting image in Figure 2.1e shows the typical

sixfold symmetry expected for graphene/graphite^{67,68} and further confirms (0002) plane of multilayer graphene shells and the (111) plane of gold nanoparticles.

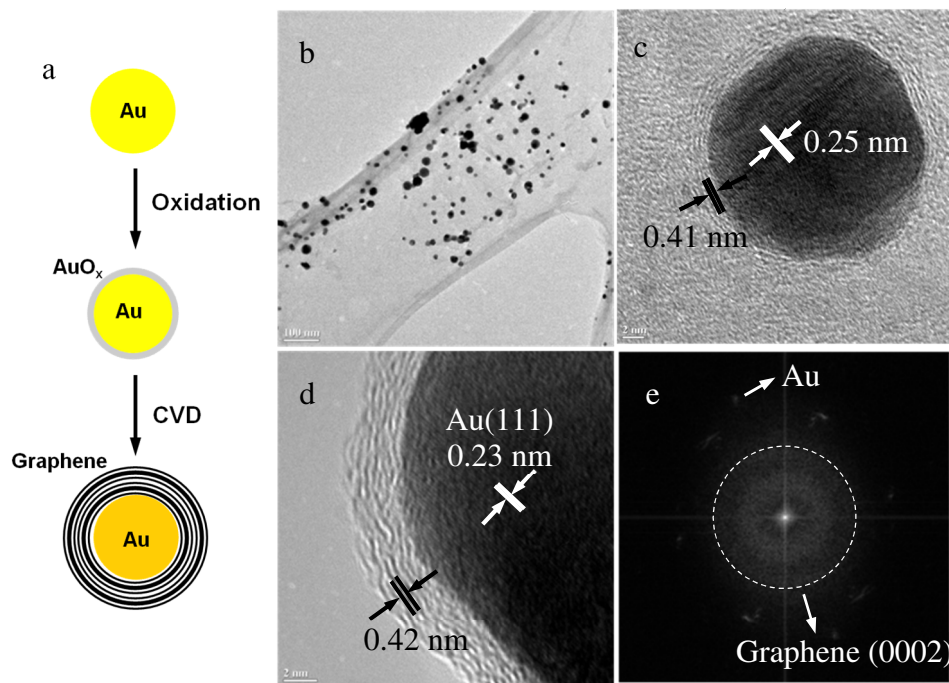


Figure 2.1. (a) Schematic showing the growth of graphene shell on gold nanoparticles. (b-d) TEM images and (e) FFT corresponding to (d) showing the as-produced graphene-encapsulated gold nanoparticles (GNPs).

2.3.2. Oxygen plasma treatment to GNPs

With the purpose of creating surface oxygen-containing functionalities (-COH and -COOH), removing amorphous carbon and further adjusting the graphene shell thickness, oxygen plasma treatment was conducted to the as-produced GNPs. Three sets of experimental conditions including oxidation duration, power and pressure (Table 2.1) were studied to fully understand the oxidation mechanism and further obtain the optimum condition for above purpose. Representative TEM images of the GNPs treated at various conditions were shown in Figure 2.2a-l. Significant structure changes were observed at each condition, as schematically summarized in Figure 2.2m. The variation of graphene shell thickness according to different condition was also shown in Figure 2.2n. We observed that oxygen plasma, even as short as 5 s (Figure 2.2b), has a significant etching effect on the graphene shells (Figure 2.2n). When the plasma treatment was continued for 60 s, graphene shells in some region of gold surface were completely removed, resulting in partially covered graphene shells on the gold nanoparticles (Figure 2.2d). Meanwhile, at constant duration (15 s, for the power set), plasma treatment with low power (30 W or 60 W, for instance), rather than etch away the graphene shells, convert them into an amorphous structure (diamond-like carbon^{69,70}) and resulted in an increase of shell thickness (Figure 2.2o). This is probably due to the gentle incorporation of oxygen atoms in the graphene shells without formation of carbon oxides (CO₂ or CO), which led to strong distortion to the crystallized graphene shells.⁶⁹ However, when the plasma power exceeds 90 W, significant etching effect was observed. The graphene shells were partially etched away but retained their graphite crystalline structure. In addition, varying plasma pressure presented a relatively weak effect on the graphene shell structure. The shell thickness was slightly increased at high pressure. This is probably because of the shortening of the mean free

path of oxygen atoms due to the increased possibility of self-collision at high pressure,⁷¹ which further resulted in the decrease of collision speed of oxygen atoms to the graphene shells.

Since the oxygen plasma showed high power in etching away graphene shells, it may have a significant effect on the quality of graphene shells. This was characterized in detail via the Raman spectroscopy and the results were shown in Figure 2.3. All of these samples before and after plasma treatment show the well-defined D-band at $\sim 1310\text{ cm}^{-1}$ and G-band at $\sim 1584\text{ cm}^{-1}$.⁷² In addition, the G-band was split and an additional D'-band was observed at $\sim 1595\text{ cm}^{-1}$ for all untreated/treated samples. G-band for carbon materials is due to the E_{2g} mode at the Γ -point, arising from the stretching of C-C bond in graphite materials, and is common for all sp² carbon systems. G-band is highly sensitive to strain effects in sp² hybridized atoms. Meanwhile, the D-band is caused by the disordered sp² hybrid structure of graphene and sp³ carbon system such as amorphous carbon.⁷³ Thus, D-band is a direct reflection of the content of defects and impurities in graphene. In addition, the emergence of D'-band was attributed to the randomly distributed impurities and the surface charges in graphene.⁷⁴ For GNPs, the observed D'-band is due to the interaction between the localized vibration mode of surface plasma from gold nanoparticles and the extended phonon mode of graphene shells.⁷³

The intensity ratio of D-band and G-band (ID/IG) is critical for identifying the crystallizing quality of graphene materials. As shown in Figure 2.3a, as-produced GNPs show large D-band due to the curvature-induced disorder of multilayer graphene shells and amorphous carbon.²⁶ The plasma treatment resulted in significant intensity decrease for both D-band and G-band due to the etching of graphene shells. Plasma treatment for 5 s and 15 s lead to a decrease of ID/IG from ~ 1.52 for

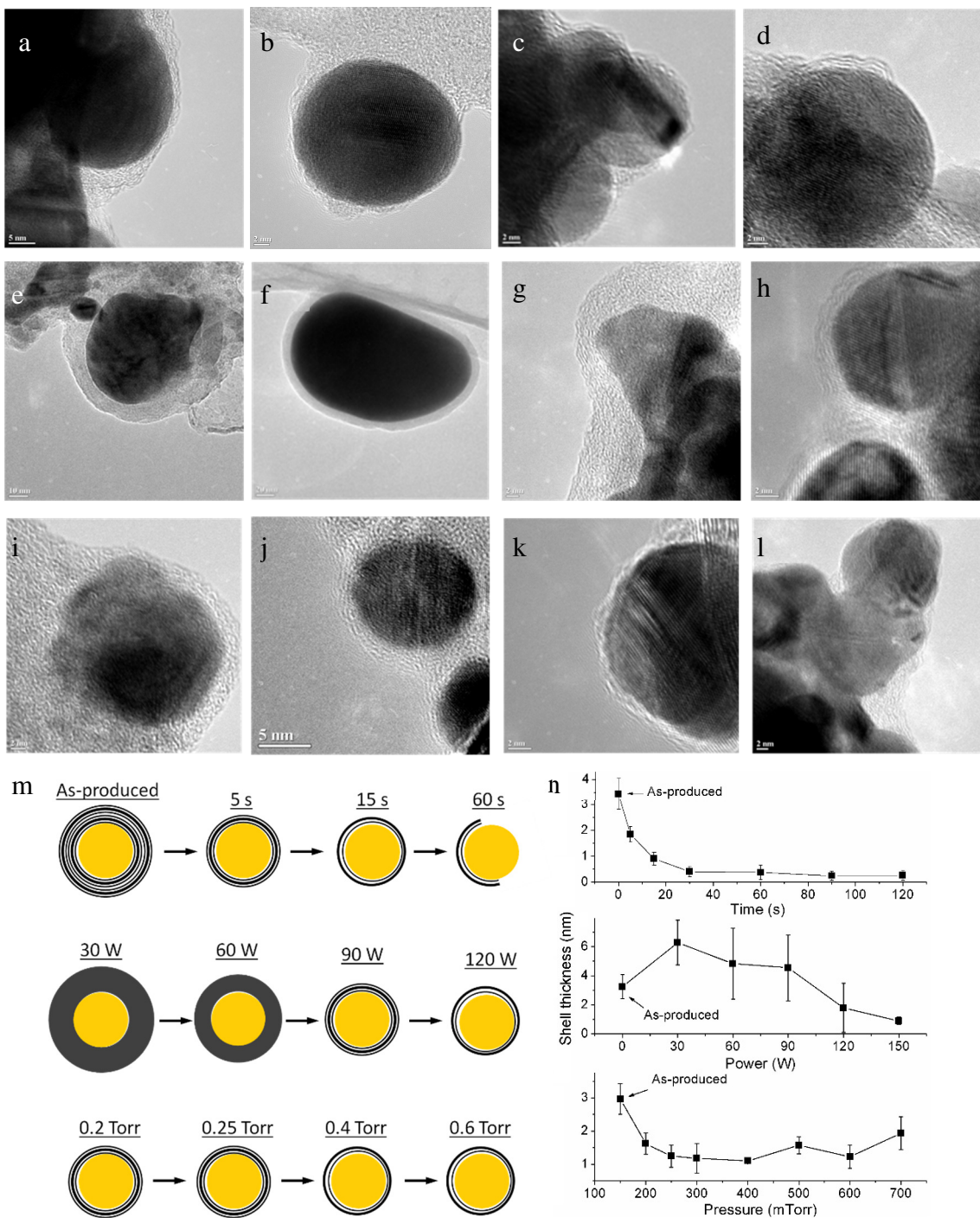


Figure 2.2. (a-l) TEM images showing the influence of plasma treatment on the structure of GNPs: (a-d) duration of 5 s, 15 s, 60 s, and 90 s; (e-h) power of 30 W, 60 W, 90 W, and 120 W; (i-l) pressure of 200 mTorr, 250 mTorr, 400 mTorr, and 600 mTorr. (m) Schematic illustration of the GNP structure at various conditions. (n-p) Variation of graphene shell thickness according to treatment time (n), power (o), and pressure (p).

the as-produced GNPs to ~ 1.34 and ~ 0.97 , respectively, due to the remove of amorphous carbon. However, when the treatment duration exceeds 40 s, I_D/I_G was increased compared with the as-produced GNPs, probably due to the damage of crystalline structure of graphene shells at long treatment. When the treatment lasted for 90 s and 120 s, both D-band and G-band are very low due to the lack of graphene shells, gives small values of I_D/I_G .

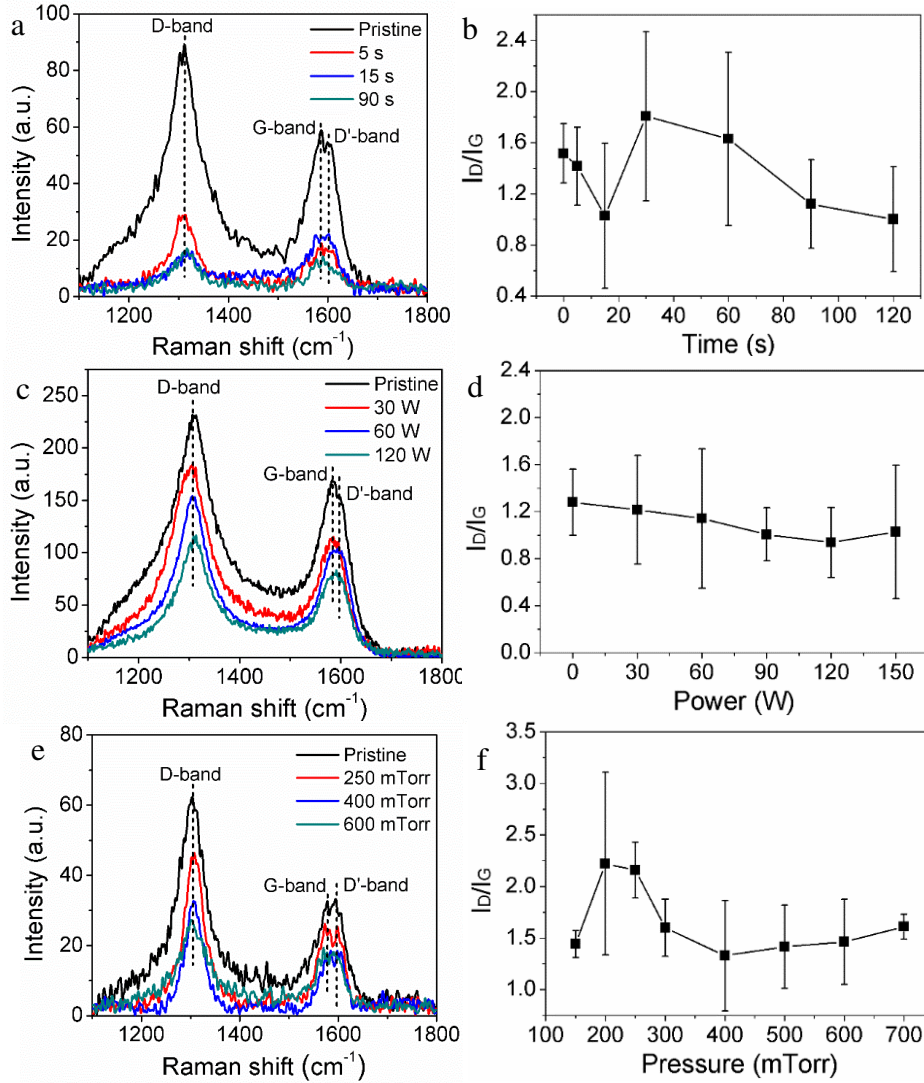


Figure 2.3. Raman spectra (a, c and e) and corresponding I_D/I_G (b, d and f) of GNPs before and after plasma treatment at (a,b) different time, (c,d) different power, and (e,f) different pressure.

Figure 2.3c and d show the Raman spectra and corresponding I_D/I_G of GNPs after plasma treatment at various power. For this set of study, new-prepared fresh GNPs were used and it needs to notice that the I_D/I_G is slightly different for the as-produced GNPs grown for different set. As described above, plasma treatment at lower powers induced the formation of amorphous carbon shell on the gold nanoparticles. Thus, obvious decrease of I_D/I_G was not observed at 30 W and 60 W. Further increasing the plasma power resulted in decrease of I_D/I_G . However, when the power was at 150 W, I_D/I_G slightly increased due to the severe damage of graphene shells. The influence of plasma pressure on the Raman spectra and I_D/I_G was shown in Figure 2.3e and f. Lower pressure gave high mean free path of oxygen plasma and thus they reacted with graphene shells with a higher speed. This led to more damage to the graphene shells and thus I_D/I_G obtained at 200 mTorr and 250 mTorr were largely increased (Figure 2.3f). However, at high pressure, the weak interaction between oxygen plasma and graphene shells led no significant change to I_D/I_G .

Quantitative analysis of the surface functionalities on GNPs was conducted using XPS, which gives signals for various elements including Au, C, O and Si on the as-produced GNPs in the wide-range (0 ~ 1000 eV) survey scan. The Si peaks arise due to the substrate. Pure element Au peaks for intact gold nanoparticle cores were observed at ~84.59 eV and ~88.27 eV, which are consistent with Au 4f_{7/2} and Au 4f_{5/2} respectively.⁶¹ For O 1s peaks, there could be several origins, such as absorbed molecules and native oxide (SiO₂) from the substrate. Thus, O 1s peaks should not be utilized for analyzing plasma oxidized Au nanoparticles and surface-modified GNPs. High-resolution scan was conducted for C 1s peaks, and these were further deconvoluted into several carbon groups (C-C, -COOH and -COH). The molar fraction of carboxyl and hydroxyl radicals in the graphene shells was obtained from their area percentages in the whole C 1s spectrum area.

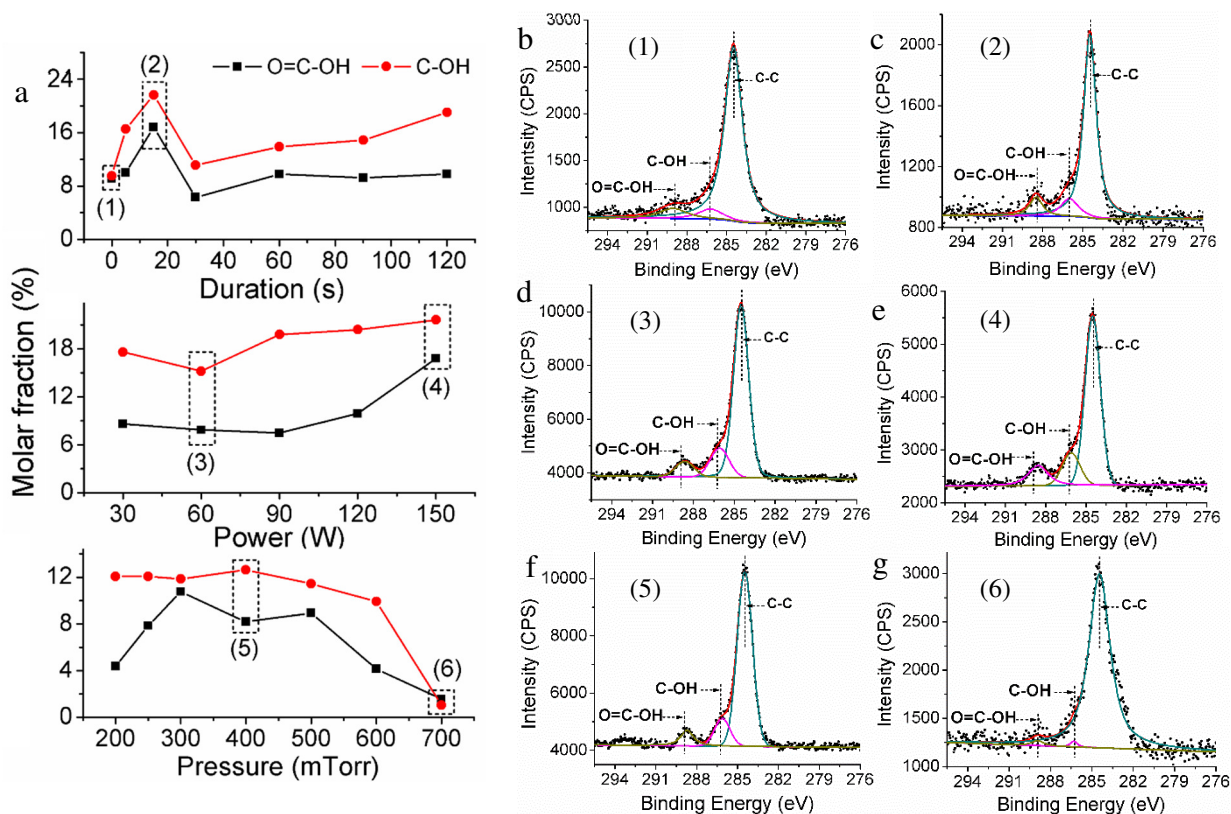


Figure 2.4. (a) Variation of -COOH and -COH fraction in the graphene shells before and after plasma treatment at different duration (top), different power (middle), different oxygen pressure (bottom). (b-g) Deconvoluted XPS spectra of C 1s for various samples marked in Figure 2.4a.

Such XPS survey scan and C 1s spectra analysis were also conducted for GNPs after plasma treatment at various conditions. The variation of hydroxyl and carboxyl content in the graphene shells according to the plasma duration, power and pressure were shown in Figure 2.4a-c. Several representative deconvoluted XPS spectra of C 1s were further shown in Figure 2.4d-i. The as-produced GNPs show a carboxyl content of 4.82% and hydroxyl content of 6.53%. Plasma treatment for 5 s and 15 s resulted an increase of carboxyl to 10.00% and 16.79%, and an increase of hydroxyl to 16.51% and 21.62%, respectively (Figure 2.4a, top). However, when the plasma treatment exceeds 30 s, the carboxyl and hydroxyl contents significantly decreased. This is consistent with the change of I_D/I_G observed in Figure 2.3b and due to the over-etching of graphene

shells. With respect of plasma power, strong powers (e.g. 120 W, 150 W) led to high content of carboxyl and hydroxyl groups in the graphene shells because of the intensive interaction between oxygen plasma and graphene (Figure 2.4a, middle). In the pressure study, GNPs treated with low plasma pressure (e.g. 200 mTorr, 250 mTorr) show relatively low content of carboxyl groups due to the lack of oxygen atoms. However, when the pressure increased to 600 mTorr or 700 mTorr, the generated plasma becomes weak, resulting decreased content of carboxyl and hydroxyl (Figure 2.4a, bottom). Thus, only proper plasma pressure resulted in high content of carboxyl and hydroxyl functionalities.

To sum up the oxygen plasma study of GNPs, we found that controlling plasma conditions as duration – 15 s, power – 120 W, and pressure – 300 mTorr (referred as the optimum conditions in the following) led to highest creation of surface functionalities, appropriate graphene shell thickness and effective remove of amorphous carbon. This was further characterized by the hydrophilicity test showing in Figure 2.5. A 10 μ l DI-water droplet shows a contact angle of $\sim 55.71^\circ$ on clean silicon wafer (Figure 2.5a). The contact angle of the same droplet on the as-produced GNP substrate is $\sim 71.40^\circ$ (Figure 2.5b) while this value decreased to $\sim 31.86^\circ$ on the plasma-treated GNP substrate (Figure 2.5c). Such hydrophilicity variation was further illustrated in Figure 2.5d. The as-produced GNPs were highly hydrophobic due to the presence of amorphous carbon and lack of surface functionalities.⁷⁵ However, after the plasma treatment, the surface of GNPs become hydrophilic due to the generation of carboxyl and hydroxyl groups, which are favorable for the formation of hydrogen bonds with water molecules. This hydrophilicity test indicates that the optimum conditions are feasible for above purpose and can be further used for the subsequent bio-functionalization.

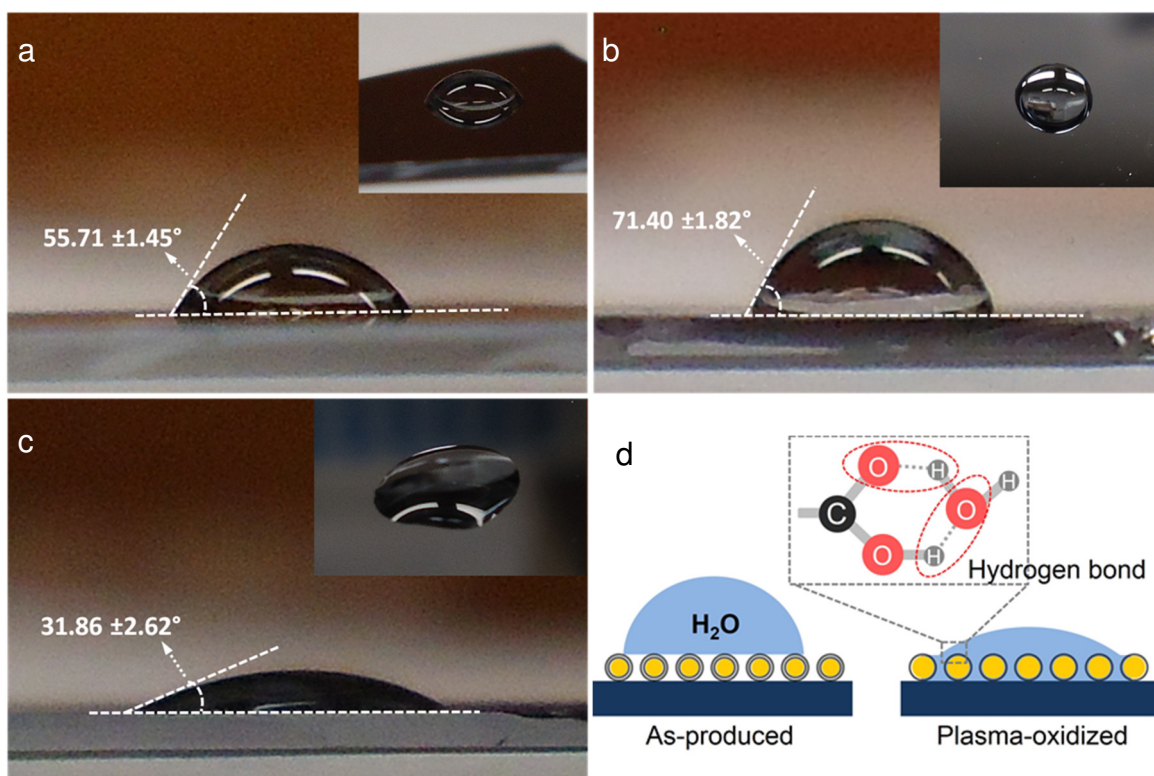


Figure 2.5. Hydrophilicity test of GNP substrate before and after plasma treatment. (a) Blank silicon wafer, (b) as-produced GNP substrate, (c) plasma treated GNP substrate under the optimum conditions (time 15 s, power 120 W, and pressure 300 mTorr). (d) Schematic showing the principle of the interactions between water and the GNP substrates.

2.3.3. Heterostructuring of GNPs for SERS

Bio-functionalization of plasma-treated GNPs includes heterostructuring attachment of extraneous gold nanoparticles and immobilization of λ -DNA segments. The well-defined carbodiimide chemistry was used for the bio-conjunction in both processes.⁷⁶ As schematically illustrated in Figure 2.6, the carboxyl radicals (-COOH) on the plasma-treated GNPs was first reacted with EDC to form an amine-reactive *o*-acylisourea intermediate. This intermediate was further reacted with NHS to form a semi-stable ester, which may then be reacted with primary amines (-NH₂)-terminated NDA or cysteamine to form the amide crosslinks. Then extraneous gold nanoparticles

were able to attach on the GNPs *via* the thiol chemistry. The presence of NHS in the reaction system greatly enhances coupling efficiency (although it is not essential). TEM images of the GNPs functionalized with extraneous gold nanoparticles (~10 nm) were shown in Figure 2.7. The heterostructures with the same configuration as illustrated in the inset of Figure 2.7a were observed exclusively. According to these TEM images, a surface coverage of $32 \pm 15\%$ was estimated for the gold nanoparticles distributed on GNPs.

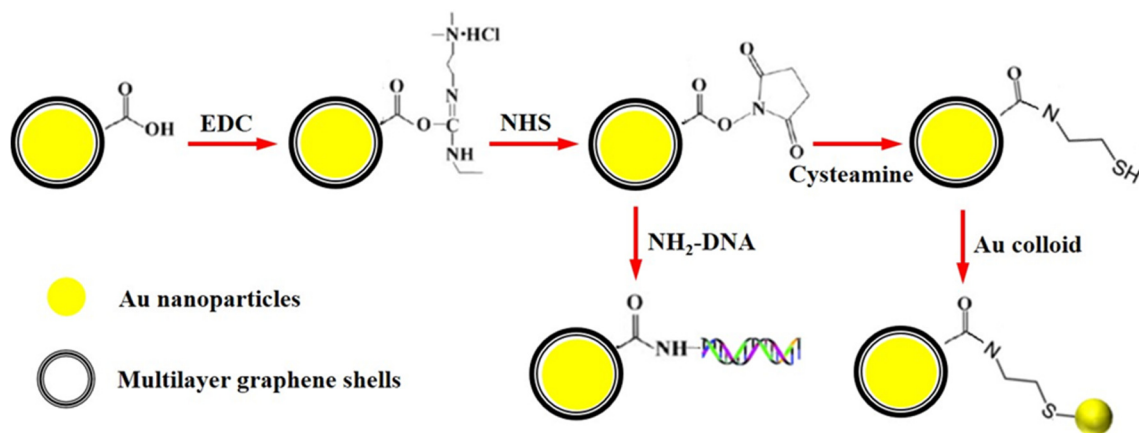


Figure 2.6. Schematic showing the carbodiimide chemistry used for functionalizing extraneous gold nanoparticle and λ -DNA onto the plasma-treated GNPs.

Raman spectra of the extraneous gold nanoparticle attached GNPs (referred as GNP-Au nanoparticle heterostructures in the following) were shown in Figure 2.8a. Significantly enhanced Raman signals for D-band and G-band were observed on the GNP-Au nanoparticle heterostructures as compared with the as-produced and plasma-treated GNPs (see the inset in Figure 2.8a). These GNP-Au nanoparticle heterostructures were further used as the SERS substrate for the detection of trace amount of dye containing in water. Figure 2.8c and d show the Raman signal obtained in 10^{-6} M R6G- and MB-aqueous solution. In both system, the Raman signals of R6G/MB were increased significantly enlarged as compared with that obtained on plasma-treated

GNP substrate and blank substrate. Such Raman enhancement can be mainly attributed to (1) the interaction of localized surface plasma among different gold nanoparticles, resulting in significantly increased or overlapped electric field at the interface area of the nanoparticles (Figure 2.8b), this is so-called electromagnetic enhancement mechanism;⁷⁷ (2) graphene naturally present a hexagonal structure, which is quite similar with the molecule structure of R6G and MB and thus these GNP substrates are more favorable than naked gold nanoparticles for absorbing the target molecules and this was defined as the chemical enhancement mechanism.⁷⁸

The optical properties of GNP-Au nanoparticle heterostructures were simulated using the Discrete Dipole Approximation (DDA) method. This method has been well-demonstrated by our group for estimating the extinction properties and simulating the near-field electric field distribution of gold-based nanomaterials. The simulation target was shown in Figure 2.9a. The central GNP was considered to be 20 nm in diameter including 1 nm thick graphene shell corresponding to the plasma-treated GNPs. Gold nanoparticles with a diameter of 10 nm were closely-packed around GNPs. A simulation for the plasma-treated GNPs with no surrounding gold nanoparticles was also conducted as comparison.

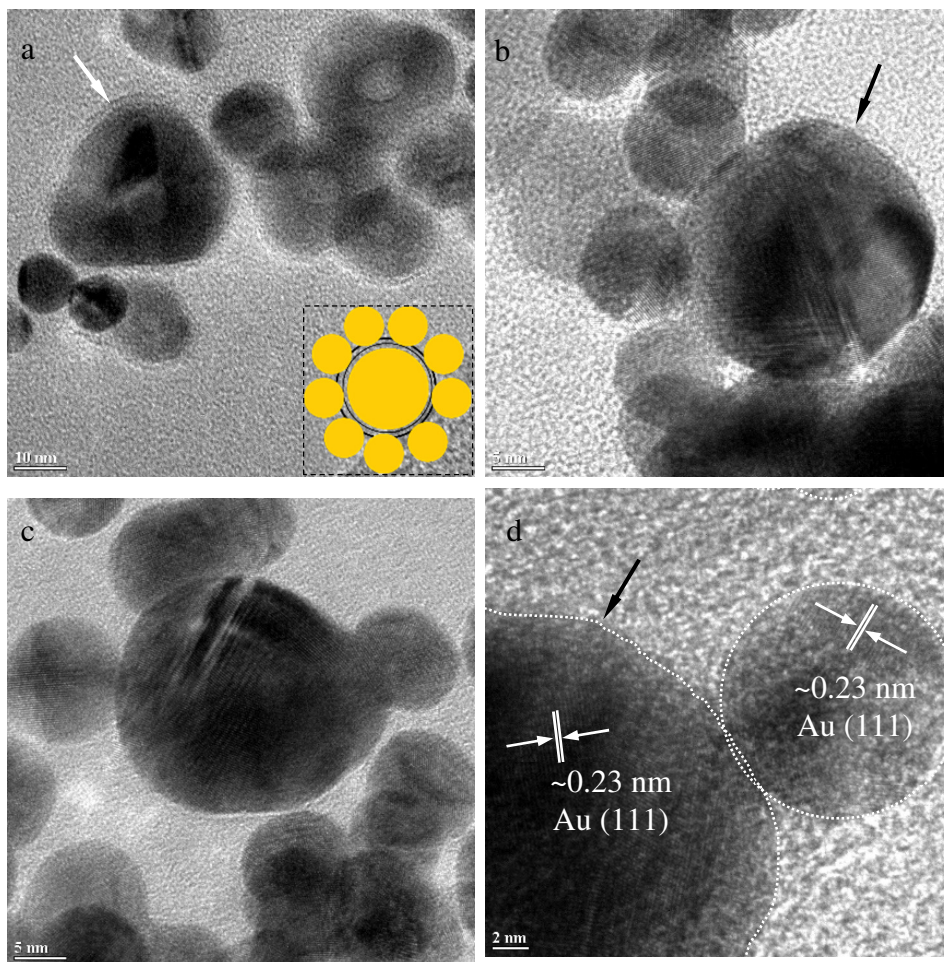


Figure 2.7. (a-c) TEM images extraneous gold nanoparticles functionalized GNPs (GNP-Au nanoparticle heterostructures). Note: Inset in Figure 2.7a illustrates the structure of the heterostructures, and the arrows show the graphene shells after plasma oxidation. (d) HRTEM image showing the lattice and interface between GNPs and the extraneous gold nanoparticles.

The obtained extinction efficiency spectra were shown in Figure 2.9b. The extinction efficiency of the GNP-Au nanoparticle heterostructures was significantly increased as compared with the plasma-treated GNPs due to the enhancement of surface plasmon resonance. The extinction spectra were further deconvoluted into absorbance and scattering, indicating that the extinction for both targets is dominantly contributed by the absorbance. The plasma-treated GNPs show the two extinction maximum peaks at ~ 210 nm and ~ 518 nm, corresponding to the $\pi \rightarrow \pi^*$ transition of

aromatic C-C bonds⁷⁹ and surface plasmon resonance of gold nanoparticle,⁸⁰ respectively. After heterostructuring with extraneous gold nanoparticles, an obvious red-shift of ~27 nm and ~22 nm was observed respectively for these two peaks. To further evaluate the influence of extraneous gold nanoparticles on the electromagnetic field strength and distribution, the normalized electric field map was generated for both targets under incidents equivalent to the extinction maximum wavelength (~518 nm for plasma-treated GNPs and ~540 nm for the GNP-Au nanoparticle heterostructures). The normalized electric field intensity is defined as the ratio between electric field generated on the nanostructures and the incident electric field ($|E|/|E_0|$). As shown in Figure 2.9d and e, the GNP-Au nanoparticle heterostructures exhibited significantly enhanced electric field overall the target and the strongest electric field places (hot spots) are mainly at the interface of different nanoparticles. This was further confirmed by the $|E|/|E_0|$ spectra across the center of the targets in the incident direction (Figure 2.9c). These hot spots have been considered to play a critical role in SERS sensing and have a dominant contribution to the Raman enhancement.

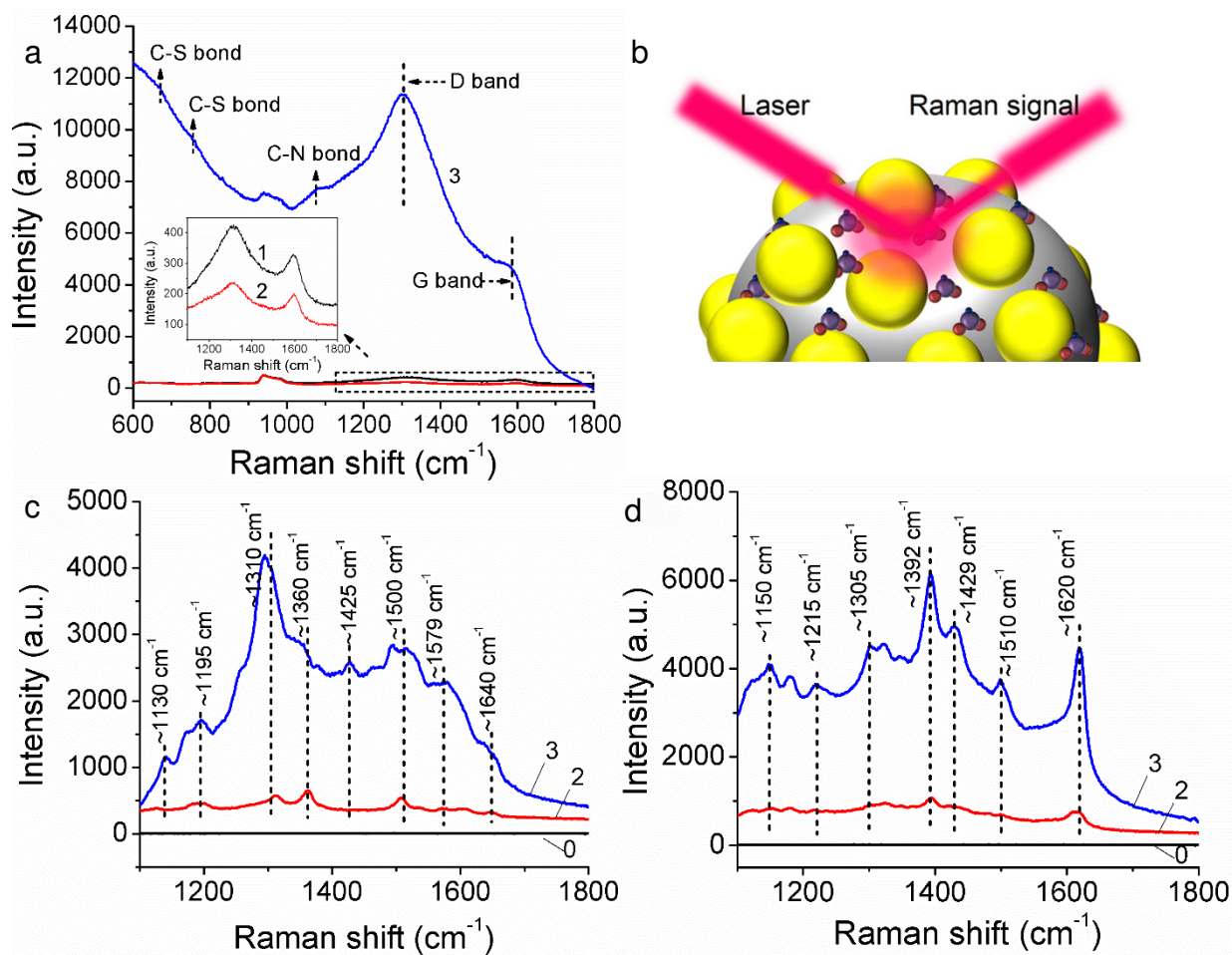


Figure 2.8. (a) Raman spectra of the as-produced GNPs (1), plasma-treated GNPs (2), and the GNP-DNA hybrids (3). (b) Schematic showing the SERS-based organic sensing on the GNP-AuNP hybrids. (c,d) Raman spectra R6G (c) and MB (d) that absorbed on (0) blank silicon substrate, (2) plasma-treated GNPs and (3) GNP-DNA hybrids.

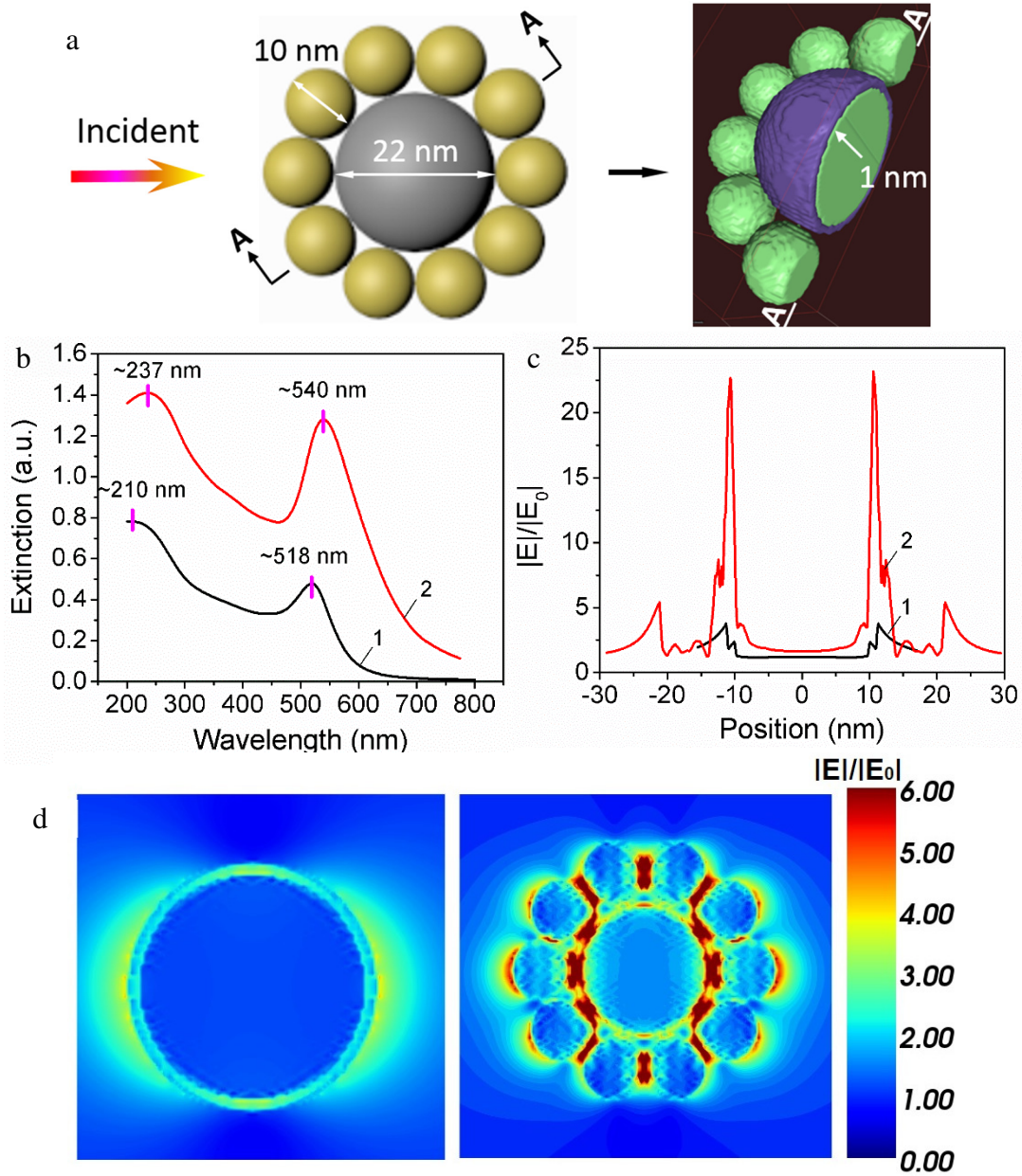


Figure 2.9. (a) Schematic for the GNP-Au nanoparticle heterostructures used for the plasmonic modeling. (b) Extinction spectra of (1) plasma-treated GNPs and (2) GNP-Au nanoparticle heterostructures. (c) Normalized electric field across the heterostructures in the incident direction. (d) Distribution of electromagnetic field near the surface of the plasma-treated GNPs (left, incident 518 nm) and the GNP-Au nanoparticle heterostructures (right, incident 540 nm).

2.3.4. Immobilization of DNA on GNPs

The carbodiimide chemistry used for the covalent attachment of DNA to the plasma-treated GNPs was described above (Figure 2.6). The Hind III cleaving technique resulted λ -DNA segments with amine terminations at the both ends (Figure 2.10a), which opens the possibility for attaching λ -DNA to the carboxyl-terminated GNPs *via* the formation of amide bonds. FTIR spectra for the as-produced GNPs, plasma-treated GNPs, the pristine λ -DNA and the GNP-DNA architectures were shown in Figure 2.10b. For the pristine λ -DNA, the band at $\sim 1023\text{ cm}^{-1}$ indicates Thymine (CH_3), $\sim 1080\text{ cm}^{-1}$ indicates the PO_2^- stretch, $\sim 1176\text{ cm}^{-1}$ indicates thymidine (C5-CH_3 bond and in-plane ring stretching), $\sim 1376\text{ cm}^{-1}$ indicates thymidine (C5-CH_3 str, C6-H in-plane bending), and $\sim 1480\text{ cm}^{-1}$ indicates deoxyguanosine/deoxyadenosine (N7-C8 stretching).⁸¹⁻⁸⁴ For the as-produced GNPs and the plasma-treated GNPs, appearance of C=C and C=O stretches were observed at $\sim 1530\text{ cm}^{-1}$ and $\sim 1650\text{ cm}^{-1}$. The weak signal of C=O is due to the natural oxidation of graphene shells in air, which was observed in above XPS study. After plasma treatment, the C=O signal was enhanced, allowing for further covalent immobilization of DNA as shown in Figure 2.6.

FTIR spectrum of GNPs after DNA immobilization shows several main peaks same as that obtained on the pristine λ -DNA (Figure 2.10b), indicating the presence of DNA structures on the plasma-treated GNP substrate. Moreover, the appearance of amide I ($1650\sim 1670\text{ cm}^{-1}$, C=O stretch), amide II and amide III stretches (1550 cm^{-1} and 1240 cm^{-1} , respectively, stretching of C-N and/or bending of N-H) further indicate the formation of covalent bond between $-\text{COOH}$ on the graphene shell and $-\text{NH}_2$ at the end of the λ -DNA fragment.⁸⁵⁻⁸⁷ Representative SEM/TEM images of the DNA-functionalized GNPs heterostructures were shown in Figure 2.11 a-d. One side or both sides of the λ -DNA segments were immobilized on GNPs. AFM was further used for characterizing large-area of GNP-DNA substrate. As shown in Figure 2.11e, most of the DNA

segments were wrapped on GNPs due to the natural van der Waals attraction force.⁸⁸ To further stretch the DNA structure and align the heterostructures in a highly-ordered pattern, the substrate was spin-stretched with the assistant of 1 mM MgCl₂ aqueous solution.⁸⁹ The resulting patterned substrate was shown in Figure 2.11f, indicating highly-ordered alignment of GNP-DNA architectures. Such ordered assembly of GNP-DNA architectures will be of great use and interest in future bio-nano electronic devices, sensors and biopolymer molecule analysis.

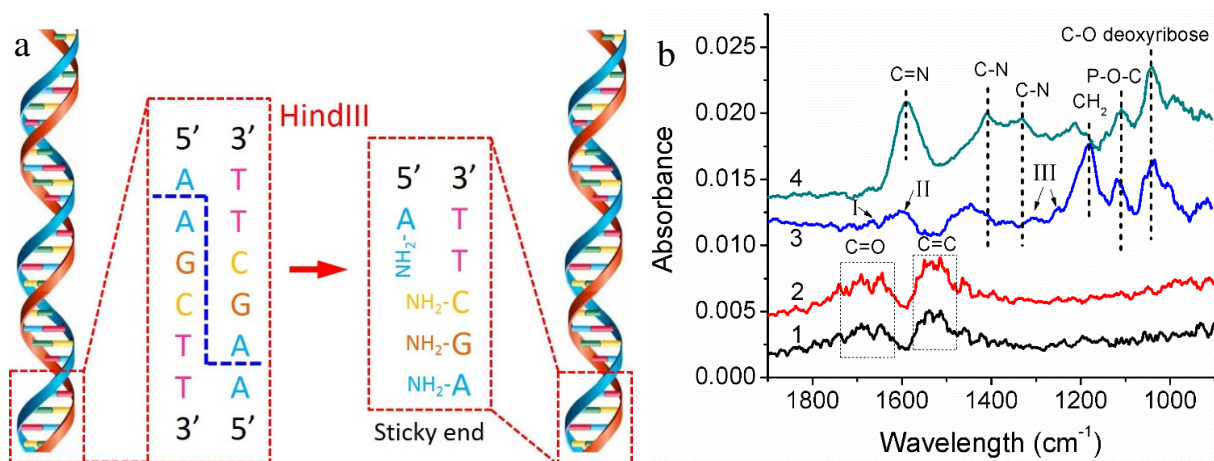


Figure 2.10. (a) Schematic showing the Hind III technique for cleaving λ -DNA into fragments. (b) FTIR spectra of (1) as-produced GNPs, (2) plasma-treated GNPs, (3) covalently-linked GNP-DNA architectures, and (4) Pristine λ -DNA segments.

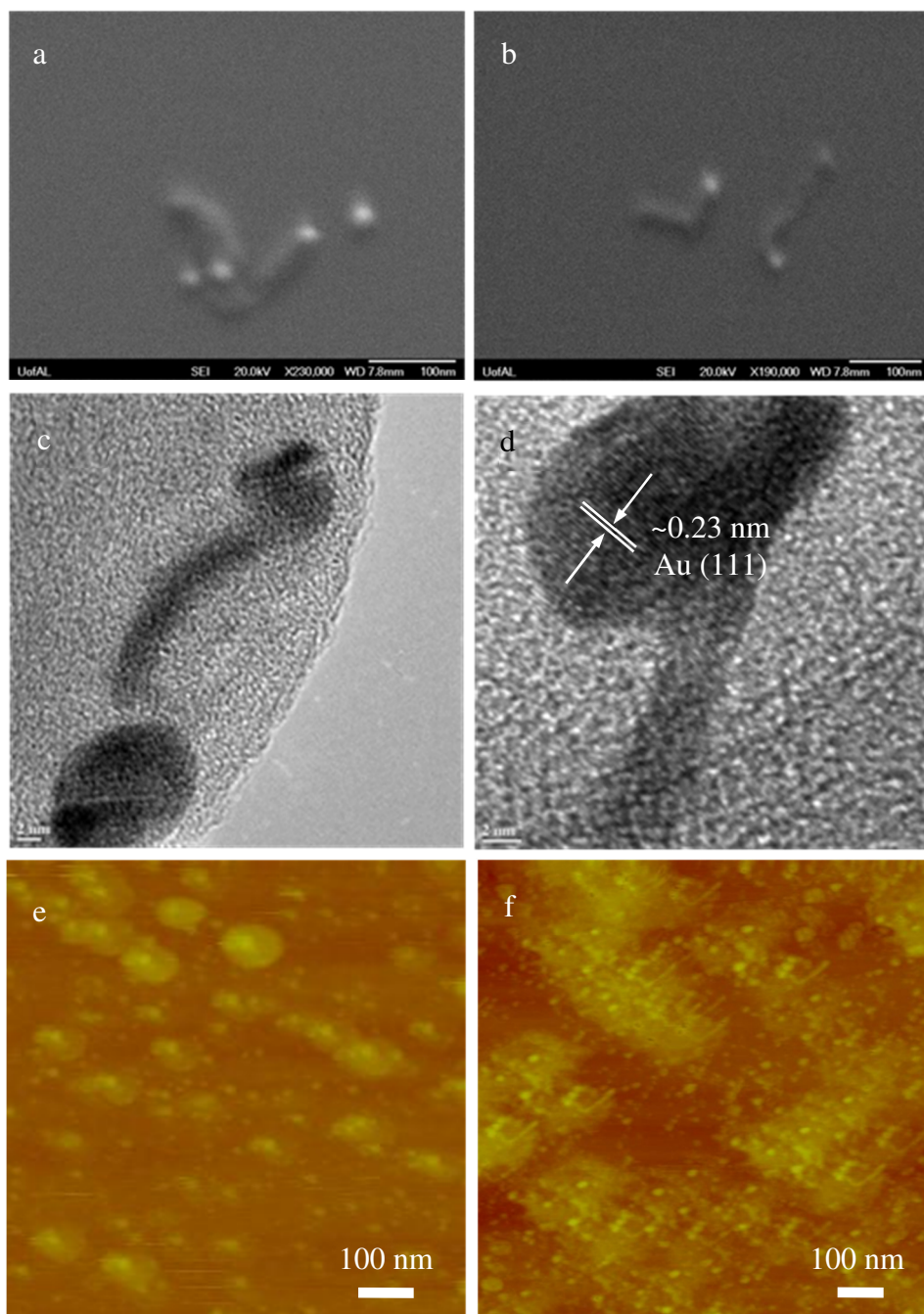


Figure 2.11. SEM images (a,b) and HRTEM images (c,d) of the covalently-linked GNP-DNA architectures. (e,f) AFM images of the GNP-DNA architectures before (e) and after (f) spin stretching with 1 mM MgCl₂.

2.4. Conclusions

In summary, we reported facile approaches for the production of graphene shells-encapsulated gold nanoparticles (GNPs) and their further plasma treatment and bio-functionalization. First, GNPs were obtained *via* a xylene-based CVD process, resulting multilayer graphene shells with a thickness of ~ 3.8 nm encapsulated on gold nanoparticle of ~ 20 nm. Their subsequent structure modification was carried out using oxygen plasma treatment, which was found effective to remove the natural amorphous carbon, reduce the graphene thickness and create the surface functionalities (-COOH, -COH). This opens the possibility of further bio-functionalization *via* the well-defined carbodiimide chemistry. The resulting gold nanoparticles-attached GNPs heterostructures exhibit excellent SERS sensitivity in the detection of trace amount of R6G and MB in water with an enhancement factor of $\sim 10^6$. Highly-ordered assembly of GNP-DNA architectures were also obtained with this manner. Such combination may be of importance in future DNA detection/recognition and other bio-compatible device applications.

CHAPTER 3

PLASMON-ENHANCED PHOTOCATALYTIC DEGRADATION USING NANOSCALE HETEROSTRUCTURES COMPRISED OF GRAPHENE-ENCAPSULATED GOLD NANOPARTICLES AND SEMICONDUCTING QUANTUM DOTS

Yuan Li,¹ and Nitin Chopra^{1,2,}*

¹Metallurgical and Materials Engineering Department, Center for Materials for Information Technology (MINT), The University of Alabama, Tuscaloosa, AL 35487, U.S.A.

²Department of Biological Sciences, The University of Alabama, Tuscaloosa, AL 35487, U.S.A.

***Corresponding Author**

E-mail: nchopra@eng.ua.edu

Tel: [205-348-4153](tel:205-348-4153)

Abstract

We report a facile technique for patterned growth of multilayer graphene shell encapsulated gold nanoparticles (referred as graphene nanoparticles or GNPs) and their surface chemical functionalization for integration with $\text{CdS}_x\text{Se}_{1-x}/\text{ZnS}$ quantum dots. The compositions, morphologies, crystallinity, and surface functionalization of GNPs and their heterostructures with quantum dots were evaluated using microscopic, spectroscopic, and analytical methods. Further, GNPs and their heterostructures were experimentally studied and simulated for the optical properties. Such nanoscale heterostructures demonstrate unique multi-functionality in optics and electronics that makes them of interest for plasmon-enhanced photocatalysis. The heterostructures were used for the photodegradation of phenol and their photocatalytic behavior/mechanism was studied in detail.

Keywords: plasmon-enhanced photocatalysis, multilayer graphene shell encapsulated gold nanoparticles, quantum dots, heterostructures

3.1. Introduction

Efficient photocatalytic degradation of organic pollutants using high-performance nanostructured photocatalysts has been considered as one of the most promising and sustainable strategies for future water cleaning and environment protection [90-92]. Metal oxide semiconductors such as TiO_2 , Fe_2O_3 and Co_3O_4 exhibit good photocatalytic behavior and are mostly used as the preferred photocatalytic materials [93]. Meanwhile, semiconducting quantum dots (QDs) such as CdSe, CdS, ZnS, etc. are another set of interesting photocatalytic materials due to their unique properties such as broad excitation regions, narrow emission areas, size-dependent band gaps, and high extinction coefficients [94]. However, in long-term practical process, these photocatalysts are limited due to their wide band gap, rapid recombination of excited electrons, high over-potential for H_2 production, and/or low chemical stability [95].

The combination of these semiconductor photocatalysts with plasmonic noble metal nanostructures such as gold (Au) and silver (Ag) was recently found to be of interest for band gap modification and catalytic efficiency improvement [96]. The advantages are mainly attributed to the unique optical properties of Au nanostructures such as strong visible absorption and localized surface plasma resonance (LSPR) [97]. Such photocatalytic materials and process have been widely studied and regarded as plasmonic-enhanced photocatalysis [98]. The interactions between Au/Ag nanostructures and quantum dots lead to interesting light-matter interactions and energy transfer processes. Two main mechanisms have been discussed regarding the plasmonic-enhanced photocatalysis: charger transfer and local electric field enhancement. In the former charger transfer mechanism, the plasmon resonance excites electrons in Au or Ag, which are then transferred to the conduction band of the adjacent semiconductors and thus prompt the photocatalytic efficiency. Meanwhile, the local electric field enhancement mechanism is due to the intense local plasmonic

“hot spots”, which significantly increase the amount of photo-induced charger for photocatalytic reaction. Since such plasmonic enhancement involves direct interface charger transfer and meanwhile the generation of local electric field has significant distance dependence, the effective combination of quantum dots and noble metal nanostructures becomes of importance and still is the main challenge for plasmonic-enhanced photocatalysis [99].

Carbon nanostructures such as carbon nanotubes (CNTs), graphene, etc. exhibit a diverse range of surface chemistry necessary for developing hierarchical heterostructures [100]. The combination of these carbon nanostructures with nanoparticles/quantum dots has been performed for defect labeling, sensors, and surface chemical analysis [101]. For instance, chemically-exfoliated graphene wrapped around Au nanoparticles has been reported for biosensors and bioelectronics [102]. However, the corrosive nature of the exfoliation process and the inability of wrapped graphene to form an impervious shell around Au nanoparticles limited their electrical transport and did not completely prevent exposure of the encapsulated Au nanoparticle. Thus, spherical carbon nanostructures such as fullerene, onion-like carbon (OLC), and carbon nanocapsules hold great potential [103]. The morphology, dimension, and surface functionality of spherical carbon nanostructures can result in tunable properties, which can be further modulated by loaded Quantum dots. For instance, hierarchical heterostructures comprised of spherical carbon nanostructures loaded with quantum dots have been reported to be a promising electron donor-acceptor system for energy harvesting [104].

With this regard, a novel configuration is multilayer graphene shell or carbon encapsulated noble metal nanoparticles coordinated with quantum dots. Here, the shell provide a robust surface passivation to the encapsulated Au nanoparticle and also serve as a multifunctional interface between the Au nanoparticle and the bound quantum dots. Past research in the growth of carbon

encapsulated Au nanoparticles has been majorly focused on in-situ TEM based synthesis converting lacey carbon on TEM grids to a graphitic shell around the Au nanoparticles or pyrolysis of polymer coatings around the Au nanoparticles [105]. However, the former method resulted in difficulty in the extraction of hybrid nanoparticles from the TEM grid while the latter approach involved tedious cleaning steps to remove amorphous carbon from around the encapsulated Au nanoparticles. Recently, the authors demonstrated a facile and scalable xylene-based CVD approach for the growth of multilayer graphene shell around Au nanoparticles (referred as graphene nanoparticles or GNPs) [106]. The presence of multilayer graphene shell modulated or improved the optical properties (LSPR) and chemical stability of the Au nanoparticles [107]. Most importantly, this process gives Au nanoparticles enriched carbon-based surface chemistry, allowing their further surface functionalization and heterostructuring.

Herein, we report a facile and controlled approach for the assembly of fluorescent $\text{CdS}_x\text{Se}_{1-x}/\text{ZnS}$ quantum dots onto GNPs (hereafter referred as GNP-QD heterostructures) as efficient photocatalyst for plasmonic-enhanced photodegradation of organics. Uniformly-dispersed Au nanoparticles were formed on a silicon (Si) substrate, followed by the CVD growth multilayer graphene shell as we reported before. Further plasma or acid treatment of the patterned GNPs resulted in carboxylic (-COOH) group derivatization on the multilayer graphene shell. The (-COOH)-derivatized GNPs were covalently and selectively linked with amine (-NH₂)-terminated quantum dots using the well-defined carbodiimide chemistry. The GNP-QD heterostructures were evaluated for their binding chemistry, phases, structure, and morphology using spectroscopic, diffraction, and microscopic methods. Their band gap energies, and their optical, electrical, and photocatalytic properties were also demonstrated in detail.

3.2. Experimental section

Materials and Methods: Si substrate (111) was purchased from IWS (Colfax, CA). Potassium gold (III) chloride was purchased from Sigma-Aldrich (St. Louis, MO). Hydrogen fluoride (~50 wt.%) was purchased from VWR (Atlanta, GA). Ammonium fluoride was purchased from Alfa Aesar (Ward Hill, MA). 1-ethyl-3-(3-dimethylaminopropyl) carbodiimide (EDC), N-hydroxysuccinimide (NHS), and 2-(N-morpholino) ethanesulfonic acid (MES) were purchased from Thermo scientific (Rockford, IL). (-NH₂)-terminated CdSe_xS_{1-x}/ZnS fluorescent quantum dots were purchased from Cytodiagnosics Inc. (Burlington, Canada). All chemicals were used as such. Buffered oxide etch (BOE) solution was prepared by mixing NH₄F and HF in DI-water. DI-water (18.1 MΩ-cm) was obtained from a Barnstead International DI-water system (E-pure D4641). The GNP growth was carried out in a Lindberg blue three-zone tube furnace (Watertown, WI) with the quartz tube purchased from ChemGlass (Vineland, NJ). Oxygen plasma was performed in Nordson March Jupiter III Reactive Ion Etcher (Concord, CA).

Patterning of GNPs on Si substrate and their carboxylic derivatization: Au film was deposited on the Si substrate using an acid-based wet-chemical method [113]. In this method, cleaned Si substrate was treated with BOE solution to remove the surface oxide layer. This was followed by immersing the substrate in an acidic solution comprised of ~1 mM KAuCl₄ and 1% HF. This reaction resulted in Au film (~20 nm thick) on the Si substrate. The substrate was washed with DI-water, dried, and annealed in air for 15 min at 850 °C to dewet Au film that resulted in Au nanoparticles patterned on the Si substrate.

CVD process was employed for the growth of multilayer graphene shell. First, Au nanoparticles patterned on Si substrate were treated with oxygen plasma for 15 min to result in surface gold

oxide. This was followed by CVD growth of multilayer graphene shell between 600 and 700 °C for 1 h. Xylene was utilized as the carbon source. The carrier gas was H₂/Ar with a flow rate of 1.15 SLM. This process resulted in patterned growth of GNPs on the Si substrate. The -COOH derivatization on the GNPs was carried out by treating the as-grown GNPs with oxygen plasma for 15 s. In order to compare the plasma oxidation-based derivatization process, nitric acid treatment was also carried out for the as-produced GNPs. This involved treatment of the Si substrate with patterned GNPs in a 3 M HNO₃ solution at 60 °C for 5 h.

Covalent binding of quantum dots on the patterned GNPs: The binding approach employed the well-established carbodiimide chemistry [108]. The Si substrate patterned with (-COOH)-terminated GNPs was immersed in a ~50 mM MES buffer solution with ~2 mM EDC and incubated for 10 min. This was followed by the addition of ~4 mM NHS. This process allowed the formation of a stable amine-reactive NHS ester. The substrate was washed with PBS buffer (pH = 7.4) and then immersed in the same solution containing 2 mM quantum dots. This reaction continued for 12 h to form amide bonds (-CONH-) between the GNPs and quantum dots, resulting in covalently linked GNP-QD heterostructures. Finally, the substrate with patterned assembly of GNP-QD heterostructures was washed with DI-water and dried in N₂. This washing step removed physically adsorbed quantum dots from the surface of Si substrate and patterned GNPs.

Optical properties, plasmonic modeling and photocatalytic degradation of phenol: The optical transition energy for the pristine quantum dots and the GNP-QD heterostructures was further determined using equation (3.1) [109],

$$ah\nu = A(h\nu - E_g)^n, \quad (3.1)$$

where a is absorbance coefficient, A is a constant, $h\nu$ is the energy of light and n is a constant depending on the nature of the electron transition (n is 1/2, 2, 3/2 and 3 for allowed direct, allowed indirect, forbidden direct and forbidden indirect transitions, respectively). CdS_xSe_{1-x}/ZnS quantum dots have been reported as an allowed direct band gap semiconductor [110]. Thus, the optical band gap energies were calculated by extrapolating the linear portion of the Tauc plots [$(ah\nu)^2$ vs. $h\nu$] to the $h\nu$ -axis where $(ah\nu)^2 = 0$.

Discrete dipole approximation (DDA) method was used to simulate the plasmonic properties (scattering and absorbance) of the as-produced Au nanoparticles, GNPs (before and after plasma treatment), and GNP-QD heterostructures. This method is based on the solution of the 3D Maxwell equation *via* the DDSCAT code developed by Draine and Flatau [111]. Detailed simulation procedures have been demonstrated earlier by the authors [107]. Briefly, DDSCAT 7.2 was utilized to estimate the normalized electric field or surface plasmon generation for all these mentioned samples or targets. The normalized electric field intensity is defined as the ratio between the electric field generated near the target surface and the incident electric field ($|E|/|E_0|$). The geometrical targets were generated using 3D max software for various simulated nanostructures. The effective radius of the dipoles was calculated using: $r_{\text{eff}} = (3V/4\pi)^{1/3}$, where V is the total volume of the target and is calculated with $V = Nd^3$ (N is the number of dipoles and d is the lattice spacing in cubic array).

To demonstrate the plasmonic-enhanced photocatalysis, Si substrates (2 cm × 2 cm) patterned with the as-produced GNPs, or GNP-QD heterostructures were sonicated to disperse the nanostructures in DI-water. In the following, ~0.2 mL of phenol (3 mM) was added into these nanostructure suspensions and sonicated for another 1 min. This was followed by further addition of ~0.1 mL H₂O₂ (37%) as the sacrificial agent [112]. A UV illumination lamp (~254 nm, 8W) was utilized as

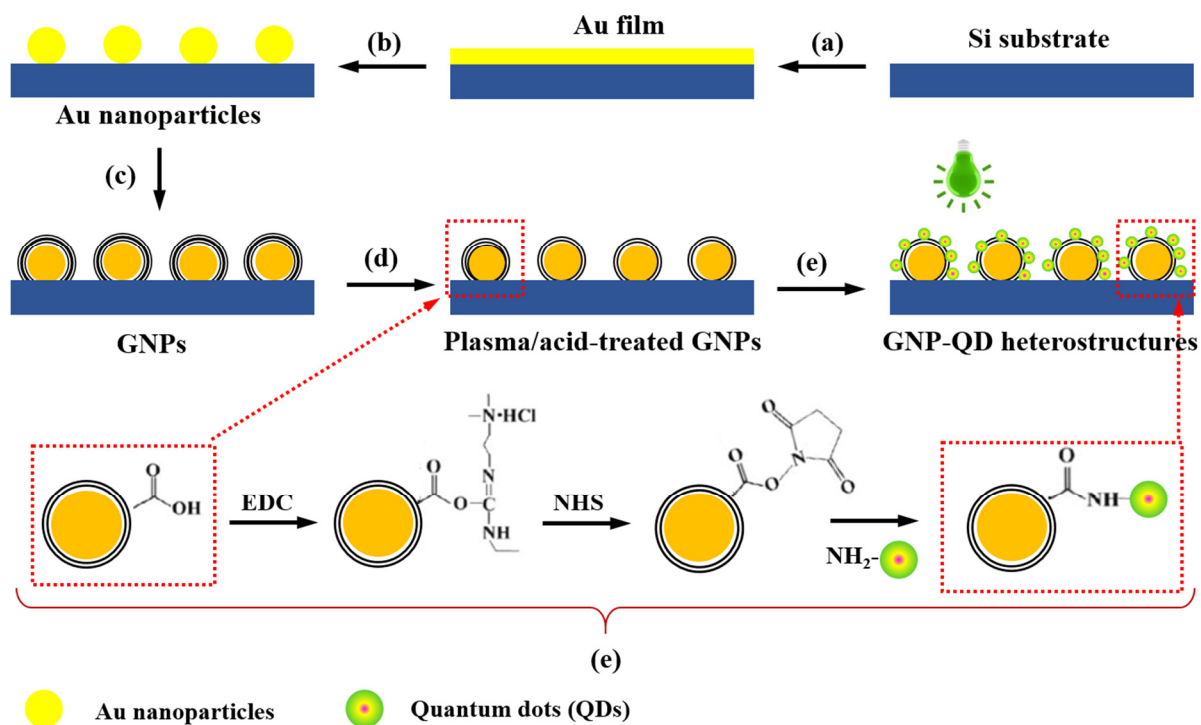
the light source and the solution was gently stirred during the photodegradation experiment. At 30 min intervals, the solution was centrifuged and UV-vis spectra for the supernatant were recorded to estimate the concentration of phenol. The samples were re-dispersed in the supernatant and the degradation experiment and analysis was conducted for 6 h. The same photodegradation process was also conducted using the pristine quantum dots as comparison.

Characterizations: FE-SEM (JEOL-7000) and Tecnai F-20 TEM were used to characterize the morphology, crystal structure, and/or interfaces present in Au nanoparticles, as-produced GNPs, and GNP-QD heterostructures. X-ray photoelectron spectra (XPS) were gathered by a Kratos Axis 165 with a mono-aluminum gun at 160 eV pass energy for full range scan and 40 eV pass energy for detailed scan. Raman spectra were collected using the Bruker Senterra system (Bruker Optics Inc.). A neon laser with wavelength of 785 nm and power of 10 mW was used. The integral time and co-additions were 15 s and 2, respectively. FTIR spectra were obtained on a Nicolet 4700 FTIR instrument. The UV-vis absorbance spectra were obtained using a DH-2000 UV-VIS-NIR light source. Fluorescence images were captured using the Zeiss Axiovert 200 Inverted Fluorescence Microscopy with an excitation wavelength of ~490 nm. The electrical characterization (I-V test) of the Si substrates patterned with various nanostructures was carried out using a two-point probe micromanipulator set-up equipped with Keithley source meters.

3.3. Results and discussion

Scheme 3.1 (steps a-e) outlines the approach for the patterned growth of GNPs, their surface functionalization, and attachment with quantum dots. This involves the following steps: (a) Deposition of Au film on a Si substrate, (b) high-temperature annealing and dewetting of Au film

to result in Au nanoparticles patterned on the Si substrate, (c) CVD growth of multilayer graphene shell on plasma-oxidized Au nanoparticles (patterned GNPs formation), (d) plasma oxidation or acid treatment of patterned GNPs to create carboxylic (-COOH) functionalities on the multilayer graphene shell, and (e) covalent binding of quantum dots on GNPs to result in the GNP-QD heterostructures. Carbodiimide chemistry (Scheme 3.1, step e) was used to link -COOH (on GNPs) with -NH₂ (on quantum dots) *via* the formation of amide bonds.



Scheme 3.1. Schematic representation of GNP-QD heterostructure fabrication on Si substrate.

3.3.1. Synthesis and chemical modification of GNPs

Wet-chemical approach and thermal annealing process were utilized for patterning Au nanoparticles onto the Si substrate. Au film was first deposited onto the Si substrate by treating the latter in a solution of HF and gold salt. This Au film formation is attributed to an electroless mechanism, where Au^{3+} replaces Si atoms of the substrate as follows [113]:



In the following, The Au film was dewetted at a high temperature ($\sim 850^\circ\text{C}$) to result in uniform dispersion or patterning of Au nanoparticles (Figure 3.1a) on the Si substrate. This approach circumvented the challenges associated with the patterning of metal nanoparticles using chemical and nanofabrication techniques [114]. The dewetting process is known to involve void/defect formation and vacancy nucleation at the interface of Au film and Si substrate and is responsible for minimal surface energy and stable shape and size of the patterned nanoparticles. Au nanoparticles patterned on the Si substrate were then plasma oxidized to create a surface gold oxide and further utilized for the xylene-based CVD growth of multilayer graphene shell around Au nanoparticles (Figure 3.1b). This approach resulted in uniformly-patterned growth of multilayer graphene shell-encapsulated Au nanoparticles (referred as GNPs) on the Si substrate. The inset in Figure 3.1b shows the presence of graphene shell around the Au nanoparticle as compared with the inset in Figure 3.1a, which shows the bare as-dewetted Au nanoparticle.

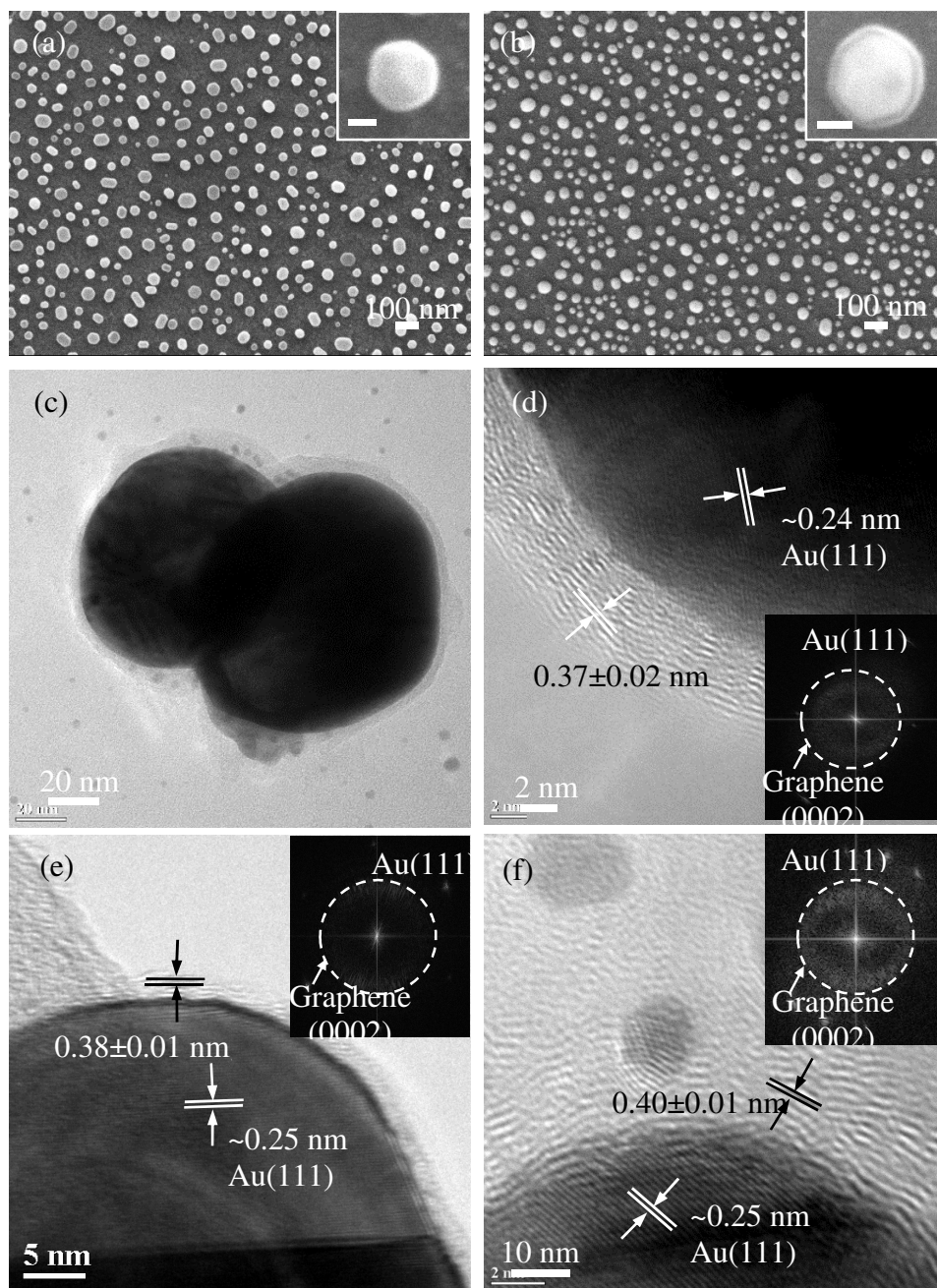


Figure 3.1. SEM images for the as-produced and uniformly-patterned Au nanoparticles (a) and GNPs (b). The insets show high-resolution SEM images (scale bar: 25 nm). TEM images of the as-produced GNPs (c and d), GNPs after plasma treatment (e) and acid treatment (f). The insets show corresponding FFT images indicating diffraction of carbon and gold.

High resolution TEM images indicate (Figure 3.1c and d) the multilayer graphene shell encapsulated on the Au nanoparticles. Inter-spacing between the carbon layers in the shell was observed to be $\sim 0.37 \pm 0.02$ nm. This is slightly larger than the c-axis lattice spacing of graphite (~ 0.34 nm) and could be attributed to the strains existed in the arcuate graphene shell [115]. The average thickness of the multilayer graphene shell for as-produced GNPs was $\sim 3.8 \pm 0.2$ nm. In addition, it was observed that dewetted Au nanoparticles before CVD growth have an average diameter of $\sim 47.3 \pm 11.3$ nm with an inter-particle spacing of $\sim 49.5 \pm 16.8$ nm on the Si substrate. A minor increase in the average nanoparticle diameter ($\sim 52.2 \pm 11.3$ nm, including shell thickness) and a slight decrease in inter-particle spacing to $\sim 45.1 \pm 13.3$ nm were observed for GNPs after CVD growth.

Since it was intended to create surface functionalities on GNPs, the substrates with patterned GNPs were treated in acid or oxygen plasma to result in -COOH groups on the multilayer graphene shell. These -COOH groups could facilitate diverse carbon chemistry, which will be of use in modifying surface structure, creating new functionalities, and improving the purity of GNPs [116]. GNPs after acid or plasma treatment remained intact and patterned on the Si substrates. As shown in Figure 3.1e, plasma oxidation (performed for 10 s) resulted in significant etching of multilayer graphene shell and the shell thickness was decreased to $\sim 0.8 \pm 0.2$ nm. The carbon lattice spacing for plasma-treated GNPs was observed to be $\sim 0.38 \pm 0.02$ nm. The nitric acid treatment had lesser influence on the shell thickness ($\sim 3.4 \pm 0.3$ nm) while lattice spacing increased to $\sim 0.40 \pm 0.01$ nm (Figure 3.1f). The minor increase in the carbon lattice spacing after plasma or acid treatment could be attributed to the removal of carbon layers from the shell and the subsequent strain relaxation within the carbon layers [117].

A decrease in GNP diameters observed after the plasma/acid treatment is due to the etching of multilayer graphene shell. Meanwhile, negligible changes in inter-particle spacing were observed. With minor differences in spatial density of nanoparticles on the Si substrate, a decreasing trend was observed as follows: Si substrate patterned with Au nanoparticles > Si substrate patterned with GNPs ~ Si substrate patterned with plasma-treated GNPs > Si substrate patterned with acid-treated GNPs. The CVD growth process involved Ostwald's ripening and Au surface migration, and thus resulted in a slight decrease in nanoparticle spatial density as compared to that before CVD growth. Overall, both plasma and acid treatment processes demonstrate a unique approach for surface modification of patterned GNPs and control of the shell thickness. In this regard, the plasma treatment is preferred because of its dry and non-corrosive features for functionalization or etching of the multilayer graphene shell.

Raman spectra of the as-produced GNPs (Figure 3.2a) showed the well-defined G band at $\sim 1595\text{ cm}^{-1}$ and D band at $\sim 1310\text{ cm}^{-1}$. The D band in GNPs was observed due to the curvature-induced disorder in the multilayer graphene shell and the existence of amorphous carbon while the G band is a significant indicative of the sp^2 hybridized carbon atoms from the graphitized structure [118]. Overall, the peak location of G band for treated or untreated GNPs was different from that for the flat graphene ($\sim 1580\text{ cm}^{-1}$). Such shifts in Raman peaks have been attributed to strains in the multilayer graphene shell lattice, shell thickness, and the size of GNPs. The acid or plasma treatment of GNPs resulted in a red shift of the G band and D band. The estimated intensity ratio of the D band and G band (I_D/I_G) changed from $\sim 1.34 \pm 0.21$ to $\sim 1.25 \pm 0.30$ after acid treatment due to the purification of GNPs. On the other hand, the plasma treatment significantly decreased the intensity of the D band and G band, indicating this process was more rigorous than acid purification [119]. This observation was also proved by the TEM result (Figure 3.1e). The

estimated I_D/I_G ratio for plasma-treated GNPs was $\sim 1.75 \pm 0.25$, which indicates that this process led to more defects and disordered structure within the multilayer graphene shell.

To better understand the plasma/acid treatment process, XPS studies were performed for Au nanoparticles, surface oxidized Au nanoparticles, and GNPs (before and after acid/plasma treatment) [120]. XPS survey scans ranging between 0 eV and 1000 eV indicated the presence of various elements such as Au, C, O, and Si. The Si peaks arise due to the substrate. For O 1s peaks, there could be several origins, such as absorbed molecules and native oxide (SiO_2) from the substrate. So, O 1s peaks should not be utilized for analyzing plasma oxidized Au nanoparticles and surface-modified GNPs. For the as-prepared Au nanoparticles, pure element Au peaks consistent with Au $4f_{7/2}$ and Au $4f_{5/2}$ were observed at ~ 84.59 eV and ~ 88.27 eV, respectively. After the plasma oxidation of Au nanoparticles, two new and additional peaks corresponding to surface gold oxide at ~ 85.34 eV and ~ 88.90 eV emerged. These two additional peaks disappeared after the GNP growth but re-emerged after the plasma treatment. However, these two oxide peaks were not observed after the acid treatment. This further confirmed the rigorosity of the plasma treatment process, which must have partially exposed some Au nanoparticles (see Figure 3.1e) and surface oxidized them.

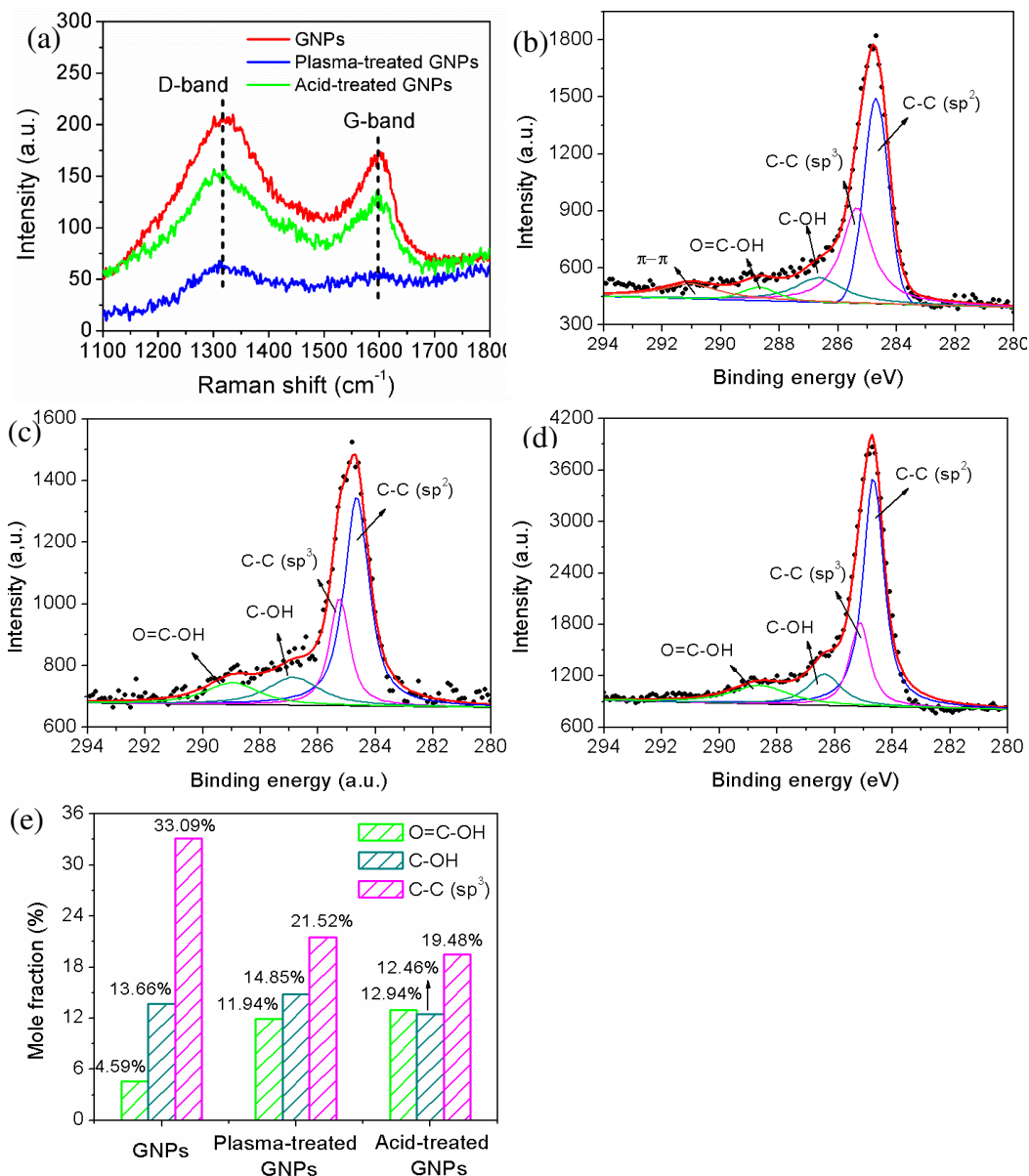


Figure 3.2. (a) Raman spectra of the as-produced GNPs, GNPs after plasma, and GNPs after acid treatment. (b-d) Deconvoluted XPS spectra (C 1s) for as-produced GNPs (b) and GNPs after plasma treatment (c) and acid treatment (d). (e) Surface chemical groups (-COH, -COOH, and C-C) for GNPs before and after plasma/acid treatment estimated using C 1s peaks observed in XPS results. *NOTE: The scatters in (b-d) show the XPS results and the solid lines show the fitted data.*

XPS C 1s peak was evaluated for the as-produced GNPs as well as GNPs after plasma or acid treatment (Figure 3.2b-d). This peak is asymmetric with long tail extending to the higher energy region and has been explained in terms of the metallic conduction electron interactions induced by low energy electron-hole excitations resulting from the absorption of X-rays. Further deconvolution of C 1s peak showed five Gaussian peaks centered at $\sim 284.7 \pm 0.1$ eV (C-C in sp^2), $\sim 285.2 \pm 0.2$ eV (C-C in sp^3), 286.6 ± 0.2 eV (-COH), 288.7 ± 0.2 eV (-COOH), and 291.2 eV (π - π^* transition loss peak). The peak at ~ 291.2 eV corresponds to the electron energy loss peak due to the π -plasmon excitations. The delocalized π -conjunctions are attributed to graphene and also reported to disappear with increasing oxidation [121]. This phenomenon was also observed for GNPs after acid or plasma treatment in this study (Figure 3.2c and d). Moreover, electronegative oxygen atoms induce positive charges to carbon atoms, thus peaks with high binding energies located at ~ 286.6 eV and ~ 288.7 eV are considered to originate from carbon-oxygen links, corresponding to -COH and -COOH groups, respectively. The peak at ~ 285.2 eV was attributed to the photoelectrons emitted from the diamond-like carbon atoms hybridized *via* the sp^3 bond. This has been reported as evidence for the presence of amorphous carbon resulting from the CVD growth of carbon materials [122]. Meanwhile, the peak at ~ 284.7 eV is associated with the hexagonal carbon atoms in sp^2 hybridization. As a result, the area ratio of C-C sp^2 and sp^3 peaks is an indicative of degrees of graphitization.

Figure 3.2e show the percentages of various functional groups (-COH, -COOH, and sp^3 hybridized C-C) estimated using the deconvoluted C 1s spectra for GNPs before and after plasma or acid treatment. The presence of carbon-oxygen groups (-COOH and -COH) before treatment of GNPs could be attributed to the absorption of water vapor and the contamination due to air exposure [123]. The content of sp^3 C-C bonds was considerably decreased after the plasma and acid

treatment, indicating both approaches improved the quality of graphitic carbon in GNPs, which further supports the microscopic and Raman spectroscopy results (Figure 3.1d-f and Figure 3.2a). Moreover, negligible changes in -COH groups were observed before and after the plasma or acid treatment of GNPs. However, the -COOH groups percentage increased from ~4.5%, for the as-produced GNPs, to 11%-12% after plasma or acid treatment. It must be noted that -COOH groups were most critical for further chemical functionalization of GNPs. Overall, a 15 s plasma oxidation of GNPs was much more rigorous and controlled as compared to the 5 h acid treatment. In addition, the former provides a dry processing route and results in thinner graphene shell (< 1 nm).

3.3.2. Fabrication of GNP-QD heterostructures

Chemical functionalization of GNPs with surface -COOH groups facilitated their combination with (-NH₂)-terminated QD (referred as GNP-QD heterostructures) by using the well-established carbodiimide linking chemistry (Scheme 1). This process mainly involves the formation of covalent amide bonds between GNPs and quantum dots, as illustrated in Figure 3.3a [5,124]. Both, acid- and plasma-treated GNPs were utilized for fabricating GNP-QD heterostructures. FTIR was used to study the surface functional groups for various samples including (1) as-produced GNPs, (2) acid-treated GNPs, (3) plasma-treated GNPs, (4) acid-treated GNPs linked with Quantum dots, and (5) plasma-treated GNPs linked with quantum dots (Figure 3.3b). Spectra for all these samples (Figure 3.3b) shows broad peaks within 1510-1540 cm⁻¹, which is corresponding to the stretching of C-C bonds and/or C-H bonds on multilayer graphene shell [5]. Peaks for -COH stretch was observed at ~1450 cm⁻¹ for all the samples. Meanwhile C=O stretches originated from the surface carboxylic groups were observed at ~1690 cm⁻¹ after plasma or acid treatment [125]. These

observations show a good consistence with the XPS results in Figure 3.2e. Further, after carbodiimide-based linking of quantum dots on GNPs, FTIR spectra show the emergence of amide I, II, and III peaks (Figure 3.3a) at $1650\sim 1670\text{ cm}^{-1}$, $1550\sim 1570\text{ cm}^{-1}$, and $1230\sim 1240\text{ cm}^{-1}$ [126]. This further confirms the presence of covalent amide bonds (-CONH-) between the (-NH₂)-terminated quantum dots and (-COOH)-terminated GNPs. Amide I band appeared around $\sim 1660\text{ cm}^{-1}$ was assigned to the C=O stretch. Amide II and III bands appeared at 1550 cm^{-1} and 1240 cm^{-1} were attributed to the stretching of C-N and/or blending of N-H, respectively.

The approach of functionalizing GNPs and linking with quantum dots was achieved directly on the Si substrate and the processes resulted in patterned GNP-QD heterostructures (Figure 3.3c-e). Prior to microscopic evaluations, substrates were washed with DI-water to remove non-specifically bound or physically-adsorbed quantum dots. Although difficult to differentiate, a careful examination of SEM images shows small aggregated dots around plasma- or acid-treated GNPs (Figure 3.3c and d). This was not observed for the as-produced GNPs that only immersed in a quantum dots solution but without processing the carbodiimide chemistry (Figure 3.3e), suggesting that surface -COOH groups on GNPs and carbodiimide-based linkages were critical for fabricating GNP-QD heterostructures. These observations were supported by fluorescence microscopy of the respective samples, where quantum dots were observed as green dots (excitation $\lambda \sim 365\text{ nm}$ and emission $\lambda \sim 490\text{ nm}$, Figure 3.3f and g), which were absent in the case of the as-produced GNPs with no functional chemistry (Figure 3.3h). In other words, functional chemistry on patterned GNPs provides a unique route to not only assemble quantum dots but also was proved to be a selective tagging approach.

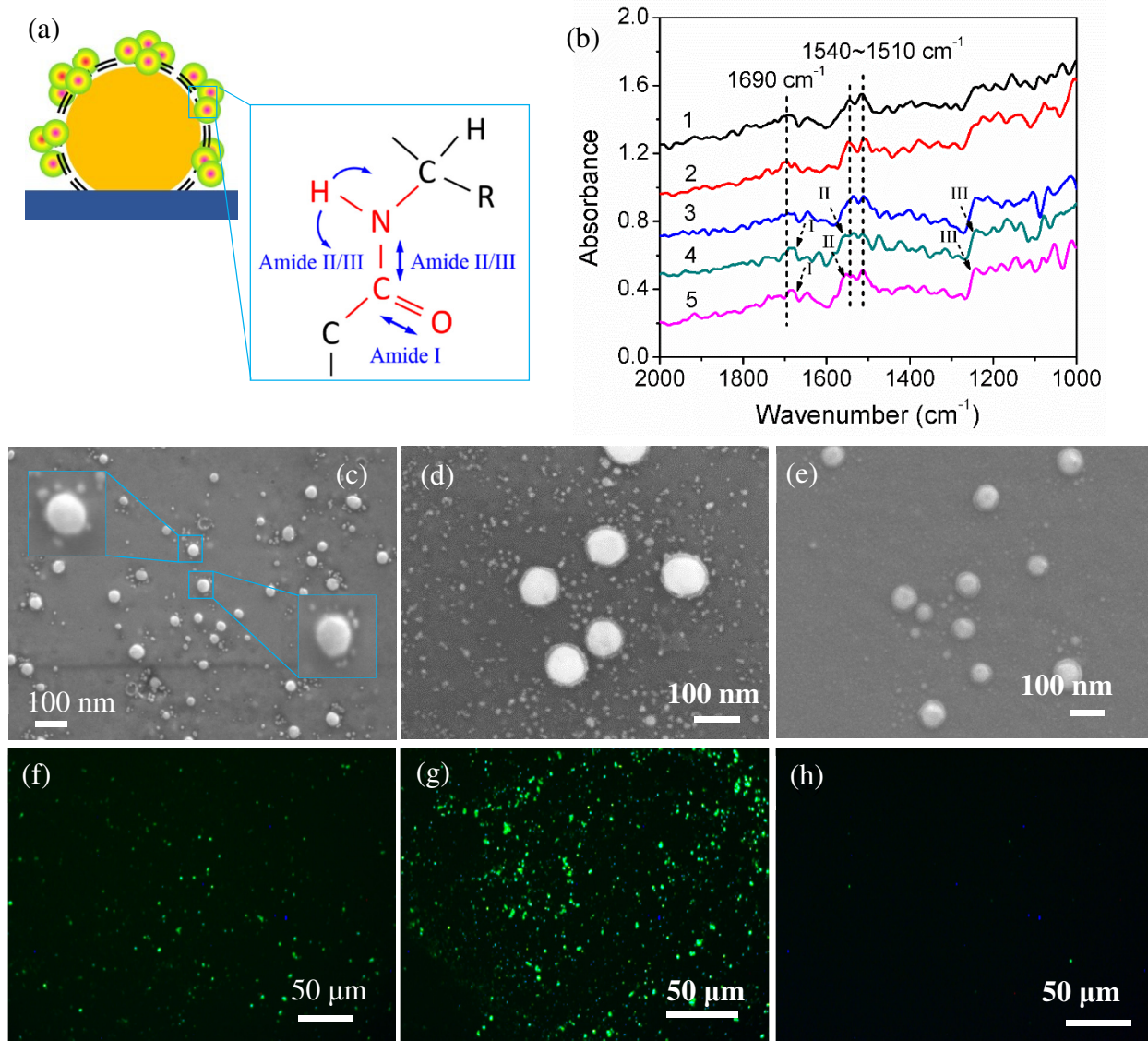


Figure 3.3. (a) Schematic of the GNP-QD heterostructures and the necessary amide bonds formed between GNPs and quantum dots. (b) FTIR spectra of (1) as-produced GNPs, (2) GNPs after plasma treatment, (3) GNPs after acid treatment, (4) GNP(plasma-treated)-QD heterostructures, and (5) GNP(acid-treated)-QD heterostructures. SEM images of the GNP-QD heterostructures fabricated using (c) plasma- and (d) acid- treated GNPs. (e) Control sample that used as-produced GNPs with no -COOH surface derivatization for physically binding with quantum dots. (d-f) Fluorescence images corresponding to samples (c-e).

High resolution TEM images (Figure 3.4a-c) demonstrate GNPs coated with quantum dots (diameter ~4 nm, lattice spacing ~0.35 nm). Pristine quantum dots showed similar size and lattice spacing, which helped in differentiating quantum dots from GNPs in the TEM analysis (Figure 3.4). Approximately, ~22% of the GNP surface was covered with quantum dots. Electron diffraction, EDS spectra, and scanning transmission electron microscopy (STEM)-mode line profile showed the crystal structure, chemical composition, or elements present in the GNP-QD heterostructures (Figure 3.4d-g). This provides another strong evidence for the effective linking of quantum dots on the surface of GNPs and, at the same time, indicates that GNPs and quantum dots were structurally and chemically intact in the heterostructures. To further confirm this EDS elemental study, XPS analysis of the quantum dots and GNP-QD heterostructures was conducted. The XPS survey scans of the pristine quantum dots and the covalently-linked GNP-QD heterostructures. Different elements such as Cd, Zn, S, O, C, and Au were observed [127]. Deconvoluted spectra for Cd, Se, Zn and S for the quantum dots were evaluated. Cd peaks consistent with Cd 3d_{3/2} and Cd 3d_{5/2} were observed at ~412.78 eV and ~406.07 eV, respectively. These were slightly shifted from ~405.0 eV and ~411.7 eV of the standard peak of pure Cd element due to the sulfuration (formation of CdS). Similarly, Zn peaks corresponding to Zn 2p_{1/2} and Zn 2p_{3/2} were observed at ~1045.76 eV and ~1022.52 eV, which were also shifted from standard peaks of pure Zn (~1044.8 eV and ~1021.8 eV) due to the sulfuration. For S peaks, S 2p_{1/2} and S 2p_{3/2} were observed at 163.94 eV and 162.75 eV. These values were also shifted from standard S peaks (~165.1 and ~163.9). No obvious peaks were observed for Se or were not detected due to instrumental limitations. This suggests that Se content in the quantum dots was negligible and the configuration can be recognized as CdS/ZnS structure. It also needs to mention that insignificant

shifts were observed for peaks corresponding to quantum dots after covalent binding with GNPs, which further confirms that all the components in the heterostructures remains chemically intact.

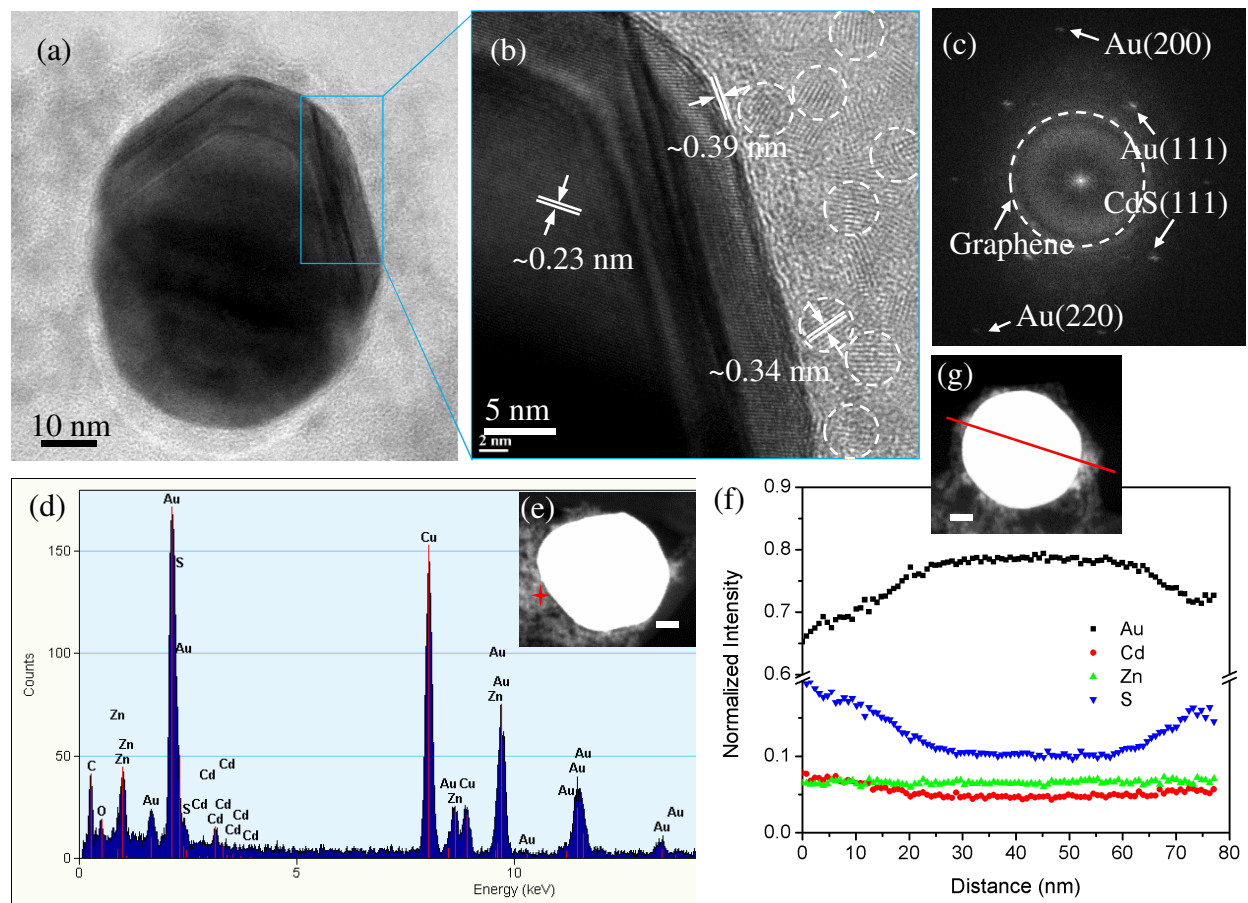


Figure 3.4. (a, b) TEM images of the GNP-QD heterostructures formed on the plasma-treated GNPs. (c) FFT image corresponding to (b). (d and e) Representative STEM mode spot EDS analysis and (f and g) STEM mode EDS line profile analysis of the GNP-QD heterostructures. *Note: The dotted circles in (b) indicate quantum dots and the red spot and line in (e) and (g), respectively, shows the analysis spot and line for EDS profiling.*

3.3.3. Optical properties of GNPs and GNP-QD heterostructures

UV-vis absorbance spectra (Figure 3.5a) for Au nanoparticles, GNPs, and GNPs after plasma or acid treatment were studied. The inset in Figure 3.5a shows the sample dispersions in DI-water. Bare Au nanoparticles resulted in characteristic visible absorption peak ~ 546 nm. After the GNP formation and their acid or plasma treatment, absorbance peaks centered at ~ 280 - 293 nm and ~ 500 - 650 nm were observed. The former peak is associated with the presence of multilayer graphene shell and attributed to the π - π^* transition of electrons in the aromatic double bonds [128]. The latter peak (~ 500 - 650 nm) is due to the encapsulated Au nanoparticles. The shift of such broad peak is hard to comment but overall no significant shift can be estimated after the multilayer graphene shell encapsulation or after the acid or plasma treatment of GNPs. Thus, one can understand that the presence of multilayer graphene shell around Au nanoparticles and their further acid/plasma treatment did not suppress the optical properties (e.g. surface plasmon resonance) of the latter, which is consistent with the simulated absorption spectra for GNPs with approximately similar size and shell thickness.

Plasma-treated GNPs were utilized for fabricating GNP-QD heterostructures and the UV-vis spectra of the latter (Figure 3.5c) shows broadened and red-shifted Au absorption peak (~ 580 nm) and graphene absorbance peak (~ 305 nm) with respect to the plasma-treated GNPs. This could be attributed to the attachment of quantum dots, which enhanced the absorbance spectrum of GNPs and lowered the absorbed energy [129]. The peak corresponding to quantum dots was observed at ~ 460 nm and remained unchanged from that of the pristine quantum dots [130]. In addition, a control sample was studied for absorbance peaks, where quantum dots were physically mixed with plasma-treated GNPs. For this control sample the Au absorption peak was remaining at ~ 500 - 650 nm and no significant shift was observed with respect to the plasma-treated GNPs. Digital images

for these samples were also put as inset for further confirmation. This absorbance property study indicates that quantum dots have a strong interaction with Au nanoparticles when covalently linked with GNPs, where multilayer graphene shell acted as a unique interface between Au nanoparticles and quantum dots.

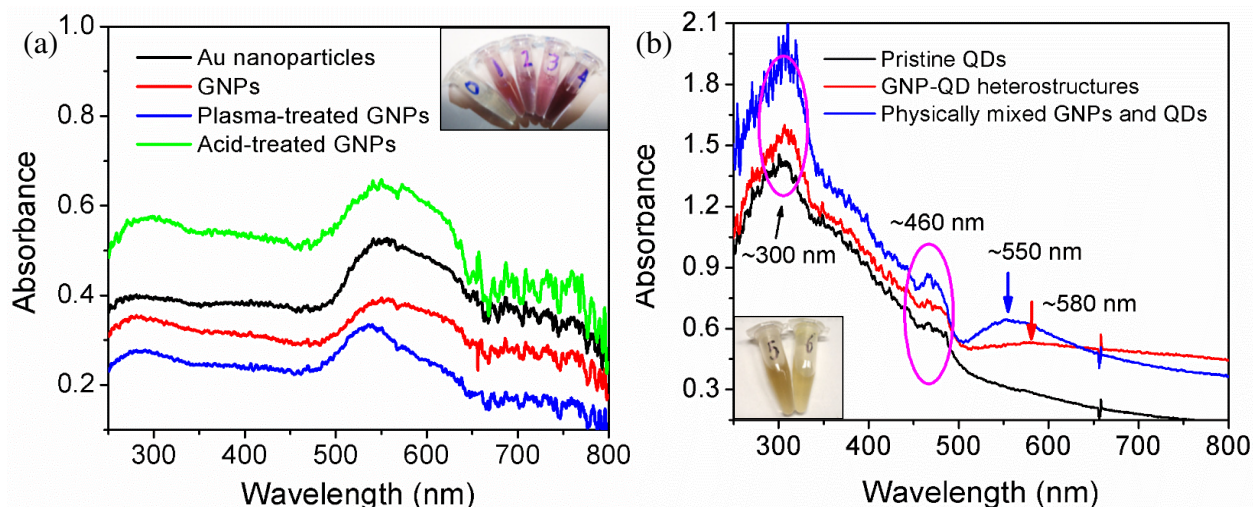


Figure 3.5. (a) UV-vis spectra for Au nanoparticles, as-produced GNPs, and GNPs after plasma and acid treatment. (b) UV-vis spectra of pristine quantum dots, GNP-QD heterostructures, and physically mixed GNPs and quantum dots. *Note: The insets showing digital images of (0) dispersed pristine quantum dots, (1) Au nanoparticles, (2) as-produced GNPs, (3) plasma-treated GNPs, (4) acid-treated GNPs, (5) physically mixed GNPs with quantum dots, and (6) GNP-QD heterostructures.*

Previous simulation studies have shown that the resonance peak of Au nanoparticle encapsulated within multilayer graphene shell varies within a broad range (~527-663 nm) according to the size and shell thickness of GNPs [107]. And the scattering component of the extinction efficiency spectra was negligible for the small-sized GNPs (< 50 nm). Thus, the optical properties of Au nanoparticles, GNPs (before and after plasma treatment), and the GNP-QD heterostructures were further simulated and compared using the Discrete Dipole Approximation (DDA) through the

available DDSCAT code (version 7.2). These targets were comprised of an arrangement of dipoles for which extinction spectra and normalized electric field distributions were numerically solved. It is important to mention here that the quantum dot target was only comprised of CdS/ZnS core/shell structure as Se content was negligible. UV-vis reflectance and absorbance spectra were collected for the pristine quantum dots and further utilized to estimate effective refractive index (real and imaginary components) [131] for the quantum dots. The spherical targets (Figure 3.6a-h) were derived by considering experimental Au nanoparticle size (~50 nm), multilayer graphene shell thickness (~3.8 nm for as-produced GNPs or 0.8 nm for plasma-oxidized GNPs), and size of quantum dots (~4 nm). Quantum dots were assumed to be closely-packed around the GNPs. The surrounding environment was set as water, which is nearly consistent with the experimental UV-vis spectroscopy study (Figure 3.5).

The extinction efficiency is given by a combination of scattering and absorption components as follows:

$$Q_{ext} = Q_{sca} + Q_{abs}, \quad (3.2)$$

where Q_{ext} is the extinction efficiency factor, Q_{sca} is the scattering efficiency factor and Q_{abs} is the absorbance factor. The extinction spectra (Figure 3.6i) were deconvoluted into absorbance and scattering spectra. DDA calculations for bare Au nanoparticles resulted in extinction efficiency peak at ~538 nm [132]. Another peak in the UV region (~270 nm) was observed for bare Au nanoparticles and could be attributed to the interband transition because of the excitation of d electrons [133]. This peak was significantly suppressed for experimental absorbance (Figure 3.5a) probably due to the difference in dielectric environment in experiment and simulation, where the latter presented an ideal environment. For the as-produced GNPs with a shell thickness of ~3.8

nm, insignificant suppression of Au absorption peak (~562 nm) was observed but this peak was red shifted with respect to the bare Au nanoparticles. The red shift is attributed to the presence of multilayer graphene shell. This observation is hard to comment on the experimental UV-vis spectra (Figure 3.5a) due to the broad peak feature. After plasma treatment, this peak shifted back to ~540 nm due to the etching of graphene shell. Moreover, The Au absorption peak of GNP-QD heterostructures show minor intensity increase and slight red-shift (~543 nm) with respect to bare Au nanoparticle, indicating the light-matter interaction happened between Au nanoparticle, graphene shell and the attached quantum dots.

For all the targets simulated here, the scattering component was significantly suppressed as compared to the absorption component. This is due to the defect-free target structure and their significantly smaller size relative to incident wavelength [134]. As reported earlier [135], when nanoparticles are much smaller compared to the wavelength of incident light, the scattering is in the Rayleigh regime. In that case, the scattering (Q_{sca}) can be written as:

$$Q_{sca} = \frac{8\pi}{3} k^4 R^6 F(m) \quad (3.3)$$

where $k = \frac{2\pi}{\lambda}$ (λ is the wavelength), R is the radius of the particles, and $F(m)$ is a function of the refractive index (m). The absorption (Q_{abs}) can be written as:

$$Q_{abs} = 4\pi k R^3 E(m) \quad (3.4)$$

where $E(m)$ is also the function of the refractive index relying on a non-zero imaginary part. Thus, the ratio of scattering to absorbance is $\sim \frac{2}{3} (kR)^3 \frac{F}{E}$, which is further equivalent to $(kR)^3$. In this simulation, the average diameter of the heterostructures is ~50 nm ($R = 25$ nm). And considering

an incident wavelength of ~ 500 nm, the ratio is: $(kR)^3 = 0.03$. This result demonstrates a good agreement with the ratio of scattering to absorbance.

The normalized electric field distribution on or near the surface of the targets was further generated (Figure 3.6j-m). The incident wavelength was selected to regard to the maximum of the Au visible absorption peak. One can observe that the electric field intensity was maximized on the surface of the spherical target for the Au nanoparticle and GNPs (before and after plasma treatment) and at the interface of GNP and quantum dots for the GNP-QD heterostructures. The plots corresponding to $|E|/|E_0|$ vs. position along the center of the targets across the incident direction are shown in Figure 3.6n. It can be observed that intense ‘hot spots’ or normalized electric field (~ 8.64) was present on and near the surface of bare Au nanoparticle. For GNPs with ~ 3.8 nm shell thickness, this intensity was significantly suppressed though with a greater surface area spread of the normalized electric field. After the plasma treatment of GNPs, the intensity was re-gained (~ 7.06) and the spread on greater surface area of the target remained. For the GNP-QD heterostructure target, this spread of normalized electric field was suppressed but intense hot spots ($|E|/|E_0| \sim 11$) emerged at the interface of GNP and quantum dots. Such simulation results indicate that the GNP-QD heterostructures preserved/improved the plasmonic features of Au nanoparticles and will be of particular interest for potential applications such as Förster Resonance Energy Transfer or the plasmonic-enhanced photocatalysts.

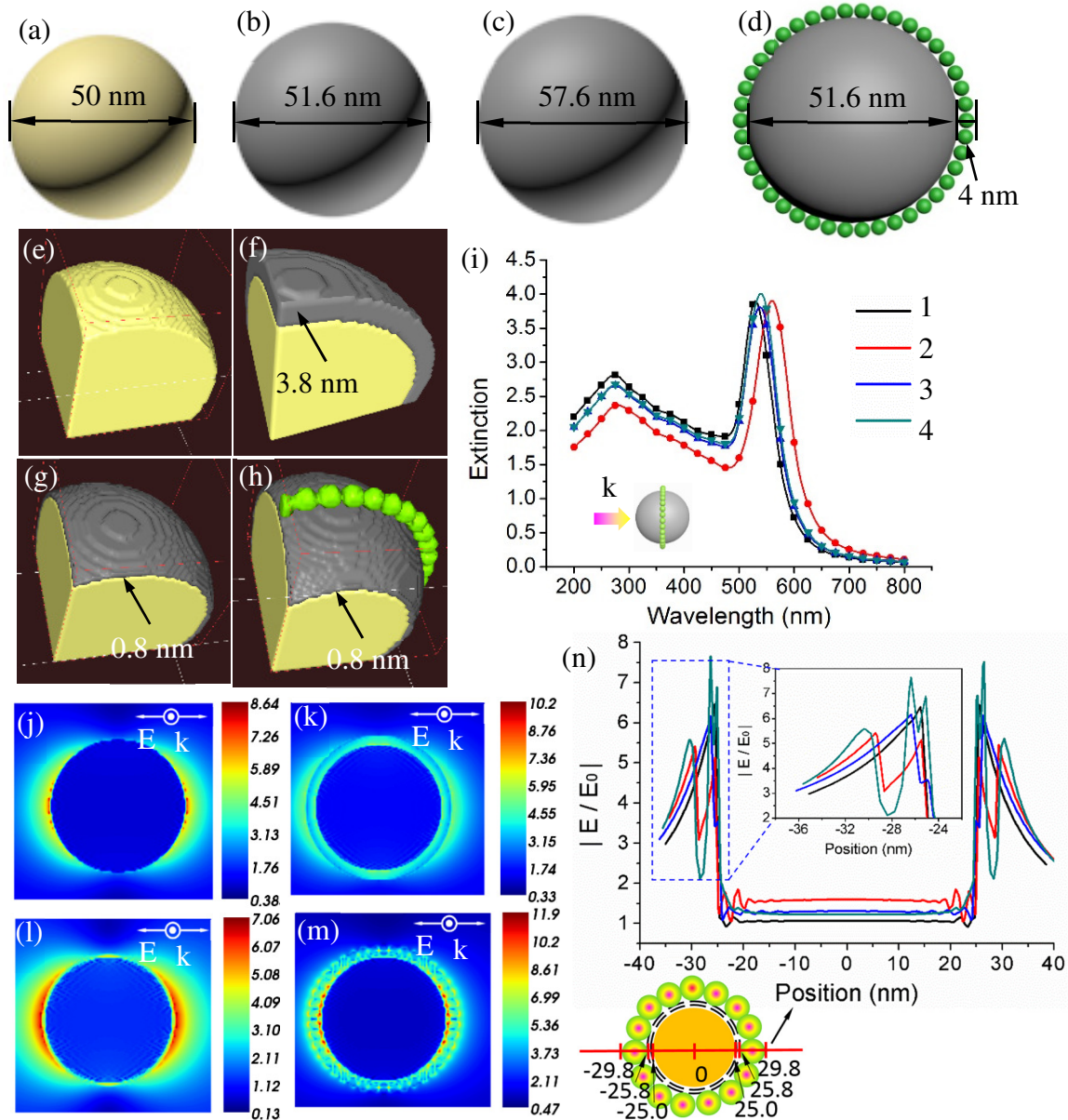


Figure 3.6. Targets: (a, e) Au nanoparticle, (b, f) GNP, (c, g) plasma-treated GNP, and (d, h) GNP-QD heterostructure. (i) Simulated extinction spectra for Au nanoparticles (1), GNPs (2), plasma-treated GNPs (3) and GNP-QD heterostructures (4). (j-m) Normalized electrical field distribution ($|E/E_0|$) near the surface of (j) Au nanoparticle (incident wavelength ~ 538 nm), (k) as-produced GNPs (shell thickness ~ 3.8 nm, incident wavelength ~ 562 nm), (l) plasma-treated GNPs (shell thickness ~ 0.8 nm, incident wavelength ~ 540 nm), and (m) GNP-QD heterostructure (incident wavelength ~ 543 nm). (n) $|E/E_0|$ vs. position along the center of the targets across the incident direction for target 1-4 in (i). *Note: Schematic in (i) shows the target and incident wavevector (k). Schematic in (n) shows ideal GNP-QD heterostructure and various positions plotted in (n)*

3.3.4. Plasmonic-enhanced photodegradation of phenol

Tauc plots (Figure 3.7a) were generated from the UV-vis absorbance spectra (Figure 3.5b) to estimate the band gap energies of the pristine quantum dots, GNP-QD heterostructures, and physically-mixed GNP-QD. For all these three samples, band gap energies of ~ 3.4 eV and ~ 2.6 eV were estimated corresponding to ZnS and CdS, respectively, present in the quantum dots [136]. A band gap tail corresponding to ~ 1.5 eV was also observed for the samples due to quantum confinement effects. Since all the samples including pristine quantum dots shows same band gap energies, the photoactivity of GNP-QD heterostructures is dominated by these attached semiconducting quantum dots. This further indicates that GNPs have metallic character, which was confirmed by the electrical characterization in Figure 3.7b. The inset digital image shows the device for I-V test. Embedded I-V curves in Figure 3.7b indicate that the blank Si substrate has semiconducting behavior and a rectifying diode effect was observed with a turn-on voltage of ~ 0.25 V [137]. The metallic characteristics (conducting) emerged after the Au nanoparticles patterning. The remaining rectification effect on this Au nanoparticle-patterned substrate was due to the Schottky barrier between the Au and Si. On further growth of GNPs, almost linear I-V relationship was observed and the estimated resistance is ~ 16790 Ω . For GNP-QD heterostructure patterned substrate, the estimated resistance increased to ~ 70040 Ω and loss of metallic character was observed with respect to GNPs due to the low conductivity of quantum dots.

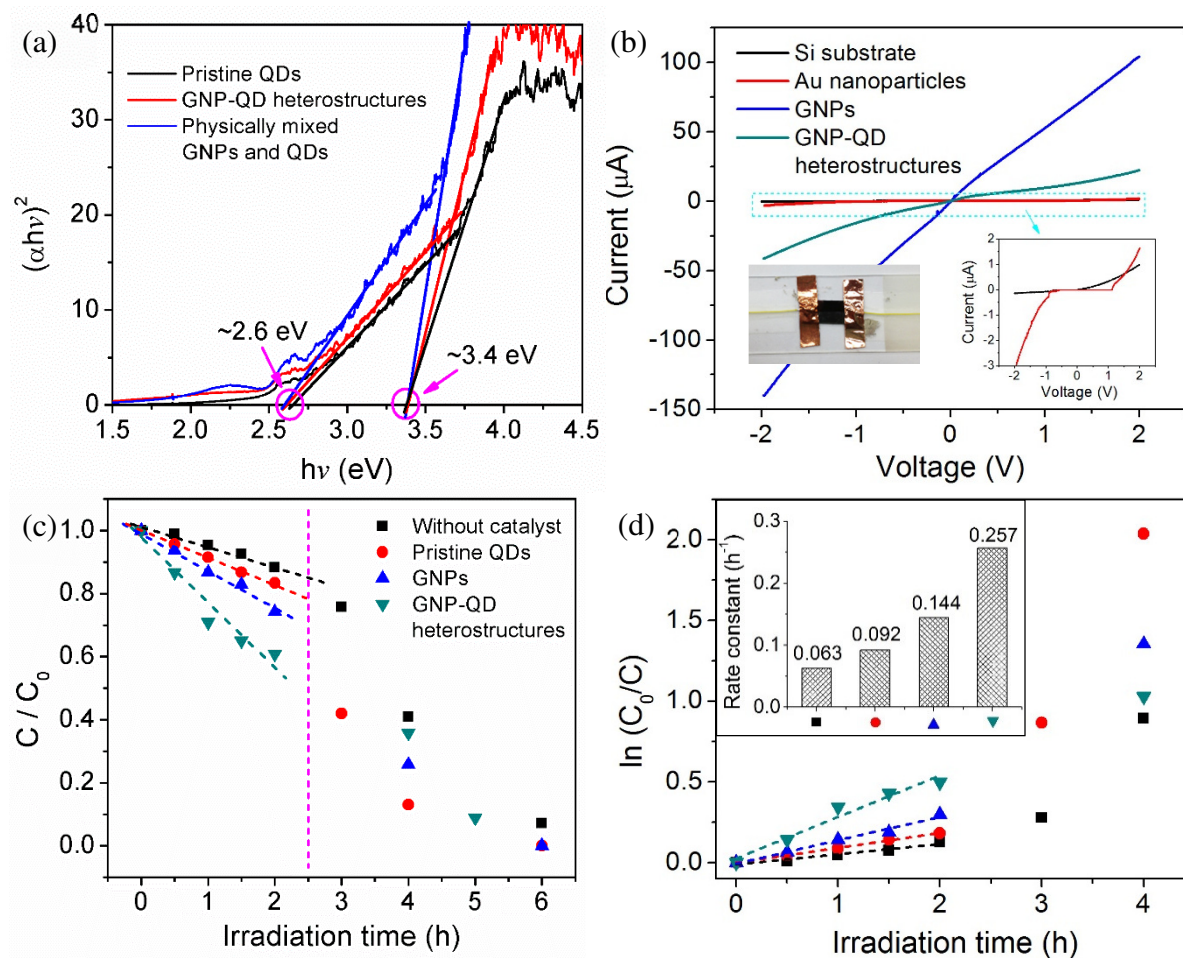


Figure 3.7. (a) Tauc plots obtained from the UV-vis spectra (Figure 3.5b) indicating band gap energies and tailings for various samples. (b) I-V curves for various samples (all samples were on the Si substrate). The inset DC image shows the digital image of the device. (c) Experimental photodegradation of phenol under UV irradiation (8 W lamp) in presence of sacrificial agent (H_2O_2) and different samples as photocatalyst. (d) First order fit of various phenol degradation processes indicated in (C). *Note: The legend in (d) is as shown in (c).*

Above band gap and electric characterizations are of use in understanding the photocatalytic behaviors of the GNP-QD heterostructures. In this regard, photodegradation of phenol was studied with the absence or presence of various photocatalysts including the pristine quantum dots, the as-produced GNPs as well as the GNP-QD heterostructures. As shown in Figure 3.7c, the GNP-QD heterostructures showed the best photocatalytic efficiency (~40%) within 2 h of degradation reaction. The other samples demonstrated the following order of photodegradation efficiencies: GNPs (26%) > pristine quantum dots (17%) > without any photocatalyst (12%). The degradation without any photocatalyst could be attributed to the presence of sacrificial agent and UV-based self-degradation of phenol [138]. The activity of GNPs could be due to the plasmonically-enhanced light harvesting and their improved electrical conductivity (Figure 3.7b). Pristine quantum dots show lower photodegradation efficiency than GNPs because of their natural narrow band gap energy, which resulted in significant self-recombination of the excited electrons [139].

To further study the photodegradation kinetics, the first order rate constant (k) was estimated using the following kinetic equation [112]:

$$k = \frac{1}{t} \ln \frac{C_0}{C} \quad (3.5)$$

where t is the degradation time, C_0 is the initial phenol concentration in water and C is the phenol concentration at specific t . As shown in Figure 3.7d, the plots of $\ln(C_0/C)$ vs. time show good linear trend for these photodegradation processes within 2 h, which allows for the estimation of their apparent first order kinetic constant (showing as inset in Figure 3.7d). Photodegradation in the presence of pristine quantum dots shows a rate constant of 0.092 h^{-1} , which is comparable with the values reported in previous studies [140]. The GNP photodegradation shows increased rate constant of 0.144 h^{-1} while photodegradation with the GNP-QD heterostructures show the highest

(0.257 h^{-1}). This rate constant value is much higher as compared with that reported in similar photocatalysis processes using semiconducting quantum dots or metal oxide nanostructures [112], indicating such GNP-QD heterostructures can be a preferred photodegradation catalyst.

Schematic of the GNP-QD heterostructures under illumination and the corresponding electron transfer band diagram was derived in Figure 3.8a-c. As demonstrated above, GNP-QD heterostructures preserved the unique plasmonic features of Au nanoparticles. Plasmonic charges will be generated on/near the heterostructure surface under illumination and that are especially strong at the interface of GNP and quantum dots (Figure 3.8a). It has been reported that these plasmonic charges reside at the Fermi energy level of the metal and their energy is too low to drive the reduction or oxidation half reaction. However, in the case of GNP-QD heterostructures, these plasmonic electrons/holes are of use for the effective separation of excited electrons on quantum dots from recombination to the valence band. For instance, at the side where positive charges accumulated (Figure 3.8b), the excited electrons on quantum dots are preferred to transfer to the GNPs and occupied with the plasmonic holes. Thus, sufficient holes are remaining on the valence band of quantum dots for the degradation of phenol. This electron transfer and photodegradation process was further detailed in Figure 3.8c, of which the band diagram further indicates that graphene shell and Au nanoparticle present lower band energy than the conduction bands of CdS and ZnS, which further facilitated the electron transfer from quantum dots to the GNP. On the other hand, it is easy to understand that at the negative charges accumulated side of the heterostructure, holes on the quantum dots are preferred to transfer to GNPs and occupied with the plasmonic electrons. This results in enough electrons on the conduction band of quantum dots for the decomposition of the sacrificial H_2O_2 , which provides $\text{OH}\cdot$ residues for the phenol degradation process. In addition, it is worthy to mention that since the strongest plasmonic electrons will be

generated with incident of 500-600 nm, we can predict that such GNP-QD heterostructures will also be favorable for visible light-driven photocatalysis processes.

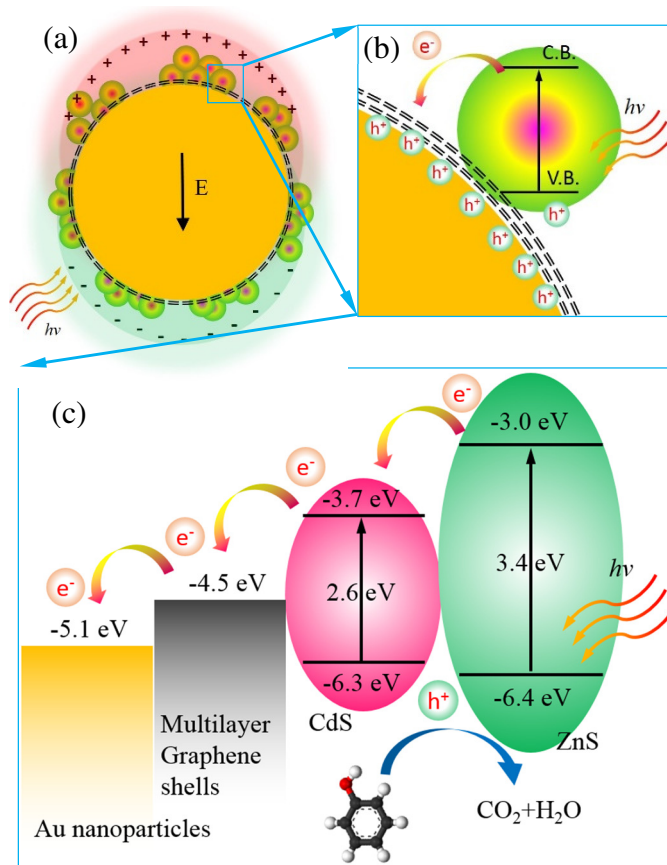


Figure 3.8. (a) Schematic of the GNP-QD heterostructures under illumination. (b) Excited electron transfer at the positive charge accumulated side of the heterostructures. (c) Derived band gap energy and relative band edge locations for GNP-QD heterostructures. *The electron transfer as well as degradation reaction under illumination are indicated by arrows.*

3.4. Conclusions

For the first time we report the patterned growth of GNPs in a facile CVD approach and their hybridization with semiconducting quantum dots directly on a Si substrate. Sequential steps for the heterostructure synthesis involved the electroless deposition of Au film, high-temperature annealing (to form Au nanoparticles), CVD growth of multilayer graphene shell around the Au nanoparticles, and covalent binding of quantum dots on GNPs. The surface functionalization of GNPs was achieved through both plasma and acid treatment and this processing had no significant impact on the distribution of GNPs on the substrate. XPS analysis of plasma- or acid-treated GNPs indicated that both processes were able to create carboxylic (-COOH) groups (~12% *via* plasma treatment and ~13% *via* acid treatment) on the surface of GNPs, which facilitated the covalent linking of (-NH₂)-terminated semiconducting quantum dots. The covalent linking was achieved *via* carbodiimide chemistry, resulting in the formation of amide bond as confirmed by FITR. Optical studies, both experimental and simulated, indicated that the encapsulation of multilayer graphene shell around the Au nanoparticles did not suppress the extinction/plasmonic characteristics of the latter. The simulation of optical behavior of GNP-QD heterostructures showed intense “hot spots” at the interface of GNP and quantum dots. Band gap and electrical characterization indicated that the heterostructuring process has minimal influence on the band gap energies of quantum dots and meanwhile the GNPs exhibited strong metallic behavior. Thus, GNP-QD heterostructures were further employed for the plasmon-enhanced photocatalytic phenol degradation. The results indicate that such heterostructures exhibited the highest degradation efficiency (~40%) or rate constant (0.257 h⁻¹) as compared to Au nanoparticles or GNPs.

CHAPTER 4

GOLD NANOPARTICLE MODIFIED BY CARBON AND QUANTUM DOTS: SYNTHESIS AND OPTICAL PROPERTIES

Yuan Li,¹ and Nitin Chopra^{1,2,3,}*

¹Department of Metallurgical and Materials Engineering, Box 870202, The University of Alabama, Tuscaloosa, AL 35401, USA

²Department of Biological Sciences, Box 870344, The University of Alabama, Tuscaloosa, AL 35401, USA

³ Department of Chemistry, Box 870336, The University of Alabama, Tuscaloosa, AL 35401, USA

***Corresponding author**

E-mail: nchopra@eng.ua.edu

Tel: [205-348-4153](tel:205-348-4153)

Abstract

Multilayer graphene shell encapsulated gold nanoparticle – quantum dot hybrids were derived by combining wet-chemical, thermal, and covalent chemistry approaches. Uniformly patterned gold nanoparticles on a silicon substrate were obtained *via* gold film deposition in an electroless method followed by a thermal dewetting process. The resulting gold nanoparticles were further surface oxidized and utilized as catalysts for the chemical vapor deposition growth of multilayer graphene shell encapsulated on the gold nanoparticles (referred as “multilayer graphene shell encapsulated Au nanoparticle” or GNPs). As a next step, the surface of GNPs was modified to result in carboxylic (-COOH) functionalities, which enabled carbodiimide-based covalent linking of amine-terminated CdS_xSe_{1-x}@ZnS quantum dots (QDs) on the GNP surface. The GNPs and GNP-QD heterostructures were characterized using scanning and transmission electron microscopy for size, morphology, spatial distribution, and crystal structure evaluation. In addition, UV-vis, fluorescence spectroscopy and Discrete Dipole Approximation modeling were utilized for understanding the band gap energies, fluorescence quenching, and light-matter interactions of the derived hybrids/heterostructures.

Keywords: graphene, gold nanoparticles, quantum dots, optical properties, fluorescence quenching, Discrete Dipole Approximation

4.1. Introduction

The surface modification of photonic nanostructures such as gold (Au) nanoparticles can lead to novel physical phenomena including selective light-matter interactions and rapid energy transfer processes [141]. The surface modification of Au nanoparticles could be achieved by using ligand coatings, inorganic material shells, or covalent/physical adsorption of nanoparticles or quantum dots of another material. However, the challenge is to achieve stable coating, which prevents the exposure of Au nanoparticles to unwanted solution environment [142]. Overcoming this challenge will also enable conservative utilization of Au nanoparticles in photonic applications. In addition, the need is also for imparting diverse surface chemistry to Au nanoparticles. A promising approach in this direction is to encapsulate Au nanoparticles in a sub-5 nm thin carbon or graphene shell. Such modification of Au nanoparticles can also enable creating higher order architectures of Au nanoparticles by utilizing rich carbon chemistry. An attractive architecture will be to bind quantum dots [143] onto carbon encapsulated Au nanoparticles. The carbon component can also influence the light-matter interactions for such hybrid systems, by reducing scattering effects [144].

Recently, surface decoration of Au nanoparticles with chemically-exfoliated graphene was reported for biosensors and bioelectronics [145]. However, the corrosive nature of the exfoliation process and the inability of wrapped graphene to form an impervious shell around Au nanoparticles limited their electrical and optical properties. In this regard, encapsulation of Au nanoparticles in a sub-5 nm thick carbon shell or a multilayer graphene shell has been recently demonstrated by the authors [146]. This scalable approach employs a chemical vapor deposition (CVD) of multilayer graphene shells directly onto patterned Au nanoparticles (referred as “multilayer graphene shell encapsulated Au nanoparticle” or GNPs). The presence of multilayer graphene shell (sub-5 nm thickness) had significantly favorable influence on the optical properties and stability

(chemical and thermal) of the encapsulated Au nanoparticles [144]. In addition, carbon surface chemistry allowed for target-receptor bioanalysis and sensing.

In this short note, we report an approach for the controlled patterning of multilayer graphene-modified Au nanoparticles (or GNPs) on a silicon substrate and covalent linking of GNPs with semiconducting $\text{CdS}_x\text{Se}_{1-x}/\text{ZnS}$ quantum dots (referred as GNP-QD heterostructures). High resolution electron microscopy was utilized to study the crystal structure, interfaces, and binding of quantum dots with GNPs. Optical properties of heterostructures were analyzed using UV-vis and fluorescence spectroscopy. For understanding the light-matter interactions, Discrete Dipole Approximation (DDA) modeling method was further utilized to simulate surface plasmonic characteristics of GNPs and GNP-QD heterostructures.

4.2. Experimental section

Materials and Methods: Silicon (Si) wafers (111) were purchased from IWS (Colfax, CA). Potassium gold (III) chloride was purchased from Sigma-Aldrich (St. Louis, MO). Hydrogen fluoride (~50 wt.%) was purchased from VWR (Atlanta, GA). Ammonium fluoride was purchased from Alfa Aesar (Ward Hill, MA). 1-ethyl-3-(3-dimethylaminopropyl) carbodiimide (EDC) and N-hydroxysuccinimide (NHS), 2-(N-morpholino) ethanesulfonic acid (MES) were purchased from Thermo scientific (Rockford, IL). Amine-terminated $\text{CdSe}_x\text{S}_{1-x}/\text{ZnS}$ core/shell fluorescent quantum dots were purchased from cytodiagnosics (Burlington, Canada). DI-water (18.1 M Ω -cm) was obtained using a Barnstead International DI water system (E-pure D4641). All chemicals were used without further purification. Buffered oxide etch (BOE) solution was prepared by mixing ~40 wt.% NH_4F and ~50 wt.% HF in DI-water (volume ratio of 6:1). The GNP growth was

carried out in a Lindberg blue three-zone tube furnace (Watertown, WI) with a quartz tube purchased from ChemGlass (Vineland, NJ).

Synthesis of multilayer graphene shell encapsulated Au nanoparticles: Au film was deposited on the silicon substrate using acid-based wet-chemical method [147,148]. In this method, cleaned silicon substrate was treated with BOE solution to remove the surface oxide layer. This was followed by immersing the substrate in the acidic solution comprised of ~1 mM KAuCl_4 in ~1 wt.% HF. This reaction (also referred as electroless or galvanic deposition) was carried out for 45 s, 90 s and 120 s to result in Au films with different thicknesses. The substrate was washed with DI-water, dried, and subsequently annealed at 850 °C in air for 10 min. This annealing step led to de-wetting of Au film and resulted in Au nanoparticles patterned onto the silicon substrate. Growth of multilayer graphene shell around Au nanoparticles (GNPs) was accomplished in a CVD process [146] for patterned Au nanoparticles after dewetting of three samples (i.e., Au films) on silicon substrates deposited for 45 s (GNP_45), 90 s (GNP_90), and 120 s (GNP_120). The GNP growth was conducted as described next. Briefly, Au nanoparticles patterned on silicon substrate were treated with oxygen plasma for 15 min to result in surface gold oxide. This was followed by the CVD growth of multilayer graphene shell at ~675 °C for 1 h. Xylene was used as the carbon source. The carrier gas was 10% H_2/Ar with a total flow rate of 1.15 SLM. This process resulted in patterned growth of GNPs on the silicon substrate. Finally, the -COOH derivatization on the GNPs was carried out by treating the as-grown GNPs with oxygen plasma for 15 s (power 120 W, oxygen pressure 300 mTorr).

Covalent binding of quantum dots on GNPs: Commercially-bought and amine (-NH₂)-terminated CdS_xSe_{1-x}@ZnS quantum dots were covalently linked with (-COOH)-derivatized GNPs *via* the carbodiimide chemistry [149]. Briefly, the (-COOH)-terminated GNPs patterned on the silicon substrate were immersed in a ~50 mM MES buffer (pH = 6.1) solution containing ~2 mM EDC and incubated for 10 min under gentle shaking. This was followed by addition of ~4 mM NHS and further incubation for 1 h. This process allowed the formation of stable amine-reactive NHS ester on the surface of GNPs. The substrate was gently washed with PBS buffer (pH = 7.4) and then immersed in the PBS buffer (pH = 7.4) containing 2 mM (-NH₂)-terminated CdSe_xS_{1-x}/ZnS quantum dots. This reaction was continued for 12 h to form the amide bonds (-CONH-) and result in the covalently-linked GNP-QD heterostructures. The final product was washed with DI-water and dried in N₂.

Characterization methods: FE-SEM (JEOL-7000) and Tecnai F-20 TEM were used to characterize the morphology, crystal structure, and/or interfaces of the GNPs and GNP-QD heterostructures. The dimension, number density, and shell thickness were estimated accordingly. UV-vis absorbance spectra were obtained using DH-2000 UV-VIS-NIR light source. Fluorescence spectroscopy (JASCO FP-8200) was used to characterize the fluorescence quenching effect of GNP-QD heterostructures.

The band gap energies for the as-purchased quantum dots and the GNP-QD heterostructures was further determined using equation (4.1) [150,151]:

$$ah\nu = A(h\nu - E_g)^n, \quad (4.1)$$

where a is absorbance coefficient, A is a constant, $h\nu$ is the energy of light and n is a constant depending on the nature of the electron transition (n assumes 1/2, 2, 3/2 and 3 for allowed direct, allowed indirect, forbidden direct and forbidden indirect transitions, respectively.). CdS_xSe_{1-x}/ZnS quantum dots have been reported as a allowed direct semiconductor, as a result, the optical band gaps were calculated by extrapolating straight lines of the Tauc plots [$(ah\nu)^2$ vs. $h\nu$] to the intercept where $(ah\nu)^2 = 0$ [152,153].

Discrete dipole approximation (DDA) method was used to simulate the plasmonic properties of the GNPs and GNP-QD heterostructures. This method is based on the solution of 3D Maxwell equation using the DDSCAT code developed by Draine and Flatau [154,155]. Briefly, DDSCAT 7.2 was utilized to estimate the normalized electric field or surface plasmon generation for various nanostructure/heterostructure targets. The normalized electric field intensity is defined as the strength ratio between the electric field generated near the nanostructures and the incident electric field ($|E|/|E_0|$). The geometrical targets were created using the 3D max software for GNPs and GNP-QD heterostructures with various sizes. The effective radius of the targets was calculated via: $r_{\text{eff}} = (3V/4\pi)^{1/3}$, where V is the total volume of the 3D targets and is calculated with $V = Nd^3$ (N is the number of dipoles and d is the lattice spacing in cubic array). Near-field electric field distributions were extracted using the DDFIELD utility in DDSCAT 7.2 and processed using MayaVi 2 from Python(x,y).

4.3. Results and Discussion

The patterning of Au nanoparticles on the silicon substrate was achieved in an electroless or galvanic deposition process [147] followed by the high-temperature annealing. Electroless Au

deposition reaction was performed for different durations (45 s, 90 s, and 120 s). Increasing reaction time led to thicker Au films. The electroless deposition process involved the replacement reaction between Au^{3+} and Si in an aqueous solution containing F⁻, which resulted in deposition of a uniform Au film on the silicon substrate [156]. Followed by this, the dewetting of Au films resulted in uniformly-sized and patterned Au nanoparticles on the silicon substrate. For the growth of multilayer graphene shell, Au nanoparticles were surface oxidized [146], and utilized as catalysts in a xylene-based CVD process [146].

Figure 4.1A-C show the SEM images of the GNPs (GNP_45, GNP_90, and GNP_120) obtained for three different samples with increasing Au nanoparticle sizes. The microscopic images clearly show that GNPs were uniformly patterned onto the substrate (Figure 4.1A-C) and a multilayer graphene shell (Figure 4.1D-F) was observed with a core Au nanoparticle encapsulated within. The carbon inter-planar spacing is observed to be between 0.37 and 0.40 nm (Figure 4.1D-F). This carbon inter-planar spacing larger than that for c-axis lattice spacing of graphite (~0.34 nm) could be attributed to the curvature state of graphene shell. Using microscopic characterization, the GNP size, inter-particle spacing, and spatial density for various samples were estimated. It can be noted (Figure 4.1G) that the GNP size increases with increasing electroless deposition duration of Au film. This suggests that longer deposition time led to thicker Au film, which further resulted in larger-sized Au nanoparticles for a fixed dewetting condition. In addition, the size distribution of GNPs was broader for larger-sized GNPs than for smaller-sized ones. This indicates that Ostwald's ripening effect and surface migration of species enhanced with the size of the nanoparticles increasing. It is also noted that with the increase of GNP size, an increasing trend in inter-particle spacing and decreasing trend in spatial density of GNPs is observed. The thickness of multilayer graphene shell corresponding to Figure 4.1A-C is observed to be $\sim 2.5 \pm 0.3$ nm, $\sim 3.8 \pm 0.2$ nm,

and $\sim 4.2 \pm 0.5$ nm for GNP_45, GNP_90, and GNP_120 samples, respectively. This increasing shell thickness with increasing GNP size/Au nanoparticle size suggests that larger Au nanoparticles can result in thicker graphene shell.

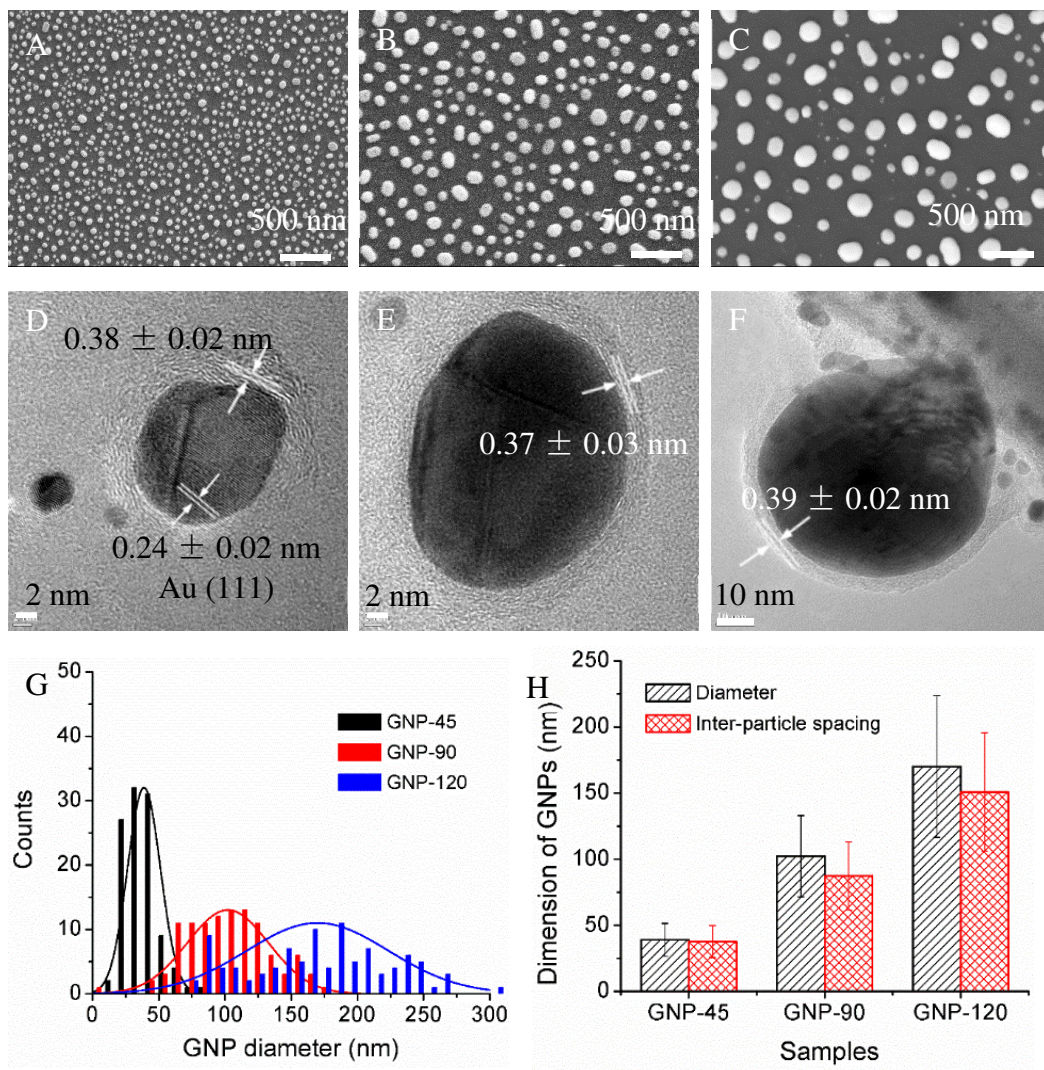


Figure 4.1. (A-C) SEM images of GNPs with different size that were uniformly patterned onto silicon substrate. (D-F) TEM images of GNPs corresponding to (A-C). (G) Histogram showing the distribution of GNP diameter for various GNP samples. (H) Histogram of GNP diameters and inter-particle spacing for various GNP samples.

The as-produced and patterned GNPs on the silicon substrate were further subjected to plasma oxidation process to enable the formation of -COOH groups on the multilayer graphene shell. In addition, this controlled process also assists in removing the amorphous carbon present on the shell or etching the shell [157]. As a next step, these (-COOH)-functionalized GNPs were covalently linked with (-NH₂)-terminated CdS_xSe_{1-x}/ZnS quantum dots [149]. Figure 4.2A-C shows TEM images of the resulting GNP-QD heterostructures that were derived using GNP_45, GNP_90, and GNP_120 samples. These three samples are referred as GNP-QD_1, GNP-QD_2, and GNP-QD_3. High resolution TEM images (Figure 4.2A, D and E) clearly show the attached quantum dots with sizes between 4 nm and 5 nm and lattice spacing of ~0.34 nm (which is corresponding to (111) plane of CdS). Since TEM images are 2D images, it is impossible to identify the spatial location of the quantum dots on GNPs but their presence on the shell can be easily identified as shown in Figure 4.2. As shown in Figure 4.2A-C, it is clear that quantum dots are uniformly coated around the GNPs. Based on this observation, the surface coverage of quantum dots on the GNPs is estimated to be ~40% for GNP-QD_1, ~18% for GNP-QD_2, and ~15% for GNP-QD_3. Thus, this unique approach presents a simple method to develop highly-ordered assemblies comprised of multiple components (Au nanoparticles, multilayer graphene shell, and quantum dots).

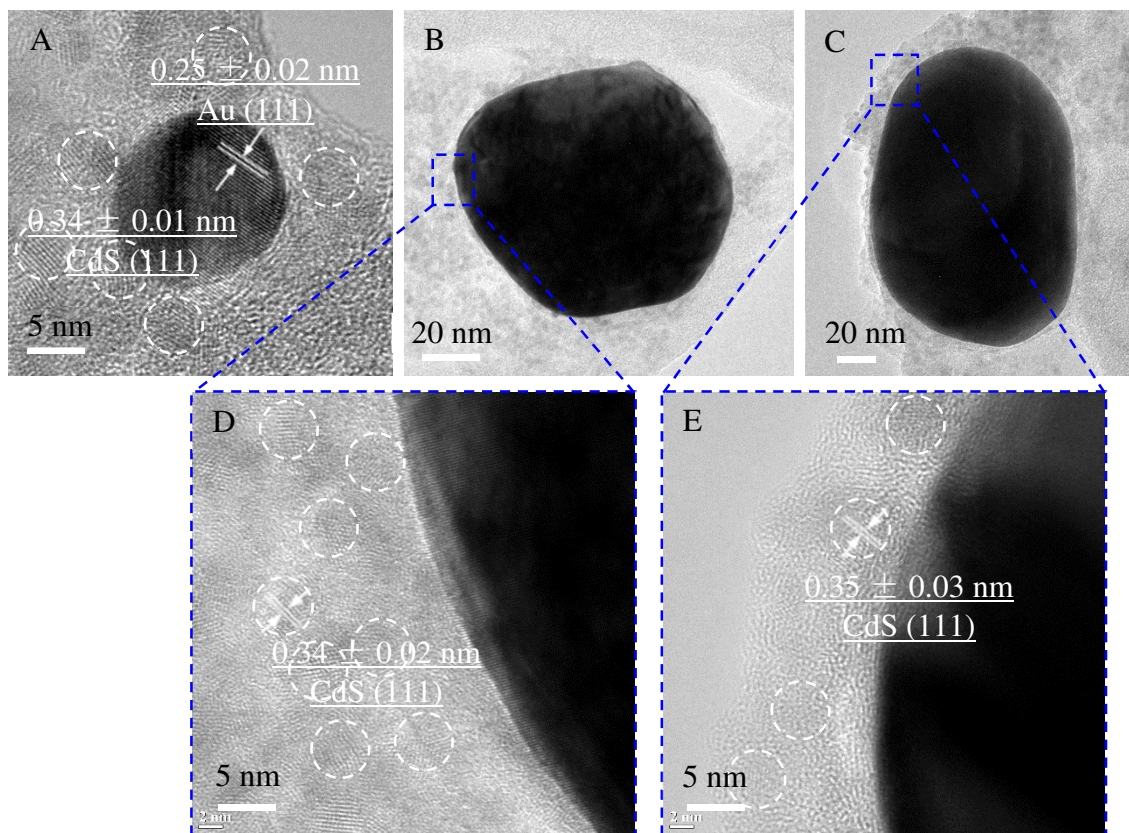


Figure 4.2. TEM images of the GNP-QD heterostructures corresponding to (A) GNP_45, (B, D) GNP_90, and (C, E) GNP_120. Note: (D) and (E) show the high resolution TEM for attached quantum dots on GNPs as shown in (B) and (C). The blue dotted lines indicate the regions observed at higher resolution.

It is known that Au nanoparticles and quantum dots have unique plasmonic and photonic characteristics [144]. However, these characteristics are difficult to manipulate except by varying the size and aggregation of such photonic nanostructures. In this regard, mathematical modeling has predicted that GNPs can exhibit modulated plasmonic and photonic properties by simply varying the thickness of the multilayer graphene shell [144]. In addition, multilayer graphene shell around Au nanoparticles allow for enhanced absorption with minimal scattering. Thus, GNP-QD heterostructures are of particular interest for optical applications. The optical properties of GNPs and GNP-QD heterostructures were studied using UV-vis absorbance spectroscopy (Figure 4.3A).

The as-produced GNPs showed broad absorbance peaks at ~550 nm, ~570 nm, and ~590 nm. These peaks could be attributed to the visible absorption of the encapsulated Au nanoparticle in GNP [158]. The red shift in this peak for the three GNP samples could be attributed to the different thickness of the multilayer graphene shell and the size of the encapsulated Au nanoparticle and is largest for GNP_90 sample [158]. Another absorbance peak was observed in the UV region (280-290 nm) and attributed to the overlapping of UV absorption of multilayer graphene shell and inter-band transition of Au nanoparticles [159]. Suppression of this peak for thicker multilayer graphene shell was observed and could be due to the weakening of inter-band transition of Au nanoparticles or presence of amorphous carbon on thicker multilayer graphene shell. Apart from the peaks described above, all the three GNP-QD heterostructure samples exhibited peaks at ~485 nm corresponding to the absorption of quantum dots (Figure 4.3B). It must be noted that attachment of quantum dots onto GNPs resulted in red-shifted peaks (from ~280-290 nm to ~300-310 nm) corresponding to Au inter-band transition or multilayer graphene shell. This could be attributed to light-matter interactions between GNP and quantum dots. Overall, these aspects indicate that individual component in hybrid assembly retained its optical behaviors and the presence of multilayer graphene shell modulated this further.

Tauc plots (Figure 4.3C) were derived using the absorbance spectra in Figure 4.3B to evaluate the band gap energies of the GNP-QD heterostructures. The inset in Figure 4.3C shows that the as-purchased quantum dots exhibited two band gaps at ~2.6 eV and ~3.4 eV, which are attributed to CdS and ZnS, respectively [160]. One can observe in Figure 4.3C that covalent linking of quantum dots onto GNPs has no significant effect on their band gap energies or band structure. This indicates that GNPs provide an excellent support for quantum dots while preserving the optical properties of latter in the heterostructure configuration. Such heterostructures with complex

architectures hold strong potential for solar energy harvesting devices, photocatalysis and Förster resonance energy transfer (FRET).

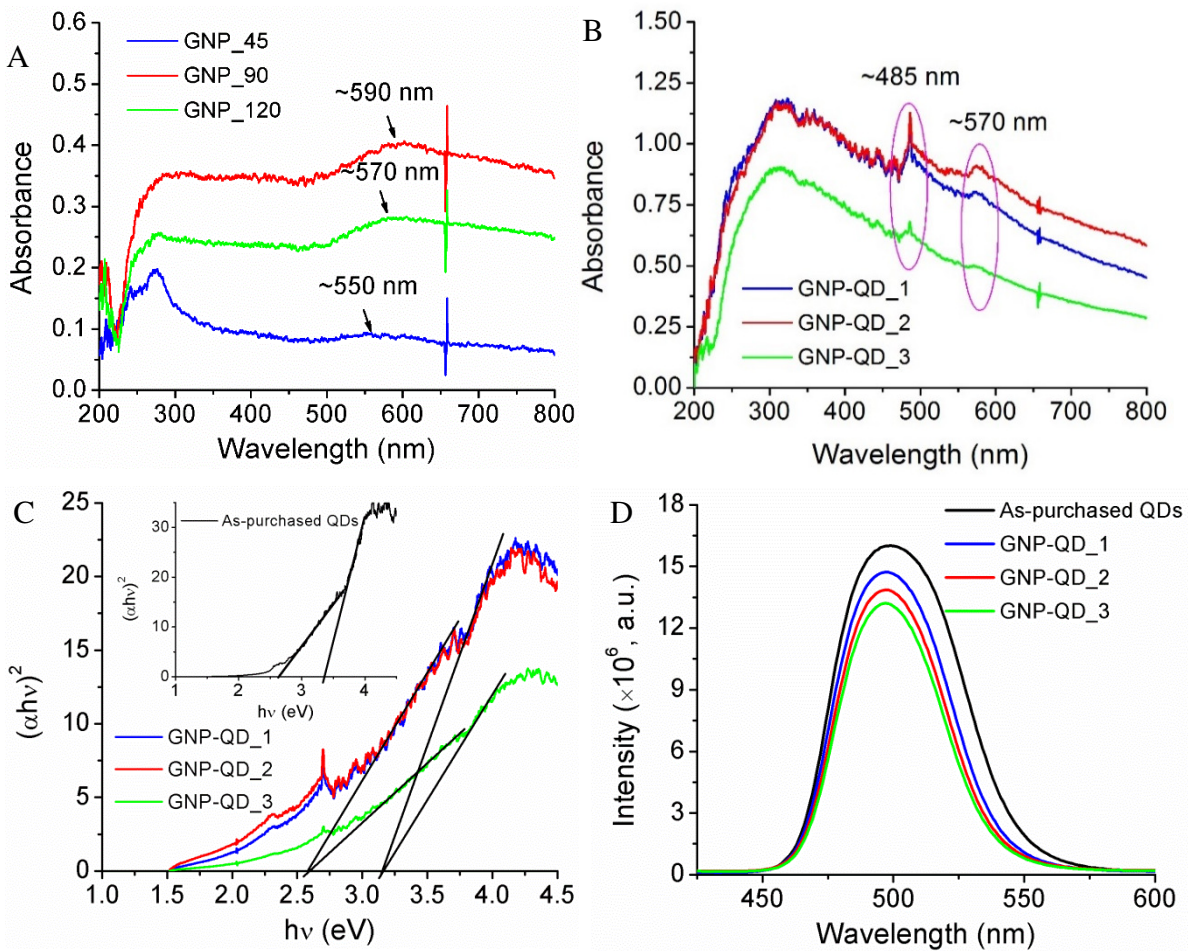


Figure 4.3. UV-vis absorbance spectra for GNP samples (A) and corresponding GNP-QD heterostructures (B). (C) Tauc plots or $(\alpha h\nu)^2$ vs. $h\nu$ plots used for the band gap energies estimation of the as-purchased quantum dots and GNP-QD heterostructures. (D) Fluorescence spectra of the as-purchased quantum dots and GNP-QD heterostructures.

The fluorescence characteristics of GNP-QD heterostructures was characterized using the fluorescence spectroscopy. Since the emission of fluorescence from quantum dots occurs during the recombination of excited electron with the ground state, the intensity of fluorescence spectra is indicative of the charge recombination processes. The attachment of quantum dots onto electron-accepting surfaces (Au, graphene, or GNPs) prevents recombination of charge carriers. This resulted in fluorescence quenching effect (around 500 nm, Figure 4.3D) for the GNP-QD heterostructures, which show reduced fluorescence intensity. In addition, the quenching effect becomes more pronounced with the increase of GNP size. As compared with the as-purchased quantum dots, the quenching efficiency (estimated by the percentage ratio of spectral area in Figure 4.3D) is 83.16%, 75.93%, and 70.43% for GNP-QD_1, GNP-QD_2, and GNP-QD_3, respectively.

GNP-QD heterostructures as derived in this study are potentially important for applications such as Surface-enhanced Raman Scattering (SERS), plasmonic-enhanced photocatalysis, and optoelectronic devices. Aimed at these potential applications, it is necessary to understand the role of multilayer graphene shell, encapsulated Au nanoparticles, and attached quantum dots on the influence of the plasmonic properties of GNP-QD heterostructures. This was achieved by simulating the extinction spectra (including absorbance and scattering) and surface electric field distribution for GNPs and GNP-QD heterostructures using the Discrete Dipole Approximation (DDA) method [154]. The targets were comprised of an arrangement of dipoles for which extinction spectra and normalized electric field distributions were numerically solved [154]. Three spherical GNP targets (Figure 4.4A-F) were derived by considering Au nanoparticles with size varied at an equal spacing (20 nm, 50 nm, and 80 nm in diameter, referred as Target#1, Target#2, and Target#3, respectively), which are encapsulated in multilayer graphene shell with a thickness of ~0.8 nm (corresponding to plasma-treated GNPs). The GNP-QD targets were derived by

considering quantum dots with diameter of 5 nm that were closely-packed around above three GNP targets (Figure 4.4G-K, referred as Target#4, Target#5, and Target#6, respectively). The simulation assumes all these targets are in air environment. The extinction efficiency is given by a combination of scattering and absorption as follows:

$$Q_{ext} = Q_{sca} + Q_{abs}, \quad (4.2)$$

where Q_{ext} is the extinction efficiency factor, Q_{sca} is the scattering efficiency factor and Q_{abs} is the absorbance efficiency factor.

The extinction spectra for all the GNPs and GNP-QD targets were deconvoluted into absorbance and scattering spectra (Figure 4.5). The main extinction peaks were observed around 530~570 nm and ~270 nm, which are consistent with the experimental findings in Figure 4.3A and B and attributed to the visible absorption of gold and the overlap of UV absorption of graphene and interband transition Au d-electrons [161]. For small GNP and GNP-QD targets ($R_{GNP} = 10$ nm), the scattering component was significantly suppressed as compared to the absorption component (Figure 4.5A and D) [159]. However, as the increase of GNP size ($R = 25$ nm and 40 nm), the scattering component for both GNP and GNP-QD targets were obviously enhanced (Figure 4.5B, E and C, F). This observation can be well-explained by the theoretical calculation reported earlier [159]. When nanoparticles are small compared to the wavelength of light, the scattering is in the Rayleigh regime. In that case, the scattering (Q_{sca}) can be written as:

$$Q_{sca} = \frac{8\pi}{3} k^4 R^6 F(m) \quad (4.3)$$

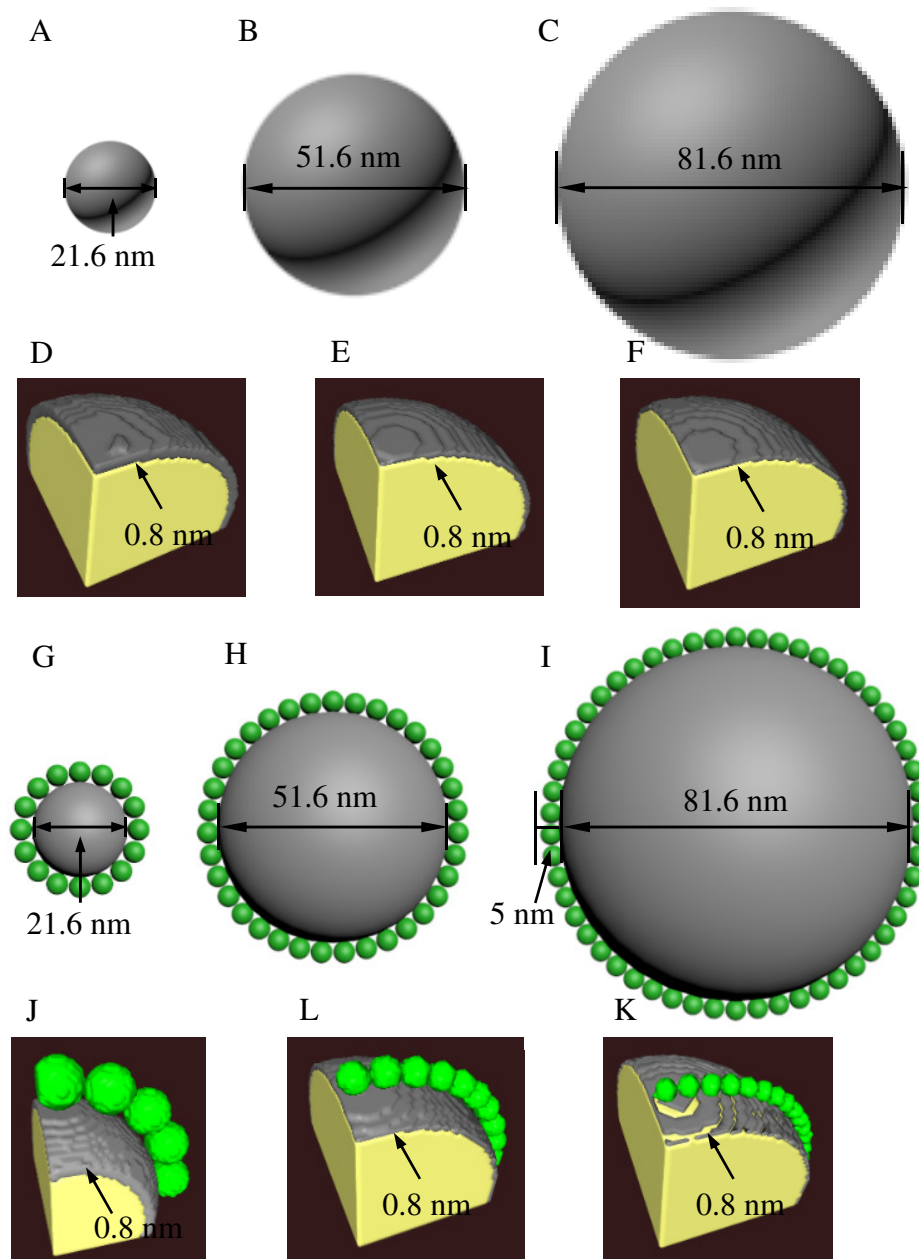


Figure 4.4. 3-D targets for various GNP samples (A-F) and GNP-QD heterostructure (G-K) samples developed by the 3ds Max software (A-C, G-I) and the LiteBil software (D-E, J-K). *Note: The LiteBil images were used for the chemical configuration identification. GNP samples (A-C) were named as Target#1-#3 and the GNP-QD samples (G-I) were named as Target #4-#6.*

where $k = \frac{2\pi}{\lambda}$ (λ is the wavelength), R is the radius of the particles, and $F(m)$ is a function of the refractive index (m). The absorption (Q_{abs}) can be written as:

$$Q_{abs} = 4\pi k R^3 E(m) \quad (4.4)$$

where $E(m)$ is also the function of the refractive index relying on a non-zero imaginary part. Thus, the ratio of scattering to absorbance is $\sim \frac{2}{3}(kR)^3 \frac{F}{E}$, which is further equivalent to $(kR)^3$.

Considering a wavelength of ~ 500 nm, for GNPs with R equals to 10 nm, 25 nm, and 40 nm, the value of $(kR)^3$ is 0.002, 0.031 and 0.127, respectively. This result demonstrates a consistent trend with the ratio of scattering to absorbance in Figure 4.5.

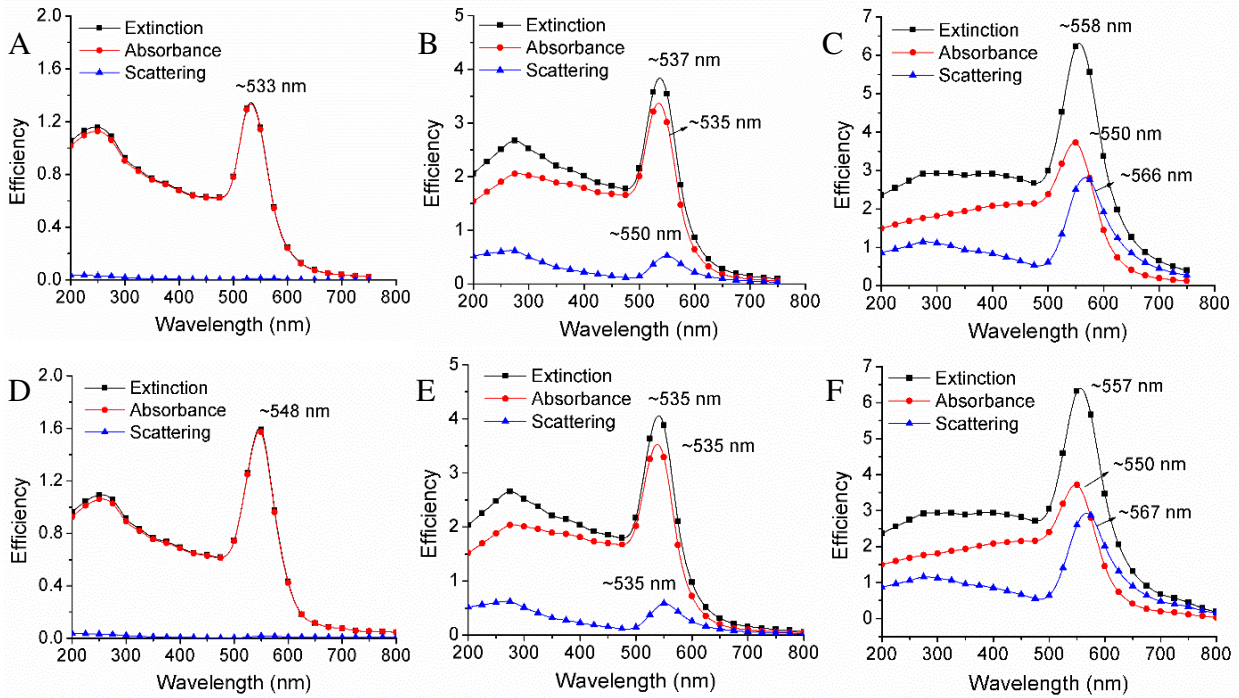


Figure 4.5. Simulated extinction spectra as a function of wavelength for the GNP targets (A-C: Target#1-#3) and the GNP-QD heterostructure targets (D-F: Target#4-#6) showing in Figure 4.4. *Note: These extinction spectra were further deconvoluted into absorbance and scattering spectra.*

The Extinction spectra for all the targets that simulated here were further summarized in Figure 4.6A. One can observe that large GNP and GNP-QD targets show significantly enhanced extinction as compared with the smaller ones. The attachment of quantum dots shows very weak influence on the extinction of large GNP and GNP-QD targets ($R_{\text{GNP}} = 40$ nm). However, when the targets are small ($R_{\text{GNP}} = 25$ nm and 10 nm), extinction spectra of GNP-QD targets are enhanced and show obvious blue-shift. This indicates strong light-matter interactions are preferred to happen between quantum dots and GNPs with small size. Normalized electric field distribution on or near the surface of the targets were further generated under the incident wavelength corresponding to the maximum of visible extinction peak of each target (Figure 4.6C-H). For GNPs, the strongest electric field is accumulated on the surface of the spherical targets, where the incident electromagnetic wave was parallel to the localized surface area vector. With respect to the GNP-QD heterostructures, the strongest electric field areas (normally called “hot spots”) were mainly accumulated at the interface of GNP and quantum dots.

The variation of normalized electric field intensity ($|E|/|E_0|$) along the central line of the target across the incident direction was shown in Figure 4.6B. The symmetrical sharp peaks indicate the strongest electric field accumulated at the surface of GNPs or the interface of GNP-QD targets. One can also observe that GNPs show enhanced electric field near the surface with increased particles size. This trend is consistent with the extinction spectra showing in Figure 4.6A. However, the varying trend of electric field intensity at the interface of GNP-QD heterostructures is reversed from the GNP targets. It was observed that large GNP and GNP-QD targets ($R_{\text{GNP}} = 40$ nm) show equivalent electric field intensity, while small GNP-QD target ($R_{\text{GNP}} = 10$ nm) shows significantly enhanced electric field at the “hot spot” as compared with the corresponding GNP. This again indicates that strong light-matter interaction is prone to happen between small GNPs

and quantum dots. Such simulation provides interesting fundamental knowledge and enlightenment for understanding and designing of future plasmonic-enhanced photocatalysts and FRET devices.

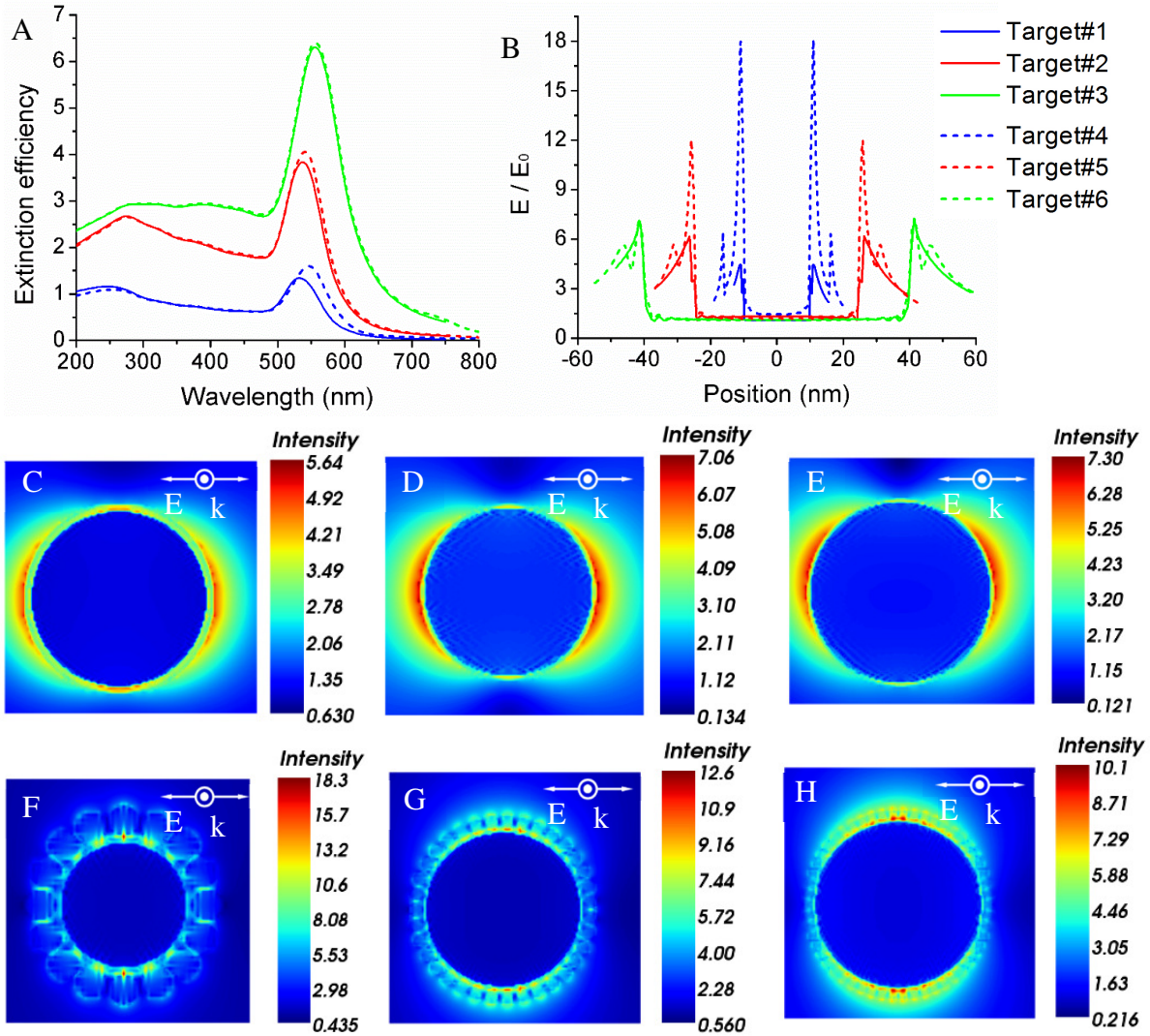


Figure 4.6. (A) Simulated extinction spectra of the GNP and GNP-QD targets. (B) Normalized electric field intensity (E/E_0) vs. positions along the center of the targets across the incident direction for the GNP and GNP-QD targets. (C-H) Normalized electric field distributions near/around the GNPs (C-E: Target#1-#3) and GNP-QD heterostructures (D-F: Target#4-#6).

4.4. Conclusions

In summary, multilayer graphene shell encapsulated Au nanoparticle – quantum dot hybrids were fabricated using the electroless deposition, thermal annealing, CVD, and self-assembly chemistry. The fabrication process also demonstrates a unique combination of both, top-down and bottom-up approaches. The thermal dewetting of Au films led to controlled patterning of Au nanoparticles, which further enabled patterned growth of GNPs in a CVD process. The presence of encapsulating multilayer graphene shell around Au nanoparticles enhanced the surface chemistry of the GNPs and allowed their linking with quantum dots in a simple carbodiimide functionalization approach. The high resolution electron microscopy showed that crystal structure of individual components present in the heterostructures or hybrids. UV-vis spectroscopy showed that presence of multilayer graphene shell did not suppress but modulated the absorbance peaks corresponding to encapsulated Au nanoparticles. GNPs could be successfully utilized as substrates for loading quantum dots without influencing the absorbance characteristics and their band gap energies. It was observed that fluorescence response for the quantum dots was quenched for the quantum dots loaded onto GNPs and this was attributed to the electron accepting characteristics of the latter. This fluorescence quenching was dependent on both, the size of GNPs and quantum dot loading on the GNPs. Meanwhile, the plasmonic simulation indicates that Au nanoparticles preserved their plasmonic properties after graphene encapsulation and quantum dots linking. Strong light-matter interaction between GNP and quantum dots (especially for GNP with smaller size) was observed in the DDA modeling. The $|E/E_0|$ for the GNP-QD heterostructures was estimated to be 10.1 as compared with that of 5.46 for the pristine Au nanoparticles.

CHAPTER 5

GRAPHENE ENCAPSULATED GOLD NANOPARTICLE – QUANTUM DOTS HYBRIDS DECORATED SILICON ELECTRODE

Yuan Li,¹ Nitin Chopra^{,1,2}*

¹Metallurgical and Materials Engineering Department, Center for Materials for Information Technology (MINT), The University of Alabama, Tuscaloosa, AL 35487, U.S.A.

²Department of Biological Sciences, The University of Alabama, Tuscaloosa, AL 35487, U.S.A.

***Corresponding Author**

E-mail: nchopra@eng.ua.edu

Tel: [205-348-4153](tel:205-348-4153)

Abstract

For the first time we report a facile technique for patterning multilayer graphene shell encapsulated gold nanoparticles (graphene nanoparticles or GNPs) on the silicon substrate and their further surface decoration with semiconducting quantum dots (QDs). This leads to a novel silicon electrode decorated with GNP-QD heterostructures. The morphology, structure and composition of the GNPs and GNP-QD heterostructures were evaluated using various microscopic and spectroscopic techniques. The heterostructure-decorated silicon electrode was also evaluated for the electronic and electrochemical properties. The results indicate that the electrical conductivity of the silicon substrate was significantly improved by decorating with GNPs and quantum dots. Meanwhile, significantly increased electrochemical charge transfer activity was observed on the GNP-QD heterostructure electrode through the CV and EIS characterization.

Keywords: multilayer graphene shell encapsulated gold nanoparticles, semiconducting quantum dots, silicon electrode, electrochemical activity

5.1. Introduction

Carbon nanotubes (CNTs), graphene, and fullerene exhibit a diverse range of surface chemistry necessary for developing hierarchical heterostructures.¹⁶² Surface functionalization of these carbon nanostructures with extraneous nanoparticles or quantum dots (QDs) is of interest for surface chemical analysis, sensors and various photocatalysis or photovoltaic applications. Such attempts leads to the present innovations in heterostructures development.¹⁶³ Recently, chemically-exfoliated graphene wrapped around gold (Au) nanoparticles for biosensors and bioelectronics was reported.¹⁶⁴ However, the corrosive nature of the exfoliation process and the inability of wrapped graphene to form an impervious shell around Au nanoparticles limited their electrical transport. With this regards, spherical carbon nanostructures such as fullerene, onion-like carbon (OLC), and carbon nanocapsules hold great potential.¹⁶⁵

Hierarchical heterostructures comprised of spherical carbon nanostructures loaded with quantum dots have been reported.¹⁶⁶ The morphology, dimension, and surface functionality of spherical carbon nanostructures can result in tunable properties, which can be further modulated by loaded quantum dots. Herein, we report a novel heterostructure configuration of multilayer graphene shell encapsulated Au nanoparticles (GNPs), which were further coordinated with $\text{CdS}_x\text{Se}_{1-x}/\text{ZnS}$ quantum dots. Such graphene shells provide a robust surface passivation to the encapsulated Au nanoparticle and also serve as a multifunctional interface between the Au nanoparticles and the bound quantum dots. Moreover, the in-situ patterning of such GNP-QD heterostructures on a highly-doped conductive silicon (Si) electrode was also achieved during the fabrication process. Detailed heterostructure fabrication and patterning procedures were described in the experimental section (see the Supplementary Information). The GNP-QD heterostructures were evaluated for their morphology, structure and chemical composition using microscopic (SEM/TEM) and

spectroscopic (XPS) methods. The GNP-QD heterostructures decorated Si electrode was further demonstrated for their electrical and electrochemical properties.

5.2. Experimental section

Materials and methods: Heavily B-doped conductive silicon (Si) substrate (111) was purchased from IWS (Colfax, CA). Potassium gold (III) chloride was purchased from Sigma-Aldrich (St. Louis, MO). Hydrogen fluoride (~50 wt.%) was purchased from VWR (Atlanta, GA). 1-ethyl-3-(3-dimethylaminopropyl) carbodiimide (EDC) and N-hydroxysuccinimide (NHS), 2-(N-morpholino) ethanesulfonic acid (MES) were purchased from Thermo scientific (Rockford, IL). (-NH₂)-terminated CdS/ZnS core/shell fluorescent quantum dots were purchased from Cytodiagnosics Inc. (Burlington, Canada). FE-SEM (JEOL-7000) and Tecnai F-20 TEM were used to characterize morphology, crystal structure, and/or interfaces present in Au nanoparticles, as-produced GNPs, and GNP-QD heterostructures. X-ray photoelectron spectra (XPS) were gathered by a Kratos Axis 165 with a mono-aluminum gun at 160 eV pass energy for full range scan and 40 eV pass energy for detailed scan.

Fabrication and patterning of Au nanoparticles on the Si substrate: Au film was deposited on the Si substrate using acid-based wet-chemical method.¹⁶⁷ Briefly, cleaned Si substrate was treated with Buffered oxide etch (BOE) solution to remove the surface oxide layer. This was followed by immersing the substrate in an acidic solution comprised of ~1 mM KAuCl₄ in HF. This reaction resulted in Au film (~20 nm thick) on Si substrate. The substrate was washed with DI-water, dried, and annealed in air for 15 min at 850 °C to dewet Au film that resulted in Au nanoparticles patterned onto the Si substrate.

Chemical Vapor Deposition of multilayer graphene shell: CVD process was employed for the growth of multilayer graphene shells. First, Au nanoparticles patterned on Si substrate were treated with oxygen plasma for 15 min to result in surface gold oxide. This was followed by CVD growth of multilayer graphene shell between 600 and 700 °C for 1 h. Xylene was utilized as the carbon source, carried with 10% H₂/Ar with a flow rate of 1.15 SLM. This process resulted in patterned growth of GNPs on Si substrate. The -COOH derivatization on the GNPs was carried out by treating the as-grown GNPs with oxygen plasma for 15 s.

Covalent binding of CdS/ZnS quantum dots: The binding approach employed well-established carbodiimide chemistry.¹⁶⁸ The (-COOH)-terminated GNPs patterned on Si substrate was immersed in a ~50 mM MES buffer solution with ~2 mM EDC and incubated for 10 min. This was followed by the addition of ~4 mM NHS. This process allowed the formation of a stable amine-reactive NHS ester. The substrate was washed with PBS buffer (pH = 7.4) and then immersed in the same containing 2 mM quantum dots. This reaction continued for 12 h to form amide bonds (-CONH-) resulting in GNP-QD heterostructures. Finally, the substrate with patterned assembly of GNP-QD heterostructures was washed with DI-water and dried in N₂.

Electronic/electrochemical study: The electrical characterization (I-V test) of the Si substrate patterned with Au nanoparticles, as-produced GNPs, or GNP-QD heterostructures was carried out using a two-point probe micromanipulator set-up equipped with Keithley source meters. Metal contacts were fabricated on the two edges of the Si substrate using silver paint. The electrochemical characterization was carried out on the PARSTAT 2273 Potentiostat/Galvanostat (Princeton Applied Research, Oak Ridge, TN). The standard three-electrode system was used. The Si electrodes (1.5 cm × 0.5 cm) patterned with Au nanoparticles, as-produced GNPs, or GNP-QD heterostructures were used as the working electrode. This electrode was sealed with epoxy gel to

selectively allow exposure of the front surface of the electrode. A Pt wire was used as the counter electrode and NaCl saturated Ag/AgCl electrode was utilized as the reference electrode. All potentials/voltages were measured with respect to Ag/AgCl electrode. CV and EIS were carried out in the solution containing 1.0 mM $\text{Fe}(\text{CN})_6^{3-/4-}$ and 0.1 M KCl. The impedance spectra were recorded from 100 KHz to 10 mHz with an AC amplitude of 5 mV rms.

5.3. Results and discussion

Gold film (~20 nm thick) was first deposited on the Si substrate *via* a galvanic deposition method.¹⁶⁹ This process involves the typical replacement reaction between Si and Au^{3+} , resulting uniform metallic Au layer deposited on the substrate.¹⁷⁰ SEM image of the Au film was shown in Figure 5.1a. The following rapid heat treatment process at high temperature (850 °C) leads to dewetting of the Au film, which forms uniformly patterned Au nanoparticles on the Si substrate. The average size of the Au nanoparticles is 48.25 ± 10.67 nm, dispersed on the substrate with an inter-particle spacing of 50.33 ± 15.74 nm (Figure 5.1b). The growth of multilayer graphene shell on these Au nanoparticles were conducted in a xylene-based chemical vapor deposition (CVD) process that recently reported by the authors.¹⁷¹ The resulting GNPs on the Si substrate were shown in Figure 5.1c. A slightly increased average particles size was observed (53.46 ± 17.23 nm) as compared with the former Au nanoparticles. Meanwhile, the inter-particles spacing of GNPs (49.44 ± 12.93 nm) shows no significant change, indicating the CVD process led to little particles loss. Representative TEM images of the GNPs were further shown in Figure 5.1d. A lattice spacing of ~0.24 nm was observed for Au nanoparticles (corresponding to (111) plane of gold). Multilayer graphene shell with a thickness of 2.0 ~2.5 nm was observed closely encapsulated around the Au

nanoparticles. The shell inter-lattice spacing is ~ 0.37 nm. This distance is slightly larger than the standard c-axis spacing of graphite (0.34 nm) due to the curvature of the graphene shell.

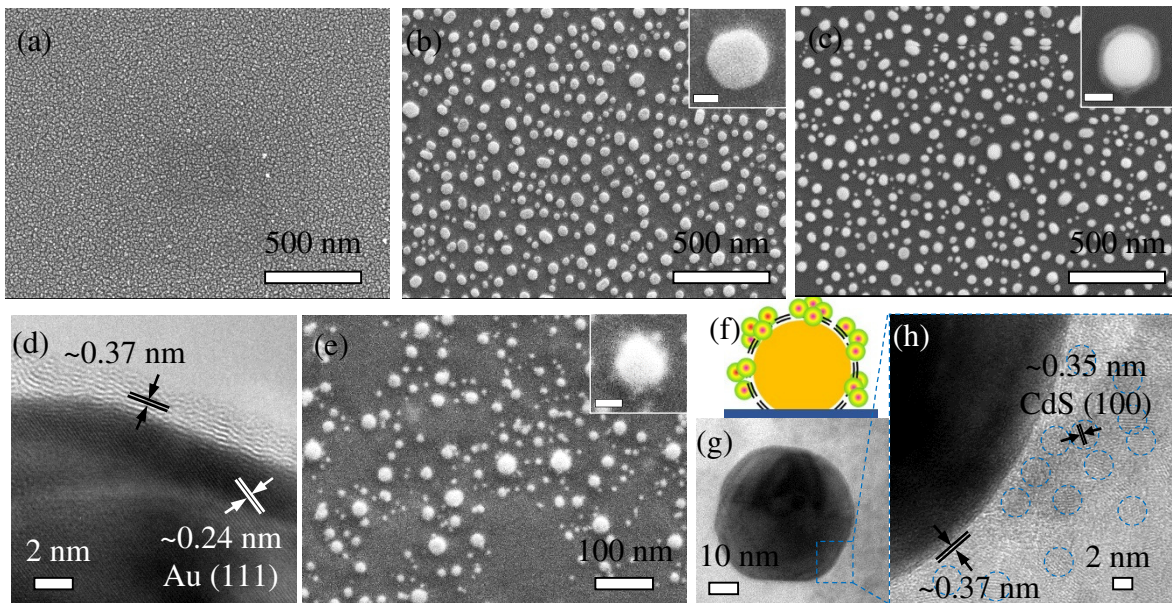


Figure 5.1. (a) SEM image of the Au film obtained through galvanic deposition on the Si substrate. (b) SEM image of the Au nanoparticles after annealing of Au film in (a). (c) SEM image of the as-produced GNPs. (d) SEM image of the GNP-QD heterostructures on the Si substrate. (e) HRTEM image of the as-produced GNPs. (f-h) Schematic and TEM/HRTEM images of the GNP-QD heterostructures.

The as-produced GNPs were subjected to a short-duration (15 s) plasma treatment process, which led to surface functionalization of GNPs with carboxyl (-COOH) groups and reduce of the shell thickness.¹⁷² Covalent attachment of amine (-NH₂)-terminated CdS_xSe_{1-x}/ZnS quantum dots to the (-COOH)-functionalized GNPs was achieved *via* the well-defined carbodiimide chemistry.¹⁷³ The chemical linking was completed through the formation of amide bonds (-NHCO-). SEM image of the obtained GNP-QD heterostructures were shown in Figure 5.1e and S1d (low-resolution image). Instead of separately dispersed single quantum dot, we observed that these quantum dots were

attached to the GNP surface in the form of clusters or aggregated dots.¹⁷⁴ The schematic of the heterostructures were illustrated in Figure 5.1f and the corresponding TEM images were shown in Figure 5.1g. High resolution TEM image in Figure 5.1h clearly indicates that quantum dots with size of 4~5 nm in diameter and lattice spacing of ~0.35 nm (corresponding to (111) plane of CdS) were closely-packed around the surface of GNPs. Approximately we can estimate that the surface coverage of quantum dots on GNPs is ~22%.

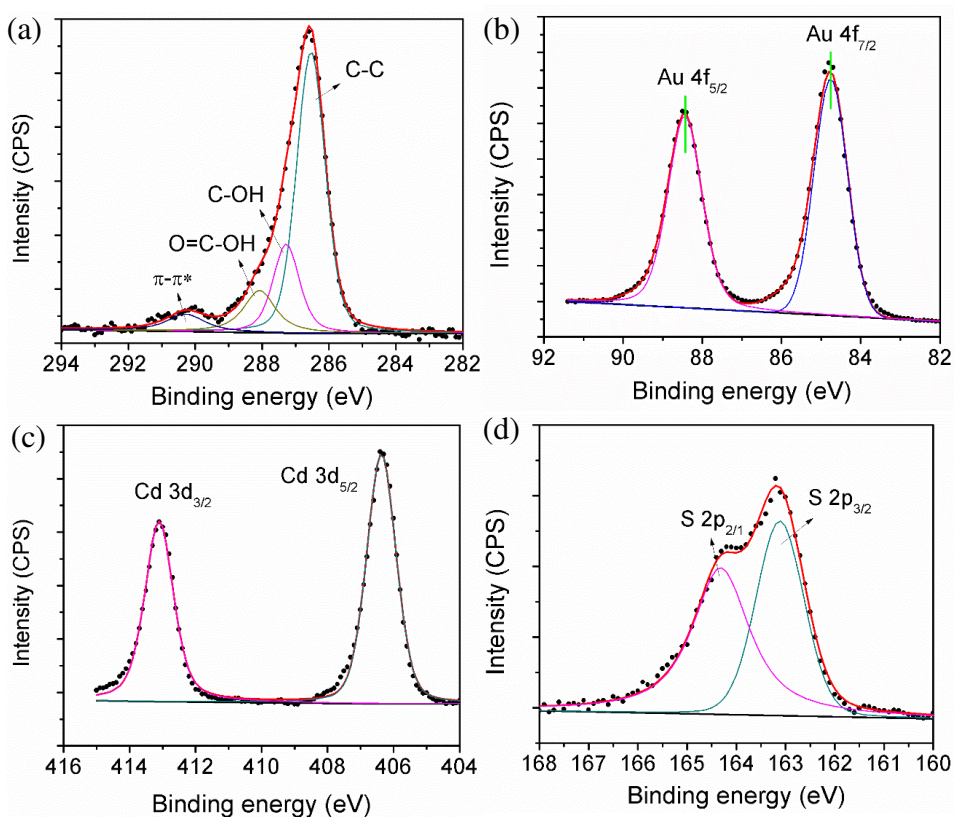


Figure 5.2. Deconvoluted XPS spectra of C 1s (a), Au 4f (b), Cd 3d (c) and S 2p (d) obtained on the GNP-QD heterostructures decorated Si substrate.

XPS spectra were obtained on the GNP-QD heterostructures decorated Si electrode for chemical composition evaluation. Full range XPS spectrum shows various elements including Cd, Zn, S, O, C, and Au were observed.¹⁷⁵ Deconvoluted spectra for C 1s, Au 4f, Cd 3d and S 2p were further demonstrated in detail (Figure 5.2a-d). The deconvoluted C 1s peak shows four Gaussian peaks centered on ~286.54 eV, 287.28 eV, 288.07 eV, and 290.28 eV. The peak at ~290.28 eV corresponds to the electron energy loss peak due to π -plasmon excitations.¹⁷⁶ Electronegative oxygen atoms induced positive charges to carbon atoms, thus peaks with high binding energies located at ~287.28 eV and ~288.07 eV are considered to originate from carbon-oxygen links, corresponding to -COH and -COOH groups, respectively.¹⁷⁷ The peak at ~286.54 eV (C-C) is associated with photoelectrons emitted from the diamond-like carbon atoms hybridized *via* sp^3 bond and hexagonal carbon atoms hybridized *via* sp^2 bond.¹⁷⁸ Pure element Au peaks consistent with Au 4f_{7/2} and Au 4f_{5/2} were observed at ~84.75 eV and ~88.43 eV, respectively (Figure 5.2b). For spectra associated with quantum dots, Cd peak consistent with Cd 3d_{3/2} and Cd 3d_{5/2} were observed at ~413.12 eV and ~406.39 eV, respectively (Figure 5.2c). These were slightly shifted from ~405.0 eV and ~411.7 eV of the standard peak of pure Cd element, which is due to sulfuration for the formation of CdS. For S peaks, S 2p_{1/2} and S 2p_{3/2} were observed at 163.94 eV and 162.75 eV. These values were also shifted from standard S peaks (~165.1 and ~163.9). It needs to mention that no significant peak shifts were observed as compared with the pristine quantum dots,¹⁷⁹ indicating that all the components in the heterostructures remained chemically intact.

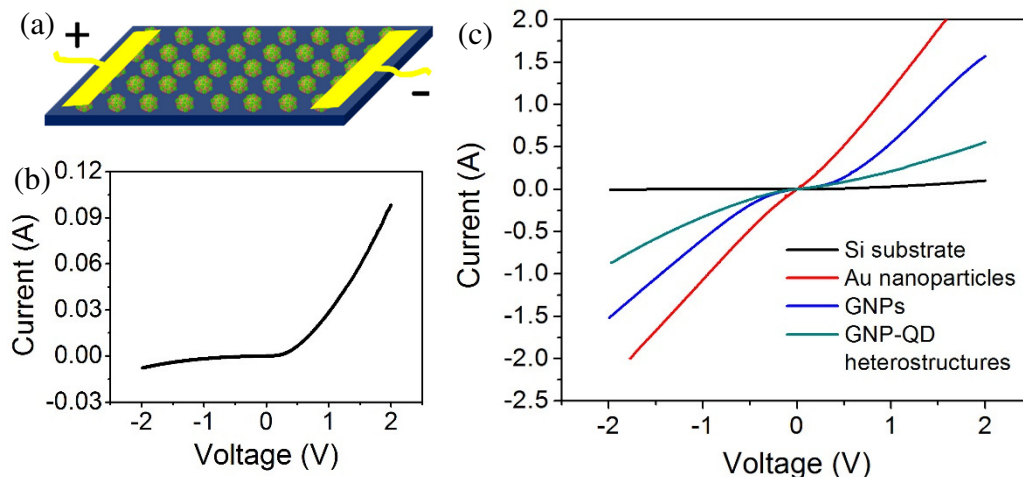


Figure 5.3. I-V curves obtained on the as-received Si substrate, on the Au nanoparticles, as-produced GNPs, and GNP-QD heterostructures decorated Si electrode.

The blank Si electrode as well as the Au nanoparticles decorated, GNPs decorated, and GNP-QD heterostructures decorated Si electrode was evaluated for these electric and electrochemical properties. The electric test set-up was schematically illustrated in Figure 5.3a. The obtained I-V curves were further shown in Figure 5.3b and c. The blank Si substrate (Figure 5.3b) exhibited semiconducting behavior and exhibited rectifying diode behavior with a turn-on voltage of ~ 0.25 V.¹⁸⁰ From the linear part we can estimate that the resistance is $\sim 13.85 \Omega$. The metallic characteristics emerged after the Au nanoparticle decoration as the I-V curve becomes linear (Figure 5.3c), and an electric resistance of $\sim 0.83 \Omega$ was estimated for the Au nanoparticles decorated Si electrode. On further growth of GNPs on Si substrate, a rectification effect was observed, which is probably due to the Schottky barrier between the Au and graphene. The estimated resistance is $\sim 1.07 \Omega$. For GNP-QD heterostructures, the estimated resistance increased to $\sim 1.79 \Omega$. This electric characterization indicates that decoration the Si electrode with Au

nanoparticles, GNPs and GNP-QD heterostructures improved its electric conductivity and thus these composite electrodes can be used for further electrochemical processes.

Figure 5.4a shows the digital images of these decorated electrodes for electrochemical experiments. CV of the blank Si substrate showed a well-defined redox peaks of $\text{Fe}(\text{CN})_6^{3-/4-}$ with a peak-to-peak separation of ~ 300 mV. The Si substrate decorated with Au nanoparticles or GNPs resulted in suppressed redox peaks (Figure 5.4b). It is known that the electrocatalytic activity of Au nanoparticles depends on their size and only sub-10 nm nanoparticles exhibit excellent electrocatalytic behavior.¹⁸¹ The size of Au nanoparticles used here (~ 47.27 nm) was larger than 10 nm and may have led to decreased redox activity. The redox peaks (Figure 5.4b) for the GNPs decorated electrode were negligible and could be due to thick (~ 3.8 nm) multilayer graphene shells on GNPs and their larger resistance than single layered flat graphene, which is consistent with the I-V curves in Figure 5.3c.¹⁸² In contrast to these two electrodes, GNP-QD heterostructures decorated electrode showed enhanced redox activity (Figure 5.4b). This could be attributed to a) improved electron transfer between GNPs and quantum dots¹⁸³ and b) reduced multilayer graphene shell thickness (~ 0.8 nm) for plasma-treated GNPs that were utilized for fabricating GNP-QD heterostructures in this study.

EIS spectrum of blank Si substrate showed a large capacitive arc in the whole frequency range. In contrast, Au nanoparticles and GNPs exhibited two capacitive arcs in the low and high frequency region (Figure 5.4c). These could be attributed to the film impedance of the modified electrode and the electron transfer impedance associated with the faradaic reactions.¹⁸⁴ In addition, the Warburg impedance line associated with the semi-infinite linear diffusion (unrestricted diffusion to a large planar electrode) was observed in the low frequency region for the GNP-QD

heterostructures. Accordingly, the following equation can be used to describe the total impedance of this faradaic reaction system:¹⁸⁴

$$Z_T = R_s + \frac{1}{\frac{1}{R_f} + \frac{1}{C_f}} + \frac{1}{\frac{1}{C_d} + \frac{1}{R_t + Z_w}}. \quad (5.1)$$

The R_s , R_f , and R_t are the solution, film, and electron transfer resistances, respectively. The film resistance, R_f , indicates the resistance of the blank Si substrate or the same patterned with Au nanoparticles, GNPs, or GNP-QD heterostructures. The C_f and C_{dl} represent the capacitance of the modified Si substrate and the double layer, respectively. The Z_w stands for the Warburg diffusion element defined as: $Z_w = s(1 - j)/\omega^{1/2}$, where s is a constant related to the Warburg impedance, $j = (-1)^{1/2}$, and ω is the angular frequency. The corresponding Equivalent Electrical Circuit (EEC) was shown in Figure 5.4d.¹⁸⁵ This EEC was used to simulate the experimental EIS spectra in the ZSimpWin® software. Considering the surface complexity of these modified electrode, Constant Phase Elements (CPEs) were used to replace the capacitors (C) in the EEC for the simulation of EIS. CPE can model the behavior of double layer or imperfect capacitor by considering factors such as surface roughness and non-uniformity in distribution of surface reaction sites.¹⁸⁵ The impedance of CPE can be written as:

$$Z_{CPE} = 1/Q(j\omega)^n, \quad (5.2)$$

where Q representing the capacity parameter expressed in $S\ cm^{-2}\ s^n$, $j = (-1)^{1/2}$ and n represents the deviation from the ideal behavior, n being 1 for the perfect capacitors.

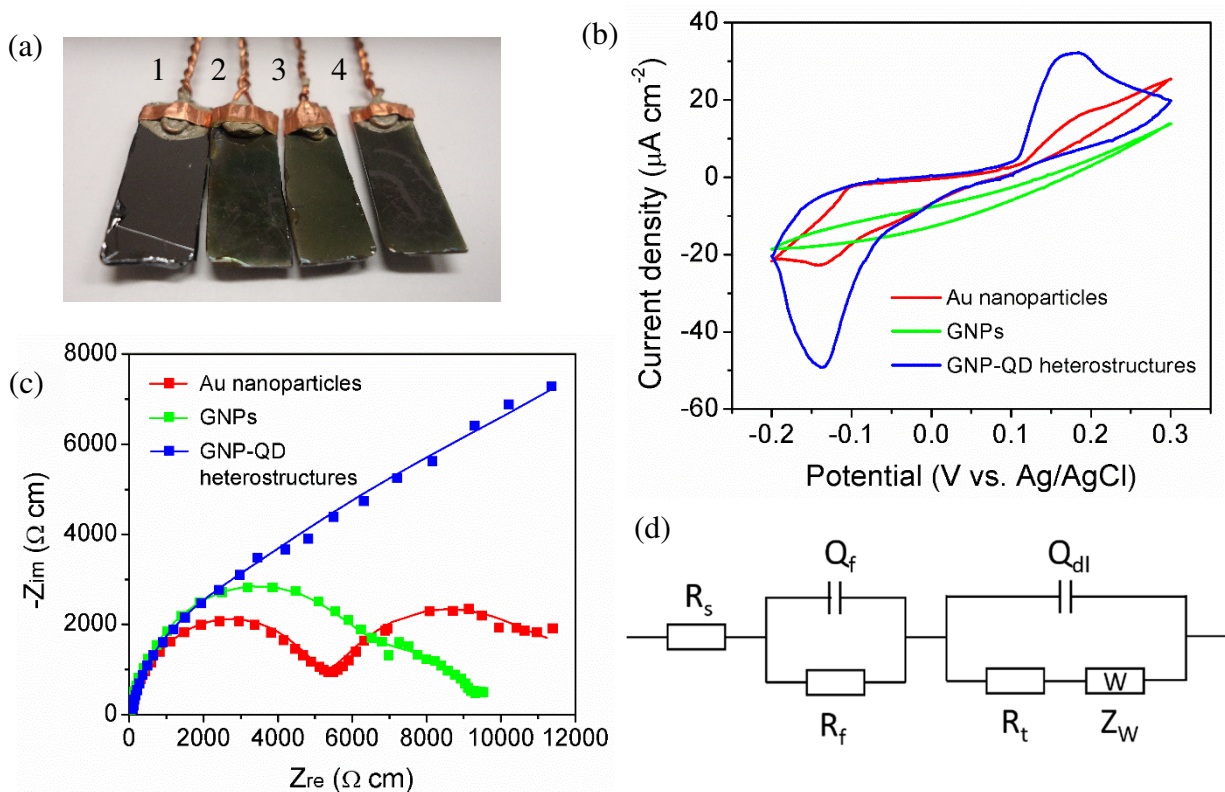


Figure 5.4. (a) Digital images of electrodes comprised of various samples: (1) blank Si substrate, (2) Au nanoparticles, (3) as-produced GNPs, (4) GNP-QD heterostructures. (b) CV diagrams and (c) EIS for Au nanoparticles, as-produced GNPs, and GNP-QD heterostructures. (d) EEC used for the simulation of EIS data in the ZSimpWin software. *NOTE: Scatters in (c) show the experimental data and the solid fitted lines correspond to simulated data.*

The simulated impedance spectra for various samples studied are shown in Figure 5.4c (solid lines) and compared with experimental values (scatters). The simulated spectra (solid lines) showed a good agreement with the experimental spectra (scatters). The simulation-based impedance parameters are shown in Table 5.1. The blank Si substrate showed one capacitive arc in the whole frequency region and could be attributed to film resistance ($\sim 10920 \Omega \text{ cm}^2$, Table 5.1). The capacitive arcs in the high frequency region for Au nanoparticles and GNPs were also attributed to the film resistance. These film resistances were decreased as compared with the blank Si substrate due to the higher electrical conductivity of Au nanoparticles and GNPs. The estimated

film resistance (Table 5.1) of GNP-QD heterostructures was slightly increased due to the attachment of semiconducting quantum dots.

Table 5.1. Impedance parameters of the blank Si electrode, Au nanoparticles, GNPs, and GNP-QD heterostructures obtained using the EEC (Fig. 4d). *Note: R_s , R_f , and R_t are the solution, film, and electron transfer resistances, respectively. The Q_f and Q_{dl} represent the CPE of the film and double layer capacitance, respectively.*

	R_s ($\Omega \text{ cm}^2$)	Q_f ($\text{S s}^n \text{ cm}^{-2}$)	n	R_f ($\Omega \text{ cm}^2$)	Q_{dl} ($\text{S s}^n \text{ cm}^{-2}$)	n	R_t ($\Omega \text{ cm}^2$)	W
Si electrode	46.5	1.15×10^{-5}	0.59	10020	1.94×10^{-6}	0.98	920	5.36×10^{-4}
Au nanoparticles decorated electrode	25.46	2.16×10^{-8}	0.85	5026	3.24×10^{-6}	0.78	7220	2.43×10^{-4}
GNPs decorated electrode	30.44	7.46×10^{-8}	0.90	6618	5.58×10^{-6}	0.79	3052	1.05×10^{-3}
GNP-QD heterostructures decorated electrode	27.15	7.77×10^{-6}	0.70	8070	2.99×10^{-6}	1	330	2.50×10^{-5}

The electron transfer resistance, R_t , is critical as it is a direct measure of the electrochemical activity for the electrode.¹⁸⁴ The estimated R_t value for blank Si substrate was lowest as compared to other samples (Table 5.1). This could be the reason for the highest redox activity for the blank Si substrate. The capacitive arcs in the low frequency region for Au nanoparticles and GNPs correspond to the reaction impedance (Figure 5.4c). The corresponding estimated R_t (Table 5.1) was much larger than that of Si substrate due to the surface silicon oxide and the multilayer graphene shells. This is consistent with the observation that the redox peaks were suppressed for Au nanoparticles and GNPs (Figure 5.4b). The estimated R_t value for the GNP-QD heterostructures was lower than Au nanoparticles and GNPs (Table 5.1) and explains enhanced redox peaks for the heterostructures in Figure 5.4b. The electrical conduction in semiconducting quantum dots is based on the mobility of sulfur vacancies.¹⁸⁶ In this case, S^{2-} donate electrons to the conductive GNPs under positive bias and resulting in sulfur vacancies. These positively charged vacancies further act as the active sites to accept electrons from the $Fe^{2+/3+}$ system.¹⁸⁷ Accordingly, the electron transfer in GNP-QD heterostructures based electrode was significantly enhanced. This is probably the reason that the heterostructures showed enhanced redox peaks and low electron transfer resistance (R_t). In addition, the GNP-QD heterostructure electrode exhibited decreased Warburg diffusion impedance, indicating that the film structure was disintegrated, improving the ionic diffusion of electrolyte on the local surface of the electrode.¹⁸⁸

5.4. Conclusions

In summary, fabrication of GNP-QD heterostructure decorated silicon electrode was demonstrated. The controlled patterning of the heterostructures was achieved *via* several critical processes including galvanic deposition of Au film, annealing, CVD growth of multilayer graphene shell on Au nanoparticles and covalent linking of quantum dots on GNPs. The microscopic characterization indicates that the nanostructures (Au nanoparticles, GNPs, and GNP-QD heterostructures) were uniformly patterned on the silicon substrate. Meanwhile, the spectroscopic results shown that various components in the heterostructures are chemically intact. Decoration of silicon electrodes with these nanostructures improved the electrical conductivity, making them feasible for the aqueous-based electrochemical processes. The CV and EIS demonstrated that the GNP-QD heterostructure decorated silicon electrode shows significantly increased electrochemical charge transfer activity due to the possible interactions within quantum dots, graphene shell and Au nanoparticles. The charge transfer resistance of the GNP-QD heterostructure decorated electrode is $330 \Omega \text{ cm}^2$, which is significantly decreased as compared with that of Au nanoparticle electrode ($7220 \Omega \text{ cm}^2$) and GNP electrode ($3052 \Omega \text{ cm}^2$). Such heterostructure-decorated silicon electrode will be of interest in future small-sized electronic/electrochemical devices.

CHAPTER 6

FABRICATION AND OPTICAL PROPERTIES OF GRAPHENE SHELLS ENCAPSULATE GOLD NANOPARTICLE – CARBON NANOTUBE HETEROSTRUCTURES

Yuan Li¹, John Connor Dykes², Todd Gilliam³, Nitin Chopra,^{1,4,}*

¹Metallurgical and Materials Engineering Department, Center for Materials for Information Technology (MINT), The University of Alabama, Tuscaloosa, AL 35487, U.S.A.

²REU, Department of Mathematics, The University of Alabama, Tuscaloosa, AL 35487, U.S.A

³Department of Chemical Engineering, The University of Alabama, Tuscaloosa, AL 35487, U.S.A

⁴Department of Biological Sciences, The University of Alabama, Tuscaloosa, AL 35487, U.S.A.

*Corresponding Author

E-mail: nchopra@eng.ua.edu

Tel: 205-348-4153

Abstract

We reported a facile route for the fabrication of multilayer graphene shells encapsulated gold nanoparticles – single-walled carbon nanotube (SWCNTs) heterostructure by means of the combination of the carbodiimide chemistry and biotin-streptavidin affinity. In the first step, Au nanoparticles were prepared through the galvanic deposition – annealing process. This was followed by encapsulation of multilayer graphene shells on these Au nanoparticles (GNPs) via a chemical vapor deposition process. Carbodiimide chemistry was further used to covalently link the NH₂-terminated biotin to the GNPs. Finally, streptavidin-wrapped SWCNTs were attached to these graphene encapsulated Au nanoparticle (GNPs) by means of the affinity of biotin and streptavidin. The morphology and structure of the GNPs and the GNP-CNT heterostructures were studied using SEM and TEM. The optical properties of the GNP-QD heterostructures were further modeled using the discrete dipole approximation (DDA) method.

Keywords: multilayer graphene shell encapsulated gold nanoparticles, carbon nanotubes, heterostructures, Discrete dipole approximation

6.1. Introduction

Single-walled carbon nanotubes (SWCNTs) has exceptional thermal, mechanical, electrical, and optical properties and has been considered of specially great interest in the applications of molecule electrons, electron-analytical sensors and field emission transistors [189]. Self-assembly of SWCNTs can result in single molecule transistor, which shows great potential in dealing with the miniaturization problem and reducing the fabrication cost [190]. Dekker et al. reported the application of such single electron transistor (SET) in realizing the logical gates mimicking the CMOS ones but with a lateral channel extension reduced to 1 nm [191]. Recently, more effort was contributed to improve the reproducibility and sensitivity of such SETs for applications such as DNA recognition and other biological systems [192]. One of the most important approach is the complexation or hybridization of these SNCNTs with other materials such as fullerene, quantum dot, etc. to form multifunctional heterostructures [193]. However, all of these demonstrations are conducted on randomly arranges SNCNTs, which is not desirable for the bottom-up philosophy of such molecular electronics [190]. Realizing the controlled arrangement or positioning of these single or complex SWCNTs by means of self- or possibly directed-assembly is still a big challenge.

Recently, the authors demonstrated a facile and scalable xylene-based chemical vapor deposition (CVD) approach for the growth of graphene shells on Au nanoparticles (GNPs) [194]. The encapsulation of graphene shell significantly modified the optical properties and chemical stability of Au nanoparticles, and most important, further grafted the nanostructures with enriched surface chemistry. Thus, development of GNPs based complex architectures becomes possible. In this paper, we reported a facile and controlled approach for the fabrication of ordered assembly of GNP-CNT heterostructures through a covalent linking method. Uniformly dispersed Au nanoparticles on the Si substrate were obtained through the galvanic deposition – annealing

process. Further graphene shell encapsulation was achieved by the xylene-based CVD method. Oxygen plasma was conducted to remove amorphous carbon, optimize the graphene shell thickness and create surface functional carboxyl groups on GNPs. This was followed by covalently attaching NH₂-terminated biotin to these GNPs using carbodiimide chemistry. Such biotin-GNPs were further reacted with streptavidin warped SWCNTs to form the GNP-CNT heterostructures.

6.2. Experimental section

Materials and Methods: P-doped Si wafers (111) were purchased from IWS (Colfax, CA). Potassium gold (III) chloride was purchased from Sigma-Aldrich (St. Louis, MO). Hydrogen fluoride (~50 wt.%) was purchased from VWR (Atlanta, GA). Ammonium fluoride was purchased from Alfa Aesar (Ward Hill, MA). 1-ethyl-3-(3-dimethylaminopropyl) carbodiimide (EDC) and N-hydroxysuccinimide (NHS), 2-(N-morpholino) ethanesulfonic acid (MES) were purchased from Thermo scientific (Rockford, IL). All chemicals were used without further purification. Buffered oxide etch (BOE) solution was prepared by mixing ~40 wt.% NH₄F and ~50 wt.% HF in DI-water (volume ratio of 6:1). DI-water (18.1 MΩ-cm) was obtained using a Barnstead International DI water system (E-pure D4641). The GNP growth was carried out in a Lindberg blue three-zone tube furnace (Watertown, WI) with a quartz tube purchased from ChemGlass (Vineland, NJ). The gas flow rates were controlled by Teledyne Hasting 400 mass flow controllers (Hampton, VA). H₂ (10% in Ar), N₂, and Ar gas cylinders (UHP grade) were purchased from Airgas South (Tuscaloosa, AL). Oxygen plasma treatment was performed in a Nordson March Jupiter III Reactive Ion Etcher (Concord, CA).

Synthesis of graphene shells encapsulated Au nanoparticles (GNPs): Au film was deposited on a Si substrate using acid-based wet-chemical method [195,196]. In this method, an acetone-cleaned Si substrate was treated with BOE solution for 30 s to remove the surface oxide layer. This was followed by immersing the substrate in the acidic solution comprised of ~1 mM KAuCl_4 in ~1 wt.% HF. The reaction was carried out for 30 s, 60 s and 90 s to result in Au films with different thickness. The substrate was washed with DI-water, dried, and subsequently annealed in air for 15 min at 850 °C. This annealing step led to de-wetting of Au film and resulting in Au nanoparticles patterned onto the Si substrate. Chemical vapor deposition process was used for the growth of multilayer graphene shells. As a first step, these Au nanoparticles patterned on Si substrate were treated with oxygen plasma for 15 min to result in surface gold oxide. This was followed by the CVD growth process at ~675 °C for 1 h. Xylene was used as the carbon source and was fed into the reactor at a rate of ~10 mL/h. The carrier gas was 10% H_2/Ar with a total flow rate of 1.15 SLM. Once the reaction was completed, the reactor was allowed to naturally cool down under the Ar flow. This process resulted in orderly patterned GNPs. Finally, the $-\text{COOH}$ derivatization on the GNPs was carried out by treating the as-produced GNPs with oxygen plasma for 15 s.

Chemical linking of SWCNTs on GNPs: GNPs were covalently linked with NH_2 -terminated biotin using the carbodiimide chemistry [197]. Briefly, the $-\text{COOH}$ terminated GNPs patterned on the Si substrate was immersed in a ~50 mM MES buffer (pH = 6.1) solution with ~2 mM EDC and incubated for 10 min under gentle shaking. This was followed by adding ~4 mM NHS and incubated for 1 h. This process allowed the formation of stable amine-reactive NHS ester. The substrate was gently washed with PBS buffer (pH = 7.4) and then immersed in the PBS buffer (pH = 7.4) containing 2 mM NH_2 -biotin. This reaction was allowed for 12 h to form the amide bonds ($-\text{CONH}$). At the same time, SWCNTs were treated with $\text{H}_2\text{SO}_4/\text{HNO}_3$ solution (v/v=3/1) for 3 h

at 60 °C. The product was centrifuged and washed for several times until the pH of superant became ~7. These treated SWCNTs were incubated in 5 mM streptavidin solution for 12 h. As a last step, the biotin-terminated GNPs were immersed in this SWCNTs solution and further incubated for 12 h to form the GNP-CNT heterostructures. This final product was washed with DI-water and dried in N₂.

Characterization methods: FE-SEM (JEOL-7000) and Tecnai F-20 TEM were used to characterize the morphology, crystal structure, and/or interfaces present in Au nanoparticles, GNPs, and GNP-QD heterostructures. The dimension, number density, and shell thickness was measured using more than 100 nanoparticles/hybrid assemblies per sample. This was utilized to calculate average values as well as standard deviations. Discrete dipole approximation (DDA) method was used to simulate the plasmonic properties of the as-produced GNPs and the GNP-QD heterostructures. This method is based on the solution of 3-D Maxwell equation via the DDSCAT code developed by Draine and Flatau [198,199]. Detailed simulation procedures have been demonstrated by our group in [200]. Briefly, DDSCAT 7.2 was utilized to estimate the normalized electric field or surface plasmon generation for the GNPs and the GNP-QD heterostructures. The normalized electric field intensity is defined as the ratio between the electric field generated near the nanostructures and the incident electric field ($|E|/|E_0|$). The geometrical targets were generated using 3-D max software for different heterostructures. The effective radius of the dipoles was calculated using: $R_{\text{eff}} = (3V/4\pi)^{1/3}$, where V is the total volume of the material in the target and is calculated with $V = Nd^3$ (N is the number of dipoles and dis the lattice spacing in cubic array). Near-field electric field distributions were extracted using the DDFIELD utility of DDSCAT 7.2 and processed using MayaVi 2 from Python(x,y).

6.3. Results and discussion

Figure 6.1 outlines the schematic for the preparation of multilayers graphene shells encapsulated Au nanoparticles (GNPs) and further attachment of acid-treated SWCNTs using the affinity of biotin and streptavidin. The schematic for the linking chemistry were further shown in Figure 6.2. Briefly, the GNPs were prepared by a xylene based chemical vapor deposition process (CVD). The as-produced GNPs were first treated with oxygen plasma to create surface carboxyl functional group. This was followed by the chemical reaction of EDC and NHS, which allowed the formation of stable amine-reactive NHS ester. This ester was further reacted with NH_2 -terminated biotin, which allowed the formation of peptide linked GNP-biotin structures. In the last step, streptavidin-warped SWCNTs were attached to the surface of GNPs *via* the biotin-streptavidin affinity.

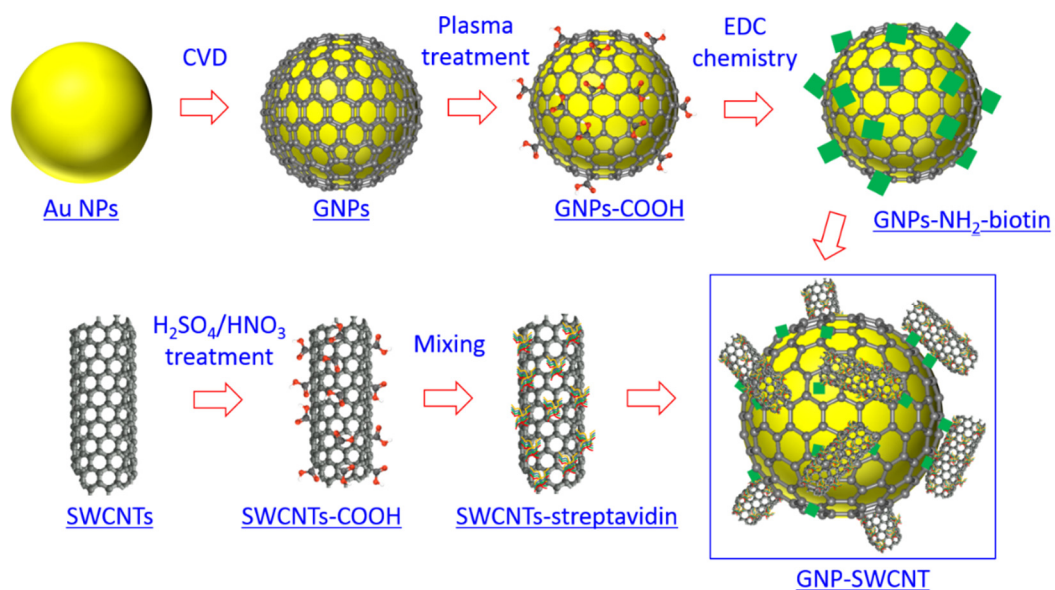


Figure 6.1. Schematic showing the preparation of multilayer graphene shells encapsulated gold nanoparticles (GNPs) and further plasma treatment for the covalent linking of single-walled carbon nanotube (SWCNT) by combining the EDC/NHS and biotin/streptavidin chemistry.

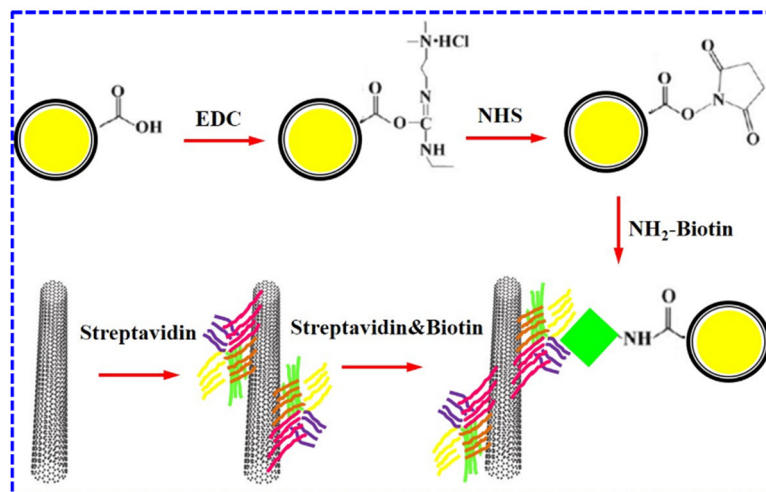


Figure 6.2. Schematic showing the principle of carbodiimide chemistry and biotin-streptavidin chemistry for the fabrication of the GNP-CNT heterostructures.

6.3.1. Fabrication of GNP-QD heterostructures

Figure 6.3A and B show the patterned Au nanoparticles and GNPs on the Si substrate. The high resolution SEM images were further demonstrated in the insets. A clear graphene shell was observed to be encapsulated on the Au nanoparticles. The estimated Au nanoparticles size is 60.13 ± 13.88 nm with an inter-particle spacing of 72.4 ± 15.6 nm. After graphene growth, the size of GNPs were slightly increased as compared to the previous Au nanoparticles. The estimated GNP size is 72.19 ± 10.17 nm nm with an inter-particle spacing of 80.8 ± 16.9 nm. The spatial density of GNPs was also observed to be decreased as compared with the pristine Au nanoparticles, which is due to the inevitable merging of Au nanoparticles during the high temperature CVD process. Figure 6.3C and D further show the SEM image of GNP-CNT heterostructures patterned on the Si substrate. Either individual SWCNTs or aggregated SWCNT clusters were observed attached on the surface of GNPs. The average size of these heterostructures was decreased to 68.48 ± 14.12 nm as compared with the as-produced GNPs due to the influence of plasma treatment on the

thickness of graphene shells. The column diagram in Figure 6.3 summarized the average diameter and inter-particle spacing of Au nanoparticles, GNPs and the GNP-CNT heterostructures.

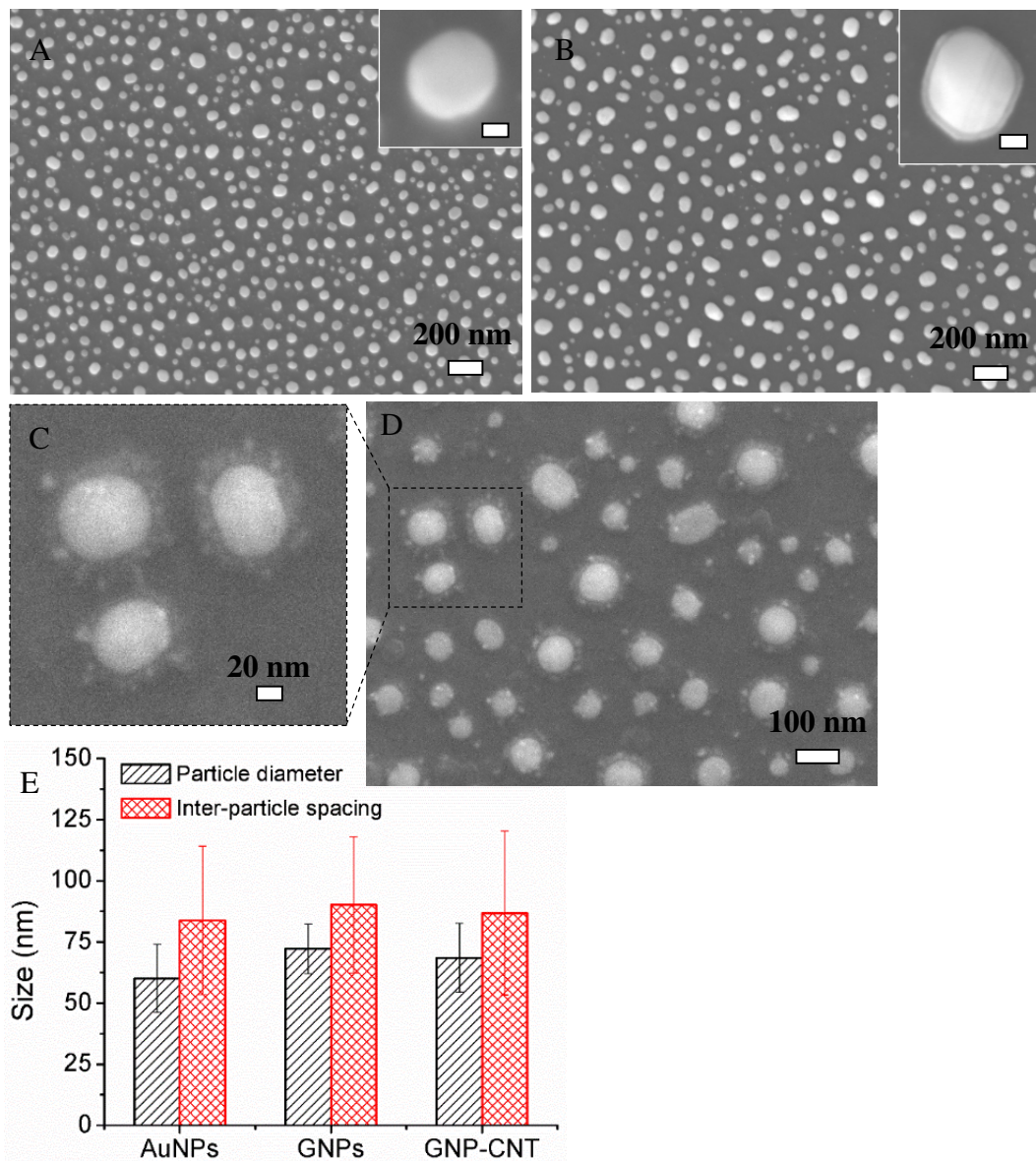


Figure 6.3. SEM images showing the as-produced Au nanoparticles (A), GNPs (B) and the GNP-CNT heterostructures (C and D). *NOTE: The insets in (A and B) show high-resolution SEM images (scale bar: 20 nm).* (E) Histogram showing the variation of particle diameter and inter-particle spacing of the Au nanoparticles, GNPs and GNP-CNT heterostructures.

Representative TEM/HRTEM images of the as-produced GNPs and the plasma-treated GNPs were shown in Figure 6.4A-C. The thickness of such graphene shells was around ~ 3.8 nm, of which the c-axis lattice spacing is ~ 0.38 nm (Figure 6.4B). This value is slightly larger than that of graphite (0.34 nm) due to the curvature of these graphene layers [194]. A thickness of ~ 0.8 nm was estimated for the plasma-treated GNPs, of which the lattice spacing was increased to ~ 0.39 due to the defects created by the plasma etching. TEM images of the GNP-CNT heterostructures were shown in Figure 6.4D-F. HRTEM image (Figure 6.4D and F) and corresponding inset FFT image further confirms the attachment of the SWCNTs on the GNPs.

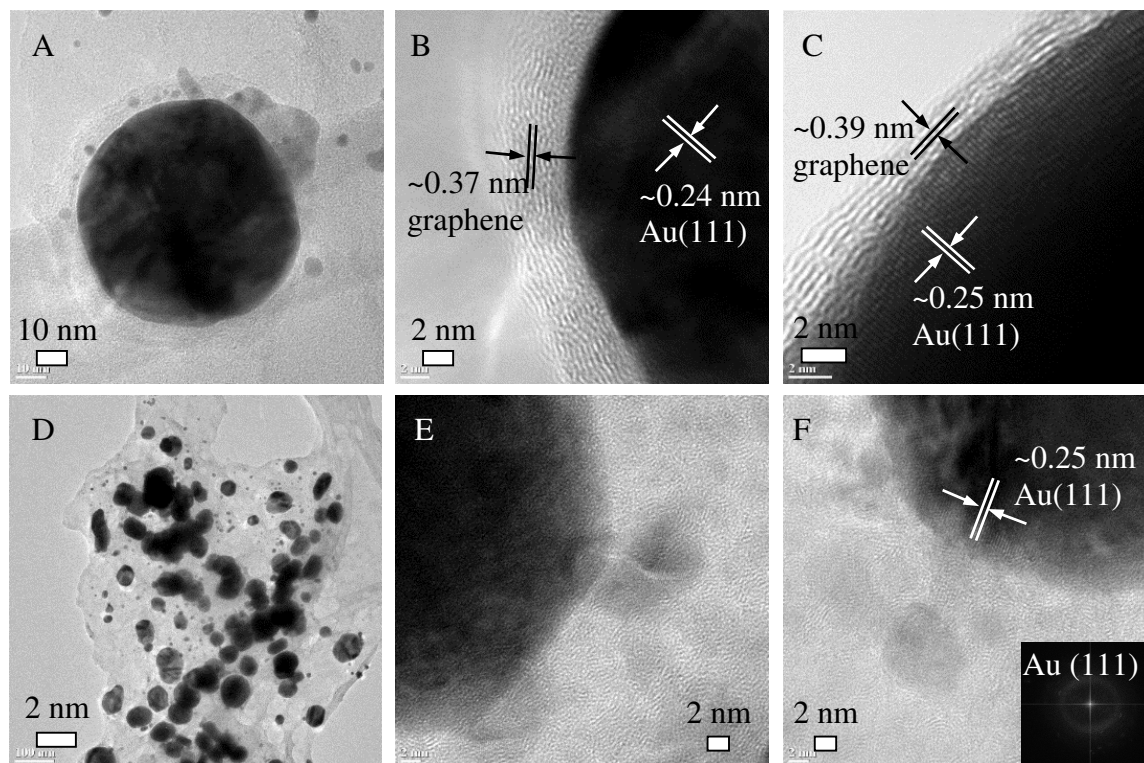


Figure 6.4. (A, B) TEM/HRTEM images of the as-produced GNPs. (C) HRTEM image of the GNPs after plasma treatment. (D-F) TEM/HRTEM images of the GNP-CNT heterostructures.

The fluorescence images in Figure 6.5A-C further confirms the attachment of SWCNTs on the GNPs. The as-produced GNPs show fluorescence effect (Figure 6.5A). However, after the attachment of SWCNTs, the regions with the presence of GNPs present green dots generated from the fluorescent streptavidin while other regions with no GNPs remained dark color (Figure 6.5B and C). Raman spectra of the as-produced GNPs (Figure 6.5D) show the well-defined G band at $\sim 1595\text{ cm}^{-1}$ and D band at $\sim 1310\text{ cm}^{-1}$ [201]. D band in GNPs was observed due to the disorder created by the curvature of graphene layers and the existence of amorphous carbon [202]. These peaks locations were different than flat graphene (G band $\sim 1580\text{ cm}^{-1}$) and such shifts in Raman peaks have been previously studied and attributed to strains in the multilayer graphene shell lattice, shell thickness, and the size of GNPs. Plasma treatment significantly decreased the intensity of D band and G band. The estimated I_D/I_G ratio after plasma oxidation was between 1.5 and 2.0, which indicates that this process led to more defects and disordered structure within the multilayer graphene shells. The GNP-CNT heterostructures show increased D band and G band as compared with the plasma-treated GNPs. In addition, the G band was split to two peaks. The additional peak (called D' band) located at $\sim 1610\text{ cm}^{-1}$ has been well-defined for carbon nanotubes and attributed to the amorphous hydrogenated carbon, which is regarded as one kind of defective graphite structure [203]. This further confirmed the attachment of SWCNTs on the GNPs.

The carbodiimide chemistry used for the covalent attachment of SWCNTs to the plasma-treated GNPs was characterized using FTIR. The results were shown in Figure 6.5E For the as-produced GNPs and the plasma-treated GNPs, appearance of C=C and C=O stretches were observed at $\sim 1530\text{ cm}^{-1}$ and $\sim 1650\text{ cm}^{-1}$. The weak signal of C=O is due to the natural oxidation of graphene shells in air, which was observed in above XPS study. After plasma treatment, the C=O signal was enhanced, allowing for further covalent attachment of biotin as shown in Figure 6.2. For the FTIR

spectra after the SWCNT attachment, the appearance of amide I ($1650\sim 1670\text{ cm}^{-1}$, C=O stretch), amide II and amide III stretches (1550 cm^{-1} and 1240 cm^{-1} , respectively, stretching of C-N and/or blending of N-H) further indicate the formation of covalent bond between -COOH on the graphene shell and -NH₂ at the end of biotin [204].

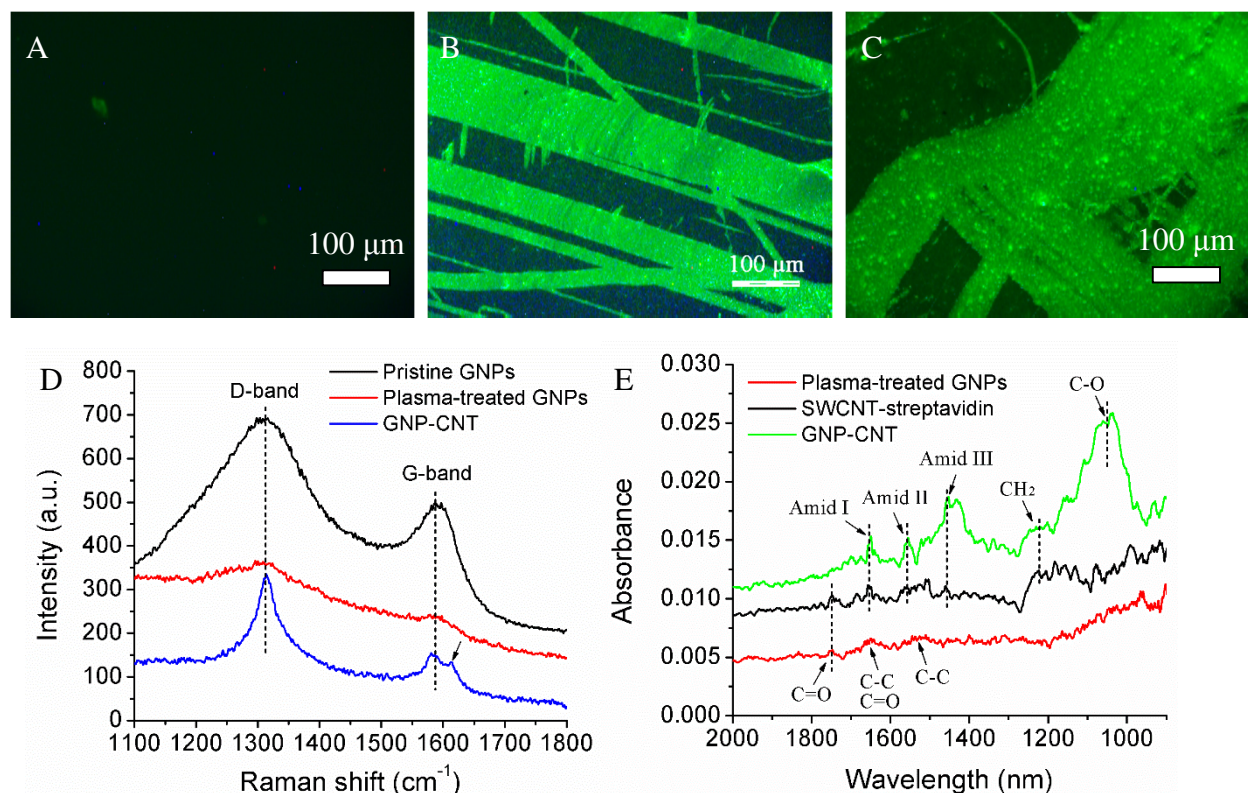


Figure 6.5. (A-C) Fluorescence images obtained from (A) the pristine GNPs and (B, C) GNP-CNT heterostructures. (D) Raman spectra of the pristine GNPs, plasma-treated GNPs and GNP-CNT heterostructures. (E) FTIR spectra of the plasma-treated GNPs, SWCNT/streptavidin, and GNP-CNT heterostructures.

6.3.2. Discrete Dipole Approximation modeling

To further demonstrate the influence SWCNTs attachment on the plasmonic properties of GNP-CNT heterostructures, DDSCAT was used to simulate their surface extinction and electric field distribution. The nanostructured configurations (or target) in this study were comprised of an arrangement of dipoles for which extinction spectra and electric field distributions were numerically solved. The extinction efficiency is given by:

$$Q_{ext} = Q_{abs} + Q_{sca} \quad (6.1)$$

where Q_{ext} is the extinction efficiency factor, Q_{sca} is the scattering efficiency factor and Q_{abs} is the absorbance factor. In the simulation, the target was assumed to be composed of a spherical plasma-treated GNP and 25 carbon nanotubes. The Au nanoparticles core was assumed to be 50 nm and the encapsulated graphene shell was assumed to be 0.8 nm thick. The size of carbon nanotubes was estimated to be equivalent to the size of SWCNT clusters surround on the GNPs (Figure 6.5A), of which the length is 10 nm, the outside diameter is 10 nm and inside diameter is 5 nm. The 3-D images of these nanostructures created by 3ds max software were shown in Figure 6.5A. The composition configuration of the corresponding targets was also analyzed by the LiteBil software, as shown in Figure 6.5B and C. Three more targets were generated accordingly by putting two GNP-QD heterostructures together with an inter-particle spacing of 0 nm, 5 nm and 10 nm. The representative 3-D images were shown in Figure 6.6D and E.

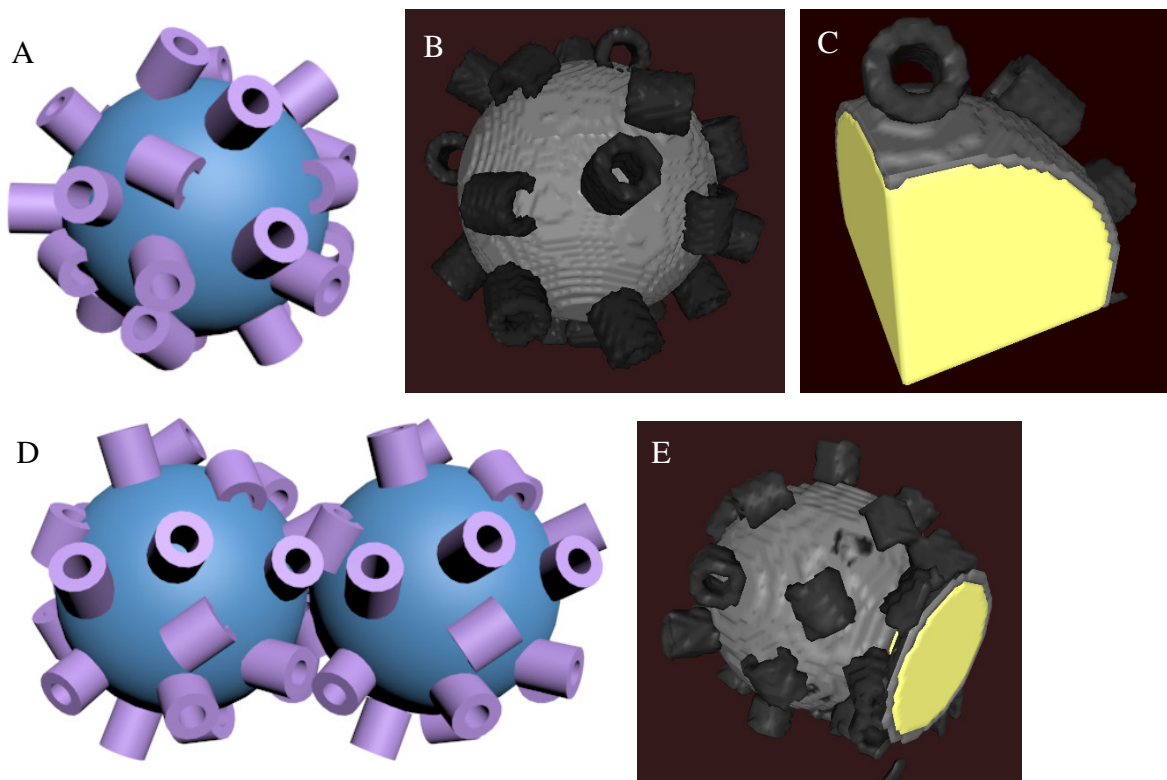


Figure 6.6. (A) 3-D image of the GNP-CNT heterostructures developed by 3ds Max software for DDSCAT-based plasmonic modeling. (B, C) Corresponding 3-D images developed by LiteBil software showing the chemical composition of the heterostructures. (D, E) 3-D images of the target composed of two GNP-CNT heterostructure with inter-particle spacing of 0 nm.

DDA simulation method allows the calculation of the extinction spectra and the normalized electric field distribution of the target. The obtained extinction efficiency spectra show the combined effect of scattering and absorption of the incident electromagnetic wave. As shown in Fig. 6.7A, the GNP-CNT heterostructures show the well-defined extinction peak at ~ 524 nm [205,206]. This extinction spectrum were further split into absorbance and scattering components. As shown in Figure 6.7A, absorbance has a dominant contribution to the extinction spectra while the effect of scattering was relatively small. The same phenomenon was also observed for other targets. This is because size of these nanostructures are much smaller than the wavelength of

incident wave. This is because size of these nanostructures is much smaller than the wavelength of incident wave [207]. This result has a good consistence with that reported before [208]. These authors pointed out that when particles are small compared to the wavelength of light, the scattering is said to be in the Rayleigh regime. Then the scattering (Q_{sca}) can be written as $Q_{sca} = \frac{8\pi}{3}k^4R^6F(m)$, where $k = \frac{2\pi}{\lambda}$ (λ is the wavelength), R is the radius of the particles, and $F(m)$ is a function of the refractive index (m). Meanwhile, the absorption (Q_{abs}) can be written as $Q_{abs} = 4\pi kR^3E(m)$, where $E(m)$ is also the function of the refractive index relying on a non-zero imaginary part. Thus, the ratio of scattering to absorbance is $\sim \frac{2}{3}(kR)^3 \frac{F}{E}$, which is further equivalent to $(kR)^3$. As we pointed out above, the average diameter of the heterostructures is ~ 72 nm ($R = 36$ nm). If consider a wavelength of ~ 500 nm, we got that the ratio $(kR)^3 = 0.1$. This result shows a good agreement with the ratio of scattering to absorbance in figure 6.7.

In addition, it is worthy to mention that another broad extinction peak was observed at the UV region. This peak has been reported before and assigned to the interband transition [205,209], which basically is due to the excitation of d electrons when the energy of incident photon is larger than the gap energy. This direct interband extinction can occur at any energy-conserved position in the brillouin zone. The energy conservation equation was given by:

$$\hbar\omega = \varepsilon_c(k) + \varepsilon_v(k) \quad (6.2)$$

where \hbar is the Plank constant, ω is the frequency. $\varepsilon_c(k)$ and $\varepsilon_v(k)$ are the dielectric function of the empty band and full band. The wavelength of the extinction peaks was further selected as the incident wavelength to generate the normalized electric field distribution.

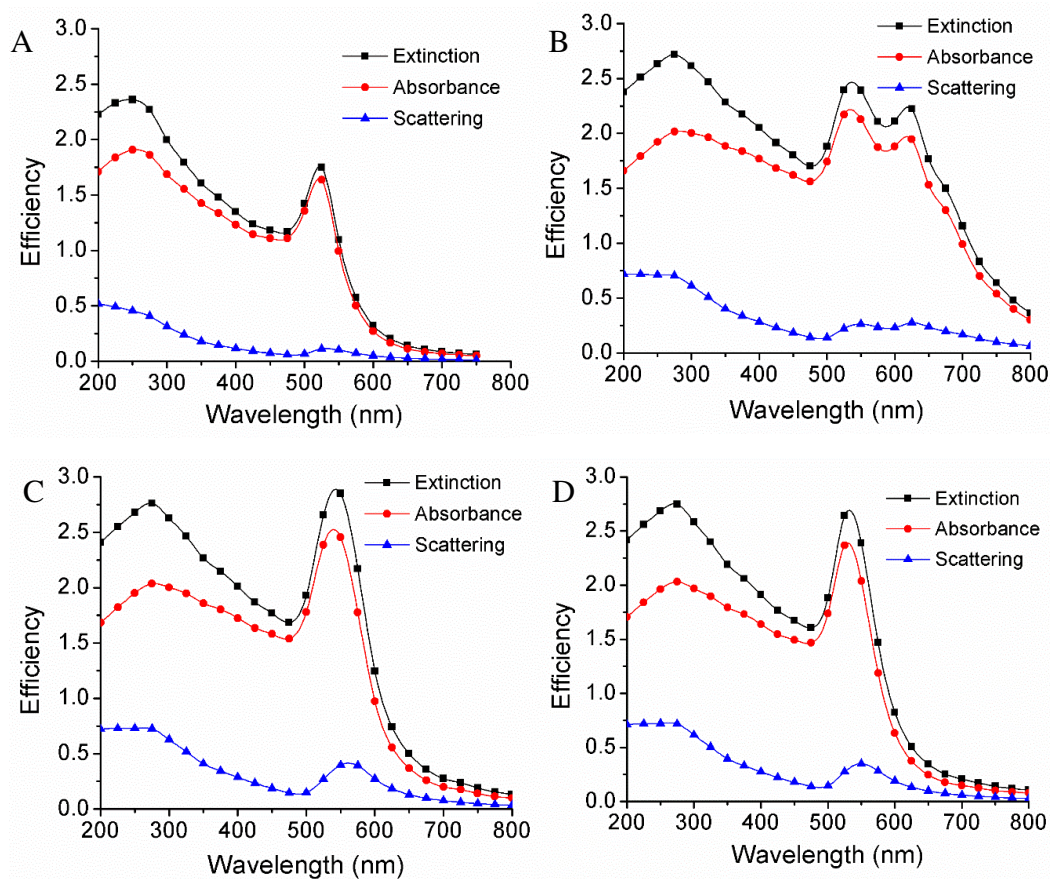


Figure 6.7. Simulated extinction, absorbance and scattering plots as a function of wavelength for a single GNP-CNT heterostructure target (A), Two GNP-CNT heterostructure target with inter-particle spacing of 0 nm (B), 5 nm (C) and 10 nm (D).

As shown in Figure 6.8, the intense electric field (generally called “hot spots”) was mainly observed in the contact interface of the SWCNTs and GNPs. This further confirmed the efficiency interactions of surface plasmon from Au nanoparticle with surrounding carbon nanostructures. For the closely settled GNP-CNT heterostructures, the electric field at the interstice of two heterostructures were significantly increased. Obvious overlapping of electric field was observed and this is of great importance of the applications in localized surface plasmon resonance (LSPR) based Raman sensing. The comparison of extinction spectra for various targets were shown in Figure 6.9A. Obvious blue shift of resonance peak were observed for the closely settled GNP-CNT

heterostructures. The $|E/E_0|$ vs. position plots showing in Figure 6.9B further confirm the strongest electric field exist at the interface or interstice of the GNP-CNT heterostructures.

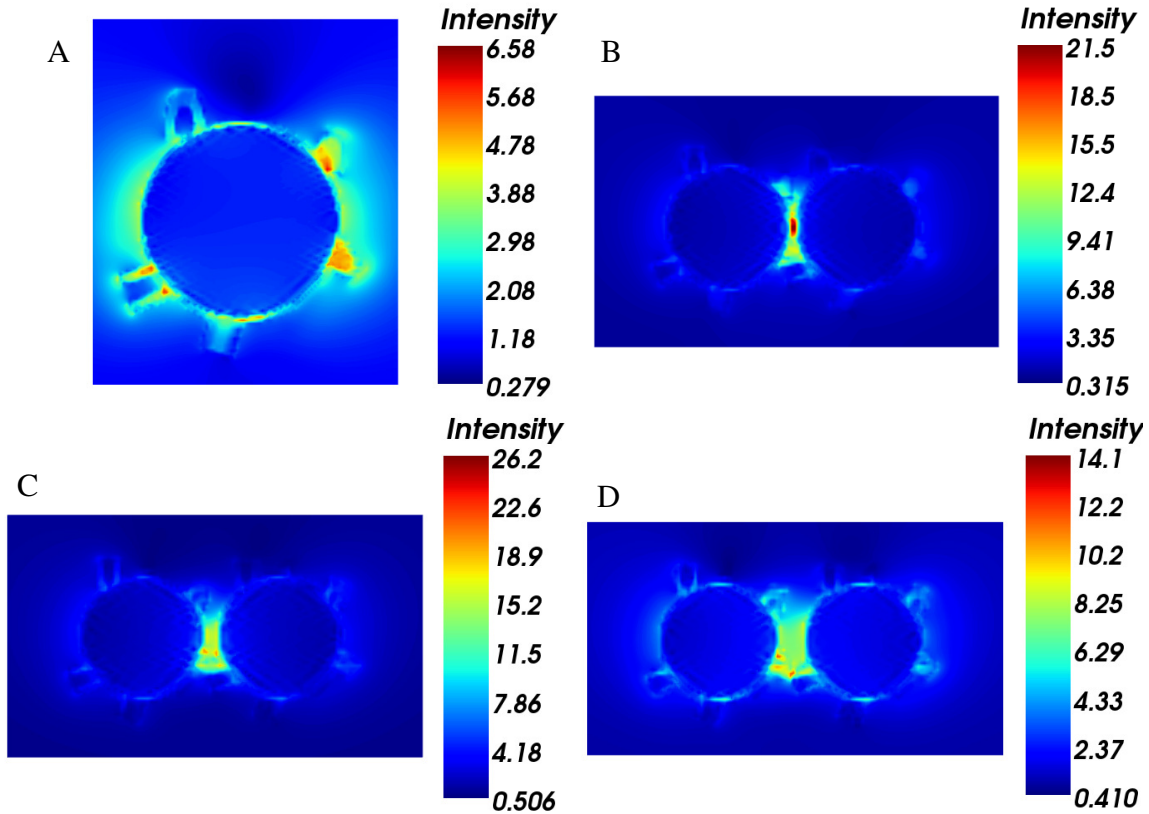


Figure 6.8. Normalized electric field distributions of a single GNP-CNT heterostructure target (A), Two GNP-CNT heterostructure target with inter-particle spacing of 0 nm (B), 5 nm (C) and 10 nm (D). The corresponding wavelength was 530 nm, 540 nm, 550 nm and 540 nm, respectively.

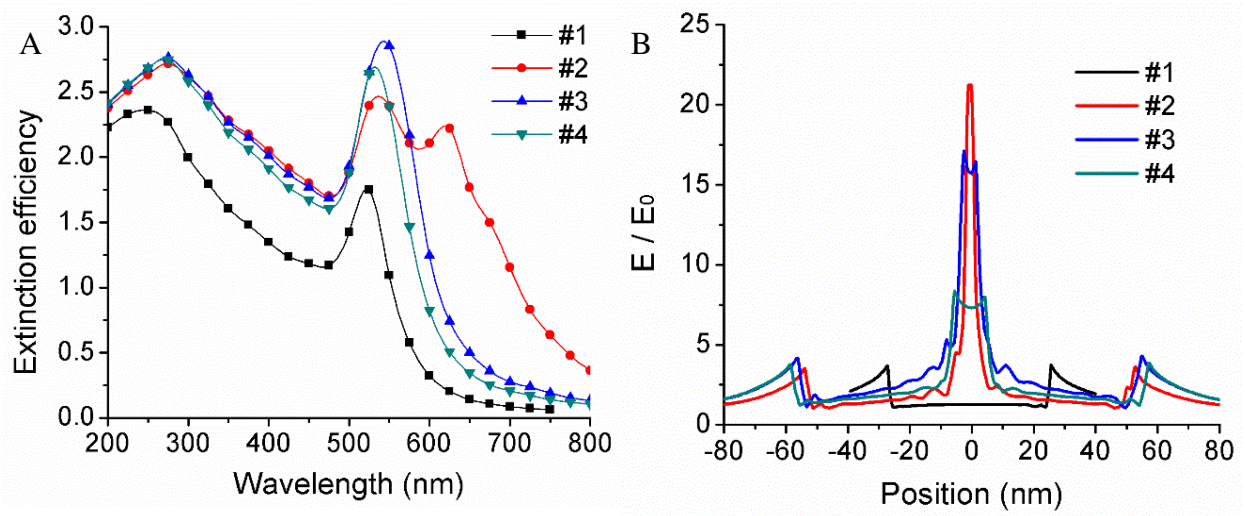


Figure 6.9. (A) Simulated extinction of single GNP-CNT heterostructure target, Two GNP-CNT heterostructure target with inter-particle spacing of 0 nm, 5 nm and 10 nm. (B) Normalized electric field intensity (E/E_0) vs. position in the incident direction for the targets corresponding to (A).

6.4. Conclusions

In this paper, multilayer graphene shells encapsulated gold nanoparticle – single-walled carbon nanotube (GNP-CNT) heterostructures were fabricated. Au nanoparticles were patterned on Si substrate through a facile galvanic deposition – high temperature annealing process. Encapsulating graphene shells on these Au nanoparticles was achieved via the well-defined xylene-based chemical vapor deposition (CVD) technique. The combination of GNPs and SWCNTs was achieved by means of the carbodiimide chemistry and the affinity of biotin and streptavidin. SEM and TEM were used to characterize the morphology and structure of the GNPs and the GNP-CNT heterostructures. The optical properties of these GNPs and GNP-QD heterostructures were further studies by simulating their plasmonic properties (absorbance and scattering) and surface electric field distribution using the discrete dipole approximation (DDA) method. The result indicated significantly improved electric field was observed on the GNP-CNT heterostructures. The well-defined hot spots were mainly observed in the contact interface of GNPs and SWCNT.

PART II

NANOSTRUCTURED METAL OXIDE HETEROSTRUCTURES FOR
PHOTOCATALYSIS AND ELECTROCATALYSIS

CHAPTER 7

WATER VAPOR-ASSISTED SINGLE-STEP THERMAL GROWTH OF FREE-STANDING COBALT OXIDE NANOWIRES

Yuan Li,¹ Nitin Chopra^{,1,2}*

¹Metallurgical and Materials Engineering Department, Center for Materials for Information Technology (MINT), The University of Alabama, Tuscaloosa, AL 35487, U.S.A.

²Department of Biological Sciences, The University of Alabama, Tuscaloosa, AL 35487, U.S.A.

***Corresponding Author**

E-mail: nchopra@eng.ua.edu

Tel: [205-348-4153](tel:205-348-4153)

Abstract

In this paper, we proposed a water vapor-assisted thermal oxidation approach for the growth of free-standing Co_3O_4 nanowires with controlled size, crystallization, and spatial density on the substrate. The fundamental thermodynamic calculation was carried out to understand the basic principle for the nanowire formation process and the function of water vapor during the formation of nanowires. Detailed parameter study were carried out for optimizing the growth process. The influence of growth environment, chemical additive in water vapor, surface treatment to the cobalt substrate were preliminarily evaluated. We found that the presence of water vapor during the thermal oxidation is critical for the growth of single crystalline Co_3O_4 nanowires with high spatial density. Other growth conductions including water vapor feeding rate, oxygen source flowing rate, temperature and duration were also investigated and analyzed in detail. It was observed that the growth temperature has a dominant control on the morphology and structure of Co_3O_4 nanostructures during the thermal oxidation process. This study provides interesting knowledge for the direct thermal growth of metal oxide nanostructure and leads to the preparation of Co_3O_4 nanowires for future device fabrication.

Keywords: Co_3O_4 nanowires, water vapor-assisted thermal oxidation, thermodynamics, growth conditions

7.1. Introduction

Compounds such as phenol, textile dyes, and poly chloro-byphenyls (PCBs) contaminate water through domestic sewage, industrial wastewater, and agriculture wastewater. Even low concentration of such contaminants ($<1 \text{ mg L}^{-1}$) is hazardous since they prevent the growth of aqueous organisms and reduce the photosynthesis activity of the marine flora [210]. Recently, catalytic oxidation method was recognized as being aggressive towards organic pollutants and presents wide applicability [211]. Especially, solar-driven heterogeneous photocatalytic degradation of water-contaminating organics was widely-proposed as a novel efficient, cost-effective and environmental friendly approach [212]. Furthermore, such photocatalysis processes are normally carried out at room temperature and atmospheric pressure, which makes their wide industrial applications technically feasible [213].

With regards to the photocatalysts, metal oxide semiconductors such as TiO_2 , ZnO , Fe_2O_3 , Co_3O_4 , WO_3 , etc. and sulphides (CdS , ZnS , etc.) were mostly studied [214]. TiO_2 is the best known photocatalyst due to its high photocatalytic activity and good photostability in aqueous medium [215]. However, its extensive application in industry was largely limited due to its wide band gap (can only be used under UV illumination) and high charge recombination [216]. Meanwhile, ZnO and Fe_2O_3 are instable in various industrial waste water streams. Metal sulphides will release toxic sulphides under illumination and thus its suitability for water decontamination was ruled out. Co_3O_4 and WO_3 are also important earth-abundant catalytically active materials with relatively narrow band gap [217]. They present unique advantages such as extended photosensitivity in the visible region, long-term physical/chemical stability and ease of preparation of high purity

Various approaches have proposed for the preparation or growth of Co_3O_4 nanostructures however most of these are all associated with the precursor-based wet-chemical or hydrothermal processes. These methods led to difficulty in the control of product morphology and chemical purity. Moreover, for the purpose of photocatalytic process, monocrystalline structure is of importance for the transfer of photo-excited electrons or holes. However, the Co_3O_4 nanostructures prepared by the wet-chemical or hydrothermal methods are normally with a relatively large size (200 nm to 300 nm) and polycrystalline structure. Preliminary reports showed the fabrication of Co_3O_4 nanowires with a high temperature thermal oxidation approach. The Co_3O_4 nanowires were directly prepared by oxidation of cobalt substrate at high temperature in the presence of O_2 . This process leads to the formation of free-standing single crystalline nanowires with controllable nanowire diameter. However, the main challenge lies in the large scale production as the spatial density of nanowires on the substrate is very low and is not uniformly.

In this paper, we proposed a water-vapor assisted thermal oxidation approach for the growth of free-standing Co_3O_4 nanowires with controlled size, crystallization, and spatial density on the substrate. Detailed parameter study were carried out for optimizing the growth process. The fundamental thermodynamic calculation was carried out to understand the basic principle for the nanowire formation process and the function of water vapor during the formation of nanowires. This study provides interesting knowledge for the direct thermal growth of metal oxide nanostructure and leads to the preparation of Co_3O_4 nanowires for future device fabrication.

7.2. Experimental details

Materials and methods: Cobalt foil was purchased from Alfa Aesar (Ward Hill, MA), Cobalt powders were purchased from ACROS (Geel, Belgium). (100), n-type silicon wafers were purchased from IWS (Colfax, CA). 68% nitric acid was purchased from VWR (Atlanta, GA). DI water (18.1 M Ω -cm) was obtained using a Barnstead International DI water system (E-pure D4641). All chemicals were used without further purification. Branson 2510 Sonicator (Danbury, CT) was used to assist the surface cleaning of Co foil/powders in acetone and DI-water. Thermal oxidation growth of cobalt oxide nanostructures was carried out in a MTI GSL-1100X CVD furnace. ATC ORION sputtering system (AJA international, Inc., North Scituate, MA) was used. Cobalt targets (99.999%) were supplied by AJA International, Inc. 5% O₂/Ar gas cylinders were purchased from Airgas South (Tuscaloosa, AL).

Thermal oxidation growth of cobalt oxide nanostructures: Scratching of the Co foil was carried out using an X-ACTO blade. Surface dents on the Co foil were produced by pressing the pristine foil between sand papers (LECO FJ 120) in the CARVER Lab Press. Surface polishing of Co foil was done using BASI PK-4 polishing kit. Before the thermal growth, these pre-treated samples, as well as the Co powders, were first cleaned in acetone and DI-water for 10 min, respectively. The samples were further treated with 10% HNO₃ solution for 15 s to remove pristine surface oxide layers. The growth of Co oxide nanostructures was carried out in the installations showing in Figure 7.1. The investigated growth parameters were shown in Table 7.1.

Characterizations: Scanning Electron Microscopy (SEM) images were obtained using FE-SEM JEOL-7000 equipped with energy dispersed X-ray spectroscopy (EDX). Tecnai F-20 was used to collect Transmission Electron Microscopy (TEM) images at 200 kV. TEM samples were prepared

by dispersing as-prepared samples on lacey carbon TEM copper grids purchased from Ted Pella Inc. (Redding, CA). Raman spectra were collected using Bruker Senterra system (Bruker Optics Inc. Woodlands, TX) equipped with 785 nm laser source at 10 mW laser powers. Uv-vis reflectance spectra of the cobalt oxide nanostructures were obtained using DH-2000 UV-VIS-NIR light source. The optical transition energy value can be determined using the equation (7.1):

$$ahv = A(hv - E_g)^n, \quad (7.1)$$

where a is absorption coefficient, A is a constant, hv is the energy of light and n is a constant depending on the nature of the electron transition (n assumes the values 1/2, 2, 3/2 and 3 for allowed direct, allowed indirect, forbidden direct and forbidden indirect transitions, respectively.).

Since the absorption coefficient a is proportional to Kubelka–Munk function ($F(R)$):

$$F(R) = (1 - R)^2 / 2R = a / s, \quad (7.2)$$

(where R is the reflectance, k is the absorption coefficient and s is the scattering coefficient) the band gap energy can be obtained from the plots of $[F(R)hv]^{1/2}$ vs. hv as the intercept at $[F(R)hv]^{1/2} = 0$ of the extrapolated linear part of the plot.

7.3. Results and discussion

7.3.1 Thermodynamic analysis

Figure 1 shows two basic experimental set-up for the growth of cobalt oxide nanostructures via the direct thermal oxidation with the assistant of water vapor. We designed two approaches for the feeding of water vapor into the furnace. As shown in Figure 7.1A, water vapor was generated by

evaporating DI-water on a hot plate, and then the water vapor was mixed with air and fed into the furnace for the growth process. The flow rate can be modulated by controlling the temperature of the hot plate. In the second design, air and water vapor was fed into the furnace separately. DI-water was pushed into the furnace with a syringe under accurate control of the liquid feeding controller. As the DI-water reached the high-temperature region, it will be evaporated and flow into the furnace with air. The first design allowed a good mixing of water vapor and air when flowing into the furnace however the feeding rate of water vapor can't be controlled accurately. Since the feeding of water vapor is of great importance for the growth of Co_3O_4 nanowires, the second design is preferably used after several preliminary experiments.

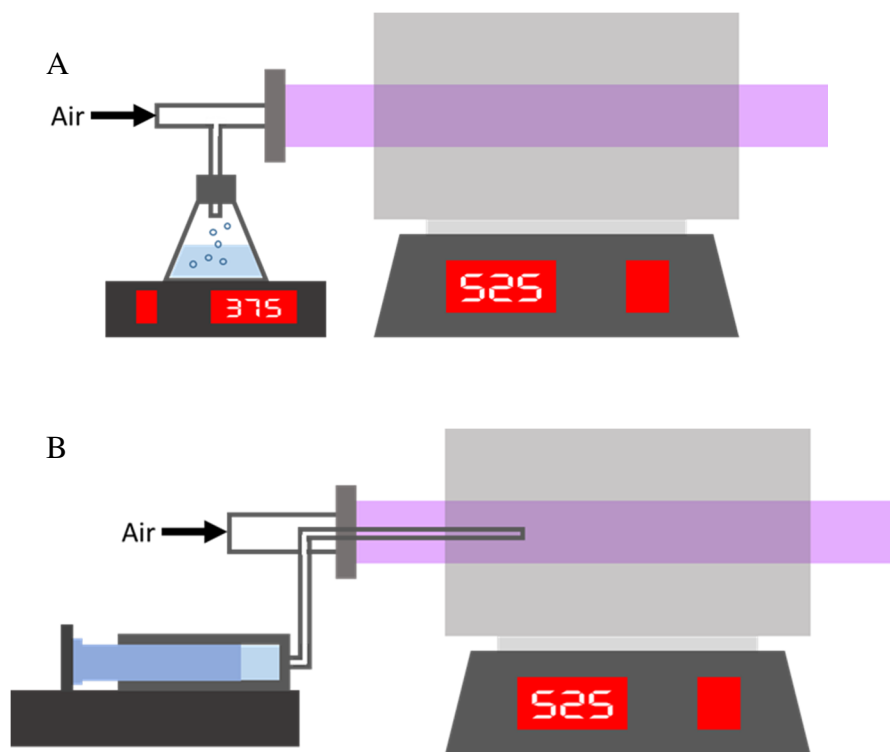


Figure 7.1. Scheme showing the set-up for growth of Co_3O_4 nanowires: (A) water vapor and air flowed simultaneously, (B) water vapor and air flowed separately.

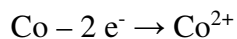
To understand the basic principle of cobalt oxide on the cobalt substrate, thermodynamic calculations were carried out for various possible chemical reactions at a temperature range of 200 K to 1400K. As shown in Figure 7.2A. The direct formation of CoO and Co₃O₄ through the reaction of Co and O₂ presents negative Gibbs free energy and is thermodynamically possible. However this oxidation approach is prone to the formation of cobalt oxide film on the surface of cobalt substrate and leads to less formation of nanowire structure. With the feeding of water vapor in the growth system, the Gibbs energy for the formation cobalt oxide becomes positive, indicating the direct formation of oxide is difficult and the nanowire growth is completed in several steps as shown in Figure 7.2B. In the first step, the system forms a galvanic cell, leading to the decomposition of H₂O to OH⁻ and oxidation of cobalt substrate to Co²⁺. The reaction of Co²⁺ and OH⁻ resulted in the formation of Co(OH)₂. The Co(OH)₂ is not stable at high temperature, which will further convert to CoO. At the third step, the oxidation of CoO to Co₃O₄ has a much negative Gibbs energy and is thermodynamically feasible.

Electrochemical cell reactions:

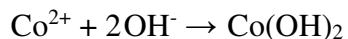
(1) Reduction of O₂:



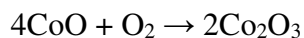
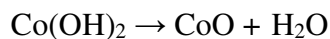
(2) Oxidation of Co:



(3) Acid-base reaction:



(4) Dehydration and further oxidation:



The proposed growth mechanism were further illustrated in Figure 7.2C. In the absence of water vapor, the oxidation process first leads to the formation of cobalt oxide film and the very few nanowires were formed on the surface. With the presence of water vapor, the water vapor first absorbed on the substrate, which effective presented the formation of cobalt oxide film and led to the formation nanowires with higher spatial density. In this study, surface cracks were created, which led to intensive local surface strain. These active sites is preferred for the absorption of water vapor and lead to facilitated growth of nanowires.

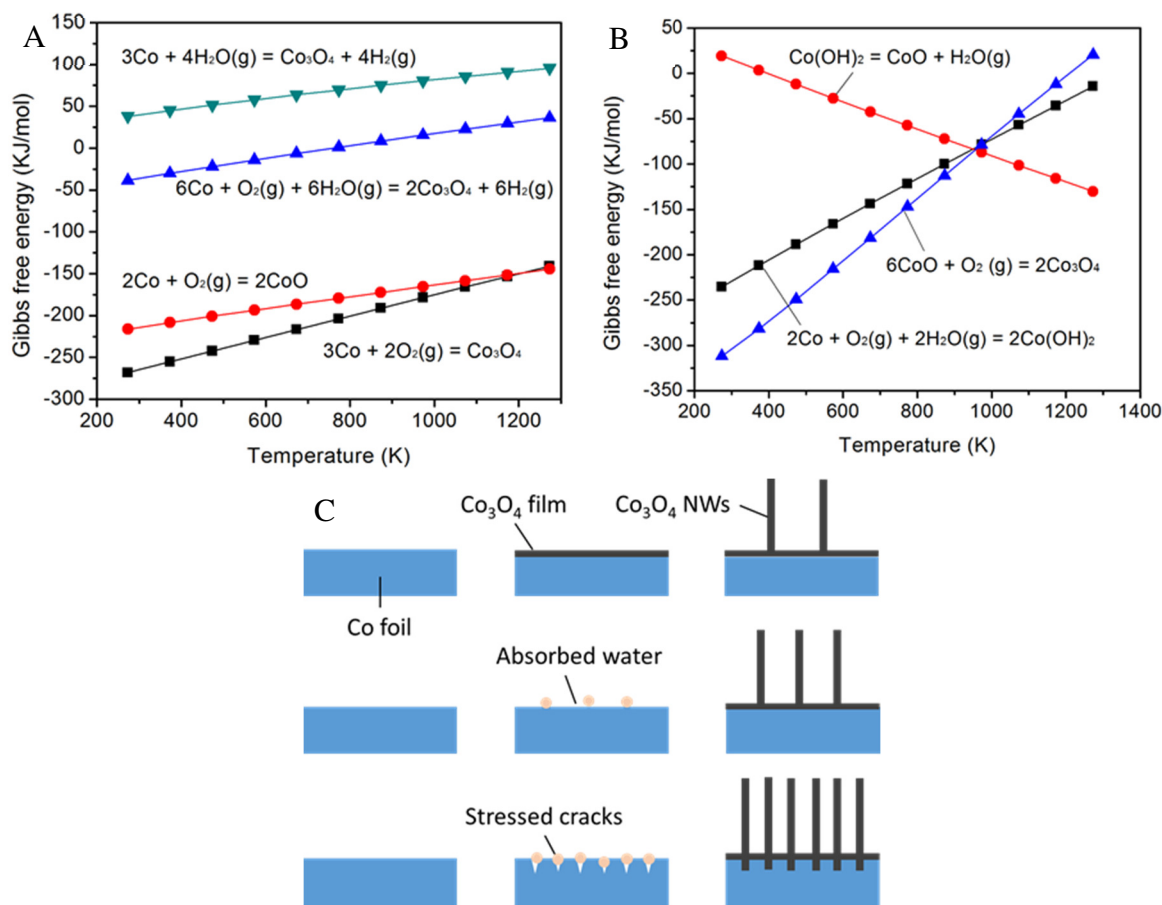


Figure 7.2. (A, B) Thermodynamics calculation of Co oxidation reaction in the absence and presence of water vapor: (A) approach 1, (B) approach 2. (B) Schematic showing the growth mechanism of Co_3O_4 nanowires in the presence of water vapor and stress.

7.3.2. Morphology and structure of final Co_3O_4 nanowires

Figure 7.3A and B show the cross-section of finally obtained Co_3O_4 nanowire product. Free-standing Co_3O_4 nanowires with high spatial density were observed on the film substrate composed of CoO top layer and Co_3O_4 and under layer. TEM images in Figure 7.3C and D further show the detailed morphology and lattice structure of the Co_3O_4 nanowires. The Co_3O_4 nanowires were observed to grow mainly in (111) direction with a single crystalline structure. This is further confirmed by the inset FFT image. To provide evidence for the formation of Co_3O_4 nanowires and CoO/ Co_3O_4 underlayers, EDS analysis was carried out and shown Figure 7.4.

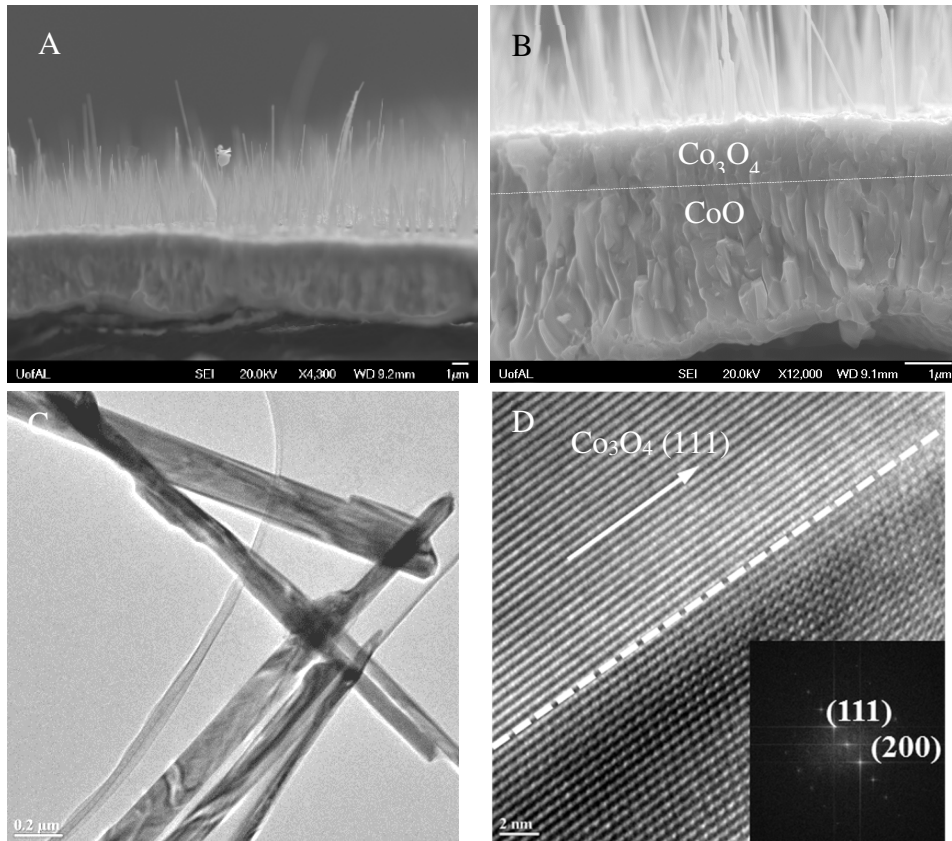


Figure 7.3. SEM (A-B) and TEM (C-D) images showing the cobalt oxide nanostructures produced by the thermal oxidation of Co foil.

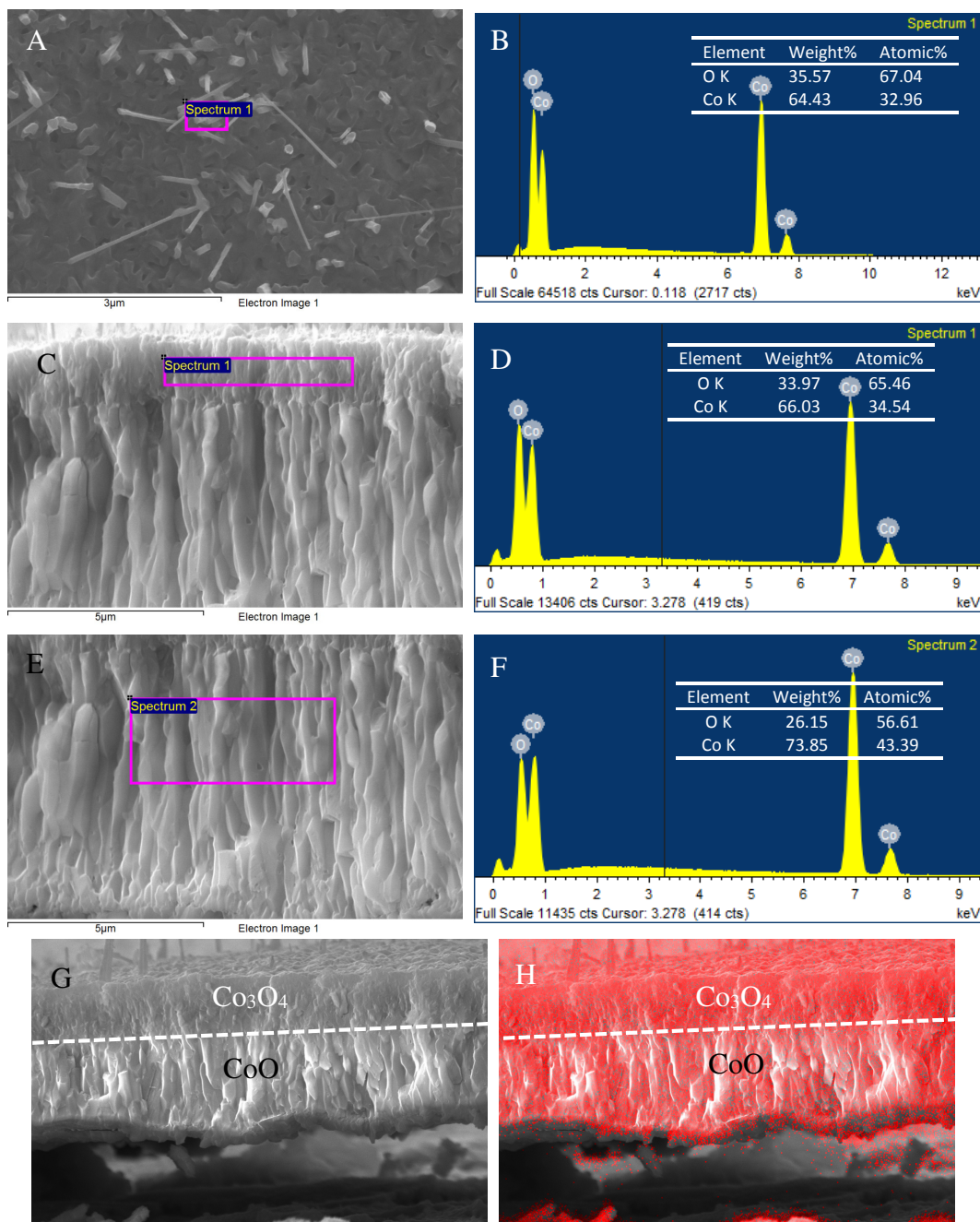


Figure 7.4. SEM image and EDS spectra showing the morphology and chemical content of Co_3O_4 nanowires (A-B), Co_3O_4 film (C-D) and CoO film (E-F). (G-H) EDS mapping showing the distribution of oxygen in the cobalt oxide film.

7.3.3. Parameter study for the growth of Co_3O_4 nanowires

The optimization of growth conditions was conducted at various conditions as shown in Table 7.1. These include the variation of growth environment (air, water vapor, or air and water vapor), shape or treatment of the substrate, vapor/air flow rate, growth temperature and time. The influence of growth environment on the growth of nanowire was demonstrated in Figure 7.5. Co_3O_4 nanowires with low spatial density were observed for the growth in air environment, while the environment only containing water vapor led to little growth of nanowire. However, with the presence of both air and water vapor, the spatial density of Co_3O_4 nanowire obviously increased. Figure 7.6 further demonstrated the influence of surface treatment on the growth of Co_3O_4 nanowires. It was observed that when cracks or dents were created on the cobalt surface, the formation of nanowires were obviously promoted. This is due to the generation of surface defects, which provided numerous of active sites for absorb of water vapor and growth of nanowires. The influence of additives in DI-water on the growth of Co_3O_4 nanowires were further demonstrated in Figure 7.7. One can observe that addition of KI in DI-water led to the formation of Co_3O_4 “nano-cookies” (Figure 7.7A). The addition of NH_4F resulted in rough surface with growth of Co_3O_4 nanorods (Figure 7.7B). We also attempted to drop the DI-water droplets on hot cobalt substrate. This process lead to the formation of Co_3O_4 nano-flakes on the substrate with very high spatial density. Figure 7.8 shows the SEM images of the thermal grown product obtained by treating the initial cobalt substrate with sand blaster at different duration. However, no significant growth of nanowire were observed on these substrate. Moreover, the growth was also carried out on Si substrate coated with cobalt film of various thickness (Figure 7.9). No nanowire was observed on these substrate, which is probably due to the limited cobalt source and amorphous structures of as-sputtered cobalt film. In addition, no nanowire growth was observed on the cobalt powders (Figure 7.10).

Table 7.1. Detailed experimental parameters for the optimization of Co_3O_4 nanowire growth on the cobalt substrate using the direct oxidation approach.

Sample #	Environment	Substrate	Flow rate		Temperature ($^{\circ}\text{C}$)	Time (h)
			Water (ml/h)	Air (sccm)		
1	Air	Pristine	6	10	525	10
2	Water vapor	Pristine	6	10	525	10
3	Vapor + air	Pristine	6	10	525	10
3	Vapor + air	Pristine	6	10	525	10
4	Vapor + air	Polished	6	10	525	10
5	Vapor + air	Scratched	6	10	525	10
6	Vapor + air	Dented	6	10	525	10
7	Vapor + air	Sand blaster	6	10	525	10
8	Vapor + air	Co powders	6	10	525	10
9	Vapor + air	Co film	6	10	525	10
5	Vapor + air	Scratched	6	1	525	10
10	Vapor + air	Scratched	9	4	525	10
11	Vapor + air	Scratched	12	8	525	10
12	Vapor + air	Scratched	15	12	525	10
13	Vapor + air	Scratched	18	16	525	10
14	Vapor + air	Scratched	12	1	525	10
15	Vapor + air	Scratched	12	4	525	10

11	Vapor + air	Scratched	12	8	525	10
16	Vapor + air	Scratched	12	12	525	10
17	Vapor + air	Scratched	12	16	525	10
18	Vapor + O ₂	Scratched	12	5%O ₂ / Air (1 2)	525	10
19	Vapor + O ₂	Scratched	12	12	375	10
20	Vapor + O ₂	Scratched	12	12	425	10
21	Vapor + O ₂	Scratched	12	12	475	10
18	Vapor + O ₂	Scratched	12	12	525	10
22	Vapor + O ₂	Scratched	12	12	575	10
23	Vapor + O ₂	Scratched	12	12	625	10
24	Vapor + O ₂	Scratched	12	12	475	1
25	Vapor + O ₂	Scratched	12	12	475	5
21	Vapor + O ₂	Scratched	12	12	475	10
26	Vapor + O ₂	Scratched	12	12	475	15
27	Vapor + O ₂	Scratched	12	12	475	20

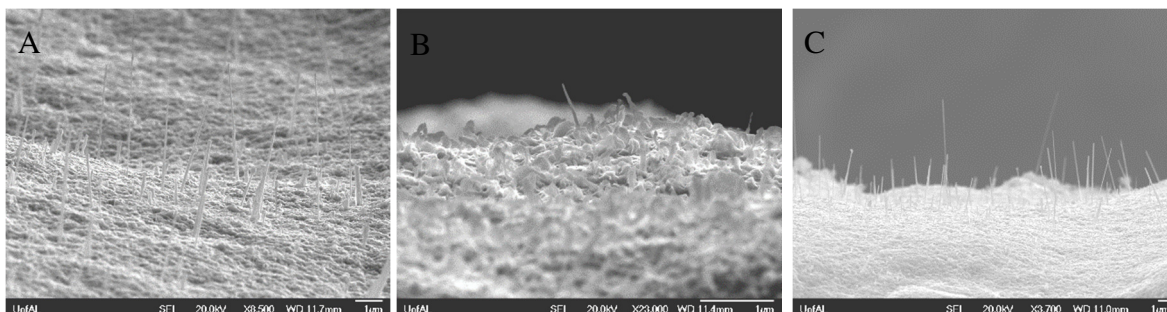


Figure 7.5. Influence of growth environment on the structure and density of Co_3O_4 nanowires (A-C) in air, (D-F) in water vapor, (G-I) in air and water vapor.

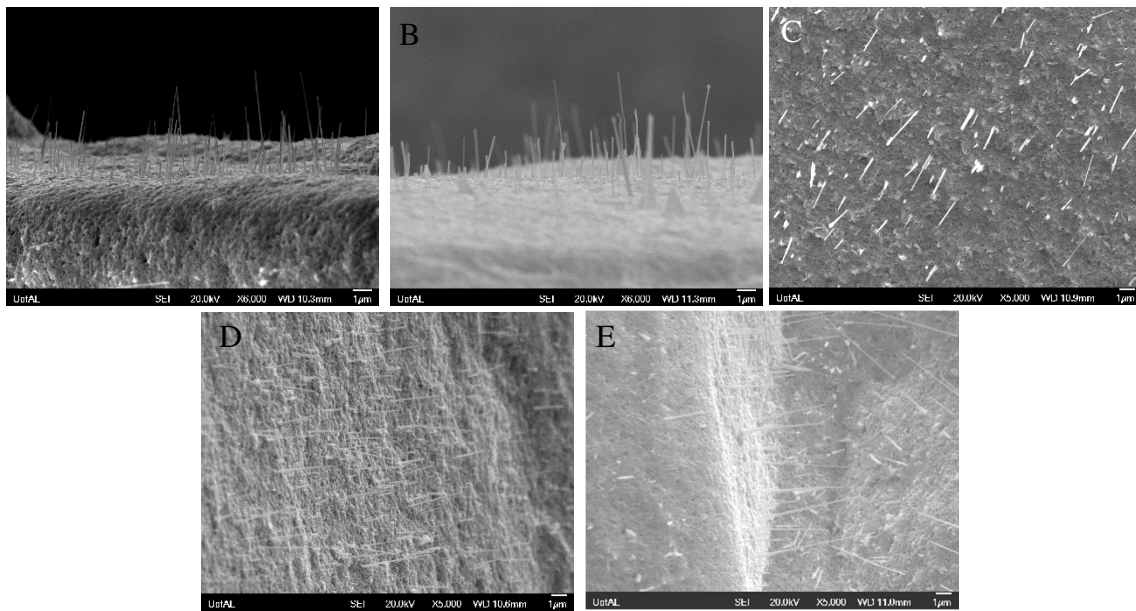


Figure 7.6. Influence of substrate treatment on the growth of Co_3O_4 nanowires (A-C) Polished, (D-F) Blended, (G-I) Scratched, (J-L) Penetrated, (M-O) Pressed with sand paper.

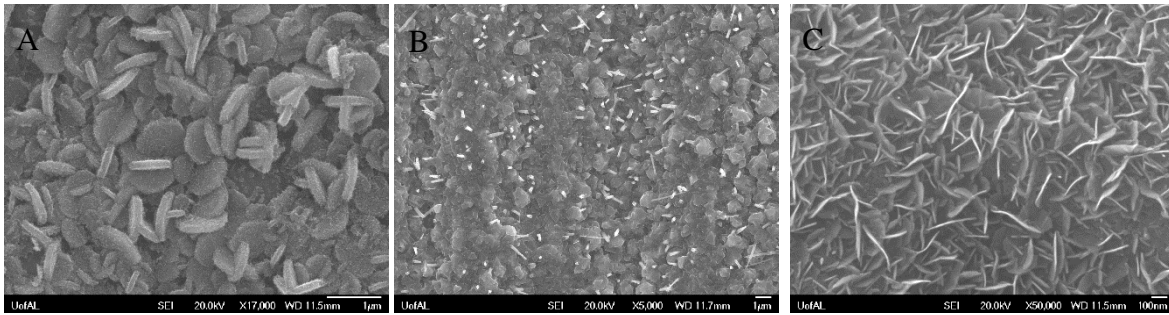


Figure 7.7. Influence of additives on the growth of Co_3O_4 nanostructures (A-C) KI, (D-F) NH_4F , (G-I) continuous water droplet.

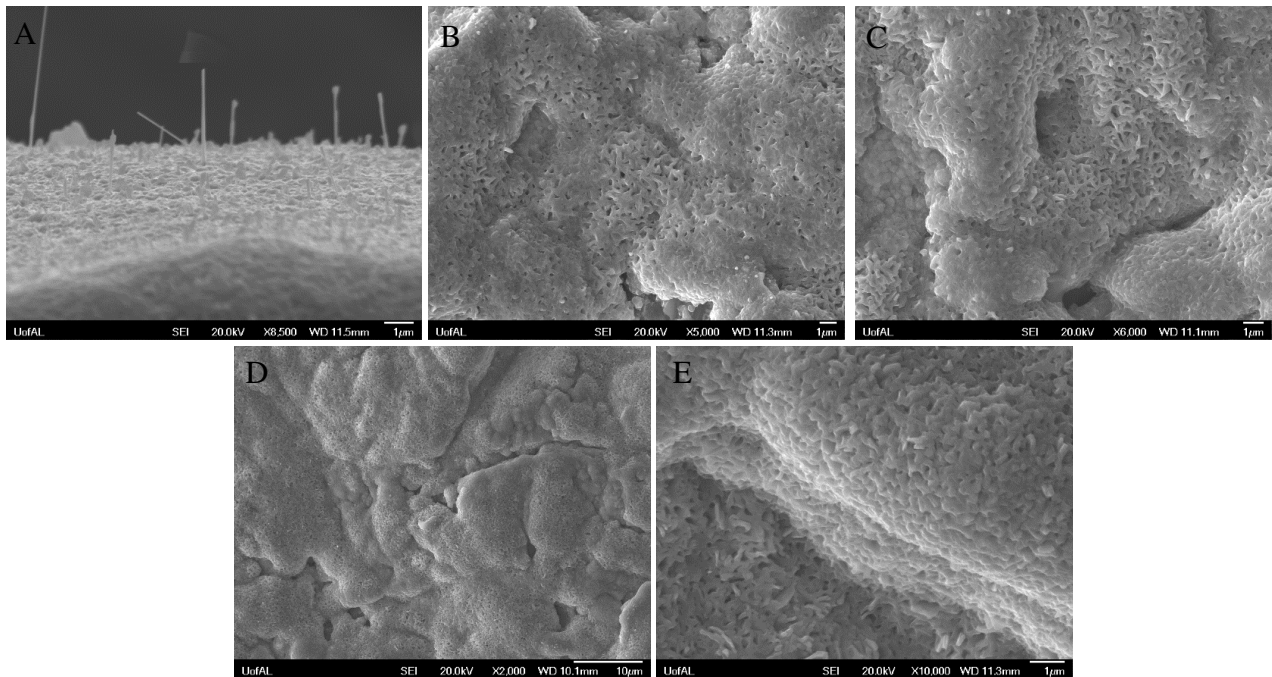


Figure 7.8. Sand blaster treated Co foils as substrate (A) 15 s, (B) 30 s, (C) 1 min, (D) 1.5 min, (E) 2 min.

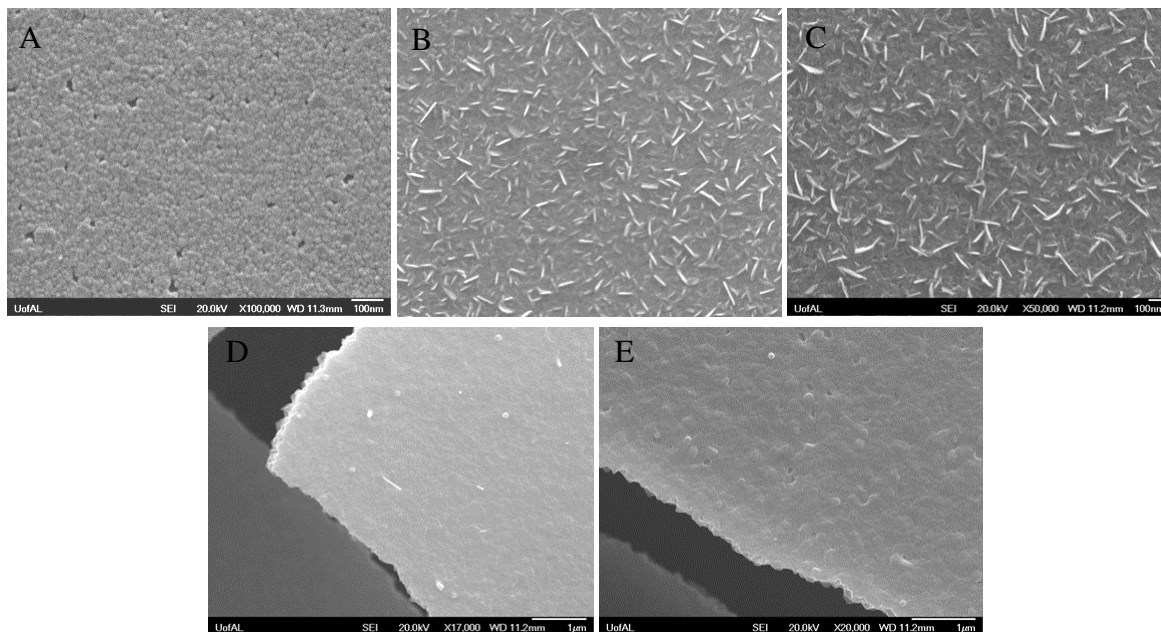


Figure 7.9. Sputtered Co film on Si wafer as substrate: (A) 5 nm, (B) 50 nm, (C) 100 nm, (D) 300 nm, (E) 500 nm.

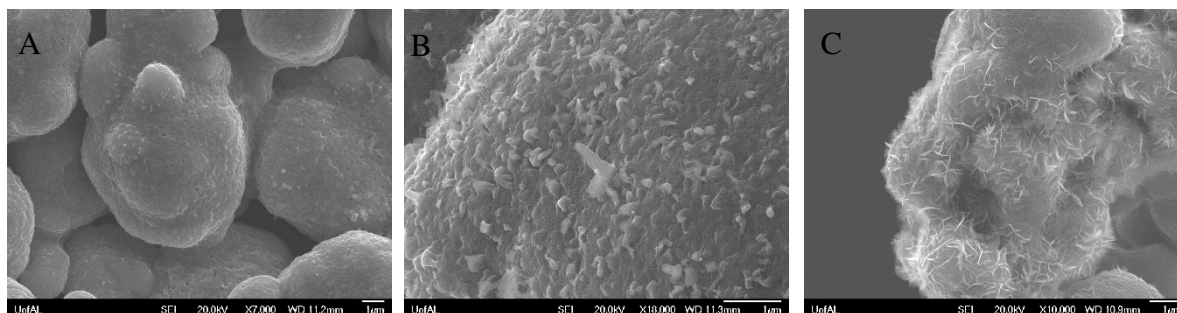


Figure 7.10. Co powder (300 mesh) as the growth substrate: (A-C) in air, (D-F) in water vapor, (G-I) in water vapor and air.

Figure 7.11 shows the SEM images of various substrate after thermal oxidation with feeding of water at different flow rate. One can observe when the flow rate is either too high or too low, no obvious nanowires were formed the surface of cobalt substrate. Meanwhile, the formation of CoO/Co₃O₄ underlayers were always observed. The influence of water vapor on the morphology and structure of Co₃O₄ nanowires as well as on the thickness of CoO/Co₃O₄ underlayer will be discussed in detail later. Raman spectra (Figure 7.12) were collected for understanding the chemical and phase composition of the nanowires. The as-produced Co₃O₄ nanowires show consistent Raman signal for spinel Co₃O₄.^{218,219} These include F_{2g} at ~196 cm⁻¹, ~525 cm⁻¹ and 623 cm⁻¹, E_g at ~484 cm⁻¹, and A_{1g} at ~695 cm⁻¹. As reported before, the A_{1g} mode is assigned to the octahedral sites in spinel Co₃O₄ and the E_g and F_{2g} modes are related to the combined vibrations of tetrahedral sites and octahedral oxygen motions. The UV-vis reflectance spectra and corresponding band gap analysis were shown in Figure 7.12C and D.

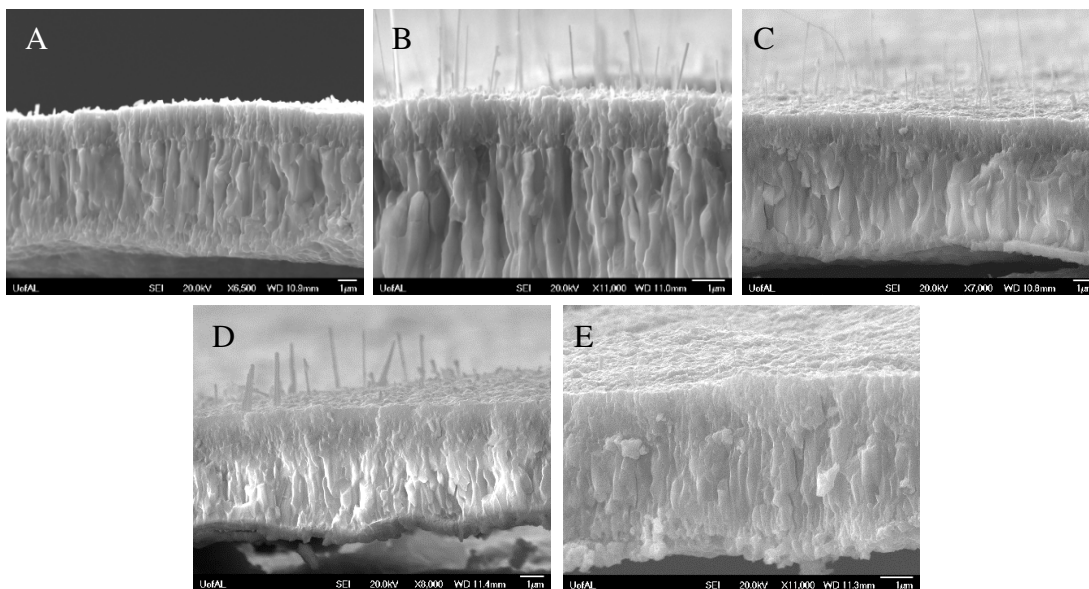


Figure 7.11. Influence of water vapor flow rate on the structure and density of Co₃O₄ nanowires: (A-C) 6 ml/h, (D-F) 9 ml/h, (G-I) 12 ml/h, (J-L) 15 ml/h, (M-O) 18 ml/h.

XRD further confirmed the presence of different phases and elements within the nanowires. Crystallographic planes for CoO, Co₃O₄ and Co are shown in the XRD spectra (Figure 7.12B). The presence of CoO peaks is due to the formation of CoO underlayer during the thermal growth, which is consistent with above SEM images. The peaks for the Co₃O₄ are attributed to both the Co₃O₄ underlayer and the standing nanowires. The dominant (111) peak for Co₃O₄ shows a good match with the lattice spacing observed in Figure 7.3D.

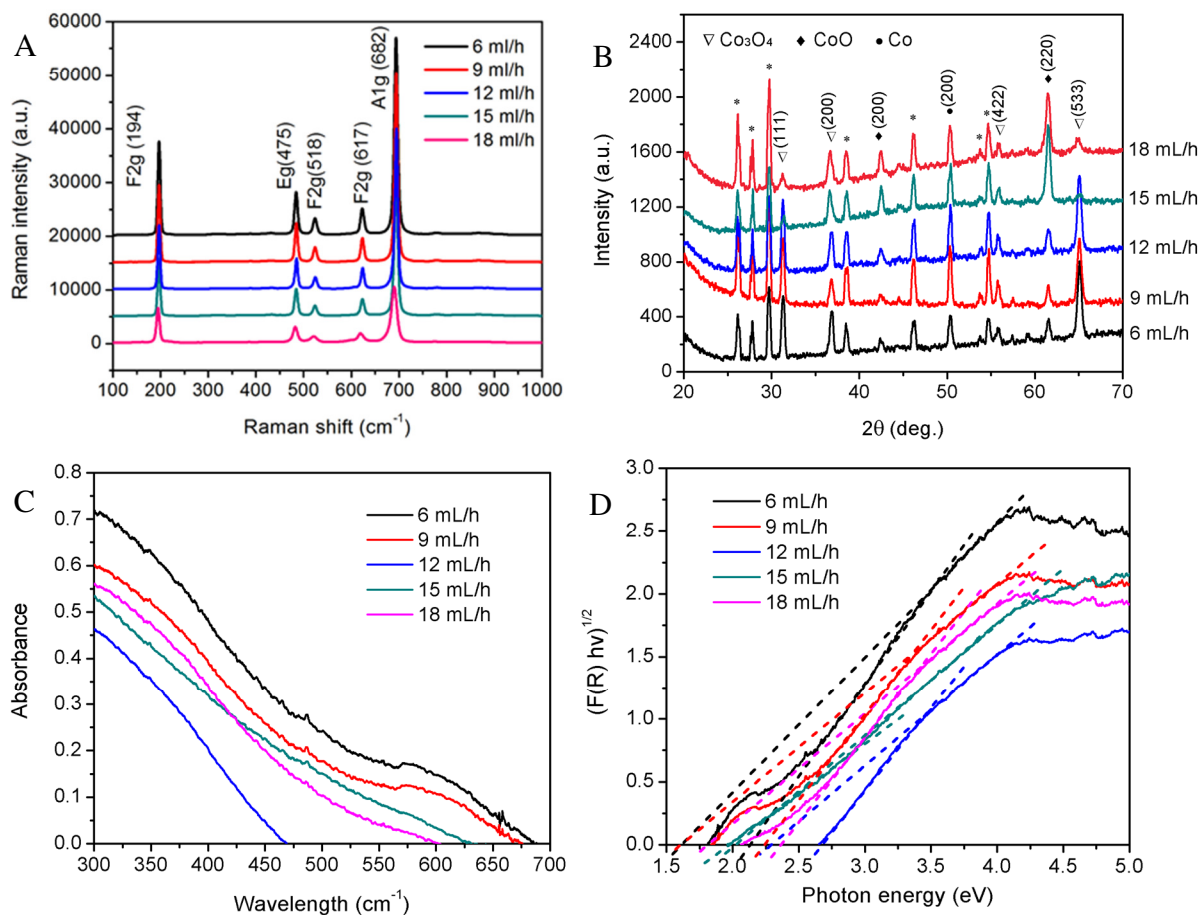


Figure 7.12. (A) Raman spectra of Co₃O₄ nanowires obtained at different water vapor feeding rate; (B) XRD characterization of Co₃O₄ nanowires (water vapor set). (C) Uv-vis Absorbance spectra of Co₃O₄ nanowires with different structures. (D) Band gap of Co₃O₄ nanowires based on the UV-vis reflection spectra.

Figure 7.13 shows the SEM images of various substrate after thermal oxidation with feeding of various oxygen sources. We observed that with a low flow rate of oxygen, the nanowires grown on the substrate showed a low spatial density. However, when high spatial density nanowires were observed after increase the flow rate. Moreover, when the 5%O₂/Ar was used, further increased spatial density of Co₃O₄ nanowires were observed. Meanwhile, the formation of CoO/Co₃O₄ underlayers were always observed. The influence of oxygen flow rate on the morphology and structure of Co₃O₄ nanowires as well as on the thickness of CoO/Co₃O₄ underlayer will be discussed in detail later. Raman spectra (Figure 7.14) were collected for understanding the chemical and phase composition of the nanowires obtained at different flow rate of oxygen source. The as-produced Co₃O₄ nanowires show consistent Raman signal for spinel Co₃O₄.^{220,221} These include F_{2g} at ~196 cm⁻¹, ~525 cm⁻¹ and 623 cm⁻¹, E_g at ~484 cm⁻¹, and A_{1g} at ~695 cm⁻¹.

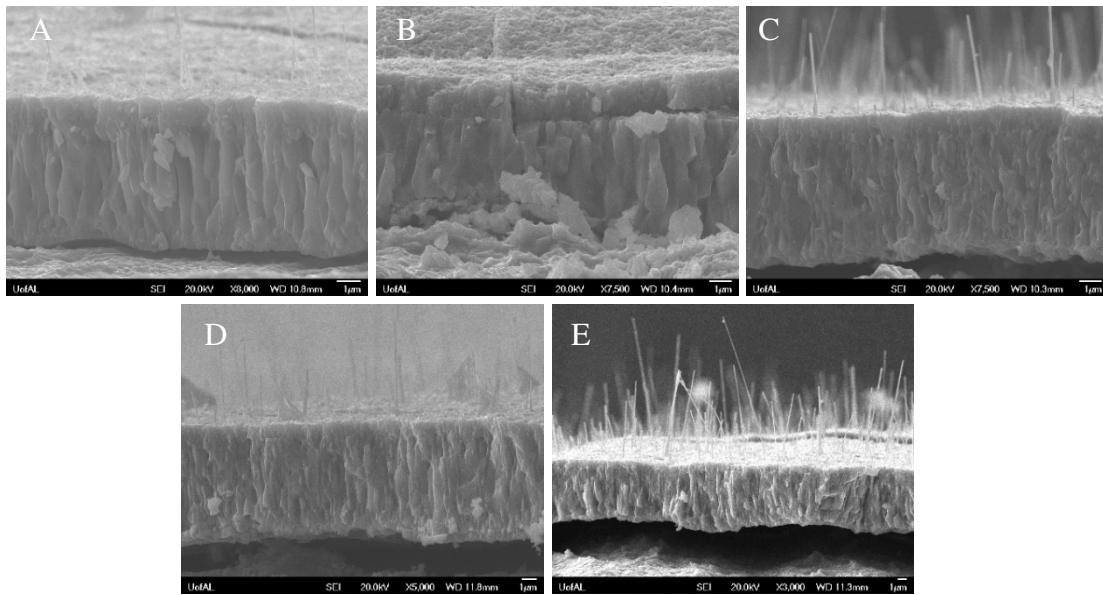


Figure 7.13. Influence of the flow rate oxygen source on the structure and density of Co₃O₄ nanowires: (A-C) air 0.1 SLM, (D-F) air 0.8 SLM, (G-I) air 1.2 SLM, (J-L) air 1.6 SLM, (M-O) 5% O₂/Ar 1.2 SLM.

Figure 12.B further confirmed the presence of different phases and elements within the nanowires. Crystallographic planes for CoO, Co₃O₄ and Co are shown in the XRD spectra. The presence of CoO peaks is again due to the formation of CoO underlayer during the thermal growth. The peaks for the Co₃O₄ are attributed to both the Co₃O₄ underlayer and the standing nanowires. The dominant (111) peak for Co₃O₄ was also observed. The UV-vis reflectance spectra and corresponding band gap analysis were shown in Figure 7.12C and D.

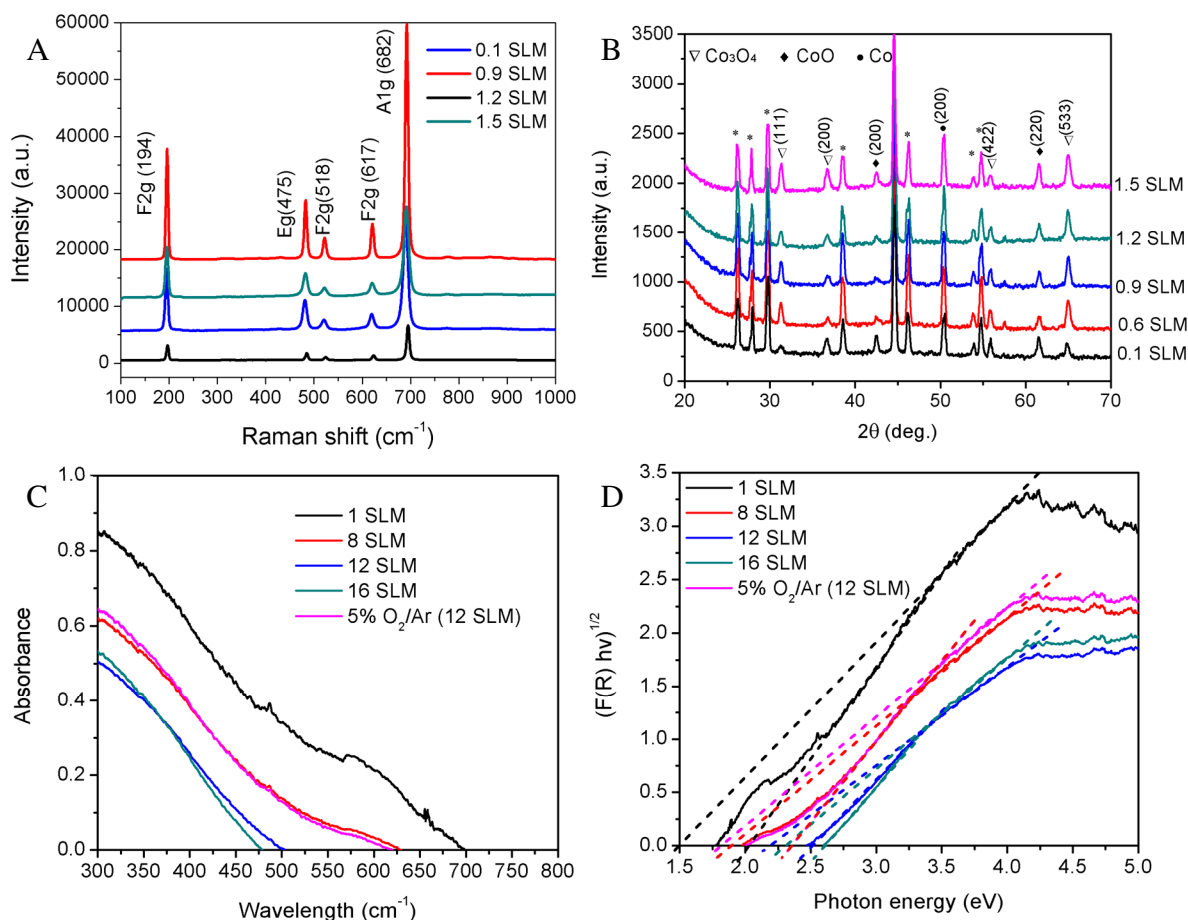


Figure 7.14. (A) Raman spectra of Co₃O₄ nanowires obtained at different oxygen source feeding rate; (B) XRD characterization of Co₃O₄ nanowires. (C) UV-vis Absorbance spectra of Co₃O₄ nanowires with different structures. (D) Band gap of Co₃O₄ nanowires based on the UV-vis reflection spectra.

The influence of growth temperature on the morphology of Co_3O_4 nanostructures was shown in Figure 7.15. We observed the formation of Co_3O_4 nanoflakes at a growth temperature of 375°C (Figure 7.15A). Further increase of growth temperature (425°C) resulted in the formation of nanopyramids. When the temperature was above 475°C , the Co_3O_4 presented a nanowire morphology. This observation can be explained by the thermodynamic analysis showing in Figure 7.2. The low temperature gives preferred oxidation of Co substrate to Co^{2+} , however, the formation of $\text{Co}(\text{OH})_2$ is not favorable at lower temperature. This led to the formation of large amount of CoO on substrate but a slow growth rate of Co_3O_4 . Thus, the nano-flakes with high density was observed. However, when the temperature was increased beyond 625°C . Meanwhile, the formation of $\text{CoO}/\text{Co}_3\text{O}_4$ underlayers were always observed. The influence of growth temperature on the morphology and structure of Co_3O_4 nanowires as well as on the thickness of $\text{CoO}/\text{Co}_3\text{O}_4$ underlayer will be discussed in detail later.

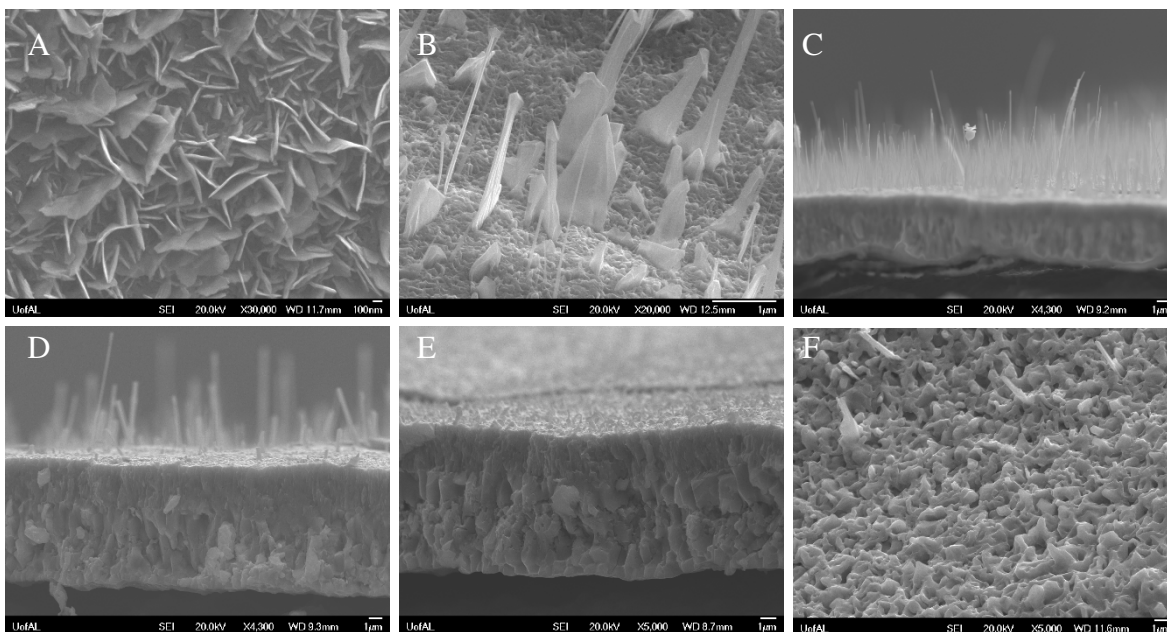


Figure 7.15. Influence of temperature on the structure and density of Co_3O_4 nanowires: (A-C) 375°C , (D-F) 425°C , (G-I) 475°C , (J-L) 575°C , (M-O) 625°C , (P-R) 725°C .

The chemical and phase composition of the nanowires obtained at different growth temperature were demonstrated in Figure 7.16A. The Co_3O_4 nanowires show consistent Raman signal for spinel Co_3O_4 .^{222,223} These include F_{2g} at $\sim 196\text{ cm}^{-1}$, $\sim 525\text{ cm}^{-1}$ and 623 cm^{-1} , E_g at $\sim 484\text{ cm}^{-1}$, and A_{1g} at $\sim 695\text{ cm}^{-1}$. XRD spectra were further demonstrated in Figure 7.16B. The presence of CoO peaks is again due to the formation of CoO underlayer during the thermal growth. The peaks for the Co_3O_4 are attributed to both the Co_3O_4 underlayer and the standing nanowires. The UV-vis reflectance spectra and corresponding band gap analysis were shown in Figure 7.12C and D.

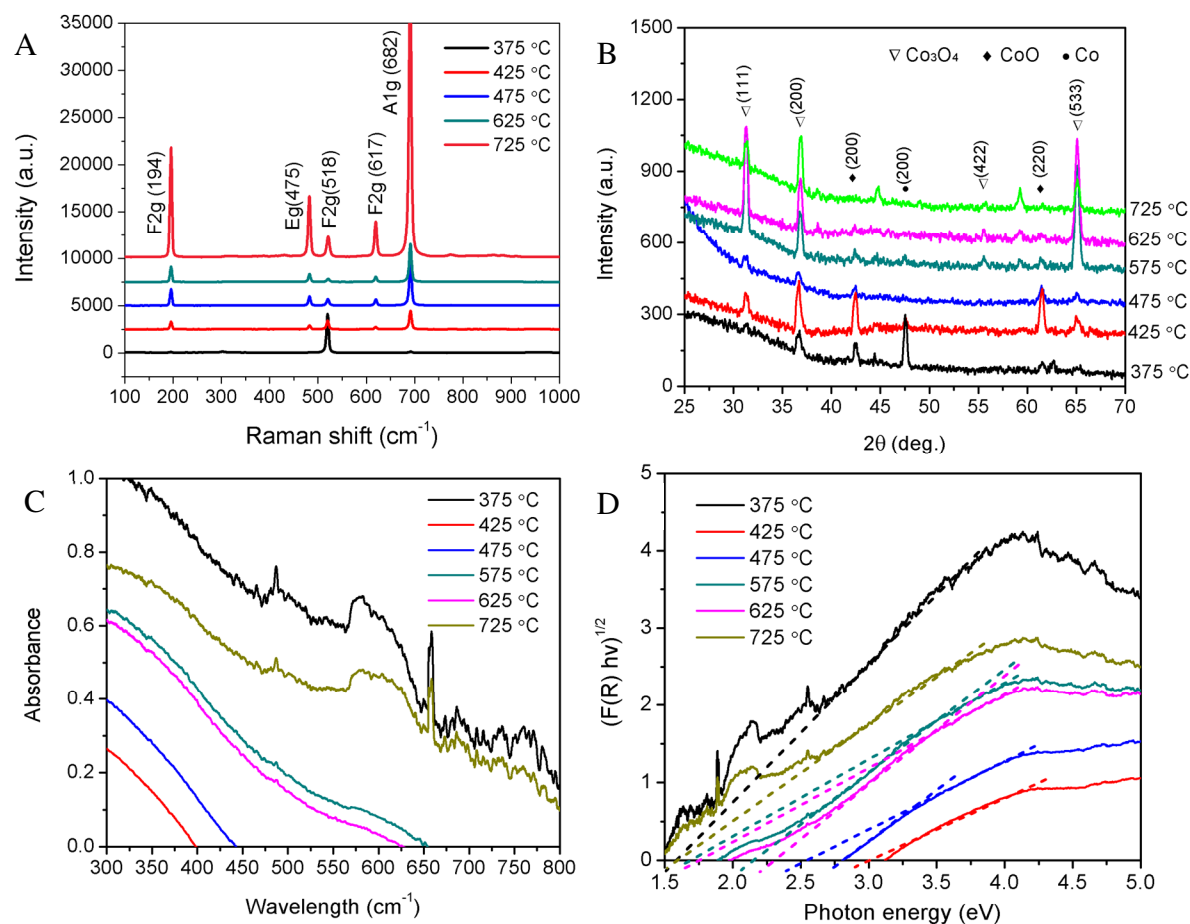


Figure 7.16. (A) Raman spectra of Co_3O_4 nanowires obtained at different temperature; (B) XRD characterization of Co_3O_4 nanowires. (C) UV-vis Absorbance spectra of Co_3O_4 nanowires with different structures. (D) Band gap of Co_3O_4 nanowires based on the UV-vis reflection spectra.

The influence of growth duration on the morphology of Co_3O_4 nanostructures was shown in Figure 7.17. Growth of 10 min and 30 min gave very less Co_3O_4 nanowires on the substrate. With the increase of growth duration, the density of nanowires obvious increased. However, when the growth is processed to 20 h, most of the nanowires were disappeared. This is probably due to the re-fuse and fracture of Co_3O_4 nanowires because of the flowing of water vapor and oxygen. Meanwhile, the formation of $\text{CoO}/\text{Co}_3\text{O}_4$ underlayers were always observed. The influence of growth temperature on the morphology and structure of Co_3O_4 nanowires as well as on the thickness of $\text{CoO}/\text{Co}_3\text{O}_4$ underlayer will be discussed in detail later. From this time study, we observed that Co_3O_4 nanowires can be obtained within a long duration range.

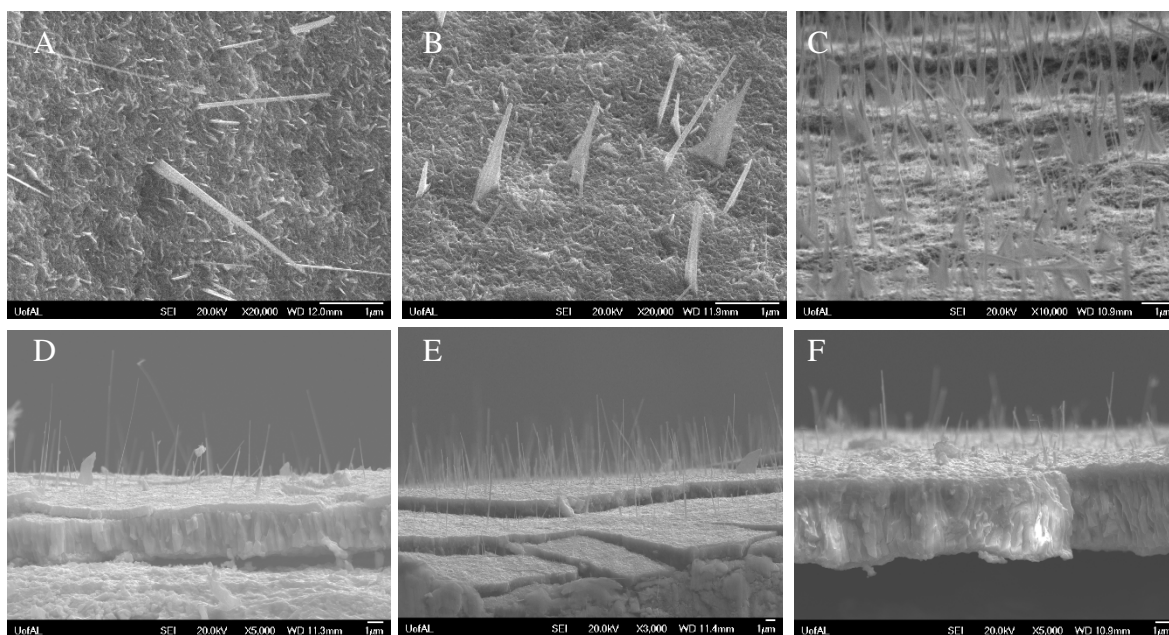


Figure 7.17. Influence of growth duration on the structure and density of Co_3O_4 nanowires: (A-C) 10 min, (D-F) 30 min, (G-I) 1 h, (J-L) 5 h, (M-O) 20 h, (P-R) 30 h.

Raman spectra and XRD patterns were collected for chemical and phase composition analysis for the nanowires obtained at different duration. As shown in Figure 7.18A, the Co_3O_4 nanowires show consistent Raman signal for spinel Co_3O_4 .^{224,225} These include F_{2g} at $\sim 196\text{ cm}^{-1}$, $\sim 525\text{ cm}^{-1}$ and 623 cm^{-1} , E_g at $\sim 484\text{ cm}^{-1}$, and A_{1g} at $\sim 695\text{ cm}^{-1}$. XRD spectra were further demonstrated in Figure 7.18B. The presence of CoO peaks is again due to the formation of CoO underlayer during the thermal growth. The peaks for the Co_3O_4 are attributed to both the Co_3O_4 underlayer and the standing nanowires. The UV-vis reflectance spectra and corresponding band gap analysis were shown in Figure 7.12C and D.

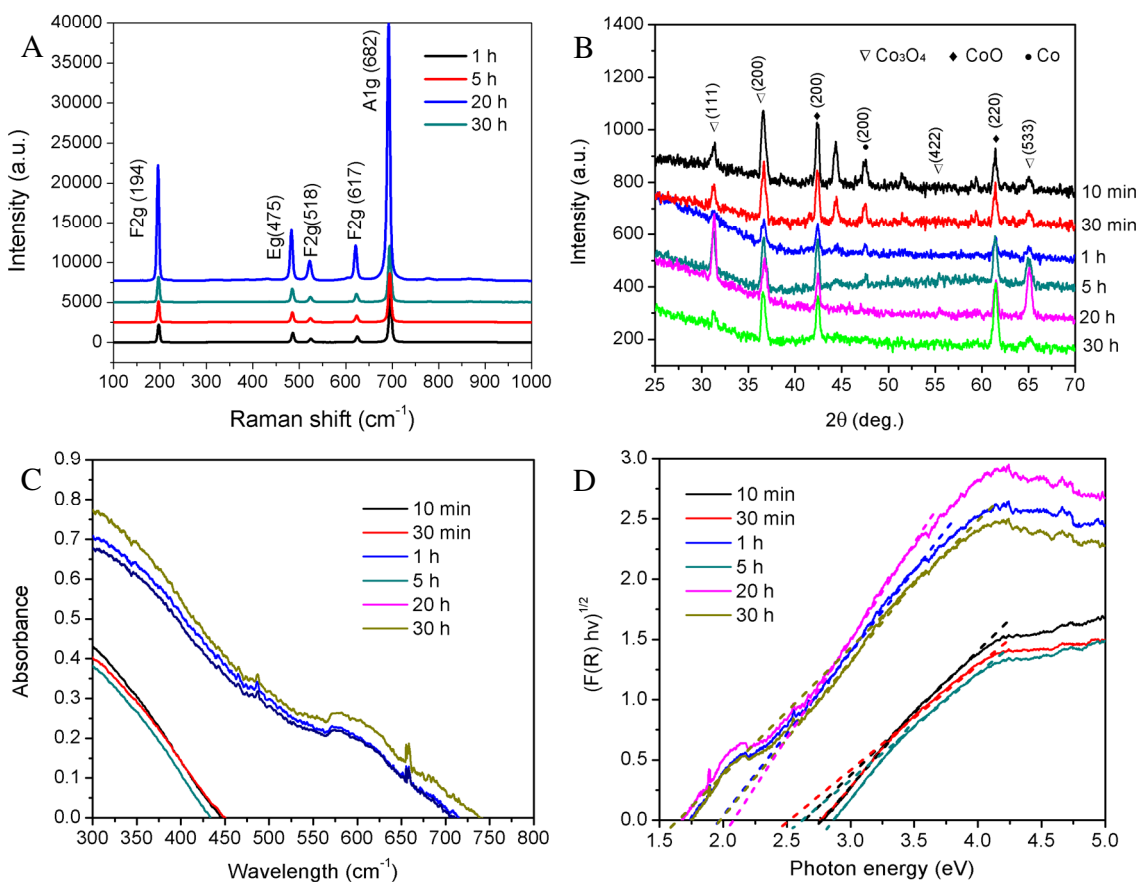


Figure 7.18. (A) Raman spectra of Co_3O_4 nanowires obtained at different growth time; (B) XRD characterization of Co_3O_4 nanowires. (C) UV-vis Absorbance spectra of Co_3O_4 nanowires with different structures. (D) Band gap of Co_3O_4 nanowires based on the UV-vis reflection spectra.

7.3.4. Analysis of parameter study results

TEM analysis was conducted on the representative Co_3O_4 nanostructures obtained in previous parameter study. As shown in Figure 7.19A-C, the nanowires obtained in dry environment presents a polycrystalline structure. The main nanowires were grown in the (111) direction. This is because that the formation of Co_3O_4 nanowires is based on the single step oxidation process without the assistant of water vapor. As a result, the formation of nanowires is rapid and leads to multiple crystalline direction. The Co_3O_4 nanorods obtained in water vapor environment were shown in Figure 7.19D-F. With the absence of oxygen in this case, the formation of Co_3O_4 is a slow process, leading to short nanorods distributed on the substrate. A lattice spacing of (0.25 nm) were obtained for these nanorods, corresponding to the (311) plane of Co_3O_4 . The Co_3O_4 nanowires obtained in the 5% O_2 /Ar and water vapor environment presented a good single crystalline structure. The lattice analysis indicate that the growth is in the (311) direction. The nano-flakes obtained at low temperature (375 °C) was also demonstrated using TEM. An average flake size of 158.6 ± 20.3 nm were observed. The lattice spacing was ~ 0.25 nm, indicating the growth direction of (311). The lattice structure of these nanostructures were further confirmed by the inset FFT images.

As we demonstrated above, the band gap analysis was conducted using the UV-vis reflectance spectra, which were further converted into the Tauc plots. This leads to the estimation of band gaps energies for various Co_3O_4 nanostructure samples. Considering Co_3O_4 is an indirect band gap semiconductor,^{270,226} Band gap energies of ~ 1.50 eV and ~ 1.86 eV were estimated for the as-produced Co_3O_4 nanowires. The former is considered as transitions from O^{2-} to Co^{3+} while the latter is near to the transitions from O^{2-} to Co^{2+} .²⁶⁸ We can observe that the band gap energies varied with different morphology and structure of Co_3O_4 nanowires. In addition, it needs to mention that the band gap energies are also due to the formation of $\text{CoO}/\text{Co}_3\text{O}_4$ underlayers.

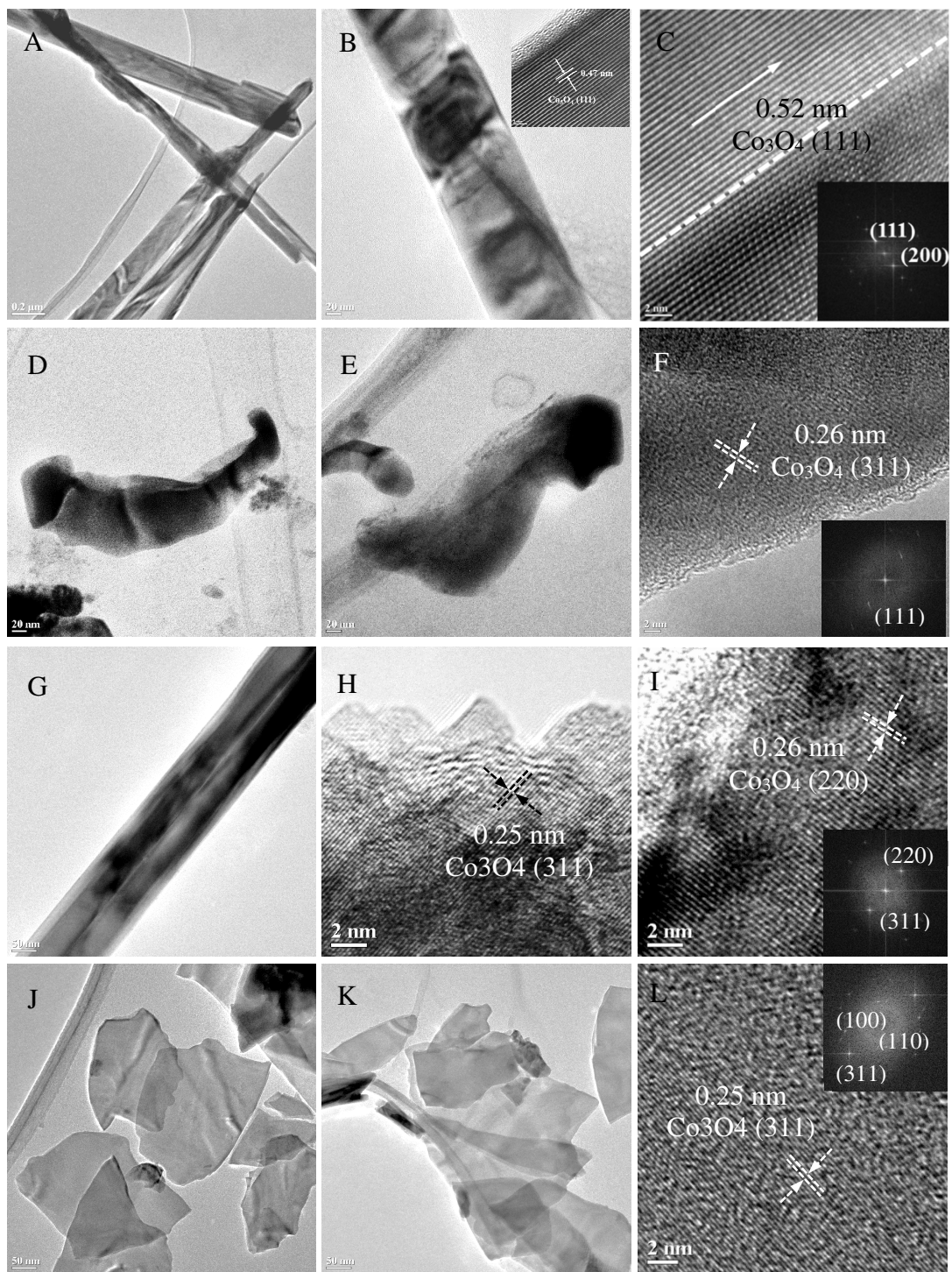


Figure 7.19. TEM characterization of Co_3O_4 nanowires obtained in air (A-C), nanorods (D-F), nanowires obtained in 5% O_2/Ar (G-I) and nanowalls (J-L).

Table 7.2. Band gap of cobalt oxide nanostructures formed on the surface of cobalt foil. The samples were obtained at various experimental conditions as listed in Table 7.1. These band gap energies were based on the Tauc plot generated from the Uv-vis reflectance spectra for various Co_3O_4 nanostructure samples.

Water vapor feeding rate (mL/h)	CoO (eV)	Co_3O_4 (eV)	Oxygen flow rate (SLM)	CoO (eV)	Co_3O_4 (eV)
6	1.62	2.14	1	1.50	2.05
9	1.62	2.25	4	2.29	2.68
12	2.29	2.68	8	1.90	2.36
15	1.99	2.02	12	2.20	2.52
18	1.82	2.37	16	2.31	2.60
			5% O_2/Ar (12)	1.81	2.36
Temperature ($^{\circ}\text{C}$)	CoO (eV)	Co_3O_4 (eV)	Growth duration (h)	CoO (eV)	Co_3O_4 (eV)
375	1.59	---	1/6	2.55	2.78
425	---	3.01	0.5	2.53	2.78
475	2.55	2.82	1	1.97	---
525	1.81	2.36	5	2.66	2.86
575	1.71	2.16	10	2.55	2.82
625	1.76	2.31	20	1.98	---
725	1.58	---	30	1.98	---

The analysis of spatial density of these Co_3O_4 nanostructures on the cobalt substrate were shown in Figure 7.20. The variation of spatial density was summarized as a function of water vapor feeding rate, oxygen source flowing rate, growth temperature, and growth duration. As we observed, the highest spatial density was observed with appropriate feeding rate of water vapor. Either high flow rate or low flow rate led to decreased spatial density (Figure 7.20A). From Figure 7.20B, one can observe that the highest Co_3O_4 spatial density was obtained with the feeding of 5% O_2/Ar . Moreover, the spatial density was obviously decrease with the increase of temperature and growth duration due to the fracture and re-fuse of nanowires.

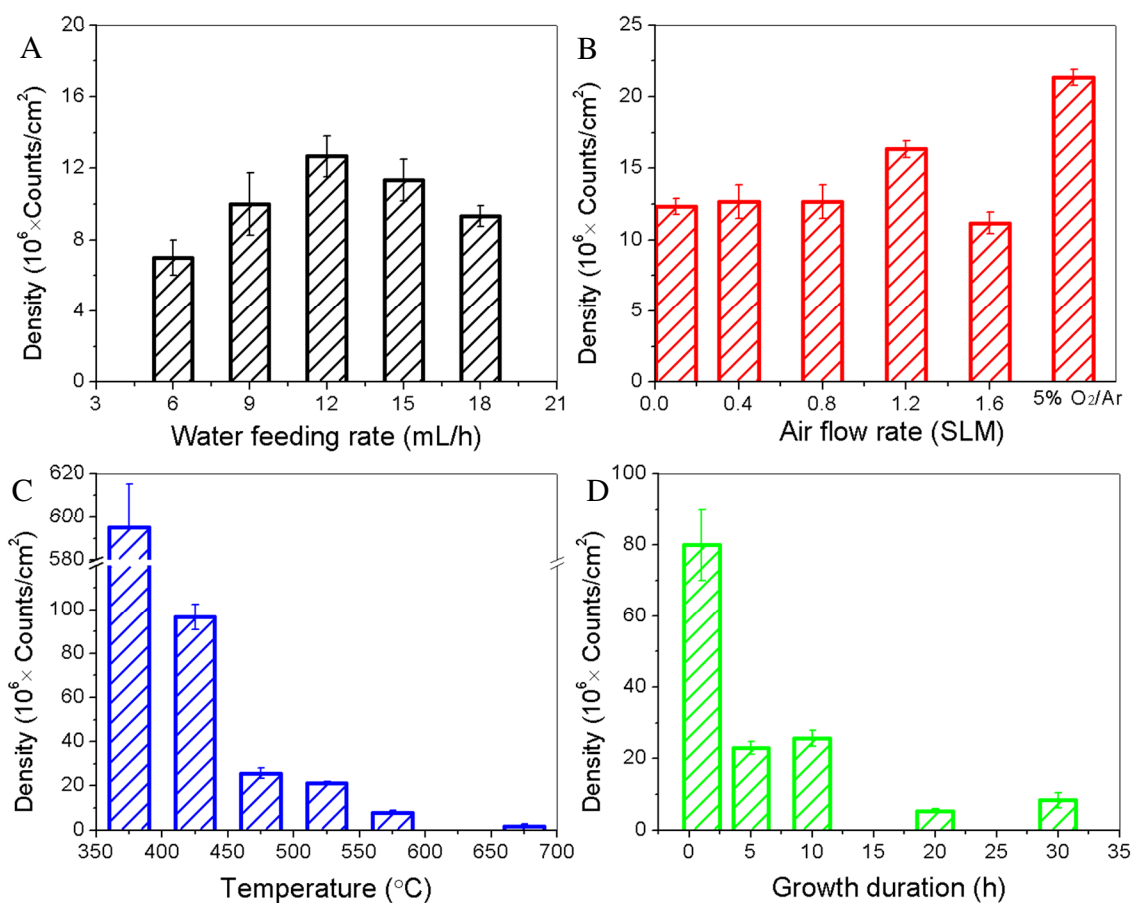


Figure 7.20. Influence of growth parameter on the density of nanowires: (A) water feeding rate, (B) oxygen source flow rate, (C) temperature, (D) growth duration.

The influence of growth conditions on the length and diameter of nanowires were further summarized in Figure 7.21. The water vapor flow rate of 9 ml/h and 12 ml/h resulted in the highest nanowire length, however, further increase the feeding rate led to decrease of nanowire length. For the air flow rate set, 0.8 SLM of air flow gives longest nanowire. When the air flow rate was increased, the nanowire length decreased due to the facture of nanowires. However, when 5% O₂/Ar was used, long nanowires were obtained. The growth temperature has a significant influence on the length of nanowires. This is due to its influence on the morphology of nanostructures, and also, high temperature leads to re-fuse of nanowires. In addition, the variation of growth conditions show no significant influence on the diameter of Co₃O₄ nanowires.

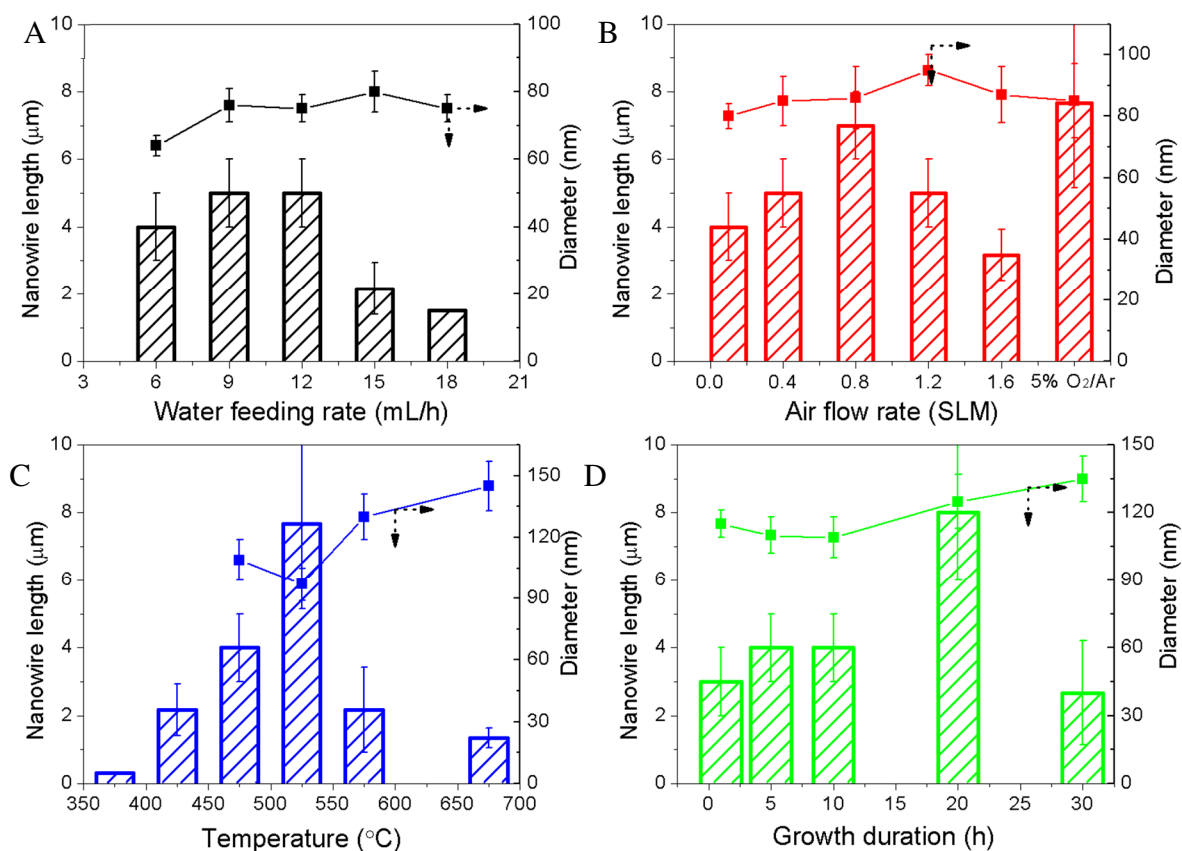


Figure 7.21. Influence of growth parameter on the length and diameter of nanowires: (A) water feeding rate, (B) oxygen source flow rate, (C) temperature, (D) growth duration.

The influence of growth conditions on the thickness of CoO/Co₃O₄ underlayer was further summarized in Figure 7.22. Increased water vapor feeding rate led to decreased underlayer thickness. This is because that the absorption of water molecules on the substrate presented the formation of oxide. The variation of air flow rate has no significant influence on the underlayer thickness. However, the highest thickness was observed at different temperatures. As shown in Figure 7.22C, the underlayer thickness significantly increase with the increase of temperature. High temperature (500-800 °C) leads to the formation of more Co₃O₄ film. The film thickness increased at the first stage of growth (0-10 h) however no significant changes were observed after.

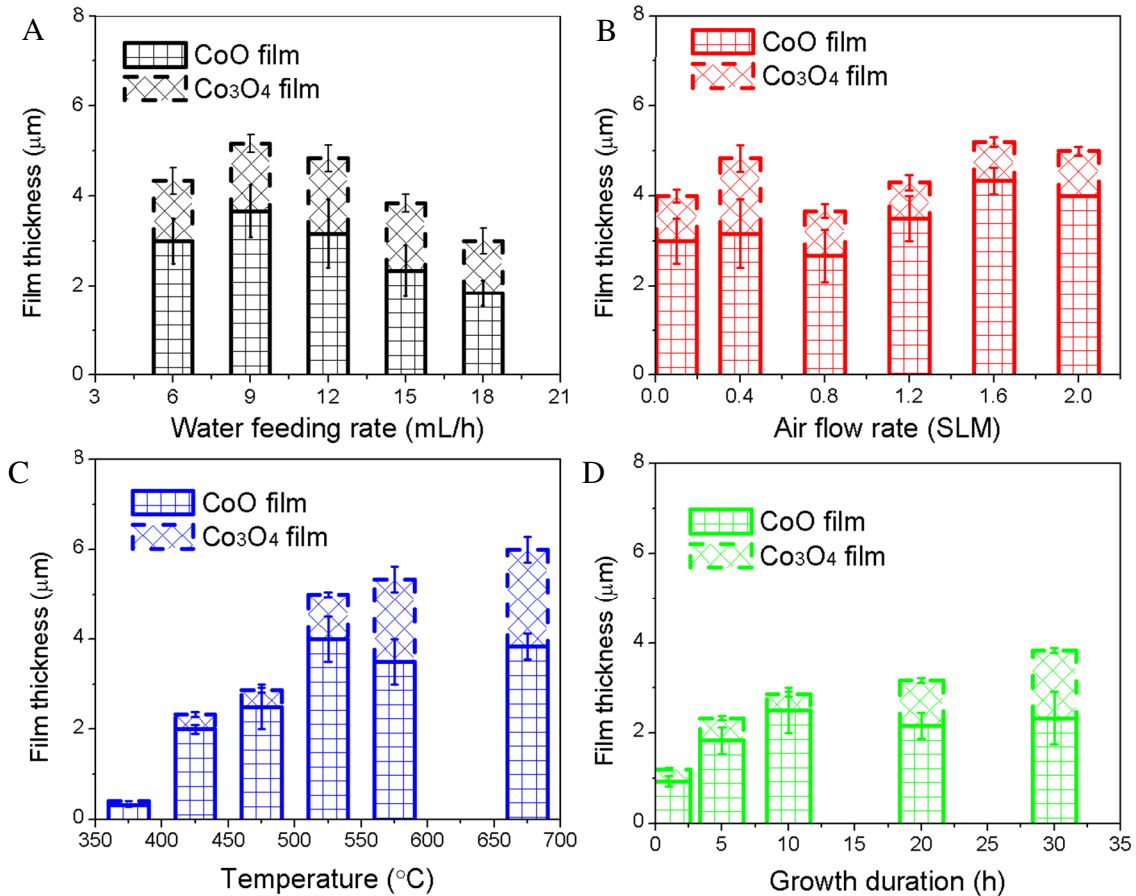


Figure 7.22. Influence of growth parameter on the thickness of under layer CoO and Co₃O₄ film: (A) water feeding rate, (B) oxygen source flow rate, (C) temperature, (D) growth duration.

For a summary, the influence of various growth condition on the morphology, length, and diameter of Co_3O_4 nanostructures as well as their influence on the thickness of underlayer were summarized in Figure 7.23.

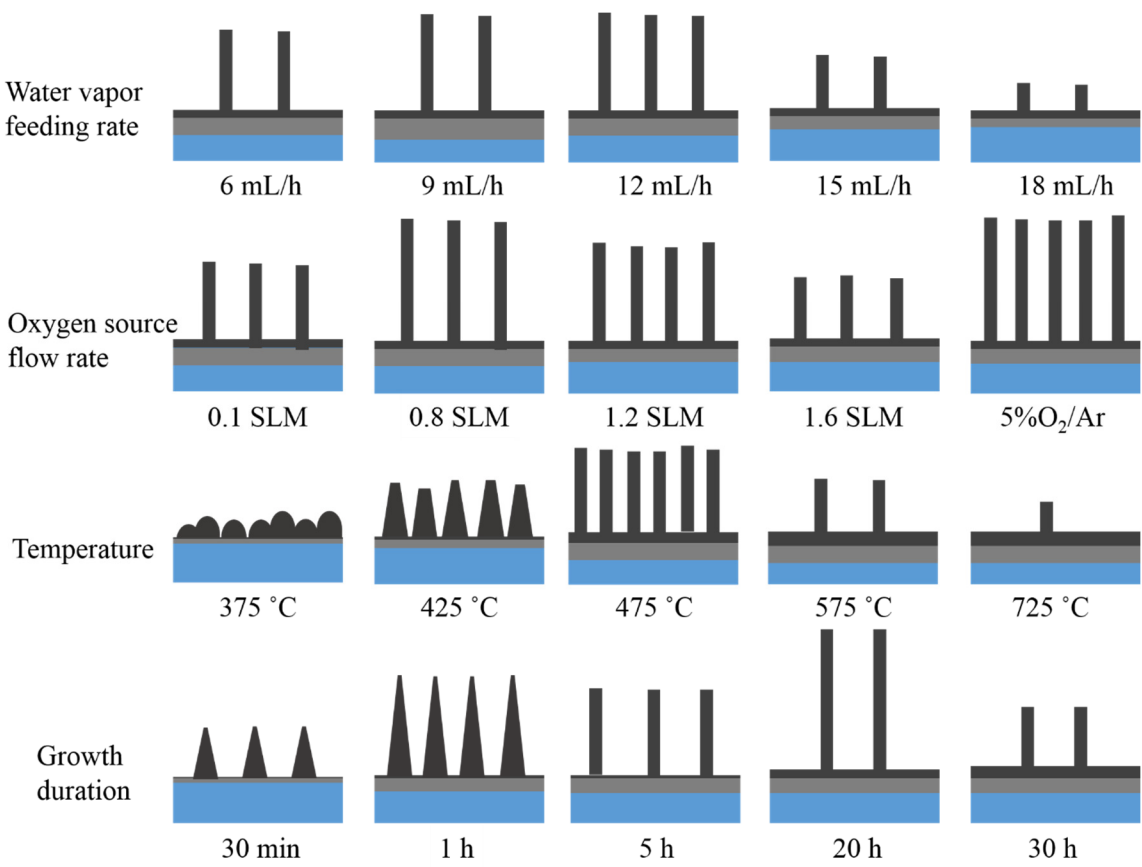


Figure 7.23. Schematic showing the influence of growth conditions on the structure of cobalt oxide nanowires.

7.4. Conclusions

In summary, we proposed a water-vapor assisted thermal oxidation approach for the growth of free-standing Co_3O_4 nanowires with controlled size, crystallization, and spatial density on the substrate. Detailed parameter study were carried out for optimizing the growth process. The fundamental thermodynamic calculation was carried out to understand the basic principle for the nanowire formation process and the function of water vapor during the formation of nanowires. The feeding of water vapor has a critical influence on the formation of Co_3O_4 nanostructures. Thermal oxidation in the dry air environment with the absence water vapor resulted in polycrystalline Co_3O_4 nanowires with (111) growth direction, while the growth in the environment only containing water vapor gave short nano-rods. The single crystalline with a growth direction of (311) can be obtained in the environment containing both water vapor and oxygen. In addition, in such mixture environment, the growth temperature have a dominant influence on the structure and morphology of Co_3O_4 nanostructures. We observed the formation of Co_3O_4 nanoflakes at a growth temperature of 375°C . Further increase of growth temperature (425°C) resulted in the formation of nano-pyramids. When the temperature was above 475°C , the Co_3O_4 presented a nanowire morphology. This study provides fundamental understanding for the direct thermal growth of metal oxide nanostructure and leads to the preparation of single crystalline free-standing Co_3O_4 nanowires with diameter of $60\sim 70$ nm, length of $3\sim 8$ μm , and spatial density of 10^8 per cm^2 .

CHAPTER 8

FABRICATION AND ELECTROCHEMICAL PROPERTIES OF COPPER OXIDE NANOWIRE-COBALT OXIDE NANOPARTICLE HETEROSTRUCTURES FOR OXYGEN EVOLUTION REACTION

Yuan Li,¹ Nitin Chopra^{1,2,*}

¹Metallurgical and Materials Engineering Department, Center for Materials for Information Technology (MINT), The University of Alabama, Tuscaloosa, AL 35487, U.S.A.

²Department of Biological Sciences, The University of Alabama, Tuscaloosa, AL 35487, U.S.A.

*Corresponding author

E-mail: nchopra@eng.ua.edu,

Tel: [205-348-4153](tel:205-348-4153)

Abstract

Nanoscale heterostructures of metal oxides with controlled morphology, interface, and phase purity have been considered of great importance for efficient and cost-effective water splitting. Here, we report the fabrication of CuO nanowire-Co₃O₄ nanoparticle heterostructures for oxygen evolution reaction in the electrocatalytic water splitting process. The synthesis was achieved in a facile and surfactant-free two-step thermal growth process, where free-standing CuO nanowires were first produced by directly annealing copper foil in air. This was followed by dip-coating cobalt salt on the surface of CuO nanowires and subsequent thermal treatment in air to result in the uniform formation of Co₃O₄ nanoparticles on the CuO nanowires. The morphology and structure of the heterostructures were characterized by microscopic and diffraction methods. CuO nanowires or the heterostructures were further coated onto a glassy carbon electrode for oxygen evolution in an electrochemical water splitting. The effective surface area of the electrodes were measured using the Randles-Sevcik equation. Their electrocatalytic activity was evaluated using Cyclic Voltammetry (CV), Electrochemical Impedance Spectroscopy (EIS), and Tafel methods.

Keyword: CuO nanowire; Co₃O₄ nanoparticle; heterostructures; microscopy; oxygen evolution reaction, electrochemical impedance spectroscopy

8.1. Introduction

Electrochemical splitting of water into oxygen and hydrogen provides a promising yet challenging strategy for chemical fuel generation.²²⁷ The reaction of Water splitting is composed of two parts: anodic oxygen evolution and cathodic hydrogen evolution. Of these two half-reactions, oxygen evolution is considered to be more complex since it involves a four-electron oxidation process and presents high overpotential.²²⁸ Thus, finding efficient catalysts for oxygen evolution reaction is critical as well as difficult than that for hydrogen evolution reaction. Noble metal oxides such as RuO_2 , IrO_2 and PtO_2 demonstrate good electrocatalytic activity towards oxygen evolution reaction and have been preferred as catalysts.²²⁹ However, their industrial applications have been largely limited owing to their high-cost and scarcity of Ru, Ir and Pt.²²⁸

Cobalt is an earth-abundant element and its oxide, cobalt oxide (Co_3O_4), has shown good electrocatalytic activity in relation to oxygen evolution reaction.²³⁰ Structure control and heterostructuring of cobalt oxide would be key in developing highly-active and industrially-feasible catalyst for oxygen generation.²³¹ For instance, chemical doping of Co_3O_4 has been reported to play a significant role in improving the electrocatalytic activity, increasing electrical conductivity and reducing causticity of Co_3O_4 in alkaline solution.²³² Moreover, heterostructuring of Co_3O_4 with other supporting materials hold promise for hybrid systems with enhanced electrocatalytic activity, durability, and cost-effectiveness.²³³ Synthesis of Co_3O_4 supported carbon nanotubes (CNTs) with improved electrocatalytic activity for oxygen evolution reaction has been reported.²³¹ However, this synthesis process is based on the surfactant-assisted hydrothermal method, resulting in damage to the CNTs. In addition, Co_3O_4 nanoparticles were physically attached to CNTs according to the van der Waals force and would be prone to separate during the evolution of oxygen bubbles.²³⁴

Recently, the authors have developed wet-chemical²³⁵ and dry sputter-deposition²³⁶ based techniques for CuO nanowires heterostructured with Co₃O₄ nanoparticles or polycrystalline shells. These heterostructures are photoactive in a broad range of wavelengths and led to efficient degradation of organic contaminants. In addition, heterostructured configuration allowed for the manipulation of band gap with a possibility of morphology-dependent multi-level transition states in band diagram. The choice of these oxide is also due to their stability and ability to survive multiple processing steps. With respect to crystal structure, both oxides form a clean interface (CuO and Co₃O₄ are chemically intact) with minimal lattice mismatch at the interface.²³⁶ Thus, this seems to be an ideal geometry for alternative energy production system such as a water splitting. Here, we report fabrication and electrochemical characterization of CuO nanowire-Co₃O₄ nanoparticle heterostructures. The morphology and structure of the heterostructures were characterized using microscopy and diffraction methods. The effective (or active) surface area of the heterostructure electrode was evaluated using the Randles-Sevcik equation. The oxygen evolution activity was evaluated using CV, EIS, and Tafel plots.

8.2. Experimental Section

Materials and methods: Copper foil was purchased from VWR (Atlanta, GA). Cobalt nitrate hexahydrate (Co(NO₃)₂·6H₂O) was obtained from Alfa Aesar (Ward Hill, MA). Nitric Acid (HNO₃, 69.5%) and ethyl alcohol were purchased from Fisher Scientific (Pittsburg, PA). All chemicals were used without further purification. De-ionized (DI) water (18.1 MΩ cm) was obtained using a Barnstead International DI water system (Epure D4641). Microscopic characterization and Energy-dispersive X-ray (EDX) spectroscopy were performed using Field Emission Scanning Electron Microscope (FE-SEM, JEOL-7000, equipped with Oxford EDX detector) and transmission electron microscopy (HR-TEM, Tecnai FEI-20). X-ray diffraction

(XRD) data of samples was recorded with a Philips diffractometer (XRG 3100, Cu K α radiation, 35 mA and 40 kV). The electrochemical experiments were carried out on the PARSTAT 2273 Potentiostat/Galvanostat (Princeton Applied Research, Oak Ridge, TN).

Synthesis of CuO nanowire-Co₃O₄ nanoparticle heterostructures: Copper foil (4 cm \times 4 cm) was cleaned with diluted HNO₃ solution (23%, v/v) to remove surface oxide layer. Further, it was rinsed thoroughly with DI water and dried with N₂ gas. The cleaned foil was placed in a box furnace (LindBerg/Blue) at ambient pressure and heated to 400 °C. After 6 h, the furnace was turned off and the sample was cooled down naturally. In the next step, Co(NO₃)₂·6H₂O aqueous solution (1 M) was uniformly drop-casted on the surface of as-produced CuO nanowires, and placed in a vacuum oven (VWR Scientific, Model No. 1430), at 80 °C. The dried sample was air-annealed in the box furnace (LindBerg/Blue) at 400 °C for 4 h to result in CuO nanowire-Co₃O₄ nanoparticle heterostructures. Heterostructures were characterized by SEM, TEM, and XRD for their crystal orientations, morphologies, interfaces, and phases.

Electrochemical studies: The CuO nanowires as well as the CuO nanowire-Co₃O₄ nanoparticle heterostructures were carefully peeled off from the copper substrate and attached to a glassy carbon electrode with silver paint. The edges of the electrodes were further sealed with Nail oil, which resulted in a geometrical surface area of ~0.5 cm \times ~0.5 cm only containing CuO nanowires or CuO nanowire-Co₃O₄ nanoparticle heterostructures.²³⁷ The former was referred as CuO electrode and the latter as CuO-Co₃O₄ electrode. In this experiment, the standard three-electrode system was used with glassy carbon electrode loaded with nanowires or heterostructures as a working electrode. A Pt wire was used as the counter electrode and an Ag/AgCl electrode saturated with NaCl was the reference electrode. Cyclic Voltammetry (CV) and electrochemical impedance spectroscopy (EIS) measurements were conducted in 1.0 mM Fe(CN)₆^{3-/4-} and 0.1 M KCl aqueous

solutions. This allowed for measuring the electron transfer efficiency of the nanowires or heterostructures. The CV scan was carried out from -0.2 V to 0.4 V with a scanning rate of 10 mV s⁻¹. The EIS was conducted at 0.2 V, and the impedance spectra were recorded from 100 KHz to 10 MHz with an AC amplitude of 5 mV rms. The water splitting experiment was carried out in 1 M KOH solution using the same three-electrode system. CV scan in this solution was conducted from 0 V to 1.5 V and with a scanning rate of 10 mV s⁻¹. Tafel study was further carried out to evaluate the over-potential of the heterostructure electrode for oxygen evolution reaction at a specific current.

8.3. Results and discussion

8.3.1. Growth of CuO nanowire-Co₃O₄ nanoparticle heterostructures

High aspect ratio (~75) and standing CuO nanowires (Figure 8.1A) were grown directly on a copper foil utilizing vapor-solid method.²³⁸ The average diameter and length of the as-produced CuO nanowires were observed to be 65.4 nm and 5 μm, respectively. The spatial density was estimated to be ~10⁸ per cm². TEM images (Figure 8.1C and 1D) of the as-produced CuO nanowires revealed lattice spacing of ~0.28 nm, which corresponds to (110) plane of monoclinic CuO.²³⁹ The FFT image in the inset of Figure 8.1D further confirms the monoclinic structure of CuO nanowires. Heterostructuring of CuO nanowires with Co₃O₄ nanoparticles was achieved by air annealing of CuO nanowires coated with cobalt salt. After the growth of Co₃O₄ nanoparticles on CuO nanowires, SEM image of the heterostructure (Figure 8.1B) revealed that the nanowires remained intact after heterostructure formation. HRTEM images of these heterostructures (Figure 8.1E and 1F) indicated Co₃O₄ nanoparticles with an average diameter of 3.4 nm were uniformly

dispersed on CuO nanowires. These nanoparticles demonstrated an inter-lattice spacing of ~ 0.245 nm, corresponding to the (311) plane of Co_3O_4 .²⁴⁰ FFT images in the inset of Figure 8.1F confirms the lattice spacing of CuO nanowire- Co_3O_4 nanoparticle heterostructures. XRD results further revealed (Figure 8.2) the presence of various crystal planes corresponding to CuO nanowires (JCPDS: 48-1548) and CuO nanowire- Co_3O_4 nanoparticle heterostructures. CuO is a base centered monoclinic structure with $a = 0.46837$ nm, $b = 0.34226$ nm, $c = 0.51288$ nm and $\alpha = 90^\circ$, $\beta = 99.5^\circ$, $\gamma = 90^\circ$.²⁴¹ The presence of Cu_2O peaks (JCPDS: 65-3288) with body-centered cubic structure ($a = b = c = 0.4269$ nm and $\alpha = \beta = \gamma = 90^\circ$) could be attributed to the presence of oxide film beneath CuO nanowires.²⁴² Co_3O_4 nanoparticles in the heterostructured configuration exhibited spinel structure, where oxygen ions form a cubic-packed structure with Co^{2+} ions in tetrahedral sites and Co^{3+} ions in octahedral site ($a = b = c = 0.8089$ nm and $\alpha = \beta = \gamma = 90^\circ$).²³⁵

8.3.2. Effective surface area and electron transfer resistance

Figure 8.3 demonstrates CVs for glassy carbon electrode modified with CuO nanowire (CuO electrode) and heterostructures (CuO- Co_3O_4 electrode) in the $\text{Fe}(\text{CN})_6^{3-/4-}$ aqueous solution. CuO electrode displayed weak redox peaks with a peak-to-peak separation of ~ 0.6 V, which could be attributed to poor electrical conductivity ($\sim 10^5 \Omega \text{ cm}$).²⁴³ In addition, a minor oxidation peak at ~ 0.1 V was observed in the positive scan. This peak may be attributed to the oxidation of underlayer Cu_2O film that formed during the growth of CuO nanowires.²³⁸ The reduction peak at 0 V in the negative scan was due to the reduction of CuO. The CuO- Co_3O_4 electrode showed obviously enhanced redox peaks with peak-to-peak separation of ~ 0.4 V as compared with CuO electrode. This enhancement is attributed to the high electrocatalytic activity and low electrical resistivity ($0.5 - 5.3 \Omega \text{ cm}$)²⁴⁴ of cobalt oxide and the increased specific surface area of the electrode.

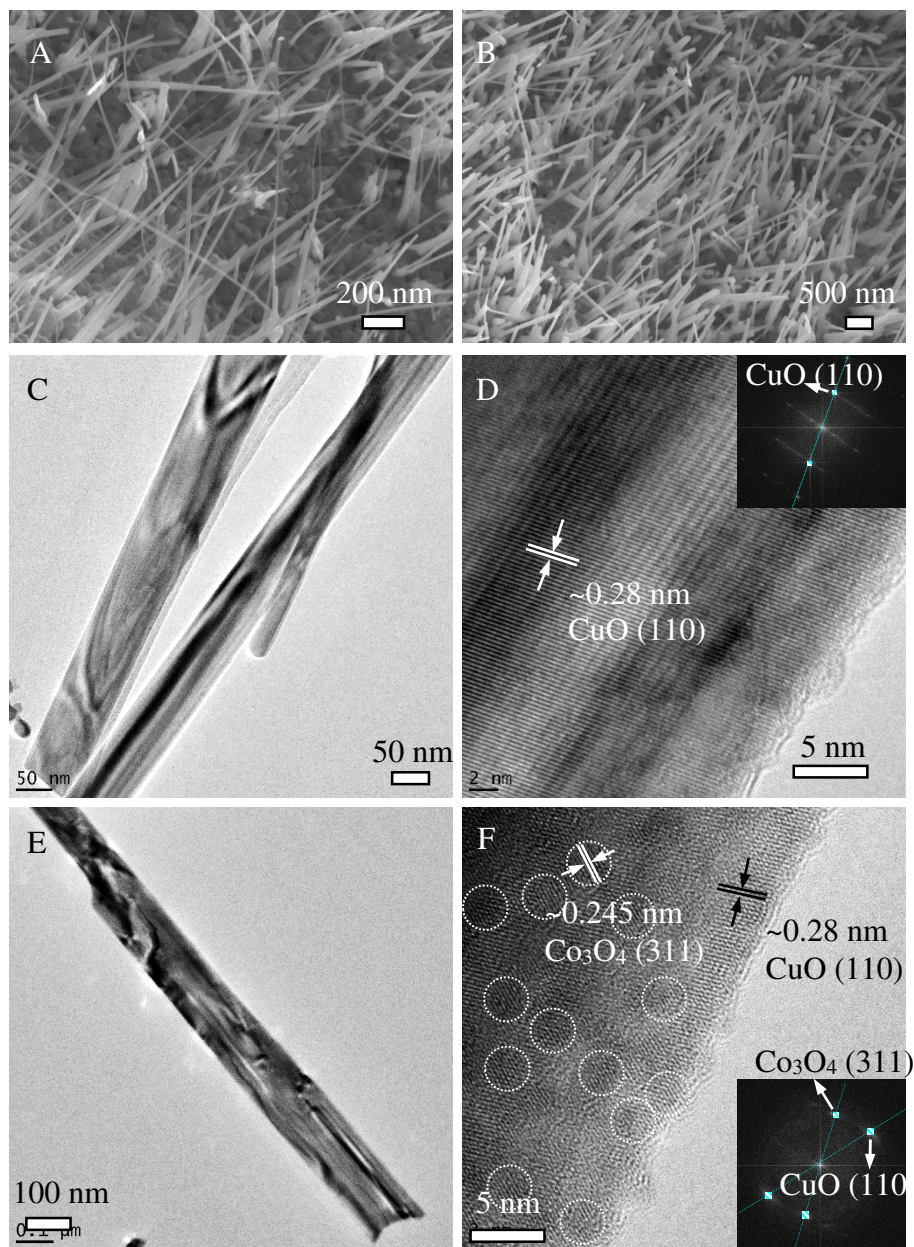


Figure 8.1. SEM images of (A) standing CuO nanowires and (B) CuO nanowire-Co₃O₄ nanoparticle heterostructures grown on the copper foil. TEM images of (C and D) CuO nanowires and (E and F) CuO nanowire-Co₃O₄ nanoparticle heterostructures. *Note: Insets in (D) and (F) show the corresponding FFT images with indexed diffraction spots. Dotted circles in (F) indicate Co₃O₄ nanoparticles on CuO nanowire.*

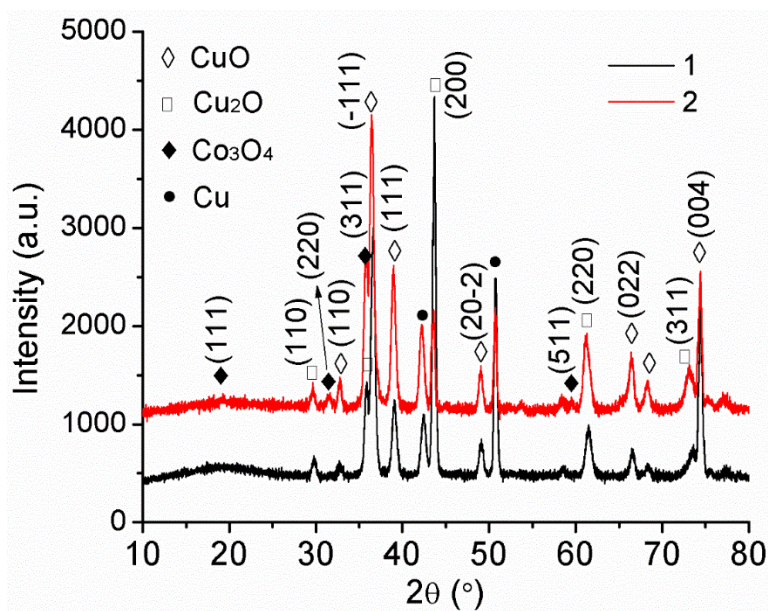


Figure 8.2. XRD patterns of the CuO nanowires (1) and CuO nanowire-Co₃O₄ nanoparticle heterostructures (2) and corresponding indexing of planes.

The electroactive surface area of CuO and CuO-Co₃O₄ electrode was estimated using the Fe(CN)₆^{3-/4-} solution as a redox probe. CVs of the electrodes (Figure 8.4) as a function of different scan rates were obtained. The dependence of the peak current on the square root of the scanning rate was plotted using Randles-Sevcik equation:²⁴⁵

$$I_p = (2.69 \times 10^5) n^{3/2} A D_0^{1/2} C_0^* \nu^{1/2}, \quad (8.1)$$

where n represents the number of electrons participating in the redox reaction, ν is the scan rate of the potential perturbation (ν , mV/s), A is the area of the electrode (cm^2), D is the diffusion coefficient of the molecules in the solution (cm^2/s), C^* is the concentration of the probe molecule in the bulk solution (mol/cm^3), and I_p is the peak current of the Fe(CN)₆^{3-/4-} redox couple. At both of the nanostructured electrodes, the peak current (I_p , mA cm^{-2}) increased linearly with the increasing value of square root of the potential scan rate ($\nu^{1/2}$), which indicates that the reactions

occurring on the modified electrode were nearly reversible. This result also means that the mass transfer phenomenon in the double layer region of the electrodes was mainly diffusion controlled.²⁴⁶

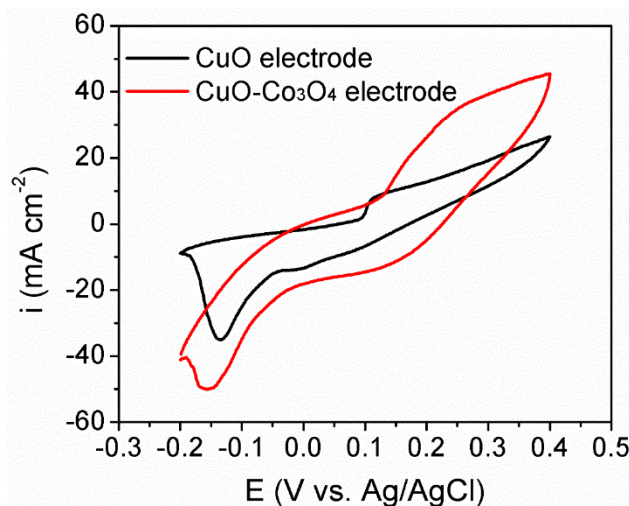


Figure 8.3. CV diagram of the CuO electrode and CuO-Co₃O₄ electrode obtained in 1.0 mM Fe(CN)₆^{3-/4-} and 0.1 M KCl aqueous solution.

As shown in Figure 8.4A, the slope and calculated effective surface area for CuO electrode was ~1.81 ($R = 0.8246$) and ~6.26 cm², respectively. This surface area is ~25 times larger than the geometric area (0.5 cm × 0.5 cm) of the electrode. In Figure 8.4B, the slope obtained for CuO-Co₃O₄ electrode was ~5.78 ($R = 0.9956$) and the calculated effective surface area was ~19.99 cm². Thus, after decorating CuO nanowires with Co₃O₄ nanoparticles, the effective surface area of the CuO-Co₃O₄ electrode was further increased by ~3.19 times as compared with the CuO electrode leading to significantly enhanced electrocatalytic activity of the CuO-Co₃O₄ electrode.

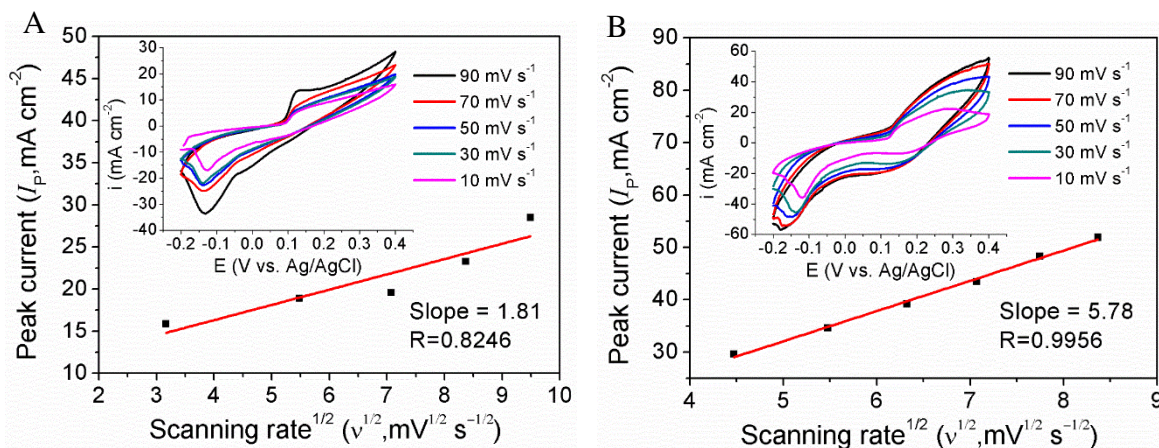


Figure 8.4. Peak current vs. scanning rate for the determination of effective surface area of the (A) CuO electrode and (B) CuO-Co₃O₄ electrode.

EIS was further used to evaluate the electron transfer efficiency of CuO-Co₃O₄ electrode for the Fe(CN)₆^{3-/4-} redox couple (at ~0.3 V corresponding to the oxidation of Fe²⁺). The obtained impedance spectrum for CuO-Co₃O₄ electrode is shown in Figure 8.5A. The spectrum is mainly composed of two capacitive arcs and one Warburg line. The capacitive arc in the high frequency region is considered to be a measure of the film impedance of the modified electrode whereas the capacitive arc in the low frequency region is considered to be associated with the electron transfer resistance of the faradaic reactions.²⁴⁷ The Warburg impedance line observed in the low frequency region is attributed to the semi-infinite linear diffusion (unrestricted diffusion to a large planar electrode).²⁴⁸ Accordingly, the following equation can be used to calculate the total impedance of this faradaic reaction:²⁴⁹

$$Z_T = R_s + \frac{1}{\frac{1}{R_f} + \frac{1}{C_f}} + \frac{1}{\frac{1}{C_d} + \frac{1}{R_t + Z_w}} \quad (8.2)$$

The R_s , R_f and R_t represent the solution resistance, film resistance and electron transfer resistance, respectively. The C_f and C_{dl} represent the capacitance modified film and double layer capacitance, respectively. The Z_W stands for the Warburg diffusion element and is defined as $Z_W = s(1-j)/\omega^{1/2}$, where s is a constant related to the Warburg impedance, $j = (-1)^{1/2}$, and ω is the angular frequency. The corresponding Equivalent Electrical Circuit (EEC) is shown in Figure 8.5B.²⁵⁰ This EEC was further used to simulate the experimental EIS spectra in the ZSimpWin software. Considering the surface complexity of these modified electrodes, Constant Phase Elements (CPEs) were used to replace the capacitors (C) in the simulation.²⁴⁹ It is known that the introduction of CPE can reach a good match to the surface roughness, physical non-uniformity or the non-uniform distribution of surface reaction site.²⁵¹ The impedance of CPE can be written as $Z_{CPE} = 1/Q(j\omega)^n$, where Q represents the capacity parameter expressed in $S\ cm^{-2}\ s^n$, $j = (-1)^{1/2}$ and n , the deviation from the ideal behavior, $n = 1$ is defined for perfect capacitors. The simulation results have been shown in Figure 8.6 and Table 8.1, which concurs strongly with the experimental results. As shown in Table 8.1, the film resistance, R_f , of the CuO-CO₃O₄ electrode is much smaller than that of CuO electrode. This is due to the increase of electrical conductivity of the heterostructures after CO₃O₄ nanoparticles were deposited onto CuO.²⁵² The electron transfer resistance, R_t , of the CuO-CO₃O₄ electrode was ~5.5 times smaller than that of the CuO electrode, indicating that the reaction activity of this heterostructure electrode had significantly improved. This finding is consistent with the CV in Figure 8.3, and the increase of reaction efficiency could be attributed to the good electrocatalytic activity of CO₃O₄ nanoparticles and the large effective surface area of the heterostructure electrode.

Table 8.1. Equivalent Electrical Circuit (EEC) parameters obtained from simulation results as shown in the impedance spectra in Figure 8.6.

Electrodes	Q_f ($S\ s^n\ cm^{-2}$)	n	R_f ($\Omega\ cm^2$)	Q_{dl} ($S\ s^n\ cm^{-2}$)	n	R_t ($\Omega\ cm^2$)	W
CuO	1.87×10^{-5}	0.38	8170	6.46×10^{-8}	0.66	6486	2.92×10^{-4}
CuO-CO ₃ O ₄	5.43×10^{-10}	1	553.4	6.48×10^{-5}	0.73	1190	1.59×10^{-4}

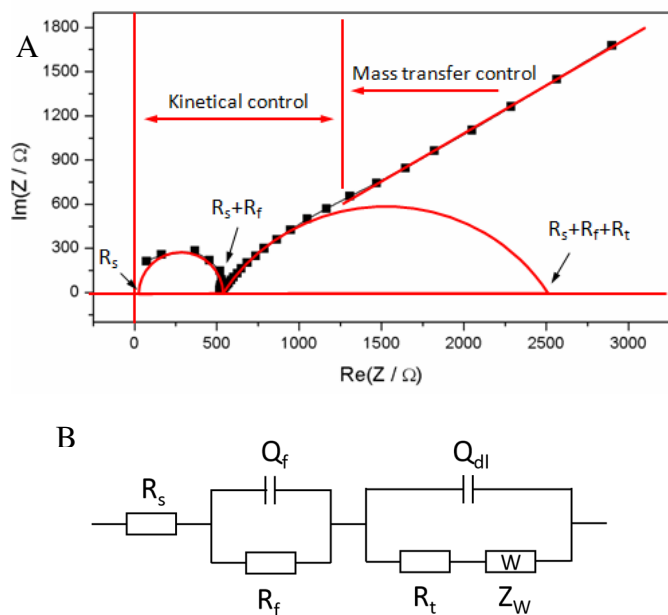


Figure 8.5. (A) EIS spectra of the CuO-Co₃O₄ electrode and corresponding impedance contributing regions. (B) Equivalent electric circuit (EEC) for impedance spectra shown in (A).

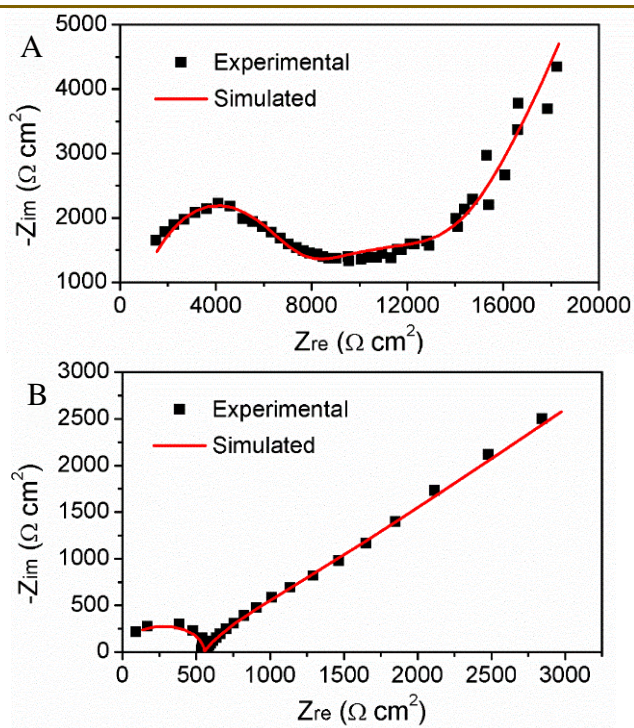


Figure 8.6. Experimental and simulated impedance spectra of (A) CuO electrode and (B) CuO-Co₃O₄ electrode.

8.3.3. Oxygen evolution reaction on the heterostructures

To evaluate the electrocatalytic activity of the heterostructures in relation to oxygen evolution reaction in the water splitting process, cyclic voltammetry and Tafel test were carried out in 1 M KOH solution. The CVs of the CuO electrode and CuO-Co₃O₄ electrode are shown in Figure 8.6A. The anodic branch of oxygen evolution reaction was observed in the high potential region (0.6 V to 1.5 V) for both electrodes. As compared to the CuO electrode, the branch of CuO-Co₃O₄ electrode is significantly shifted towards the negative direction, indicating that the oxygen evolution reaction on these heterostructures is efficient. In addition, small redox peaks corresponding to Cu₂O oxidation (~0.3 V) and CuO reduction (~0.6 V) were observed on the CuO electrode but not on the CuO-Co₃O₄ electrode.

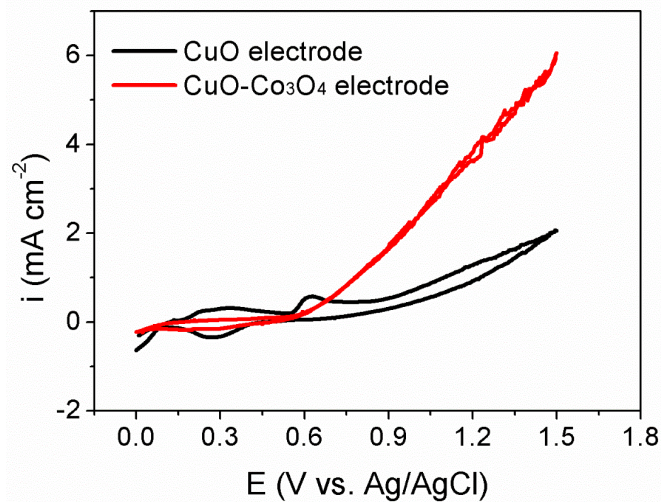


Figure 8.7. CVs for the CuO electrode and CuO-Co₃O₄ electrode obtained in 1 M KOH aqueous solution.

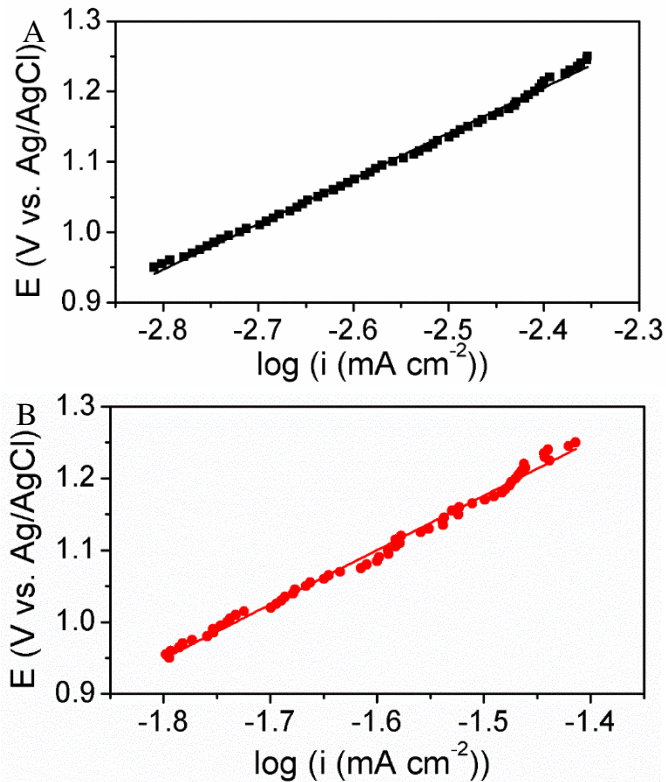


Figure 8.8. Tafel plots for oxygen evolution reaction for (A) CuO electrode and (B) CuO-Co₃O₄ electrode. The polarization was conducted in 1 M KOH aqueous solution.

Tafel plots were further recorded from 0.95 V to 1.25 V, as shown in Figure 8.8. Table 8.2 shows the slopes and the intercepts fitted using OriginLab. The over-potential, η_a , for the oxygen evolution reaction at specific current density of 50 mA cm⁻¹ was calculated using the Tafel equation:

$$\eta_a = (a_0 - \varphi) + b \log i, \quad (8.3)$$

where a_0 represents the Tafel intercept obtained from OriginLab and φ represents the equilibrium electrode potential corresponding to the oxygen evolution reaction:²⁵¹



On comparing the Tafel equation (8.3) with the Butler-Volmer equation in high anodic polarization region ($\eta_a \geq 0.116\text{V}$),²⁵³ the exchange current density J_0 can be described as $\log J_0 = -(a_0 - \varphi)/b$. As shown in Table 8.2, the calculated J_0 for all the three anodes was very small, indicating the oxygen evolution reaction on these electrodes was highly irreversible.²⁵⁴ In addition, these small J_0 values were considered to be negligible in evaluating the electrocatalytic activity of anode materials. As a result, the over-potential η_a was used as the only important criterion.

The calculated over-potential ($i = 50 \text{ mA cm}^{-2}$) for the CuO electrode was 667 mV. Considering the moderate electrocatalytic activity of CuO, this value is not very large as compared to the industrial metal oxide electrode (~850 mV for lead oxide, for example).²⁵⁵ This may be attributed to the significantly increased effective surface area of such nanowire electrode resulted in small real current density. Consequently, the over-potential value would decrease according to the Tafel equation (8.3). For CuO-Co₃O₄ electrode, the measured over-potential was 67.2 mV, which is decreased by ~600 mV as compared with the CuO electrode. This can be attributed to the increased effective surface area and good electrocatalytic activity of Co₃O₄ nanoparticles.

Table 8.2. Kinetic parameters of oxygen evolution reaction obtained from the Tafel plots as shown in Figure 8.8.

Anodes	a_0 (V)	b (mV/dec)	η_a (mV)	J_0 (A/cm ²)
CuO	2.76	645	662	1.74×10^{-4}
CuO-Co ₃ O ₄	2.31	756	67.2	2.26×10^{-4}

8.4. Conclusions

CuO nanowire-Co₃O₄ nanoparticle heterostructures were fabricated for efficient oxygen evolution during electrochemical water splitting. The heterostructures were fabricated by coupling wet-coating of cobalt salt followed by thermal annealing to decompose the cobalt salt to Co₃O₄ nanoparticles uniformly coating the CuO nanowires. These heterostructures were coated on glassy carbon electrode and used as oxygen evolution anode for the electrochemical water splitting. The effective surface area evaluation indicated that the CuO nanowire electrode demonstrated a ~25 times increase as compared to the geometrical surface area of the electrode. For CuO-Co₃O₄ electrode, the effective surface area was further increased by ~3.19 times. Moreover, the CuO-Co₃O₄ electrode showed significantly enhanced electrocatalytic activity for the oxygen evolution reaction. The oxygen evolution over-potential for the CuO-Co₃O₄ electrode was decreased by ~600 mV as compared to that of the CuO electrode (~662 mV).

CHAPTER 9

NOVEL MULTI-COMPONENT P-N JUNCTION COBALT OXIDE-TUNGSTEN OXIDE NANOWIRE HETEROSTRUCTURES FOR EFFICIENT ORGANIC PHOTODEGRADATION

Yuan Li,¹ Nitin Chopra^{1,2,}*

¹Metallurgical and Materials Engineering Department, Center for Materials for Information Technology (MINT), The University of Alabama, Tuscaloosa, AL 35487, U.S.A.

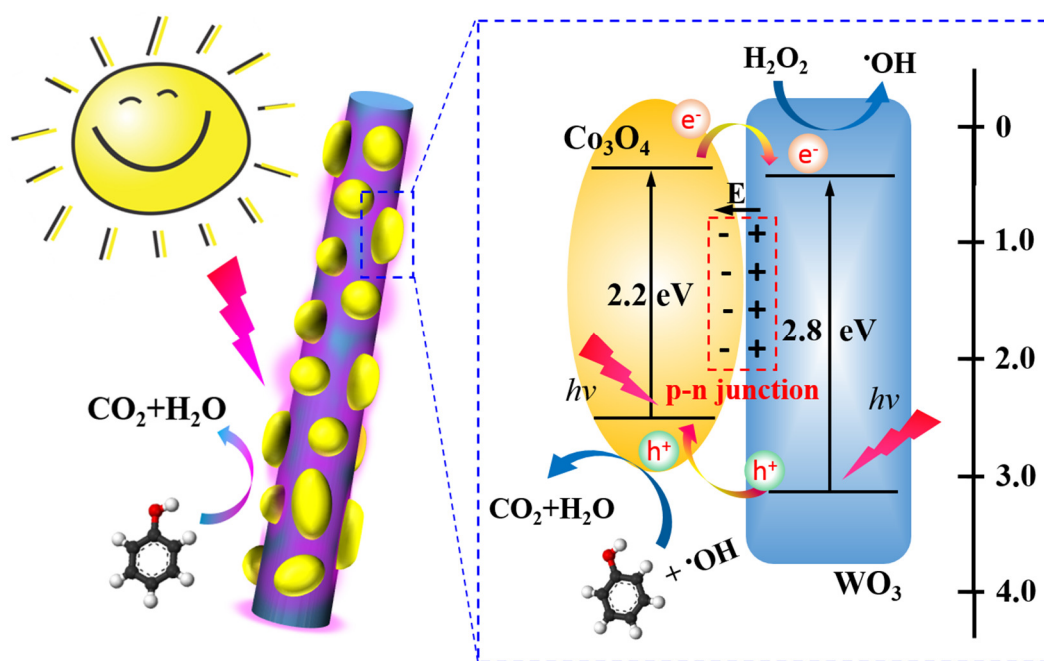
²Department of Biological Sciences, The University of Alabama, Tuscaloosa, AL 35487, U.S.A.

***Corresponding Author**

E-mail: nchopra@eng.ua.edu

Tel: [205-348-4153](tel:205-348-4153)

Table of Content (TOC)



Abstract

Tungsten oxide (WO_3) and cobalt tungstate (CoWO_4) decorated one-dimensional cobalt oxide (Co_3O_4) p-n junction nanowire heterostructures were fabricated through a facile and cost-effective approach. The process includes vapor-solid growth of cobalt oxide nanowires *via* a thermal oxidation method and sputtering coating of tungsten oxide on the standing Co_3O_4 nanowires. To further modulate the structure, morphology and improve the crystallization of tungsten oxide, the product was subjected to a post-annealing process, which resulted in free-standing Co_3O_4 - $\text{WO}_3/\text{CoWO}_4$ multi-component nanowire heterostructures. The crystal structures, morphologies, and chemical composition at each fabrication stage were studied in detail using microscopy and spectroscopy techniques. The investigation for the first time showed the dry processing route for formation of such novel nanowire heterostructures. The photocatalytic performance and behavior of such nanowire heterostructures were further demonstrated for the degradation of water-contaminating organics (*via* a phenol photodegradation process). The photocatalytic efficiency was estimated by ~42% for visible illumination and ~25% for UV illumination as compared with the as-produced Co_3O_4 nanowires.

Keywords: Cobalt oxide, tungsten oxide, p-n junction nanowire heterostructure, photocatalysis

9.1. Introduction

Environmental remediation technologies for efficient water cleaning *via* the photocatalytic methods are of particular interest.²⁵⁶ Here, the demands are for using cheap catalysts with suitable energy and electronic structure. Compounds such as phenol, textile dyes, and poly chloro-biphenyls (PCBs) contaminate water through domestic sewage, industrial wastewater, and agriculture wastewater. Even low concentration of such contaminants ($<1 \text{ mg L}^{-1}$) is hazardous since they prevent the growth of aqueous organisms and reduce the photosynthesis activity of the marine flora.²⁵⁷ Various physical and chemical methods for the removal of these contaminants from water have been studied, including absorption (using activated carbon), thermal degradation, and wet-air oxidation/ozonation.²⁵⁸ However, these processes are cost-intensive and mainly suitable for higher-concentration contaminants. Thus, catalytic or photocatalytic degradation of organic pollutants is critical and holds potential for efficient, cost-effective, and environmental-friendly decontamination.²⁵⁷ Furthermore, photocatalytic degradation of organics can be conducted at room temperature and atmospheric pressure, which makes this approach commercially favorable.²⁵⁷

Various metal oxide semiconductors such as TiO_2 , ZnO , Fe_2O_3 , and sulfides (CdS , ZnS) exhibit photocatalytic behavior attributed to their suitable electronic, surface, and crystal structure.²⁵⁹ Among these oxides, TiO_2 is the best known photocatalyst due to its high photocatalytic activity and good photostability in aqueous medium.²⁶⁰ However, its sustainable application are largely limited due to the wide energy band gap (only UV-active) and high charge recombination.²⁶¹ Meanwhile, ZnO and Fe_2O_3 are unstable in various industrial waste water streams. Metal sulfides will release toxic sulfides under illumination and thus their suitability for water decontamination was also constricted. Out of several material choices, Co_3O_4 and WO_3 are earth-abundant

catalytically active materials with relatively narrow band gap energies.²⁵⁸ These two oxides present advantages such as extended photosensitivity in the visible region, long-term physical/chemical stability, and/or ease of preparation. However, band gap engineering of such oxides is a challenge and mainly depends on their morphology, size, and configuration. If the aim is to develop a photocatalyst that can also survive multiple processing or treatment cycles then catalysts based on single component nanostructure or oxide cannot surpass the advantages of heterostructured photocatalysts. The latter implies nanoscale systems combining two or more materials or nanostructures, where the synergistic effect of all the components results in a multifunctional catalytic architecture.

Nanowire heterostructures are novel one-dimensional nanoarchitectures that possess unique surface functionality, chemical and electrical properties.²⁶² Such heterostructures can exhibit anisotropic light-matter interactions and thus are promising for photocatalysis processes.²⁶³ For instance, one-dimensional geometry (e.g., core-shell nanowires) can allow for greater absorption of light in longitudinal direction and result in efficient charge transport (or charge carrier generation) in radial direction.²⁶⁴ However, such merit exhibition shows significant dependence on the structure, morphology, size, and material selection. Meanwhile, another challenge for photoactive nanostructures is to eliminate or mitigate the use of noble metals.²⁶⁵ This further narrows down the materials selection criteria for photoactive systems. In this regard, we propose an interesting and novel photocatalyst design through the hybridization of cobalt oxide and tungsten oxide, which can result in one-dimensional multi-component heterostructures with specific structure and tunable band gap energies.²⁶⁶ Moreover, tungsten oxide (WO_3) is n-type semiconductor with band gap energy of ~ 2.8 eV while cobalt oxide (Co_3O_4) is a p-type semiconductor with band gap energy ~ 1.6 eV.²⁶⁷ Their combination can form a stable p-n junction

at the interface and further generate a constant electric field at equilibrium.²⁶⁰ Under illumination, the photo-excited electrons is prone to move to the positive field and the holes flow into the negative field. As a result, the electron-hole pairs can be separated in an efficient manner, leading to significantly improved photocatalytic activity.²⁶⁸

The major goal of this work is to develop novel oxide-based nanowire heterostructures with controlled morphology, chemical composition, and interfaces. The fabrication of the cobalt oxide-tungsten oxide nanowire heterostructures was achieved in a surfactant-free and dry processing route. Free-standing Co_3O_4 nanowires were grown in a water vapor-assisted thermal oxidation process,²⁶⁹ further sputtering-coated with WO_3 thin shell, and annealed in air. The resulting nanowire heterostructures remained standing on the substrate after multiple processing steps. The morphology, interfaces, chemical composition, and crystal structure of the heterostructures were characterized by various microscopic and spectroscopic techniques. The photocatalytic performance and kinetics of the same were also studied for the degradation of phenol.

9.2. Experimental section

Materials and methods: Cobalt (Co) foil was purchased from Alfa Aesar (Ward Hill, MA). Tungsten oxide (WO_3) target (99.99%) were provided by AJA International, Inc. Phenol was purchased from Sigma-Aldrich (St. Louis, MO). DI water (18.1 $\text{M}\Omega\text{-cm}$) was obtained using a Barnstead International DI water system (E-pure D4641). All chemicals were used without further purification. Branson 2510 Sonicator (Danbury, CT) was used to assist the surface cleaning of Co foil/powders in acetone and DI-water. ATC ORION sputtering system (AJA international, Inc.,

North Scituate, MA) was used. 5% O₂/Ar gas cylinders were purchased from Airgas South (Tuscaloosa, AL).

Growth of Co₃O₄ nanowires: Roughened Co foil with a thickness of ~0.2 mm was used as the initial substrate. Before the thermal growth, the pre-treated samples were first cleaned in acetone and then in DI-water. The samples were further treated with 10% HNO₃ solution for 15 s to remove pristine surface oxide layers. The growth of Co₃O₄ nanowires was carried out in a quartz tube furnace (at ~450 °C for 10 h) in the presence of humidity (flow rate ~12 mg/min) and 5% O₂ in Ar (flow rate ~12 SLM).

Fabrication of Co₃O₄-WO₃ nanowire heterostructures: The as-produced Co₃O₄ nanowire were sputtering-coated with WO₃ in a RF sputtering process at chamber pressure of ~3×10⁻³ Torr. The sputtering was carried out at 50 W for 10 min. The measured sputtering rate (by a crystal quartz monitor) was ~0.02 nm/s. This resulted in a WO₃ thickness of ~12 nm on a flat substrate. In the following, this as-sputtered Co₃O₄-WO₃ nanowire heterostructures were further subjected to a high-temperature (450 °C) air-annealing process for 30 min, which leads to the final annealed nanowire heterostructures.

Photodegradation of phenol: To test the photocatalytic performance of the nanowire heterostructures, degradation of phenol (~ 3 mM in DI-water) was carried out under visible light or UV illumination. Standing nanowire heterostructures on the Co foil (2 × 2 cm²) were immersed in ~3 ml phenol solution. This was followed by further addition of ~100 μL H₂O₂ (37%) as the sacrificial agent.^{270,271} Either UV illumination lamp (~254 nm, 8W) or visible illumination lamp (~360 nm, 8W) was utilized as the light source. The solution was gently stirred during the

photodegradation. UV-vis absorbance spectra of the phenol solution were recorded every 30 min for estimating the concentration of phenol. This photodegradation process was continued for ~8 h.

Characterizations: Scanning Electron Microscopy (SEM) images were obtained using FE-SEM JEOL-7000. Tecnai F-20 was used to collect Transmission Electron Microscopy (TEM) images and Energy Dispersion Spectroscopy (EDS) line-profiles in the Scanning Transmission Electron Microscopy (STEM) model. Philips X'Pert-MPD X-ray Diffraction (XRD) System was used for the phase analysis. Raman spectra were collected using Bruker Senterra system (Bruker Optics Inc. Woodlands, TX) equipped with 785 nm laser source. Kratos Axis 165 X-ray photoelectron spectroscopy (XPS) with a mono-aluminum gun was used. Full range XPS spectra were collected at 160 eV pass energy for high-resolution spectra were collected at 40 eV pass energy. UV-vis reflectance spectra of the cobalt oxide nanostructures were obtained using DH-2000 UV-VIS-NIR light source. The optical transition energy value can be determined using the equation (9.1):

$$ah\nu = A(h\nu - E_g)^n, \quad (9.1)$$

where a is absorption coefficient, A is a constant, $h\nu$ is the energy of light and n is a constant depending on the nature of the electron transition (n assumes the values 1/2, 2, 3/2 and 3 for allowed direct, allowed indirect, forbidden direct and forbidden indirect transitions, respectively).

Since the absorption coefficient (a) is proportional to Kubelka-Munk function ($F(R)$):

$$F(R) = (1 - R)^2 / 2R = a / s, \quad (9.2)$$

where R is the reflectance, k is the absorption coefficient and s is the scattering coefficient, the band gap energy can be obtained from the plots of $[F(R)h\nu]^{1/2}$ vs. $h\nu$ by estimating the intercept of their linear extrapolation at the $h\nu$ axis.

9.3. Results and discussion

High aspect ratio and standing Co_3O_4 nanowires were grown *via* a water vapor-assisted thermal oxidation approach, where the growth was governed by the vapor-solid mechanism.²⁷² Figure 9.1A and B show the SEM images of the as-produced Co_3O_4 nanowires. An oxide film composed of CoO bottom layer and Co_3O_4 top layer (Figure 9.1A, marked by arrows) was observed on the cobalt foil after the Co_3O_4 nanowire growth process. Such underlayer formation has been confirmed previously for similar thermal growth of metal oxide nanowires on metal foils (e.g. Cu, Fe).²⁷³ The EDS analysis and elemental imaging for the formation of CoO/ Co_3O_4 film was further detailed. The average diameter and length of nanowires was observed to be $\sim 76.81 \pm 14.37$ nm and $\sim 5.33 \pm 2.23$ μm , respectively. TEM images of the as-produced Co_3O_4 nanowires were shown in Figure 9.1C and D. A lattice spacing of $\sim 0.24 \pm 0.01$ nm was observed corresponding to the (311) plane of Co_3O_4 . In the next step, surface decoration of Co_3O_4 nanowires with WO_3 was achieved in a sputtering process. Figure 9.1E shows the SEM image of the resulting Co_3O_4 - WO_3 nanowire heterostructures. Due to the coating of WO_3 film on the Co_3O_4 nanowires, the average diameter and length was observed to be $\sim 88.66 \pm 11.39$ nm and $\sim 5.01 \pm 2.50$ μm . This indicates that ~ 12 nm thick WO_3 film (Figure 9.1F) was deposited on the Co_3O_4 nanowires. It is important to note that the line-of-sight deposition of WO_3 leads to self-shadowing of nanowires,²⁷⁰ as a result, thicker WO_3 coating was observed at on one side of Co_3O_4 nanowires (Figure 9.1G). In addition, it was also observed that the as-deposited WO_3 was in amorphous structure and further crystalizing process is necessary for improving the photocatalytic features.

High temperature air-annealing was carried out on the as-sputtered Co_3O_4 - WO_3 nanowire heterostructures to modulate their structure, morphology and improve the crystallization of tungsten oxide. As shown in Figure 9.2A, the annealed Co_3O_4 - WO_3 nanowire heterostructures

exhibited diameter of $\sim 102.66 \pm 20.63$ nm. The average length of these nanowires was decreased to 3.22 ± 1.80 μm after annealing. TEM images of the annealed heterostructures were shown in Figure 9.2B-E. These microscopy images indicate this post-annealing process resulted in redistribution of the decorated tungsten oxide, which was then partially covered on the surface of the nanowires with a thickness of 25~28 nm (Figure 9.2B). These surface-decorating nanostructures were observed to be either a composite of tungsten oxide and cobalt oxide with a slightly increased lattice spacing of ~ 0.25 nm (corresponding to the (200) plane of CoWO_4 ,²⁷⁴ Figure 9.2C and D), or pure WO_3 with a lattice spacing of 0.38 nm (corresponding to (010) plane of WO_3 , Figure 9.2D and E). As further observed in Figure 9.2C-E, the interfaces in the heterostructures were mostly composed of CoWO_4 composite zone, transition zone (in amorphous structure), pure WO_3 zone and Co_3O_4 nanowire zone (with its original lattice spacing of 0.24 nm). The lattice distribution of the annealed nanowire heterostructures were further confirmed by the FFT images in Figure 9.2F.

To further demonstrate the chemical composition of the nanowire heterostructures, STEM-model EDS line profile analysis were carried out on both as-sputtered and annealed nanowire heterostructures (Figure 9.2G and H). Consistent with that shown in Figure 9.1F and G, obvious self-shadowing effect was observed on the as-sputtered nanowire heterostructures (Figure 9.2I). The WO_3 shell thickness at one side of the Co_3O_4 nanowire was higher than the other side ($\Delta d \sim 12$ nm). However, most of these surface-decorating nanostructures after the annealing were uniformly distributed on both sides of the nanowire. Tungsten was dominantly distributed in these decorating nanostructures while the original Co_3O_4 nanowire core was chemically intact. This is consistent with the previous observations of the authors and indicates that the post-annealing process involves surface migration and recrystallization of the sputtered tungsten oxide and/or its diffusion and

compositing with cobalt oxide.²⁶³ Such surface migration and diffusion have been attributed to surface tension, capillary forces, and chemical potential differences between the nanowire and coatings.

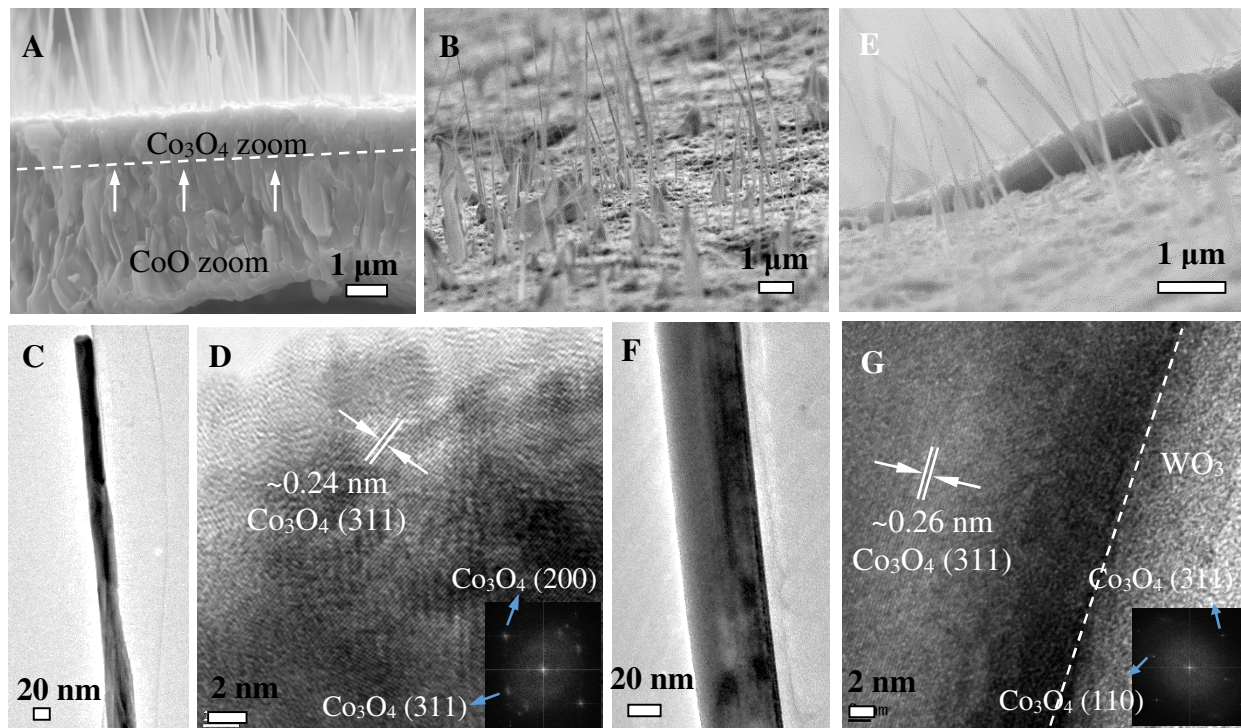


Figure 9.1. (A, B) SEM images showing the cross-section and top view of the pristine Co_3O_4 nanowires produced by water vapor-assisted thermal oxidation. (C) Top view of the as-sputtered Co_3O_4 - WO_3 nanowire heterostructures. (D-G) TEM/HRTEM images showing the structure and lattice of the Co_3O_4 nanowires (D and E) and the as-sputtered Co_3O_4 - WO_3 nanowire heterostructures (F and G).

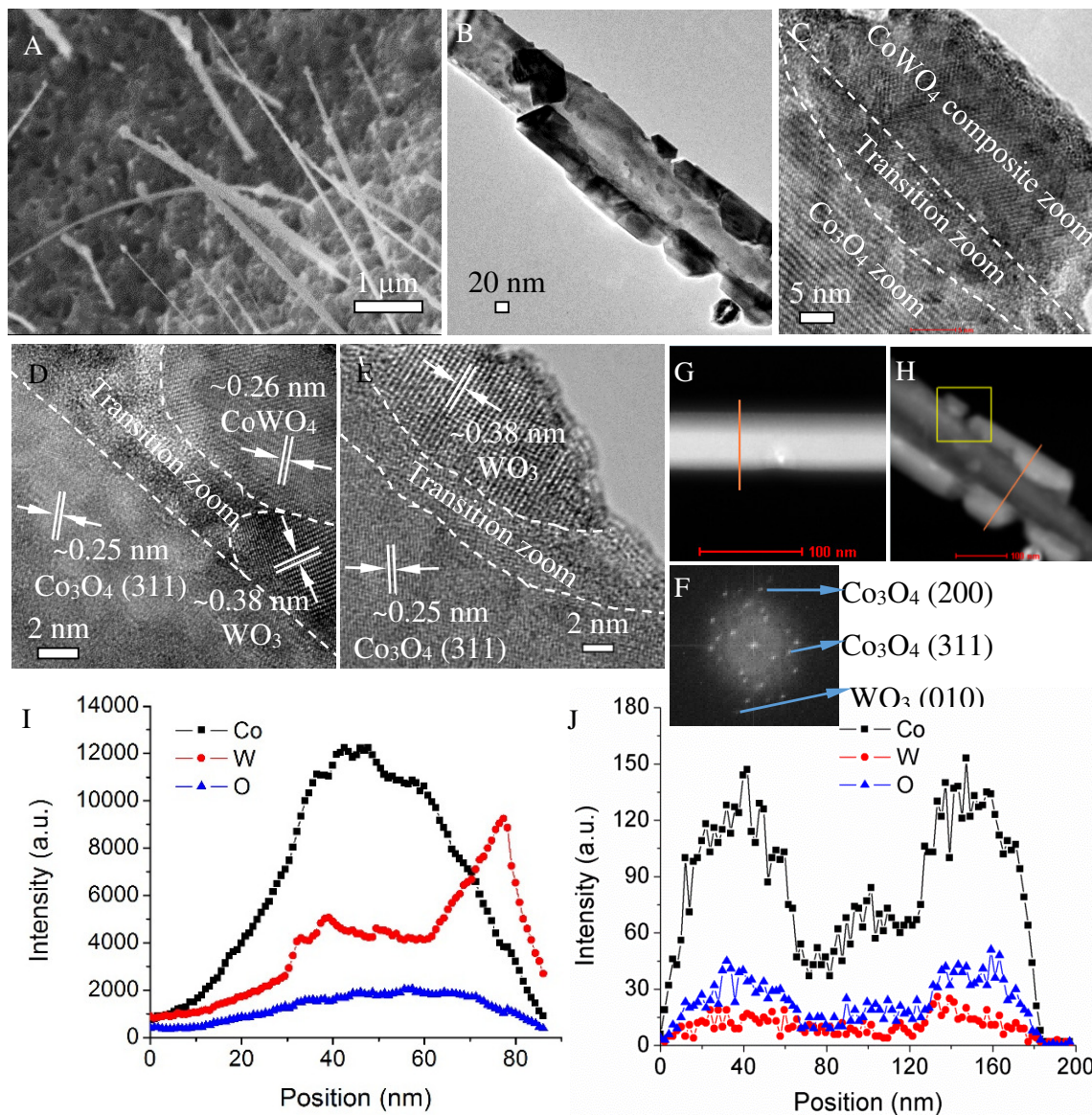


Figure 9.2. (A) SEM images of the annealed $\text{Co}_3\text{O}_4\text{-WO}_3$ nanowire heterostructures. (B-E) TEM/HRTEM images showing the structure and lattice of the annealed heterostructures. (F) FFT image generated from E. (G and H) STEM images of the $\text{Co}_3\text{O}_4\text{-WO}_3$ nanowire heterostructures before (G) and after (H) annealing. (I, J) EDS line profiles cross the nanowire heterostructures corresponding to G and H, respectively.

XRD further confirmed the presence of different phases and elements within the nanowire heterostructures at each stage of fabrication. Various crystallographic planes for CoO, Co₃O₄, WO₃ and CoWO₄ are shown in the XRD spectra (Figure 9.3A and B). The presence of CoO peaks is due to the formation of CoO underlayer during the thermal growth, which is consistent with SEM images showing in Figure 9.1A and S1 (see supporting information). The peaks for the Co₃O₄ are attributed to both the Co₃O₄ underlayer and the standing nanowires. The dominant (311) peak for Co₃O₄ shows a good match with the lattice spacing observed in Figure 9.1D. Furthermore, after the sputtering deposition of tungsten oxide, an obvious negative shift for Co₃O₄ peaks ($\Delta_{2\theta} \sim 0.45^\circ$) were observed (Figure 9.3B) and suggests that deposition of tungsten oxide layers led to strains within the nanowire lattice.²⁷⁵ According to the Bragg's law, this deduction is consistent with the slightly increase of lattice spacing of Co₃O₄ (Figure 9.1G) after WO₃ sputtering. After the post-annealing process, the Co₃O₄ peaks were slightly shifted back due to the release of strain during the annealing. And the remaining negative shift of $\sim 0.37^\circ$ (Figure 9.2B) is also consistent with the emergence of CoWO₄ peaks.²⁷⁴ The peaks of WO₃ and CoWO₄ for the heterostructures before and/or after annealing were overall very small due to their less amount however provide evidence for the existence/formation of both as the indicative crystal plane are consistent with the TEM observations in Figure 9.2.

Raman spectra (Figure 9.3C) were collected for understanding the chemical and phase composition of the nanowire heterostructures at the different fabrication stages. The as-produced Co₃O₄ nanowires, as-sputtered and annealed Co₃O₄-WO₃ nanowire heterostructures all show consistent Raman signal for spinel Co₃O₄.²⁷⁶ These include F_{2g} at $\sim 196\text{ cm}^{-1}$, $\sim 525\text{ cm}^{-1}$ and 623 cm^{-1} , E_g at $\sim 484\text{ cm}^{-1}$, and A_{1g} at $\sim 695\text{ cm}^{-1}$.

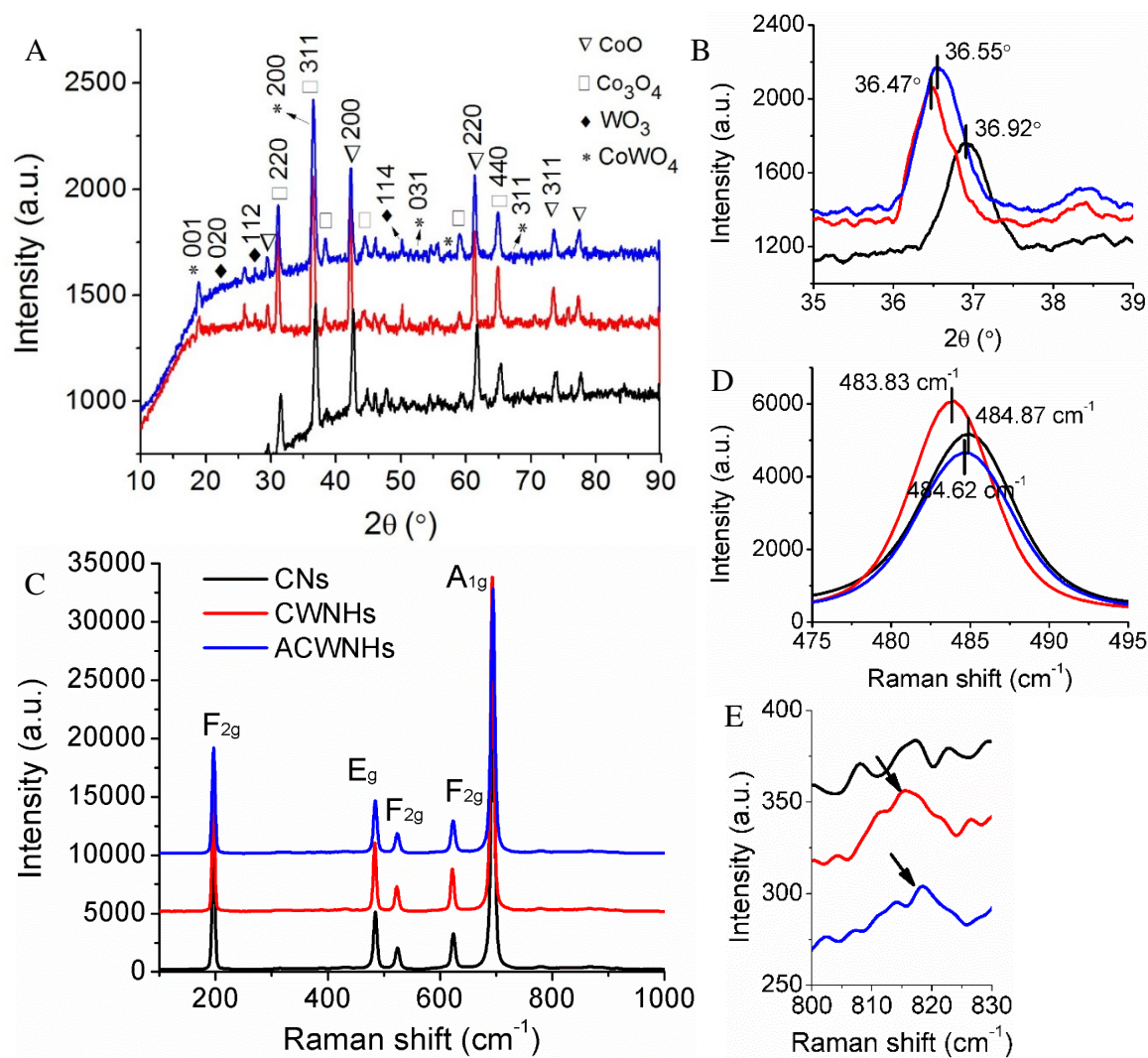


Figure 9.3. (A) XRD patterns of the Co₃O₄ nanowires, Co₃O₄-WO₃ nanowire heterostructures before and after annealing. (B) Detailed XRD spectra for the typical (311) peak of Co₃O₄ in (A). (C) Raman spectra of the Co₃O₄ nanowires, Co₃O₄-WO₃ nanowire heterostructures before and after annealing. (D, E) Detailed Raman spectra for (D) the E_g band of Co₃O₄ and (E) representative ν(O-W⁶⁺-O) band of WO₃ in (C). *Note: The as-produced Co₃O₄ nanowires were referred as (CNs), the as-sputtered Co₃O₄-WO₃ nanowire heterostructures are referred as (CWNHs) and the annealed nanowire heterostructures were referred as (ACWNHs) as shown in Figure 9.3C.*

As reported before, the A_{1g} mode is assigned to the octahedral sites in spinel Co_3O_4 and the E_g and F_{2g} modes are related to the combined vibrations of tetrahedral sites and octahedral oxygen motions. After WO_3 sputtering, all the Raman peaks of Co_3O_4 were slightly shifted to the negative direction ($\Delta = 1.0 \text{ cm}^{-1}$, as representatively shown in Figure 9.3D). This is consistent with the XRD observation in Figure 9.3A and probably because the sputtered WO_3 shell brought extra strain to the lattice of Co_3O_4 nanowires, which resulted in frequency change to the equilibrium vibration of cobalt and oxygen atoms.²⁷⁷ As mentioned above, the amount sputtered WO_3 was very less as compared with that of Co_3O_4 , and thus only weak signal can be found for WO_3 component. As shown in Figure 9.3E, the peak at $\sim 815 \text{ cm}^{-1}$ observed for the as-sputtered and annealed Co_3O_4 - WO_3 nanowire heterostructures were assigned to the $\nu(\text{O}-\text{W}^{6+}-\text{O})$ vibrational stretching mode of the W-O-W bridging oxygen.²⁷⁸

Surface information on the purity and composition of the nanowire heterostructures at the different fabrication stages was further demonstrated using XPS. The binding energies obtained in the XPS analyzer were corrected for possible specimen charging by referencing C 1s peak at 284.7 eV.²⁷⁹ Wide-range XPS spectra indicate that the predominant elements are Co and O for the as-produced Co_3O_4 nanowire, W and O for the as-sputtered nanowire heterostructures, and Co, W, and O for the annealed nanowire heterostructures. High-resolution Co 2p spectrum of the Co_3O_4 nanowires were shown in Figure 9.4A, which was further deconvoluted to various sub-peaks according different oxidation state and binding energy of cobalt. The asymmetric peaks located at 779.63 eV and 794.69 eV (with a spin-orbit splitting of 15.06 eV) are characteristic of octahedral Co^{3+} in spinel Co_3O_4 .²⁸⁰ The peaks at $\sim 780.80 \text{ eV}$ and ~ 796.00 are assigned to the Co^{2+} species.²⁸⁰ Another three important peaks, located at $\sim 786.00 \text{ eV}$, $\sim 770.00 \text{ eV}$ and $\sim 804.20 \text{ eV}$, have been assigned to the satellite shake-up structures of divalent cobalt ions.²⁸⁰ All of these peaks has been regarded as

important evidence for the presence of pure spinel Co_3O_4 .²⁷⁹ It also needs to mention that the peaks at ~ 781.97 eV and ~ 797.78 eV were considered as chemical shift of the main spin-orbit components because of the chemical interaction of cobalt cations with some contamination ions such as hydroxyls.²⁸¹ In addition, Figure 9.4B indicates that no tungsten presence in the as-produced Co_3O_4 nanowires.

Considering XPS is a surface characterization technique with a detection depth limit of ~ 3 nm,²⁸² Co_3O_4 core component would hardly been detected for the as-sputtered core-shell nanowire heterostructures. As shown in Figure 9.4C, the Co 2p spectra of the as-sputtered $\text{Co}_3\text{O}_4\text{-WO}_3$ nanowire heterostructures only show very weak signal of cobalt. However, in this case strong signal of tungsten oxide was observed (Figure 9.4D). The peaks located at ~ 36.19 eV and ~ 38.31 eV were attributed to the presence of W^{6+} .²⁸³ Besides, a small peak was also observed at ~ 34.25 eV, which has been assigned to the characteristics of W^{4+} . The appearance of this valence of tungsten is probably due to the random deposition and arrangement of tungsten atoms during sputtering.²⁸³ For the annealed nanowire heterostructures, the air-annealing process led to possible inter-diffusion and surface migration of tungsten and cobalt species. As a result, the tungsten oxide-based surface decorating materials were significantly re-distributed (Figure 9.2B) and large surface of Co_3O_4 nanowires was exposed. Thus, similar XPS spectrum of Co_3O_4 (Figure 9.4E) with the as-produced Co_3O_4 nanowires was observed. However, since most of tungsten oxide was interacted with cobalt oxide and appeared in the form of CoWO_4 composite (Figure 9.2C-F), relative weak signal of tungsten was observed for this annealed nanowire heterostructures (Figure 9.4F).

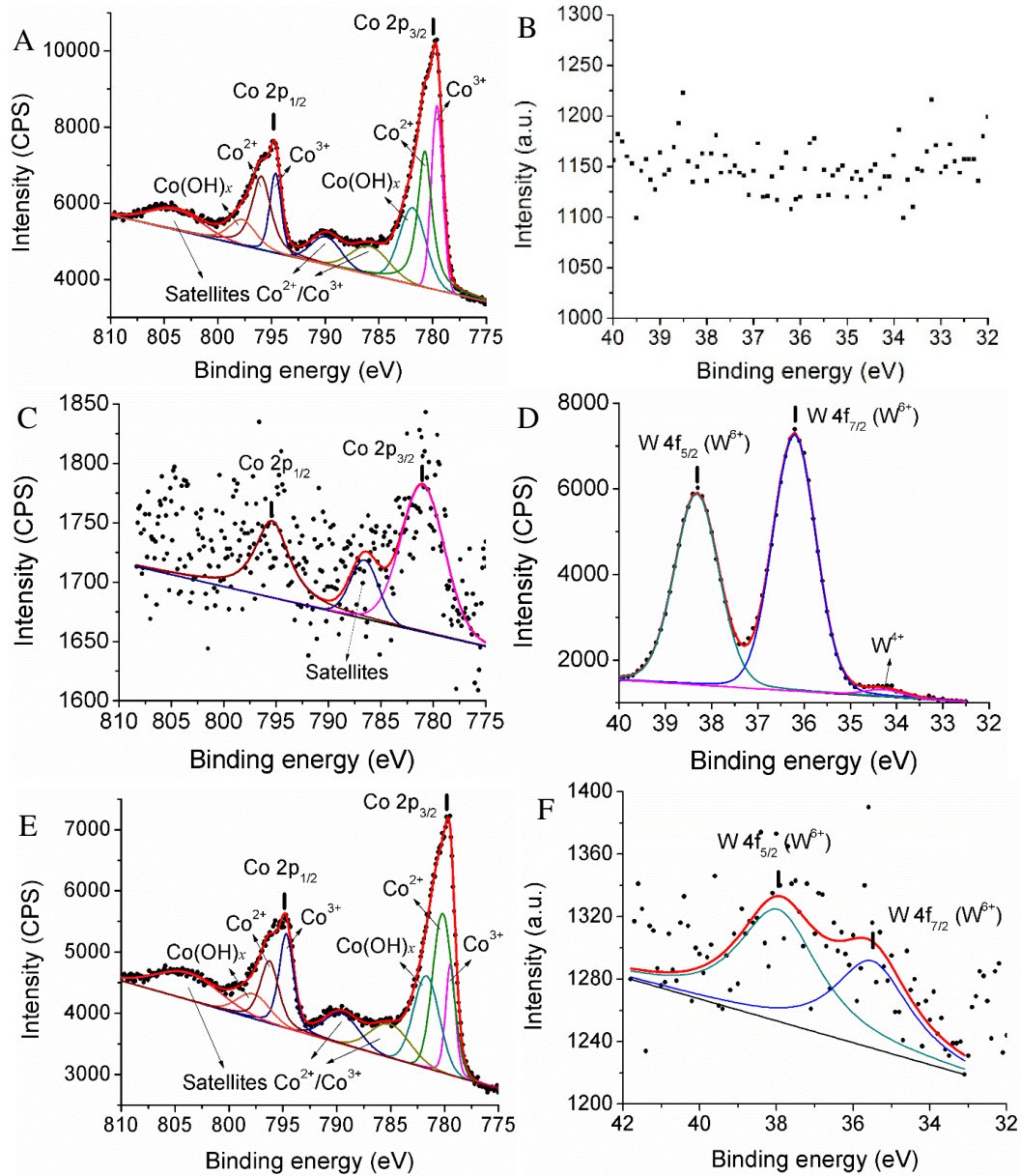


Figure 9.4. Deconvoluted XPS spectra corresponding to Co 2p (A, C and E) and W 4f (B, D and F) of the Co₃O₄ nanowires (A, B), Co₃O₄-WO₃ nanowire heterostructures before (C, D) and after (E, F) annealing.

The influence of surface decoration of $\text{WO}_3/\text{CoWO}_4$ nanostructures on the UV-vis reflectance characteristics and band gap energies of Co_3O_4 nanowires was evaluated in the following. The UV-vis spectra (Figure 9.S3, Supporting Information) indicates that the annealed nanowire heterostructures show reduced reflectance compared with the pristine Co_3O_4 nanowires. This can be attributed to the increase of surface roughness.²⁸⁴ Several reflectance edges were observed on both samples. Considering both Co_3O_4 and WO_3 are indirect band gap semiconductors,^{270,285} the spectra can be converted into Tauc plots (Figure 9.5A), of which the intercepts of the extrapolated linear region on x -axis correspond to the band gap energy of the heterostructures. Band gap energies of ~ 1.50 eV and ~ 1.86 eV were estimated for the as-produced Co_3O_4 nanowires. The former is considered as transitions from O^{2-} to Co^{3+} while the latter is near to the transitions from O^{2-} to Co^{2+} .²⁶⁸ For the annealed nanowire heterostructures, two band gaps were observed at ~ 1.50 eV and ~ 2.17 eV. This indicates that incorporation of tungsten oxide has little influence on the transition energy of Co^{3+} , but has a significant modification on that of Co^{2+} . Such observation confirms the former observation (Figure 9.2B) that Co^{2+} dominantly diffused and hybridized with WO_3 during the annealing, resulting the formation of CoWO_4 .

Photodegradation of water-containing phenol under UV and visible light was carried out to demonstrate the photocatalytic performance of the as-produced Co_3O_4 nanowires and the annealed $\text{Co}_3\text{O}_4\text{-WO}_3$ nanowire heterostructures. The degradation efficiency ($\eta = (1 - C/C_0) \times 100\%$) vs. time were plotted in Figure 9.5B. We observed that after 8 h of visible light illumination, 12% of phenol was removed on the as-produced Co_3O_4 nanowires and the degradation efficiency increased to 17% by use of the annealed nanowire heterostructures. The UV illumination is much more powerful for such photocatalytic degradation processes. A degradation efficiency of 57% was obtained for Co_3O_4 nanowires while that for the annealed nanowire heterostructures was increased

to 71%. This indicates that the photocatalytic efficiency of Co_3O_4 nanowire was increased by $\sim 42\%$ ($\frac{17\%-12\%}{12\%} \times 100\%$) for visible illumination and by $\sim 25\%$ ($\frac{71\%-57\%}{57\%} \times 100\%$) for UV illumination after the surface heterostructuring process.

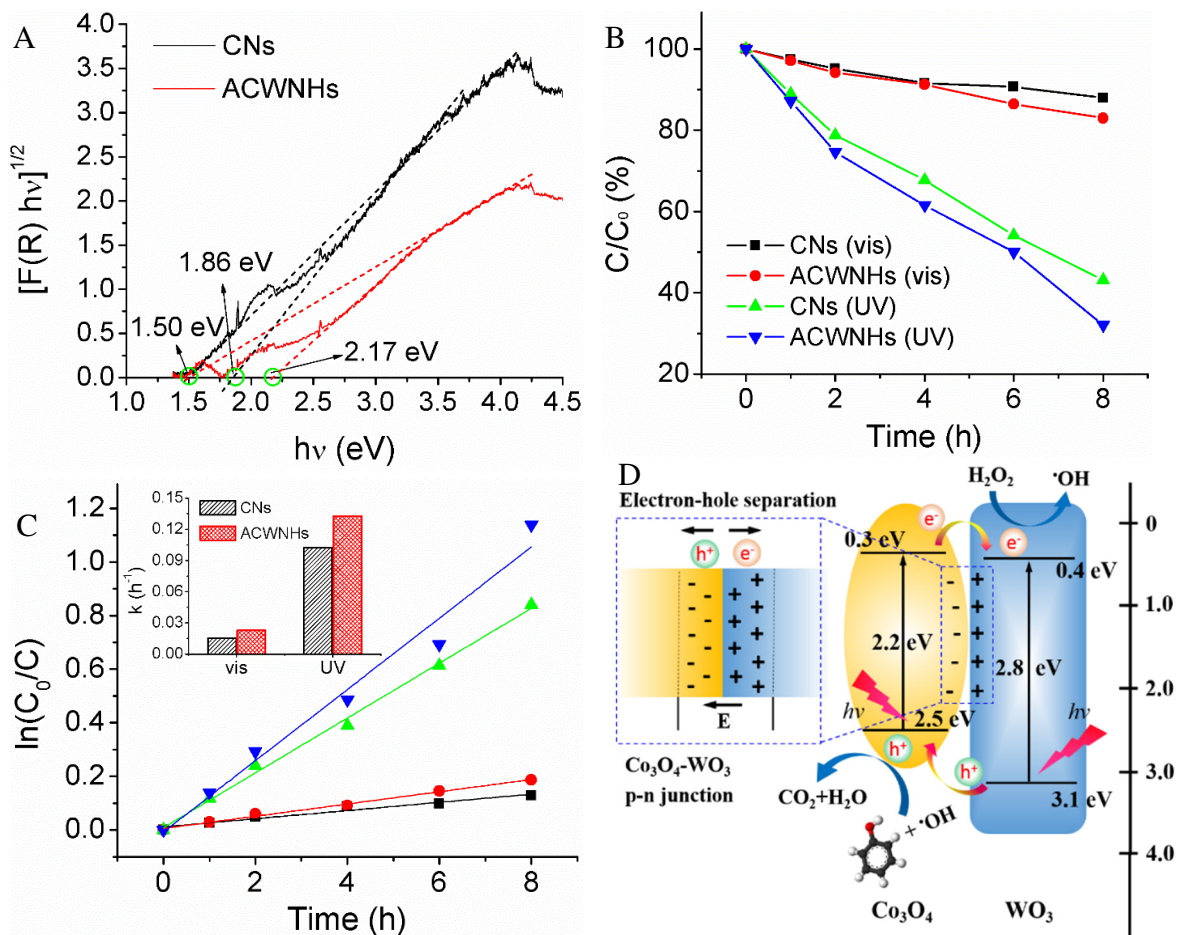


Figure 9.5. (A) Tura plots based on the UV-vis reflectance spectra showing the band gap of the Co_3O_4 nanowires (CNs) and the annealed Co_3O_4 - WO_3 nanowire heterostructures (ACWNHs). (B) Photocatalytic degradation of phenol with various nanostructures under UV or visible light. (C) Kinetics study for the photodegradation of phenol. (4) Schematic illustration of band gap of the annealed Co_3O_4 - WO_3 heterostructures and possible charge transfer and separation mechanism.

To further study the photodegradation kinetics, the first order rate constant (k) was estimated using the following kinetic equation:²⁵⁷

$$k = \frac{1}{t} \ln \frac{C_0}{C} \quad (9.3)$$

where t is the degradation time, C_0 is the initial phenol concentration in water and C is the phenol concentration at specific t . As shown in Figure 9.5C, the plots of $\ln(C_0/C)$ vs. t show good linear trend, allowing to estimate the first order kinetic constant of 0.015 h^{-1} and 0.023 h^{-1} for the Co_3O_4 nanowires and annealed $\text{Co}_3\text{O}_4\text{-WO}_3$ nanowire heterostructures under visible illumination and 0.102 h^{-1} and 0.133 h^{-1} for each under UV illumination.

The improvement of photocatalytic activity observed on the annealed $\text{Co}_3\text{O}_4\text{-WO}_3$ nanowire heterostructures can be well-explained based on the catalyst design. First of all, as shown in the TEM images (Figure 9.2B-E), these multi-component heterostructures are basically composed of $\text{WO}_3/\text{CoWO}_4$ nanostructures that supported on one-dimensional Co_3O_4 nanowires. This leads to significantly increased surface area and interface area for the photocatalytic reaction on the heterostructures. Second, the band gap arrangement for Co_3O_4 and WO_3 is one of the most efficient design for charge transfer and excited electron-hole separation (Figure 9.5D). One of the major challenge for most of photocatalysts lies in the recombination of photogenerated electrons. In this case, the conduction band of WO_3 is lower than that of Co_3O_4 and the valence band of Co_3O_4 is higher than that of WO_3 . This leads to the excited electrons, rather than combination, transfer from the conduction band of Co_3O_4 to that of WO_3 and meanwhile holes transfer from the valence band of WO_3 to that of Co_3O_4 . As a result, the photogenerated charge separation was effectively enhanced. Moreover, in such heterostructure design, Co_3O_4 and WO_3 form a constant p-n junction at the interface (as magnified in Figure 9.5D), the inner electric field (from WO_3 to Co_3O_4) further accelerated the transfer of electron and hole, which results the electrons mainly accumulated on

the conduction band of WO_3 for decomposing H_2O_2 to $\text{OH}\cdot$ radicals, while the holes mainly accumulated on the valence band of Co_3O_4 for the degradation of phenol (with the assistant of $\text{OH}\cdot$ radicals). In addition, such charge separation mechanism can also be applied to the interface between WO_3 and CoWO_4 since the latter is another well-defined p-type semiconductor.²⁸⁶ Thus, one can predict that the catalyst design reported in this paper is of great interest and efficiency for further photocatalytic water purification and organic degradation.

9.4. Conclusions

This study for the first time shows the facile fabrication of free-standing cobalt oxide-tungsten oxide nanowire heterostructures *via* a surfactant-free and dry fabrication method. The cobalt oxide nanowire growth was achieved using a water vapor-assisted thermal oxidation approach directly conducted on a cobalt substrate. This was followed by sputtering deposition of tungsten oxide and further annealing process to result in polycrystalline $\text{WO}_3/\text{CoWO}_4$ composite nanostructures supported on the cobalt oxide nanowires. The heterostructures were studied for their crystal structure and lattice variation across the interface and various phase transformations were observed along the heterostructure diameter. Interesting p-n junctions were formed between Co_3O_4 and WO_3 or between WO_3 and CoWO_4 , which is of importance for the excited charge separation during a photocatalysis process. As we observed, the final annealed nanowire heterostructures show improved photocatalytic activity in the degradation of water-containing phenol. The photocatalytic efficiency was improved by ~42% for the visible illumination and by ~25% for the UV illumination as compared with the Co_3O_4 nanowires. Such novel nanowire heterostructures can be interesting and promising for future solar-driven devices and catalytic applications.

PART III

SURFACE-ENHANCED RAMAN SPECTROSCOPY (SERS)

CHAPTER 10

CONTROLLED GROWTH OF SILICON NANOWIRES AND THEIR FURTHER DECORATION WITH GOLD NANOPARTICLE FOR SURFACE-ENHANCED RAMAN SENSING

Yuan Li¹, Nitin Chopra^{1,2,}*

¹Metallurgical and Materials Engineering, Center for Materials for Information Technology (MINT), The University of Alabama, Tuscaloosa, AL 35401, USA

²Department of Biological Sciences, The University of Alabama, Tuscaloosa, AL 35487, U.S.A.

*Corresponding Author

E-mail: nchopra@eng.ua.edu

Tel: [205-348-4153](tel:205-348-4153)

Abstract

In this paper, we report a facile and combined chemical vapor deposition – wet reduction – annealing approached for the fabrication of free-standing silicon nanowire-gold nanoparticle heterostructures for organic detection or sensing based on the Surface-enhanced Raman Spectroscopy (SERS). The variation of structures morphology and chemical composition during the production procedure was carefully characterized with Transmission Electron Microscopy (TEM) and X-ray Photoelectron Spectroscopy (XPS), respectively. The surface configuration and phase transformation kinetics were further calculated and analyzed in detail. Furthermore, we demonstrated the dependence of Raman enhancement on the heterostructure configurations obtained at different annealing conditions. This study provides fundament understanding on principle of gold migration and nanoparticles rearrangement on silicon nanowire during high temperature annealing. With the analyzed result, the basic chemical transformation behaviors and kinetics is well-understood. The optimization technique of heterostructures also provides reliable reference to the development of Raman-based chemical sensors.

Keywords: silicon nanowire-gold nanoparticle heterostructures, chemical vapor deposition, annealing, phase transformation kinetics, surface-enhanced Raman spectroscopy (SERS)

10.1. Introduction

Coinage metals such as gold, silver, and copper were usually used as the preferred Surface Enhanced Raman Scattering (SERS) substrate in the form of rough surface and nanoscale structures.²⁸⁷ The enhancement of Raman signal is believed to be originated from the interaction between metallic substrate and absorbed target molecules under the electromagnetic field generated by Raman laser, which is normally called Localized Surface Plasmon Resonance (LSPR).²⁸⁸ LSPR can be simply tuned by controlling the size, shape, and distribution of nanoparticles,²⁸⁹ as well as using effective supporting substrate. Directly dispersing these nanostructures on flat medium such as silicon wafer has been initially studied.²⁹⁰ However, the further developed is thought to be confined by the limited maximum particle density, uncontrollable aggregation, and nonuniform distribution of Raman signal.²⁹¹ Consequently, heterostructures by combining these Raman sensitive nanoparticles with one-dimensional nanowire as supporting medium²⁹² were further explored. Silicon nanowire supported nanoparticles, for instance, were reported as the preferred SERS heterostructures.

Silicon nanowire has been studied for several decades due to their excellent electronic/ mechanical properties, convenient surface tailorability and industrial compatibility, which make it a promising material in field-effect transistors, solar cells, and sensors.²⁹³ Among these applications, using silicon nanowires as chemical sensors are of particularly important due to their biocompatibility, vast surface-to-bulk ratio, fast response, good reversibility and oxide-coated or H-terminated surface.²⁹⁴ However, it is now widely accepted that as-produced pristine silicon nanowires only exhibit moderate sensitivity in chemical detection. As a result, appropriate surface modification is definitely needed and well developed. We can find papers that showing the decoration/functionalization of silicon nanowires with platinum nanoparticles,²⁹⁵ boron and

magnesium,²⁹⁶ alkyl and nanotrees,²⁹⁷ diamond-like carbon (DLC)²⁹⁸ and polymers.²⁹⁹ However, in the approaches for Raman-based chemical sensors, silicon nanowires were exclusively surface-decorated with silver nanoparticles³⁰⁰ or gold nanoparticles. The significant enhancement on silicon nanowire based heterostructures was attributed to (1) the enlargement of specific substrate area, which is capable to absorb more target molecule per unit area; and (2) the appropriate distribution of nanoparticles on the nanowire, which is able to generate more hot-spots for Raman detection. For instance, silver nanostructures decorated silicon nanowires have been intensively studied as ultrasensitive SERS substrate in the detection of R6G, CV, DNA, as well as amoxicillin³⁰¹. It is found that the detection limit can reach as low as 10^{-14} M³⁰². Compared with silver-based substrate, gold nanoparticles are considered to be increasingly important due to its chemical stability, low-temperature processibility (low melting point, especially for nanoparticle), and excellent bio-compatibility. Based on these super properties, gold nanoparticle based heterostructures are of particularly promising in the up-coming bio-chemical and life science. The concept of SERS based on gold nanostructure supported on silicon nanowires has been previously confirm by the well-defined Tip Enhanced Raman Scattering (TERS) technique.³⁰³ It is found that the Raman scattering signal, compared that generated on single nano-tip, will be significantly enlarged when two or more gold tips combined together. As a result, the capability for the detection of infinite low-concentration molecules will largely increase. However, the decoration of silicon nanowire with extraneous gold nanoparticles severing as SERS substrate is really coming new. For instance, Sun et al.³⁰⁴ studied the charge-selective ability of silver/gold nanoparticles supported on silicon-carbon core-shell nanowires. Chen et al.³⁰⁵ reported the Raman scattering enhancement of gold nanoparticle decorated silicon nanowire and demonstrated its Raman photodetection ability.

Not only in the Raman based sensors, silicon nanowires decorated with gold nanoparticles have also been widely developed for other advanced chemical devices such as electrochemical sensor, field emission transistor (FET), molecule beacons and cancer cell destructor.³⁰⁶ There are generally three approaches used to arch gold nanoparticles on silicon nanowires including (1) wet-reduction of chlorauric chelate, (2) physical sputtering/evaporation³⁰⁷ of gold target, and (3) galvanic deposition.³⁰⁸ The first method was preferably used since gold nanoparticles can be directly deposited on silicon nanowires without any destruction of the pristine nanowire structure. The reduction of Au^{3+} is actually an heterogeneous nucleation process, gold atoms preferredly bond to the active sites such as defects, residue gold catalyst on the nanowire, and then grow up to nanoparticles. However, due to the random distribution of these nucleation sites, the resulting gold nanoparticles, both space and size, are also randomly dispersed. Such inhomogeneous heterostructures are not beneficial to get uniform Raman enhancement and satisfactory detection limit. Therefore, according to the facile dewetting properties of gold nanoparticle, a further high-temperature annealing approach³⁸ was proposed to optimize the space configuration of the heterostructures. The migration behaviors of gold as CVD catalyst have been studied by several groups.³⁰⁹ However, the high-temperature behaviors of gold nanoparticles on silicon nanowire during the annealing are rarely studied and still unclear.

In present paper, we propose a CVD-wet reduction-annealing procedure to produce well-configured silicon nanowire-gold nanoparticle heterostructures using in Raman scattering molecule detection. The variation of structures morphology and chemical composition during the production procedure was carefully characterized with Transmission Electron Microscopy (TEM) and X-ray Photoelectron Spectroscopy (XPS), respectively. Based on these raw experimental data, the surface configuration and phase transformation kinetics was calculated and analyzed in detail.

Furthermore, we demonstrated the dependence of Raman enhancement on the heterostructure configurations obtained at different annealing conditions. This study provides fundamental understanding on principle of gold migration and nanoparticles rearrangement on silicon nanowire during high temperature annealing. With the analyzed result, the basic chemical transformation behaviors and kinetics was clearly presented. The optimization technique of heterostructures also provides reliable reference to the development of Raman-based chemical sensors.

10.2. Experimental details

Materials and Methods: Silicon (Si) wafers (<100>, n-type) were purchased from IWS (Colfax, CA). Gold (III) chloride trihydrate ($\text{HAuCl}_4 \cdot 3\text{H}_2\text{O}$, 99.9%) was purchased from Sigma-Aldrich (St. Louis, MO). Sodium borohydride (NaBH_4 , powder, 98%) was purchased from Acros Organics (New Jersey, NJ). Acetone ($(\text{CH}_3)_2\text{CO}$) was purchased from VWR International (West Chester, PA). DI water (18.1 $\text{M}\Omega\text{-cm}$) was obtained using a Barnstead International DI water system (E-pure D4641). All chemicals were used without further purification. Gold sputtering was carried out on a Bio-Rad gold sputtering and coating system, Polaron division (Agawan, MN). Dispersion of heterostructures into ethyl alcohol was done in a Branson 2510 Sonicator (Danbury, CT). Labnet centrifuge (Edison, NJ) was used to clean, wash, and separate nanoparticles. Wet samples were dried in a VWR vacuum oven (West Chester, PA). Growth and annealing of the Silicon nanowires were accomplished inside a GSL-1100X Tube Furnace (MTI Corporation) with a quartz tube from ChemGlass (Vineland, NJ). Gas flow rates of all chemical vapor deposition and annealing processes were controlled by Teledyne Hasting powerpod 400 mass flow controllers (Hampton, VA). H_2 (UHP grade, 40% balanced with Ar), N_2 , O_2 , SiH_4 and Ar (all UHP grade) gas cylinders

were purchased from Airgas South (Tuscaloosa, AL). Low-pressure atmosphere inside the quartz tube was generated by the Gast (DOA-P74-AA) Vacuum Pump bought from GAST manufacturing inc. (Benton Harbor, MI). Oxygen plasma treatment was performed in a Nordson March Jupiter III Reactive Ion Etcher (Concord, CA). Syringe injector was obtained from Fisher Scientific (Suwanee, GA).

Silicon nanowires growth: (111) silicon wafer was used as the substrate. Two strategies were applied to deposit gold catalyst on the substrate. In both strategies, the silicon wafers were first sonicated in acetone for 10 min. (1) The wafer was treated with 3:1 H₂SO₄: H₂O₂ piranha solution for 30 min at 100 °C, then sputtered with gold in a Bio-Rad gold sputtering and coating systems, Polaron division (Agawan, MN). (2) The silicon wafer was placed in BOE solution for 1 min to etch away the surface oxide layer. Galvanic deposition was then carried out at room temperature to prepare the gold catalyst film. The deposition solution is 1 mM KAuCl₄ + 1% HF. The newly prepared catalyst substrate was placed in the center of a GSL-1100X (MTI Corporation) tube furnace. The nanowire growth was executed through a typical CVD process. The furnace was first heated to 850 °C in the protection of 5% H₂ in Ar. The temperature was maintained for 10 minutes to convert the catalyst film to gold nanoparticles (Au nanoparticle). Then the temperature was decreased to the growth temperature. 2% SiH₄ in He was pumped into the quartz tube as the silicon source, which was carried by 10% H₂ in Ar. When the growth process was finished, the furnace was cooled ambiently in the protection of pure Ar.

Preparation of silicon nanowire-gold heterostructures: Pristine silicon nanowires were treated with BOE solution for 5 s and then placed in a galvanic deposition solution (1 mM KAuCl₄ + 1% HF) for different times to prepare silicon-gold core-shell nanostructures. Then the sample was annealed in the quartz furnace or oven box (as specified) for 10 min at different temperatures. This

process made silicon nanowire-gold nanoparticle heterostructures, which can be used as the surface enhanced Raman scattering (SERS) substrate for dye detection.

Raman detection of Rhodamine 6G: Both pristine silicon nanowires and silicon nanowire-gold nanoparticle heterostructures were used as the SERS substrate for R6G detection. The nanostructures were first treated in BOE solution for 10 s to create surface Si-H bonds, which can largely increase the efficiency of R6G absorption on the SERS substrate. After being dried in flowing N₂, the sample was kept in 10⁻⁶ M R6G solution for 10 h with slight agitation. Then the dyed nanostructures were washed with DI-water and dried in flowing N₂. Raman measurement was carried out on the Bruker Senterra Raman System (Bruker Optics Inc. Woodlands, TX), where a Ne laser source with 785 nm wavelength was used. The applied laser power was 1 mW; the integration time was 10 s.

Characterizations: Scanning Electron Microscopy (SEM) images were obtained using a FE-SEM JEOL-7000 equipped with energy dispersed X-ray spectroscopy (EDX). Tecnai F-20 was used to collect Transmission Electron Microscopy (TEM) images at 200 kV. TEM samples were prepared by dispersing as-prepared samples on lacey carbon TEM copper grids purchased from Ted Pella Inc. (Redding, CA). (XRD, UV-Vis, DSC). The average nanoparticle size was measured from TEM and SEM images, where more than 200 nanoparticles were counted and measured per sample. Diameter was measured for spherical nanoparticles and distances less than 20nm between two Au nanoparticles were taken into account for particle interval measurements. All the measurements were done using Nano-measurer 1.2 Software. High resolution TEM image for graphene encapsulated Au nanoparticles were also converted into FFT image using Digital Micrograph software. X-ray photoelectron spectra (XPS) were gathered by Kratos Axis 165 with mono-Aluminum gun at 160 eV pass energy for full range scan and 40 eV pass energy for detailed

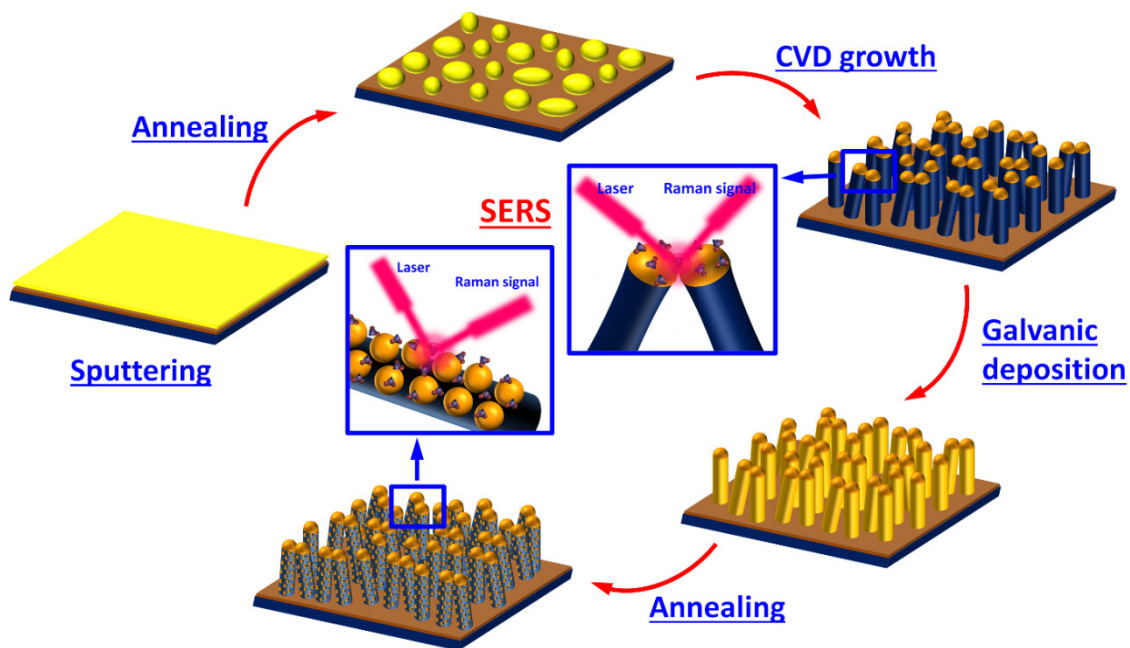
scan. The analysis spot was set as “Slot” with $>20\ \mu\text{m}$ aperture and 19.05 mm iris setting. Raman spectra and SERS of samples were collected using Bruker Senterra system (Bruker Optics Inc. Woodlands, TX) equipped with 785 nm laser source at 10-25 mW laser powers and 100X objective. The integral time and co-additions were set as 15 seconds and 2, respectively. The Raman mapping conditions for map acquisition were set at the spectral resolution of $3 - 5\ \text{cm}^{-1}$ in the range of $77 - 2658\ \text{cm}^{-1}$ with 10 mW laser power. Samples for SERS were prepared by dispersing Rhodium 6G (R6G) dye over SNW samples at various stages: as-produced, as-nucleated, annealed in different conditions, branched SNWs and graphene encapsulated Au nanoparticle on SNW (all these SNW were dispersed on a silica substrate before wetting them with dye). Around 5-6 nanowires were randomly chosen and 5-6 points were taken on each nanowire to get SERS signal enhancement data (approximately 30 data points per sample).

10.3. Results and discussion

10.3.1 Silane-based CVD growth of Si nanowires

Scheme 10.1 illustrated the process for the fabrication of Si nanowire – Au nanoparticle heterostructures for SERS-based chemical sensing. Si nanowires were grown through an atmospheric-pressure chemical vapor deposition (CVD) process, the growth mechanism can be described by the well-defined vapor-liquid-solid (VLS) principle. As shown in Scheme 1, gold film sputtering was first conducted on the silicon substrate. This was followed by a high-temperature annealing process, which lead to the dewetting of gold film to result in island-like Au nanoparticles. These Au nanoparticles have been proved served as the catalysts during the initial stage of the silicon nanowire growth process. Due to the high solubility of silicon in gold, when

SiH_4 was decomposed at the growth temperature, silicon atom diffused into liquid gold droplet and alloyed. As the silicon in gold reached the saturated state, solid silicon precipitated at the interface of gold droplet and substrate while the gold catalyst was lifted up and stayed on the top of the Si nanowires. In this study, various growth conditions including SiH_4 flow rate, growth duration, temperature, and sputtering time were evaluated for their influence on the growth of Si nanowires, which leads to further understanding on the basic principle of the VLS growth process. The detailed experiment parameters were listed in Table 10.1.



Scheme 10.1. Schematic showing the growth of silicon nanowires and synthesis of silicon nanowire-gold heterostructures for SERS detection

Table 10.1. Experimental parameters showing the optimization and control of Silicon nanowire growth on gold-sputtering substrates

Sample #	SiH ₄ flow rate (sccm)	Time (min)	Temperature(°C)	Sputtering time (s)
1A	10	1	625	60
2A	20	1	625	60
3A	30	1	625	60
2A	20	1	625	60
4A	20	2	625	60
5A	20	5	625	60
6A	20	10	625	60
4A	20	2	625	60
7A	20	2	675	60
8A	20	2	725	60
9A	20	2	625	15
10A	20	2	625	30
11A	20	2	625	45
4A	20	2	625	60

Figure 10.1 shows the SEM images of the silicon substrate decorated with as-sputtered gold film or the dewetted Au nanoparticles after annealing. One can observe the sputtering process led to uniform dispersion of Au film on the substrate, where various cracks were also observed between different crystalline grains. These self-separated crystalline grains have been found to take an important role during the following high-temperature annealing process. The resulted Au nanoparticles or islands were also uniformly dispersed with an inter-particle spacing of $\sim 92.3 \pm 30.5$ nm. The estimated average size for these nanoparticles are $\sim 112.5 \pm 20.6$ nm and meanwhile their spatial density are $\sim 9.5 \times 10^8$ per cm^2 .

In the following, various growth parameters were used for the growth of Si nanowires. Silane flow rates of 10 sccm, 20 sccm and 30 sccm were first demonstrated. As shown in Figure 10.2A, when the flow rate is small, the decomposed silicon atoms diffused into these gold droplet and alloyed with them at high temperature. However, there is not enough silicon atoms for the saturation of gold-silicon alloy droplet. As a result, no nanowire was formed at this case but only led to an increase of the average size of the pristine Au nanoparticle (to $\sim 230 \pm 50$ nm).

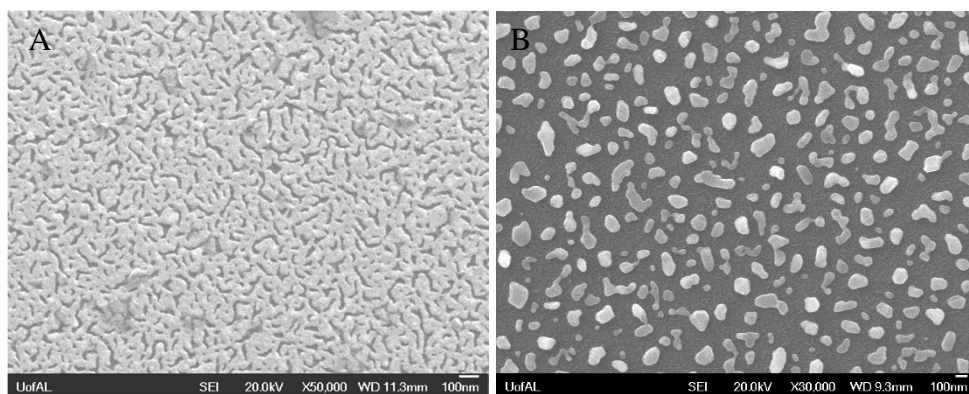


Figure 10.1. SEM showing the as-sputtered gold film (A) and dewetted gold nanoparticle catalysts after annealing (B).

With a Silane flow rate of 20 sccm, the growth of Si nanowires was observed (Figure 10.2B and C). The inset in Figure 10.2B further shows a high-resolution SEM image of a single nanowire. Au nanoparticle tips with a slightly larger diameter than the diameter of Si nanowires was constantly observed due to the above mentioned VLS mechanism. The cross-section SEM image of the Si nanowires on the silicon substrate indicates that these as-grown nanowires present the well-defined “zig-zag” morphology. We approximately estimated that the average length of the Si nanowires is $\sim 1.6 - 2.4 \mu\text{m}$, suggesting a nanowire growth speed of $\sim 27 - 40 \text{ nm/s}$. The nanowires obtained with a Silane flow rate of 30 sccm show increased overall length due to the fastened silicon precipitate speed. The morphology of the nanowires became relatively straight at this case while the zig-zag structure was still observed on some nanowires.

In addition, it is worthy to mention that small Si nanowire branches were constantly observed on these main nanowires. The branch observed on the nanowires obtained at 20 sccm was blend and with high spatial density (Figure 10.2B). However, with increased flow rate (30 sccm), these branches became straight and less (Figure 10.2D). The VLS growth of Si nanowires were further schematically illustrated in Figure 10.2F. The decomposition of SiH_4 at high temperature resulted in silicon atoms vapor, which further diffused into the gold droplets and alloyed with gold. The interface of gold droplet and silicon substrate presented the lowest surface energy due to the mismatch of atom distributions at the two sides interface, as a result, silicon is preferred to precipitate at this interface and leads to the growth of silicon nanowires. The formation of surface branches is due to the non-uniform diffusion of gold droplet during the growth. The main droplet was lifted up by the precipitation of Si nanowire while a lot of small droplets were remained on the nanowire surface. These small gold droplet acted as the new catalyst center for the growth of nanowire branches according to the aforementioned VLS mechanism. The evolution of “zig-zag”

morphology has been attributed to the atmosphere growth environment. On one hand, at high temperature, the growth of nanoscale nanowires can be influenced by even a very weak gas flow as compared with that in the high-vacuum environment proposed by other authors. On the other hand, different from the growth using SiCl_4 as the silicon source, the growth with SiH_4 led to inevitable partial surface oxidation at atmosphere environment. These oxide sites have a negative influence on the surface diffusion of gold and silicon and thus led to the change of growth direction.

Figure 10.2G-I show the TEM images of Si nanowires at various resolution. The main nanowire and the branches all show the “zig-zag” and branched structure. Gold tips were always observed on the branches, further indicating the growth of these branches also followed the VLS mechanism. High resolution image in Figure 10.2I indicates that the main nanowire and branches present the same crystal structure as a lattice spacing of ~ 0.31 nm for the (111) plane of silicon was observed for both. The lattice structure was further confirmed by the FFT images (Figure 10.2 J) developed from the high resolution image (Figure 10.2 I).

The influence of growth time on the structure and morphology of Si nanowires were demonstrated in Figure 10.3. Branched and “zig-zag” nanowires was also obtained when the growth was conducted for 2 min. However, as the growth continued for 5 min or 10 min, the nanowire become straight and branchless (see the insets in Figure 10.3C and D). This observation was further illustrated in Figure 10.3F. The disappearance of the Si branches was mainly due to the well-defined Ostwald’s ripening effect, which indicated that the branches were slowly fused with the main nanowires at high temperature with the increase of growth duration. TEM images of the Si nanowire grown for 5 min were shown in Figure 10.3G-K. The nanowires straight and uniform in Morphology, with a thin SiO_2 shell encapsulated on the surface of gold tops (Figure 10.3H). The

lattice evaluation by the high resolution image in Figure 10.3I indicate the gold (111) plane for the tips and the silicon (111) plane for the main nanowire.

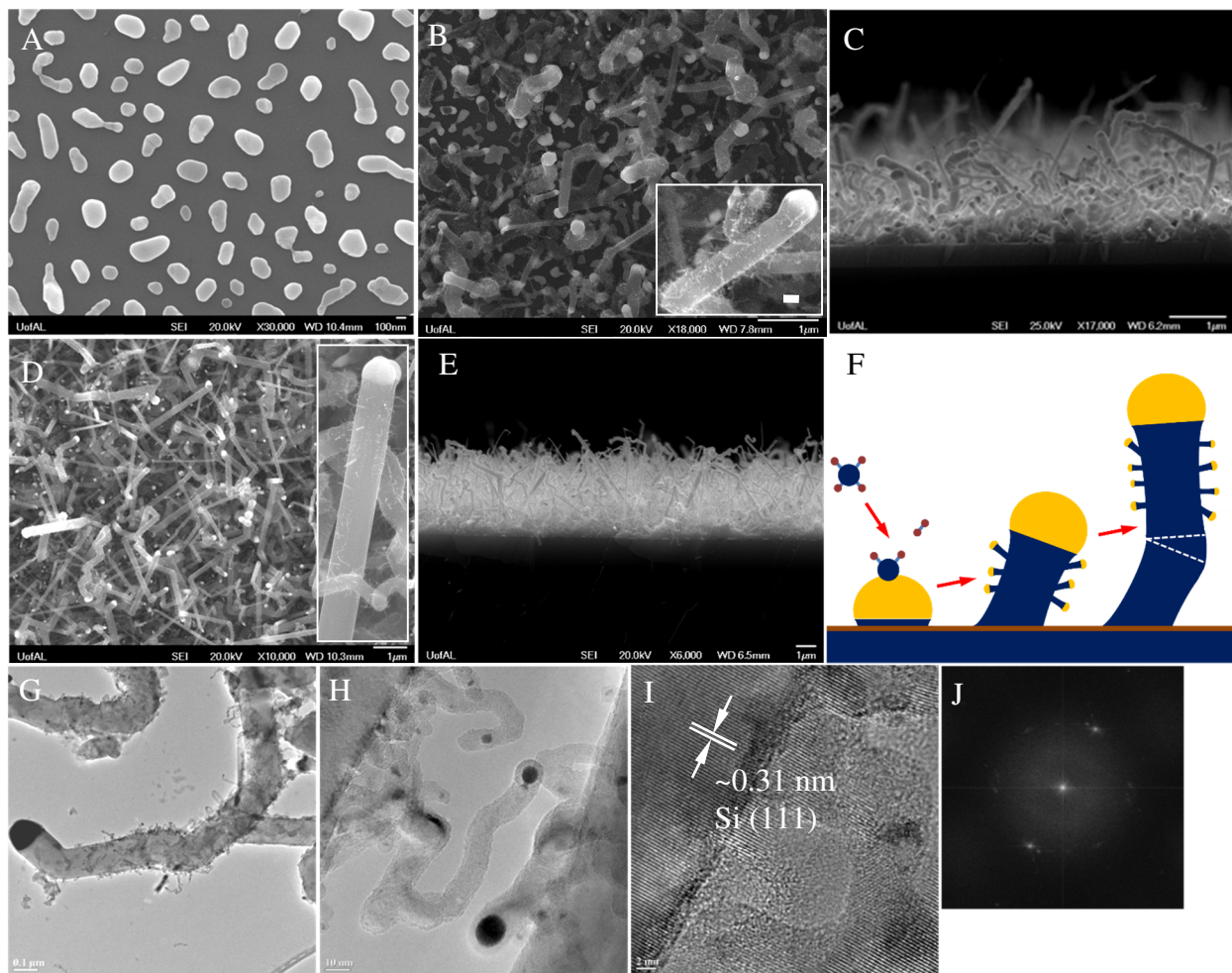


Figure 10.2. Silicon nanowire arrays grown on the gold-sputtered substrate by controlling different feeding rate of SiH_4 : (A) 10 sccm (Sample#1A); (B-C) 20 sccm (Sample#2A); (D-E) 30 sccm (Sample#3A). (F) Schematic showing the growth process of SNWA on gold-sputtering substrate. (G-J) TEM demonstration of as-grown SNWA corresponding to (D-E). (Baseline conditions: growth temperature 625 °C; carrier gas: 100 sccm 5% H_2/Ar ; growth duration: 1 min; gold sputtering 60 s.)

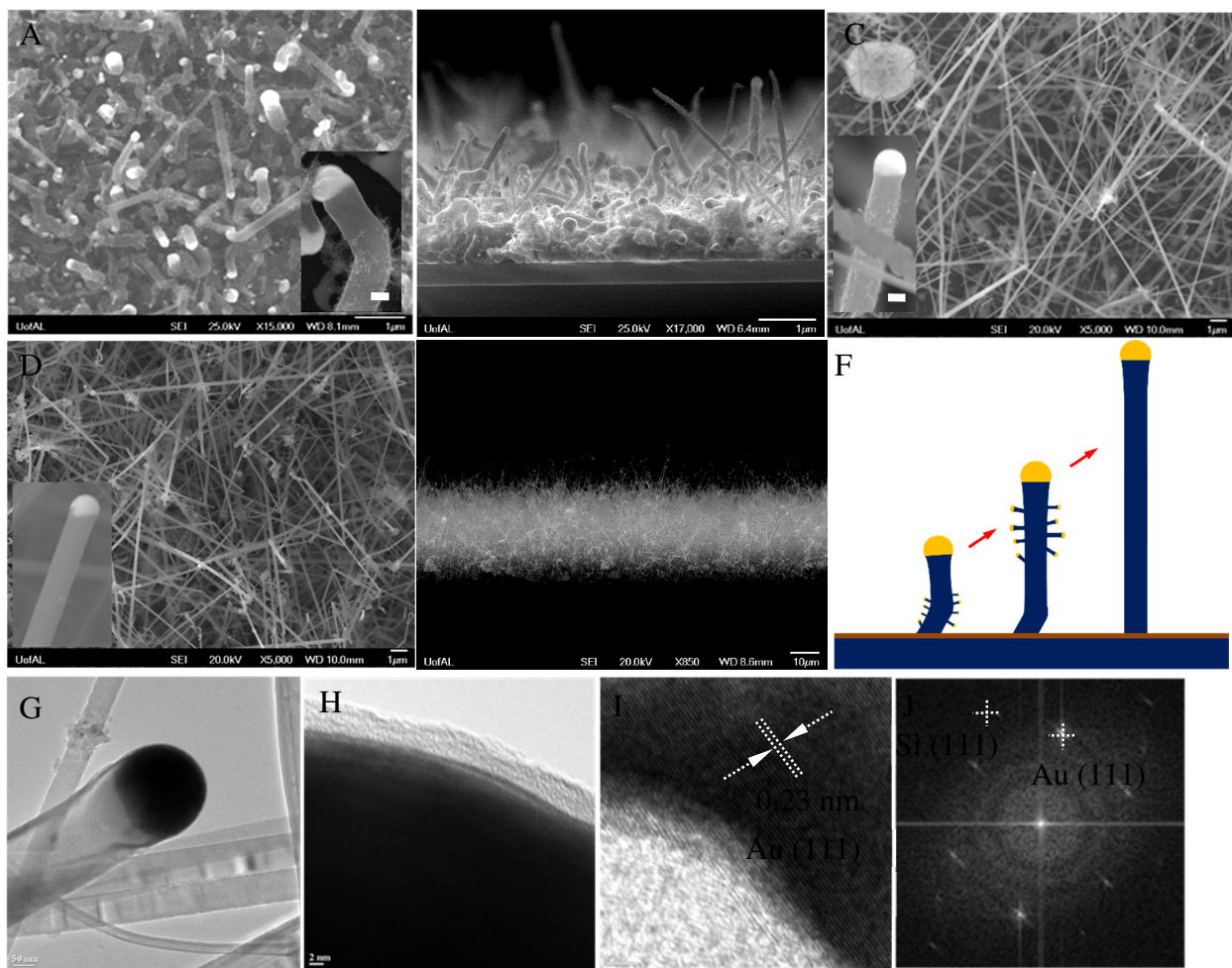


Figure 10.3. Silicon nanowires with high aspect ratio grown on the gold-sputtered substrate by controlling different grow time: (A-B) 2 min (Sample#4A); (C) 5 min (Sample#5A); (D-E) 10 min (Sample#6A); (F) Schematic showing the growth of long-aspect ratio Si NWs from nanowire arrays; (G-J) TEM demonstration of as-grown SNWA corresponding to (D). (Baseline conditions: growth temperature 625 °C; carrier gas: 100 sccm 5% H₂/Ar; flow rate: 20 sccm; sputtering time: 60 s.)

Figure 10.4 demonstrates the influence of temperature on the growth of Si nanowires. The growth at relatively lower temperature (Figure 10.4A and B) led to aforementioned “zig-zag” and branched nanowires. However, as the temperature was increased, straight nanowires with relative straight branches were obtained. The influence of temperature on the morphology of nanowires is mainly due their influence on the diffusion rate of silicon atoms in gold droplets. Higher temperature led to increased growth speed of Si nanowire, and as a result, the nanowire became straight and longer, as illustrated in Figure 10.4E.

As we described above, the growth of Si nanowires is based on the alloying and saturation of gold droplets. Thus, the deposition and subsequent annealing process are of importance for the nanowire growth. This was further demonstrated in Figure 10.5. Sputtering of 15 s led to less deposition of gold film on the substrate, resulting small gold nanoparticles. At high temperature, these small gold droplets presented high surface energy and, rather than kept a completed gold tip, preferred to distribute at the defect site on the nanowires. This led to the pronounced growth of side branches. Thus on obvious large gold tips were observed on the main nanowires (Figure 10.5A). This principle was further confirmed by the growth of Si nanowires on gold droplets formed by long-time sputtering (30 s and 45 s). In these cases, less branches was observed and the gold tips became large and round (Figure 10.5B and C). The insets in Figure 10.5A-C further demonstrated the high-resolution images of the Si nanowires obtained at various gold sputtering conditions. Such parameter study on the growth of Si nanowires provides important knowledge for the VLS-based CVD process at atmosphere environment. As compared with the frequently used high vacuum process for Si nanowire growth, this atmosphere process is much more feasible, cost effective and easier to be combined with current CMOS technologies.

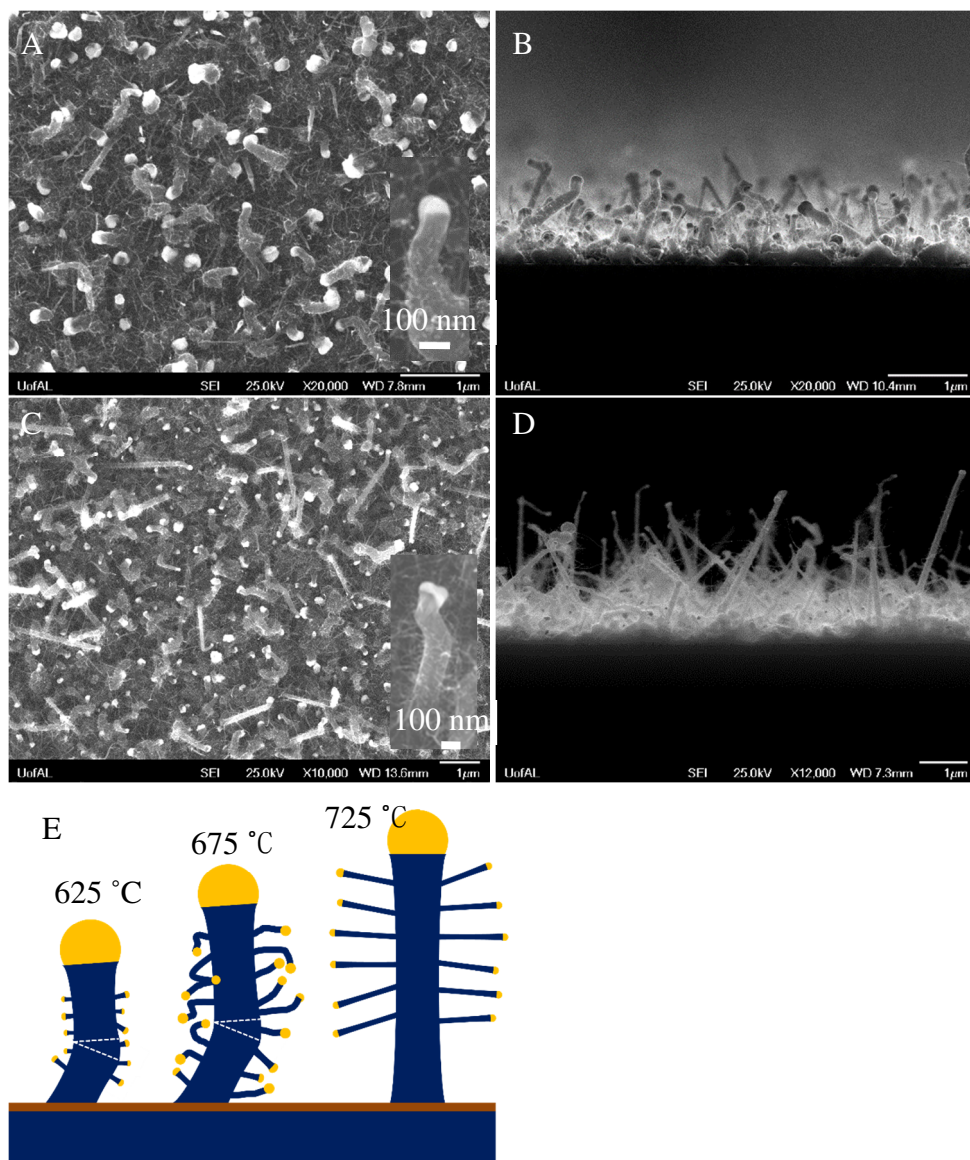


Figure 10.4. Branched silicon nanowires obtained at different growth temperature: (A-B) 675°C (Sample#7A); (C-D) 725 °C (Sample#8A); (E) Schematic showing the influence of growth temperature on the structure of silicon nanowires. (Baseline conditions: carrier gas: 100 sccm 5% H₂/Ar; flow rate: 20 sccm; grow time: 2 min; grow time 60 s.)

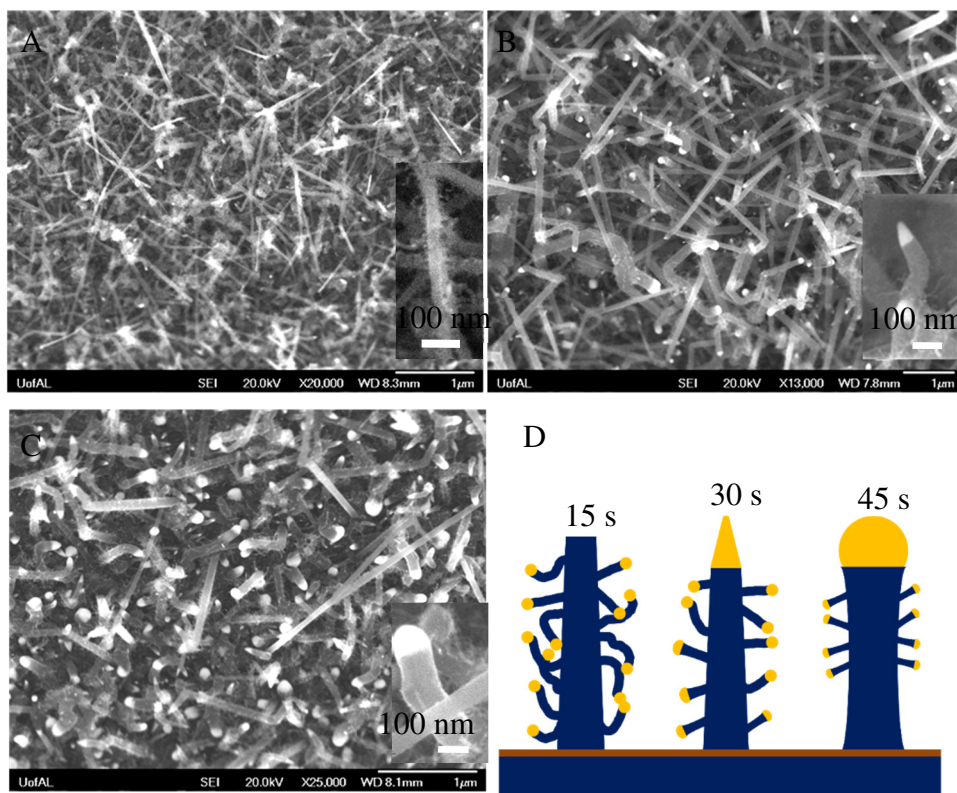


Figure 10.5. Influence of gold sputtering time on the configuration of silicon nanowires and their ability in Raman enhancement: (A) 15 s (Sample#9A); (B) 30 s (Sample#10A); (C) 45 s (Sample#11A); (D) Schematic showing the influence of growth temperature on the structure of silicon nanowires. (Baseline conditions: growth temperature 625 °C; carrier gas: 100 sccm 5% H₂/Ar; flow rate: 20 sccm; grow time: 2 min.)

The Influence of various growth conditions on the average diameter of the main nanowire and the gold tips were further summarized in Figure 10.6. In general we can observed that the average diameter of the gold tips is larger than that of main nanowires. This is due to the low melting point of Au nanoparticles. At high temperature, the Au tips were melted and have to keep a spherical surface on the top of the solid nanowires. It is also worthy to mention that the consistent various trend in the diameter of gold tips and main nanowires as a function of growth condition was observed, indicating the gold tips have obvious guide effect on the growth of Si nanowires. Specifically, the diameter of gold tips and main nanowires were decreased with the increase of

SiH₄ flow rate, which is due to the fast growth rate with large amount of silicon source. The diameters were first decreased with increase of growth time and then increased when the growth was prolonged. This can be well-explained by the appear and disappear of branches (Figure 10.3).

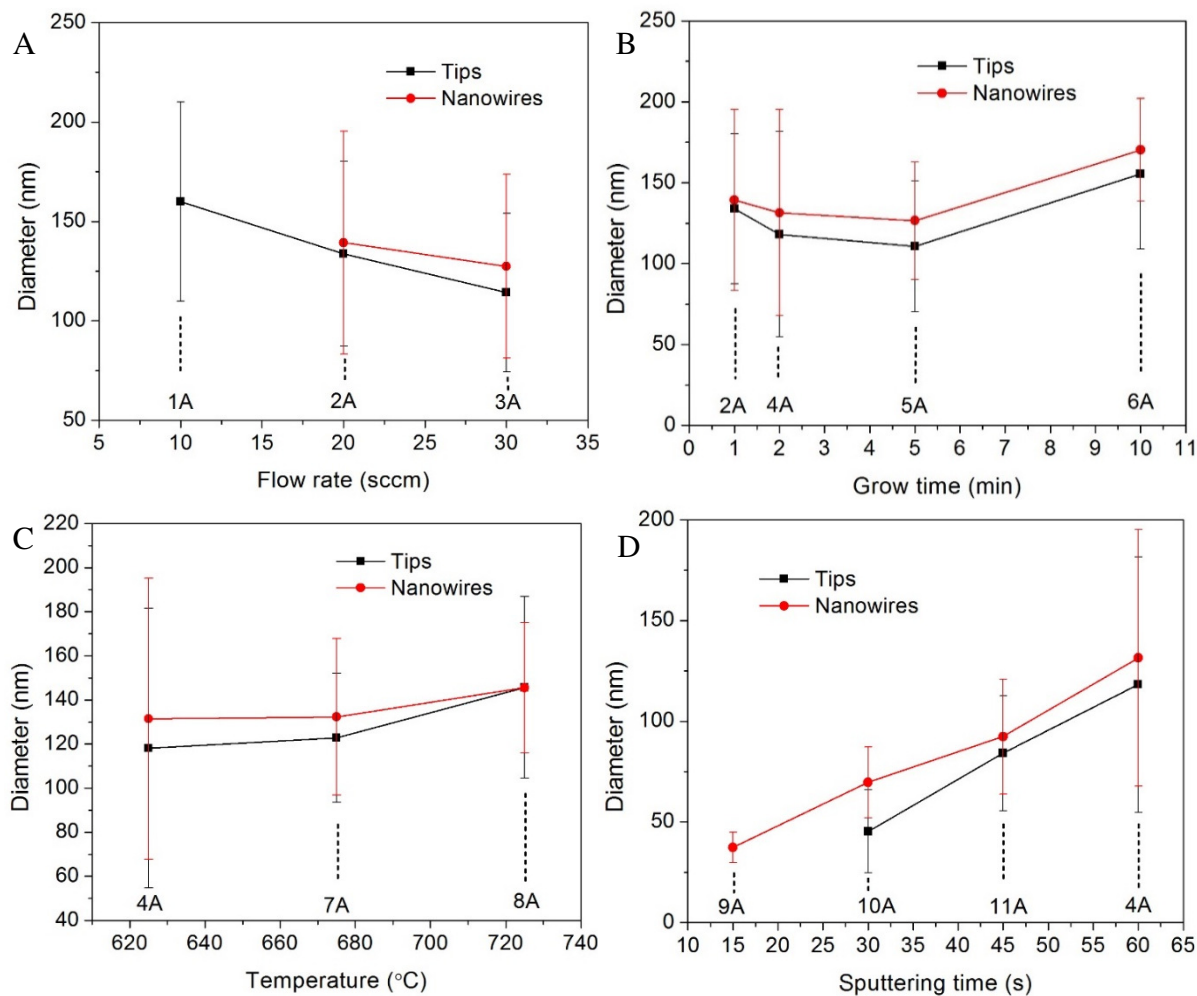


Figure 10.6. Influence of growth conditions on the diameter of silicon nanowires: (A) flow rate set, (B) grow time set, (C) sputtering time set, (D) temperature set.

10.3.2. Surface decoration of Si nanowires

Further surface decoration of Si nanowires with extraneous Au nanoparticles was conducted via a galvanic deposition – annealing process, as illustrated in Scheme 10.1. Three Si nanowire samples obtained in the parameter studies was selected (see Figure 10.7). The basic mechanism for the galvanic deposition of gold film (shell) on the Si nanowires was illustrated in Figure 10.7D. The deposition is due to the replacement reaction between silicon and Au^{3+} in HF solution.

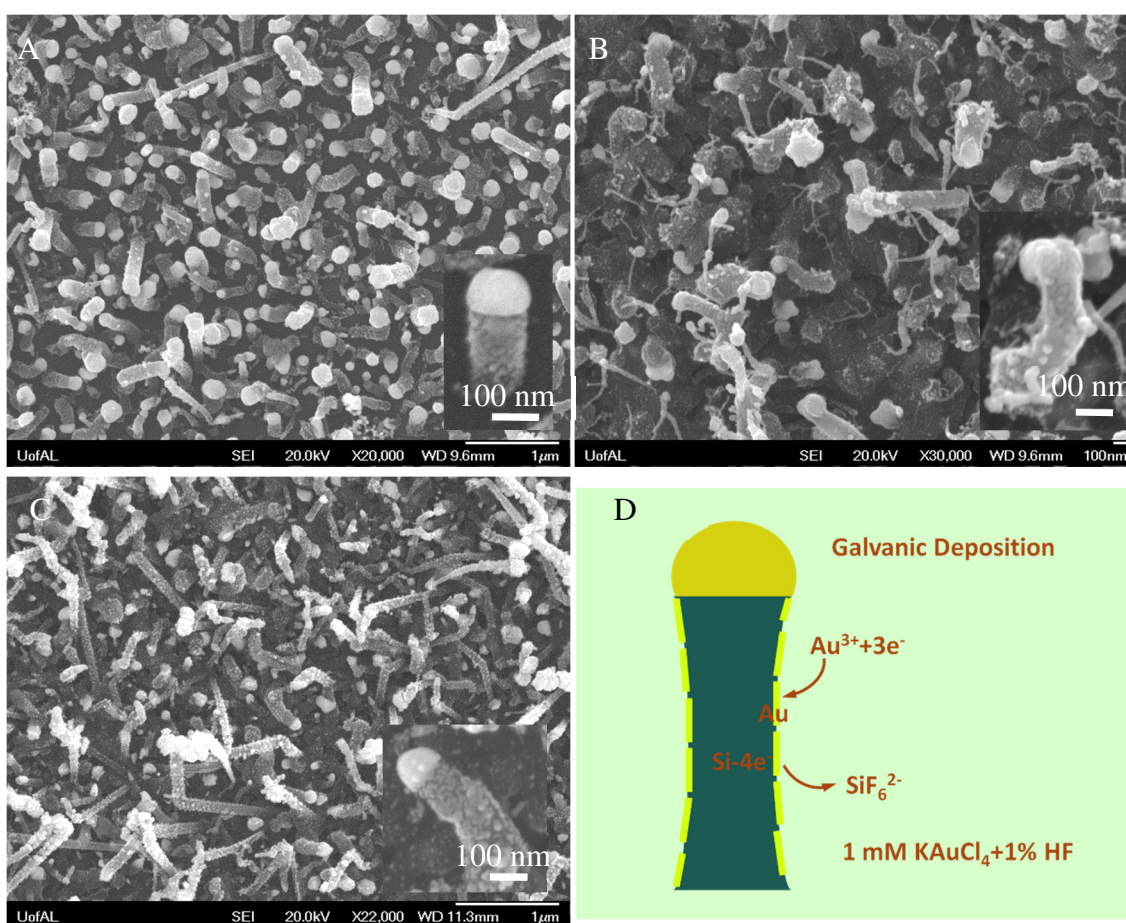


Figure 10.7. Galvanic deposition of gold film on preferred silicon nanowires selected from each set: (A) Sample#4A, (B) Sample#8A, (C) Sample#11A. (D) Schematic showing the galvanic deposition of gold shell on silicon nanowires.

The following annealing process and the resulting Si nanowire-Au nanoparticle heterostructures were demonstrated in Figure 10.8. As we observed, these deposited gold film was dewetted into Au nanoparticles that uniformly dispersed on the surface of Si nanowire. The influence of annealing environment including air and Ar was evaluated. As we observed, air-annealing led to slight surface oxidation of both main nanowire and gold nanoparticles after dewetting. Thus diffusion between gold and silicon was weakened and Au nanoparticles on the nanowire surface presented spherical morphology. However, when annealed in Ar, obvious inter-diffusion between gold and silicon was observed, rendering the Au nanoparticles gold/silicon core-shell structure.

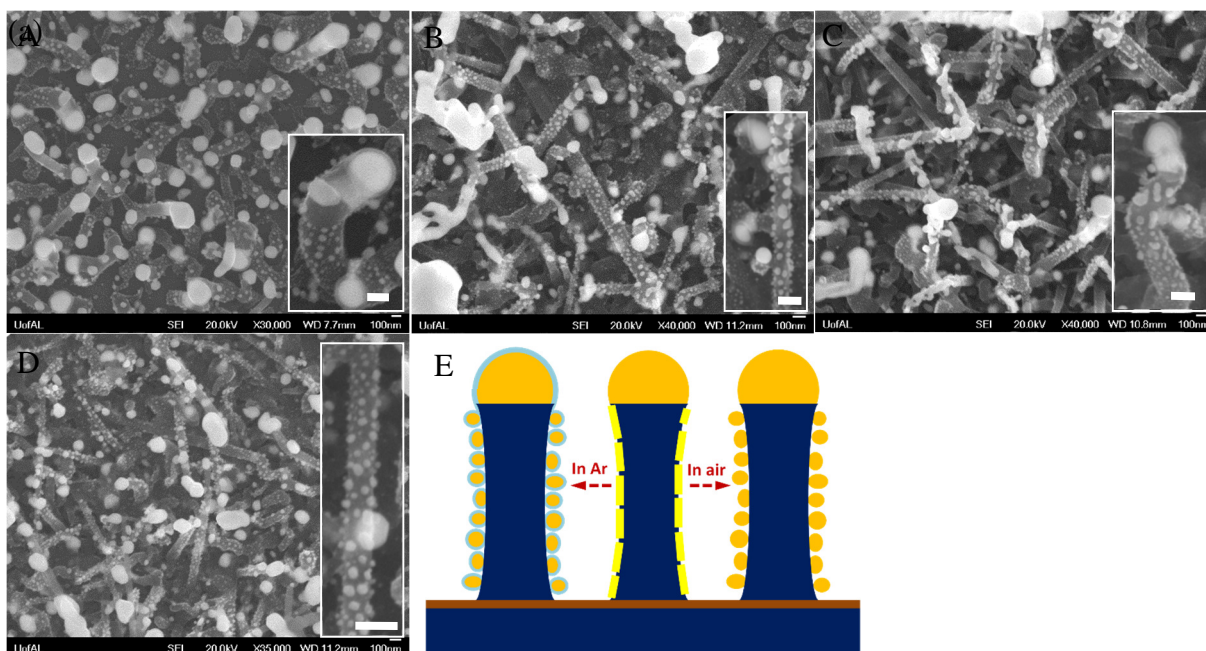


Figure 10.8. Si NWs-Au NPs heterostructures obtained by annealing above Si-Au core-shell nanowires (Sample#11A) at different temperatures: (A) 700 °C (Sample#11a), (B-D) 625 °C (Sample#11b); (C) 500 °C (Sample#11c), and at different environments: (A-C) in Ar, (D) in air (Sample#11d). (E) Schematic showing the influence of annealing on the structure of heterostructures.

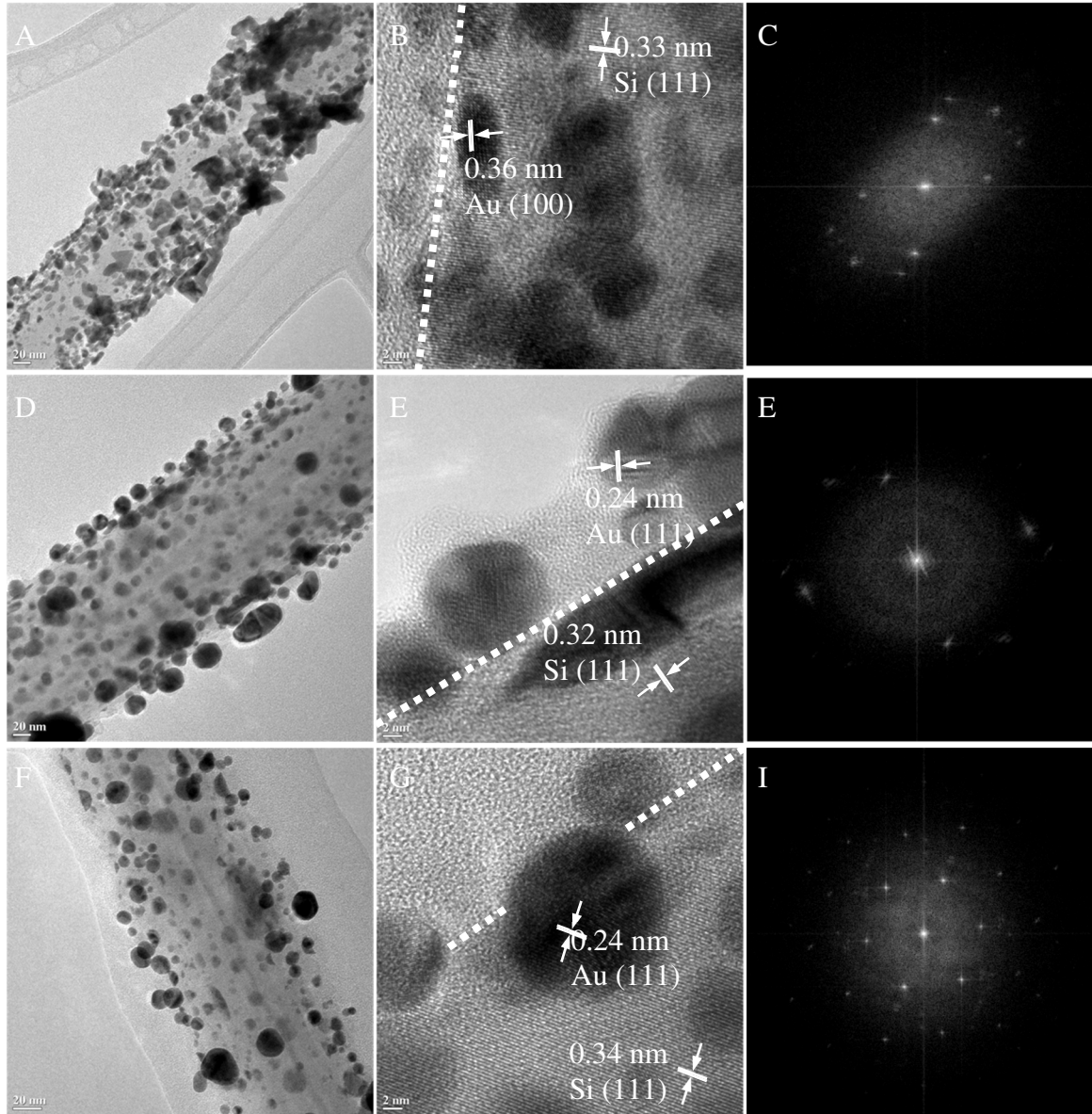


Figure 10.9. TEM images of Si NW-Au heterostructures after (A-C) galvanic deposition (sample#11B) and further annealing in (D-F) Ar and (G-I) air environment, respectively.

TEM images and analysis of the Si nanowire-Au nanoparticle heterostructures before and after annealing in air or Ar were presented in Figure 10.9. We observed that the as-deposited gold present a flake structure in high resolution images. These gold flakes were randomly dispersed on the surface of the main nanowires. However, after the annealing process both in air and Ar,

effective dewetting process happened and uniformly dispersed spherical nanoparticles were observed on the surface of Si nanowires. The estimated nanoparticle size is 25.4 ± 5.9 nm for the air-annealed heterostructures and 22.1 ± 4.6 nm for the Ar-annealed heterostructures. The slightly smaller size of the later is due to the inter-diffusion of gold into silicon nanowire during the annealing process. Lattice evaluation indicate that the as-produced Au flakes presented random distributed crystal structures. However, after annealing the standard low energy (111) plane was constantly observed for the Au nanoparticles. In addition, no obvious lattice variation was observed for the silicon nanowire before and after annealing, indicating the main nanowires are chemically and structurally stable enough to stand for these multi-step fabrication process. FFT images in Figure 10.9C, E and I further confirm the lattice distribution.

10.3.3. Surface-enhanced Raman Spectroscopy

In this study, we evaluated the Raman based organic sensing for the detection of trace amount of dyes contained in DI-water. Rhodamine 6G (R6G) was used as a Raman probe. The as-produced nanowires obtained at various growth conditions showing in Table 10.1 as well as the Si nanowire-Au nanoparticle heterostructures before and after air- or Ar-annealing was evaluated. For reference, the initial blank oxidized Si substrate, Si substrate with gold film and the substrate with dewetted Au nanoparticles were also tested. The samples were immersed in 10^{-6} M R6G solution overnight to allow the absorption of R6G molecules on the nanostructures. The Raman signals of R6G were collected directly on these R6G-absorbed substrate. Figure 10.10A shows the schematic for Raman test conducted on the Au nanoparticles decorated Si substrate. The obtained Raman spectra were further shown in Figure 10.10B. No signal was observed on the blank Si substrate or

Au film decorated substrate even they were undergone the same dye absorption process. Significantly enhanced Raman signals were observed dewetted Au nanoparticle substrate. This has been attributed to the localized surface plasmon resonance (LSPR) generated on the surface of spherical Au nanoparticles.

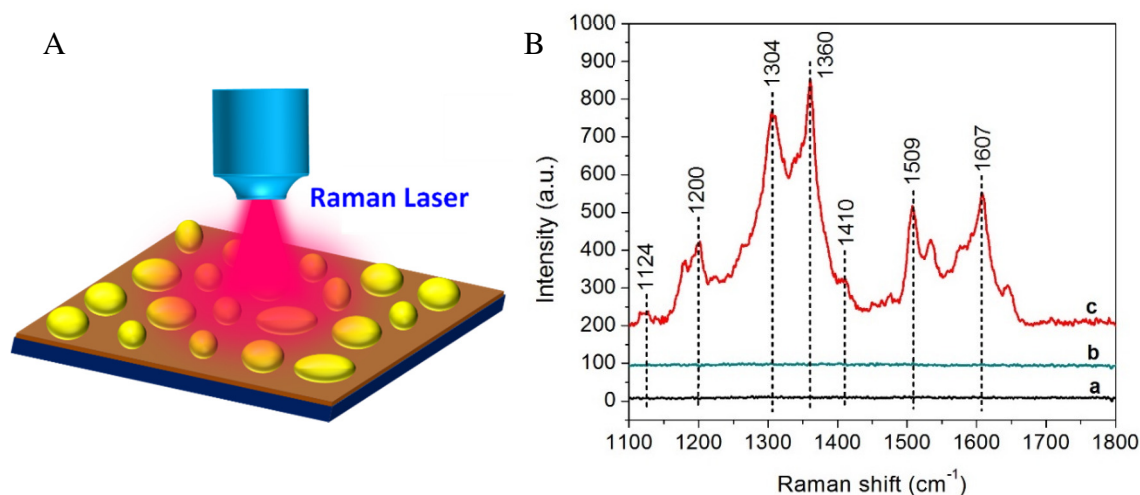


Figure 10.10. (A) Schematic showing the Surface Enhanced Raman Scattering (SERS) effect on pristine gold catalyst obtained by annealing of sputtered gold film. (B) Raman spectra of R6G obtained on: (a) oxidized silicon wafer, (b) sputtered gold film, and (c) gold island catalyst obtained by annealing of the gold film.

Figure 10.11 further demonstrated the Raman sensing conducted on the as-produced Si nanowires. The Raman enhancement is mainly due to the Au nanoparticles distributed on the tips of Si nanowires. Especially, when two or more Si nanowires put their head together, significant Raman enhancement will be observed due to the overlapping of LSPR from both nanoparticles. This has been described as TERS and is schematically illustrated in Figure 10.11A. Figure 10.11B-E further show the Raman spectra of R6G obtained on various as-produced Si nanowire substrate. The

alloyed Si-Au particles dispersed on the silicon substrate show weak Raman signals. This is probably due to their large inter-particle spacing. However, the signals collected from the “zig-zag” nanowires were significantly increased. The variation of Raman signal for nanowires obtained at different growth time were shown in Figure 10.11C. The samples obtained with 2 min of growth show the highest R6G signal due to high spatial density of gold nanoparticle tips. Further increase the growth temperature has no positive effect on the intensity of Raman signals. As shown in Figure 10.11C, the sample #7A and #8A presented depressed spectra. Variation of preliminary sputtering time has a significant influence on the morphology of Si nanowires, leading to a dominant influence on the Raman intensity. As shown in Figure 10.11E, Si nanowires with no tips or small tips shows weak signal for R6G. The highest Raman enhancement was observed on sample #11A due to the high spatial density of gold tips on these Si nanowires.

Such TERS-based chemical sensing is interesting but still didn't provide desirable Raman enhancement due to the less amount of Au nanoparticles. Thus it is important to study the SERS based sensing on the Si nanowire-Au nanoparticle heterostructures. The schematic for the sensing was shown in Figure 10.12A. The closely-packed Au nanoparticles on the body of Si nanowires presented multiple LSPR overlapping and thus the laser-induced electric field near the particle surface was significantly strengthened. This will to lead to orders of enhancement on the Raman signals. The Raman test was first conducted on the as-deposited Si-Au core-shell nanowires (Figure 10.12B). The obtained Raman signals were depressed due to the random lattice structure and shell shape of the as-deposited gold. However, the Raman intensity was significantly enhanced after the annealing process. As shown in Figure 10.12C, The Raman intensity of R6G obtained on the Si nanowire-Au nanoparticle heterostructures was enhanced by ~10 times.

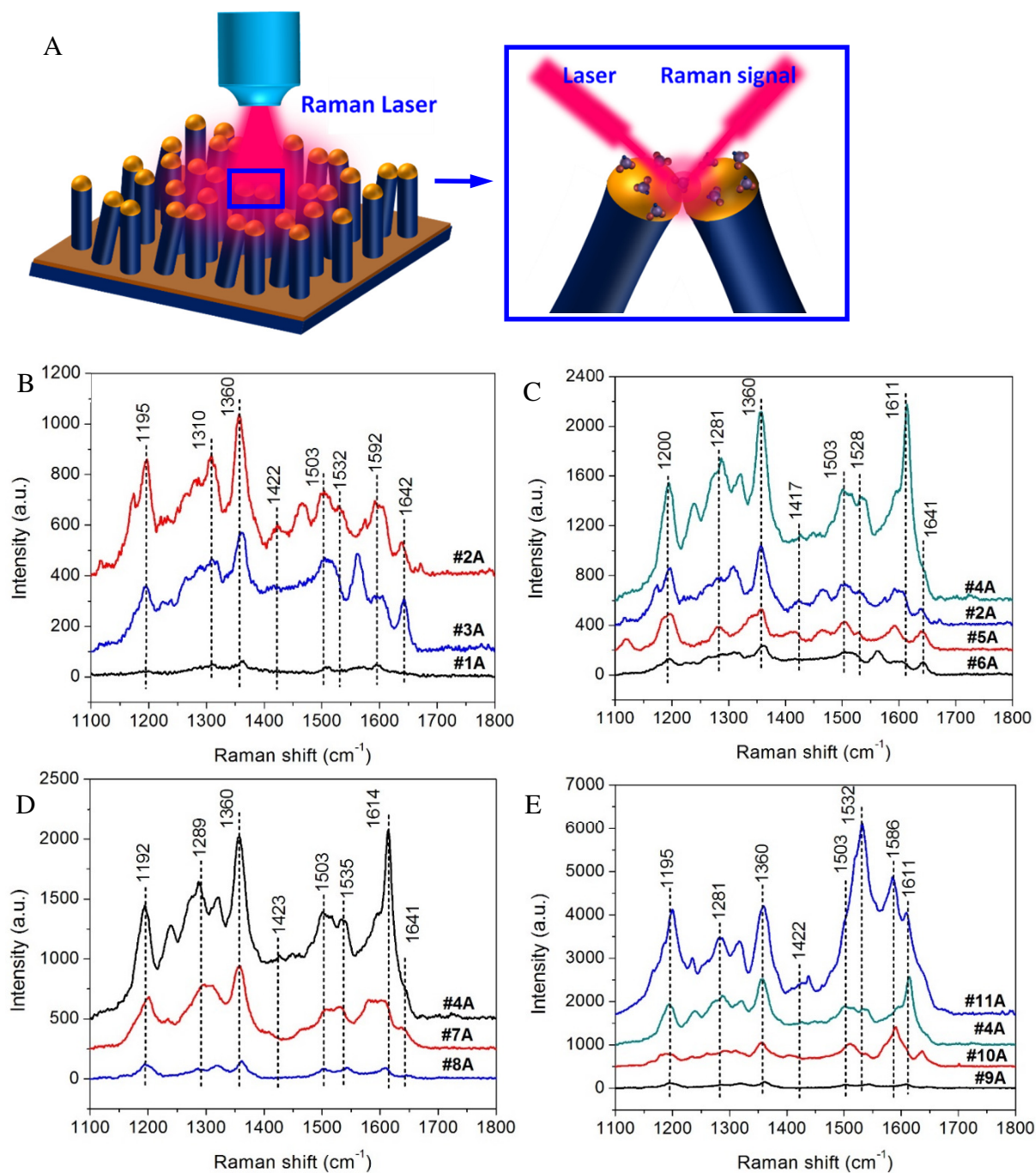


Figure 10.11. (A) Schematic showing the Surface Enhanced Raman Scattering (SERS) effect of pristine Si NW arrays. (B-E) Raman spectra of R6G obtained on silicon nanowires grown at different conditions: (A) flow rate set, (B) grow time set, (C) temperature set, and (D) gold sputtering time set. (Note: Spectra (1-11) in B-E corresponds to the sample # in Table 10.1.)

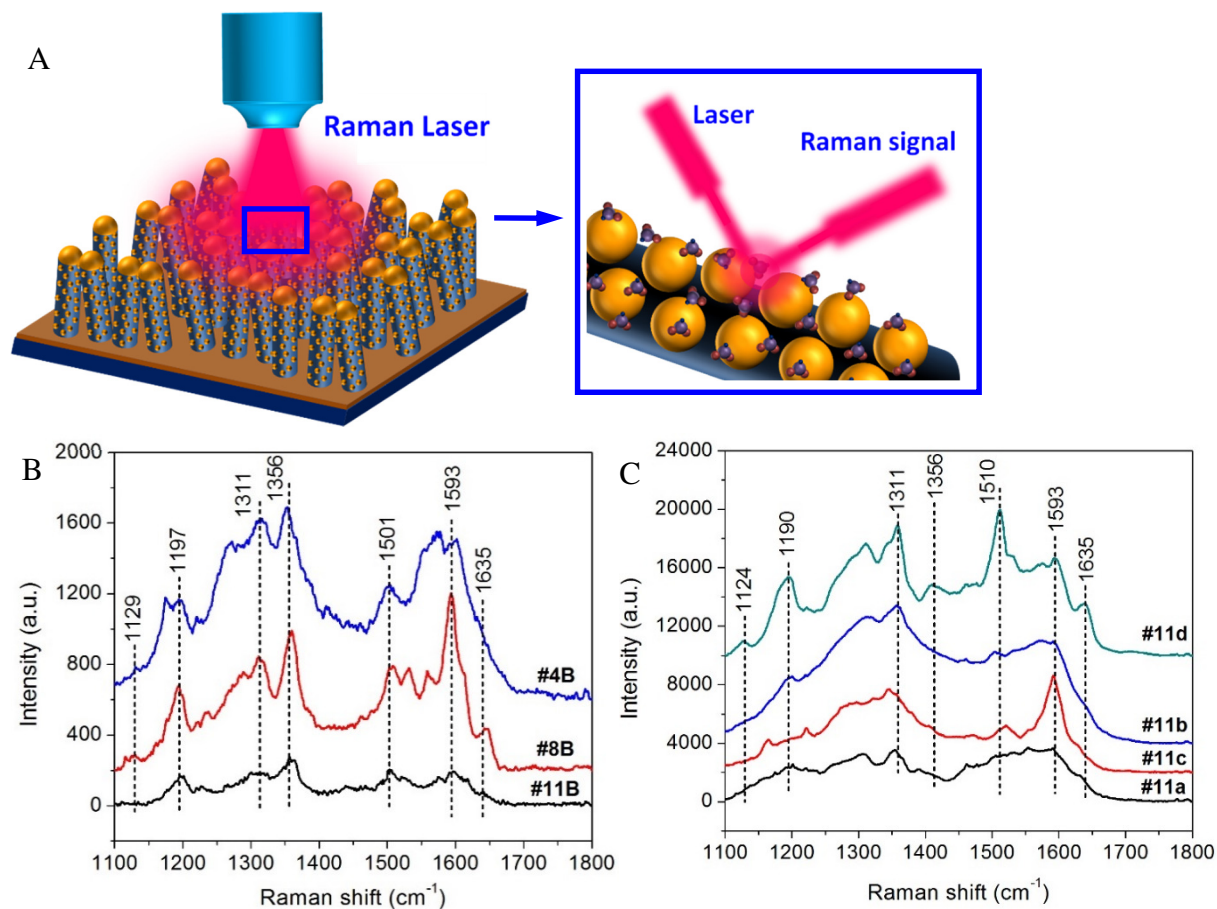


Figure 10.12. (A) Schematic showing the Surface Enhanced Raman Scattering (SERS) effect of Si NWs-Au NPs heterostructures. (B-C) Raman spectra of R6G obtained on Si-Au core-shell nanowires (B) and Si NWs-Au NPs heterostructures. (*Note: Spectra (A'~C')* in B correspond to samples in Figure. 6, and spectra (A~D) in C correspond to samples in Figure. 7.)

To evaluate the uniformity and reproductivity of TERS or SERS sensing based on the as-produced nanowires or the annealed Si nanowire-Au nanoparticle heterostructures, Raman mapping was conducted on these two nanostructure substrates after the same molecule absorption process. Figure 10.13A shows a representative optical images of the Si nanowire-Au nanoparticle heterostructures marked with numbers of points for conducting the Raman test on each. The obtained Raman mapping images on both the as-produced Si nanowires and the annealed Si nanowire-Au nanoparticle heterostructures were shown in Figure 10.13B and C. These two images

were generated using the indicative Raman signal of RG at 1360 cm^{-1} . We can observe that the distribution of “hot-spot” was much more uniform and intensive on the annealed Si nanowire-Au nanoparticle heterostructures as compared with that observed on the as-produced Si nanowires.

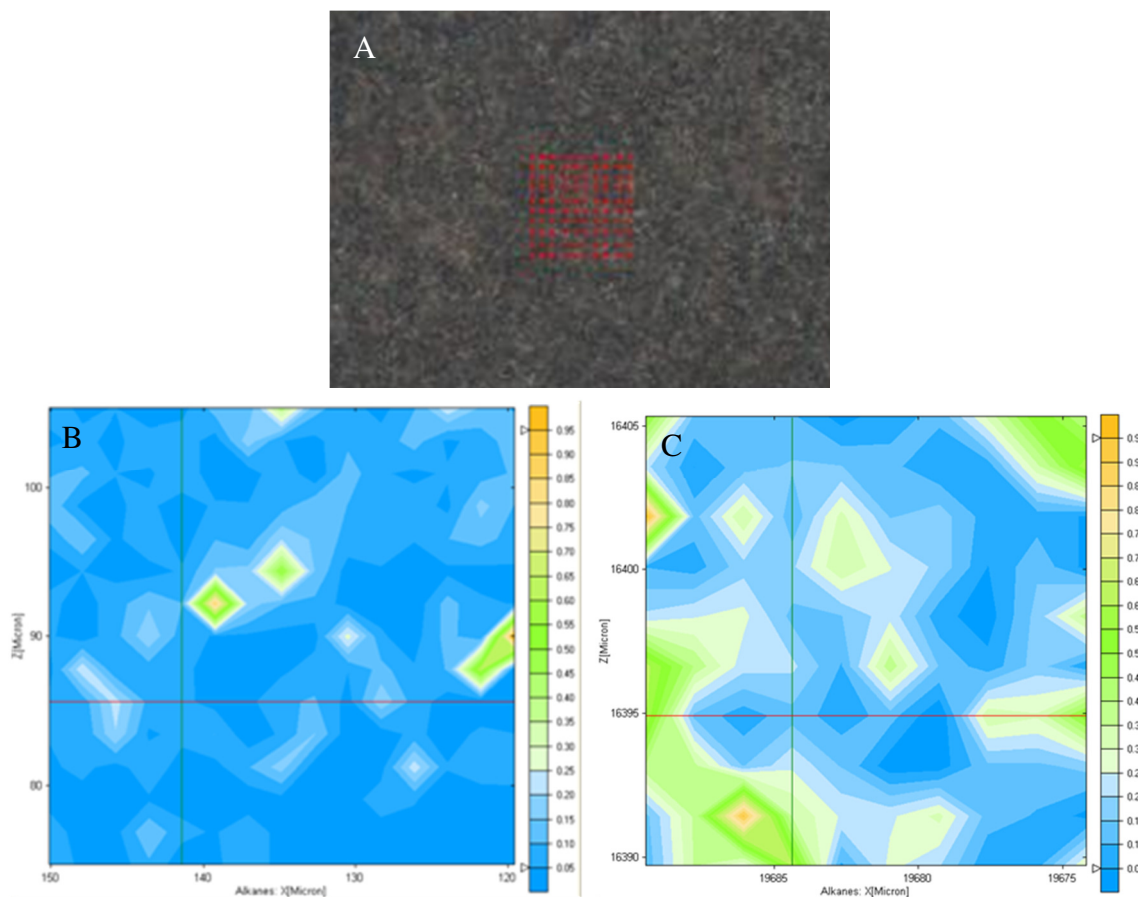


Figure 10.13. Raman mapping on Si NW array and Si nanowire-Au NPs heterostructures: (A) Optical images showing the Raman measurement, (B-C) distribution of Raman signal of R6G at 1360 cm^{-1} for (B) Si nanowire arrays (Sample#11A) and (C) Si nanowire-Au nanoparticle heterostructures(Sample#11C).

The Raman sensitivity or detection limit of the TERS based on the as-produced Si nanowires and the SERS based on the annealed Si nanowire-Au nanoparticle heterostructures were further evaluated using R6G solution with various concentrations (Figure 10.14A and B). The nanostructure substrates were put in these R6G solutions (10^{-8} M, 10^{-10} M, and 10^{-12} M) for the same time. We observed that the detection limit of the as-produced Si nanowire is 10^{-8} M and that of the annealed nanowire heterostructures can reach 10^{-10} M (Figure 10.14C).

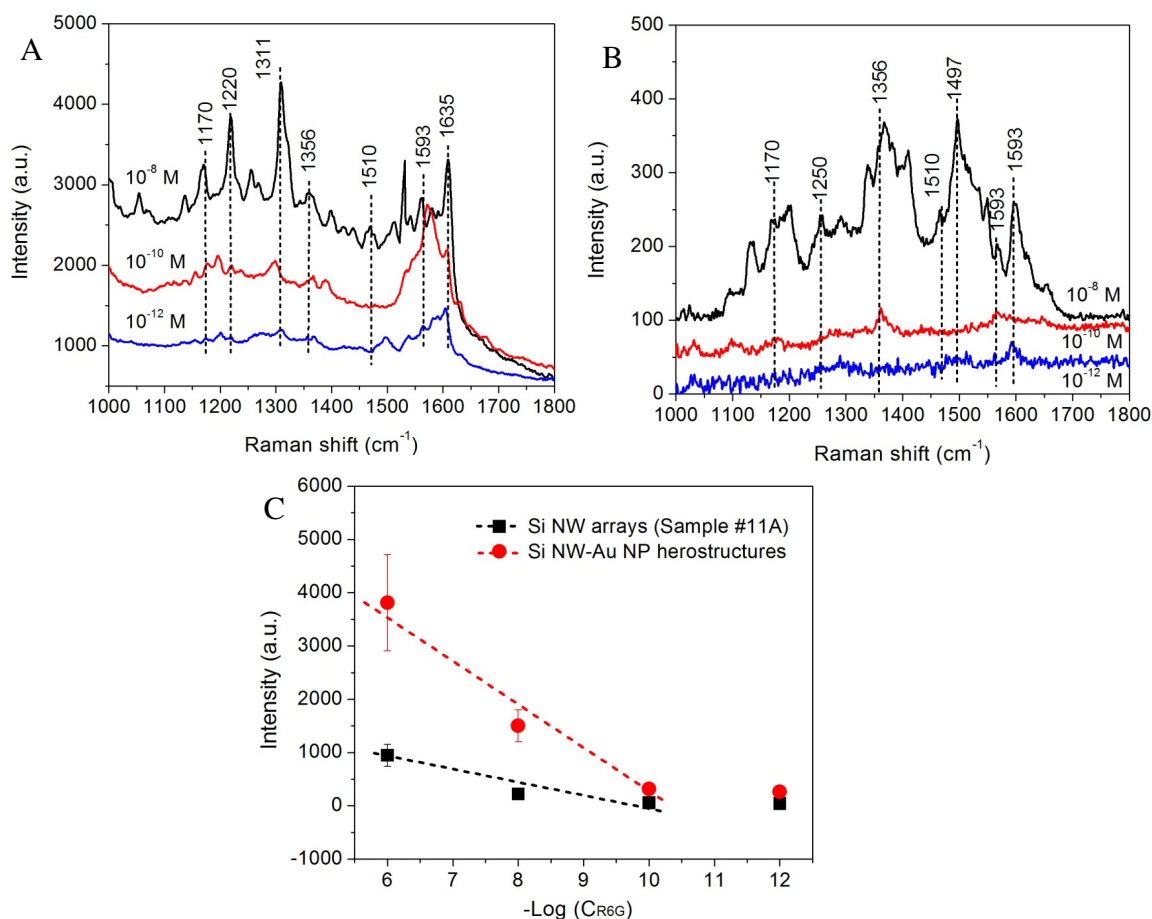


Figure 10.14. Detection limit of (A) pristine nanowire and (B) nanowire-gold nanoparticle heterostructures; (C) Variation of Raman peak (at 1360 cm^{-1}) intensity according to the concentration of target R6G solution.

10.4. Conclusions

In summary, we study the growth of Si nanowires in a chemical vapor deposition (CVD) method employing silane/hydrogen as precursors and gold film as a nanowire growth catalyst. We fundamentally understand the growth mechanism of the Si nanowires and the surface migration of catalytic gold nanoparticle as a function of growth parameters. Different architectures of Si nanowires are produced such as branched, standing, and horizontally residing on the substrates. Morphology/structure (diameter, length, branches) of Si nanowires can be obtained by controlling the growth conditions during the CVD process. These Si nanowires with attached Au nanoparticles on it by virtue of CVD growth are further studied for SERS effect using Raman dyes. Molecule detection based on TERS largely depends on the structure and configuration of as-produced nanowires. The Raman enhancement as high as 10^4 in the dye signals are observed as compared to blank silicon substrate. Decoration of Au nanoparticles on Si nanowires results in effective red-shift of Localized Surface Plasmon Resonance (LSPR), as well as the significant increase of extinction efficiency. The detection limit on these heterostructures can reach as high as 10^{-12} M. Such sensitive Raman nano-architectures are critical for scalable chemical sensing devices with high sensitivity and improved detection limits.

CHAPTER 11

THERMAL TREATMENT OF SILICON NANOWIRE – GOLD NANOPARTICLE HETEROSTRUCTURES FOR SURFACE-ENHANCED RAMAN SCATTERING SENSING

Yuan Li,¹ Aditya Gupta,¹ Wenwu Shi,¹ Nitin Chopra,^{1,2}*

¹Metallurgical and Materials Engineering Department, Center for Materials for Information Technology (MINT), The University of Alabama, Tuscaloosa, AL 35487, U.S.A.

²Department of Biological Sciences, The University of Alabama, Tuscaloosa, AL 35487, U.S.A.

*Corresponding Author

E-mail: nchopra@eng.ua.edu

Tel: [205-348-4153](tel:205-348-4153)

11.1. Introduction

Surface-enhanced Raman Spectroscopy (SERS) has been considered as a powerful analytical tool allowing for significantly-enhanced Raman signals for the target molecules with even a single molecule sensitivity.³¹⁰ In this regard, nanostructured gold and silver have been widely studied as the SERS substrate due to their excellent surface plasmonic properties (or localized surface plasmon resonance, LSPR).³¹¹ LSPR can be effectively modulated by controlling the size, shape, and arrangement of the nanostructures,³¹² or by using suitable supporting materials. Direct dispersion or patterning of the nanostructures on a flat substrate, for instance, has been widely reported.³¹³ However, further development of such SERS substrates is limited by the poor nanostructure density, uncontrollable aggregation, and nonuniform distribution of the nanostructures.³¹⁴ Recently, heterostructures of one-dimensional nanowires integrated with extraneous nanoparticles were demonstrated to be of great interest due to their excellent detection sensitivity, reproducibility, stability, and biocompatibility.³¹⁵

Silicon (Si) nanowires have been utilized in bioelectronics, nanoelectronics, optical devices, and energy devices.³¹⁶ The pristine Si nanowires only exhibit moderate Raman sensitivity for molecular detection, and thus proper surface modification or heterostructuring of the nanowires are of particular interest for the purpose of SERS sensing. Surface decoration for Si nanowires have been well-studied and the decorating materials including metal nanoparticles, boron and magnesium, diamond-like carbon (DLC) and polymers.³¹⁷ In regard to SERS, gold (Au) and silver (Ag) nanoparticles decorated Si nanowires have been fabricated and used for chemical and biological species detection.³¹⁸ Enhancement in Raman signals was observed on such heterostructures and was attributed to (1) the increase of specific substrate surface area, which resulted in increased absorption of target molecules per unit area, and (2) The modulation of

surface plasmonic properties of Au or Ag by integrating with supporting nanowires, which led to generation of more SERS “hot-spots”.³¹⁹ To further increase the performance of SERS devices, Tip-enhanced Raman Spectroscopy (TERS) using the Au nanoparticles supported on the tips of Si nanowires have also been demonstrated.³²⁰ However, the aligned arrangement of nanowires and size of Au nanoparticle on the tips were normally hard to control and resulted in weak plasmonics or “hot-spots”. In addition, other hybridized configurations based on the surface decoration of Si nanowires (e.g., Au/C decorated Si nanowires) were also studied for SERS.³²¹ However, the major challenges are still lying in the control of morphology and distribution of plasmonic nanostructures on the one-dimensional nanostructures and lack of knowledge in understanding the structure-processing-plasmonic performance relationships. With this regard, development of simple and facile fabrication routes for realizing complex plasmonic heterostructures becomes of interest and importance.

Various approaches have been reported for growing Au nanoparticles on the Si nanowires. These including (1) wet-chemical reduction of the gold salt, (2) physical sputtering/evaporation of gold target, and (3) electroless deposition.³²² In all these methods, Au nanoparticles can be directly deposited on the Si nanowires with very little damage to the pristine nanowires. However, since the active sites for particle nucleation are randomly dispersed on the nanowires, the resulting Au nanoparticles are normally non-uniform in shape and size. Meanwhile, their inter-particle spacing and density are hard to control. Thus, proper further treatment for these as-produced heterostructures is necessary to control the distribution and modulate the shape and size of these surface nanostructure. It is hypothesized in this paper that a controlled high-temperature treatment (annealing) process will significantly change the surface distribution, shape and size of the Au nanoparticles supported on Si nanowires. This annealing process allows for controlled surface

migration and material re-distribution on the surface of curvature Si nanowires, leading to the minimal surface energy configuration for the heterostructures,³²³ and thus making annealed heterostructures perform as multifunctional and robust SERS substrates.

The fabrication of Si nanowire-Au nanoparticle heterostructures in this paper is completed by combining a wet-chemical nucleation method with the post high-temperature annealing process. This led to the formation of uniformly distributed Au nanoparticles on the surface of Si nanowires with controlled shape, size and inter-particle spacing. The morphology, crystal structure, and chemical composition of the heterostructures before and/or after annealing was demonstrated using various microscopic and spectroscopic methods. The heterostructures were also studied for their surface migration or diffusion kinetics during the annealing at different conditions. Finally, we demonstrated the dependence of SERS enhancement (using R6G as Raman probe) on the configurations of the heterostructures obtained at various annealing conditions. This study provides fundamental understanding on the migration behaviors/kinetics of Au nanoparticles on the Si nanowires during high temperature annealing. The proposed surface decoration strategy of heterostructure fabrication also provides reliable reference for future development of SERS-based chemical sensors.

11.2. Experimental section

Materials and methods: N-type silicon wafers (100) were purchased from IWS (Colfax, CA). Gold (III) chloride trihydrate ($\text{HAuCl}_4 \cdot 3\text{H}_2\text{O}$, 99.9%) was purchased from Sigma-Aldrich (St. Louis, MO). Sodium borohydride (NaBH_4 , powder, 98%) was bought from Acros Organics (New Jersey, NJ). Acetone ($(\text{CH}_3)_2\text{CO}$) was purchased from VWR International (West Chester, PA). DI water

(18.1 M Ω -cm) was obtained using a Barnstead International DI water system (E-pure D4641). All chemicals were used without further purification. Gold sputtering was carried out on a Bio-Rad gold sputtering and coating systems (Agawan, MN). Growth and annealing of Si nanowires were carried out in a GSL-1100X (MTI Corporation) with a quartz tube purchased from ChemGlass (Vineland, NJ).

Chemical vapor deposition of Si nanowires: Atmosphere pressure chemical vapor deposition (CVD) method was used for the growth of Si nanowires. Briefly, the silicon substrate was treated in the piranha solution for 30 min at 100 °C. This was followed by sputtering of gold film (~20 nm) for 1 min. The substrate was then placed in the center of the reactor tube for the growth of Si nanowires *via* the vapor-liquid-solid (VLS) mechanism. This CVD process was conducted at ~625 °C with the flowing silane (SiH₄, 30 sccm) as the silicon source and 10% H₂/Ar (100 sccm) as the carrier gas. The growth was continued for 5 min and then the furnace was cooled down to room temperature with protection of Ar.

Fabrication of Si nanowire-Au nanoparticle heterostructures: The as-produced Si nanowires were dispersed in ethanol by sonicating the substrate (1×1 cm²) for 10 min. This was followed by addition of ~30 μ L as-prepared NaBH₄ solution (60 g/L) into the nanowire dispersion. After slightly stirred for 1 min, ~50 μ L of HAuCl₄ (~5 × 10⁻³ M) was further added. The nucleation reaction was continued for 10 min. The product was washed with ethanol for 3 times and finally dispersed in ~1 mL ethanol. This process led to the preparation of the as-produced Si nanowire-Au nanoparticle heterostructures. For the subsequent annealing process, the as-produced heterostructures were first dispersed on a surface oxidized silicon substrate (1×1 cm²) *via* the simple drop-casting method. In the following, the heterostructures containing substrates were annealed at various durations, temperatures, and environments as planned in Table 11.1.

Surface-enhanced Raman spectroscopy studies: Rhodamine 6G (R6G) was used as the Raman probe or model molecule to evaluate the enhancement of Raman signal on the Si nanowire-Au nanoparticle heterostructures. 50 μL of R6G solution ($\sim 10^{-4}$ M in ethanol) was drop-casted on the heterostructure-dispersed substrate. Single nanowire heterostructure was captured under the optical spectroscopy in the Raman system. Raman signal of R6G was collected at various spots along the heterostructures. Approximately ten nanowire heterostructures were selected on each substrate and similar Raman analysis was carried out to get the average intensity of Raman signals for various heterostructure samples.

Characterization Methods: FE-SEM JEOL-7000 Scanning Electron Microscopy (SEM) and Tecnai F-20 Transmission Electron Microscopy (TEM) were used for the morphological analysis. TEM samples were prepared by drop-casting the heterostructures dispersion on the lacey carbon TEM grids. Nanoparticle density, size and inter-particle spacing were estimated according to the TEM analysis. Philips X'Pert-MPD X-ray Diffraction (XRD) System was used for the phase analysis. UV-vis absorbance spectra were collected using DH-2000 UV-VIS-NIR light source. Kratos Axis 165 X-ray photoelectron spectroscopy (XPS) with mono-aluminum gun was used for binding energy or chemical composition analysis. Raman spectra of R6G on various heterostructures were collected using the Bruker Senterra Raman system. The wavelength of the Raman laser is 785 nm and the diameter of the laser spot is 1 μm . The integration time was set as 10 s with co-conditions of 2.

Table 11.1. Detailed experimental parameters for the annealing of Si nanowire-Au nanoparticle heterostructures. Note: Sample #2, #6 are the baseline samples (bold and italics) and were repeated in each set (shaded).

Sample #	Duration (min)	Temperature(°C)	Atmosphere
1	15	625	Ar
2	45	625	Ar
3	75	625	Ar
4	120	625	Ar
5	45	300	Ar
6	45	500	Ar
2	45	625	Ar
7	45	700	Ar
8	45	800	Ar
9	45	1000	Ar
6	45	500	Ar
10	45	500	5%O ₂ /Ar
11	45	500	Vaccum
12	45	500	10%H ₂ /Ar
13	45	500	N ₂

11.3. Results and discussion

Figure 11.1 shows the fabrication steps for Si nanowire-Au nanoparticle heterostructures as a novel substrate for SERS-based organic dye sensing. The following steps (Figure 11.1) were involved: (1) growth of Si nanowires in the CVD approach, (2) wet-chemical synthesis and direct nucleation of Au nanoparticles on the Si nanowires, (3) dispersion of the as-produced Si nanowire-Au nanoparticle heterostructures on the oxidized silicon substrate, (4) morphological evolution of Au nanoparticles on the Si nanowires in a controlled annealing process, and (5) correlation of heterostructure morphology with Raman signal enhancement effect for the organic molecules.

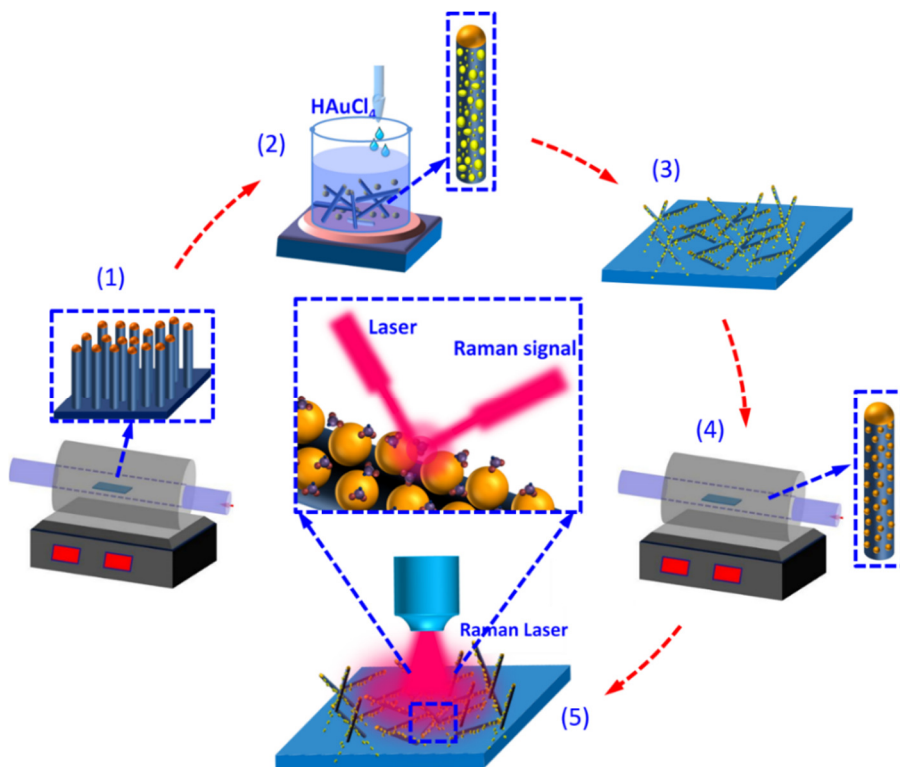


Figure 11.1. Schematic representation of the process for fabricating Si nanowire-Au nanoparticle heterostructures and their application for SERS sensing. (1) CVD growth of Si nanowires, (2) direct and wet-chemical nucleation of Au nanoparticles on Si nanowires, (3) dispersion of the heterostructures on substrate, (4) thermal annealing, and (5) SERS-based organic dye detection.

11.3.1. Growth of Si nanowires and their surface decoration with Au nanoparticles

Figure 11.2A and B show the SEM images of the as-produced Si nanowires. Au nanoparticle was always found at the tip of each Si nanowire, indicating the growth was governed by well-known VLS mechanism.³²⁴ This growth process utilized sputtered and dewetted Au film on the Si substrate. The authors have thoroughly studied the dewetting of Au films to result in uniform dispersion of nanoparticles in their previous study.³²⁵ The resulting Au nanoparticles/islands were further served as the catalysts/seeds for the CVD growth of Si nanowires. The growth was conducted for 5 min and resulted in Si nanowires with a length of ~8 - 12 μm , suggesting a nanowire growth speed of ~27 - 40 nm/s. The diameter of Si nanowires was observed to be consistent with the size of Au nanoparticle tips on the nanowires. From Figure 11.2C, it can be estimated that the diameter of Si nanowire was $\sim 172.44 \pm 90$ nm. Figure 11.2D-F shows the HRTEM images of the as-produced Si nanowires. A lattice spacing of ~0.31 nm was observed for silicon (111) planes. Gold (111) planes with a lattice spacing of ~0.23 nm was also observed for Au nanoparticle tips. The lattice structure of both gold and silicon present in the nanowires were further confirmed by the Fast Fourier Transform (FFT) image in the inset of Figure 11.2F.

As the next step, Si nanowires were decorated with extraneous Au nanoparticles in a wet-chemical nucleation process. This approach involves the chemical reduction of metal salt (HAuCl_4) in presence of NaBH_4 , allowing for direct nucleation of Au nanoparticles on the Si nanowires. Figure 11.3A-C show TEM images of the as-produced Si nanowire-Au nanoparticle heterostructures. Significant nanoparticle aggregation on nanowires was observed. The Au nanoparticles exhibited lattice spacing of ~0.23 nm corresponding to the (111) planes. It is worthy to mention that this direct nucleation process has no significant damage the structure of Si nanowires, as the silicon (111) crystal planes with a lattice spacing of ~0.32 nm was also observed. XRD spectra of the as-

produced Si nanowires and the Si nanowire-Au nanoparticle heterostructures further confirmed their crystal structure (Figure 11.3D). Figure 11.3E shows the estimation of size (average diameter $\sim 10.40 \pm 3.59$ nm) and inter-particle spacing ($\sim 6.19 \pm 2.30$ nm) for the as-nucleated Au nanoparticles on the Si nanowires.

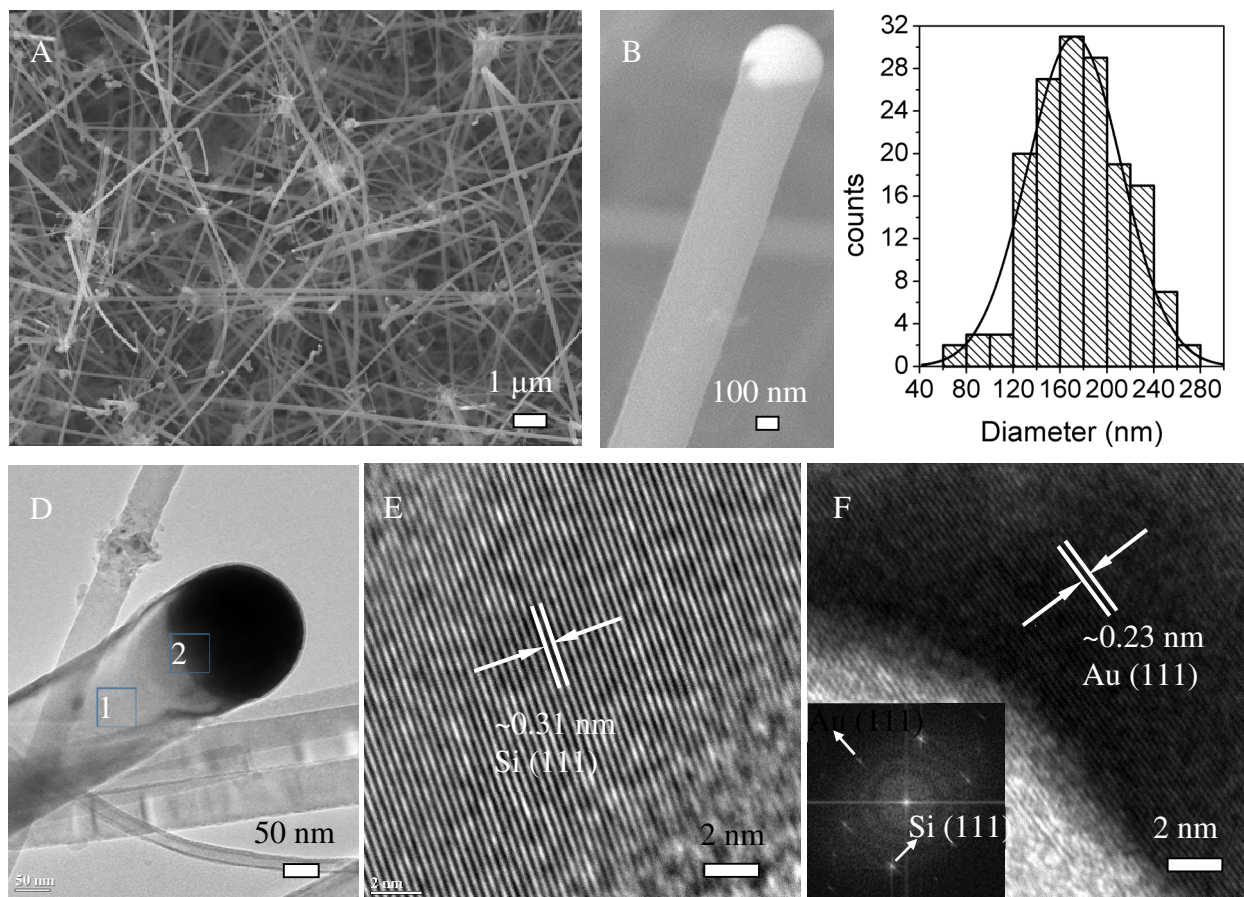


Figure 11.2. (A and B) SEM images of the as-produced Si nanowires. (C) The diameter distribution ($\sim 172.44 \pm 90$ nm) of Si nanowires. (D) TEM image of the as-produced Si nanowires. (E) HRTEM image indicating the lattice structure of the Si nanowire (marked as “1” in D). (F) HRTEM image indicating the lattice structure of the Au nanoparticle (catalyst/seed) at the tip of the Si nanowire (marked as “2” in D). *Note: The inset in (F) show the corresponding FFT image for diffraction spots for silicon and gold.*

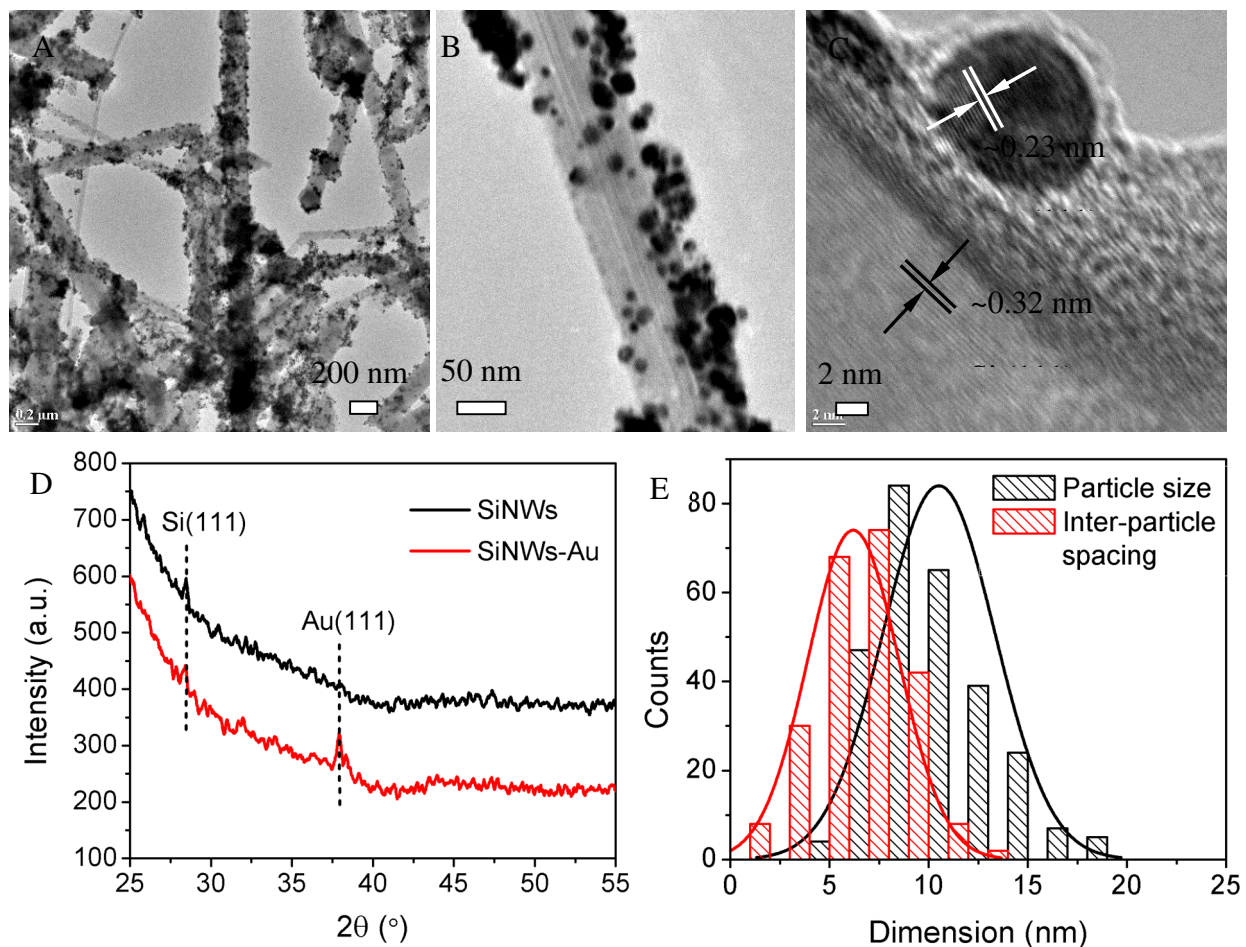


Figure 11.3. (A-C) TEM images of the as-produced Si nanowire-Au nanoparticle heterostructures (before annealing). (D) XRD spectra of the as-produced Si nanowires and the Si nanowire-Au nanoparticle heterostructures before annealing. (E) Size and inter-particle spacing of the Au nanoparticle on Si nanowires.

11.3.2. Annealing of Si nanowire-Au nanoparticle heterostructures

In order to modulate the shape, size and surface distribution of Au nanoparticles on the Si nanowires, subsequent high-temperature annealing was conducted under various conditions including duration, temperature, and environment. The detailed experimental parameters can be found. Figure 11.4A-D show TEM images of the Si nanowire-Au nanoparticle heterostructures after annealing for various durations (15-120 min). As compared to the as-produced

heterostructures (Figure 11.3A, B), the distribution of Au nanoparticles is much more uniform and with minimized aggregation on the Si nanowires. HRTEM images of the heterostructures (Figure 11.4E-H) show the lattice spacing for both silicon and gold. It could be observed that after the annealing process, the lattice spacing increased at the outer edge of the Au nanoparticle as compared to the inner core, resulting a core/shell nanoparticle configuration on the surface of Si nanowire. This could be attributed to the formation of gold silicide (AuSi_x) at the interface of Au nanoparticle and Si nanowire, which was growing into a shell structure with increasing annealing duration.³²⁶ As shown in Figure 11.4E, 15 min annealing resulted in core/shell configuration of Au nanoparticles, where the core lattice spacing is observed to be ~ 0.20 nm (corresponding to Au (200) plane) and the outer shell region (marked with dotted circle) exhibited lattice spacing of ~ 0.22 nm. The shell thickness was observed to increase with annealing duration. When beyond 75 min, the whole nanoparticle exhibited a lattice spacing of ~ 0.25 nm. This indicates that prolonged annealing duration (>75 min) resulted in complete phase transformation of Au nanoparticles into gold silicide nanoparticles. The details on kinetics of this transformation are discussed later.

It was also observed that the diameter of Au nanoparticles on Si nanowires increased as a function of annealing duration from 15 min to 75 min (Figure 11.4I). The as-produced heterostructures exhibited an Au nanoparticles diameter of ~ 10.4 nm, which was increased to ~ 16.2 nm, 18.7 nm, and 22.6 nm after annealing for 15 min, 45 min, and 75 min, respectively. This increase can be explained by the Ostwald's ripening effect and surface migration of Au species, which resulted in growth of larger nanoparticle at the expense of smaller ones.³²⁵ However, when the annealing beyond 75 min, a sudden decrease in nanoparticle diameter (~ 15 nm) is observed. It has been reported for annealing of Au/Si thin film structure, the silicide formation takes place at much lower temperatures than that used for the annealing. It is proposed that the possibility of Au diffusing

towards Si or vice versa can lead to consumption of Au and result in shrinking of nanoparticle as observed in case of 120 min annealing. This further corroborates with the TEM observations that shows complete phase transformation of Au nanoparticles to gold silicide nanoparticles beyond 75 min of annealing. In regard to inter-particle spacing on Si nanowires, the as-produced heterostructures exhibited inter-particle spacing of ~6.2 nm, which was increased to ~10.1 nm after annealing of 15 min and remained nearly the same beyond this duration. This is an interesting observation as it suggests that surface migration of Au nanoparticles at the annealing conditions used was restricted and the process allowed for the formation of thermally-stable or sinter-resistant nanoparticle dispersion on Si nanowires. Similar observation have been reported for other one-dimensional heterostructures based on oxide nanowire-nanoparticle or carbon nanotube-nanoparticle systems.³²⁷

The microscopic observations were further utilized to develop contour maps correlating annealing duration and nanowire diameter with the nanoparticle diameter and spatial density (Figure 11.4J and K). This uniquely shows that Si nanowires with large diameter favored the growth of nanoparticles, resulting in largest nanoparticles dispersed on the heterostructures. On the other hand, nanowires with small diameter allowed for greater nucleation of nanoparticles and thus, resulted in highest spatial density of the coated nanoparticles. Figure 11.4J shows that annealing of 45 min resulted in largest nanoparticle diameters between ~45-50 nm coated on surface of Si nanowires with largest diameters between ~250-275 nm. This also suggests that higher the radius of curvature of nanowires, faster the surface migration of nanoparticles with enhanced Ostwald's ripening effect.³²⁸ Meanwhile, Si nanowires with small radius of curvature present higher surface energy, resulting restricted surface migration and enhanced heterogeneous nucleation for the Au

nanoparticles. Thus, the highest nanoparticle spatial density ($9-11 \times 10^{10}$ per cm^2) region observed at the intersection of 75 min duration and 50-100 nm diameter for Si nanowires (Figure 11.4K).

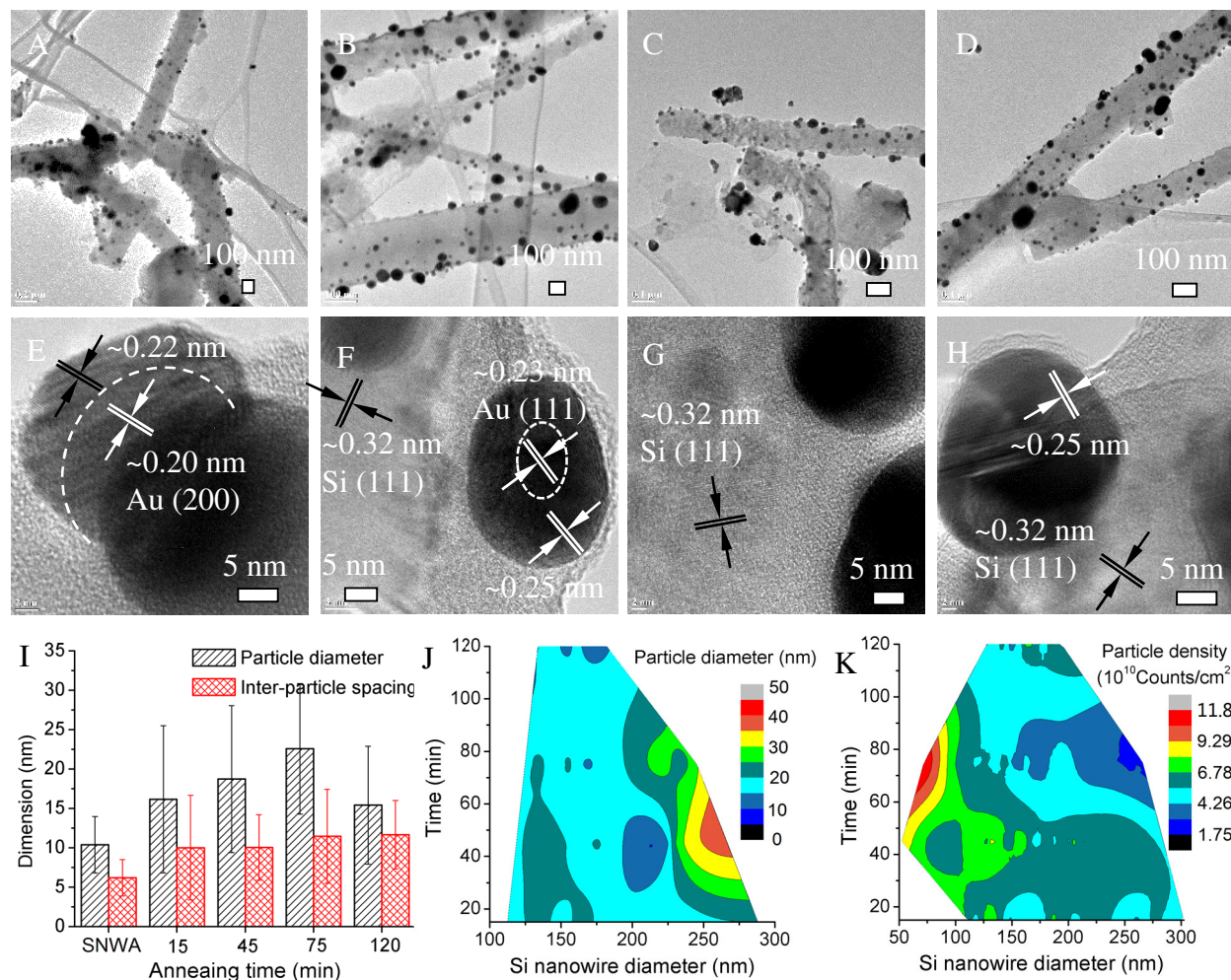


Figure 11.4. TEM images and lattice structure of the Si nanowire-Au nanoparticle heterostructures after annealing for (A, E) 15 min, (B, F) 45 min, (C, G) 75 min, and (D, H) 120 min. (I) Average diameter and inter-particle spacing of Au nanoparticles on Si nanowires after annealing for different durations. Contour graphs showing the distribution of Au nanoparticle (J) diameter and (K) spatial density as a function of the Si nanowire diameter and the annealing duration.

The influence of annealing temperature on the morphology of Si nanowire-Au nanoparticle heterostructures was shown in Figure 11.5A-D. Figure 11.5E-H further show the corresponding HRTEM images. Annealing at 300 °C only resulted in slight morphology change (Figure 11.5A) of the heterostructures as compared to the as-produced. Meanwhile, no obvious formation of gold/gold silicide core/shell nanoparticles was observed on this sample and the nanoparticle lattice spacing (~ 0.23 nm) was similar to that of pristine Au nanoparticles (Figure 11.5E). However, significantly improved Au nanoparticle uniformity was observed on the heterostructures annealed at 500 °C. The core/shell structure for the nanoparticles was also observed with the lattice spacing increased from ~ 0.23 nm of the core to ~ 0.25 nm of the shell (Figure 11.5F). When the annealing temperature increased to 700 °C and 800 °C, the nanoparticles on the heterostructures show constant lattice spacing of ~ 0.25 nm (Figure 11.5G and H), indicating the phase transformation or gold diffusion process becomes more pronounced at high temperatures and the Au nanoparticles were completely converted to gold silicide. In addition, annealing at 1000 °C led to the partially fusion of Si nanowires and severe destruction of the heterostructures was observed.

Figure 11.5I further summarized the variation of size and inter-particle spacing of Au nanoparticles on the heterostructures after annealing at various temperatures. Annealing at 300 °C showed obvious influence on the distribution of Au nanoparticle size (even not much on the morphology as shown in Figure 11.5A), which was increased from ~ 10.4 nm of the as-nucleated (Figure 11.3B) to ~ 16.8 nm (Figure 11.5A). Further increase the annealing temperature (from 500 °C to 800 °C) resulted in continuous increase of particle size. This is understandable since the diffusion efficiency of gold is increased at higher temperature, which is prone to the migration and merging of Au nanoparticles. The inter-particle spacing of Au nanoparticles increased from ~ 6.19 nm

(Figure 11.3B) to ~ 7.55 nm when annealed at 300 °C (Figure 11.5A) and to ~ 9.66 nm when annealed at 500 °C (Figure 11.5B).

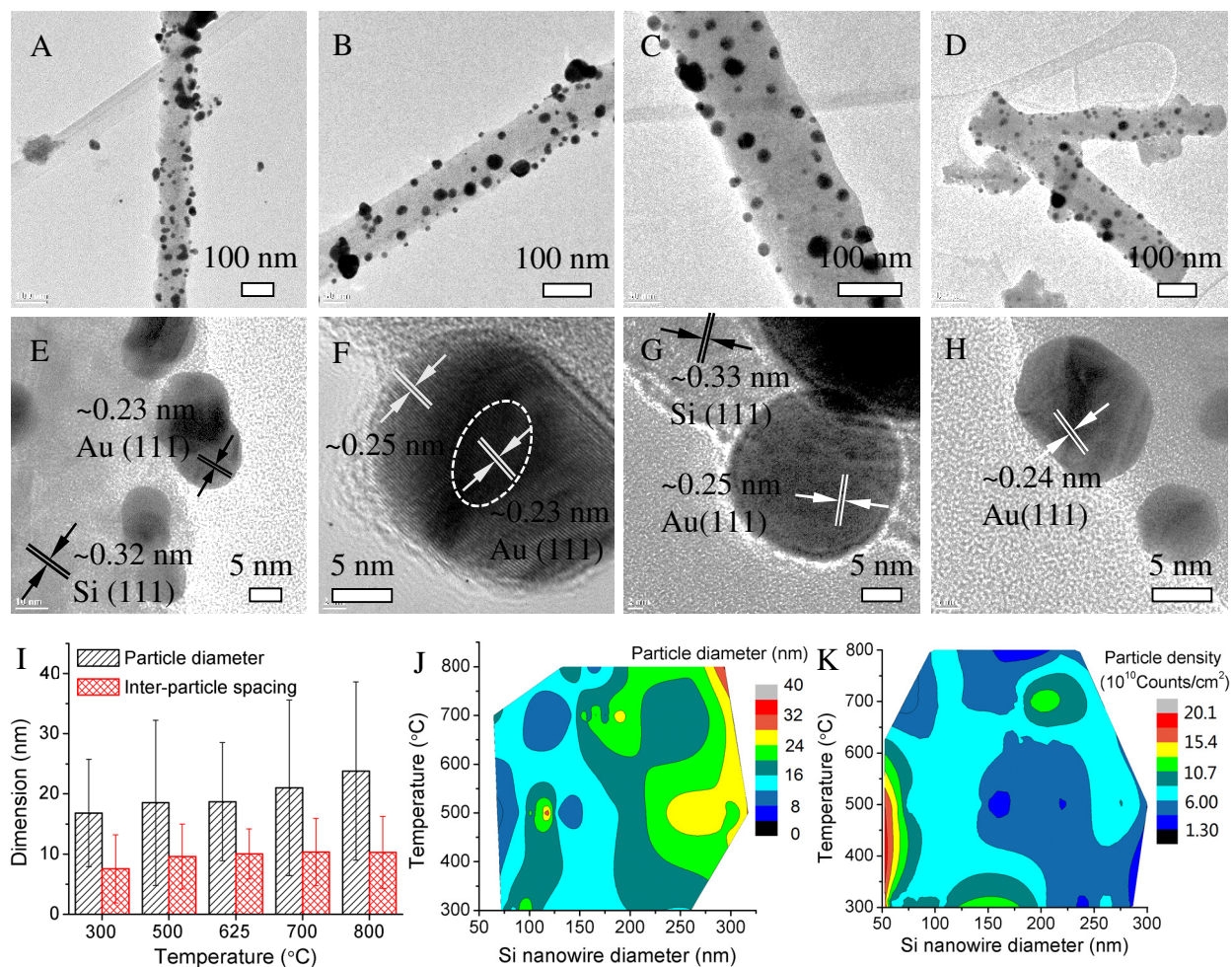


Figure 11.5. TEM images and lattice structure of the Si nanowire-Au nanoparticle heterostructures after annealing at (A, E) 300 °C, (B, F) 500 °C, (C, G) 700 °C, and (D, H) 800 °C. (I) Average diameter and inter-particle spacing of Au nanoparticles on Si nanowires after annealing for different temperatures. Contour graphs showing the distribution of Au nanoparticle (J) diameter and (K) spatial density as a function of Si nanowire diameter and the annealing temperature. *Note: Baseline annealing conditions were 45 min duration and in Ar environment.*

Further increase the temperature showed little effect on the inter-particle spacing, which kept a constant value of ~10 nm (Figure 11.5C and D). Figure 11.5J and K show the correlation of particle size and spatial density with the annealing temperature and the diameter of Si nanowires. The largest Au nanoparticles were mainly distributed on the heterostructures with largest Si nanowire diameter and that treated with high temperature. This is due to the increase of gold migration rate on the low curvature nanowires and at high temperature. With this regard, one can understand that the lowest spatial density of Au nanoparticles was mainly observed on the small-diameter nanowires and the heterostructures annealed in low temperatures (Figure 11.5K).

TEM images of the Si nanowire-Au nanoparticle heterostructures annealed in various environments were shown in Figure 11.6A-H. The aforementioned core/shell nanoparticles can be observed on the heterostructures that annealed in 5%O₂/Ar and N₂ environments (Figure 11.6E and G). Meanwhile, the lattice spacing of nanoparticles on the heterostructures annealed in 10%H₂/Ar and vacuum environment was increased from ~0.23 nm of the pristine to ~0.24 nm - ~0.25 nm due to the formation of gold silicide. Figure 11.6I further summarized the variation of particle diameter and inter-particle spacing of the heterostructures. The heterostructures annealed in 5%O₂/Ar environment show smaller average nanoparticle diameter (~16.3 nm) as compared with that annealed in pure Ar (~18.5 nm). This is because the outer layer of Si nanowires and Au nanoparticles was partially oxidized in the presence of O₂. The oxide layers mitigated the direct diffusion of gold into Si nanowires as well as the surface migration of Au nanoparticles, leading to less changes in nanoparticle size during the annealing.^{329, 330} The average diameter of nanoparticles after annealing in 5%H₂/Ar was ~16.8 nm (Figure 11.6B and I). This relatively smaller size is due to the presence of hydrogen, which removed the pristine surface oxide layer on

the Si nanowires and facilitated the diffusion of Au nanoparticles into Si nanowires.⁵⁶ As a result, the surface migration and aggregation of Au nanoparticles was not significant.

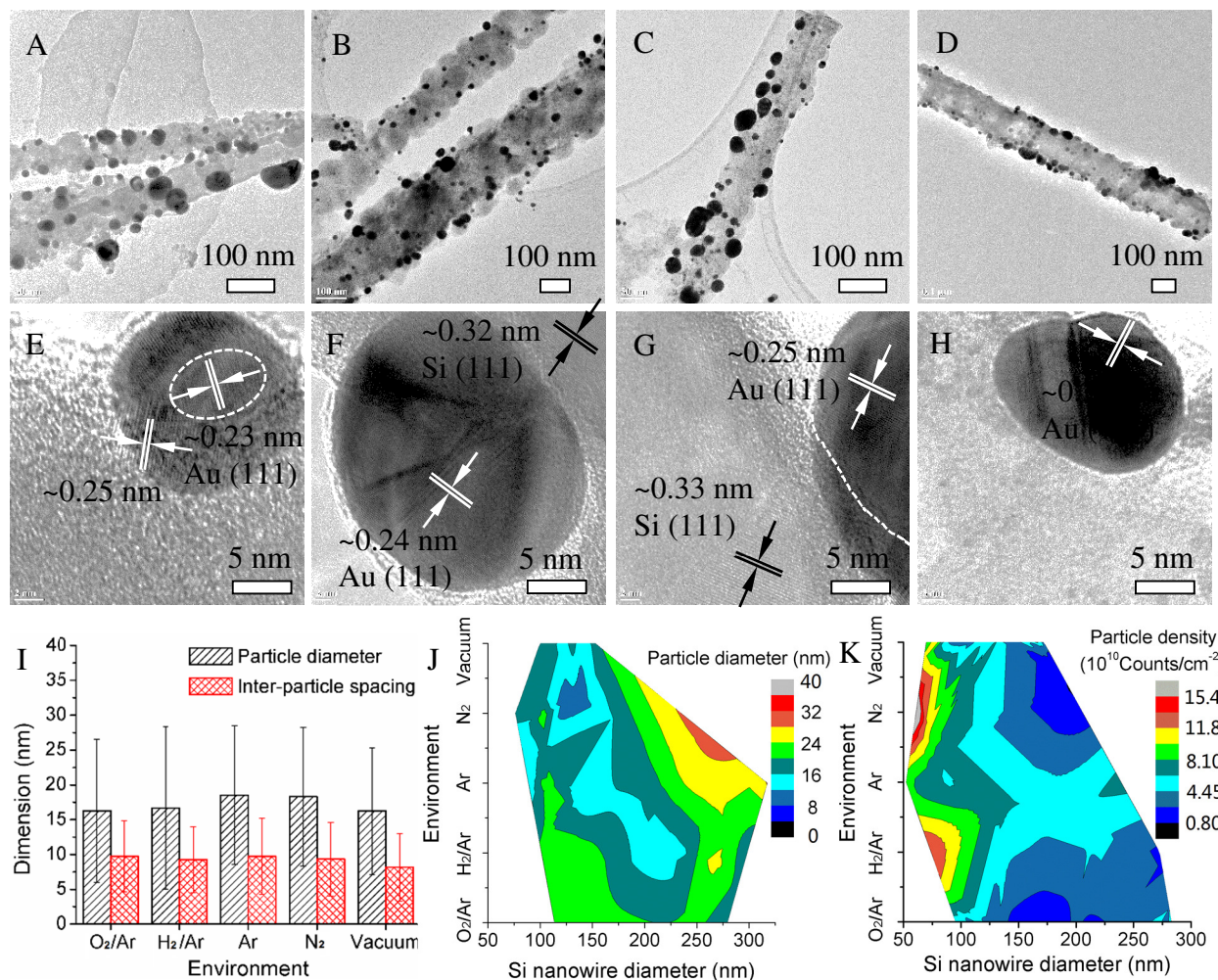


Figure 11.6. TEM images and lattice structure of the Si nanowire-Au nanoparticle heterostructures after annealing in various environments including (A, E) 5%O₂/Ar, (B, F) 10%H₂/Ar, (C, G) N₂, and (D, H) vacuum. (I) Average diameter and inter-particle spacing of Au nanoparticles on Si nanowires after annealing for different environments. Contour graphs showing the distribution of Au nanoparticle (J) diameter and (K) spatial density as a function of Si nanowire diameter and the annealing environment.

Annealing in vacuum also resulted in a less increased nanoparticle diameter (~16.2 nm, Figure 11.6D and I), which is probably due to the high diffusion rate of gold in silicon at low pressure.³³¹ In addition, heterostructures annealed in N₂ environment (Figure 11.6C and I) show no significant difference on particle size and inter-particle spacing with that annealed in Ar.³³² Contour images in Figure 11.6J-K show the distribution of particle size and spatial density according to various environments and nanowire diameter. Similar with that observed in previous duration and temperature study, nanoparticles with the largest diameter were observed on large Si nanowires while the region with highest spatial density were observed on small nanowires. In addition, the region with highest spatial density was observed on heterostructures treated in the H₂/Ar environment owing to the mitigation of surface migration and merging of Au nanoparticles in the presence of hydrogen.

Histograms summarized the size distribution and inter-particle spacing distribution of Au nanoparticles on the heterostructures before and after annealing at various conditions. Composition analysis for the heterostructures before and after annealing (at 500 °C, 45 min and Ar environment) was conducted using STEM-mode EDS line profile. STEM images show different contrast of gold and silicon in the heterostructures, which were further identified by the EDS spectra (corresponding to spot “1” and “2”). Representative EDS line profiles of the nanowire heterostructures before and after annealing process were studied. These line profiles clearly show the elements present and their maps as a function of location on the nanowire.

11.3.3. XPS study for the formation of gold silicide

Above TEM images clearly demonstrate a lattice spacing shift for nanoparticles on the heterostructures from ~0.23 nm to ~0.25 nm before and after annealing. This has been attributed to the formation of gold silicide according to the previous literatures. In order to make further quantitative conclusions, XPS was utilized to study the variation of chemical composition for the heterostructures annealed at various annealing conditions and further understand the surface migration/diffusion kinetics of Au nanoparticles on the Si nanowires. Wide-range XPS spectra and further deconvoluted Au 4f spectra show different elements such as Si, Au, O, C, and Na were observed for all the tested samples. The existence of Na is due to NaBH₄ used in the Au nanoparticle nucleation process.³³³ However, this peak was only observed on the as-produced nanowire heterostructures and was almost disappeared after annealing. In addition, C and O are common contaminations resulted from the oxidized silicon substrate.

The peaks observed at ~83.86 eV and ~87.50 eV were assigned to Au 4f_{7/2} and Au 4f_{5/2} of metallic Au nanoparticles that nucleated on the Si nanowires (Figure 11.7A).⁶³ The further deconvolution fitting of this Au 4f spectrum shows nearly 100% pure metallic gold. This indicates that no gold oxide or Au³⁺ remaining on the heterostructures after Au nanoparticle nucleation. At the same time, the gold and silicon phases are chemically intact, which is consistent with the TEM images in Figure 11.3A-C and EDS line profile. The Au 4f spectrum for the heterostructures annealed for 15 min (corresponding to sample #1) was shown in Figure 11.7B. The deconvolution resulted in two additional peaks in high binding energy region (~84.43 eV and ~88.55 eV) and the peak area of metallic gold (at ~86.65 eV and ~87.68 eV) became relatively small. The emergence of these two peaks was also observed by several authors before and was attributed to the chemical reaction of gold and silicon atoms owing to the formation of gold silicide.³³⁴⁻³³⁶ This observation is

consistent with the core/shell nanoparticles observed in the TEM image (Figure 11.4E) and will be a solid confirmation for statement of gold silicide formation. The same phenomenon was also observed on the spectrum obtained on the heterostructures annealed for 45 min (Figure 11.7C, corresponding to sample #2). Further decreased peak area for metallic gold (at ~83.53 eV and ~87.68 eV) was observed on this sample. After annealing the heterostructure for 75 min (sample #3) and 120 min (sample #4), no peaks for the metallic gold was observed in the deconvoluted spectra. This further confirmed the lattice variation observed in Figure 11.4G and H since no metallic gold core was observed on these heterostructures (Sample #3 and #4).

Since XPS is a surface characterization technique with the detection depth of ~8 nm,⁶³ and meanwhile the diameter of Au nanoparticles on the annealed heterostructures was varying from ~15 nm to ~20 nm, the metallic gold detected by the photoelectrons will be only from part of the nanoparticles. Thus, it is necessary to establish a theoretical model to calculate the accurate molar fraction of metallic gold and thickness of the gold silicide shell. This will also lead to further understanding on the kinetics of the gold silicide formation process. The model was schematically shown in Figure 11.7D. Here we assume the nanoparticles on Si nanowires are spherical and composed of a concentric gold core and gold silicide shell. The incident X-ray is from the top of the core/shell structure with a penetrating depth of 8 nm. Accordingly, one can realize that the molar fraction (F_{Au}) directly calculated by the area ratio from the XPS spectra is only for the spherical cap in Figure 11.7D (photoelectron region). The volume of this spherical cap (V) being detected by XPS was given by

$$V = \pi RH^2 - \frac{1}{3}\pi H^3, \quad (11.1)$$

where R is the outside radius of the core/shell structure, H is the photoelectron emission depth and was assumed to be 8 nm. Thus, according to Figure 11.7D, F_{Au} calculated from the area ratio of XPS spectra can be written as

$$F_{Au} = \frac{(r-R+H)^2 \cdot (2r+R-H)}{H^2 \cdot (3R-H)} \quad (11.2)$$

where r represents the radius of the metallic gold core. It needs to mention here that Eq. (11.2) is only suitable for the core/shell nanoparticles with $R - r \geq H$ (these show metallic gold peaks in XPS spectra). Furthermore, knowing F_{Au} from the XPS spectra, the real molar fraction ($F_{Au,real}$) of the core/shell nanoparticles can be calculated by

$$F_{Au,real} = (r/R)^3 \quad (11.3)$$

The obtained molar fraction values were summarized. It has been reported that diffusion of silicon atoms in the gold at the elevated temperature is a thermodynamically feasible process due to its high solubility in gold and the low eutectic temperature of gold and silicon (~ 363 °C).³²⁴ It can be observed that annealing the heterostructures at 625 °C for 15 min resulted in a metallic gold content of 19.23% (Sample #1). When the annealing was conducted for 45 min, the remaining metallic gold is 4.10%.

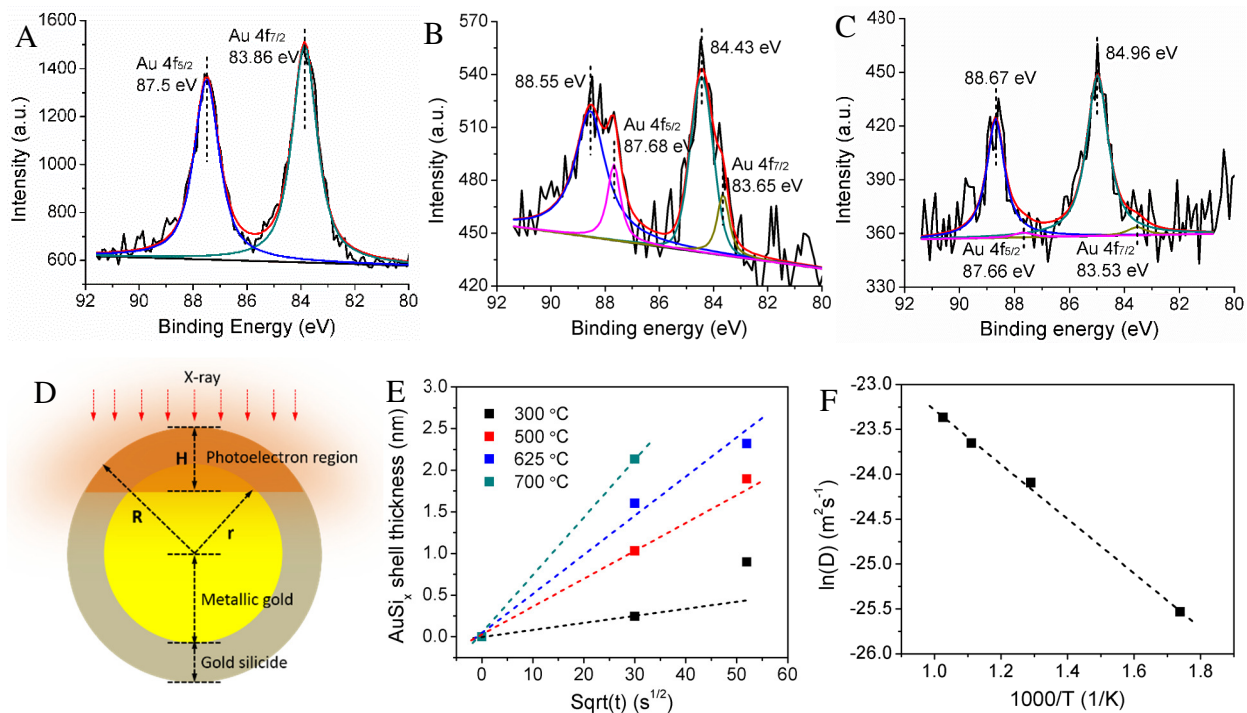


Figure 11.7. (A-C) Deconvoluted XPS spectra (Au 4f) of the Si nanowire-Au nanoparticle heterostructures (A) before and after annealing for (B) 15 min and (C) 45 min. (D) Schematic showing the formation of gold Silicide (AuSi_x) shell on Au nanoparticles and the geometrical model for the XPS analysis. (E) Variation of AuSi_x shell thickness as a function of annealing duration at different temperature. (E) Linear plot showing the relationship between the diffusion coefficient and temperature for the AuSi_x formation activation energy calculation.

XPS spectra of Au 4f for the nanowire heterostructures annealed at various temperatures and environments (sample #5-#13) were also deconvoluted. The peak locations were further summarized. For all these annealed samples, two additional gold silicide peaks were observed in the positive direction (with a binding energy shift of ~ 1 eV compared to the metallic gold). Metallic gold peaks were only observed on heterostructures annealed at 300 °C and 500 °C, but not on those annealed at 700 °C, 800 °C and 1000 °C. This is because the diffusion rate of silicon in gold is much higher at high temperature, resulting in complete phase transformation from gold to gold silicide. In the environment set, we observed the metallic gold peaks on the heterostructures

annealed in Ar, N₂, and 5% O₂/Ar but not on the samples annealed in 5%H₂/Ar and vacuum environments. This is consistent with the TEM observations in Figure 11.6 and further confirmed above reasoning that the presence of hydrogen or low pressure facilitated the diffusion and alloying of silicon and gold.

11.3.4. Kinetics for the formation of gold silicide

Considering that the formation of gold/gold silicide core/shell nanoparticles on the heterostructures during the annealing fundamentally involves the diffusion of Si atoms in Au nanoparticles, one can apply the Fick's second law (Eq. (11.4)) to this process and further study the formation kinetics of gold silicide.

$$\frac{\partial c}{\partial t} = D \frac{\partial^2 c}{\partial x^2} \quad (11.4)$$

where c is the concentration of Si in Au nanoparticles, t is the time and D is the chemical interdiffusion coefficient and only depends on temperature. Solving Eq. (11.4) with the following boundary conditions: $c = c_0$ at $t = 0$ and $c = c_s$ at $x = 0$, we can get:

$$\frac{c(x,t)-c_0}{c_s-c_0} = 1 - \operatorname{erf}\left(\frac{x}{2\sqrt{Dt}}\right), \quad (11.5)$$

where x can be considered as the thickness of gold silicide shell, ($x = R - r$, the values for various samples were shown), erf is the Gauss error function and can be express as $\operatorname{erf}(x) = \frac{2}{\sqrt{\pi}} \int_0^x e^{-t^2} dt$.

Further consider $c(x,t) = c_s$, the following equation can be obtained,

$$x = 2\sqrt{Dt} \quad (11.6)$$

Accordingly, we were able to calculate D at various temperatures according to the slopes of $x \sim t^{1/2}$ plots (Figure 11.7E).³³⁷ These linear plots further indicate that the formation of AuSi_x is

controlled by the Si diffusion process and thus the following Arrhenius equation can be used to describe the activation energy (E_a) of this diffusion process.³³⁸

$$D(T) = D_0 \exp\left(-\frac{E_a}{kT}\right) \quad (11.7)$$

where T is the temperature, D_0 is pre-exponential factor and k is the Boltzmann's constant. The plot of $\ln D(T) \sim 1/T$ was further shown in Figure 11.7F and the calculated activation energy is 1.23 eV. This value is slightly lower than the previously calculated activation energy for the formation of platinum silicide,⁷¹⁻⁷³ which can be explained by the high solubility of silicon atoms in gold.

11.3.5. SERS-based chemical sensing

Controlled annealing of the heterostructures resulted in uniform dispersion of Au nanoparticles on the Si nanowires with specific size, inter-particle spacing and density, which further opens a great opportunity for reproductive and sensitive organic detection based on the Surface-enhanced Raman Spectroscopy (SERS). Various heterostructure samples were dispersed on the oxidized silicon substrate. This was followed by anchoring R6G molecules on the heterostructures as Raman probe. As shown in Figure 11.8A, Raman tests were conducted at various locations along the heterostructures to evaluate their reproducibility and sensitivity. Figure 11.8B further shows the representative optical image of the heterostructures dispersed on the oxidized silicon substrate. The colored spots marked on the nanowire heterostructure represents various locations for Raman test. The resulting Raman signal intensity (estimated for Raman peak of R6G at $\sim 1360 \text{ cm}^{-1}$) for the as-produced Si nanowires, Si nanowire-Au nanoparticle heterostructures before and after annealing at different duration were shown in Figure 11.8C. The columns with different colors for each sample are corresponding to the spots marked in Figure 11.8B. The same test were conducted

on ten nanowires for each sample to evaluate the Raman detection sensitivity. The average intensity values for all the tested spots on these nanowires/heterostructures were summarized in Figure 11.8D.

Representative Raman spectra of R6G for various samples were further shown in Figure 11.8E. No signal of R6G was observed on the blank substrate (without any nanowire heterostructure), indicating the substrate is nearly insensitive for this Raman probe molecules. The as-produced Si nanowires show weak signals for R6G while the signals on the as-produced Si nanowire-Au nanoparticle heterostructures were significantly increased. As described above, such Raman enhancement has been attributed to the presence of localized surface plasmon resonance (LSPR) on Au nanoparticles.³⁻⁶ The heterostructures annealed at 625 °C for 15 min (sample #1) and 45 min (sample #2) show further enhanced Raman signal of R6G due to the reconfiguration (size, inter-particle spacing, and density, see Figure 11.4) of surface nanoparticles. However, the Raman signals on the heterostructures annealed for 75 min (sample #3) and 120 min (sample #4) were decreased as compared with that for 45 min. This can be attributed to the increase of inter-particle spacing (Figure 11.4I) and decrease of particle density (Figure 11.4K) on the Si nanowires. Another possible reason is that after annealing for a long duration (>45 min), most of these Au nanoparticles have been converted to gold silicide and the Au core was nearly disappeared.

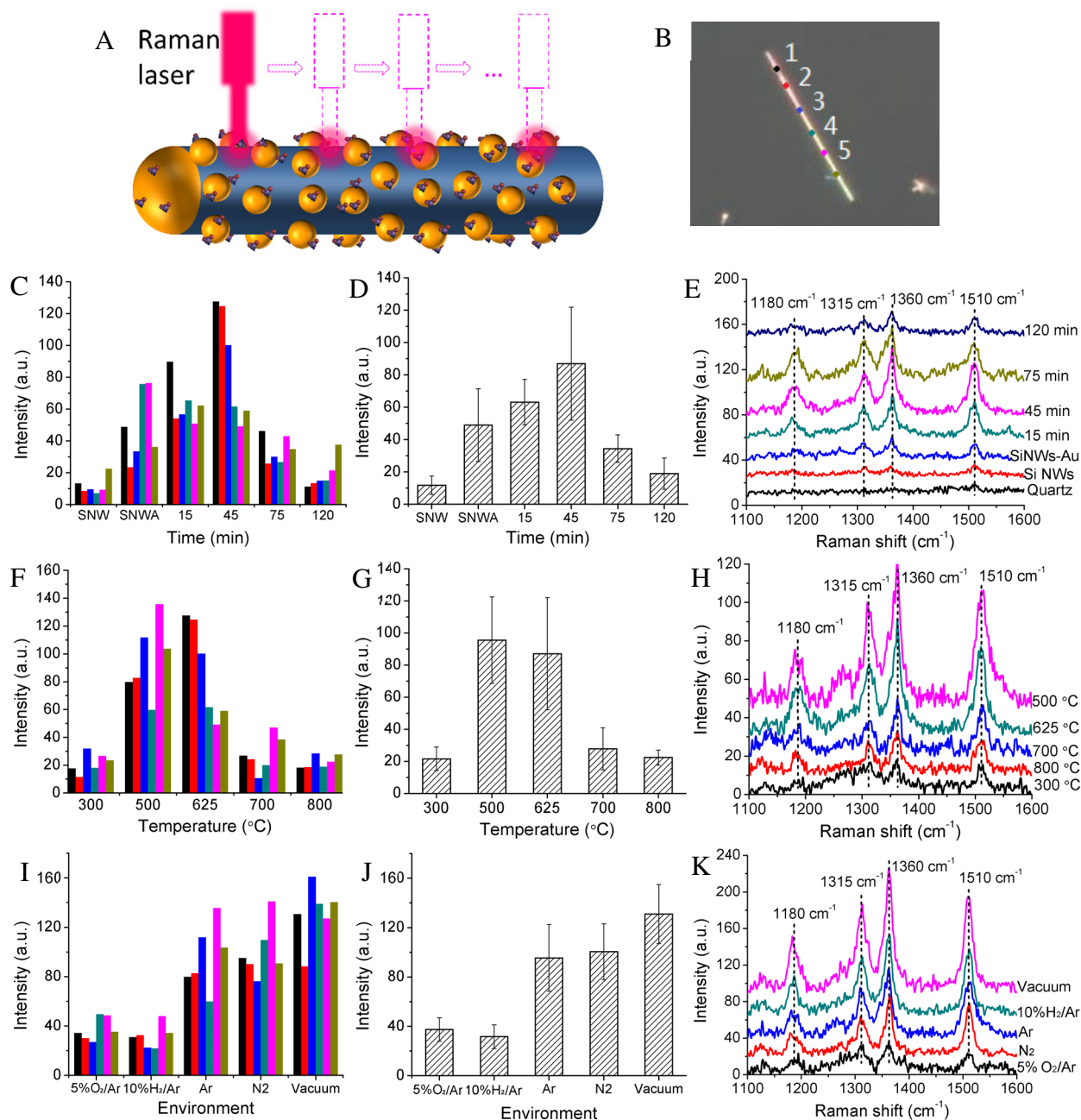


Figure 11.8. (A) Schematic showing the collection of Raman signal along the Si nanowire-Au nanoparticle heterostructures. (B) Optical images of the heterostructures and corresponding spots for the Raman measurement. (C) Intensity of Raman signal for R6G at various spots along the Si nanowires or Si nanowire-Au nanoparticle heterostructures. (D) Average Raman intensity for various samples corresponding to (C). (E) Raman spectra of R6G on samples corresponding to (C). The same Raman test was conducted on samples in the temperature and environment study and the results were shown in (F-H, temperature set) and (I-K, environment set).

The same Raman tests were also conducted on the Si nanowire-Au nanoparticle heterostructures annealed at various temperatures and environments (sample #5-#13). The heterostructures (sample #5) annealed at 300 °C show no obvious enhancement of Raman signal since the size and inter-particle spacing of this sample (Figure 11.5A and I) was not significantly changed as compared with the as-produced heterostructures. The highest Raman enhancement was observed on the heterostructures annealed at 500 °C. This is consistent with that observed in Figure 11.5K, where the highest particle density was observed on the sample annealed at this temperature. These closely located nanoparticles have high possibility to overlap their surface electrical field, which will significantly enhance the Raman spectra of the anchored molecules.³³⁹ The heterostructures annealed at 700 °C and 800 °C show weakened Raman signals than these annealed at 500 °C and 625 °C. This is because the diffusion of silicon in gold nanoparticles was facilitated at high annealing temperature (>700 °C) and most of the particles have converted to silicide.

The heterostructures annealed in the oxygen and hydrogen environments show weak enhancement on the Raman signal while these annealed in inert environments (Ar, N₂, and vacuum) show significant signal improvement (Figure 11.8I). These observations can be explained by the particle configuration (size, inter-particle spacing, and density) showing in Figure 11.6. The heterostructures annealed in oxygen environment resulted in formation of surface SiO₂ and this might shadow the surface plasmon resonance effect of Au nanoparticles.³⁴⁰ For the heterostructures annealed in the hydrogen environment, the existence of H₂ facilitated the diffusion between gold and silicon, resulting Au nanoparticles partially diffused into the Si nanowires. As a result, the particle size becomes small and the Raman enhancement was not significant. The heterostructures annealed in N₂ environment show similar enhancement with that annealed in the Ar environment. Further improved Raman enhancement was observed on these heterostructures

annealed in the vacuum environment. This can be attributed to the relatively small inter-particle spacing of surface nanoparticles that formed during the annealing at low pressure.

11.4. Conclusions

In this paper, we report a facile approach for the fabrication of Si nanowire-Au nanoparticle heterostructures using a wet-chemical nucleation – annealing approach. The surface migration behaviors (including variation of chemical composition and phase transformation kinetics) of Au nanoparticles on the Si nanowire during annealing were further studied in detail. The results indicate that the surface dispersion (size, inter-particle spacing and spatial density) of Au nanoparticles has a significant dependence on the annealing conditions including duration, temperature and environment. TEM and XPS study further show that such high temperature annealing led to significant migration/diffusion of Au nanoparticles and further resulted in the formation of gold silicide in the nanoparticles. Kinetics analysis indicates that this silicide formation process was controlled by the diffusion of silicon atoms in Au nanoparticles. The activation energy for this process is ~ 1.23 eV. For the SERS-based organic detection, Raman enhancement showed a significant dependence on the distribution and chemical state of Au nanoparticles on the heterostructures. Highest Raman enhancement was observed on the heterostructures annealed at 500 °C in Ar for 45 min. This study provides fundamental knowledge on the surface migration and diffusion behavior of Au nanoparticles on Si nanowire at high temperature process and leads to reliable guidance for future development of SERS-based chemical sensors.

CHAPTER 12

HIGHLY-ORDERED GRAPHEN-ENCAPSULATED GOLD NANOPARTICLES FOR SERS SENSING

Yuan Li,¹ Kelly Burnham,¹ John Dykes,¹ Nitin Chopra^{1,2,}*

¹Metallurgical and Materials Engineering Department, Center for Materials for Information Technology (MINT), The University of Alabama, Tuscaloosa, AL 35487, U.S.A.

²Department of Biological Sciences, The University of Alabama, Tuscaloosa, AL 35487, U.S.A.

*Corresponding Author

E-mail: nchopra@eng.ua.edu

Tel: [205-348-4153](tel:205-348-4153)

Abstract

In this paper, we reported a facile cost-effective approach for the fabrication Si substrate supported highly ordered assembly of graphene-encapsulated gold nanoparticles (GNPs) as the SERS substrate. In the first step, gold (Au) nanoparticles with controlled size and inter-particle spacing were uniformly coated on Si substrate through a galvanic deposition – annealing process. Graphene shells with a pristine thickness of ~3 nm were further encapsulated on the Au nanoparticles via the well-defined xylene-based chemical vapor deposition method. The influence of GNPs size and density on the SERS sensitivity was demonstrated. GNPs with optimized size and density were further used to evaluate the detection limit by utilizing R6G solution with different concentration. Moreover, mixture of R6G and MB solution was used to demonstrate the SERS selectivity. To demonstrate the reproducibility of such GNP substrate, electric current was applied to remove the absorbed molecules and the substrate was recycled for further continuous SERS detection.

Keywords: patterned assembly, multilayer graphene shell encapsulated gold nanoparticles, galvanic deposition, annealing, chemical vapor deposition (CVD), surface enhanced Raman spectroscopy (SERS)

12.1. Introduction

Surface enhanced Raman spectroscopy (SERS) has been considered to be one of promising techniques in molecular detection. By exciting the surface plasmon resonance on noble metal nanoparticles, the Raman signal for low concentration molecular can be significantly increased. It is reported that the enhancement factor (EF) of SERS molecular detection can be as high as 10^{14} - 10^{15} . Coinage metals such as gold, silver, and copper were usually used as the preferred Surface Enhanced Raman Scattering (SERS) substrate in the form of rough surface and nanoscale structures³⁴¹. The enhancement of Raman signal is believed to be originated from the interaction between metallic substrate and absorbed target molecules under the electromagnetic field generated by Raman laser, which is normally called Localized Surface Plasmon Resonance (LSPR).³⁴² LSPR can be simply tuned by controlling the size, shape, and distribution of nanoparticles,³⁴³ as well as using effective supporting substrate.

The major challenge in practical application of surface enhanced Raman scattering (SERS) sensing lies in the low uniformity, poor reproducibility and limited selectivity. Recently graphene was proposed as a promising substrate for uniformly dispersing the coinage metal nanoparticles for SERS sensing. Graphene itself was also demonstrated as an effective SERS substrate due to the ability to absorb and concentrate target molecules. The abundant graphene-molecule interactions result in significantly increased sensitivity based on the chemical enhancement mechanism and further give such graphene-based Raman sensor good molecule selectivity.

Herein we proposed a facile cost-effective approach to fabricate Si substrate supported highly ordered assembly of graphene-encapsulated gold nanoparticles (GNPs) as the SERS substrate. The gold nanoparticles (Au nanoparticles) with controlled size and inter-particle spacing were uniformly coated on Si substrate through a galvanic deposition – annealing process. Graphene

shells with a pristine thickness of ~3 nm were further encapsulated on the Au nanoparticles via the well-defined xylene-based chemical vapor deposition method. The influence of GNPs size and density on the SERS sensitivity was demonstrated. GNPs with optimized size and density were further used to evaluate the detection limit by utilizing R6G solution with different concentration. Moreover, mixture of R6G and MB solution was used to demonstrate the SERS selectivity. To demonstrate the reproducibility of such GNP substrate, electric current was applied to remove the absorbed molecules and the substrate was recycled for further continuous SERS detection.

12.2. Experimental section

Materials and Methods: Silicon (Si) wafers (111) were purchased from IWS (Colfax, CA). Potassium gold (III) chloride was purchased from Sigma-Aldrich (St. Louis, MO). Hydrogen fluoride (50%) was purchased from VWR (Atlanta, GA). Ammonium fluoride was purchased from Alfa Aesar (Ward Hill, MA). Xylene used for CVD growth of graphene was purchased from Fisher Scientific (Pittsburg, PA). Rhodamine 6G (R6G) and Methylene blue (MB) were purchased from Alfa Aesar (Ward Hill, MA). All chemicals were used without further purification. Buffered oxide etch (BOE) solution was prepared by mixing 40% NH₄F and 50% HF in DI-water at a volume ratio of 6:1. DI water (18.1 MΩ-cm) was obtained using a Barnstead International DI water system (E-pure D4641). High-temperature annealing was done using a CMF 1100 oven furnace (MTI Corporation). Graphene growth was carried out in a Lindberg blue three-zone tube furnace (Watertown, WI) with a quartz tube from ChemGlass (Vineland, NJ). The gas flow rates were controlled by Teledyne Hasting powerpod 400 mass flow controllers (Hampton, VA). H₂ (10% in Ar), N₂, and Ar gas cylinders were purchased from Airgas South (Tuscaloosa, AL). Plasma treatment was performed in a Nordson March Jupiter III Reactive Ion Etcher (Concord, CA).

Gold (Au) nanoparticles dispersion on Si wafer: A layer of gold film was first deposited onto the Si wafer by a typical galvanic deposition process as reported before. [344,345] Briefly, Si wafers were cleaned in acetone for 10 min with sonication. The wafer was further treated in BOE solution for 30 s to remove the surface oxide layer. This was followed by directly putting the wafer in the galvanic deposition solution (1 mM KAuCl_4 + 1% HF) for 1 min. The film was rinsed with DI-water and dried in flowing N_2 . Continuously, the sample was put in an oven box and annealed for 10 min at 850 °C to form dewetted Au nanoparticles.

Graphene growth on Au nanoparticles: Growth of graphene on the Au nanoparticles was conducted using a xylene-based Chemical Vapor Deposition (CVD) process as reported before [346,347]. Briefly, the Au nanoparticles dispersed on the Si wafer were oxidized under oxygen plasma for 15 min to produce a gold oxide layer (power: 160 W; oxygen pressure: 600 mTorr). The samples after plasma oxidation were put in the center of the quartz tube furnace. The growth process was carried out at 675 °C for 1 h. Xylene was used as the carbon source with a feeding rate of 10 mL/h, which was carried by 10% H_2/Ar with a total flow rate of 1.15 SLM. To create carboxyl groups on the surface of graphene shell, the as-produced graphene was either treated with oxygen plasma for 15 s (power 120 W, oxygen pressure 300 mTorr) or treated in 3 M HNO_3 solution for 5 h at 80 °C.

Dyes anchoring on Au nanoparticles and GNPs: The pristine Au nanoparticles and GNPs dispersed on Si wafer were used as the SERS substrate for MB and R6G detection. The nanostructures were first treated in BOE solution for 10 s to create surface Au-H bonds, which can largely increase the efficiency of MB/R6G absorption on the SERS substrate. After being dried in flowing N_2 , the sample was kept in MB or R6G solution with different concentration overnight (10 h) with slight agitation. Then the nanostructures were washed with DI-water and dried in N_2 .

Characterization methods: FE-SEM (JEOL-7000) and Tecnai F-20 TEM were used to characterize the morphology and structure of Au nanoparticles, GNPs and that after plasma treatment. Raman spectra were collected using a BrukerSenterra system (Bruker Optics Inc. Woodlands, TX) equipped with a 785 nm laser source at 10 mW laser power. The integral time and co-additions were set as 15 seconds and 2, respectively. XRD

12.3. Results and discussion

12.3.1. Fabrication and patterning of Au nanoparticles and GNPs on the silicon substrate

The fabrication and patterning of Au nanoparticle and GNPs on the Si substrate were conducted *via* the process described in Figure 12.1A, which shows the procedures for the fabrication of assembly of multilayer graphene shells encapsulated on gold (Au) nanoparticles for Surface-enhanced Raman Spectroscopy (SERS): (1) galvanic deposition, (2) annealing, (3) chemical vapor deposition (CVD) of multilayer graphene shells, (4) oxygen plasma treatment. (b-d) Schematic showing the basic principle of (b) galvanic deposition, (c) CVD, (d) molecule detection using SERS. The Au film or nanostructures obtained at various fabrication stages were characterized for their morphology, structure and chemical composition. The sample labeling was further shown in Table 12.1. Figure 12.1B further shows the basic principle for the galvanic deposition process, which involves the replacement reaction between the silicon substrate and the Au³⁺ in the HF-containing solution. Figure 12.1C illustrated the xylene based chemical vapor deposition process for the growth of multilayer graphene shell on the surface of Au nanoparticles and Figure 12.1D shows the Surface-enhanced Raman Spectroscopy (SERS)-based Raman sensing on these patterned GNP substrate.

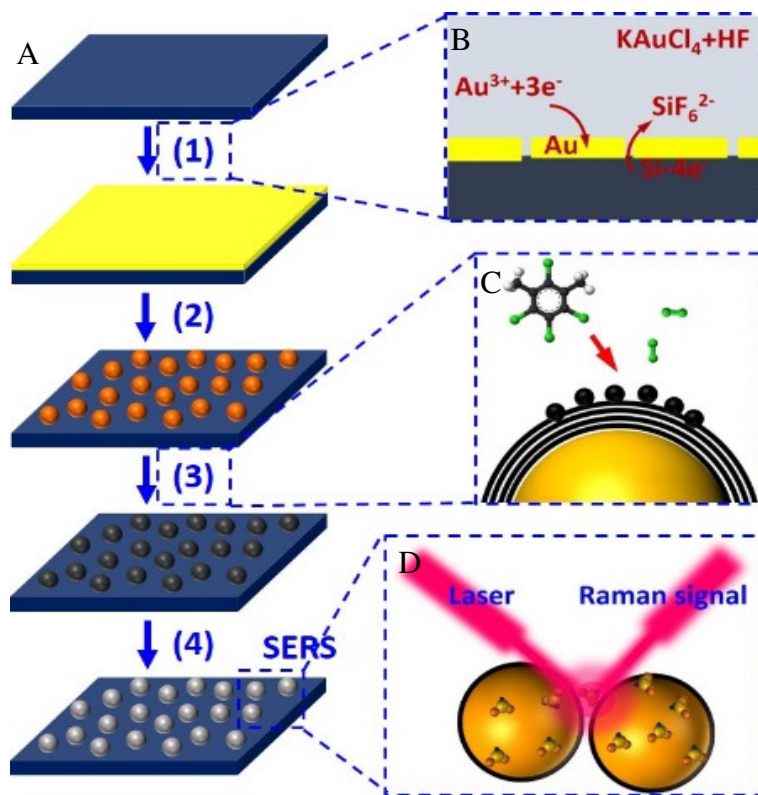


Figure 12.1. (a) Schematic showing the procedures for the fabrication of assembly of multilayer graphene shells encapsulated on gold (Au) nanoparticles for Surface-enhanced Raman Spectroscopy (SERS): (1) galvanic deposition, (2) annealing, (3) chemical vapor deposition (CVD) of multilayer graphene shells, (4) oxygen plasma treatment. (b-d) Schematic showing the basic principle of (b) galvanic deposition, (c) CVD, (d) molecule detection using SERS.

Table 12.1. Labeling of various samples in this study according to different galvanic deposition time for preparation of Au film.

Samples	Galvanic deposition time (min)				
	0.5	1	3	5	7
Au film	A1	A2	A3	A4	A5
Au nanoparticles	B1	B2	B3	B4	B5
As-produced GNP	C1	C2	C3	C4	C5
Plasma-treated GNP	D1	D2	D3	D4	D5

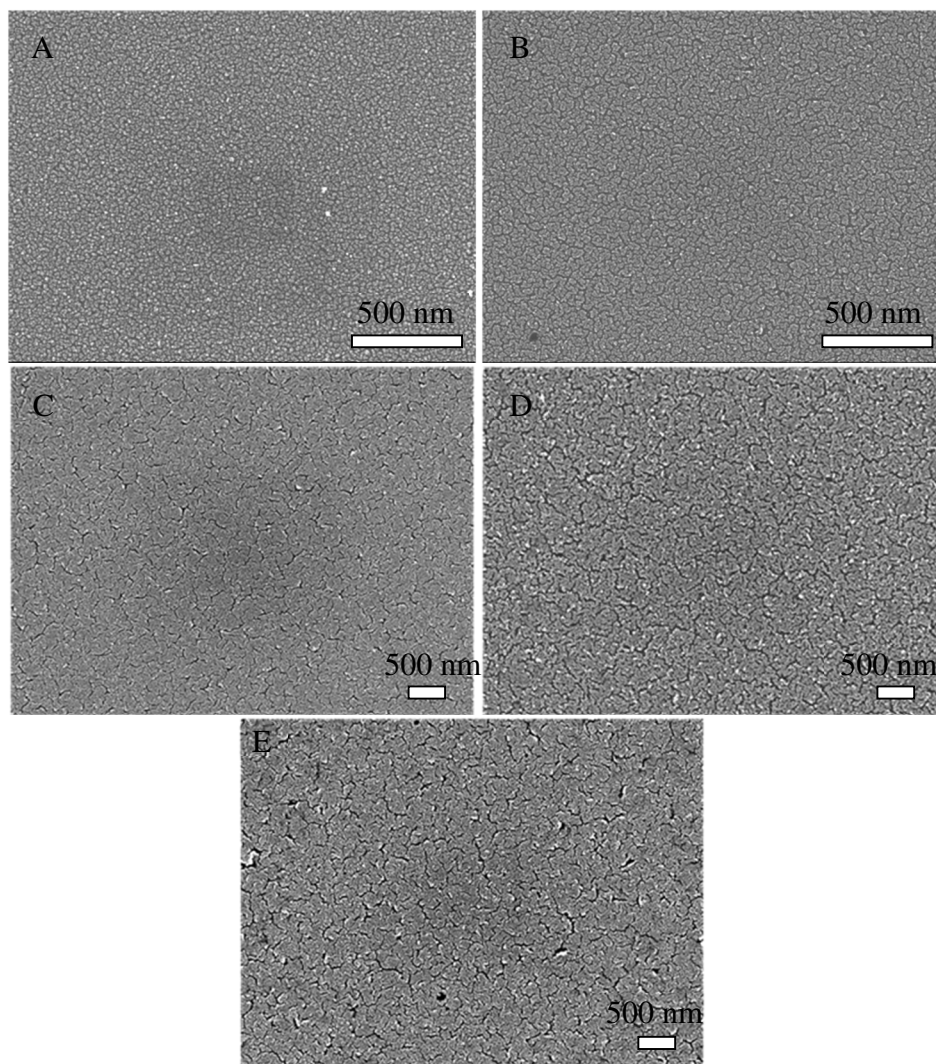


Figure 12.2. SEM images of Au film prepared by galvanic deposition at various deposition times: (A) 0.5 min, (B) 1 min, (C) 3 min, (D) 5 min, and (E) 7 min.

SEM images of the Au film prepared by the galvanic deposition process were shown in Figure 12.2. Various Au films with different thickness were obtained by varying the duration of galvanic deposition. Figure 12.2 illustrates that the Au film with a flat surface were uniformly deposited on the surface of silicon substrate. Short galvanic deposition time such as 0.5 min and 1 min lead to small crystal grains with little interstice or cracks between them. When the galvanic deposition time was increased to 5 min or 7 min, the grain size obviously increased, with large cracks

observed among these crystal grains. These cracks have been demonstrated to play a critical role during the following high temperature annealing or dewetting process. Figure 12.3A shows the XRD spectra of the Au films according to their galvanic deposition time. The dominant Au (111) peak was observed consistently for all the samples while a small Au (200) peak was also observed. The increased of the Au peaks with the increase of galvanic deposition time is due to the increased of film thickness, which is further demonstrated in Figure 12.3B. The film thickness was evaluated by the equivalent volume estimated from the size and spatial density of Au nanoparticles obtained in the following annealing process. A linear trend of film thickness as a function of galvanic deposition time was observed in Figure 12.3B, indicating the formation of Au film have no significant effect on the contact of electrolyte and the silicon substrate due to the existence of inter-grain cracks and this wet-chemical deposition process is continued uniformly with 7 min. This is critical for the control of particle size by simply varying the galvanic deposition time.

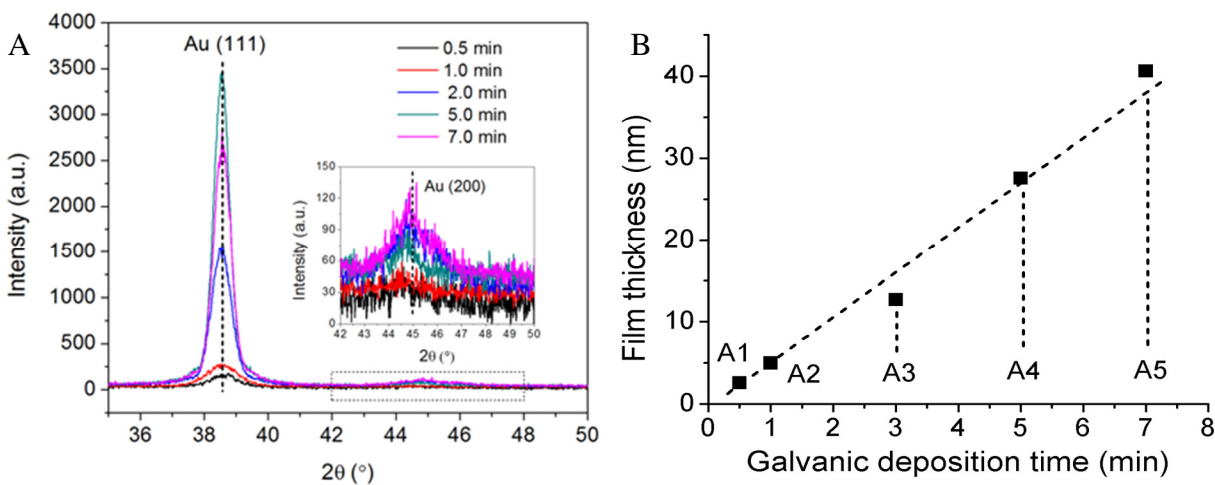


Figure 12.3. (A) XRD patterns for the as-deposited Au films corresponding to Figure 12.2. (B) Au film thickness calculated according the density and size of Au nanoparticle in Figure 12.4.

Figure 12.4A-E show the SEM images of the Au nanoparticles patterned on the silicon substrate. The size and spatial density control of these Au nanoparticle samples were achieved by varying the galvanic deposition time as we stated above. From these SEM images we can observe that the Au nanoparticles are uniformly dispersed on the substrate with equally increased size and spatial density, indicating such galvanic deposition – annealing approach is a simple and effective method for patterning Au nanoparticle on the Si substrate. The following graphene growth on the Au nanoparticles were conducted via a xylene based chemical vapor deposition process. Briefly, the Au nanoparticles were first surface-oxidized in an oxygen plasma chamber. These surface oxide layer has been considered to take a function of catalysis for the formation of initial carbon layers. The resulting graphene shell encapsulated Au nanoparticles (referred as graphene nanoparticle or GNPs) patterned on the silicon substrate were shown in Figure 12. 4F-J.

The corresponding high resolution SEM images were also shown in these insets. We observed that GNPs were also uniformly patterned on the substrate and a carbon shell is closely encapsulated on the surface of Au nanoparticles. High resolution TEM images were collected for the as-produced GNPs, as shown in Figure 12. 5A-E. Low energy Au (111) plane was consistently observed for the Au nanoparticles and lattice spacing of 0.37~0.38 nm was estimated for these graphene shells. This lattice spacing is slightly larger than the c-axis spacing of graphite (~0.34 nm), indicating the curvature structure of graphene shell introduced extra strain between the lattice and changed the atom arrangement. It needs to mention here that the as-produced GNPs is highly hydrophobic and lack of surface functionality for further surface decoration or anchoring probe molecules. Meanwhile, extra amorphous carbon was always produced as by-product during the CVD process and the as-grown graphene is relatively too thick, which may hinder the optical properties of the Au core. As a result, the subsequent plasma treatment process is essential (Figure 12. 5F-J).

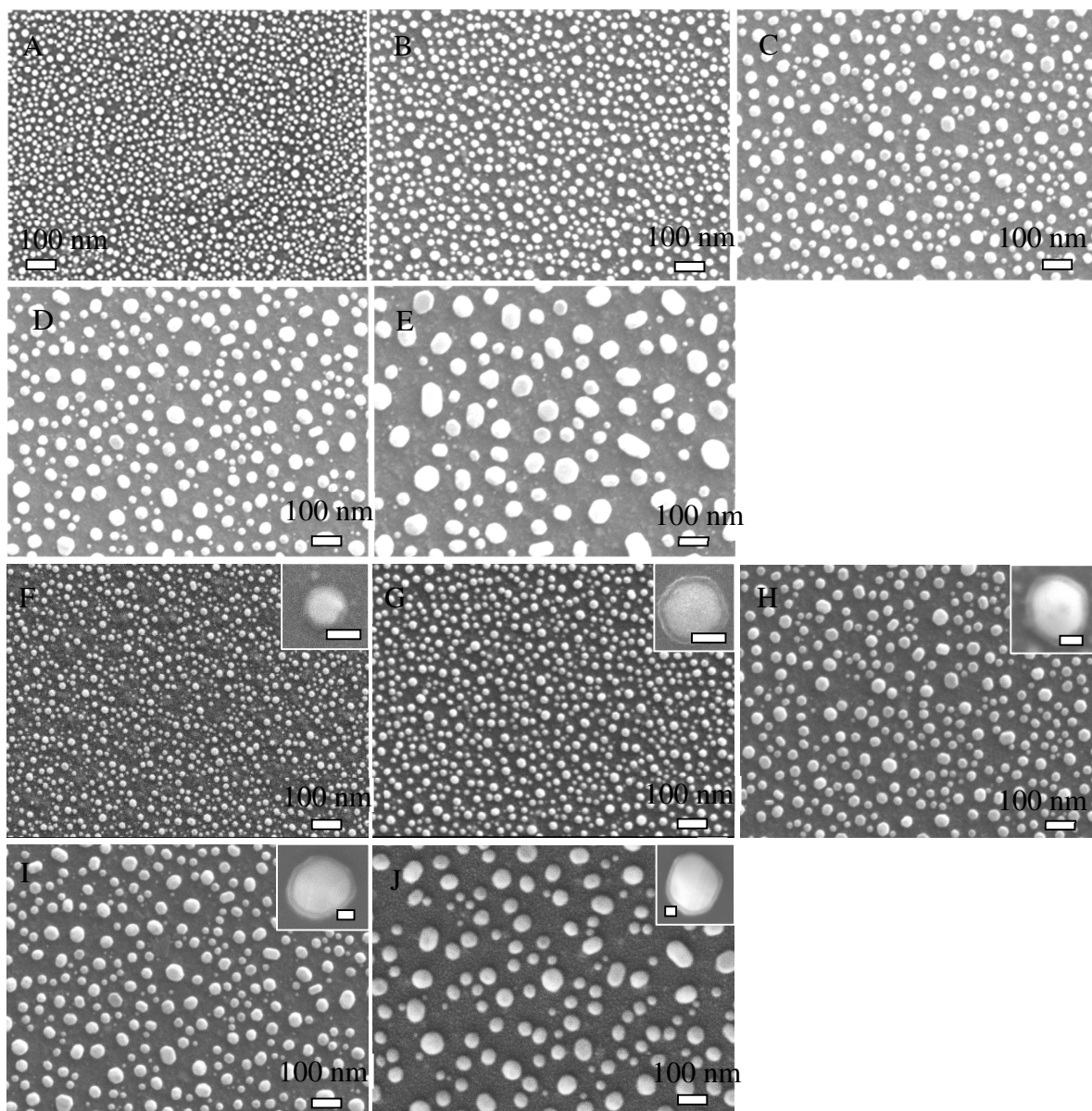


Figure 12.4. SEM images of Au nanoparticles obtained by annealing various Au films corresponding to Figure 12.1: (A) 0.5 min, (B) 1 min, (C) 3 min, (D) 5 min, (E) 7 min. SEM images of multilayer graphene shells encapsulated Au nanoparticles (GNPs) with different size corresponding to Figure 12.3: (F) 0.5 min, (G) 1 min, (H) 3 min, (I) 5 min, (J) 7 min. *Note: The insets in (B) and (E) show the representative SEM images for a single GNP (scale bar: 20 nm).*

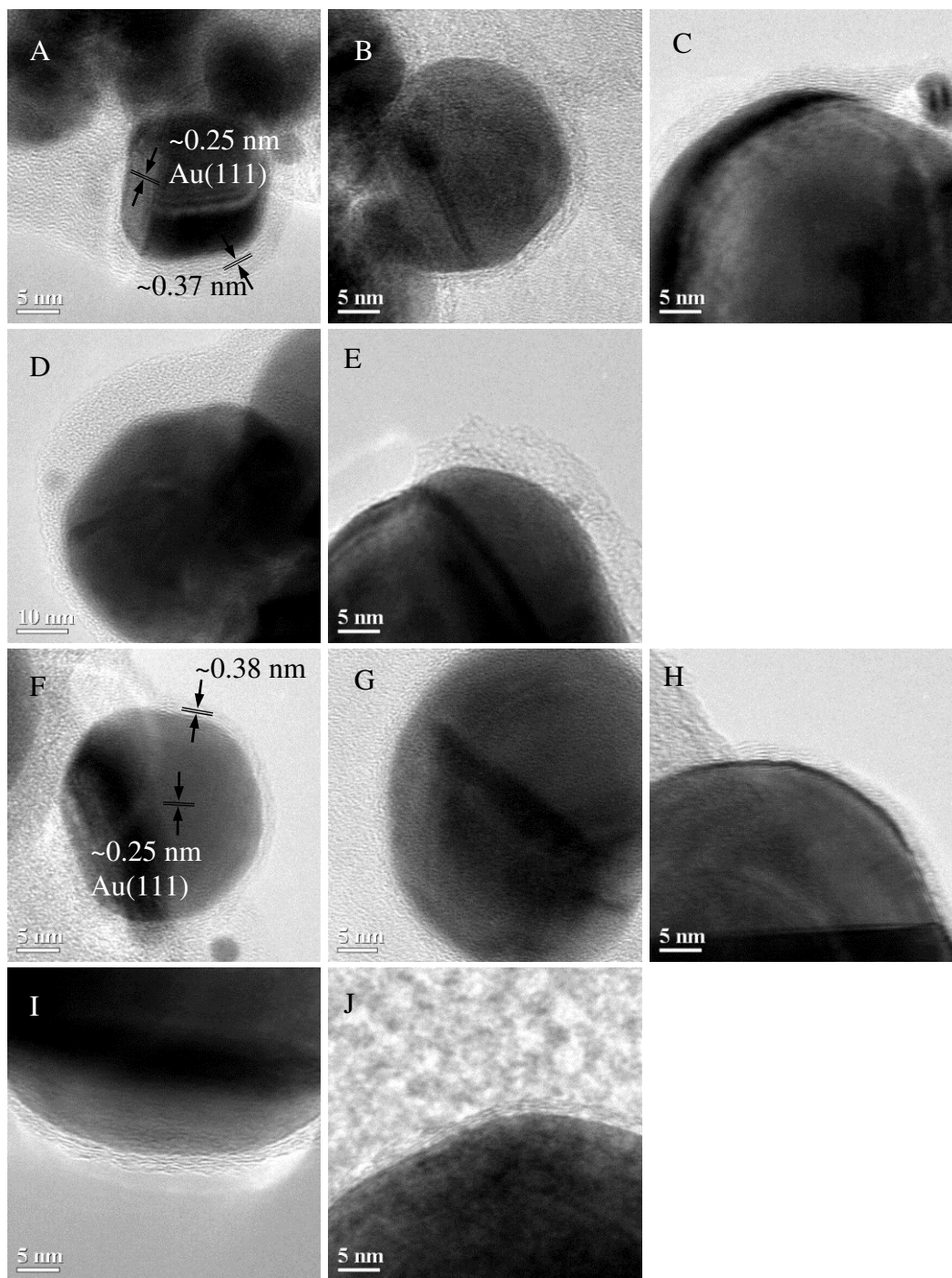


Figure 12.5. TEM images of the as-produced (A-E) GNPs and (F-J) plasma-treated GNPs. These samples are corresponding to various galvanic deposition time: (A,F) 0.5 min, (B,G) 1 min, (C,H) 3 min, (D,I) 5 min, (E,J) 7 min.

The variation of size, inter-particle spacing and spatial density as a function of the initial galvanic deposition time for the Au nanoparticles and GNPs were summarized in Figure 12.6A-C. The size of Au nanoparticles and GNPs presents a linear increase trend with the increase of galvanic deposition time, indicating the galvanic deposition of Au film was uniformly continued within 7 min. The average size of Au nanoparticles is larger than the corresponding GNPs, which is due to the inevitable evaporation of Au nanoparticles during the high-temperature CVD process. The trend observed for the inter-particle spacing is consistent with that for size. As shown Figure 12.6C, the spatial density of Au nanoparticles decreased as the increase of galvanic deposition time, indicating the dewetting of Au film during the annealing has a large dependence on the film thickness. This is mainly due to the inter-grain cracks formed during the galvanic deposition, which actually divided the Au film into numerous of micro islands, and finally decided the size of Au nanoparticles. The spatial density of GNPs decreased as compared with the corresponding Au nanoparticles. Since the size of GNPs also decreased as compared with pristine Au nanoparticle, we can't simply attributed the loss of density to the merge of Au nanoparticle during the CVD process. The density loss is actually a comprehensive result of particle merge and evaporation.

The variation of graphene shell thickness before and after plasma treatment was demonstrated in Figure 12. 6D. We observed that with the increase of particle size, the graphene shell thickness presents an increase general trend. This phenomenon can also be explained by the curvature structure of graphene shell. Large curvature shell on the small Au nanoparticles introduced high strain energy within the graphene shells. As a result, large lattice mismatch presented within the graphene layers, which will make the deposition of further graphene layer difficult and rendering a thin shell. However, large particles shows small curvature, leading to less lattice mismatch and is favorable for the continuous deposition of graphene layers.

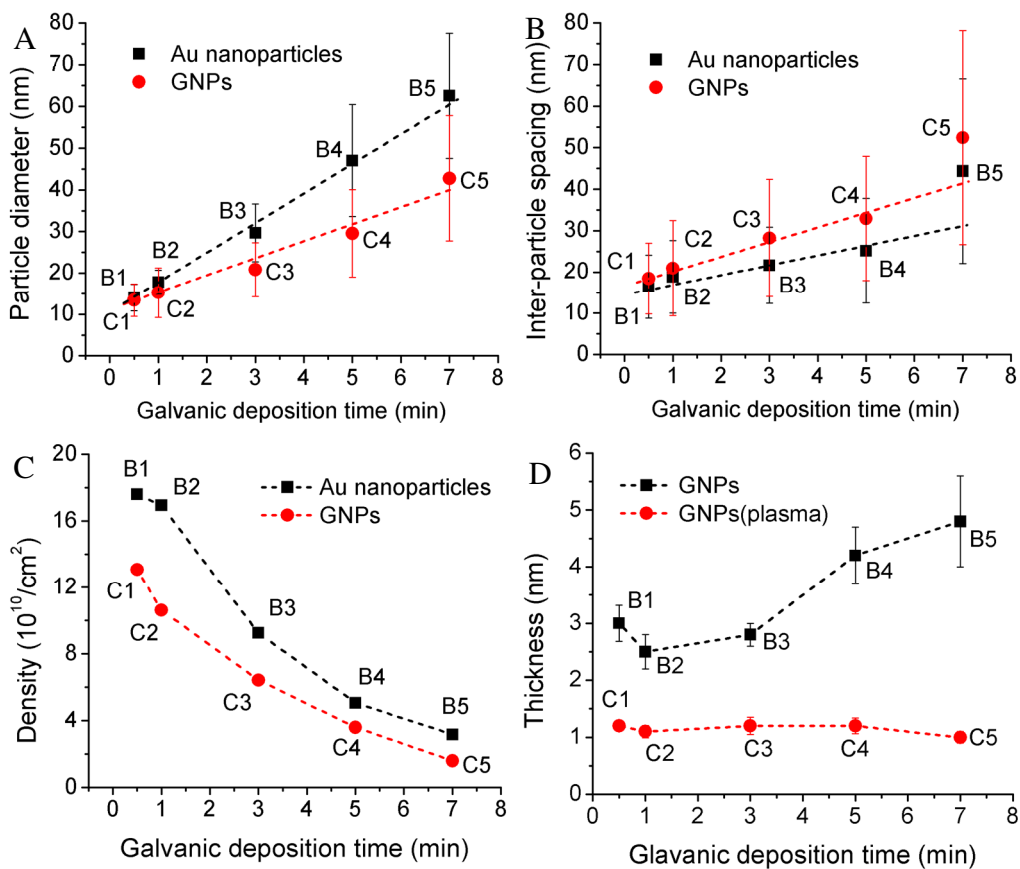


Figure 12.6. (A-C) Variation of particle size (A), inter-particle spacing (B), and particle density (C) for the Au nanoparticles and GNPs according to the galvanic deposition time. (D) Variation of thickness of the multilayer graphene shells before and after oxygen plasma treatment.

12.3.2. SERS sensing on the patterned substrate

To evaluate the Raman detection efficiency of these Au nanoparticles and plasma-treated GNPs samples, R6G and MB were used as the Raman probes, which were first dispersed in DI-water with a concentration of 10^{-6} M. The Au nanoparticles or GNPs decorated substrates were then immersed in this dye-containing solution overnight for the absorption of these probe molecules onto the Au nanoparticle or GNP targets. Raman spectra were collected directly in the washed and dried Au nanoparticle or GNP substrate. The representative Raman spectra were shown in Figure

12.7. As shown in Figure 12.7A and B, small Au nanoparticle substrate (sample #B1) shows no obvious signals for R6G and MB. However, the intensity of Raman signals increased as the increase of particle size (Sample #B2 and #B3). This have been approved by the theoretical modeling of plasmonic properties of the Au nanostructures previous completed by our group. Such plasmonic modeling indicates that the electric field generated on or near the surface of nanostructures has a large size dependence. With the increase of particle size, the electric field generated on the particle surface was significantly improved.

Another reason for the Raman enhancement is the overlapping of electric field, which resulted in significantly enhanced localized surface plasmon resonance (LSPR). Since the basic Raman enhancement mechanism is based on the LSRP, the overlapping of electric field will be a direct contribution to the signal capture and magnification. Further increase of the particle size leads to the decrease of Raman signals (sample #B4 and #B5), which is mainly due to the larger inter-particle spacing between the Au nanoparticles and GNPs, resulted in less overlapping of electric field for the plasmon enhancement. Almost the same trend was observed for the signals of R6G and MB on the GNPs substrate. As shown in Figure 12. 7C, small GNP substrate only shows the G-band and D-band for graphene shells. The highest Raman enhancement was observed on sample #D3. Further increased GNP size gives much weakened Raman signals similar to what we described above. However, for the detection of MB using the GNP substrate (Figure 12.7D), sample #D3 exhibited the highest Raman signal but equivalent Raman enhancement was also observed for the other samples. This is mainly due to the effective absorption of MB molecules on the graphene shells. In addition, the overall Raman signals observed on the GNP substrate is much weaker than that on the Au nanoparticle substrate mainly due to the less absorbed dye molecules.

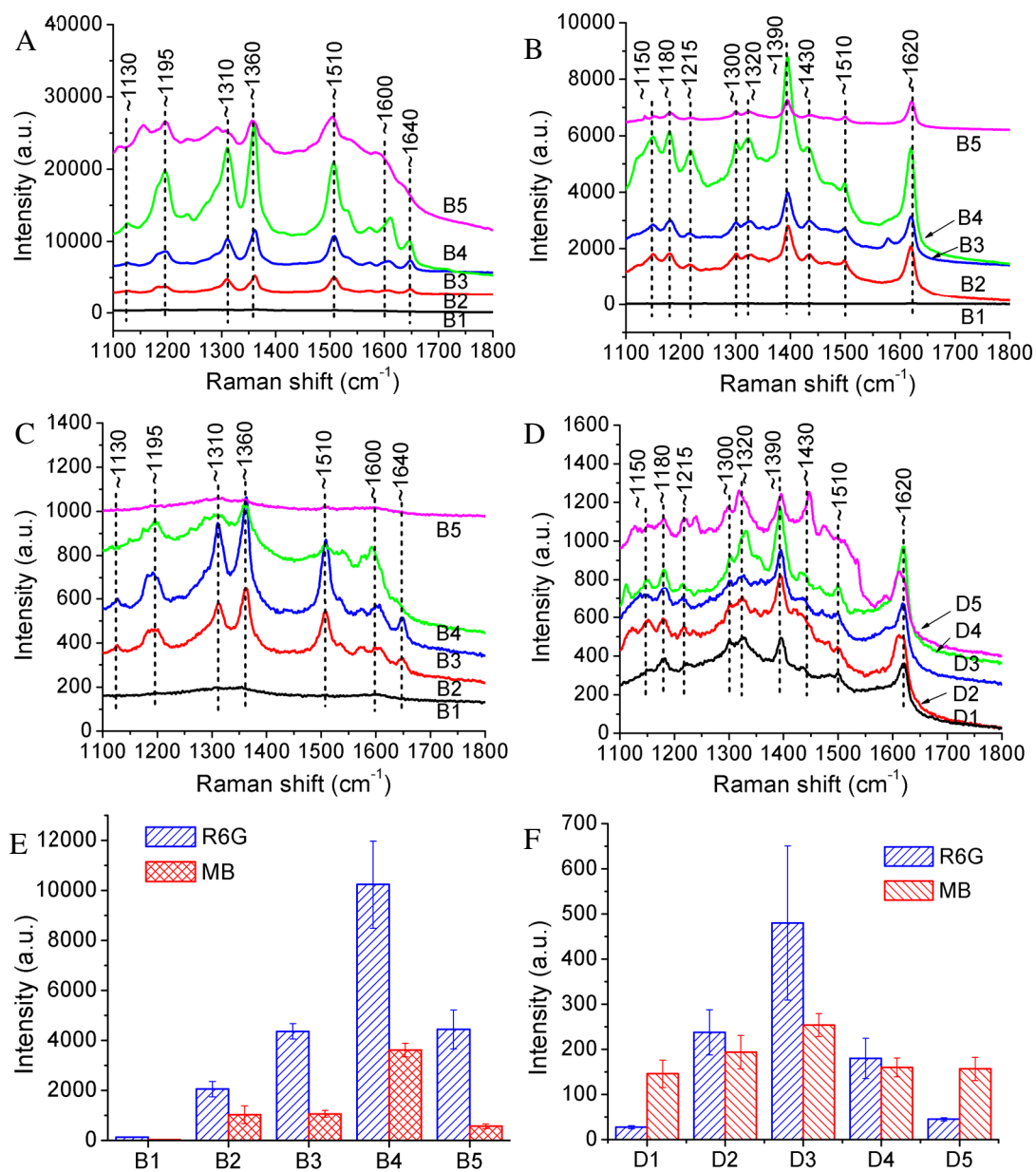


Figure 12.7. (A, B) SERS spectra of R6G (A) and MB (B) on the Au nanoparticle samples corresponding to various galvanic deposition time. (C, D) SERS spectra of R6G (C) and MB (D) on the GNP samples corresponding to various galvanic deposition time. (E) Average Raman intensity of R6G and MB corresponding to A and B. (F) Average Raman intensity of R6G and MB corresponding to C and D. *Note: The peak locations (cm⁻¹) were mark on the top of these spectra. The Raman intensity of R6G was estimated to the peak centered at ~1360 cm⁻¹ and that of MB was estimated using the peak centered at 1390 cm⁻¹.*

The influence of dye concentration in DI-water was further demonstrated. Various concentrations of MB were prepared and the same Raman process was conducted. The obtained spectra were shown in Figure 12.8A and B for Au nanoparticles and GNPs, respectively. The average Raman intensity (Figure 12.8C) was estimated using the peak located at 1390 cm^{-1} . We observed that the Raman intensity presented a linear trend as a function of concentrations. Such linear trend will be of great importance for the application of SERS device for real molecule detection.

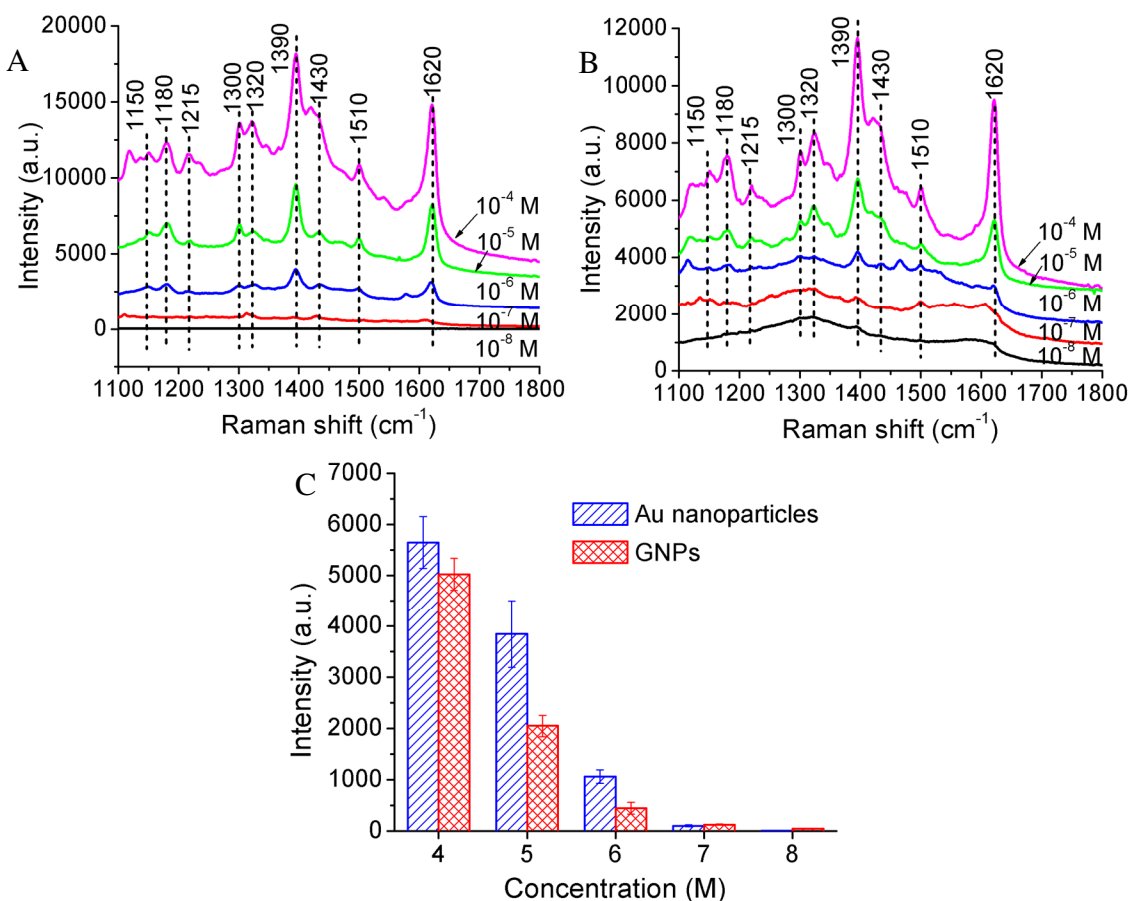


Figure 12.8. (A,B) SERS spectra of MB. These spectra correspond to the Au nanoparticle (A) and GNP (B) samples immersed in MB solution with various concentration. The peak locations (cm^{-1}) were mark on the top of these spectra. (C) Average Raman intensity MB corresponding to A and B. Note: The Raman intensity of MB was estimated using the peak centered at 1390 cm^{-1} .

12.3.3. Evaluation of selectivity and enhancement factor

The selectivity of Au nanoparticle and GNP substrate was demonstrated using a mixture of 10^{-6} MB and 10^{-6} R6G. The substrates were immersed in the mixture overnight for the competitive absorption of R6G and MB molecules. Since Au nanoparticle sample #B4 and GNP sample #B3 exhibited the highest Raman enhancement for both R6G and MB, the selectivity test was conducted on sample #B3, #B4, #D3 and #D4. The Raman spectra for R6G and MB were shown in Figure 12.9A. As we can observe, the main signals observed are for MB while the signal of R6G are very weak. The corresponding Raman intensity was further summarized in Figure 12.9B. Both Au nanoparticle and GNP substrates exhibited much higher Raman enhancement for MB than that for R6G. As shown in the inset, the selectivity of GNP is much higher than that of Au nanoparticles. This is mainly attributed to the structure of MB molecules, which are much easier to be absorbed on the substrate with proper orientation. Moreover, the hexagonal structure of MB is similar to that of graphene structure, making it is prone to be absorbed on GNPs.

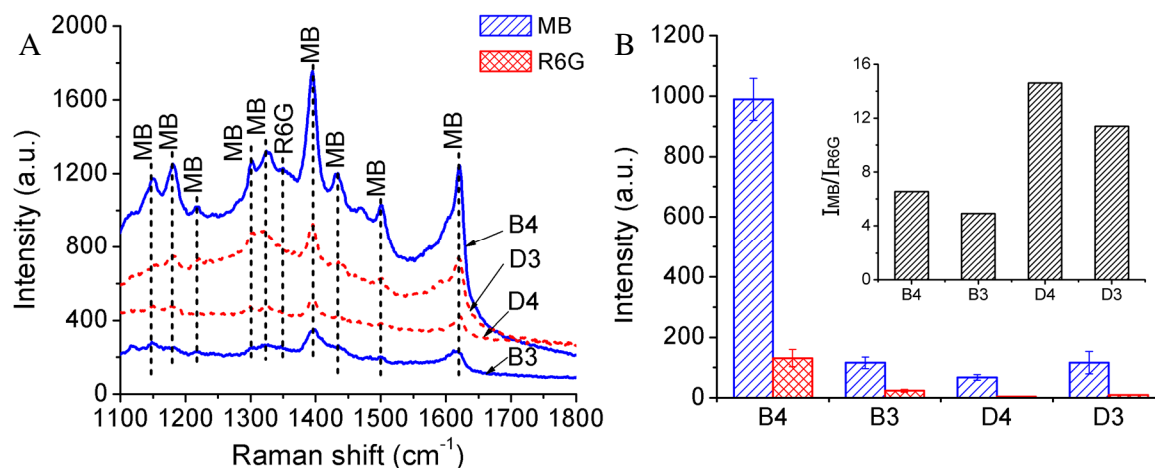


Figure 12.9. (A) SERS spectra of MB and R6G obtained on Au nanoparticles and GNPs immersed in a mixture of 10^{-6} M R6G and 10^{-6} M MB. (B) Average Raman intensity MB and R6G corresponding to A. The inset further shows the intensity ratio of MB and R6G.

The evaluation of enhancement factor (EF) are based on the well-defined equation as follows:

$$EF = \frac{I_{SERS}}{N_{SERS}} / \frac{I_{bulk}}{N_{bulk}} \quad (12.1)$$

where I_{SERS} and I_{bulk} indicate the Raman intensity obtained on the nanostructures decorated substrate and that obtained on the bulk MB solution, respectively, meanwhile, N_{SERS} and I_{bulk} indicate the number of molecules used for the generation of Raman signal, respectively. Figure 12.10A shows the digital image of the 10^{-6} M MB solution before and after the absorption of Au nanoparticle and GNP substrates. The color of solution (2) after the absorption of Au nanoparticle for overnight become light, indicating the intensive absorption of MB molecules on this substrate. Meanwhile, the absorption on the GNP substrate is much less since no significant color change was observed for solution (3) as compared with the pristine MB solution (1). This was further confirmed by the UV-vis spectra in Figure 12.10B. As the peak intensity for solution (2) is much weaker than that of the other two. The Raman signal of the bulk MB solution was shown in Figure 12.10C, where very weak signals were observed for the bulk MB solution. This is another contrast for above observed Raman enhancement. Using this spectra we calculated the enhancement factor according to above EF equation. The result for sample #B3 and #D3 were shown in Figure 12.10D. The estimated EF for #B3 is 4.88×10^5 and for #D3 is 6.87×10^5 , respectively. This EF data is of importance since they indicate that GNPs naturally show better Raman enhancement than the Au nanoparticles. The higher experimental Raman intensity observed for Au nanoparticle substrate is mainly due to the large amount of molecules absorbed on their surface. This study provides unique approach for the fabrication and patterning of Au nanoparticles as well as GNPs on the substrate and fundamental understanding of SERS effect of graphene encapsulated Au nanoparticles.

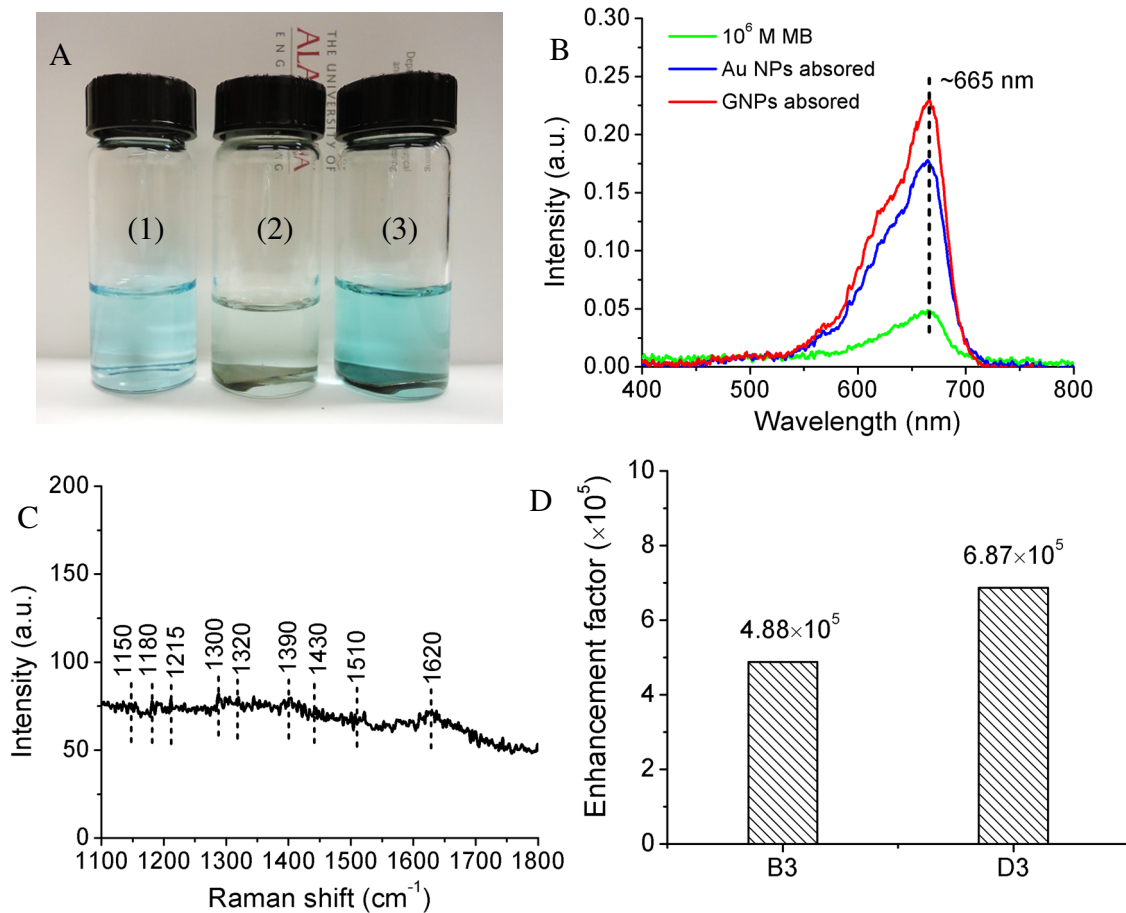


Figure 12.10. (A) Digital image showing (1) pristine MB solution (10^{-6} M), (2) MB solution after immerse Au nanoparticle sample (B3) for 10 h, and (3) MB solution after immerse GNPs sample (D3) for 10 h. (B) UV-vis spectra of MB solution corresponding to (A). (C) Representative Raman spectra of 10^{-6} M MB in DI-water. (D) Calculated enhancement factor for Au nanoparticles (B3) and GNPs (D3).

12.4. Conclusions

To sum up, we reported a facile cost-effective approach to fabricate Si substrate supported highly ordered assembly of graphene-encapsulated gold nanoparticles (GNPs) as the SERS substrate. The gold nanoparticles (Au nanoparticles) with controlled size and inter-particle spacing were uniformly coated on Si substrate through a galvanic deposition – annealing process. Graphene shells with a pristine thickness of ~3 nm were further encapsulated on the Au nanoparticles via the well-defined xylene-based chemical vapor deposition method. The influence of GNPs size and density on the SERS sensitivity was demonstrated. GNPs with optimized size and density were further used to evaluate the detection limit by utilizing R6G solution with different concentration. Moreover, mixture of R6G and MB solution was used to demonstrate the SERS selectivity. The Au nanoparticle and GNP substrates show preferred Raman selectivity of MB instead of R6G. The estimated enhancement factor for these samples are around 10^5 . GNPs naturally show better Raman enhancement than the Au nanoparticles. The higher experimental Raman intensity observed for Au nanoparticle substrate is mainly due to the large amount of molecules absorbed on their surface. This study provide unique approach for the fabrication and patterning of Au nanoparticles as well as GNPs on the substrate and fundamental knowledge to the SERS sensing based on the patterned Au nanoparticle and GNPs.

CHAPTER 13

GROWTH AND DECORATION OF SILICON NANOWIRES WITH GRAPHENE-ENCAPSULATED GOLD NANOPARTICLES FOR SURFACE-ENHANCED RAMAN SENSING

Yuan Li,¹ Nitin Chopra^{1,2,}*

¹Metallurgical and Materials Engineering Department, Center for Materials for Information Technology (MINT), The University of Alabama, Tuscaloosa, AL 35487, U.S.A.

²Department of Biological Sciences, The University of Alabama, Tuscaloosa, AL 35487, U.S.A.

*Corresponding Author

E-mail: nchopra@eng.ua.edu

Tel: [205-348-4153](tel:205-348-4153)

Abstract

In this paper, we reported a fundamental study on morphological and structural evolution of gold nanoparticles onto silicon nanowires by combining chemical vapor deposition method with wet-chemical synthesis followed by high temperature treatment. The latter step led to controlled spatial densities, inter-particle spacing, and diameters of gold nanoparticles on high curvature silicon nanowires. The encapsulation of multilayer graphene shell the decorated gold nanoparticles were further achieved via a xylene-based chemical vapor deposition process. This lead to the preparation of graphene nanoparticles (GNPs) decorated silicon nanowire heterostructures with unique plasmonics, chemical and electronic properties. These nanowire heterostructures were characterized using high-resolution electron microscopy, X-ray photoelectron spectroscopy, and Raman spectroscopy. Raman active organic molecules were further studied for Raman signal enhancement using the developed silicon nanowire-gold nanoparticle or GNP heterostructures, and improved sensitivity and detection limits were observed. Such controlled nanowire heterostructures with significant plasmonic activities hold promise for the future of analytical devices as well as NEMS/MEMS architectures.

Keywords: Si nanowires, multilayer graphene shell encapsulated gold nanoparticles, surface decoration, surface-enhanced Raman spectroscopy (SERS)

13.1 Introduction

Understanding the nucleation and growth of nanoparticles on high curvature nanowire surfaces is necessary to develop controlled assemblies with enhanced multifunctionality. Coinage metals such as gold, silver, and copper were usually used as the preferred Surface Enhanced Raman Scattering (SERS) substrate in the form of rough surface and nanoscale structures.³⁴⁸ The enhancement of Raman signal is believed to be originated from the interaction between metallic substrate and absorbed target molecules under the electromagnetic field generated by Raman laser, which is normally called Localized Surface Plasmon Resonance (LSPR). LSPR can be simply tuned by controlling the size, shape, and distribution of nanoparticles,³⁴⁹ as well as using effective supporting substrate. However, the further developed is thought to be confined by the limited maximum particle density, uncontrollable aggregation, and nonuniform distribution of Raman signal.³⁵⁰

Silicon nanowire has been studied for several decades due to their excellent electronic/ mechanical properties, convenient surface tailorability and industrial compatibility, which make it a promising material in field-effect transistors, solar cells, and sensors.³⁵¹ Among these applications, using silicon nanowires as chemical sensors are of particularly important due to their biocompatibility, vast surface-to-bulk ratio, fast response, good reversibility and oxide-coated or H-terminated surface.³⁵² However, it is now widely accepted that as-produced pristine silicon nanowires only exhibit moderate sensitivity in chemical detection. As a result, appropriate surface modification is definitely needed and well developed. Towards this end, coating silicon nanowires with gold nanoparticles is of particular interest as it leads to an interesting Schottky device geometry. In addition, silicon nanowire-gold nanoparticle heterostructures have been of recent interest for Raman active substrates. The significant enhancement on silicon nanowire based heterostructures

was attributed to (1) the enlargement of specific substrate area, which is capable to absorb more target molecule per unit area; and (2) the appropriate distribution of nanoparticles on the nanowire, which is able to generate more hot-spots for Raman detection. For instance, silver nanostructures decorated silicon nanowires have been intensively studied as ultrasensitive SERS substrate in the detection of R6G, CV, DNA, as well as amoxicillin.³⁵³

Graphene was demonstrated as an effective SERS substrate due to the ability to absorb and concentrate target molecules. The abundant graphene-molecule interactions result in significantly increased sensitivity based on the chemical enhancement mechanism and further give such graphene-based Raman sensor good molecule selectivity. It is critical to evolve knowledge of gold nanoparticles with controlled morphologies and spacing on such nanowire substrates, and this remains a significant challenge to date. Here, we report a detailed fundamental study on morphological and structural evolution of gold nanoparticles onto silicon nanowires by combining chemical vapor deposition method with wet-chemical synthesis followed by high temperature treatment. The latter step led to controlled spatial densities, inter-particle spacing, and diameters of gold nanoparticles on high curvature silicon nanowires. Interestingly, it was observed that diffused interfaces between gold and silicon existed, which could potentially alter the plasmonics, chemical and electronic properties of such heterostructures. These nanowire heterostructures were characterized using high-resolution electron microscopy, X-ray photoelectron spectroscopy, and Raman spectroscopy. Raman active organic molecules were further studied for Raman signal enhancement using the developed silicon nanowire-gold nanoparticle heterostructures, and improved sensitivity and detection limits were observed. Such controlled nanowire heterostructures with significant plasmonic activities hold promise for the future of analytical devices as well as NEMS/MEMS architectures.

13.2 Experimental section

Materials and Methods: Silicon (Si) wafers (<100>, n-type) were purchased from IWS (Colfax, CA). Gold (III) chloride trihydrate ($\text{HAuCl}_4 \cdot 3\text{H}_2\text{O}$, 99.9%) was purchased from Sigma-Aldrich (St. Louis, MO). Sodium borohydride (NaBH_4 , powder, 98%) was purchased from Acros Organics (New Jersey, NJ). Acetone ($(\text{CH}_3)_2\text{CO}$) was purchased from VWR International (West Chester, PA). DI water (18.1 M Ω -cm) was obtained using a Barnstead International DI water system (E-pure D4641). All chemicals were used without further purification. Gold sputtering was carried out on a Bio-Rad gold sputtering and coating system, Polaron division (Agawan, MN). Dispersion of heterostructures into ethyl alcohol was done in a Branson 2510 Sonicator (Danbury, CT). Labnet centrifuge (Edison, NJ) was used to clean, wash, and separate nanoparticles. Wet samples were dried in a VWR vacuum oven (West Chester, PA). Growth and annealing of the Silicon nanowires were accomplished inside a GSL-1100X Tube Furnace (MTI Corporation) with a quartz tube from ChemGlass (Vineland, NJ). Gas flow rates of all chemical vapor deposition and annealing processes were controlled by Teledyne Hasting powerpod 400 mass flow controllers (Hampton, VA). H_2 (UHP grade, 40% balanced with Ar), N_2 , O_2 , SiH_4 and Ar (all UHP grade) gas cylinders were purchased from Airgas South (Tuscaloosa, AL). Low-pressure atmosphere inside the quartz tube was generated by the Gast (DOA-P74-AA) Vacuum Pump bought from GAST manufacturing inc. (Benton Harbor, MI). Oxygen plasma treatment was performed in a Nordson March Jupiter III Reactive Ion Etcher (Concord, CA). Syringe injector was obtained from Fisher Scientific (Suwanee, GA).

Growth and decoration of Si nanowires: (111) silicon wafer was used as the substrate. Two strategies were applied to deposit gold catalyst on the substrate. In both strategies, the silicon wafers were first sonicated in acetone for 10 min. (1) The wafer was treated with 3:1 H_2SO_4 : H_2O_2

piranha solution for 30 min at 100 °C, then sputtered with gold in a Bio-Rad gold sputtering and coating systems, Polaron division (Agawan, MN). (2) The silicon wafer was placed in BOE solution for 1 min to etch away the surface oxide layer. Galvanic deposition was then carried out at room temperature to prepare the gold catalyst film. The deposition solution is 1 mM KAuCl_4 + 1% HF. The newly prepared catalyst substrate was placed in the center of a GSL-1100X (MTI Corporation) tube furnace. The nanowire growth was executed through a typical CVD process. The furnace was first heated to 850 °C in the protection of 5% H_2 in Ar. The temperature was maintained for 10 minutes to convert the catalyst film to gold nanoparticles (Au nanoparticle). Then the temperature was decreased to the growth temperature. 2% SiH_4 in He was pumped into the quartz tube as the silicon source, which was carried by 10% H_2 in Ar. When the growth process was finished, the furnace was cooled ambiently in the protection of pure Ar. Pristine silicon nanowires were treated with BOE solution for 5 s and then placed in a galvanic deposition solution (1 mM KAuCl_4 + 1% HF) for different times to prepare silicon-gold core-shell nanostructures. Then the sample was annealed in the quartz furnace or oven box (as specified) for 10 min at different temperatures. This process made silicon nanowire-gold nanoparticle heterostructures, which can be used as the surface enhanced Raman scattering (SERS) substrate for dye detection.

Graphene growth on the heterostructures: Growth of graphene on the GNPs was conducted using a typical Chemical Vapor Deposition (CVD) process as reported before. Briefly, the GNPs dispersed Si wafer were oxidized under oxygen plasma for 15 min to produce a gold oxide layer (power: 160 W; oxygen pressure: 600 mTorr). The sample after plasma oxidation were put in the center of the quartz tube furnace. The growth process was carried out at 675 °C for 1 h. Xylene was used as the carbon source with a feeding rate of 10 mL/h, which was carried by 10% H_2/Ar with a total flow rate of 1.15 SLM. To create carboxyl groups on the surface of graphene shell, the

as-produced graphene was either treated with oxygen plasma for 15 s (power 120 W, oxygen pressure 300 mTorr) or treated in 3 M HNO₃ solution for 5 h at 80 °C.

Raman detection of Rhodamine 6G: Both pristine silicon nanowires and silicon nanowire-gold nanoparticle heterostructures were used as the SERS substrate for R6G detection. The nanostructures were first treated in BOE solution for 10 s to create surface Si-H bonds, which can largely increase the efficiency of R6G absorption on the SERS substrate. After being dried in flowing N₂, the sample was kept in 10⁻⁶ M R6G solution for 10 h with slight agitation. Then the dyed nanostructures were washed with DI-water and dried in flowing N₂. Raman measurement was carried out on the Bruker Senterra Raman System (Bruker Optics Inc. Woodlands, TX), where a Ne laser source with 785 nm wavelength was used. The applied laser power was 1 mW; the integration time was 10 s.

Characterizations: Scanning Electron Microscopy (SEM) images were obtained using a FE-SEM JEOL-7000 equipped with energy dispersed X-ray spectroscopy (EDX). Tecnai F-20 was used to collect Transmission Electron Microscopy (TEM) images at 200 kV. TEM samples were prepared by dispersing as-prepared samples on lacey carbon TEM copper grids purchased from Ted Pella Inc. (Redding, CA). (XRD, UV-Vis, DSC). The average nanoparticle size was measured from TEM and SEM images, where more than 200 nanoparticles were counted and measured per sample. Diameter was measured for spherical nanoparticles and distances less than 20nm between two Au nanoparticle were taken into account for particle interval measurements. All the measurements were done using Nano-measurer 1.2 Software. High resolution TEM image for graphene encapsulated Au nanoparticles were also converted into FFT image using Digital Micrograph software. X-ray photoelectron spectra (XPS) were gathered by Kratos Axis 165 with mono-Aluminum gun at 160 eV pass energy for full range scan and 40 eV pass energy for detailed

scan. The analysis spot was set as “Slot” with $>20\ \mu\text{m}$ aperture and 19.05 mm iris setting. Raman spectra and SERS of samples were collected using Bruker Senterra system (Bruker Optics Inc. Woodlands, TX) equipped with 785 nm laser source at 10-25 mW laser powers and 100X objective. The integral time and co-additions were set as 15 seconds and 2, respectively. The Raman mapping conditions for map acquisition were set at the spectral resolution of $3 - 5\ \text{cm}^{-1}$ in the range of $77 - 2658\ \text{cm}^{-1}$ with 10 mW laser power. Samples for SERS were prepared by dispersing Rhodium 6G (R6G) dye over SNW samples at various stages: as-produced, as-nucleated, annealed in different conditions, branched SNWs and graphene encapsulated Au nanoparticle on SNW (all these SNW were dispersed on a silica substrate before wetting them with dye). Around 5-6 nanowires were randomly chosen and 5-6 points were taken on each nanowire to get SERS signal enhancement data (approximately 30 data points per sample).

13.3 Results and discussion

13.3.1. Silane-based CVD growth of Si nanowires

Silicon nanowires (Si nanowires) were grown through an atmospheric-pressure chemical vapor deposition (CVD) process, the growth mechanism can be described by the well-defined vapor-liquid-solid (VLS) principle. As shown in Figure 13.1, galvanic deposition was first carried out on Si wafer, the replacement reaction between Au and Si will rendering a layer of gold film. Followed with high-temperature annealing, the gold film were dewetted into island-like gold nanoparticles, which served as the catalyst during the silicon nanowire growth process. Due to the high solubility of silicon in gold, when SiH_4 was decomposed at the growth temperature, silicon atom diffused into liquid gold droplet and alloyed. As the silicon in gold reached the saturated state, solid silicon

precipitated at the interface of gold droplet and substrate while the gold catalyst was held up and kept on the top of silicon nanowire. In this study, various growth conditions were used to the growth of Si nanowire for understanding the basic principle of the CVD growth. The experiment parameters were listed in Table 13.1.

It was widely proposed that in the typical VLS growth process, the diameter of Si nanowires will be dominated by the size of Au catalysts. As a result, different galvanic deposition time was applied to control the thickness of gold film (as shown in Figure 13.2A-E). As a result, controllable Au nanoparticles size was obtained after high-temperature annealing (Figure 13.2F-J). XRD was used to characterize the crystal structure of the gold film, as shown in Figure 19K, the as-deposited films were mainly existed in (111) structure. The variation of particles size according to different galvanic deposition time was shown in Figure 19L-M. Linear relationship between galvanic deposition time and particle size was observed.

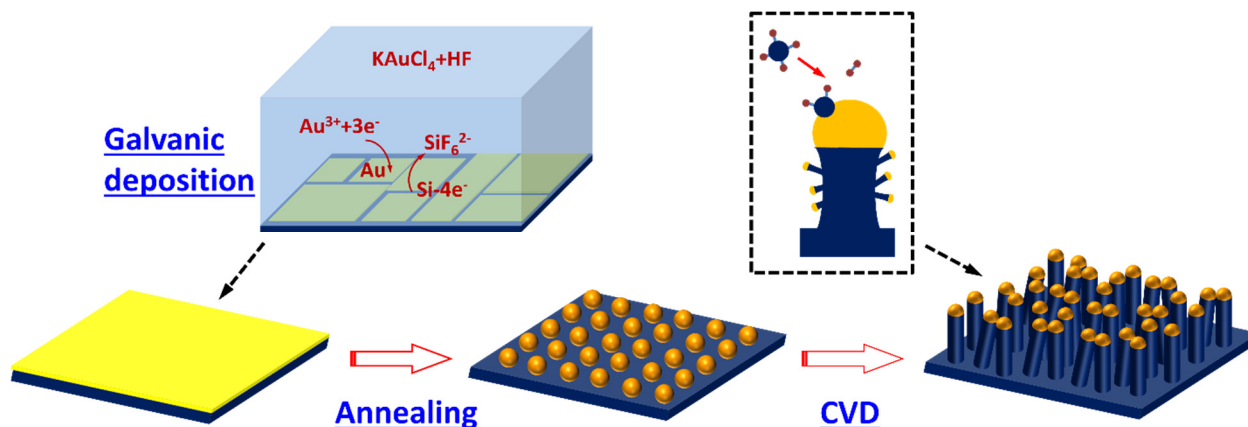


Figure 13.1. Schematic showing the galvanic deposition of gold film on Si substrate and CVD growth of silicon nanowires.

Table 13.1. Experimental parameters showing the optimization and control of Silicon nanowire growth on substrates prepared by galvanic deposition.

Sample #	Galvanic deposition (min)	Temperature (°C)	Time (min)	SiH ₄ flow rate (sccm)
1A	0.5	725	5	30
2A	1	725	5	30
3A	3	725	5	30
4A	5	725	5	30
5A	7	725	5	30
6A	5	675	5	30
4A	5	725	5	30
7A	5	775	5	30
8A	5	725	1	30
4A	5	725	5	30
9A	2	725	15	30
10A	2	725	30	30
11A	2	725	60	30
12A	2	725	30	20
10A	2	725	30	30
13A	2	725	30	40
14A	2	725	30	50

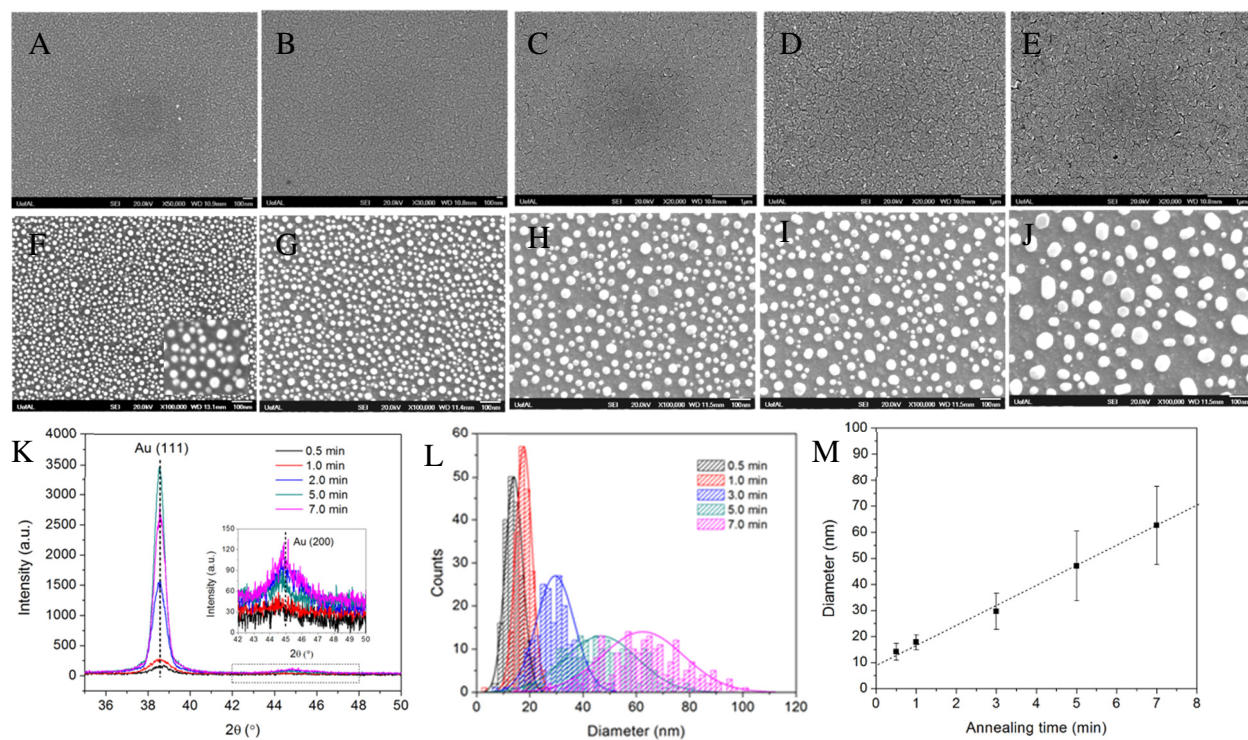


Figure 13.2. Au film and corresponding Au nanoparticles prepared by galvanic deposition under different times: (A, F) 0.5 min, (B, G) 1 min, (C, H) 3 min, (D, I) 5 min, (E, J) 7 min. (K) XRD pattern of Au films. (L-M) Variation of particle size according to the galvanic deposition time.

All of these Au nanoparticles were used as catalyst to grow Si nanowires. The corresponding SEM images of Si nanowires were shown in Figure 13.3A-F. The structure obtained at different catalysts were summarized in Figure 13.3G. When the catalysts size was small (0.5 min, 1 min), no gold tip can be found on the silicon rods and diameter of the rods was very large ($\sim 1 \mu\text{m}$). The CVD growth is an atom diffusion process, so the small amount of gold catalyst will be distributed in Si nanowire. Only when the amount of catalyst increased, the Au nanoparticles appeared at the tips of Si nanowires, and most important is the diameter of Si nanowires was approximately the same as the tip size. In addition, small diameter ($\sim 10 \text{ nm}$) silicon branches were instantly observed on the Si nanowires. This is because even at high temperature, the diffusion of gold in solid silicon was inefficient. Some gold remained on the surface of Si nanowires will act as the new catalyst for the

growth of silicon branches. TEM images showing the structure of Si nanowires and the branches were presented in Figure 13.3G-I. The diameter of Si nanowires was around ~200 nm. A silica shell can be observed to encapsulate on the surface of the nanowires and the tips. Small Au nanoparticles catalyst (~10 nm) can be found to distribute in the branches.

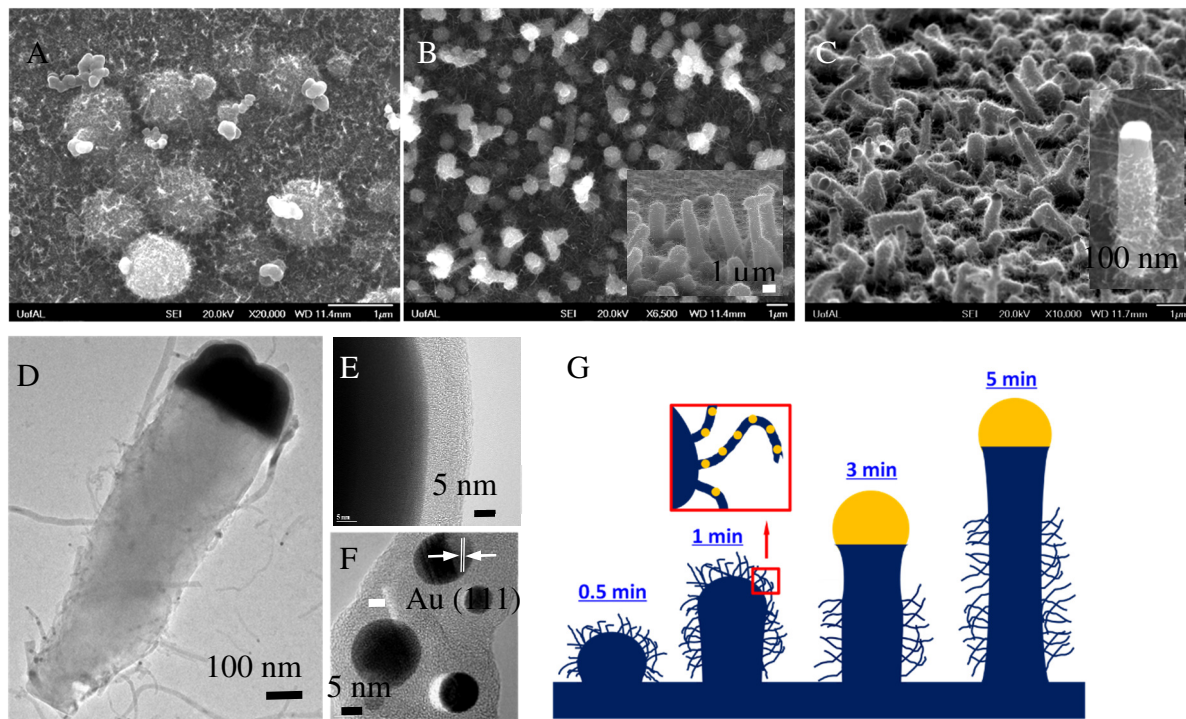


Figure 13.3. (A-C) SEM images showing the Si nanostructures obtained on different Au nanoparticles catalysts. (D-F) HRTEM images showing the morphology of gold tip (E) and branches (F). (G) Schematic showing the CVD products obtained on different substrates.

The Si nanowires obtained at different temperature were shown in Figure 13.4. At higher temperature, the length of the nanowire decreased while the length of branches largely increased. Gold catalysts can be observed to distribute uniformly in these branches. This is because at higher temperature the diffusion rate of gold in silicon was increased and the gold catalysts become more active. As a result, more gold was distributed on the surface Si nanowires. The length and diameter of the branches were both increased. Under this principle, we can understand that the Si nanowires obtained at lower temperature present increased length and decreased diameter. Also, less branches were found on these low temperature Si nanowires. Their TEM characterizations were shown in Figure 13.4C-E.

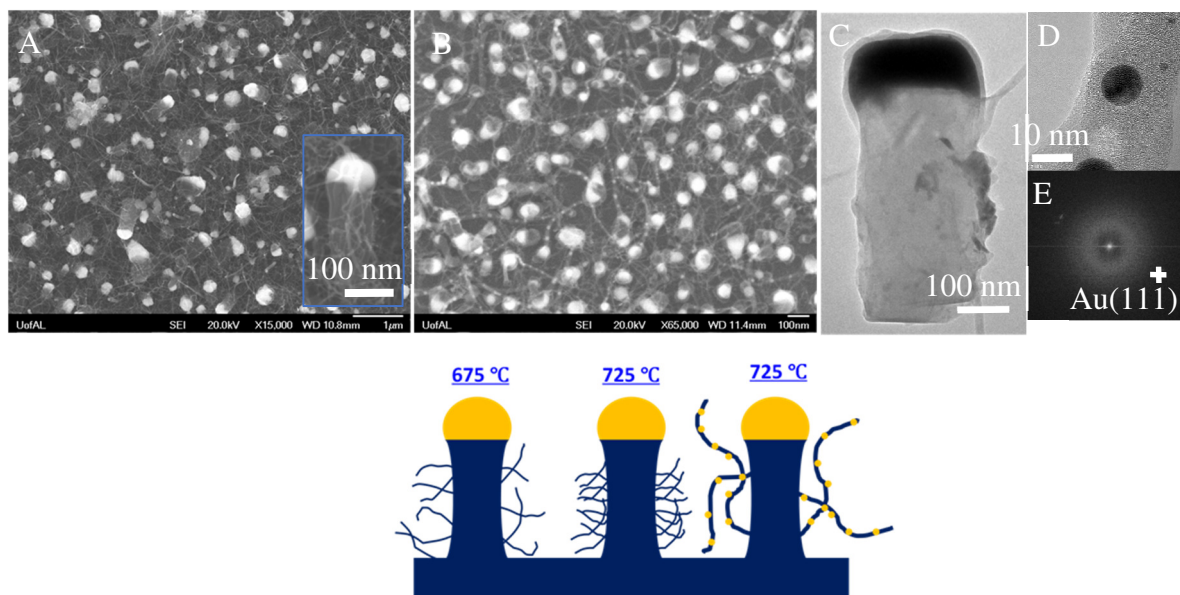


Figure 13.4. (A-B) Silicon nanowire arrays obtained at different temperatures: (A) 675 °C, (B) 775 °C. (C-E) TEM image corresponding to (A). (F) Schematic showing the structure of Si nanowires obtained at different temperature.

Studying the growth of Si nanowires at different duration provide an important chance to understand the formation principle of Si nanowires at the initial stage and the continuous growth period. The Si nanowires obtained at different growth time were shown in Figure 13.5 (A-F). The schematic showing the growth process were presented in Figure 13.5 (J). At the very early stage of the growth, Si atoms became saturate and precipitate on the surface of gold catalyst as a shell (Figure 13.5A). With increased growth time, more silicon atoms precipitated. The place with lowest surface energy will be the most preferred region. Due to the mismatch of crystal structures of gold and silicon, plenty of defects existed between the interface of gold catalyst and (111) silicon substrate, making the interface the most preferred region for the growth of Si nanowires. The Si nanowires obtained at 60 min present a diameter of ~150 nm with of length of 3~5 μm . The estimated average growth rate was around 800 nm/min.

Si nanowires growth at different silane flow rate was also carried out. As shown Figure 13.6A-C, the silane flow rate can definitely control the growth rate of Si nanowires, which will directly result in a different length. In addition, at higher flow rate, less amount of branches can be found on the Si nanowires. In addition, it is worthy to mention that small Si nanowire branches were constantly observed on these main nanowires. The branch observed on the nanowires obtained at 30 sccm was blend and with high spatial density (Figure 13.5B). However, with increased flow rate (40 sccm and 50 sccm), these branches became straight and less (Figure 14.6D and E). The VLS growth of Si nanowires were further schematically illustrated in Figure 14.6H. The decomposition of SiH_4 at high temperature resulted in silicon atoms vapor, which further diffused into the gold droplets and alloyed with gold. The interface of gold droplet and silicon substrate presented the lowest surface energy due to the mismatch of atom distributions at the two sides interface, as a result, silicon is preferred to precipitate at this interface and leads to the growth of silicon

nanowires. The formation of surface branches is due to the non-uniform diffusion of gold droplet during the growth. The main droplet was lifted up by the precipitation of Si nanowire while a lot of small droplets were remained on the nanowire surface. These small gold droplet acted as the new catalyst center for the growth of nanowire branches according to the aforementioned VLS mechanism. Thus, we demonstrated the growth of Si nanowire in atmosphere environment (without vacuum) by optimizing the growth conditions and finally straight, branchless and free-standing Si nanowires were grown on the Si substrate. This parameter study is of importance since it provide fundamental knowledge for the VLS growth of Si nanowire at atmosphere environment and a feasible approach for growth of high-quality Si nanowires.

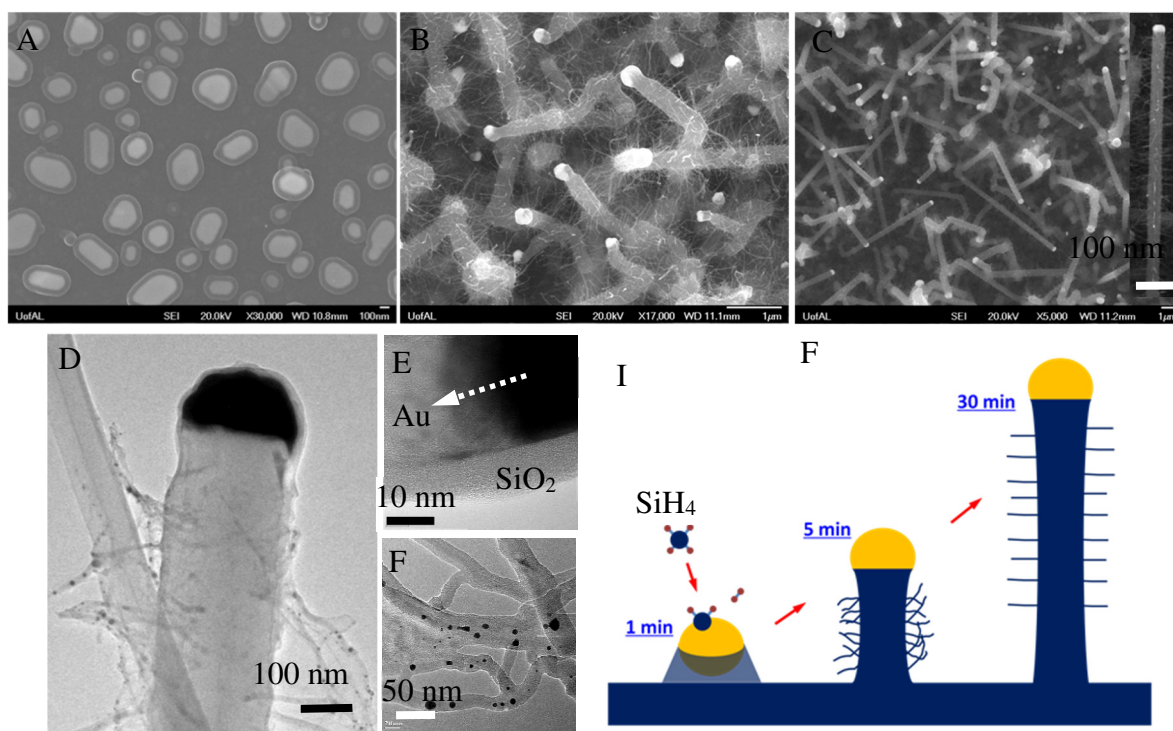


Figure 13.5. (A-C) Silicon nanowires obtained at different growth times: (A) 1 min, (B) 15 min, (C) 60 min. (D-E) HRTEM image showing the gold tip-silicon nanowire-silica shell interface and branch structure. (I) Schematic showing the Si nanowires obtained at different growth times.

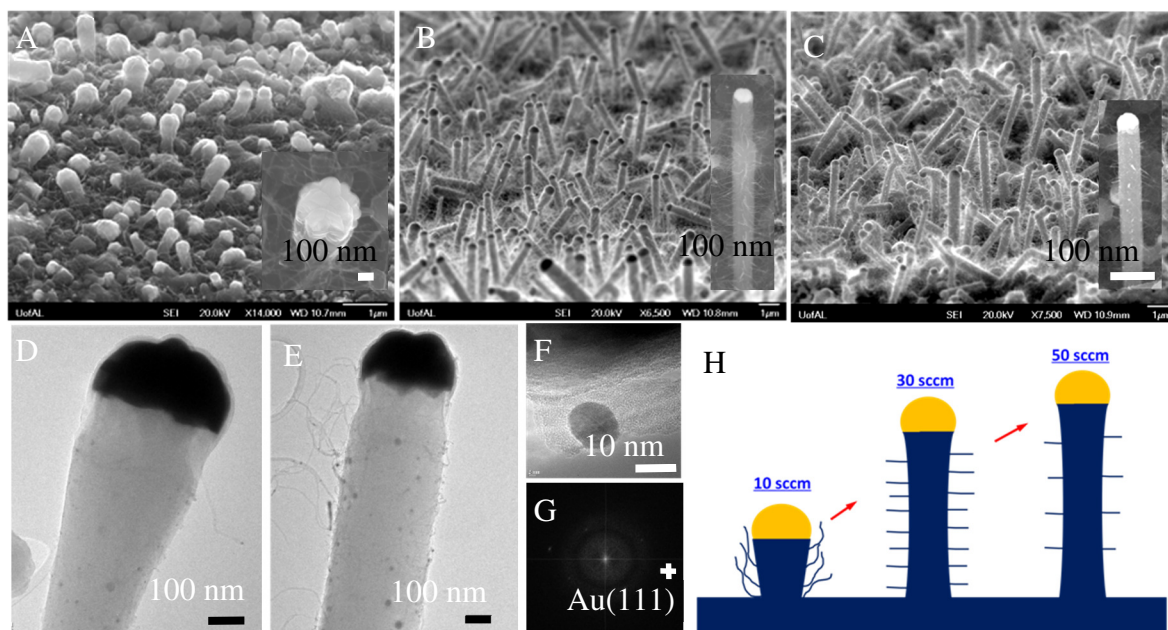


Figure 13.6. (A-C) Silicon nanowires obtained at different SiH_4 flow rates: (A) 20 sccm, (B) 40 sccm, (C) 50 sccm. (D) TEM image corresponding to (A). (E) TEM image corresponding to (B). (I-J) HRTEM and FET image showing the silicon branch structure. (K) Schematic showing the Si nanowires obtained at different SiH_4 feed rates.

13.3.2. Surface decoration of Si nanowire with Au nanoparticles and GNPs

Further surface decoration of Si nanowires with extraneous Au nanoparticles was conducted via a galvanic deposition – annealing process, as illustrated in Scheme 13.7A. Three Si nanowire samples obtained in the parameter studies was selected. The basic mechanism for the galvanic deposition of gold film (shell) on the Si nanowires was illustrated in Figure 10.7D. The deposition is due to the replacement reaction between silicon and Au^{3+} in HF solution, which led to the formation of Au film or shell on the surface of Si nanowires. In the following annealing process, the Au film was dewetted and converted to Au nanoparticles decorated on the nanowire surface. The further graphene growth was completed *via* a well-defined chemical vapor deposition process. The Au nanoparticles were used as the supporting materials, which were first subjected to a plasma

oxidation process to create surface oxide layer. This surface gold oxide layer on Au nanoparticles have been proved to be of importance for the formation of initial graphene layers on the Au nanoparticles. These surface decorated Au nanoparticle standing on the Si substrate was further used for the SERS-based chemical sensing, as illustrated in Figure 13.7B and C.

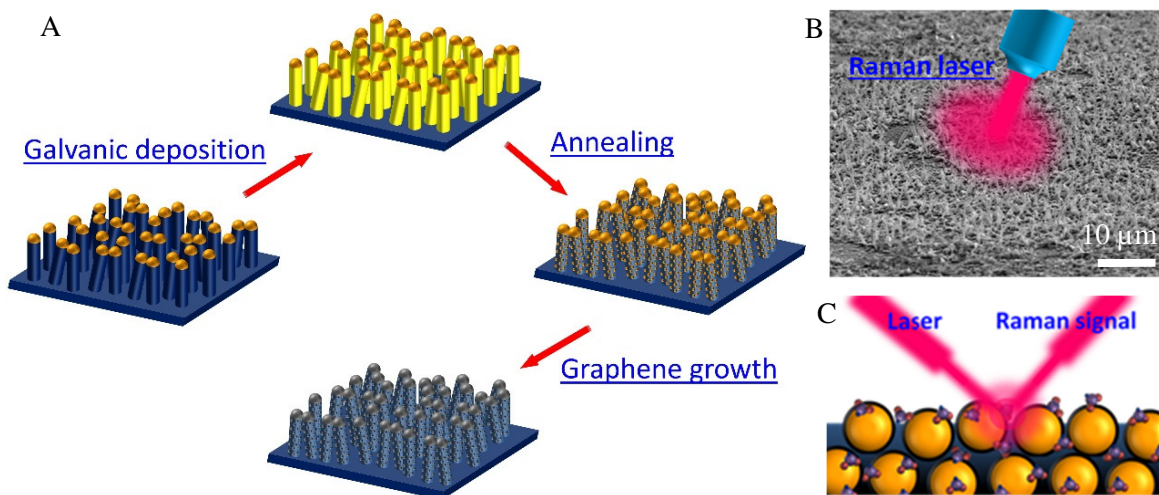


Figure 13.7. (A) Schematic showing the surface decoration of Si nanowires with Au nanoparticles and GNPs. (B) Representative low-resolution SEM image of the Si nanowire based heterostructure substrate for SERS sensing. (C) Schematic showing the SERS sensing on the molecule attached Si nanowire-GNP heterostructures.

SEM images of the Si nanowires after gold deposition were shown in Figure 13.8A-C. The following annealing process and the resulting Si nanowire-Au nanoparticle heterostructures were demonstrated in Figure 13.8D-F. As we observed, these deposited gold film was dewetted into Au nanoparticles that uniformly dispersed on the surface of Si nanowire. As we observed, air-annealing led to slight surface oxidation of both main nanowire and gold nanoparticles after dewetting. Thus diffusion between gold and silicon was weakened and Au nanoparticles on the nanowire surface presented spherical morphology.

TEM images and analysis of the Si nanowire-Au nanoparticle heterostructures before and after annealing in air were presented in Figure 13.8G-L. We observed that the as-deposited gold present a flake structure in high resolution images. These gold flakes were randomly dispersed on the surface of the main nanowires. However, after the annealing process both in air, effective dewetting process happened and uniformly dispersed spherical nanoparticles were observed on the surface of Si nanowires. The estimated nanoparticle size is 28.9 ± 5.3 nm for the air-annealed heterostructures. Lattice evaluation indicate that the as-produced Au flakes presented random distributed crystal structures. However, after annealing the standard low energy (111) plane was constantly observed for the Au nanoparticles. In addition, no obvious lattice variation was observed for the silicon nanowire before and after annealing, indicating the main nanowires are chemically and structurally stable enough to stand for these multi-step fabrication process. FFT images in Figure 13.9I and L and E further confirm the lattice distribution. This annealed Si nanowire-Au nanoparticle heterostructures were further used as the supporting materials for the decoration of graphene. This is according to the xylene based chemical vapor deposition process for the growth of multilayer graphene shell on the decorated Au nanoparticles.

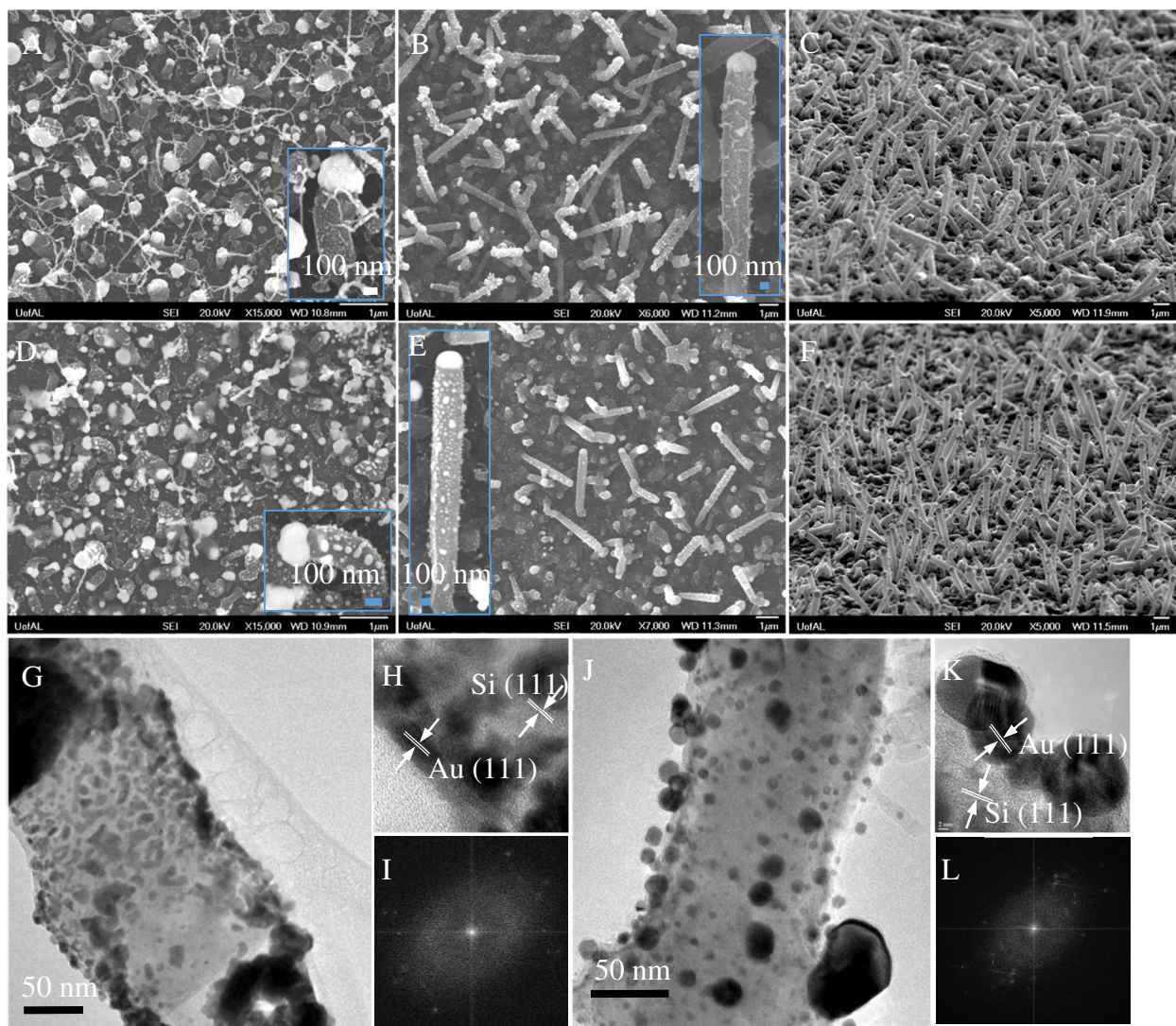


Figure 13.8. (A-C) Si nanowire-Au core-shell structures obtained by galvanic deposition of gold film on silicon nanowires: (A) sample 6B, (B-C) sample 13B. (D-F) Si nanowire-Au nanoparticle heterostructures obtained by annealing the core-shell structure: (D) sample 6C and (E-F) sample 13C. (G) Representative TEM image corresponding to (A). (H-I) HRTEM and FET images corresponding to (G). (J) Representative TEM image corresponding to (D). (K-L) HRTEM and FET images corresponding to (J). (Note: Galvanic deposition solution: 1mM KAuCl_4 + 1% HF, deposition time: 2 min, annealing temperature: 625 °C, time: 10 min, environment: air.)

Figure 13.9A-D show the TEM and HRTEM images of the Si nanowire-GNP heterostructures. One can observe that the chemical vapor deposition process has no significant influence on the structure and distribution of Si nanowires and Au nanoparticles. The GNPs were uniformly dispersed on the Si nanowire with average size of 22.54 ± 10.32 nm and inter-particle spacing of 28.22 ± 12.54 nm. The average diameter of GNPs was slightly decreased as compared with Au nanoparticle due to the inevitable diffusion of gold into Si nanowires during the chemical vapor deposition process. High resolution images in Figure 13.9C and D further demonstrated the lattice structure of Au nanoparticle and graphene shell. Lattice spacing of 0.25 nm was observed for Au nanoparticle core (111) and spacing of 0.37 nm were estimated graphene shell. Raman spectra of the Si nanowire-Au nanoparticle heterostructures were shown in Figure 13.9E and further magnified in F, when the well-defined G-band and D-band were demonstrated for GNPs.

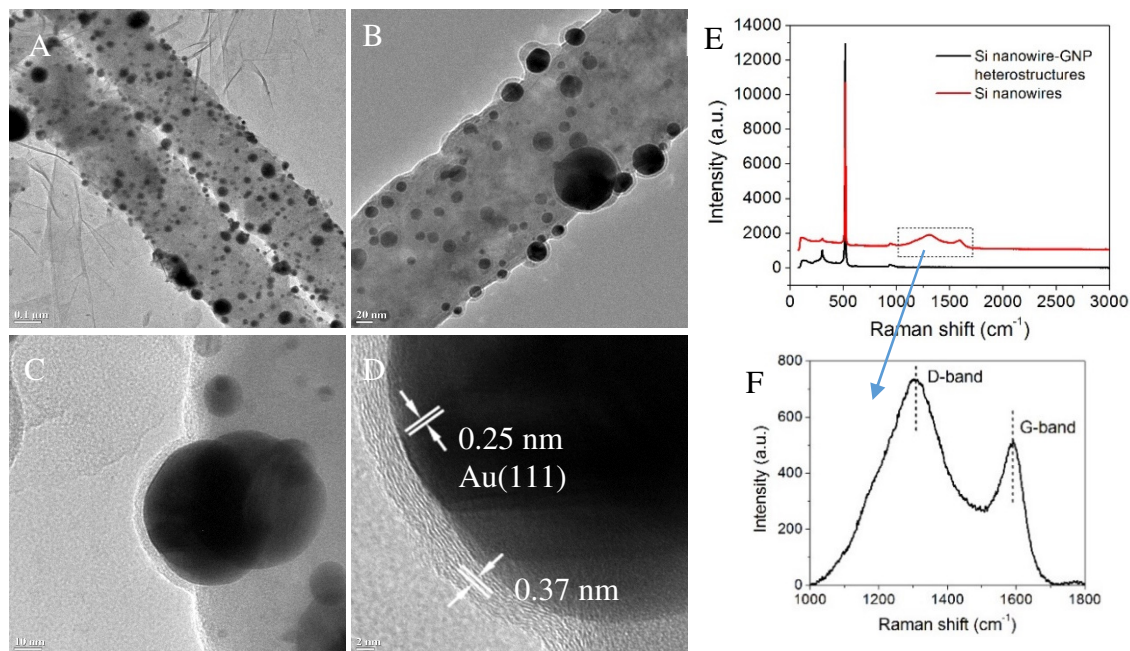


Figure 13.9. Growth of graphene on the gold nanoparticles decorated on the silicon nanowires: (A-D) TEM/HRTEM images of the Si nanowire-GNP heterostructures. (E-F) Raman spectra obtained on the as-produced Si nanowires and the Si nanowire-GNP heterostructures.

13.3.3. SERS sensing on the Si nanowire-GNP heterostructures

We evaluated the Raman based organic sensing for the detection of trace amount of dyes contained in DI-water. Rhodamine 6G (R6G) was used as a Raman probe. The test was conducted on several Si nanowire and Si nanowire-Au nanoparticle or GNP heterostructure samples. The samples were immersed in 10^{-6} M R6G solution overnight to allow the absorption of R6G molecules on the nanostructures. The Raman signals of R6G were collected directly on these R6G-absorbed substrate. The obtained Raman spectra were shown in Figure 13.10. The Au nanoparticle decorated Si nanowires presented obviously increased Raman intensity as compared with the previous Au nanoparticles on the Si substrate and the as-grown Si nanowires. This Raman enhancement is mainly due to the overlapping of electric field between various Au nanoparticles dispersed on the Si nanowires, which led to significantly increased Localized Surface Plasma Resonance (LSPR). Further increase Raman enhancement was observed on the Si nanowire-GNP heterostructures, which can be attributed to both electromagnetic and chemical mechanism.

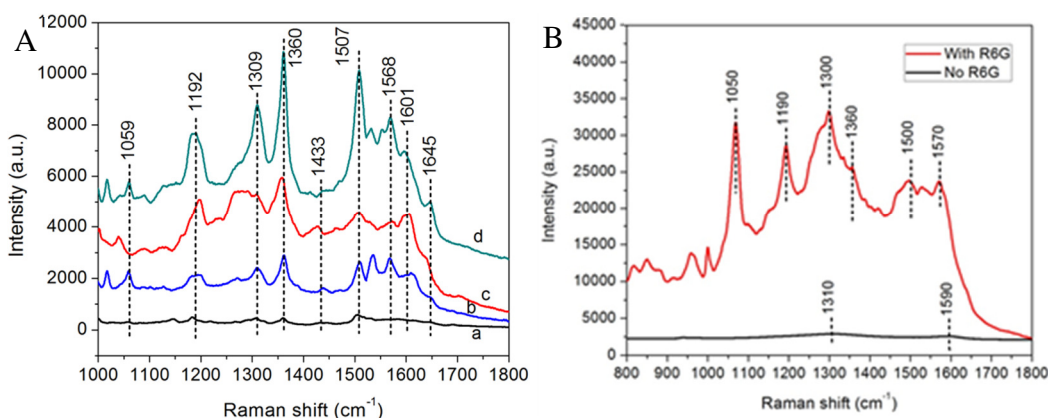


Figure 13.10. (A) Raman spectra of R6G (1×10^{-6} M) obtained on different substrates: (a) Annealed Au nanoparticle catalysts, (b) pristine Si nanowire arrays (Sample 6A), (c-d) Si nanowire-Au nanoparticle heterostructures (sample 6C, 11C). (B) Raman spectra obtain on the Si nanowire-GNP heterostructure with or without R6G.

13.3.4. Discrete Dipole Approximation modeling

Based on the calculation of diameters of Si nanowires and Au nanoparticles, we constructed four types of targets for calculation of extinction spectra (scattering and absorption) and mapped normalized electric field at the peak extinction wavelength. Since the targets are anisotropic, two incident directions (X: radial and Y: axial, Figure 13.11A) were considered. Figure 13.11B-E show four targets: (a) Si nanowire, (b) Si nanowire-Au nanoparticles heterostructure, (c) a section of Si nanowires-Au nanoparticles heterostructure from (b), and (d) Si nanowires-GNP heterostructure corresponding to section in (c) and with 2 nm thick graphene shells. Due to much thinner graphene shells compared with diameters of Au nanoparticles and Si nanowire, only sections of heterostructures were considered, where numbers of dipoles are less than a million and enough dipoles were allocated to 2 nm graphene shells. This could significantly reduce the computation time and improve the accuracy. As seen in Figure 13.11F and G, Si nanowire for X and Y directions showed extinction peaks at 512 nm. For Si nanowires-Au nanoparticles heterostructures, plasmonic peak red-shifted to ~674 nm for X direction and ~597 nm for Y direction. This is from the electromagnetic coupling between Au nanoparticles and Si nanowire. Peak intensity also differed for different orientations of incoming wave vectors. Extinction peak intensity in X direction for Si nanowire decorated with nanoparticles is 2.3 times higher than intensity in Y direction. This indicates that electromagnetic field effects are stronger when incident wave propagates in the radial direction rather than axial direction. When only a section of heterostructure was considered (Figure 13.11D), peaks shifted toward lower wavelength (557 nm at X direction and 545 nm at Y direction). The shift of peaks and change of intensity indicated that geometry of Si nanowires and distribution density of Au nanoparticles is critical for plasmonic properties. However, Si nanowires-GNP heterostructures (with 2 nm shell thickness), extinction spectra at

both directions diminished sharply. Only a broad peak at ~ 535 nm was observed in Y direction but scattering dominated in X direction. The reduction in peak intensity could be attributed to the thickness of graphene shells. Overall, it shows that optical properties after graphene shell encapsulation can be spatially resolved and depend on incident wave vector direction. It is also anticipated that to retain optical properties of encapsulated Au nanoparticles, the shell thickness should be lower than 2 nm.

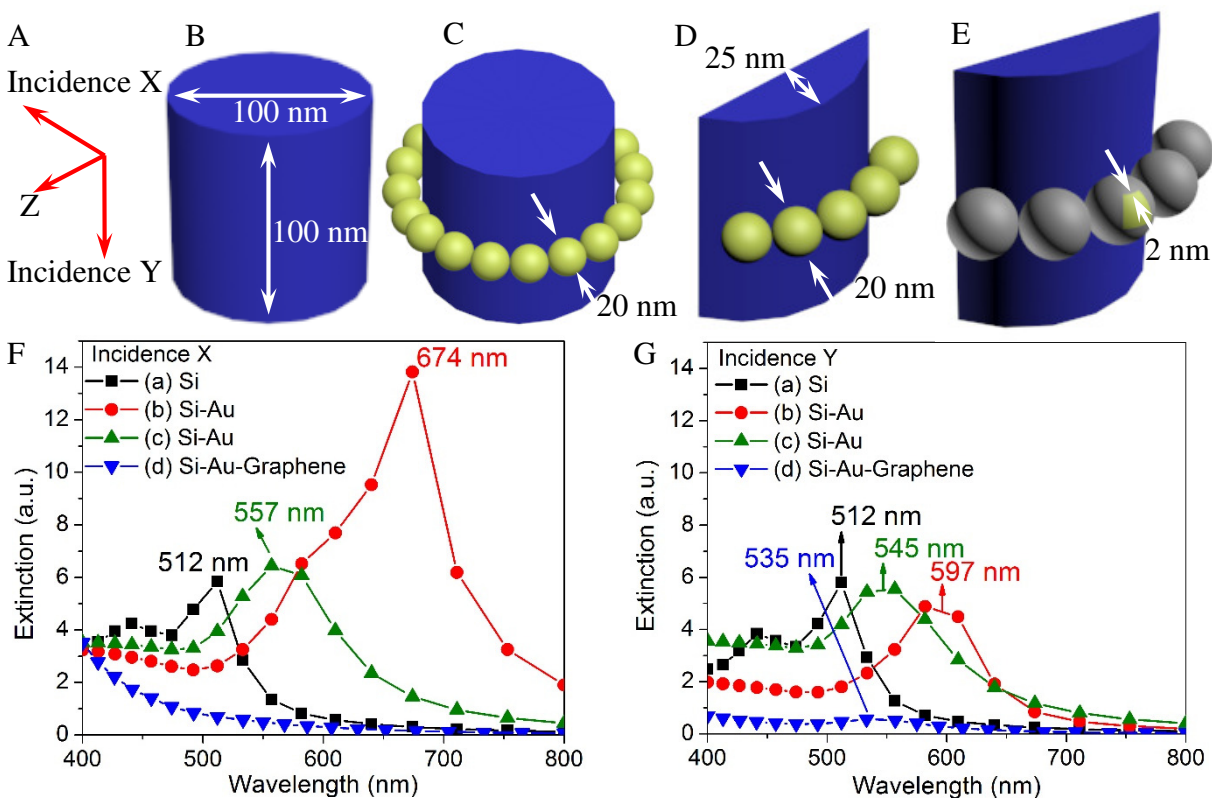


Figure 13.11. Schematics showing (A) two directions of incident lights (X: radial to nanowire, Y: axial to nanowire), (B) Si nanowire, (C) Si nanowire-Au nanoparticles, (D) a section of Si nanowire-Au nanoparticles, (E) a section of Si nanowire coated with GNPs (shell ~ 2 nm thickness), (F) and (G) comparison of extinction spectra for two directions for k vectors (X and Y) and peak locations.

Normalized electric field distributions were mapped using extinction results (Figure 13.12). Three major conclusions could be derived. (1) The field or plasmon are concentrated at the interface between Si and Au. This is also observed by others and is mainly caused by induction of image charge on the substrate surface as well as multiple scattering and reflection by nanoparticles.³⁵⁴ (2) Normalized electric field could be enhanced by decoration of Au nanoparticles. However, the increment is depending on incident wave vector direction (increase from 30.7 in X direction to 37.9 in Y direction). (3) Graphene shells (~2 nm) greatly depressed the intensity for both directions (75% drop in X direction and 72.5% decrease in Y direction) but enhanced the distribution of plasmon over larger surface area of GNPs as compared to only interfacial hot spots in case of Si nanowire-Au nanoparticle heterostructures.

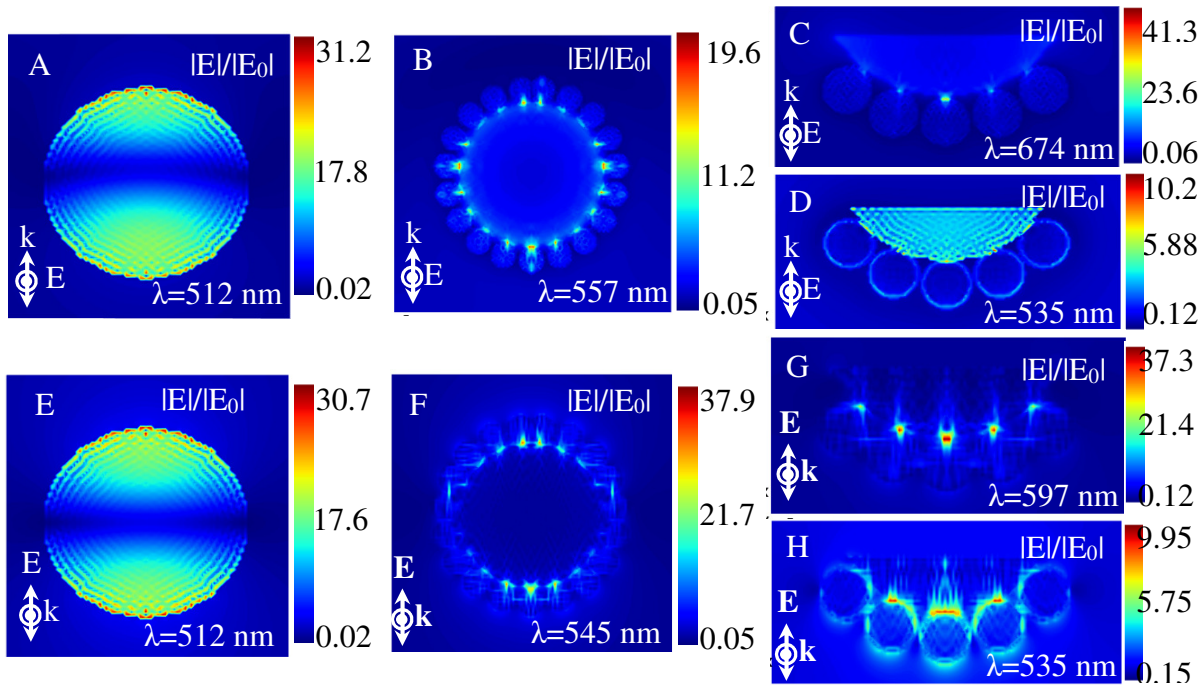


Figure 13.12. Distribution of normalized electric field in X direction for (A) Si nanowire, (B) Si nanowire-Au nanoparticles, (C) a section of (B), (D) Si nanowire-GNP heterostructures and in Y direction for (E) Si nanowire, (F) Si nanowire-Au nanoparticles, (G) a section of (F), (H) Si nanowire-GNP heterostructures.

13.4 Conclusions

CVD approach is demonstrated to grow Si nanowires, which were subsequently utilized to nucleate Au nanoparticles to result in Si nanowires-Au nanoparticles heterostructures. These heterostructures were further surface plasma oxidized to allow for the selective growth of graphitic shells encapsulating Au nanoparticles while the exposed regions of Si nanowires were encapsulated within an amorphous carbon. Such hybrid combinations based on Si nanowires were further studied for their optical properties using DDA calculations. It was estimated that the bare Si nanowires showed an extinction efficiency peak at ~ 512 nm, which was significantly red shifted to ~ 674 nm after decorating with Au nanoparticles. However, this activity is suppressed when encapsulated inside graphene shells. At the same time presence of graphene shells make the heterostructures spatially-resolved with a broad extinction efficiency peak at ~ 535 nm when the incident wave vector is in the nanowire axial direction and no peak in case of wave vector in nanowire radial direction. In addition, normalized electric field of plasmons were distributed over larger surface of GNPs in Si nanowire-GNP heterostructures as compared to only limited to interfaces in Si nanowire-Au nanoparticles heterostructures. Overall, incident light wavelength, morphologies of components, distribution density, and the encapsulating shell thickness strongly influence the intensity, peak location of extinction spectra, and distribution of normalized electric field. Results also indicate strong field intensity mainly concentrated at the Si-Au interface and quenched sharply as well as broadly distributed by ~ 2 nm graphene shells.

PART IV

THERMAL MANAGEMENT ON NANO-CARBON MATERIALS

CHAPTER 14

CHEMICALLY MODIFIED AND DOPED CARBON NANOTUBE-BASED COMPOSITES WITH TUNABLE THERMAL CONDUCTIVITY GRADIENT

Yuan Li,¹ Nitin Chopra^{1,2,}*

¹Metallurgical and Materials Engineering Department, Center for Materials for Information Technology (MINT), The University of Alabama, Tuscaloosa, AL 35487, U.S.A.

²Department of Biological Sciences, The University of Alabama, Tuscaloosa, AL 35487, U.S.A.

*Corresponding Author

E-mail: nchopra@eng.ua.edu

Tel: [205-348-4153](tel:205-348-4153)

Abstract

Nitrogen (N)-doped and un-doped MWCNTs grown using a chemical vapor deposition (CVD) process were studied for their surface chemical modification and thermal characteristics. Various surface functional groups developed through acid purification or controlled plasma oxidation of MWCNTs were analyzed using X-ray photoelectron spectroscopy (XPS). High resolution electron microscopy was used to understand the structure and morphology of the surface-modified/unmodified MWCNTs. Thermal conductivities of surface-modified/unmodified MWCNT films were estimated using the shifts in Raman peaks for MWCNTs as a function of incident laser power (1 – 50 mW) and film temperature (60 – 120 °C). The thermal conductivity of pristine un-doped MWCNT films was much higher (~70 W/m-K) than that of N-doped MWCNT films (~16-27 W/m-K). Plasma oxidation or acid treatment further reduced the conductivity (~8-14 W/m-K). Thermal maps or temperature distribution profiles for MWCNT films were theoretically evaluated. Finally, different combinations of doped/un-doped and plasma/acid-treated MWCNTs were stacked and impregnated within a polystyrene matrix to result in a gradient of thermal conductivity across the thickness direction of the nanocomposite. Temperature distribution profiles within these nanocomposites were studied using the hot wire method.

Keywords: carbon nanotubes; nitrogen-doping; oxygen plasma; acid treatment; thermal conductivity; nanocomposite

14.1. Introduction

Thermal management using carbon nanotubes (CNTs) is of significant interest [355]. Individual single-walled or multi-walled CNT (SWCNT or MWCNT) exhibit thermal conductivities as high as 2000 W/m-K to 6000 W/m-K [355]. This is nearly 10 times higher than that of copper and silver [356]. Additionally, random network/mesh of CNTs, CNT mats, buckypaper, and vertically-aligned CNT arrays are of interest for integrated circuits, flexible or transparent substrates, gas and biosensing, optoelectronics, and thermal interface layers for heat dissipation [357]. Although such CNT architectures have bulk thermal conductivities (10-220 W/m-K) much lower than single-walled and individual CNTs, they are still useful for controlled enhancement in thermal conductivities of polymers [358]. Lower thermal conductivity of bulk CNTs could be attributed to the presence of amorphous carbon, multiple walls (MWCNTs), defects, impurities and inter-tube junction resistance, all resulting in phonon scattering [359].

Surface chemical modification or doping (e.g., boron, phosphorus, and nitrogen) of pristine CNTs could influence their electrical conductivity and electrochemical properties [360]. Surface modification methods such as acid and plasma treatment [361] can alter the surface morphology and defect-density of CNTs. Furthermore, strong acid treatment can effectively purify CNTs by removing metal catalyst and amorphous carbon as well as derivatizing CNT surface with carboxylic (-COOH) groups. Gas-phase plasma oxidation allows greater control over CNT surface modification [362]. This approach is solvent-free, time-efficient, tunable, and provides a wide range of functional groups depending on the plasma conditions [363]. In addition, such treatments for tailoring CNT thermal conductivity hold great potential for realizing thermally-anisotropic/graded films or nanocomposites. However, such knowledge in regard to chemically-modified CNTs remains limited due to the lack of understanding on the thermal transport behavior

and the resulting temperature profiles across bulk CNT networks [364]. Overall, CNT fillers in polymer matrix can result in enhanced properties of the nanocomposite [358] and if thermal anisotropy is observed it is attributable to the arrangement of CNTs within the polymer matrix and distinct radial/axial phonon transport [365] across CNTs. The alignment of thermally conductive CNTs or carbon fibers within a polymer matrix is a critical challenge and calls for simplified approaches to impart thermal anisotropy/gradient in such nanocomposites [366].

To overcome the issues related to the arrangement/orientation of CNTs [367], a promising approach is to stack films of CNTs with variable thermal conductivity within the matrix. In this regard, the authors hypothesize that careful control of dopant and functional group density in CNTs or their surface modification will allow for easy manipulation of their thermal conductivities. Furthermore, stacking layers of such modified CNTs will lead to the development of a novel approach for thermally-graded nanocomposite design. The major goal is to develop multifunctional CNT-polymer nanocomposites with thermal conductivities varying across the direction of thickness of the nanocomposites. The use of MWCNTs for such a nanocomposite fabrication will be a cost-effective and simple approach for bulk thermal management applications. In this article, un-doped and nitrogen-doped MWCNTs (N-MWCNTs) grown via chemical vapor deposition (CVD) were acid-treated or plasma-oxidized. They were further characterized for their crystallinity, morphology, and surface functionality using microscopic and spectroscopic methods. Raman spectroscopy and microscopy methods [368] were used to understand the relationship between the G band location, laser power (Q) and film temperature (T). This further allowed for the estimation of the thermal conductivities of un-doped and N-doped MWCNTs before and after plasma or acid treatment. Fundamental thermal transport theory was utilized to understand temperature distribution profiles in the fabricated MWCNT films. Further, films comprised of

stacked layers of differently-treated or doped MWCNTs were impregnated within a polystyrene matrix by coupling drop casting and spin coating methods. The resulting nanocomposites exhibited controlled thermal conductivity gradient in the cross-thickness direction with a constant thermal conductivity for a specific MWCNT film. These nanocomposites were studied for temperature distribution profiles or thermal gradient using the hot wire method.

14.2. Experimental details

Materials and Methods: Silicon (Si) wafers ((100), n-type) were purchased from IWS (Colfax, CA). Xylene, pyridine, acetonitrile and ethyl alcohol were purchased from Fisher Scientific (Pittsburgh, PA). Polystyrene and toluene were bought from Acros Organics (New Jersey, USA). A-B glue was purchased from Walmart Inc. (Tuscaloosa, AL). Silver paint was purchased from SPI supplies (West Chester, PA). DI water (18.1 M Ω -cm) was obtained using a Barnstead International DI water system (E-pure D4641). All chemicals were used without further purification. Dispersion of MWCNTs in ethanol was done in a Branson 2510 Sonicator (Danbury, CT). Labnet centrifuge (Edison, NJ) was used to clean, wash, and separate nanostructures. Oxygen plasma treatment was performed in a Nordson March Jupiter III Reactive Ion Etcher (Concord, CA). ATC ORION sputtering system (AJA international, Inc., North Scituate, MA) was used. ITO and copper targets (both 99.999% purity) were purchased from AJA International, Inc. MWCNT growth was conducted in a Lindberg blue M 3-zone tube furnace (Watertown, WI). Quartz tube was purchased from ChemGlass (Vineland, NJ). Syringe injector was obtained from Fisher Scientific (Suwanee, GA). Gas flow rates during the CVD process were controlled by Teledyne Hasting powerpod 400 mass flow controllers (Hampton, VA). Thermocouples and temperature

controllers were bought from Omega Engineering (Stamford, CT). H₂ (UHP grade, 40% balanced with Ar) and Ar (UHP grade) gas cylinders were purchased from Airgas South (Tuscaloosa, AL).

Synthesis of un-doped and N-doped MWCNTs: The synthesis of N-MWCNTs (or doped MWCNTs) and un-doped MWCNTs were described in previous reports [369]. Briefly, N-doped MWCNTs and un-doped MWCNTs were synthesized in a floating-catalyst CVD process, using ferrocene as the catalyst. The feed precursor used was pyridine-ferrocene for 2.6% N-doped MWCNTs (2.6%N-MWCNTs), acetonitrile-ferrocene for 5% N-doped MWCNTs (5%N-MWCNTs), and xylene-ferrocene for un-doped MWCNTs. For un-doped MWCNTs, the carrier gas was comprised of Ar mixed with 10% H₂.

Surface modification of un-doped and N-doped MWCNTs: Un-doped MWCNTs, 2.6%N-doped MWCNTs, and 5% N-doped MWCNTs were purified by sonication in 3:1 H₂SO₄:HNO₃ for 6 h at 70 °C. This was followed by centrifuging at 6000 rpm for 60 min. Supernatant was removed and fresh DI-water was added to the remaining MWCNTs and centrifuged again. This washing process was repeated until the pH of the supernatant reached ~7. The purified MWCNTs were dispersed in ethanol (~1 mg/mL) and stored. In regard to surface modification of MWCNTs by plasma treatment, un-doped and N-doped MWCNTs without acid treatment were plasma oxidized for 30 s or 5 min at 100 W and oxygen pressure of 300 mTorr.

Dispersion of MWCNTs on silicon (Si) wafer and preparation of polymer nanocomposites: Si wafer was oxidized at ~1000 °C in air for 12 h to produce the surface oxide layer. Pristine MWCNTs, as well as the acid/plasma-treated MWCNTs were dispersed in ethanol (~1 g/L) and ~4 mL solution was drop-casted on the oxidized Si wafer (2 cm × 2 cm). This substrate was dried at ~60 °C overnight to result in uniform MWCNT films. Such films were prepared for pristine as

well as acid/plasma-treated MWCNTs, resulting in 12 samples as shown in Table 14.1 (Sample #: a1-4, b1-4, and c1-4). Thermal conductivities of these samples were estimated using the Raman spectroscopy and microscopy method [355,370-372]. A similar approach of drop-casting was utilized to fabricate multi-layer MWCNT films, where different combinations of pristine and/or plasma/acid treated MWCNTs were stacked on the oxidized Si wafer. The stacking sequence is shown in Table 14.2. Finally, these MWCNT films were spin-coated with polystyrene solution (~50% w/w in toluene) at 2500 rpm for 60 s. The excess polystyrene was removed by spin coating neat toluene solvent at 2500 rpm for 30 s. The samples were dried in a vacuum oven for 48 h (~60 °C) to eliminate air bubbles from the nanocomposite.

Table 14.1. Average diameters for pristine and acid- or plasma- treated MWCNTs and the corresponding sample #.

Samples	Pristine		Acid-treated		Plasma-treated for 30s		Plasma-treated for 5min	
	#	Diameters	#	Diameters	#	Diameters	#	Diameters
Un-doped MWCNTs	a1	85.2 ± 33.10	a2	55.79 ± 45.38	a3	65.82 ± 46.17	a4	38.09 ± 29.25
2.6%N-MWCNTs	b1	25.81 ± 5.69	b2	23.03 ± 6.99	b3	25.04 ± 6.23	b4	23.67 ± 6.30
5.0%N-MWCNTs	c1	38.93 ± 12.85	c2	38.25 ± 8.11	c3	38.68 ± 9.33	c4	37.08 ± 11.41

Thermal conductivity and temperature distribution profile measurements for MWCNT films:

Thermal conductivities of the un-doped and doped MWCNTs, before and after acid/plasma treatment, were measured using Raman spectroscopy method [372]. The following experimental steps were employed: 1) ITO film with a thickness of ~200 nm was sputtered on the back of the oxidized Si wafer, 2) Copper contact pads (~300 nm thick) were sputtered under same conditions for 60 min on the two sides of ITO film, 3) Copper wire (~0.5 mm diameter) was connected to the copper contact pads using silver paint, 4) This substrate with the ITO heat source was affixed to a piece of Teflon® substrate using insulating and sealing A-B glue, 5) MWCNT films comprised of only one kind of MWCNTs (pristine, acid-treated, or plasma-treated) were deposited on the Si wafer as described. This set-up was connected to a DC power source and Raman measurements were recorded (G band peak analysis at 785 nm laser wavelength). The integration time of 10 s and 2 co-additions were utilized for these studies and the measurements were repeated for six times on each sample to obtain the average values of G band location. The relationship between G band position and temperature (G vs. T) was obtained by heating the sample to different temperatures. The temperature was controlled by the DC current flow through the ITO heater. The relationship between G band position and laser power (G vs. Q) was obtained through Raman spectra at different laser powers (1 mW, 10 mW, 25 mW, 50 mW). Finally, thermal conductivity (K) of the MWCNTs was estimated (Eq. (14.1) - (14.11)). The steady-state temperature distribution for MWCNT films was simulated for Raman laser-based optical heating using Eq. (14.4) using Matlab® programming. The estimated thermal conductivities were used for various MWCNT films. The un-doped MWCNT films were evaluated for temperature distribution profiles as a function of Raman laser power (1 – 50 mW) and distance from the center of the laser spot (r , Eq. (14.4)). From this, low incident laser power of ~1 mW was further selected to study temperature distribution

profiles for all the remaining MWCNT films (doped, un-doped, acid-treated, and plasma-treated) as a function of r .

Temperature distribution or thermal map for MWCNT-polymer nanocomposites: The nanocomposites (Sample #1-5, Table 14.2) were peeled from the Si substrate and placed between two polystyrene insulators. A chromium (Cr) wire with diameter ~ 0.5 mm was used as the Joule heating source on one side of the nanocomposite. For all the measurements, a power of ~ 0.4 W was applied to the Cr wire, which resulted in a constant temperature of ~ 80 °C after 30 min of stabilization. The temperature distributions in-plane and through-thickness were obtained by the attached thermocouples arranged in equal spacing (~ 2 mm apart) both at the bottom and top of the nanocomposite. The obtained temperature distributions were utilized as the boundary conditions for the MATLAB®-based simulations in estimating the temperature distribution or thermal maps within the films

Table 14.2. Various nanocomposites prepared by stacking films of doped and/or un-doped MWCNTs (with/without acid/plasma treatment). These stacked MWCNTs layers were impregnated within polystyrene to result in various samples (#1 - #5).

Sample #	Bottom layer	Middle layer	Top layer
1	Pristine un-doped MWCNTs	Pristine 2.6%N-MWCNTs	Pristine 5.0%N-MWCNTs
2	Acid-treated un-doped MWCNTs	Acid-treated 2.6%N-MWCNTs	Acid-treated 5.0%N-MWCNTs
3	un-doped MWCNTs plasma-treated for 30 s	2.6%N-MWCNTs plasma treated for 30 s	5.0%N-MWCNTs Plasma-treated for 30 s
4	un-doped MWCNTs plasma-treated for 5 min	2.6%N-MWCNTs Plasma-treated for 5 min	5.0%N-MWCNTs Plasma-treated for 5 min
5	Pristine un-doped MWCNTs	Pristine 5%N-MWCNTs	Acid-treated 5%N-MWCNTs

Characterization methods: Scanning Electron Microscopy (SEM) images were obtained using FE-SEM JEOL-7000 equipped with energy dispersed X-ray spectroscopy (EDX). Tecnai F-20 was used to collect Transmission Electron Microscopy (TEM) images. TEM samples were prepared by dispersing the as-prepared samples on lacey carbon TEM copper grids purchased from Ted Pella Inc. (Redding, CA). X-ray photoelectron spectra (XPS) were gathered by Kratos Axis 165 with mono-Aluminum gun at 160 eV pass energy for a full range scan and 40 eV pass energy for a detailed scan. The analysis spot was set as “Slot” with >20 μm aperture and 19.05 mm iris setting. Raman spectra were collected using Bruker Senterra system (Bruker Optics Inc. Woodlands, TX) equipped with 785 nm laser source at 10-25 mW laser powers and 50X objective. Multiple measurements were performed on each sample indicated average values with standard deviation. The MWCNT diameters were estimated using Nano Measure software (version 1.2). More than 200 MWCNTs were included to obtain the average values. Temperature profiles were estimated using Matlab 7.1 (MathWorks, Inc.).

14.3. Results and discussion

14.3.1 Synthesis and surface modification of doped and un-doped MWCNTs

MWCNTs were grown in a hydrocarbon-based floating catalyst CVD process. Hydrocarbon-catalyst precursors such as xylene-ferrocene, pyridine-ferrocene, and acetonitrile-ferrocene were used to synthesize un-doped MWCNTs, 2.6%N-doped MWCNTs, and 5%N-doped MWCNTs, respectively. Pristine MWCNTs were treated with either acid for 6 h or oxygen plasma for 30 sec and 5 min to result in surface modification. The treated MWCNTs were drop-casted onto a Si wafer to result in a random mesh film with a thickness of $\sim 2.5 \pm 0.3 \mu\text{m}$. Figure 14.1 shows the

front and cross-section of pristine MWCNT films. Similar films were fabricated for acid- or plasma-treated MWCNTs corresponding to all the samples described in Table 14.1, and additionally indicates the average diameters of the MWCNTs. TEM images of doped and un-doped MWCNTs (before and after acid or plasma treatment) are shown in Figure 14.2. All MWCNTs exhibited wall spacing of $\sim 0.34\text{-}0.35$ nm (Figure 14.2), which is consistent with the c-axis spacing of the graphite. A well-defined bamboo-like structure was observed for the doped MWCNTs similar to earlier reports [373]. Catalytic Fe nanoparticles were observed within the cores of MWCNTs from the ferrocene precursor. Acid- or plasma-treated MWCNTs (Figure 14.2B-D, F-H, J-L) led to damaged structure (e.g., stress marks, amorphous carbon, uneven edges/sidewalls) compared to pristine MWCNTs (Figure 14.2A, E, and I). Un-doped MWCNTs were more damaged than doped MWCNTs and amorphous carbon deposits after acid or plasma treatment were observed on the latter (arrows in Figure 14.2).

The presence of N atoms inhibits the growth of MWCNTs because N atoms tend to occupy the growing edges of the nanotubes rather than the hexagonal lattices [374]. The edges of MWCNTs are most likely saturated with N atoms and hinder the incorporation of incoming carbon atoms into the growing MWCNTs [375]. This possibly led to the growth inhibition of doped MWCNTs resulting in smaller diameters as compared to un-doped MWCNTs (Table 14.1). The average diameter after acid or plasma treatment was further reduced for un-doped MWCNTs (sample # a1-4, Table 14.1). Reduction in un-doped MWCNT diameters from ~ 85 nm to ~ 55 nm after acid treatment was observed. However, plasma oxidation (a dry oxidation method) resulted in controlled etching of MWCNTs. For example, the average diameter of un-doped MWCNTs reduced from ~ 85 nm to ~ 65 nm and ~ 38 nm after 30 sec and 5 min of plasma oxidation, respectively. The greater decrease in MWCNT diameters within 5 min plasma oxidation suggests

that this process is more intense as compared to acid treatment. Interestingly, it was observed that doped MWCNTs (sample # b1-4 and c1-4) were most stable during acid or plasma treatments as indicated by the minimal changes in the average diameters before and after. This could be attributed to the graphite CN_x structure [376].

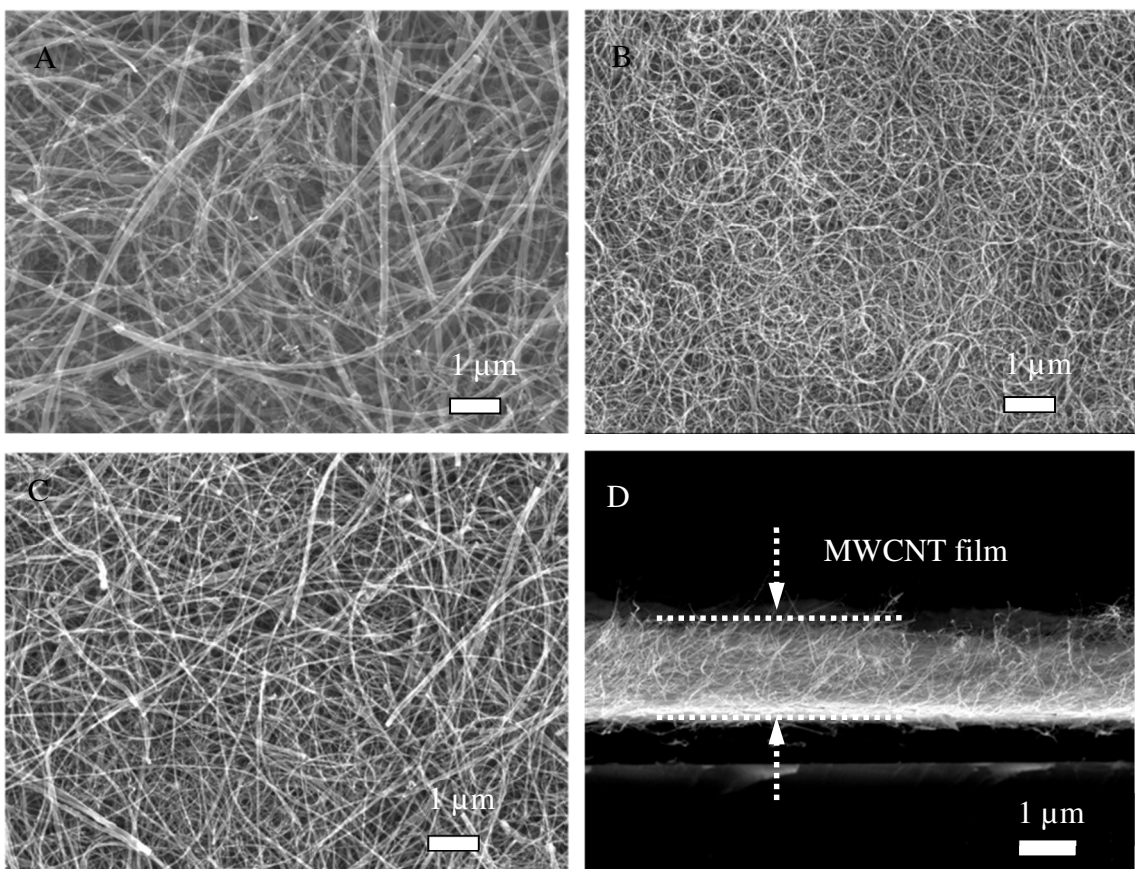


Figure 14.1. (A-C) SEM images showing the morphology and dispersion of pristine MWCNT films (sample #a1, #b1, #c1) comprised of (A) un-doped MWCNTs, (B) 2.6%N-MWCNTs, and (C) 5%N-MWCNTs. (D) A representative SEM image of the cross-section of drop-casted MWCNT film (pristine and un-doped) on the oxidized Si wafer. *Note: The sample # are detailed in Table 14.1.*

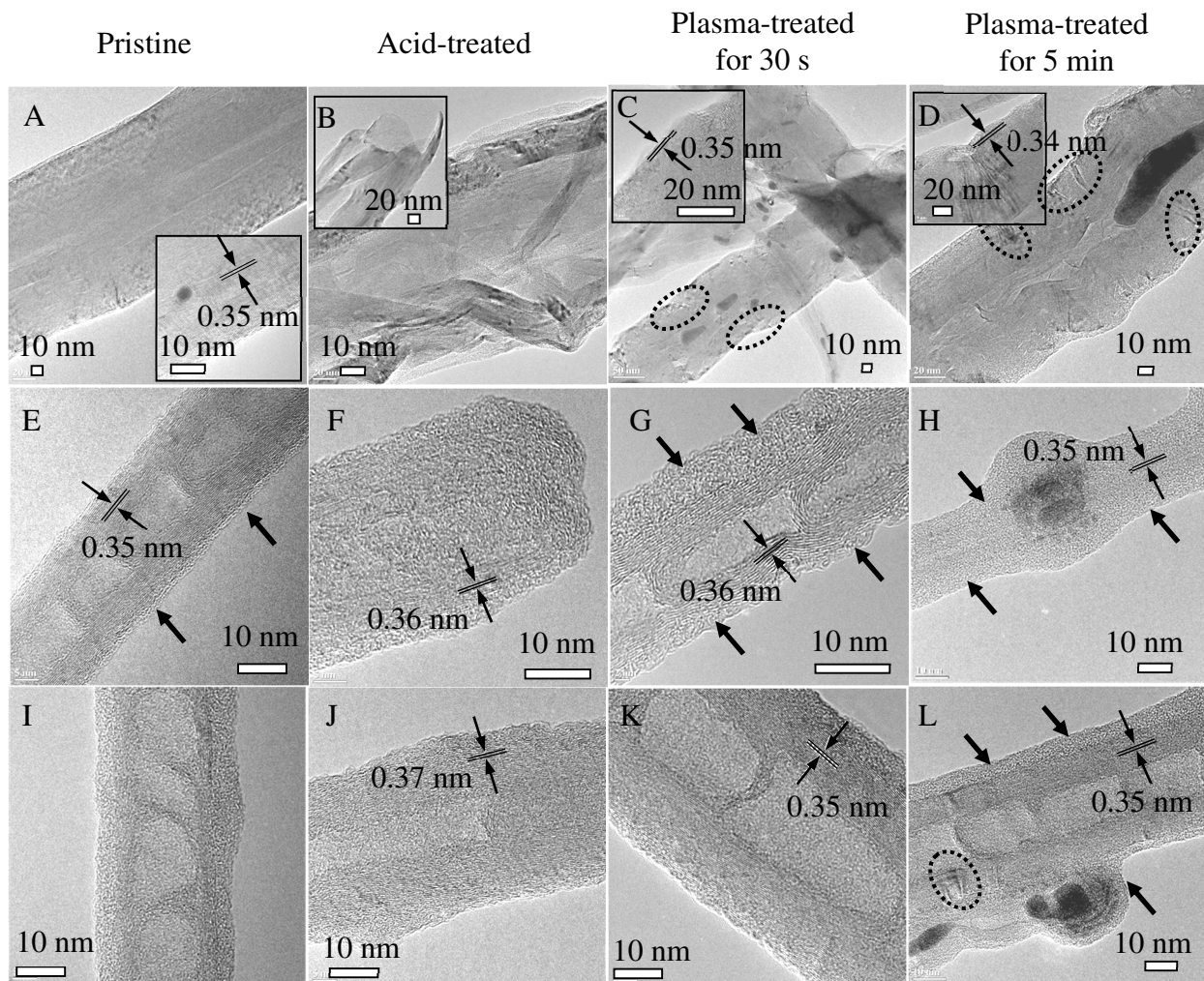


Figure 14.2. TEM images of the un-doped and N-doped MWCNTs before and after acid or plasma treatment. (A-D) Un-doped MWCNTs, (E-H) 2.6%N-MWCNTs, and (I-L) 5%N-MWCNTs. *Note: Insets show the lattice or inter-wall spacing for MWCNTs. The dotted rings indicate the defects and stress marks while arrows indicate amorphous carbon.*

To further understand acid or plasma oxidation of MWCNTs, XPS studies were conducted to estimate the percentage of carboxylic (-COOH) and other surface groups. Thus, C 1s and N 1s spectra for MWCNTs before and after acid or plasma treatment were analyzed. Un-doped MWCNTs N-based surface functionalities were absent on un-doped MWCNTs due to the absence of N 1s signals in XPS (sample #a1-4). Pristine MWCNTs (doped or un-doped) showed 4-10% of -COOH groups on the surface (Figure 14.3A), which could be attributed to air oxidation of defective sites in these MWCNTs [377]. With acid treatment, -COOH group percentages (~11-15%) increased for both doped and un-doped MWCNTs. Plasma oxidation for 30 sec resulted in -COOH groups percentages similar to acid-treated samples but 5 min plasma oxidation led to an increase by ~12-17%. This confirms that 5 min plasma treatment was more intense than 6 h acid treatment. On the other hand, doped MWCNTs (sample #b1-4 and c1-4) resulted in additional surface groups such as pyridinic-N, pyrrolic-N, quaternary-N, and N oxides (Figure 14.3B) [378]. Based on XPS results (Figure 14.3B), the pristine and doped MWCNTs exhibited pyridinic-N, pyrrolic-N, and quaternary-N groups. Pyridinic-N refers to N atoms at the outside layer, each of which is bonded to two carbon atoms and donates one π -electron to the aromatic π system. Pyrrolic-N refers to N atoms that are bonded to two carbon atoms and contributes to the π system with two p-electrons. Quaternary-N is also called "graphite nitrogen", in which N atoms are incorporated into the nanotube, represented as the bamboo-like layers. N-oxides of pyridinic-N are bonded to two carbon atoms and one oxygen atom. The high percentages of pyrrolic-N in the pristine and doped MWCNTs indicated defective structure due to N atom incorporation in the carbon ring [379]. This also explains the lower diameter of doped MWCNTs as compared to un-doped MWCNTs because such heteroatom insertion in carbon ring must have inhibited the growth of MWCNTs [374].

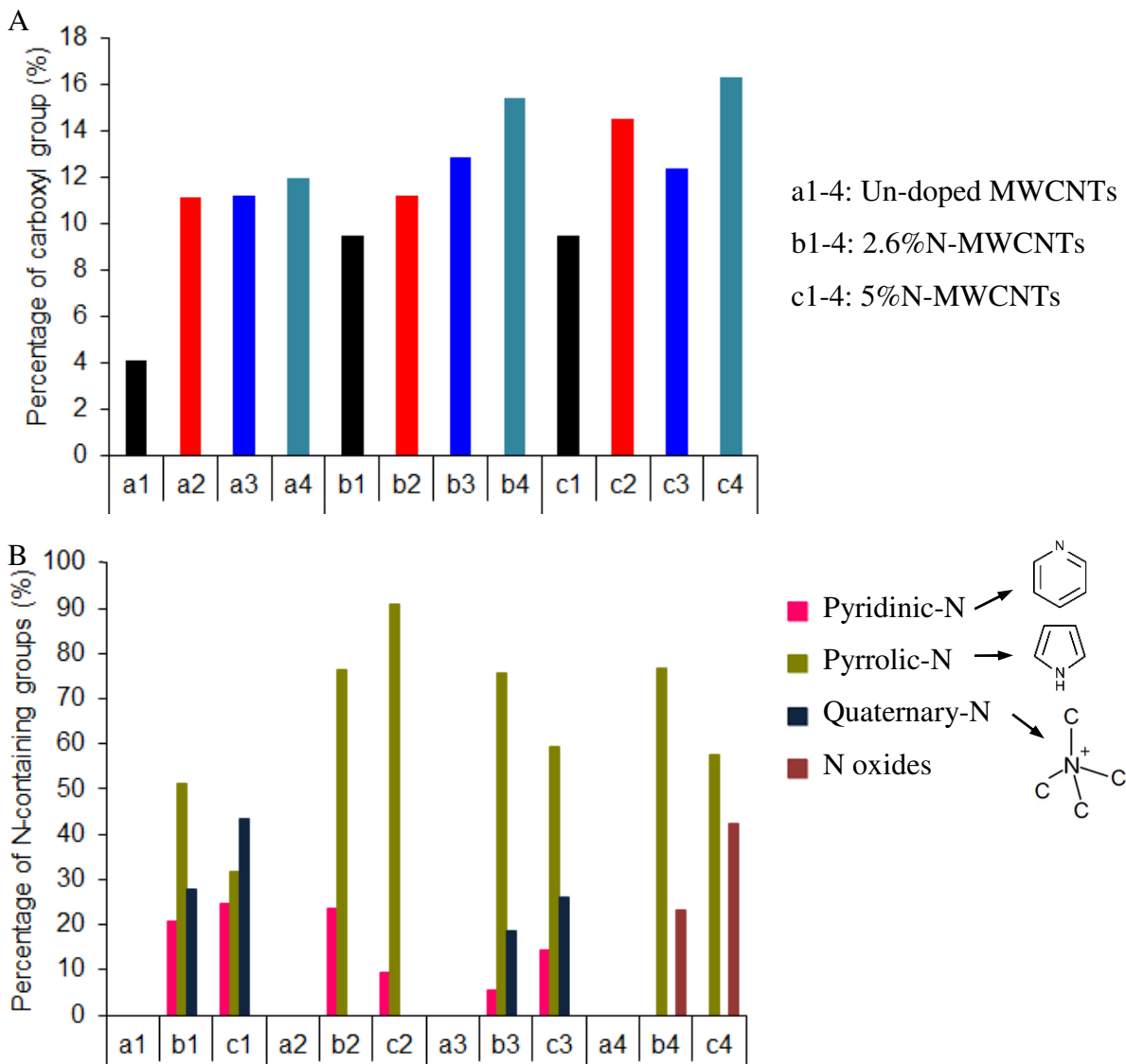


Figure 14.3. Surface groups on the MWCNTs and their percentage (mol%). (A) -COOH and (B) N-containing groups on the MWCNTs before and after acid or plasma treatments. *Note: The sample # and the corresponding treatments are detailed in Table 14.1.*

After 30 sec of plasma treatment, pyridinic-N, pyrrolic-N, and quaternary-N groups remained. However, the percentages of pyridinic-N and quaternary-N groups decreased and pyrrolic-N increased due to the etching of MWCNTs and further creation of amorphous structure. With acid treatment, quaternary-N groups disappeared and only pyridinic-N and pyrrolic-N groups remained, indicating that the quaternary graphitic structure of MWCNTs was largely broken. No N-oxide groups were observed for pristine, acid-treated, and 30 sec plasma-treated samples. However, after 5 min plasma treatment, only N-oxides and pyrrolic-N groups remained, suggesting that all the other surface groups (quaternary-N and pyridinic-N) were completely converted into the former two. Overall, pyrrolic-N groups were estimated to be highest in percentage for doped MWCNTs and could be attributed to CVD growth process and treatment conditions. A major difference between acid and 5 min plasma treatment was that the former could not result in N-oxides while the latter can. Both treatments did not allow for the formation of quaternary-N groups except for very short (30 sec) plasma treatment. The latter assisted in reducing the pyridinic-N groups. Overall, this unique study demonstrates that plasma oxidation could result in controlled surface modification of doped or un-doped MWCNTs.

14.3.2 Thermal conductivity analysis for MWCNT films

Raman spectra of pristine doped or un-doped MWCNTs showed G and D band peaks centered around $\sim 1580\text{ cm}^{-1}$ and $\sim 1312\text{ cm}^{-1}$, (Figure 14.4A) [380]. G band is related to the in-plane bond-stretching motion of pairs of sp^2 carbon atoms from the graphitized structure [380]. D band (disordered band) is the breathing mode of sp^3 rings that is related to bond-angle disorder, bond-length disorder, and hybridization. These can be caused by heteroatom (nitrogen/oxygen) doping

or structural defects. As shown in Figure 14.4A, only un-doped MWCNTs resulted in 2D band located at $\sim 2623 \text{ cm}^{-1}$, indicating zone-boundary phonon scattering in the MWCNTs [381]. The 2D band is a second-order harmonic of the D band, which is highly dispersive and is usually associated with the degree of crystallinity of MWCNTs. The disappearance of 2D band from the doped MWCNTs is due to the introduction of heteroatoms (N). Apart from fundamental information about defects, phonon modes, and graphitic/amorphous content of MWCNTs, Raman spectroscopy can be utilized for the estimation of thermal conductivity [355]. The measurement for thermal conductivity is based on the relationship between the G band shift, temperature (T), and laser power (Q). Digital image and schematic representation of the substrate with MWCNT film and in-situ ITO heater for performing the described Raman measurements is shown in Figure 14.4B and C. The incident Raman laser on the sample can be considered as an optical heat source and by varying Q, it is possible to manipulate the sample temperature (T) and observe shifts in G band peak in the corresponding Raman spectra [382]. Similarly, by using a low laser power ($\sim 1 \text{ mW}$) and controlling the temperature of the MWCNT films through ITO heater, G band peak locations as a function of T were evaluated. Raman spectra for various samples (a1-4, b1-4, and c1-4) as a function of laser power (Q $\sim 1 - 50 \text{ mW}$) was collected. For un-doped MWCNTs (with or without treatment), there was a minor decrease in I_D/I_G ratio with increasing Q. However, increasing trends in I_D/I_G ratio as a function of Q was observed for doped MWCNTs. This indicated that Raman laser influenced the MWCNT structure, altered the disordered carbon content, and etched/burnt MWCNTs. The lowering of this ratio, for un-doped MWCNTs, with increasing Q indicated that under higher Q, it was possible to remove amorphous carbon content. On the other hand, increase of this ratio with increasing Q for doped MWCNTs suggested that graphitic content or more defects were created in these under intense Raman laser exposure. Similarly, G band peak

location was also studied as a function of T and temperature showed minimal influence on the I_D/I_G ratios.

An infinitesimally-small ring of radius ($r=r$) is considered for the MWCNT film was created. The heat transfer take place across the areas given by $A_1 = 2\pi r t$ and $A_2 = 2\pi(r + dr)t$. The infinitesimal volume is given by $V_r = 2\pi r t dr$. As per heat conservation across this volume results in:

$$-KA_1 \frac{dT}{dr} \Big|_r = -KA_2 \frac{dT}{dr} \Big|_{r+dr} - q''' V_r, \quad (14.1)$$

where q''' is the incident heat flux per unit volume generated by Raman laser and given by

$q''' = \frac{q''}{t} \exp(-\frac{r^2}{r_0^2})$. So, Eq. (14.1) can be written as Eq (14.2) in following steps:

$$2\pi(r + dr)t \cdot K \frac{dT}{dr} \Big|_{r+dr} - 2\pi r t \cdot K \frac{dT}{dr} \Big|_r = -2\pi r t dr \cdot \frac{q''}{t} \exp(-\frac{r^2}{r_0^2}), \text{ and}$$

$$\frac{1}{r} \cdot \frac{r \frac{dT}{dr} \Big|_{r+dr} - r \frac{dT}{dr} \Big|_r}{dr} = -\frac{q''}{Kt} \exp(-\frac{r^2}{r_0^2}). \quad (14.2)$$

If we consider $dr \rightarrow 0$, then the second-order differential equation for heat transfer in cylindrical

coordinates is given by $\frac{1}{r} \cdot \frac{d}{dr} (r \frac{dT}{dr}) = -\frac{q''}{Kt} \exp(-\frac{r^2}{r_0^2})$. This results in:

$$\frac{d^2 T}{dr^2} + \frac{1}{r} \cdot \frac{dT}{dr} = -\frac{q''}{Kt} \exp(-\frac{r^2}{r_0^2}) \quad (14.3)$$

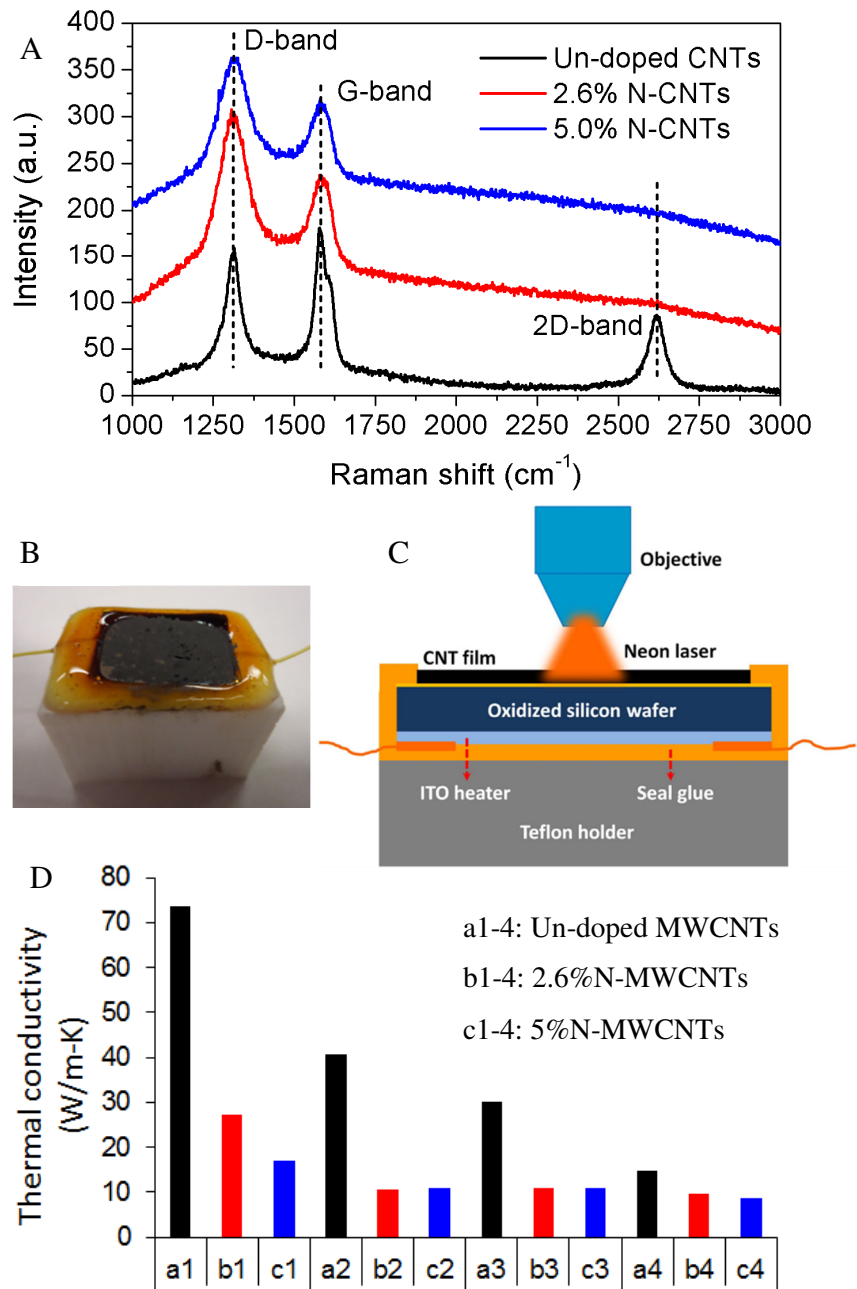


Figure 14.4. (A) Raman spectra of pristine un-doped and doped MWCNTs (sample #a1, b1, c1). (B) Digital image and (C) schematic representation of the sample-heater geometry for the thermal conductivity measurement. (D) Histogram showing the thermal conductivities for un-doped and N-doped MWCNTs before and after acid or plasma treatment.

where T is the steady-state temperature, r is the radial position measured from the center of the laser spot, r_0 is the radius of laser spot, q'' is the maximum absorbed laser power per unit area at the center of the spot, K is the thermal conductivity, and t is the film thickness. Assuming the boundary conditions as: $dT/dr|_{r=0}=0$ and $T(r=R)=T_0$, where R is the radius of the location at which the temperature is room temperature (T_0). Further integrating Eq. (14.3) using Matlab®, the temperature profile (Figure 14.5) could be estimated using:

$$T(r) = T_0 + \frac{Q}{4\pi Kt} \left[Ei\left(-\frac{r^2}{r_0^2}\right) - Ei\left(-\frac{R^2}{r_0^2}\right) + 2 \log\left(\frac{r}{R}\right) \right] \quad (14.4)$$

where $Ei(x)$ is the exponential integral, T_0 is the edge temperature, R is the radial edge of MWCNT film, Q represents the Raman laser power absorbed by the MWCNT film. Considering the thickness of MWCNT film, we assumed that the laser power was completely absorbed in this study. The temperature rise in the MWCNT film ($T_m = T(r) - T(R)$) measured by the Raman microscope is given as follows:

$$T_m \approx \frac{\int_0^R T(r) \exp\left(-\frac{r^2}{r_0^2}\right) r dr}{\int_0^R \exp\left(-\frac{r^2}{r_0^2}\right) r dr} \quad (14.5)$$

The relationship between T_m and Q was obtained by integrating Eq. (14.5) in a Matlab® programing and resulted in Eq. (14.6):

$$T_m \approx T_0 + \frac{Q}{2\pi Kt} \cdot \frac{\int_0^R \left[Ei\left(-\frac{r^2}{r_0^2}\right) - Ei\left(-\frac{R^2}{r_0^2}\right) + 2 \log\left(\frac{r}{R}\right) \right] \exp\left(-\frac{r^2}{r_0^2}\right) r dr}{\left[1 - \exp\left(-\frac{R^2}{r_0^2}\right) \right] r_0^2} . \quad (14.6)$$

Assuming $\frac{\int_0^R [Ei(-\frac{r^2}{r_0^2}) - Ei(-\frac{R^2}{r_0^2}) + 2\log(\frac{r}{R})] \exp(-\frac{r^2}{r_0^2}) r dr}{[1 - \exp(-\frac{R^2}{r_0^2})] r_0^2} = S$, The following is obtained

$$T_m \approx \frac{S}{2\pi K t} \cdot Q + T_0 \quad (14.7)$$

The estimation of K was based on Eq. (14.7), where S is a constant depends on r_0 and R . Experimentally, we obtained the linear relationship for G band position (G) and incident laser power (Q),

$$G = m_1 Q + n_1, \quad (14.8)$$

Linear relationship for G band position and MWCNT film temperature (T),

$$G = m_2 T + n_2, \quad (14.9)$$

Combining Eq. (14.8) and (14.9), a relationship between T and Q is derived as follows:

$$T = m_3 Q + n_3 \quad (14.10)$$

As shown in Table 14.3, further combining Eq. (14.7) and Eq. (14.10) allow for estimating the thermal conductivity (K) (Figure 14.4D):

$$K = \frac{S}{2\pi m_3} \quad (14.11)$$

With the help of estimated thermal conductivity (K), Matlab® was used to derive the temperature profiles at various Raman laser powers (Q) using Eq. (14.4). A mesh of 1000×1000 was built in a

2 mm diameter from the center of laser spot. The temperature profiles were estimated as a function of Raman laser power (Q), thermal conductivity of the MWCNT film (K), and distance from the center of the laser spot (r).

Table 14.3. G vs. Q , G vs. T , and T vs. Q obtained using the Raman spectroscopy and microscopy method. G represents the G band peak location in the Raman spectra.

	Methods	Un-doped MWCNT	2.6%N-MWCNT	5.0%N-MWCNT
G vs. Q	Pristine	$G=-0.17Q+1583.46$	$G=-1.01Q+1593.02$	$G=-1.20Q+1592.80$
	Acid-treated	$G=-0.46Q+1585.61$	$G=-1.78Q+1599.11$	$G=-1.63Q+1603.27$
	Plasma-treated for 30s	$G=-0.38Q+1583.18$	$G=-1.60Q+1593.76$	$G=-1.36Q+1591.59$
	Plasma-treated for 5min	$G=-0.74Q+1579.40$	$G=-1.57Q+1594.22$	$G=-1.62Q+1592.51$
G vs. T	Pristine	$G=-0.023T+1588.48$	$G=-0.050T+1609.02$	$G=-0.037T+1602.46$
	Acid-treated	$G=-0.040T+1597.95$	$G=-0.037T+1608.69$	$G=-0.033T+1623.08$
	Plasma-treated for 30s	$G=-0.018T+1588.42$	$G=-0.032T+1602.01$	$G=-0.032T+1599.99$
	Plasma-treated for 5min	$G=-0.025T+1589.48$	$G=-0.031T+1601.62$	$G=-0.027T+1598.42$
T vs. Q	Pristine	$T=7.39Q+218.26$	$T=20.20Q+320.00$	$T=32.43Q+261.08$
	Acid-treated	$T=11.50Q+308.50$	$T=48.11Q+258.92$	$T=49.39Q+279.01$
	Plasma-treated for 30s	$T=21.11Q+291.11$	$T=50.00Q+257.81$	$T=42.50Q+262.50$
	Plasma-treated for 5min	$T=29.60Q+403.2$	$T=50.65Q+238.71$	$T=60.00Q+218.89$

The Raman shifts corresponding to the G band peak for various MWCNT samples were plotted as a function of Q and T. A linear trend (negative slope) with increasing Q and T was observed. However, in some cases (for G band vs. Q), this linear trend of the plot was not observed at higher laser powers (>25 mW). This could be due to the burning/damage of MWCNTs and is addressed later. This deviation from linearity was significant for doped MWCNTs as compared to un-doped ones and this could be attributed to the presence of heteroatoms and greater extent of defects in doped MWCNTs [383]. Thus, for thermal conductivity measurements, linear fit of G vs. Q was considered for MWCNT samples. Finally, using G vs. Q and T plots, it is possible to find a relationship between T and Q and this allowed for estimating thermal conductivity (Eq. (14.1)-(14.11)). Thermal conductivities of various MWCNT samples are shown in Figure 14.4D. Irrespective of doping, it was observed that with increasing defects in MWCNTs after acid or plasma treatment, a significant drop in thermal conductivities was observed with respect to the pristine MWCNTs. Since doped MWCNTs were inherently more defective than un-doped MWCNTs, the thermal conductivities for the former (as high as ~27 W/m-K) were smaller than the latter (as high as ~74 W/m-K). In addition, acid treatment for 6 h on MWCNTs was less intensive and deteriorating in terms of thermal conductivity as compared to plasma treatment. The lowest thermal conductivity of MWCNTs was observed after 5 min plasma oxidation irrespective of doping of MWCNTs. Un-doped MWCNTs resulted in ~81% drop in thermal conductivity after 5 min plasma treatment. Similarly, a drop of ~63% and ~48% was observed for 2.6%N-doped and 5%N-doped MWCNTs, respectively. Even though the thermal conductivities dropped significantly, acid or plasma treatment of MWCNTs and their N-doping were critical for precisely modulating their bulk thermal conductivities. It is known that thermal transport in carbon nanomaterials is dominated by phonon diffusion in the hexagonal carbon lattice with strong sp^2

bonding [384]. N-containing functional groups [385] further led to defects and modified covalent bond structure of hexagonal carbon lattice, which lowered (as low as 8-11 W/m-K) bulk thermal conductivities. The N substitution also resulted in crystal distortion and acted as the phonon diffusion barrier [386] introducing greater thermal resistance. This was enhanced due to the acid or plasma treatment and poor thermal conductivity of amorphous carbon (~ 0.02 W/m-K) [387].

14.3.3 Temperature distribution profiles for MWCNT films

The thermal conductivities of various MWCNT films (Figure 14.4D) were further utilized for deriving temperature profiles or thermal maps for the MWCNT films. There were two reasons to perform these calculations: a) to develop understanding of temperature distributions within doped or un-doped MWCNTs before and after acid or plasma treatment and b) to evaluate the role of Q in damaging the MWCNT structure. The latter also explained the reason for the observed deviations from linear trends for G band peaks. For the temperature distribution profiles (Eq. (14.4)), it was assumed that the Raman laser was the only source of heat and the MWCNT films rapidly reached steady state temperatures. In addition, the oxidized Si wafer was considered as thermally insulating [388] and thus, the MWCNT films provided the dominant heat transport path. Figure 14.5A shows estimated temperature distribution profiles for un-doped MWCNTs as a function of Q (1 – 50 mW) and the distance from the center of the Raman laser spot (diameter ~ 2 μm). It is critical to analyze short distance (~ 6 μm spot diameter) and long distance (~ 2 mm spot diameter) temperature distribution profiles or thermal maps (Figure 14.5B and 5C). As Q changed, the temperature profile of pristine un-doped MWCNT films also changed. A stable temperature profile within these MWCNTs was observed for ~ 1 mW laser power. These results indicate that

understanding peak temperature ($T(r = 0)$, Eq. (14.4)) and the slope of the temperature profiles (gradient) for various MWCNT films is important.

Peak temperatures as a function of Q (~1 mW, 10 mW, 25 mW, 50 mW) are shown in Figure 14.6A. Un-doped MWCNT films with higher thermal conductivity led to improved heat transport and resulted in lower peak temperatures (Figure 14.6A). However, MWCNTs with defects showed significantly high peak temperatures (calculated to be ~2800 °C) due to poor heat transport characteristics. Representative SEM images of pristine 2.6%N-doped MWCNTs showed the burning of MWCNTs at 25 mW (peak temperature ~520 °C) and 50 mW (peak temperature ~1015 °C) (Figure 14.6B-E). It was found that 1 mW laser power resulted in lowest peak temperatures for un-doped MWCNTs before and after acid or plasma treatment (<87 °C). This is also consistent with a previous study on thermal stability of un-doped MWCNTs corroborating their sustainability until 400 oC [389]. Such low peak temperatures for MWCNT films for various laser powers also explained the linear correlation between G band and Q for un-doped MWCNTs.

Higher peak temperatures estimated for doped MWCNTs before and after acid or plasma treatment and microscopic evidence of their burning explains the deviation of G band vs. Q from linear trends at higher Q. This further re-confirms increasing trends for I_D/I_G ratios as a function of Q for doped MWCNTs. Further differentiation of the obtained temperature profiles gives dT/dr as a function of the distance from the center of the laser spot. An inflection point was observed around $r = 1.12 \mu\text{m}$, irrespective of incident Q and MWCNT sample type. MWCNT films with low thermal conductivity resulted in large dT/dr at $r = 1.12 \mu\text{m}$, indicating that the heat transfer process was difficult in such films. Overall, this fundamental knowledge is critical to fill the knowledge gap regarding surface-modified MWCNTs and their applications in bulk thermal nanocomposites as discussed next.

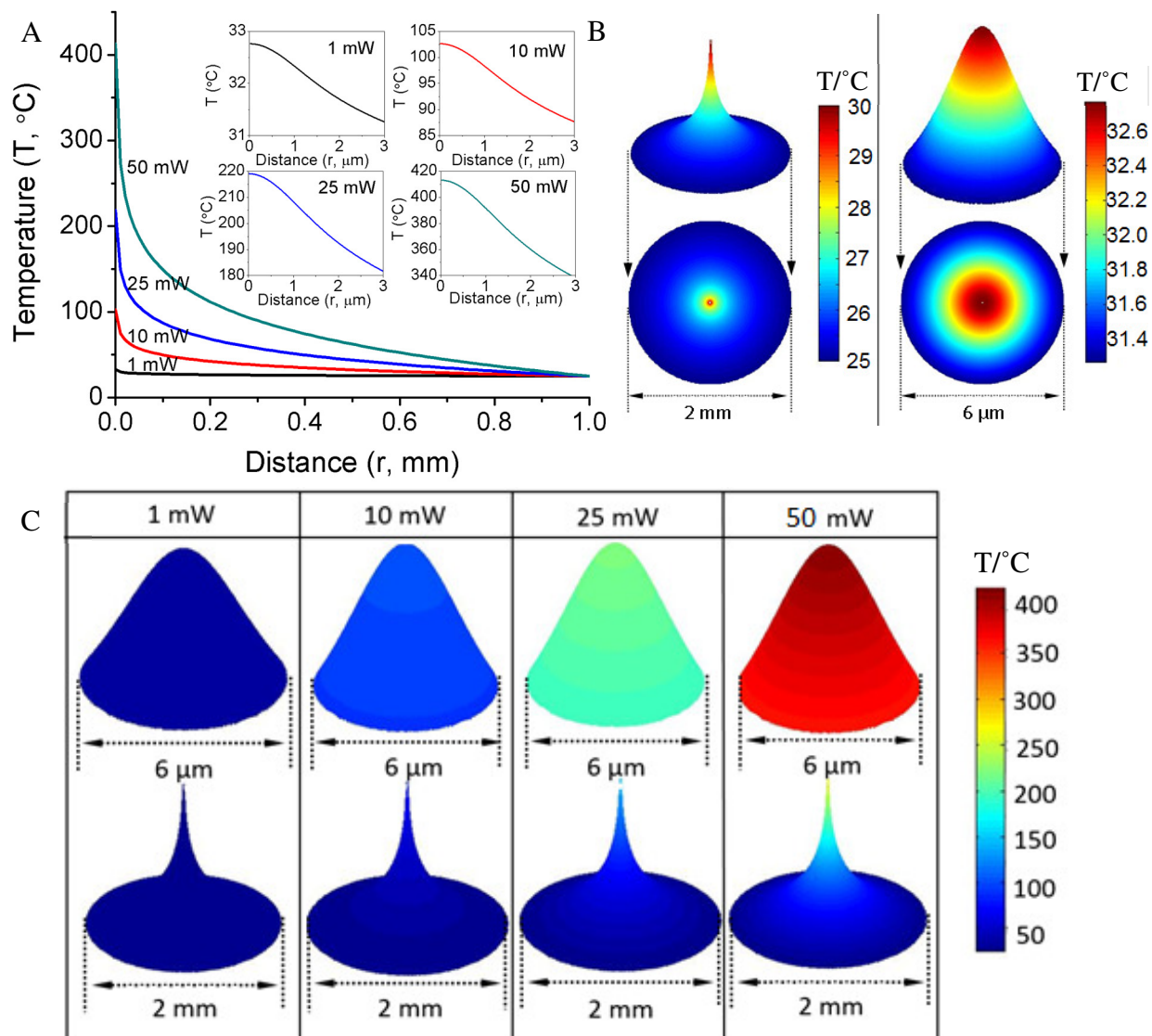


Figure 14.5. Theoretical estimation of temperature distribution profiles for the MWCNT films (sample #a1). (A) Representative profile for the pristine and un-doped MWCNT film as a function of Q . (B) Detailed thermal map for the pristine and un-doped MWCNT film at 1 mW and (C) corresponding to different Q .

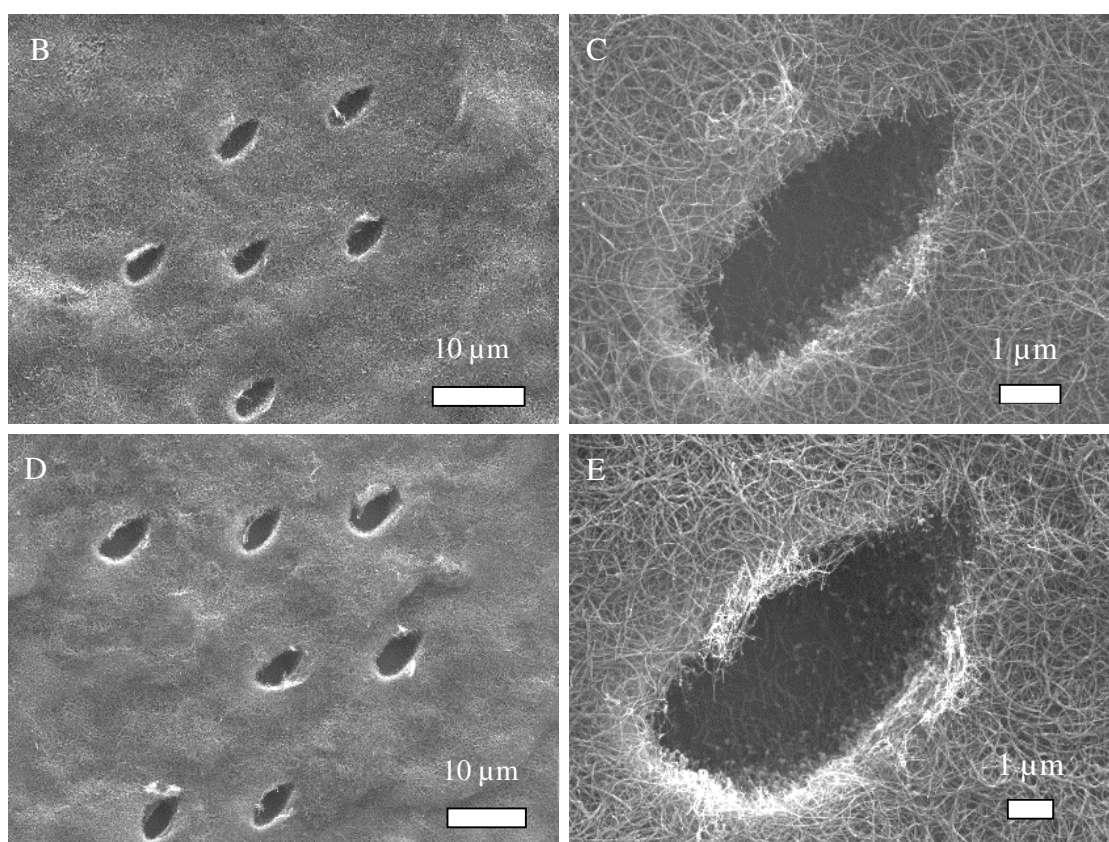
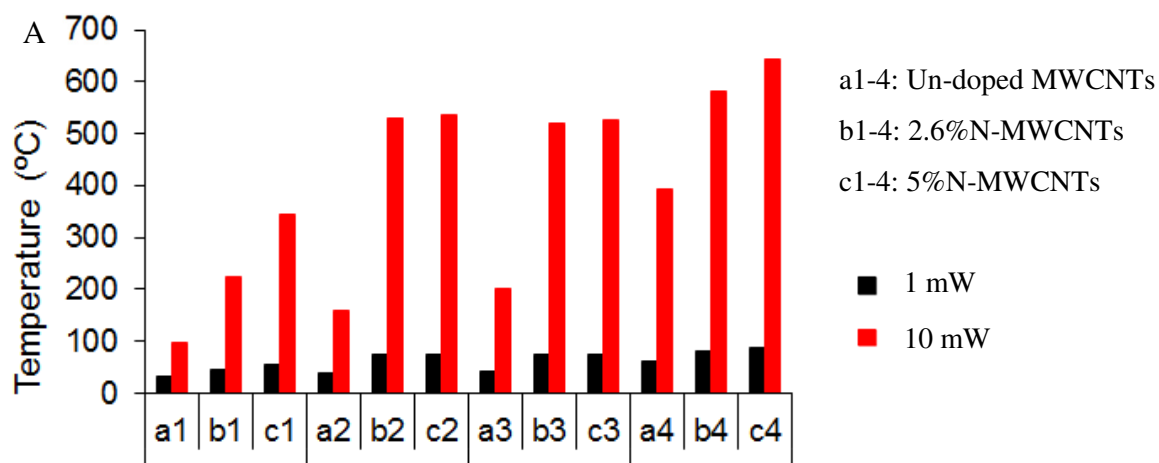


Figure 14.6. (A) Calculated peak temperatures at the center of Raman laser spot on the MWCNT films corresponding to laser power of 1 mW and 10 mW. (B-E) SEM images of 2.6%N-MWCNT film (sample #b1) after exposure to Raman laser with Q fixed at (B, C) 25 mW and (D, E) 50 mW.

14.3.4 MWCNT-polystyrene nanocomposites and their thermal behavior

A schematic of the nanocomposite studied is shown in Figure 14.7A. Individual MWCNT films were drop-casted on the substrate or on previously laid MWCNT film(s) to result in a three-layered stack. This stack was further impregnated within a thermally-insulating polystyrene matrix in a spin coating process. The aim was to enhance thermal conductivity of the polystyrene with MWCNTs as nanofillers. Importantly, stacking MWCNT films of different kinds (doped, undoped, acid- or plasma-treated) allowed for a controlled variation (or gradient) in the thermal conductivity of nanocomposites leading to distinct in-plane and cross-thickness heat transport. Thus, five different kinds of nanocomposites (Table 14.2), each having three layers of different kinds of MWCNTs, were fabricated. Figure 14.7B shows the digital image of flexible nanocomposite (15 mm × 13 mm × 0.03 mm) peeled from the substrate. SEM images show the top, bottom, and cross-sectional view of the stacked MWCNT films within the polystyrene matrix (Figure 14.7C and D). MWCNTs were present as a random mesh with each layer ~10 μm thick. It must be noted that treatment of polystyrene impregnated MWCNT films in a vacuum oven allowed for elimination of air bubbles and resulted in a compact nanocomposite with thickness ~30 μm. Finally, a hot wire method was utilized for understanding heat transport and temperature distribution within and on the surface of the nanocomposites (Figure 14.7E). Cr wire was used as a Joule heating source to maintain a stable temperature at bottom side of the nanocomposite. Temperature at various locations (uptil ~10 mm planar distance) on the top (T_T) and bottom (T_B) surface of the nanocomposite were measured by inserting five equally-spaced thermocouples. Figure 14.7F shows the location of hot wire and thermocouples. A power of ~0.4 W was applied to the Cr wire and steady state was reached within 30 min. A blank polystyrene film was also

prepared, as a control, in a similar spin coating method to result in thickness consistent with the nanocomposites.

For various nanocomposites, temperature vs. distance plots are shown in Figure 14.7G-K. It was observed that T_T and T_B were different for all the nanocomposites, which is due to thermal conductivity gradient in the cross-thickness direction of nanocomposite. The temperature difference ($T_B - T_T$) between the top and bottom surface of nanocomposites as a function of distance from the Cr wire was estimated. The temperatures along the x -axis exponentially decreased and also indicate the temperature differences generated for similarly-treated MWCNT films impregnated within polystyrene matrix (sample #1-5). Sample #5 is the one with maximum thermal conductivity difference between the stacked MWCNT films. The temperature difference between the top and bottom surface of the nanocomposites strongly depended on the thermal conductivity of the individual MWCNT film stacked within the polystyrene matrix [390]. The trend in temperature difference between the top and bottom surface of nanocomposite, for distances less than 5 mm from the hot wire, is in the following order: sample #2 < sample #3 < sample #1 < sample #4. In addition, a sharp decrease in the temperature difference was observed within 5 mm from the hot wire. For the bottom MWCNT films in the stack, sample #2 had higher thermal conductivity than sample #3. Thus, sample #2 had lower difference between the top and bottom surface temperatures than that for sample #3. On the other hand, sample #4 had lowest thermal conductivities of all the stacked MWCNT films and thus is difficult to spread heat leading to greater top-to-bottom temperature difference. Sample #1 exhibited the highest thermal conductivity for the bottom MWCNT film while much lower for the top MWCNT film. This resulted in moderate temperature distributions, placing sample #1 between sample #3 and #4. Finally, sample #5 was fabricated by stacking MWCNT films with the largest difference of thermal

conductivities resulting in the largest difference between the top and bottom surface temperature of the nanocomposite. A blank polystyrene film with similar thickness (~30 μm) was also studied and interestingly showed even higher (than sample 5) temperature difference due to thermally insulating characteristics [391]. An important observation for the blank polystyrene film was in regard to the drop in temperature difference as a function of the distance from the hot wire. Thus, for approximately 10 mm distance, the temperature difference was minimal between the top and bottom surface of the blank polystyrene film. Sample #5 showed a similar trend but did not result in higher temperature difference than the blank polystyrene film. This could be attributed to enhanced thermal conductivity of sample #5 and gradient in the cross-thickness direction. In regard to samples #1, 2, 3, and 4, for distances beyond 5 mm from the hotwire, the temperature difference stabilized. However, it remained higher than both the blank polystyrene film as well as sample #5. In sample #1, due to the higher thermal conductivity of the bottom MWCNT film resulted in lower temperature for bottom as compared to that in the case of blank polystyrene films. In addition, larger temperature difference was observed for blank polystyrene film.

To further evaluate the temperature distribution within nanocomposites, Matlab® programing was used to derive thermal maps in the cross-thickness of the nanocomposites. Each MWCNT layer within the polymer matrix was considered to be homogeneous and the thermal conductivity of a specific MWCNT layer was constant. The heat transfer in x direction, which is along the plane of a specific CNT layer and y direction (cross-thickness of the film). The top (T_T) and bottom surface (T_B) temperatures for the nanocomposites was obtained using experimental observation via hot wire experiment and by fitting ($R^2 \sim 99.5\%$) the data (OriginLab program, Figure 14.6G-K). The fitted equation is given by:

$$T = c \exp(\kappa/b) + T_0', \quad (14.12)$$

where c , b , and T_0' are constants depending on the Joule heating and the effective thermal conductivity of the nanocomposite. Since the thickness of the nanocomposite is very small (~ 0.005 times) as compared to the planer dimensions, Fourier law for 1D steady state heat conduction (Eq. 14.13) through a specific MWCNT layer, in y -direction, can be applied:

$$q = K_e A \frac{dT}{dy}, \quad (14.13)$$

where q , K_e , and A represent the heat flux, effective thermal conductivity of the nanocomposite, and area relevant to the y -direction. For 1D steady heat conduction, Eq. (14.13) can be integrated to result in linear equation (Eq. 14.14),

$$T = c' y + T_0'' \quad (14.14)$$

where c' and T_0'' are constants depending on the Joule heating and the effective thermal conductivity of a specific MWCNT film within the nanocomposite. Thus, combining Eq. (14.12) and Eq. (14.14), it is possible to estimate the temperature distribution profile or thermal map within the nanocomposite [392].

$$T = c \exp(x/b) + c' y + T_0''' \quad (14.15)$$

Following assumptions were made in regard to Eq. (14.15): (1) MWCNTs were uniformly dispersed in the polymer matrix and thermal conductivity of a specific MWCNT film in the stack was constant. (2) Interfacial thermal resistance due to the MWCNT films and interfaces present was negligible. The effective medium theory [393] was utilized to estimate the effective thermal conductivity of the nanocomposite is as follows:

$$K_e = \frac{3 + f \cdot K_c / K_m}{3 - 2f} \cdot K_m \quad (14.16)$$

where K_e represents effective thermal conductivity of the nanocomposite, K_C and K_m (~ 0.03 W/m-K) represent the thermal conductivity of MWCNTs and polystyrene, and f represents the volume fraction. The volume fraction f was estimated using the SEM images. Each MWCNT film was fabricated in a similar approach, incorporated same amount of MWCNTs, and resulted in $f \sim 0.43$. The calculated/fitted parameters for Eq. (14.12) – Eq. (14.16) are listed. Finally, Matlab® programing was utilized to solve Eq. (14.12) and Eq. (14.15) to obtain the thermal maps for various nanocomposites (Table 14.2).

Nanocomposite #1:

$$T_B = 63.71 \times e^{(-x/3.52)} + 32.67$$

$$T_T = 60.75 \times e^{(-x/3.82)} + 29.34$$

$$\text{Bottom layer (①} \rightarrow \text{②): } T = 63.71 \times e^{(-x/3.52)} + 32.67 - 42.73y - (68.34 - 68.34)$$

$$\text{Middle layer (②} \rightarrow \text{③): } T = 63.71 \times e^{(-x/3.52)} + 32.67 - 2.69 \times 42.73(y - 0.01) - (68.34 - 67.19)$$

$$\text{Top layer (③} \rightarrow \text{④): } T = 63.71 \times e^{(-x/3.52)} + 32.67 - 42.73 \times 4.36(y - 0.02) - (68.34 - 65.33)$$

Nanocomposite #2:

$$T_B = 57.93 \times e^{(-x/4.23)} + 30.31$$

$$T_T = 56.71 \times e^{(-x/4.88)} + 26.58$$

$$\text{Bottom layer (①} \rightarrow \text{②): } T = 57.93 \times e^{(-x/4.23)} + 30.31 - 31.29y - (66.41 - 66.41)$$

$$\text{Middle layer (②} \rightarrow \text{③): } T = 57.93 \times e^{(-x/4.23)} + 30.31 - 3 \times 31.29(y - 0.01) - (66.41 - 66.10)$$

$$\text{Top layer (③} \rightarrow \text{④): } T = 57.93 \times e^{(-x/4.23)} + 30.31 - 3 \times 31.29(y - 0.02) - (66.41 - 64.22)$$

Nanocomposite #3:

$$T_B = 64.62 \times e^{(-x/3.17)} + 33.85$$

$$T_T = 63.3 \times e^{(-x/3.28)} + 31.27$$

$$\text{Bottom layer (①} \rightarrow \text{②): } T = 64.62 \times e^{(-x/3.17)} + 33.85 - 61.1y - (68.23 - 68.23)$$

$$\text{Middle layer (②} \rightarrow \text{③): } T=64.62 \times e^{(-x/3.17)} + 33.85 - 1.51 \times 61.1(y-0.01) - (68.23-67.62)$$

$$\text{Top layer (③} \rightarrow \text{④): } T=64.62 \times e^{(-x/3.17)} + 33.85 - 1.68 \times 61.1(y-0.02) - (68.23-66.7)$$

Nanocomposite #4:

$$T_B=64.31 \times e^{(-x/3.32)} + 33.74$$

$$T_T=58.6 \times e^{(-x/3.74)} + 30.29$$

$$\text{Bottom layer (①} \rightarrow \text{②): } T=64.31 \times e^{(-x/3.32)} + 33.74 - 51y - (68.94-68.94)$$

$$\text{Middle layer (②} \rightarrow \text{③): } T=64.31 \times e^{(-x/3.32)} + 33.74 - 3.79 \times 51(y-0.01) - (68.94-68.43)$$

$$\text{Top layer (③} \rightarrow \text{④): } T=64.31 \times e^{(-x/3.32)} + 33.74 - 3.68 \times 51(y-0.02) - (68.94-64.62)$$

Nanocomposite #5:

$$T_B=64.79 \times e^{(-x/4.05)} + 32.34$$

$$T_T=61.77 \times e^{(-x/3.74)} + 30.04$$

$$\text{Bottom layer (①} \rightarrow \text{②): } T=64.79 \times e^{(-x/4.05)} + 32.34 - 38.77y - (71.88-71.88)$$

$$\text{Middle layer (②} \rightarrow \text{③): } T=64.79 \times e^{(-x/4.05)} + 32.34 - 4.37 \times 38.77(y-0.01) - (71.88-71.49)$$

$$\text{Top layer (③} \rightarrow \text{④): } T=64.79 \times e^{(-x/4.05)} + 32.34 - 8.43 \times 38.77(y-0.02) - (71.88-69.8)$$

All the nanocomposite samples (#1 - #5) showed temperature gradient in the cross-thickness direction (Figure 14.8A-E), which is based on the variations of thermal conductivities of the stacked MWCNT films. Since the bottom MWCNT films for all the nanocomposite samples exhibited higher thermal conductivity than any other stacked MWCNT film for a specific nanocomposite, the heat transfer was dominant through these bottom layers.

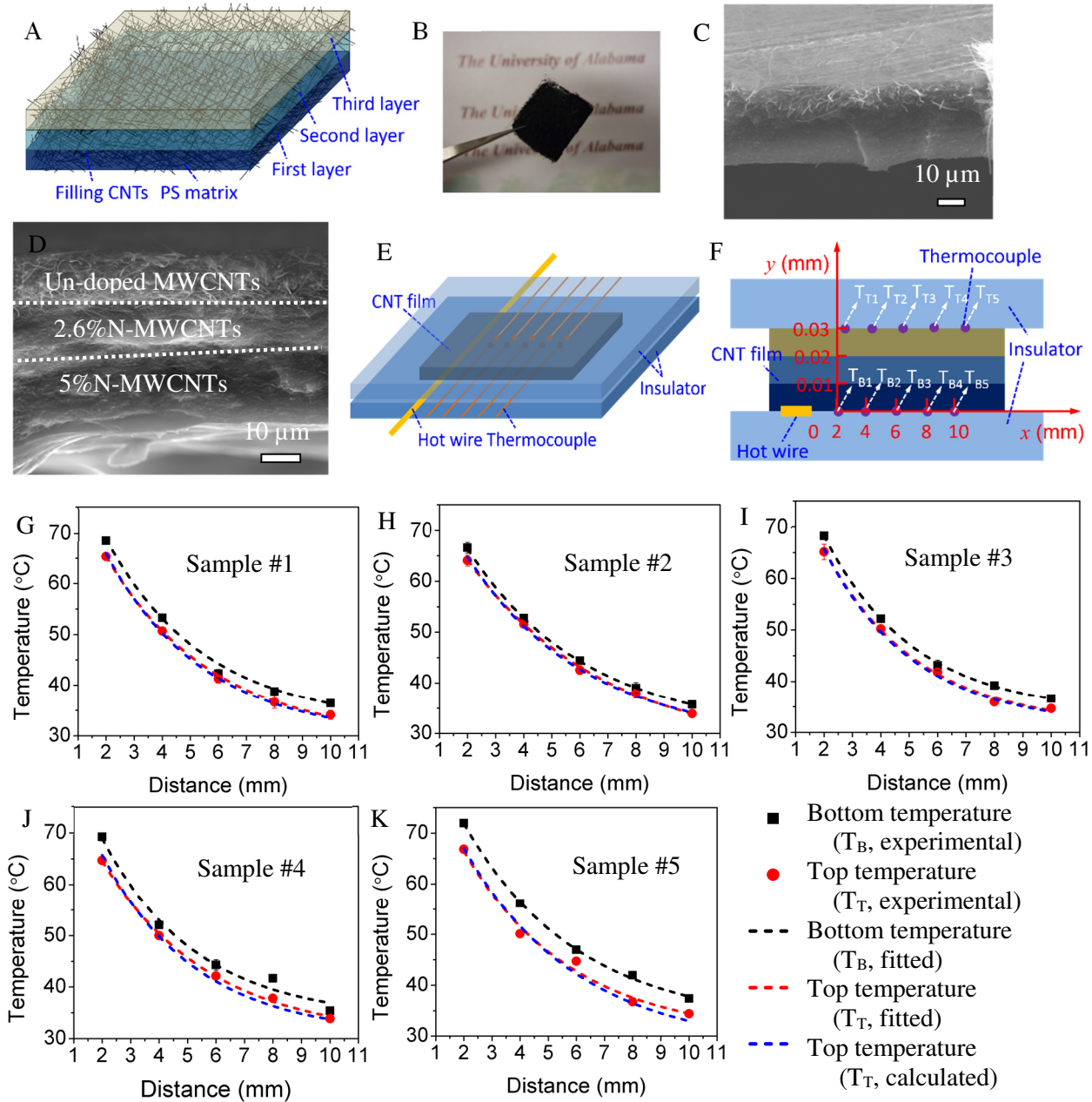


Figure 14.7. (A) Schematic of stacked multi-layered MWCNT films impregnated within polystyrene matrix (sample details in Table 14.2). (B) Digital image and (C, D) SEM image of a nanocomposite (sample #1). (E) Hot wire measurement set-up for nanocomposites showing the MWCNT film thickness (y -axis, F) and thermocouple locations (x -axis, F). Hot wire is located at $x = 0$ and $y = 0$. (G-K) Temperature distribution profiles on the top and bottom surface of the multi-layer nanocomposites (sample #1-#5, Table 14.2).

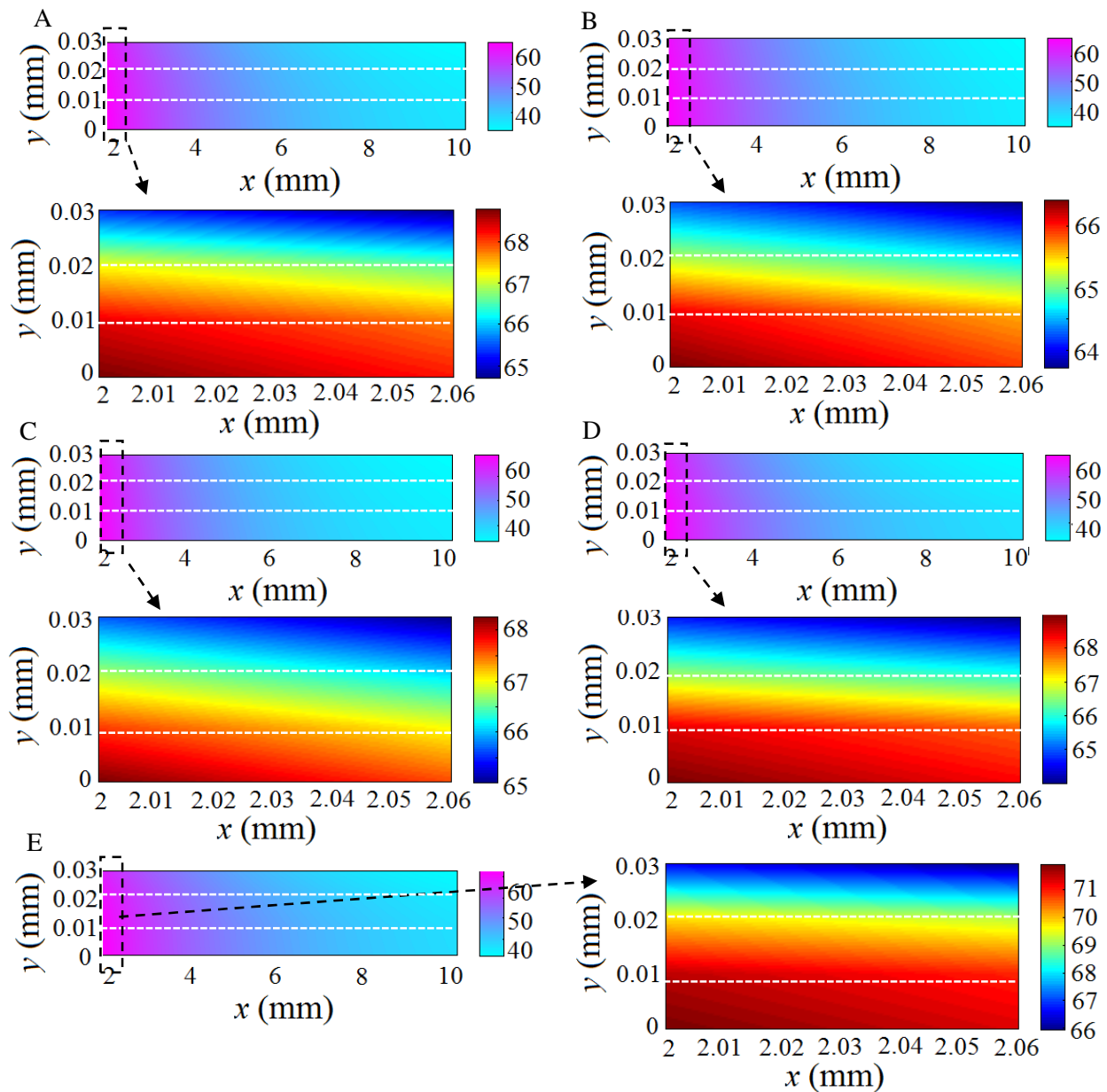


Figure 14.8. Temperature distribution profiles or thermal maps for various nanocomposites (sample #1-#5, Table 14.2). (A) Sample #1, (B) Sample #2, (C) Sample #3, (D) Sample #4, and (E) Sample #5. Note: Color bar unit: $^{\circ}\text{C}$ and each figure shows expanded temperature distribution profile for distances less than 2.1 mm.

14.4. Conclusions

Un-doped and N-doped MWCNTs were grown using a CVD method. It was observed that N-doped MWCNTs were much smaller in diameter (~25-40 nm) than un-doped MWCNTs (~85 nm). This was attributed to the incorporation of the N atoms in the hexagonal carbon lattice and inhibiting the growth of doped MWCNTs. Surface chemical modification of un-doped and N-doped MWCNTs (2.6% or 5% N) was performed in an acid or plasma oxidation. The treated MWCNTs were characterized for their morphology, defects, and average diameters. In addition, it was observed that doped MWCNTs were more resistant to acid or plasma treatment as compared to un-doped MWCNTs. The surface groups developed on MWCNTs after these treatments were thoroughly studied using XPS, which indicated 12-17% (mol%) of -COOH surface functionalization during the 5 min plasma treatment and this was higher than 6 h acid treatment of MWCNTs. On the other hand, pyrindinic-N, pyrrolic-N, quaternary-N, and N oxide groups were observed for N-doped MWCNTs. As a next step, thermal conductivities of differently-treated MWCNT films was studied using Raman spectroscopy and microscopy method. The study showed that a fine tuning of the bulk thermal conductivities of MWCNT films was possible by controlled surface chemical treatments. The thermal conductivities of defective and doped MWCNTs (as high as ~27 W/m-K) were lower than the un-doped MWCNTs (as high as ~74 W/m-K). Un-doped MWCNTs resulted in ~81% drop in thermal conductivity after 5 min plasma treatment while a drop of ~63% and ~48% was observed for 2.6%N-doped and 5%N-doped MWCNTs, respectively. Thermal conductivity values were utilized further to derive temperature distribution profiles of MWCNTs as a function of Q and distance from the center of the Raman laser spot. Finally, differently-treated MWCNT films were stacked together and impregnated within a polystyrene matrix to fabricate nanocomposites with thermal conductivity gradient. The temperature

distribution within such nanocomposites were studied. It was observed that the gradient in thermal conductivity within the nanocomposite allowed for controlled heat transport and temperature distribution with varying surface temperatures of the nanocomposite. Furthermore, this represents a unique approach to modulate the heat transfer and temperature distribution within an insulating polymer matrix, which can be envisioned as a coating, paste, or lining for a system, where heat losses are necessary to be controlled. Through this approach, it is also possible to control the direction or path of heat transport by way of thermal conductivity gradient within a nanocomposite, where this gradient is achieved by a simple, scalable, reproducible, and facile processing of defective and doped MWCNTs.

CHAPTER 15

CONCLUSIONS AND FUTURE PROSPECTS

In summary, studies in this dissertation were mainly focused on the structural evolution and fundamental understanding of the surface and interface interactions of nanoscale hybrids and heterostructures composed of Si nanowires, graphene nanoparticles (GNPs), semiconducting quantum dots and complex ceramics. This was achieved by combining multi-step fabrication approaches including chemical vapor deposition (CVD), sputtering, chemical/thermal synthesis, plasma etching, galvanic deposition, annealing, and/or nano-carbon surface chemistry, leading to the evolution of multifunctional nanoscale heterostructures with novel thermal, chemical, mechanical, electrical and optical performances for future applications in chemical sensors, SERS, photocatalysis, electrocatalysis and thermal transport management.

The main achievements or conclusions are summarized as follows:

Multilayer graphene shell encapsulated gold nanoparticles (GNPs) were prepared *via* a xylene-based CVD process, resulting graphene shell with a thickness of ~3.8 nm encapsulated on gold nanoparticle of ~20 nm. Their subsequent structure modification was carried out using oxygen plasma treatment, which was found to be effective to remove the natural amorphous carbon, reduce the graphene thickness (to 0.8 nm) and create the surface functionalities (16% of -COOH, 18% of -COH). This opens the possibility of further bio-functionalization *via* the well-defined carbodiimide chemistry. The resulting Au nanoparticles-attached GNPs heterostructures (surface coverage of ~22%) exhibit excellent SERS sensitivity in the detection of trace amount of R6G and

MB in water with an enhancement factor of 10^6 . Highly-ordered assembly of GNP-DNA architectures were also obtained with this manner. Such combination may be of importance in the future DNA detection/recognition and other bio-compatible device applications. Heterostructures composed of plasma-treated GNPs and semiconducting quantum dots were also obtained in this approach, which were demonstrated to be a promising material in light-driven energy harvesting and plasmon-enhanced photocatalysis. The photocatalytic efficiency of $\sim 40\%$ and a rate constant of $\sim 0.25 \text{ h}^{-1}$ were estimated for the photodegradation of organic phenol.

Free-standing Co_3O_4 nanowires with controlled size, crystallization, and spatial density on the substrate were obtained *via* a water-vapor assisted thermal oxidation approach. Detailed parameter study were carried out for optimizing the growth process. This was followed by sputtering deposition of tungsten oxide and further annealing process to result in polycrystalline $\text{WO}_3/\text{CoWO}_4$ composite nanostructures supported on the Co_3O_4 nanowires. The heterostructures were studied for their crystal structure evolution and lattice variation across the interface. Various phase transformations were observed along the heterostructure diameter. Interesting p-n junctions were formed between Co_3O_4 and WO_3 or between WO_3 and CoWO_4 , which is of importance for the excited charge separation during a photocatalysis process. As we observed, the final annealed nanowire heterostructures show improved photocatalytic activity in the degradation of water-containing phenol. The photocatalytic efficiency was improved by $\sim 42\%$ for the visible illumination and by $\sim 25\%$ for the UV illumination as compared with the Co_3O_4 nanowires. Such novel nanowire heterostructures can be interesting and promising for future solar-driven devices and catalytic applications.

Si nanowire-Au nanoparticle heterostructures were fabricated *via* a wet-chemical nucleation or galvanic deposition – annealing approach. The surface migration behaviors (including variation of

chemical composition and phase transformation kinetics) of Au nanoparticles on the Si nanowires during annealing were further studied in detail. The results indicate that the surface dispersion (size, inter-particle spacing and spatial density) of Au nanoparticles has a significant dependence on the annealing conditions including duration, temperature and environment. Kinetics analysis indicates that this silicide formation process was controlled by the diffusion of silicon atoms in Au nanoparticles. The activation energy for this process is ~ 1.23 eV. For the SERS-based organic detection, Raman enhancement showed a significant dependence on the distribution and chemical state of Au nanoparticles on the heterostructures. Detection limit of 10^{-10} was obtained on the final Si nanowire-Au nanoparticle heterostructures in the chemical sensing of water-containing organic dyes. The estimated enhancement factor was around 10^6 to 10^8 . The plasmonic modeling indicates that such Raman enhancement is attributed to the interfacial interaction of optical properties between Si nanowire and Au nanoparticles.

Carbon nanotubes (CNTs) network films were used for the thermal transport management. Raman spectroscopy was used for the thermal conductivity evaluation. Surface chemical modification of un-doped and N-doped MWCNTs (2.6% or 5% N) was performed in an acid or plasma oxidation. The study showed that a fine tuning of the bulk thermal conductivities of MWCNT films was possible by controlled surface chemical treatments. The thermal conductivities of defective and doped MWCNTs (as high as ~ 27 W/m-K) were lower than the un-doped MWCNTs (as high as ~ 74 W/m-K). Un-doped MWCNTs resulted in $\sim 81\%$ drop in thermal conductivity after 5 min plasma treatment while a drop of $\sim 63\%$ and $\sim 48\%$ was observed for 2.6%N-doped and 5%N-doped MWCNTs, respectively. Differently-treated MWCNT films were stacked together and impregnated within a polystyrene matrix to fabricate nanocomposites with thermal conductivity gradient. The gradient in thermal conductivity within the nanocomposite allowed for controlled

heat transport and temperature distribution with varying surface temperatures of the nanocomposite. It was demonstrated that the thermal transport efficiency was ~120 times higher in the horizontal direction as compared with the vertical direction. Furthermore, this represents a unique approach to modulate the heat transfer and temperature distribution within an insulating polymer matrix, which can be envisioned as a coating, paste, or lining for a system, where heat losses are necessary to be controlled.

REFERENCES

- 1 Banerjee, S., and Wong, S. S. (2002). Synthesis and characterization of carbon nanotube-nanocrystal heterostructures. *Nano Lett.*, 2(3), 195-200.
- 2 Peng, X., and Wong, S. S. (2009). Controlling nanocrystal density and location on carbon nanotube templates. *Chem. Mater.*, 21(4), 682-694.
- 3 Olek, M., Hilgendorff, M., and Giersig, M. (2007). A simple route for the attachment of colloidal nanocrystals to noncovalently modified multiwalled carbon nanotubes. *Colloids Surf. A*, 292(1), 83-85.
- 4 Geim, A. K., and Novoselov, K. S. (2007). The rise of graphene. *Nat. Mater.*, 6(3), 183-191.
- 5 Azamian, B. R., Coleman, K. S., Davis, J. J., Hanson, N. (2002). Directly observed covalent coupling of quantum dots to single-wall carbon nanotubes. *Chem. Commun.*, (4), 366-367.
- 6 Jeong, S., Shim, H. C., Kim, S., and Han, C. S. (2009). Efficient electron transfer in functional assemblies of pyridine-modified nQDs on SWNTs. *ACS Nano*, 4(1), 324-330.
- 7 Li, J., Lu, Y., Ye, Q., Cinke, M., Han, J., and Meyyappan, M. (2003). Carbon nanotube sensors for gas and organic vapor detection. *Nano Lett.*, 3(7), 929-933.
- 8 Peng, X., Chen, J., Misewich, J. A., and Wong, S. S. (2009). Carbon nanotube-nanocrystal heterostructures. *Chem. Soc. Rev.*, 38(4), 1076-1098.
- 9 Chaudhary, S., Kim, J. H., Singh, K. V., and Ozkan, M. (2004). Fluorescence microscopy visualization of single-walled carbon nanotubes using semiconductor nanocrystals. *Nano Lett.*, 4(12), 2415-2419.
- 10 Choi, J. H., Nguyen, F. T., Barone, P. W., Heller, D. A., Moll, A. E., Patel, D., Strano, M. S. (2007). Multimodal biomedical imaging with asymmetric single-walled carbon nanotube/iron oxide nanoparticle complexes. *Nano Lett.*, 7(4), 861-867.
- 11 Camden, J. P., Dieringer, J. A., Zhao, J., and Van Duyne, R. P. (2008). Controlled plasmonic nanostructures for surface-enhanced spectroscopy and sensing. *Acc. Chem. Res.*, 41(12), 1653-1661.
- 12 Tian, Z. Q., Ren, B., Li, J. F., and Yang, Z. L. (2007). Expanding generality of surface-enhanced Raman spectroscopy with borrowing SERS activity strategy. *Chem. Commun.*, (34), 3514-3534.
- 13 Luo, P., Li, C., and Shi, G. (2012). Synthesis of gold@ carbon dots composite nanoparticles for surface enhanced Raman scattering. *Phys. Chem. Chem. Phys.*, 39(4), 1013-1020.

- 14 Gunawidjaja, R., Kharlampieva, E., Choi, I., and Tsukruk, V. V. (2009). Bimetallic Nanostructures as Active Raman Markers: Gold-Nanoparticle Assembly on 1D and 2D Silver Nanostructure Surfaces. *Small*, 5(21), 2460-2466.
- 15 Lin, X. M., Cui, Y., Xu, Y. H., Ren, B., and Tian, Z. Q. (2009). Surface-enhanced Raman spectroscopy: substrate-related issues. *Anal. Bioanal. Chem.*, 394(7), 1729-1745.
- 16 Shao, M. W., Zhang, M. L., Wong, N. B., Ma, D. D. D., Wang, H., Chen, W., and Lee, S. T. (2008). Ag-modified silicon nanowires substrate for ultrasensitive surface-enhanced Raman spectroscopy. *Appl. Phys. Lett.*, 93(23), 233118-233118.
- 17 Deng, S., Fan, H. M., Zhang, X., Loh, K. P., Cheng, C. L., Sow, C. H., and Foo, Y. L. (2009). An effective surface-enhanced Raman scattering template based on an Ag nanocluster-ZnO nanowire array. *Nanotechnol.*, 20(17), 175705.
- 18 Peng, K. Q., and Lee, S. T. (2011). Silicon nanowires for photovoltaic solar energy conversion. *Adv. Mater.*, 23(2), 198-215.
- 19 Schmidt, V., Wittemann, J. V., Senz, S., and Gösele, U. (2009). Silicon nanowires: a review on aspects of their growth and their electrical properties. *Adv. Mater.*, 21(25-26), 2681-2702.
- 20 Cui, Y., Wei, Q., Park, H., and Lieber, C. M. (2001). Nanowire nanosensors for highly sensitive and selective detection of biological and chemical species. *Sci.*, 293(5533), 1289-1292.
- 21 Peng, K. Q., Wang, X., Wu, X. L., and Lee, S. T. (2009). Platinum nanoparticle decorated silicon nanowires for efficient solar energy conversion. *Nano Lett.*, 9(11), 3704-3709.
- 22 Shao, M. W., Shan, Y. Y., Wong, N. B., and Lee, S. T. (2005). Silicon nanowire sensors for bioanalytical applications: Glucose and hydrogen peroxide detection. *Adv. Funct. Mater.*, 15(9), 1478-1482.
- 23 Markussen, T., Jauho, A. P., and Brandbyge, M. (2009). Surface-decorated silicon nanowires: a route to high-ZT thermoelectrics. *Phys. Rev. Lett.*, 103(5), 205-210.
- 24 Fei Zhao, Dan-dan Zhao, Shao-long Wu, Guo-an Cheng, Rui-ting Zheng. (2012) Diamond-like carbon decoration enhances the field electron emission of silicon nanowires. *Surf. Coat. Technol.*, 33(6), 116-122.
- 25 Zhang, F., Song, T., and Sun, B. (2012). Conjugated polymer-silicon nanowire array hybrid Schottky diode for solar cell application. *Nanotechnol.*, 23(19), 194006.
- 26 Peng, Z., Hu, H., Utama, M. I. B., Wong, L. M., (2010). Heteroepitaxial Decoration of Ag Nanoparticles on Si Nanowires: A Case Study on Raman Scattering and Mapping. *Nano Lett.*, 10, 3940-3947.
- 27 Leng, W., Yasserli, A. A., Sharma, S., Li, Z., Woo, H. Y., Vak, D. Kelley, A. M. (2006). Silver nanocrystal-modified silicon nanowires as substrates for surface-enhanced raman and hyper-raman scattering. *Anal. Chem.*, 78(17), 6279-6282.

- 28 Leng, W., and Kelley, A. M. (2006). Surface-enhanced hyper-Raman spectra and enhancement factors for three SERS chromophores. SEHRS spectra on Ag films at pulse energies. *J. Am. Chem. Soc.*, 128(11), 3492-3493.
- 29 He, Y., Su, S., Xu, T., Zhong, Y., Zapfen, J. A., Li, J. Lee, S. T. (2011). Silicon nanowires-based highly-efficient SERS-active platform for ultrasensitive DNA detection. *Nano Today*, 6(2), 122-130.
- 30 Zhang, B., Wang, H., Lu, L., Ai, K., Zhang, G., and Cheng, X. (2008). Large-Area Silver-Coated Silicon Nanowire Arrays for Molecular Sensing Using Surface-Enhanced Raman Spectroscopy. *Adv. Funct. Mater.*, 18(16), 2348-2355.
- 31 Galopin, E., Barbillat, J., Coffinier, Y., Szunerits, S., Patriarche, G., and Boukherroub, R. (2009). Silicon nanowires coated with silver nanostructures as ultrasensitive interfaces for surface-enhanced Raman spectroscopy. *ACS Appl. Mater. Interfaces*, 1(7), 1396-1403.
- 32 Schmidt, M. S., Hübner, J., and Boisen, A. (2012). Large Area Fabrication of Leaning Silicon Nanopillars for Surface Enhanced Raman Spectroscopy. *Adv. Mater.*, 6(3), 2459-2470.
- 33 Hu, M., Ou, F. S., Wu, W., Naumov, I., Li, X., Bratkovsky, A. M. Li, Z. (2010). Gold Nanofingers for Molecule Trapping and Detection. *J. Am. Chem. Soc.*, 132(37), 12820-12822.
- 34 Baik, S. Y., Cho, Y. J., Lim, Y. R., Im, H. S., Jang, D. M., Myung, Y., Kang, H. S. (2012). Charge-Selective Surface-Enhanced Raman Scattering Using Silver and Gold Nanoparticles Deposited on Silicon–Carbon Core–Shell Nanowires. *ACS Nano*, 6(3), 2459-2470.
- 35 Chen, R., Li, D., Hu, H., Zhao, Y., Wang, Y., Wong, N. Xiong, Q. (2012). Tailoring Optical Properties of Silicon Nanowires by Au Nanostructure Decorations: Enhanced Raman Scattering and Photodetection. *J. Phys. Chem. C*, 116(7), 4416-4422.
- 36 Breuer, O. Sundararaj, U. (2004). Big Returns from Small Fibers: A Review of Polymer/Carbon Nanotube Composites. *Polym. Compos.*, 25, 630-645.
- 37 Artukovic, E. Kaempgen, M. Hecht, D. Roth, S. Gruner, G. (2005). Transparent and Flexible Carbon Nanotube Transistors. *Nano Lett.*, 5, 757-760.
- 38 Prasher, R. S. Hu, X. J. Chalopin, Y. Mingo, N. Lofgreen, K. Volz, S. Cleri, F. (2009). Turning Carbon Nanotubes from Exceptional Heat Conductors into Insulators. *Phys. Rev. Lett.*, 102, 105901.
- 39 Fujii, M. Zhang, X. Xie, H. Ago, H. Takahashi, K. Ikuta, T. Abe, H. Shimizu, T. (2005). Measuring the Thermal Conductivity of a Single Carbon nanotube. *Phys. Rev. Lett.*, 95, 065502.
- 40 A. A. Balandin, (2011). Thermal properties of grapheme and nanostructured carbon materials, *Nat. Mater.*, 10, 569-581.

- 41 Itkis, M. E. Borondics, F. Yu, A. (2012). Thermal Conductivity Measurements of Semitransparent Single-Walled Carbon Nanotube Films by a Bolometric Technique. *Nano Lett.*, 7, 900-904.
- 42 Kim, S. Kim, S. Park, J. Ju, S. Mohammadi, S. (2010). Fully Transparent Pixel Circuits Driven by Random Network Carbon Nanotube Transistor Circuitry. *ACS Nano*, 4, 2994-2998.
- 43 D. Estrada, and E. Pop, (2011). Imaging dissipation and hot spots in carbon nanotube network transistors. *Appl. Phys. Lett.*, 98, 073102.
- 44 Ayala, P. Arenal, R. Rummeli, M. Rubio, A. Picher, T. (2010). The Doping of Carbon Nanotubes with Nitrogen and Their Potential Applications. *Carbon*, 48, 575-586.
- 45 C. H. Yu, L. Shi, Z. Yao, D. Y. Li, and A. Majumdar, (2005). Thermal conductance and single-wall carbon nanotube. *Nano Lett.*, 5, 1842-1846.
- 46 J. Hone, B. Batlogg, Z. Benes, A. T. Johnson, and J. E. Fischer, (2000). Quantized phonon spectrum of single-wall carbon nanotubes, *Sci.*, 289, 1730-1734.
- 47 Yu, C. Kim, Y. S. Kim, D. Grunlan, J. C. (2008). Thermoelectric Behavior of Segregated-Network Polymer Nanocomposites. *Nano Lett.*, 8, 4428-4432.
- 48 C. Lu, H. Yang, C. Zhu, X. Chen, and G. Chen, *Angew. Chem.*, 121, 4879 (2009).
- 49 S. Daniel, T. P. Rao, K. S. Rao, S. U. Rani, G. R. K. Naidu, H. Y. Lee, and T. Kawai, *Sensor. Actuat. B-Chem.*, 122, 672 (2007).
- 50 C. Hong, X. Cao, Y. Jiang, P. He, and Y. Fang. *Anal. and Bioanal. Chem.*, 375, 287 (2003).
- 51 Park, S. Y., Lytton-Jean, A. K., Lee, B., Weigand, S., Schatz, G. C., and Mirkin, C. A. (2008). DNA-programmable nanoparticle crystallization. *Nature*, 451(7178), 553-556.
- 52 Nykypanchuk, D., Maye, M. M., van der Lelie, D., and Gang, O. (2008). DNA-guided crystallization of colloidal nanoparticles. *Nature*, 451(7178), 549-552.
- 53 Giljohann, D. A., Seferos, D. S., Daniel, W. L., Massich, M. D., Patel, P. C., and Mirkin, C. A. (2010). Gold nanoparticles for biology and medicine. *Angew. Chem. Int. Ed.*, 49(19), 3280-3294.
- 54 Li, D., Song, S., and Fan, C. (2010). Target-responsive structural switching for nucleic acid-based sensors. *Acc. Chem. Res.*, 43(5), 631-641.
- 55 Lim, D. K., Jeon, K. S., Hwang, J. H., Kim, H., Kwon, S., Suh, Y. D., and Nam, J. M. (2011). Highly uniform and reproducible surface-enhanced Raman scattering from DNA-tailorable nanoparticles with 1-nm interior gap. *Nat. Nanotechnol.*, 6(7), 452-460.

- 56 Chou, L. Y., Zagorovsky, K., and Chan, W. C. (2014). DNA assembly of nanoparticle superstructures for controlled biological delivery and elimination. *Nat. Nanotechnol.*, 9, 148-155.
- 57 Zhang, X., Servos, M. R., and Liu, J. (2012). Instantaneous and quantitative functionalization of gold nanoparticles with thiolated DNA using a pH-assisted and surfactant-free route. *J. Am. Chem. Soc.*, 134(17), 7266-7269.
- 58 Watanabe-Tamaki, R., Ishikawa, A., Tanaka, T., Zako, T., and Maeda, M. (2012). DNA-templating mass production of gold trimer rings for optical metamaterials. *J. Phys. Chem. C*, 116(28), 15028-15033.
- 59 Liu, J. (2012). Adsorption of DNA onto gold nanoparticles and graphene oxide: surface science and applications. *Phys. Chem. Chem. Phys.*, 14(30), 10485-10496.
- 60 Y. Wenrong, P. Thordarson, J. J. Gooding, S. P. Ringer, and F. Braet. *Nanotechnol.*, 18, 412001 (2007).
- 61 J. Wu, W. Shi, N. Chopra, Plasma oxidation kinetics of gold nanoparticles and their encapsulation in graphene shells by chemical vapor deposition growth. *J. Phys. Chem. C*, 116(23), 12861(2012).
- 62 Wu, J., Shi, W., and Chopra, N. (2014). Optical properties of gold/multilayer-graphene/carbon nanotube hybrid materials. *Carbon*, 68, 708-717.
- 63 Chopra, N., Bachas, L. G., and Knecht, M. R. (2009). Fabrication and biofunctionalization of carbon-encapsulated Au nanoparticles. *Chem. Mater.*, 21(7), 1176-1178.
- 64 Kumar, M., and Ando, Y. (2010). Chemical vapor deposition of carbon nanotubes: a review on growth mechanism and mass production. *J. Nanosci. Nanotechnol.*, 10(6), 3739-3758.
- 65 N. Chopra, M. Majumder, B. J. Hinds, *Adv. Func. Mater.*, 15, 858 (2005).
- 66 Wang, Y., Zhu, L., Zhang, Y., and Yang, M. (2010). Silicon nanotips formed by self-assembled Au nanoparticle mask. *J. Nanopart. Res.*, 12(5), 1821-1828.
- 67 Meyer, J. C., Geim, A. K., Katsnelson, M. I., Novoselov, K. S., Booth, T. J., and Roth, S. (2007). The structure of suspended graphene sheets. *Nature*, 446(7131), 60-63.
- 68 Lin, T., Chen, J., Bi, H., Wan, D., Huang, F., Xie, X., and Jiang, M. (2013). Facile and economical exfoliation of graphite for mass production of high-quality graphene sheets. *J. Mater. Chem. A*, 1(3), 500-504.
- 69 Li, C. Y., and Hatta, A. (2005). Preparation of diamond whiskers using Ar/O₂ plasma etching. *Diamond Relat. Mater.*, 14(11), 1780-1783.
- 70 Ladwig, A. M., Koch, R. D., Wenski, E. G., and Hicks, R. F. (2009). Atmospheric plasma deposition of diamond-like carbon coatings. *Diamond Relat. Mater.*, 18(9), 1129-1133.

- 71 Agarwal, N., Ponoth, S., Plawsky, J., and Persans, P. D. (2002). Optimized oxygen plasma etching of polyimide films for low loss optical waveguides. *J. Vac. Sci. Technol. A*, 20(5), 1587-1591.
- 72 Ferrari, A. C., Meyer, J. C., Scardaci, V., Casiraghi, C., Lazzeri, M., Mauri, F., and Geim, A. K. (2006). Raman spectrum of graphene and graphene layers. *Phys. Rev. Lett.*, 97(18), 187401.
- 73 Pimenta, M. A., Dresselhaus, G., Dresselhaus, M. S., Cancado, L. G., Jorio, A., and Saito, R. (2007). Studying disorder in graphite-based systems by Raman spectroscopy. *Phys. Chem. Chem. Phys.*, 9(11), 1276-1290.
- 74 Casiraghi, C. (2009). Probing disorder and charged impurities in graphene by Raman spectroscopy. *Physica Status Solidi (RRL)*, 3(6), 175-177.
- 75 Leenaerts, O., Partoens, B., and Peeters, F. M. (2009). Water on graphene: Hydrophobicity and dipole moment using density functional theory. *Phys. Rev. B*, 79(23), 235440.
- 76 Bielawski, C. W., Dreyer, D. R., and Todd, A. D. (2014). Harnessing the chemistry of graphene oxide. *Chem. Soc. Rev.*, 43, 5288-5301.
- 77 Halas, N. J., Lal, S., Link, S., Chang, W. S., Natelson, D., Hafner, J. H., and Nordlander, P. (2012). A plethora of plasmonics from the laboratory for nanophotonics at Rice University. *Adv. Mater.*, 24(36), 4842-4877.
- 78 Xu, W., Ling, X., Xiao, J., Dresselhaus, M. S., Kong, J., Xu, H., and Zhang, J. (2012). Surface enhanced Raman spectroscopy on a flat graphene surface. *Proc. Natl. Acad. Sci. U.S.A.*, 109(24), 9281-9286.
- 79 Zhang, Y., Ma, H. L., Zhang, Q., Peng, J., Li, J., Zhai, M., and Yu, Z. Z. (2012). Facile synthesis of well-dispersed graphene by γ -ray induced reduction of graphene oxide. *J. Mater. Chem.*, 22(26), 13064-13069.
- 80 Huang, X., and El-Sayed, M. A. (2010). Gold nanoparticles: optical properties and implementations in cancer diagnosis and photothermal therapy. *J. Adv. Res.*, 1(1), 13-28.
- 81 S. Ponkumar, P. Duraisamy, and N. Iyandurai. *Am. J. Biochem. Biotechnol.* 7, 135 (2011).
- 82 M. Liviu, J. M. Benevides, and G. J. Thomas. *J Raman Spectrosc.* 30, 637 (1999).
- 83 J. Duguid, V. A. Bloomfield, J. M. Benevides, and G. J. Thomas, *Biophys. J.* 65, 1916 (1993).
- 84 G. I. Dovbeshko, N. Y. Gridina, E. B. Kruglova, and O. P. Pashchuk. *Talanta* 53, 233 (2000).
- 85 Chang MC, Tanaka J. FT-IR study for hydroxyapatite/collagen nanocomposite cross-linked by glutaraldehyde. *Biomater.* 2002; 23(24): 4811-4818.
- 86 Barazzouk, S., and Daneault, C. (2012). Amino Acid and Peptide Immobilization on Oxidized Nanocellulose: Spectroscopic Characterization. *Nanomater.*, 2(2), 187-205.

- 87 Nakajima, N., and Ikada, Y. (1995). Mechanism of amide formation by carbodiimide for bioconjugation in aqueous media. *Bioconjugate chem.*, 6(1), 123-130.
- 88 Ma, Y., Ali, S. R., Doodoo, A. S., and He, H. (2006). Enhanced sensitivity for biosensors: multiple functions of DNA-wrapped single-walled carbon nanotubes in self-doped polyaniline nanocomposites. *J. Phys. Chem. B*, 110(33), 16359-16365.
- 89 Yokota, H., Sunwoo, J., Sarikaya, M., van den Engh, G., and Aebersold, R. (1999). Spin-stretching of DNA and protein molecules for detection by fluorescence and atomic force microscopy. *Anal. Chem.*, 71(19), 4418-4422.
- 90 Kudo, A.; Miseki, Y. Heterogeneous photocatalyst materials for water splitting. *Chem. Soc. Rev.* 2009, 38, 253-278.
- 91 Chong, M. N.; Jin, B.; Chow, C. W.; Saint, C. Recent developments in photocatalytic water treatment technology: a review. *Water Res.* 2010, 44, 2997-3027.
- 92 SanthosháBabu, S. CdSe Nanocrystal/C60-liquid composite material with enhanced photoelectrochemical performance. *J. Mater. Chem.* 2012, 22, 22370-22373.
- 93 Wang, Y.; Wang, Q.; Zhan, X.; Wang, F.; Safdar, M.; He, J. Visible light driven type II heterostructures and their enhanced photocatalysis properties: a review. *Nanoscale* 2013, 5, 8326-8339.
- 94 Empedocles, S.; Bawendi; M. Spectroscopy of single CdSe nanocrystallites. *Acc. Chem. Res.* 1999, 32: 389-396.
- 95 Asahi, R.; Morikawa, T.; Ohwaki, T.; Aoki, K.; Taga, Y. Visible-light photocatalysis in nitrogen-doped titanium oxides. *Science* 2001, 293, 269-271.
- 96 Robel, I.; Subramanian, V.; Kuno, M.; Kamat, P. V. Quantum dot solar cells. Harvesting light energy with CdSe nanocrystals molecularly linked to mesoscopic TiO₂ films. *J. Am. Chem. Soc.* 2006, 128, 2385-2393.
- 97 Liu, H.; Liang, G.; Abdel-Halim, E. S.; Zhu, J. J. A sensitive and selective quantum dots-based FRET biosensor for the detection of cancer marker type IV collagenase. *Anal. Methods* 2011, 3, 1797-1801.
- 98 Zhang, Z.; Wang, Z.; Cao, S. W.; Xue, C. Au/Pt Nanoparticle-Decorated TiO₂ Nanofibers with Plasmon-Enhanced Photocatalytic Activities for Solar-to-Fuel Conversion. *J. Phys. Chem. C* 2013, 117, 25939-25947.
- 99 Ribeiro, T.; Prazeres, T. J. V.; Farinha, J. P. S. Enhanced photoluminescence from micellar assemblies of cadmium sulfide quantum dots and gold nanoparticles. *J. Phys. Chem. C* 2013, 117, 3122-3133.
- 100 . Peng, X.; Chen, J.; Misewich, J. A.; Wong, S. S. Carbon Nanotube-nanocrystal Heterostructures. *Chem. Soc. Rev.* 2009, 38, 1076-1098.

101. Mondal, A.; Jana, N. R. Surfactant-free, Stable Noble Metal-Graphene Nanocomposite as High Performance Electrocatalyst. *ACS Catal.* 2014, 4, 593-599.
102. Kwon, O. S.; Lee, S. H.; Park, S. J.; An, J. H.; Song, H. S.; Kim, T.; Jang, J. Large-Scale Graphene Micropattern Nano-biohybrids: High-Performance Transducers for FET-Type Flexible Fluidic HIV Immunoassays. *Adv. Mater.* 2013, 25, 4177-4185.
103. McDonough, J. K.; Gogotsi, Y. Carbon Onions: Synthesis and Electrochemical Applications. *Electrochem. Soc. Interface* 2013, 22, 61-66,
104. Selinsky, R. S.; Ding, Q.; Faber, M. S.; Wright, J. C.; Jin, S. Quantum Dot Nanoscale Heterostructures for Solar Energy Conversion. *Chem. Soc. Rev.* 2013, 42, 2963-2985.
105. Banhart, F.; Redlich, P.; Ajayan, P. M. The Migration of Metal Atoms through Carbon Onions. *Chem. Phys. Lett.* 1998, 292, 554-560.
106. Chopra, N.; Bachas, L. G.; Knecht, M. R. Fabrication and Biofunctionalization of Carbon-encapsulated Au Nanoparticles. *Chem. Mater.* 2009, 21, 1176-1178.
107. Wu, J.; Shi, W.; Chopra, N. Optical Properties of Gold/Multilayer-Graphene/Carbon Nanotube Hybrid Materials. *Carbon*, 2014, 68, 708-717.
108. Hinds, B. J.; Chopra, N.; Rantell, T.; Andrews, R.; Gavalas, V.; Bachas, L. G. Aligned Multiwalled Carbon Nanotube Membranes. *Science* 2004, 303, 62-65.
109. Shi, W.; Chopra, N. Surfactant-free Synthesis of Novel Copper Oxide (CuO) Nanowire–Cobalt Oxide (Co₃O₄) Nanoparticle Heterostructures and Their Morphological Control. *J. Nanopart. Res.* 2011, 13, 851-868.
110. Wei, H.; Su, Y.; Han, Z.; Li, T.; Ren, X.; Yang, Z.; Zhang, Y. Zn_xCd_{1-x}Se Nanomultipods with Tunable Band Gaps: Synthesis and First-Principles Calculations. *Nanotechnol.* 2013, 24, 235706-235712.
111. Draine, B. T.; Flatau, P. J. User Guide for the Discrete Dipole Approximation Code DDSCAT 7.3. *arXiv preprint arXiv* 2013, 307, 1305. 6497.
112. Shi, W. Chopra, N. Controlled Fabrication of Photoactive Copper Oxide-Cobalt Oxide Nanowire Heterostructures for Efficient Phenol Photodegradation. *ACS Appl. Mater. Interfaces* 2012, 4, 5590-5607.
113. Sayed, S. Y.; Wang, F.; Malac, M.; Meldrum, A.; Egerton, R. F.; Buriak, J. M. Heteroepitaxial Growth of Gold Nanostructures on Silicon by Galvanic Displacement. *ACS nano* 2009, 3, 2809-2817.
114. Gilles, S.; Kaulen, C.; Pabst, M.; Simon, U.; Offenhäusser, A.; Mayer, D. Patterned Self-assembly of Gold Nanoparticles on Chemical Templates Fabricated by Soft UV Nanoimprint Lithography. *Nanotechnol.* 2011, 22, 295301.

- 115 Chopra, N.; Shi, W.; Bansal, A. Structural Evolution and Stability Studies of Heterostructures Comprised of Carbon Nanotubes Decorated with Nickel/Nickel Oxide Core/Shell Nanoparticles. *Carbon* 2011, 49, 3645-3662.
- 116 Zhao, B.; Zhang, L.; Wang, X.; Yang, J. Surface Functionalization of Vertically-aligned Carbon Nanotube Forests by Radio-frequency Ar/O₂ Plasma. *Carbon*, 2012, 50, 2710-2716.
- 117 Wu, J.; Chopra, N. Chemical Vapor Deposition Growth of Graphene Encapsulated Palladium Nanoparticles. *Ceram. Trans.* 2012, 238, 17-29.
- 118 Wang, H.; Chen, Q. W.; Chen, J.; Yu, B. X.; Hu, X. Y. Carboxyl and Negative Charge-functionalized Superparamagnetic Nanochains with Amorphous Carbon Shell and Magnetic Core: Synthesis and Their Application in Removal of Heavy Metal Ions. *Nanoscale* 2011, 3, 4600-4603.
- 119 Li, Y.; Chopra, N. Chemically Modified and Doped Carbon Nanotube-based Nanocomposites with Tunable Thermal Conductivity Gradient. *Carbon* 2014, 77, 675-687.
- 120 Ago, H.; Kugler, T.; Cacialli, F.; Salaneck, W. R.; Shaffer, M. S.; Windle, A. H.; Friend, R. H. Work Functions and Surface Functional Groups of Multiwall Carbon Nanotubes. *J. Phys. Chem. B* 1999, 103, 8116-8121.
- 121 Hsiao, M. C.; Liao, S. H.; Yen, M. Y.; Teng, C. C.; Lee, S. H.; Pu, N. W.; Hsiao, M. H. Preparation and Properties of a Graphene Reinforced Nanocomposite Conducting Plate. *J. Mater. Chem.* 2010, 20, 8496-8505.
- 122 Nessim, G. D.; Hart, A. J.; Kim, J. S.; Acquaviva, D.; Oh, J.; Morgan, C. D.; Thompson, C. V. Tuning of Vertically-aligned Carbon Nanotube Diameter and Areal Density Through Catalyst Pre-treatment. *Nano Lett.* 2008, 8, 3587-3593.
- 123 Bittencourt, C.; Navio, C.; Nicolay, A.; Ruelle, B.; Godfroid, T.; Snyders, R.; Ewels, C. P. Atomic Oxygen Functionalization of Vertically Aligned Carbon Nanotubes. *J. Phys. Chem. C* 2011, 115, 20412-20418.
- 124 Li, Y.; Chopra, N. Nanoscale Heterostructures Comprised of Silicon Nanowires and Gold Nanoparticles Encapsulated in Graphitic Shell for DNA Immobilization. *Mater. Res. Soc. Res. Proc.* 2013, 1572, mrss13-1572
- 125 Kim, U. J.; Furtado, C. A.; Liu, X.; Chen, G.; Eklund, P. C. Raman and IR Spectroscopy of Chemically Processed Single-walled Carbon Nanotubes. *J. Am. Chem. Soc.* 2005, 127, 15437-15445.
- 126 Chang, M. C.; Tanaka, J. FT-IR Study for Hydroxyapatite/Collagen Nanocomposite Cross-linked by Glutaraldehyde. *Biomater.* 2002, 23, 4811-4818.
- 127 Zeng, R.; Shen, R.; Zhao, Y.; Li, X.; Sun, Z.; Shen, Y. Aqueous Synthesis of Cu-doped ZnCdS/ZnS Core/Shell Nanocrystals with a New and Highly Reactive Sulfur Source. *Nanotechnol.* 2014, 25, 135602.

- 128 Shan, C.; Yang, H.; Han, D.; Zhang, Q.; Ivaska, A.; Niu, L. Graphene/Au nanoparticles/Chitosan Nanocomposites Film for Glucose Biosensing. *Biosens. bioelectron* 2010, 25, 1070-1074.
- 129 Biju, V.; Itoh, T.; Anas, A.; Sujith, A.; Ishikawa, M. Semiconductor Quantum Dots and Metal Nanoparticles: Syntheses, Optical Properties, and Biological Applications. *Anal. Bioanal. Chem.* 2008, 391, 2469-2495.
- 130 Ünlü, C.; Tosun, G. Ü.; Sevim, S.; Özçelik, S. Developing a Facile Method for Highly Luminescent Colloidal CdS_xSe_{1-x} Ternary Nanoalloys. *J. Mater. Chem. C* 2013, 1, 3026–3034.
- 131 Nadeem, M. Y.; Ahmed, W. Optical Properties of ZnS Thin Films. *Turkish J. Phys.* 2009, 24, 651-659.
- 132 Zhu, S.; Chen, T. P.; Liu, Y. C.; Liu, Y.; Fung, S. A Quantitative Modeling of the Contributions of Localized Surface Plasmon Resonance and Interband Transitions to Absorbance of Gold Nanoparticles. *J. Nanopart. Res.* 2012, 14, 1-6.
- 133 Yamada, K.; Miyajima, K.; Mafuné, F. Thermionic Emission of Electrons from Gold Nanoparticles by Nanosecond Pulse-laser Excitation of Interband. *J. Phys. Chem. C* 2007, 111, 11246-11251.
- 134 Li, Y.; Chopra, N. Optical Properties of Nanostructured Carbon and Gold Nanoparticle Hybrids. *Mater. Res. Soc. Res. Proc.* 2014, 1700, mrss14-1700.
- 135 Bohren, C. F.; Huffman, D. R. Absorption and Scattering of Light by Small Particles. *John Wiley and Sons* 2008, 130.
- 136 Meng, Z. D.; Zhu, L.; Ye, S.; Sun, Q.; Ullah, K.; Cho, K. Y.; Oh, W. C. Fullerene Modification CdSe/TiO₂ and Modification of Photocatalytic Activity Under Visible Light. *Nanoscale Res. Lett.* 2013, 8, 1-10.
- 137 Cho, H. D.; Zakirov, A. S.; Yuldashev, S. U.; Ahn, C. W.; Yeo, Y. K.; Kang, T. W. Photovoltaic Device on a Single ZnO Nanowire p-n Homojunction. *Nanotechnol.* 2012, 23, 115401.
- 138 Esplugas, S.; Gimenez, J.; Contreras, S.; Pascual, E.; and Rodríguez, M. Comparison of Different Advanced Oxidation Processes for Phenol Degradation. *Water Res.* 2002, 36, 1034-1042.
- 139 Mora-Seró, I.; Gimenez, S.; Fabregat-Santiago, F.; Gomez, R.; Shen, Q.; Toyoda, T. J. Recombination in Quantum Dot Sensitized Solar Cells. *Acc. Chem. Res.* 2009, 42, 1848-1857.
- 140 Soltani, N., Saion, E., Hussein, M. Z., Erfani, M., Abedini, A., Bahmanrokh, G., and Vaziri, P. (2012). Visible light-induced degradation of methylene blue in the presence of photocatalytic ZnS and CdS nanoparticles. *Int. J. Mol. Sci.*, 13(10), 12242-12258.

- 141 Stobiecka M, Deeb J, Hepel M (2010) Ligand exchange effects in gold nanoparticle assembly induced by oxidative stress biomarkers: Homocysteine and cysteine. *Biophys. Chem.* 146: 98-107.
- 142 Ribeiro T, Prazeres TJV, Farinha JPS (2013) Enhanced photoluminescence from micellar assemblies of cadmium sulfide quantum dots and Au nanoparticles. *J. Phys. Chem. C* 117: 3122-3133.
- 143 Mondal A, Jana NR (2014) Surfactant-free, stable noble metal-graphene nanocomposite as high performance electrocatalyst. *ACS Catal.* 4: 593-599.
- 144 Wu J, Shi W, Chopra, N (2014) Optical properties of Au/multilayer-graphene/carbon nanotube hybrid materials. *Carbon* 68: 708-717.
- 145 Kwon OS, Lee SH, Park SJ, An JH, Song HS, Kim T, Jang J (2013) Large-scale graphene micropattern nano-biohybrids: high-performance transducers for FET-type flexible fluidic HIV immunoassays. *Adv. Mater.* 25: 4177-4185.
- 146 Wu J, Shi W, Chopra N (2012) Plasma oxidation kinetics of Au nanoparticles and their encapsulation in graphene shells by chemical vapor deposition growth. *J. Phys. Chem. C* 116: 12861-12874.
- 147 Sayed SY, Wang F, Malac M, Meldrum A, Egerton RF, Buriak, JM (2009) Heteroepitaxial growth of Au nanostructures on silicon by galvanic displacement. *ACS nano* 3(9): 2809-2817.
148. Sayed SY, Wang F, Malac M, Li P, Wang D, Buriak J (2012) Preferential face deposition of Au nanoparticles on silicon nanowires by galvanic displacement. *Cryst Eng. Comm.* 14: 5230-5234.
- 149 Sorgenfrei S, Chiu CY, Gonzalez Jr RL, Yu YJ, Kim P, Nuckolls C, Shepard KL (2011) Label-free single-molecule detection of DNA-hybridization kinetics with a carbon nanotube field-effect transistor. *Nature Nanotechnol.* 6: 126-132.
- 150 Mane RS, Roh SJ, Joo OS, Lokhande CD, Han SH (2005) Improved performance of dense TiO₂/CdSe coupled thin films by low temperature process. *Electrochim. Acta* 50: 2453-2459.
- 151 Zhang G, Wu H, Li G, Huang Q, Yang C, Huang F, Lin J (2013) New high T_c multiferroics KBiFe₂O₅ with narrow band gap and promising photovoltaic effect. *Sci. Rep.* 3: 1265-1272.
- 152 Chen ML, Oh WC (2011) Synthesis and highly visible-induced photocatalytic activity of CNT-CdSe composite for methylene blue solution. *Nanoscale Res. Lett.* 6: 1-8.
- 153 Wei H, Su Y, Han Z, Li T, Ren X, Yang Z, Zhang Y (2013) Zn_(x)Cd_(1-x)Se nanomultipods with tunable band gaps: synthesis and first-principles calculations. *Nanotechnol.* 24: 235706-235712.
- 154 Flatau PJ, Draine BT (1994) Discrete-dipole approximation for scattering calculations. *J. Opt. Soc. Am. A* 11: 1491-1499.

- 155 Draine BT, Flatau PJ (2013) User guide for the discrete dipole approximation code DDSCAT 7.3. arXiv preprint arXiv:1305.6497. 2013.
- 156 Li Y, Dykes J, Chopra, N (2013) Si nanowire-gold nanoparticles heterostructures for surface enhanced Raman spectroscopy. *Mater. Res. Soc. Res. Proc.* 1551: mrss13-1551.
- 157 Li, Y. Chopra N (2014) Chemically modified and doped carbon nanotube-based nanocomposites with tunable thermal conductivity gradient. *Carbon* 77: 675-687.
- 158 Bohren CF, Huffman DR (2008) Absorption and scattering of light by small particles. John Wiley and Sons 130.
- 159 Li Y, Chopra N (2014) Optical properties of nanostructured carbon and Au nanoparticle hybrids. *Mater. Res. Soc. Res. Proc.* 1700: mrss14-1700.
- 160 Meng ZD, Zhu L, Ye S, Sun Q, Ullah K, Cho KY, Oh WC (2013) Fullerene modification CdSe/TiO₂ and modification of photocatalytic activity under visible light. *Nanoscale Res. Lett.* 8: 1-10.
- 161 Yamada K, Miyajima K, Mafuné F (2007) Thermionic emission of electrons from Au nanoparticles by nanosecond pulse-laser excitation of interband. *J. Phys. Chem. C* 111: 11246-11251.
- 162 Peng, X.; Chen, J.; Misewich, J. A.; Wong, S. S. Carbon Nanotube-nanocrystal Heterostructures. *Chem. Soc. Rev.* 2009, 38, 1076-1098.
- 163 Chopra, N.; Majumder, M.; Hinds, B. J. Bi-functional Carbon Nanotubes by Sidewall Protection. *Adv. Funct. Mater.* 2005, 15, 858-864.
- 164 Kwon, O. S.; Lee, S. H.; Park, S. J.; An, J. H.; Song, H. S.; Kim, T.; Jang, J. Large-Scale Graphene Micropattern Nano-biohybrids: High-Performance Transducers for FET-Type Flexible Fluidic HIV Immunoassays. *Adv. Mater.* 2013, 25, 4177-4185.
- 165 McDonough, J. K.; Gogotsi, Y. Carbon Onions: Synthesis and Electrochemical Applications. *Electrochem. Soc. Interface* 2013, 22, 61-66,
- 166 Lightcap, I. V.; Kamat, P. V. Graphitic Design: Prospects of Graphene-Based Nanocomposites for Solar Energy Conversion, Storage, and Sensing. *Acc. Chem. Res.* 2012, 46, 2235-2243.
- 167 S. Y. Sayed, F. Wang, M. Malac, A. Meldrum, R. F. Egerton, J. M. Buriak, *ACS nano* 3(2009): 2809-2817.
- 168 B. J. Hinds, N. Chopra, T. Rantell, R. Andrews, V. Gavalas, L. G. Bachas, *Science* 303(2004): 62-65.

- 169 Sayed, S. Y., Wang, F., Malac, M., Meldrum, A., Egerton, R. F., and Buriak, J. M. (2009). Heteroepitaxial growth of gold nanostructures on silicon by galvanic displacement. *ACS nano*, 3(9), 2809-2817.
- 170 Li, Y., Dykes, J. C., and Chopra, N. (2013). Si nanowire-gold nanoparticles heterostructures for surface enhanced Raman spectroscopy. *Mater. Res. Soc. Res. Proc.* 2013; 1551: mrss13-1551.
- 171 Wu, J.; Shi, W.; Chopra, N. Plasma Oxidation Kinetics of Gold Nanoparticles and Their Encapsulation in Graphene Shells by Chemical Vapor Deposition Growth. *J. Phys. Chem. C* 2012, 116, 12861-12874.
- 172 Li, Y., and Chopra, N. (2013, January). Nanoscale heterostructures comprised of silicon nanowires and gold nanoparticles encapsulated in graphitic shells for DNA immobilization. In *MRS Proceedings* (Vol. 1572, pp. mrss13-1572). Cambridge University Press.
- 173 A. M. Hung, C. M. Michee, L. D. Bozano, L. W. Osterbur, G. M. Wallraff, and J. N. Cha, *Nat. Nanotechnol.* 5, 121 (2009).
- 174 Kim, D., Rabbani, M. M., Ko, C. H., Nam, D. G., Yeum, J. H., Park, J. S., ... and Oh, W. (2011). Preparation and Characterization of CdSe-Decorated Multiwalled Carbon Nanotube Composites. *Jpn. J. Appl. Phys.*, 50(1).
- 175 Zeng, R.; Shen, R.; Zhao, Y.; Li, X.; Sun, Z.; Shen, Y. Aqueous Synthesis of Cu-doped ZnCdS/ZnS Core/Shell Nanocrystals with a New and Highly Reactive Sulfur Source. *Nanotechnol.* 2014, 25, 135602.
- 176 Hsiao, M. C.; Liao, S. H.; Yen, M. Y.; Teng, C. C.; Lee, S. H.; Pu, N. W.; Hsiao, M. H. Preparation and Properties of a Graphene Reinforced Nanocomposite Conducting Plate. *J. Mater. Chem.* 2010, 20, 8496-8505.
- 177 Ago, H.; Kugler, T.; Cacialli, F.; Salaneck, W. R.; Shaffer, M. S.; Windle, A. H.; Friend, R. H. Work Functions and Surface Functional Groups of Multiwall Carbon Nanotubes. *J. Phys. Chem. B* 1999, 103, 8116-8121.
- 178 Bittencourt, C.; Navio, C.; Nicolay, A.; Ruelle, B.; Godfroid, T.; Snyders, R.; Ewels, C. P. Atomic Oxygen Functionalization of Vertically Aligned Carbon Nanotubes. *J. Phys. Chem. C* 2011, 115, 20412-20418.
- 179 Veamatahau, A., Jiang, B., Seifert, T., Makuta, S., Latham, K., Kanehara, M., and Tachibana, Y. (2015). Origin of surface trap states in CdS quantum dots: relationship between size dependent photoluminescence and sulfur vacancy trap states. *Phys. Chem. Chem. Phys.*, 17(4), 2850-2858.
- 180 Cho, H. D.; Zakirov, A. S.; Yuldashev, S. U.; Ahn, C. W.; Yeo, Y. K.; Kang, T. W. Photovoltaic Device on a Single ZnO Nanowire p-n Homojunction. *Nanotechnol.* 2012, 23, 115401.

- 181 Zhou, X.; Xu, W.; Liu, G.; Panda, D.; Chen, P. Size-dependent Catalytic Activity and Dynamics of Gold Nanoparticles at the Single-molecule Level. *J. Am. Chem. Soc.* 2009, *132*, 138-146.
- 182 Keeley, G. P.; McEvoy, N.; Nolan, H.; Holzinger, M.; Cosnier, S.; Duesberg, G. S. Electroanalytical Sensing Properties of Pristine and Functionalized Multilayer Graphene. *Chem. Mater.* 2014, *26*, 1807-1812.
- 183 Chang, H.; Lv, X.; Zhang, H.; Li, J. Quantum dots Sensitized Graphene: In Situ Growth and Application in Photoelectrochemical Cells. *Electrochem. Commun.* 2010, *12*, 483-487.
- 184 Lai, Y.; Li, Y.; Jiang, L.; Xu, W.; Lv, X.; Li, J.; Liu, Y. Electrochemical Behaviors of Co-deposited Pb/Pb–MnO₂ Composite Anode in Sulfuric Acid Solution–Tafel and EIS Investigations. *J. Electroanal. Chem.* 2012, *671*, 16-23.
- 185 Li, Y.; Jiang, L.; Liu, F.; Li, J.; Liu, Y. Novel Phosphorus-doped PbO₂–MnO₂ Bicontinuous Electrodes for Oxygen Evolution Reaction. *RSC Adv.* 2014, *4*, 24020-24028.
- 186 Vuylsteke, A. A.; Sihvonen, Y. T. Sulfur Vacancy Mechanism in Pure CdS. *Phys. Rev.* 1959, *113*, 40.
- 187 Ferrer, I. J.; Salvador, P. Photoluminescence and Electroluminescence Mechanisms at Polycrystalline CdS in Air and in Contact with Aqueous Electrolytes. *J. Appl. Phys.* 1989, *66*, 2568-2577.
- 188 Zeng, X.; Xiong, D.; Zhang, W.; Ming, L.; Xu, Z.; Huang, Z.; Cheng, Y. B. Spray Deposition of Water-soluble Multiwall Carbon Nanotubes and Cu₂ZnSnSe₄ Nanoparticles Composites as Highly Efficient Counter Electrodes in Quantum dot-Sensitized Solar Cell System. *Nanoscale* 2013, *5*, 6992-6998.
- 189 K. Keren, R. S. Berman, E. Buchstab, U. Sivan, and E. Braun, *Science* 302, 1380 (2003).
- 190 L. Goux-Capes, A. Filoramo, and J. N. Patillon, *American Institute of Physics*. 17(2004).
- 191 H. W. C. Postma, T. Teepen, Z. Yao, and C. Dekker, *Science* 293, 76(2001).
- 192 A. Bachtold, P. Hadley, T. Nakanishi, and C. Dekker, *Science* 294, 1317(2001).
- 193 D. J. Hornbaker, S. J. Kahng, S. Misra, and A. Yazdani, *Science* 295, 828(2002).
- 194 J. Wu, W. Shi, and N. Chopra, *J Phys. Chem. C* 116, 12861(2012).
- 195 S. Y. Sayed, F. Wang, M. Malac, and J. M. Buriak, *ACS nano* 3, 2809(2009).
- 196 S. Y. Sayed, F. Wang, M. Malac, J. M. Buriak, *CrystEngComm* 14, 5230(2012).
- 197 S. Sorgenfrei, C. Y. Chiu, R. L. and K. L. Shepard, *Nature Nanotechnol.* 6, 126(2011).
- 198 P. J. Flatau, and B. T. Draine, *J. Opt. Soc. Am. A* 11, 1491(1994).

- 199 B. T. Draine, and P. J. Flatau, *arXiv preprint arXiv:1305. 6497* (2013).
- 200 J. Wu, W. Shi, and N. Chopra, *Carbon* 68, 708 (2014).
- 201 Y. Shao, S. Zhang, M. H. Engelhard, and Y. Lin, *J Mater. Chem.* 20, 7491(2010).
- 202 H. Wang, Q. W. Chen, J. Chen, and X. Y. Hu, *Nanoscale* 3, 4600 (2011).
- 203 N. Boutroy, Y. Pernel, J. M. Rius, and J. Robertson, *Diamond Relat. Mater.* 15, 921(2006).
- 204 Chang MC, Tanaka J. FT-IR study for hydroxyapatite/collagen nanocomposite cross-linked by glutaraldehyde. *Biomater.* 2002; 23(24): 4811-4818.
- 205 J. AlanáCreighton, *Journal of the Chemical Society, Faraday Trans.* 87, 3881(1991).
- 206 S. Zhu, T. P. Chen, Y. C. Liu, and S. Fung, *J. Nanopart. Res.* 14, 1(2012).
- 207 P. K. Jain, K. S. Lee, I. H. El-Sayed, and M. A. El-Sayed, *J. Phys. Chem. B* 110, 7238 (2006).
- 208 C. F. Bohren, and D. R. Huffman, *John Wiley and Sons.* 130, (2008)
- 209 K. Yamada, K. Miyajima, and F. Mafuné, *The J Phys. Chem. C*, 111, 11246(2007).
- 210 Stoyanova, M.; Christoskova, S. *Cent. Eur. J. Chem.* 2011, 9(6), 1000-1007.
- 211 Ahmed, S., Rasul, M. G., Martens, W. N., Brown, R., and Hashib, M. A. (2011). Advances in heterogeneous photocatalytic degradation of phenols and dyes in wastewater: a review. *Water Air Soil Pollut*, 215(1-4), 3-29.
- 212 Li, G., Wu, L., Li, F., Xu, P., Zhang, D., and Li, H. (2013). Photoelectrocatalytic degradation of organic pollutants via a CdS quantum dots enhanced TiO₂ nanotube array electrode under visible light irradiation. *Nanoscale*, 5(5), 2118-2125.
- 213 Yan, X., Zong, X., Lu, G. Q. M., and Wang, L. (2012). Ordered mesoporous tungsten oxide and titanium oxide composites and their photocatalytic degradation behavior. *Progress in Natural Science: Mater. Int.* 22(6), 654-660.
- 214 Wang, Y., Wang, Q., Zhan, X., Wang, F., Safdar, M., He, J. (2013). Visible light driven type II heterostructures and their enhanced photocatalysis properties: a review. *Nanoscale*, 5(18), 8326-8339.
- 215 Ma, D., Xin, Y., Gao, M., Wu, J. (2014). Fabrication and photocatalytic properties of cationic and anionic S-doped TiO₂ nanofibers by electrospinning. *Appl. Catal. B: Environ.*, 147, 49-57.
- 216 Kim, H., Senthil, K., and Yong, K. (2010). Photoelectrochemical and photocatalytic properties of tungsten oxide nanorods grown by thermal evaporation. *Mater. Chem. Phys.*, 120(2), 452-455.

- 217 Bignozzi, C. A., Caramori, S., Cristino, V., Argazzi, R., Meda, L., and Tacca, A. (2013). Nanostructured photoelectrodes based on WO₃: applications to photooxidation of aqueous electrolytes. *Chem. Soc. Rev.*, 42(6), 2228-2246.
- 218 Na, C. W.; Park, S. Y.; Chung, J. H.; Lee, J. H. *ACS Appl. Mater. Interfaces* 2012, 4(12), 6565-6572.
- 219 Rashad, M.; Rüsing, M.; Berth, G.; Lischka, K.; Pawlis, A. *J. Nanomater.* 2013, 82, 714853.
- 220 Na, C. W.; Park, S. Y.; Chung, J. H.; Lee, J. H. *ACS Appl. Mater. Interfaces* 2012, 4(12), 6565-6572.
- 221 Rashad, M.; Rüsing, M.; Berth, G.; Lischka, K.; Pawlis, A. *J. Nanomater.* 2013, 82, 714853.
- 222 Na, C. W.; Park, S. Y.; Chung, J. H.; Lee, J. H. *ACS Appl. Mater. Interfaces* 2012, 4(12), 6565-6572.
- 223 Rashad, M.; Rüsing, M.; Berth, G.; Lischka, K.; Pawlis, A. *J. Nanomater.* 2013, 82, 714853.
- 224 Na, C. W.; Park, S. Y.; Chung, J. H.; Lee, J. H. *ACS Appl. Mater. Interfaces* 2012, 4(12), 6565-6572.
- 225 Rashad, M.; Rüsing, M.; Berth, G.; Lischka, K.; Pawlis, A. *J. Nanomater.* 2013, 82, 714853.
- 226 González-Borrero, P. P.; Sato, F.; Medina, A. N.; Baesso, M. L.; Bento, A. C.; Baldissera, G.; da Silva, A. F. *Appl. Phys. Lett.* 2010, 96(6), 061909.
- 227 McCrory, C. C.; Jung, S.; Peters, J. C.; Jaramillo, T. F. Benchmarking Heterogeneous Electrocatalysts for the Oxygen Evolution Reaction. *J. Am. Chem. Soc.* 2013, 135(45), 16977-16987.
- 228 Zou, X.; Su, J.; Silva, R.; Goswami, A.; Sathe, B. R. Asefa, T. Efficient oxygen evolution reaction catalyzed by low-density Ni-doped Co₃O₄ nanomaterials derived from metal-embedded graphitic C₃N₄. *Chem. Commun.* 2013, 49(68), 7522-7524.
- 229 Reier, T.; Oezaslan, M.; Strasser, P. Electrocatalytic oxygen evolution reaction (OER) on Ru, Ir, and Pt catalysts: a comparative study of nanoparticles and bulk materials. *ACS Catal.* 2012, 2(8), 1765-1772.
- 230 Koza, J. A.; He, Z.; Miller, A. S.; Switzer, J. A. Electrodeposition of Crystalline Co₃O₄, A Catalyst for the Oxygen Evolution Reaction. *Chem. Mater.* 2012, 24(18), 3567-3573.
- 231 Lu, X.; Zhao, C. Highly efficient and robust oxygen evolution catalysts achieved by anchoring nanocrystalline cobalt oxides onto mildly oxidized multiwalled carbon nanotubes. *J. Mater. Chem. A* 2013, 1(39), 12053-12059.

- 232 Zhang, Q.; Wei, Z. D.; Liu, C.; Liu, X.; Qi, X. Q.; Chen, S. G.; Zhou, Y. M. Copper-doped cobalt oxide electrodes for oxygen evolution reaction prepared by magnetron sputtering. *Int. J. Hydrogen Energy* 2012, 37(1), 822-830.
- 233 Liang, Y.; Li, Y.; Wang, H.; Zhou, J.; Wang, J.; Regier, T.; Dai, H. Co₃O₄ nanocrystals on graphene as a synergistic catalyst for oxygen reduction reaction. *Nature Mater.* 2011, 10(10), 780-786.
- 234 Wu, J.; Xue, Y.; Yan, X.; Yan, W.; Cheng, Q.; Xie, Y. Co₃O₄ nanocrystals on single-walled carbon nanotubes as a highly efficient oxygen-evolving catalyst. *Nano Res.* 2012, 5(8), 521-530.
- 235 Shi, W.; Chopra, N. Surfactant-free synthesis of novel copper oxide (CuO) nanowire–cobalt oxide (Co₃O₄) nanoparticle heterostructures and their morphological control. *J. Nanopar. Res.* 2011, 13(2), 851-868.
- 236 Shi, W.; Chopra, N. Controlled fabrication of photoactive copper oxide–cobalt oxide nanowire heterostructures for efficient phenol photodegradation. *ACS Appl. Mater. Interfaces* 2012, 4(10), 5590-5607.
- 237 Jia, W.; Guo, M.; Zheng, Z.; Yu, T.; Rodriguez, E. G.; Wang, Y.; Lei, Y. Electrocatalytic oxidation and reduction of H₂O₂ on vertically aligned Co₃O₄ nanowalls electrode: Toward H₂O₂ detection. *J. Electroanal. Chem.* 2009, 625(1), 27-32.
- 238 Yuan, L.; Wang, Y.; Mema, R.; Zhou, G. Driving force and growth mechanism for spontaneous oxide nanowire formation during the thermal oxidation of metals. *Acta Mater.* 2011, 59(6), 2491-2500.
- 239 Zhao, Y.; Shl, H.; Chn, M. Splitting growth of novel CuO straw sheaves and the improved photocatalytic activity by active {110} facets exposed and crystallinity. *CrystEngCommunity* 2014, 16, 2417-2423.
- 240 Liu, Y.; Zhu, G.; Ge, B.; Zhou, H.; Yuan, A.; Shen, X. Concave Co₃O₄ octahedral mesocrystal: polymer-mediated synthesis and sensing properties. *CrystEngCommunity* 2012, 14(19), 6264-6270.
- 241 Ethiraj, A. S.; Kang, D. J. Synthesis and characterization of CuO nanowires by a simple wet chemical method. *Nanoscale Res. Lett.* 2012, 7(1), 1-5.
- 242 Ji, R.; Sun, W.; Chu, Y. One-step hydrothermal synthesis of Ag/Cu₂O heterogeneous nanostructures over Cu foil and their SERS applications. *RSC Adv.* 2014, 4(12), 6055-6059.
- 243 De Los Santos Valladares, L.; Salinas, D. H.; Dominguez, A. B.; Najarro, D. A.; Khondaker, S. I.; Mitrelias, T.; Majima, Y. Crystallization and electrical resistivity of Cu₂O and CuO obtained by thermal oxidation of Cu thin films on SiO₂/Si substrates. *Thin Solid Films* 2012, 520(20), 6368-6374.

- 244 Donders, M. E.; Knoops, H.; Van de Sanden, M. C.; Kessels, W. M.; Notten, P. Remote Plasma Atomic Layer Deposition of Co_3O_4 Thin Films. *ECS Trans.* 2009, 25(4), 39-47.
- 245 Song, M. J.; Hwang, S. W.; Whang, D. Non-enzymatic electrochemical CuO nanoflowers sensor for hydrogen peroxide detection. *Talanta* 2010, 80(5), 1648-1652.
- 246 Yu, L.; Zhang, G.; Wu, Y.; Bai, X.; Guo, D. Cupric oxide nanoflowers synthesized with a simple solution route and their field emission. *J. Cryst. Growth* 2008, 310(12), 3125-3130.
- 247 Reddaiah, K.; Reddy, M. M.; Raghu, P.; Reddy, T. M. An electrochemical sensor based on poly (solochrome dark blue) film coated electrode for the determination of dopamine and simultaneous separation in the presence of uric acid and ascorbic acid: A voltammetric method. *Colloids Surf. B* 2013, 106, 145-150
- 248 Olowu, R. A.; Arotiba, O.; Mailu, S. N.; Waryo, T. T.; Baker, P.; Iwuoha, E. Electrochemical aptasensor for endocrine disrupting 17β -estradiol based on a poly (3, 4-ethylenedioxythiophene)-gold nanocomposite platform. *Sens.* 2010, 10(11), 9872-9890.
- 249 Lin, X.; Kang, G.; Lu, L. DNA/Poly (p-aminobenzenesulfonic acid) composite bi-layer modified glassy carbon electrode for determination of dopamine and uric acid under coexistence of ascorbic acid. *Bioelectrochem.* 2007, 70(2), 235-244.
- 250 Raicopol, M.; Branzoi, V.; Necula, L.; Ionita, M.; Pilan, L. Comparative studies on the redox reaction of $\text{Fe}(\text{CN})_6^{4/3-}$ at modified glassy carbon electrodes via diazonium salts electro-reduction. *Rev. Rm. Chim.* 2012, 57(9-10), 807-814.
- 251 Lai, Y.; Li, Y.; Jiang, L.; Xu, W.; Lv, X.; Li, J.; Liu, Y. Electrochemical behaviors of co-deposited Pb/Pb- MnO_2 composite anode in sulfuric acid solution—Tafel and EIS investigations. *J. Electroanal. Chem.* 2012, 671, 16-23.
- 252 Lai, Y. Q.; Li, Y.; Jiang, L. X.; Lv, X. J.; Li, J.; Liu, Y. X. Electrochemical performance of a Pb/Pb- MnO_2 composite anode in sulfuric acid solution containing Mn^{2+} . *Hydrometallurgy* 2012, 115, 64-70.
- 253 Liu, M.; Wu, Z. Significance of interfaces in solid-state cells with porous electrodes of mixed ionic–electronic conductors, *Solid State Ionics* 1998, 107, 105-110.
- 254 Bard, A. J., Faulkner, L. R., *New York: Wiley*, 1980, 226-260.
- 255 Li, Y.; Jiang, L. X.; Lv, X. J.; Lai, Y. Q.; Zhang, H. L.; Li, J.; Liu, Y. X. Oxygen evolution and corrosion behaviors of co-deposited Pb/Pb- MnO_2 composite anode for electrowinning of nonferrous metals. *Hydrometallurgy* 2011, 109, 252-257.
- 256 Legrini, O.; Oliveros, E.; Braun, A. M. *Chem. Rev.* 1993, 93(2), 671-698.
- 257 Stoyanova, M.; Christoskova, S. *Cent. Eur. J. Chem.* 2011, 9(6), 1000-1007.
- 258 Shukla, P. R.; Wang, S.; Sun, H.; Ang, H. M.; Tadó, M. *Appl. Catal. B* 2010, 100(3), 529-534.

- 259 Wang, Y.; Wang, Q.; Zhan, X.; Wang, F.; Safdar, M.; He, J. *Nanoscale* 2013, 5(18), 8326-8339.
- 260 Dai, G.; Yu, J.; Liu, G. *J. Phys. Chem. C* 2011, 115(15), 7339-7346.
- 261 Kim, H.; Senthil, K.; Yong, K. *Mater. Chem. Phys.* 2010, 120(2), 452-455.
- 262 Shen, G.; Chen, D.; Bando, Y.; Golberg, D. *J. Mater. Sci. Technol.* 2008, 24, 541-549.
- 263 Shi, W.; Chopra, N. *ACS Appl. Mater. Interf.* 2012, 4, 5590-5607.
- 264 Tongying, P.; Plashnitsa, V. V.; Petchsang, N.; Vietmeyer, F.; Ferraudi, G. J.; Krylova, G.; Kuno, M. *J. Phys. Chem. Lett.* 2012, 3, 3234-3240.
- 265 Osterloh, F. E. *Chem. Soc. Rev.* 2013, 42, 2294-2320.
- 266 Osterloh, F. E.; Parkinson, B. A.; *MRS bulletin* 2011, 36, 17-22.
- 267 González-Borrero, P. P.; Sato, F.; Medina, A. N.; Baesso, M. L.; Bento, A. C.; Baldissera, G. *Appl. Phys. Lett.* 2010, 96, 061909.
- 268 Dai, G.; Liu, S.; Liang, Y.; Luo, T. *Appl. Surf. Sci.* 2013, 264, 157-161.
- 269 Dong, Z.; Fu, Y.; Han, Q.; Xu, Y.; Zhang, H. *J. Phys. Chem. C* 2007, 111(50), 18475-18478.
- 270 Shi, W.; Chopra, N. *ACS Appl. Mater. Interfaces* 2012, 4(10), 5590-5607.
- 271 Liu, S.; Chen, Z.; Zhang, N.; Tang, Z. R.; Xu, Y. J. *J. Phys. Chem. C* 2013, 117(16), 8251-8261.
- 272 Varghese, B.; Teo, C. H.; Zhu, Y.; Reddy, M. V.; Chowdari, B.V. R.; Wee, A. T. S. *Adv. Funct. Mater.* 2007, 17, 1932-1939.
- 273 Nasibulin, A. G.; Rackauskas, S.; Jiang, H.; Tian, Y.; Mudimela, P. R.; Shandakov, S. D.; Kauppinen, E. I. *Nano Res.* 2009, 2(5), 373-379.
- 274 Zhang, C.; Guo, D.; Hu, C.; Chen, Y.; Liu, H.; Zhang, H.; Wang, X. *Phys. Rev. B* 2013, 87(3), 035416.
- 275 Stock, S. R.; Cullity, B. D. Prentice Hall, New Jersey, 2001, 275.
- 276 Rashad, M.; Rüsing, M.; Berth, G.; Lischka, K.; Pawlis, A. *J. Nanomater.* 2013, 82, 714853.
- 277 Kreisel, J.; Weber, M. C.; Dix, N.; Sánchez, F.; Thomas, P.; Fontcuberta, J. *Adv. Funct. Mater.* 2012, 22(23), 5044-5049.
- 278 Valova, E.; Georgieva, J.; Arnyanov, S.; Sotiropoulos, S.; Hubin, A.; Baert, K.; Raes, M. J. *Electrochem. Soc.* 2010, 157(5), D309-D315.

- 279 Mei, W.; Huang, J.; Zhu, L.; Ye, Z.; Mai, Y.; Tu, J. *J. Mater. Chem.* 2012, 22(18), 9315-9321.
- 280 Todorova, S.; Kolev, H.; Holgado, J. P.; Kadinov, G.; Bonev, C.; Pereniguez, R.; Caballero, A. *Appl. Catal. B* 2010, 94(1), 46-54.
- 281 Fan, Y.; Zhang, N.; Zhang, L.; Shao, H.; Wang, J.; Zhang, J.; Cao, C. *J. Electrochem. Soc.* 2013, 160(2), F218-F223.
- 282 Wu, J.; Shi, W.; Chopra, N. *J. Phys. Chem. C* 2012, 116(23), 12861-12874.
- 283 Li, J.; Liu, Y.; Zhu, Z.; Zhang, G.; Zou, T.; Zou, Z.; Xie, C. *Sci. Rep.* 2013, 3, 2409-2455.
- 284 Dhara, S.; Giri, P. K. *Nanoscale Res. Lett.* 2011, 6(1), 1-8.
- 285 González-Borrero, P. P.; Sato, F.; Medina, A. N.; Baesso, M. L.; Bento, A. C.; Baldissera, G.; da Silva, A. F. *Appl. Phys. Lett.* 2010, 96(6), 061909.
- 286 Sun, B.; Li, H.; Wei, L.; Chen, P. *CrystEngComm* 2014, 16(42), 9891-9895.
- 287 Camden, J. P., Dieringer, J. A., Zhao, J., and Van Duyne, R. P. (2008). Controlled plasmonic nanostructures for surface-enhanced spectroscopy and sensing. *Acc. Chem. Res.*, 41(12), 1653-1661.
- 288 Luo, P., Li, C., and Shi, G. (2012). Synthesis of gold@ carbon dots composite nanoparticles for surface enhanced Raman scattering. *Phys. Chem. Chem. Phys.*
- 289 Halas, N. J., Lal, S., Link, S., Chang, W. S., Natelson, D., Hafner, J. H., and Nordlander, P. (2012). A Plethora of Plasmonics from the Laboratory for Nanophotonics at Rice University. *Adv. Mater.*.
- 290 Fan, M., Andrade, G. F., and Brolo, A. G. (2011). A review on the fabrication of substrates for surface enhanced Raman spectroscopy and their applications in analytical chemistry. *Analytica chimica acta*, 693(1), 7-25.
- 291 Shao, M. W., Zhang, M. L., Wong, N. B., Ma, D. D. D., Wang, H., Chen, W., and Lee, S. T. (2008). Ag-modified silicon nanowires substrate for ultrasensitive surface-enhanced raman spectroscopy. *Appl. Phys. Lett.*, 93(23), 233118-233118.
- 292 Fang, C., Agarwal, A., Widjaja, E., Garland, M. V., Wong, S. M., Linn, L., and Balasubramanian, N. (2009). Metallization of Silicon Nanowires and SERS Response from a single metallized Nanowire. *Chem. Mater.*, 21(15), 3542-3548.
- 293 Schmidt, V., Wittemann, J. V., Senz, S., and Gösele, U. (2009). Silicon nanowires: a review on aspects of their growth and their electrical properties. *Adv. Mater.*, 21(25-26), 2681-2702.
- 294 Lv, M., Su, S., He, Y., Huang, Q., Hu, W., Li, D., and Lee, S. T. (2010). Long-Term Antimicrobial Effect of Silicon Nanowires Decorated with Silver Nanoparticles. *Advanced Materials*, 22(48), 5463-5467.

- 295 Peng, K. Q., Wang, X., Wu, X. L., and Lee, S. T. (2009). Platinum nanoparticle decorated silicon nanowires for efficient solar energy conversion. *Nano letters*, 9(11), 3704-3709.
- 296 Shao, M. W., Shan, Y. Y., Wong, N. B., and Lee, S. T. (2005). Silicon nanowire sensors for bioanalytical applications: Glucose and hydrogen peroxide detection. *Adv. Func. Mater.*, 15(9), 1478-1482.
- 297 Markussen, T., Jauho, A. P., and Brandbyge, M. (2009). Surface-decorated silicon nanowires: a route to high-ZT thermoelectrics. *Phys. Rev. Lett.*, 103(5).
- 298 Fei Zhao, Dan-dan Zhao, Shao-long Wu, Guo-an Cheng, Rui-ting Zheng. Diamond-like carbon decoration enhances the field electron emission of silicon nanowires, in press
- 299 Eisenhawer, B., Sensfuss, S., Sivakov, V., Pietsch, M., Andrä, G., and Falk, F. (2011). Increasing the efficiency of polymer solar cells by silicon nanowires. *Nanotechnol.*, 22(31), 315401.
- 300 Peng, Z., Hu, H., Wang, S., Shen, Z., and Xiong, Q. (2010, August). Enhanced Raman Scattering of Silicon Nanowires by Ag Nanoparticles in-situ Decoration. *Am. Inst. Phys. Conf. Ser.* 1267, 53-54.
- 301 Zhang, B., Wang, H., Lu, L., Ai, K., Zhang, G., and Cheng, X. (2008). Large-Area Silver-Coated Silicon Nanowire Arrays for Molecular Sensing Using Surface-Enhanced Raman Spectroscopy. *Adv. Func. Mater.*, 18(16), 2348-2355.
- 302 Galopin, E., Barbillat, J., Coffinier, Y., Szunerits, S., Patriarche, G., and Boukherroub, R. (2009). Silicon nanowires coated with silver nanostructures as ultrasensitive interfaces for surface-enhanced Raman spectroscopy. *ACS Appl. Mater. Interf.*, 1(7), 1396-1403.
- 303 Schmidt, M. S., Hübner, J., and Boisen, A. (2012). Large Area Fabrication of Leaning Silicon Nanopillars for Surface Enhanced Raman Spectroscopy. *Adv. Mater.*
- 304 Baik, S. Y., Cho, Y. J., Lim, Y. R., Im, H. S., Jang, D. M., Myung, Y., and Kang, H. S. (2012). Charge-Selective Surface-Enhanced Raman Scattering Using Silver and Gold Nanoparticles Deposited on Silicon–Carbon Core–Shell Nanowires. *ACS nano*, 6(3), 2459-2470.
- 305 Chen, R., Li, D., Hu, H., Zhao, Y., Wang, Y., Wong, N., and Xiong, Q. (2012). Tailoring Optical Properties of Silicon Nanowires by Au Nanostructure Decorations: Enhanced Raman Scattering and Photodetection. *J. Phys. Chem. C*, 116(7), 4416-4422.
- 306 Su, Y., Wei, X., Peng, F., Zhong, Y., Lu, Y., Su, S., and He, Y. (2012). Gold Nanoparticles-Decorated Silicon Nanowires as Highly Efficient Near-Infrared Hyperthermia Agents for Cancer Cells Destruction. *Nano Lett.*, 12(4), 1845-1850.
- 307 Li, C. P., Sun, X. H., Wong, N. B., Lee, C. S., Lee, S. T., and Teo, B. K. (2002). Silicon nanowires wrapped with Au film. *J. Phys. Chem. B*, 106(28), 6980-6984.

- 308 Sayed, S. Y.; Wang, F.; Malac, M.; Meldrum, A.; Egerton, R. F., and Buriak, J. M. (2009). Heteroepitaxial Growth of Gold Nanostructures on Silicon by Galvanic Displacement. *ACS nano*, 3(9), 2809-2817.
- 309 Sivakov, V. A.; Scholz, R.; Syrowatka, F.; Falk, F.; Gösele, U., and Christiansen, S. H. (2009). Silicon nanowire oxidation: the influence of sidewall structure and gold distribution. *Nanotechnol.*, 20(40), 405607.
- 310 Gong, X.; Bao, Y.; Qiu, C.; Jiang, C. Individual Nanostructured Materials: Fabrication and Surface-Enhanced Raman Scattering. *Chem. Commun.* 2012, 48, 7003-7018
- 311 Luo, P.; Li, C.; Shi, G. Synthesis of Gold@ Carbon Dots Composite Nanoparticles for Surface Enhanced Raman Scattering. *Phys. Chem. Chem. Phys.* 2012, 14, 7360-7366
- 312 Gunawidjaja, R.; Kharlampieva, E.; Choi, I.; Tsukruk, V. V. Bimetallic Nanostructures as Active Raman Markers: Gold-Nanoparticle Assembly on 1D and 2D Silver Nanostructure Surfaces. *Small*, 2009, 5, 2460-2466.
- 313 Fan, M.; Andrade, G. F.; Brolo, A. G. A Review on the Fabrication of Substrates for Surface Enhanced Raman Spectroscopy and Their Applications in Analytical Chemistry. *Anal. Chim. Acta* 2011, 693, 7-25.
- 314 Shao, M. W.; Zhang, M. L.; Wong, N. B.; Ma, D. D. D.; Wang, H.; Chen, W.; Lee, S. T. Ag-Modified Silicon Nanowires Substrate for Ultrasensitive Surface-Enhanced Raman Spectroscopy. *Appl. Phys. Lett.* 2008, 93, 233118-233118.
- 315 Deng, S.; Fan, H. M.; Zhang, X.; Loh, K. P.; Cheng, C. L.; Sow, C. H.; Foo, Y. L. An Effective Surface-Enhanced Raman Scattering Template Based on an Ag Nanocluster–ZnO Nanowire Array. *Nanotechnol.* 2009, 20, 175705.
- 316 Peng, K. Q.; Lee, S. T. Silicon Nanowires for Photovoltaic Solar Energy Conversion. *Adv. Mater.* 2011, 23, 198-215.
- 317 Zhang, F.; Song, T.; Sun, B. Conjugated Polymer–Silicon Nanowire Array Hybrid Schottky Diode for Solar Cell Application. *Nanotechnol.* 2012, 23, 194006.
- 318 Peng, Z.; Hu, H.; Utama, M. I. B.; Wong, L. M.; Ghosh, K.; Chen, R.; Xiong, Q. Heteroepitaxial Decoration of Ag Nanoparticles on Si Nanowires: A Case Study on Raman Scattering and Mapping. *Nano Lett.* 2010, 10, 3940-3947.
- 319 Galopin, E.; Barbillat, J.; Coffinier, Y.; Szunerits, S.; Patriarche, G.; Boukherroub, R. Silicon Nanowires Coated with Silver Nanostructures as Ultrasensitive Interfaces for Surface-Enhanced Raman Spectroscopy. *ACS Appl. Mater. Interfaces* 2009, 1, 1396-1403.
- 320 Schmidt, M. S.; Hübner, J.; Boisen, A. Large Area Fabrication of Leaning Silicon Nanopillars for Surface Enhanced Raman Spectroscopy. *Adv. Mater.* 2012, 24, 11-18.

- 321 Baik, S. Y.; Cho, Y. J.; Lim, Y. R.; Im, H. S.; Jang, D. M.; Myung, Y.; Kang, H. S. Charge-Selective Surface-Enhanced Raman Scattering Using Silver and Gold Nanoparticles Deposited on Silicon–Carbon Core–Shell Nanowires. *ACS nano* 2012, 6, 2459-2470.
- 322 Li, C. P.; Sun, X. H.; Wong, N. B.; Lee, C. S.; Lee, S. T.; Teo, B. K. Silicon Nanowires Wrapped with Au Film. *J. Phys. Chem. B* 2002, 106, 6980-6984.
- 323 Hannon, J. B.; Kodambaka, S.; Ross, F. M.; Tromp, R. M. The Influence of the Surface Migration of Gold on the Growth of Silicon Nanowires. *Nat.* 2006, 440, 69-71.
- 324 Schmidt, V.; Wittemann, J. V.; Senz, S.; Gösele, U. Silicon Nanowires: A Review on Aspects of Their Growth and Their Electrical Properties. *Adv. Mater.* 2009, 21, 2681-2702.
- 325 Chopra, N.; Wu, J.; Summerville, L. Controlled Assembly of Graphene Shells Encapsulated Gold Nanoparticles and Their Integration with Carbon Nanotubes. *Carbon* 2013, 62, 76-87.
- 326 Chakraborty, S.; Kamila, J.; Rout, B.; Satpati, B.; Satyam, P. V.; Sundaravel, B.; Dev, B. N. Shape Variation in Epitaxial Microstructures of Gold Silicide Grown on Br-passivated Si (111) Surfaces. *Surf. Sci.* 2004, 549, 149-156.
- 327 Li, Y.; Chopra, N. Fabrication of Thermally-Conductive Carbon Nanotubes-Copper Oxide Heterostructures. *In MRS Proceedings*, 2013, 1543, 119-124.
- 328 Kawashima, T.; Mizutani, T.; Nakagawa, T.; Torii, H.; Saitoh, T.; Komori, K.; Fujii, M. Control of Surface Migration of Gold Particles on Si Nanowires. *Nano lett.* 2008, 8, 362-368.
- 329 Xie, T.; Schmidt, V.; Pippel, E.; Senz, S.; Gösele, U. Gold-Enhanced Low-Temperature Oxidation of Silicon Nanowires. *Small* 2008, 4, 64-68.
- 330 Lerch, W.; Stolwijk, N. A. Diffusion of Gold in Silicon during Rapid Thermal Annealing: Effectiveness of the Surface as a Sink for Self-Interstitials. *J. Appl. Phys.* 1998, 83, 1312-1320.
- 331 Nicolet, M. A. Diffusion Barriers in Thin Films. *Thin Solid Films* 1978, 52, 415-443.
- 332 Sprokel, G. J.; Fairfield, J. M. Diffusion of Gold into Silicon Crystals. *J. Electrochem. Soc.* 1965, 112, 200-203.
- 333 Wu, J.; Shi, W.; Chopra, N. Plasma Oxidation Kinetics of Gold Nanoparticles and Their Encapsulation in Graphene Shells by Chemical Vapor Deposition Growth. *J. Phys. Chem. C* 2012, 116, 12861-12874.
- 334 Sundaravel, B.; Sekar, K.; Kuri, G.; Satyam, P. V.; Dev, B. N.; Bera, S.; Caccavale, F. XPS and SIMS Analysis of Gold Silicide Grown on a Bromine Passivated Si (111) Substrate. *Appl. Surf. Sci.* 1999, 137, 103-112.

- 335 Khalfaoui, R.; Benazzouz, C.; Guittoum, A.; Tabet, N.; Tobbeche, S. Irradiation-Induced Gold Silicide Formation and Stoichiometry Effects in Ion Beam-Mixed Layer. *Vac.* 2006, *81*, 45-48.
- 336 Sarkar, D. K.; Bera, S.; Dhara, S.; Nair, K. G. M.; Narasimhan, S. V.; Chowdhury, S. XPS Studies on Silicide Formation in Ion Beam Irradiated Au/Si System. *Appl. Surf. Sci.* 1997, *120*, 159-164.
- 337 Pant, A. K.; Murarka, S. P.; Shepard, C.; Lanford, W. Kinetics of Platinum Silicide Formation during Rapid Thermal Processing. *J. Appl. Phys.* 1992, *72*, 1833-1836.
- 338 Poate, J. M.; Tisone, T. C. Kinetics and Mechanism of Platinum Silicide Formation on Silicon. *Appl. Phys. Lett.* 2003, *24*, 391-393.
- 339 Halas, N. J.; Lal, S.; Link, S.; Chang, W. S.; Natelson, D.; Hafner, J. H.; Nordlander, P. A Plethora of Plasmonics from the Laboratory for Nanophotonics at Rice University. *Adv. Mater.* 2012, *24*, 4842-4877.
- 340 Al-Ogaidi, I.; Gou, H.; Al-kazaz, A. K.; Aguilar, Z. P.; Melconian, A.; Zheng, P.; Wu, N. A Gold@ Silica Core/shell Nanoparticle-Based Surface-Enhanced Raman Scattering Biosensor for Label-Free Glucose Detection. *Anal. Chim. Acta* 2014, *811*, 76-80.
- 341 Camden, J. P., Dieringer, J. A., Zhao, J., and Van Duyne, R. P. (2008). Controlled plasmonic nanostructures for surface-enhanced spectroscopy and sensing. *Acc. Chem. Res.*, *41*(12), 1653-1661.
- 342 Luo, P., Li, C., and Shi, G. (2012). Synthesis of gold@ carbon dots composite nanoparticles for surface enhanced Raman scattering. *Phys. Chem. Chem. Phys.*
- 343 Gunawidjaja, R., Kharlampieva, E., Choi, I., and Tsukruk, V. V. (2009). Bimetallic Nanostructures as Active Raman Markers: Gold-Nanoparticle Assembly on 1D and 2D Silver Nanostructure Surfaces. *Small*, *5*(21), 2460-2466.
- 344 Sayed, S. Y., Wang, F., Malac, M., Meldrum, A., Egerton, R. F., and Buriak, J. M. (2009). Heteroepitaxial Growth of Gold Nanostructures on Silicon by Galvanic Displacement. *ACS nano*, *3*(9), 2809-2817.
- 345 Sayed, S. Y., Wang, F., Malac, M., Li, P., Wang, D., and Buriak, J. (2012). Preferential face deposition of gold nanoparticles on silicon nanowires by galvanic displacement. *CrystEngComm*, *14*(16), 5230-5234.
- 346 Chopra, N., JUNCHI, W., and Summerville, L. (2013). Controlled assembly of graphene shells encapsulated gold nanoparticles and their integration with carbon nanotubes. *Carbon*, *62*, 76-87.
- 347 Chopra, N., Bachas, L. G., and Knecht, M. R. (2009). Fabrication and biofunctionalization of carbon-encapsulated Au nanoparticles. *Chem. Mater.*, *21*(7), 1176-1178.

- 348 Camden, J. P., Dieringer, J. A., Zhao, J., and Van Duyne, R. P. (2008). Controlled plasmonic nanostructures for surface-enhanced spectroscopy and sensing. *Acc. Chem. Res.*, *41*(12), 1653-1661.
- 349 Halas, N. J., Lal, S., Link, S., Chang, W. S., Natelson, D., Hafner, J. H., and Nordlander, P. (2012). A Plethora of Plasmonics from the Laboratory for Nanophotonics at Rice University. *Adv. Mater.*
- 350 Shao, M. W., Zhang, M. L., Wong, N. B., Ma, D. D. D., Wang, H., Chen, W., and Lee, S. T. (2008). Ag-modified silicon nanowires substrate for ultrasensitive surface-enhanced raman spectroscopy. *Appl. Phys. Lett.*, *93*(23), 233118-233118.
- 351 Schmidt, V., Wittemann, J. V., Senz, S., and Gösele, U. (2009). Silicon nanowires: a review on aspects of their growth and their electrical properties. *Adv. Mater.*, *21*(25-26), 2681-2702.
- 352 Lv, M., Su, S., He, Y., Huang, Q., Hu, W., Li, D., ... and Lee, S. T. (2010). Long-Term Antimicrobial Effect of Silicon Nanowires Decorated with Silver Nanoparticles. *Adv. Mater.*, *22*(48), 5463-5467.
- 353 Zhang, B., Wang, H., Lu, L., Ai, K., Zhang, G., and Cheng, X. (2008). Large-Area Silver-Coated Silicon Nanowire Arrays for Molecular Sensing Using Surface-Enhanced Raman Spectroscopy. *Adv. Func. Mater.*, *18*(16), 2348-2355.
- 354 P. A. Atanasov, N. N. Nedyalkov, T. Sakai, M. Obara. *Appl. Surf. Sci.* 254, 794 (2005).
- 355 Balandin AA. Thermal properties of graphene and nanostructured carbon materials. *Nat. Mater.* 2011; 10: 569-581.
- 356 Chung DL, Takizawa Y. Performance of isotropic and anisotropic heat spreaders. *J. Electron. Mater.* 2012; 41(9): 2580-2587.
- 357 Cao Q, Kim S, Pimparkar N, Kulkarni JP, Wang C, Shim M, et al. Medium-scale carbon nanotube thin-film integrated circuits on flexible plastic substrates. *Nature* 2008; 454: 495-500.
- 358 Biercuk MJ, Llaguno MC, Radosavljevic M, Hyun JK, Johnson AT, Fischer JE. Carbon nanotube composites for thermal management. *Appl. Phys. Lett.* 2002; 80: 2767.
- 359 Yang J, Waltermire S, Chen Y, Zinn AA, Xu TT, Li D. Contact thermal resistance between individual multiwall carbon nanotubes. *Appl. Phys. Lett.* 2010; 96(2): 023109-023109.
- 360 Felten A, Bittencourt C, Pireaux, JJ, Van Lier G, Charlier JC. Radio-frequency plasma functionalization of carbon nanotubes surface O₂, NH₃, and CF₄ treatment. *J. Appl. Phys.* 2005; 98(7): 074308-074308.
- 361 Bittencourt C, Navio C, Nicolay A, Ruelle B, Godfroid T, Snyders R, et al. Atomic oxygen functionalization of vertically aligned carbon nanotubes. *J. Phys. Chem. C* 2011; 115(42): 20412-20418.

- 362 Li Y, Chopra N. Nanoscale heterostructures comprised of silicon nanowires and gold nanoparticles encapsulated in graphitic shells for DNA immobilization. *Mater. Res. Soc. Proc.* Symposium SS, 2013; 1572: mrss13-1572-ss06-08.
- 363 Van Hooijdonk E, Bittencourt C, Snyders R, Colomer JF. Functionalization of vertically aligned carbon nanotubes. *Beilstein J. Nanotech.* 2013; 4(1): 129-152.
- 364 Amr IT, Al-Amer A, Al-Harhi M, Girei SA, Sougrat R, Atieh MA. Effect of acid treated carbon nanotubes on mechanical, rheological and thermal properties of polystyrene nanocomposites. *Compos Part B-Eng* 2011; 42(6): 1554-1561.
- 365 Watts RJ, Kistner M, Druma AM, Alam K. Materials opportunity for spacecraft and aerospace thermal management. *AIP Con. Proc.* 2005; 746: 22.
- 366 Ivanov I, Poretzky A, Eres G, Wang H, Pan Z, et al. Fast and highly anisotropic thermal transport through vertically aligned carbon nanotube arrays. *Appl. Phys. Lett.* 2006; 89(22): 223110-223110.
- 367 Cola BA, Xu J, Cheng C, Xu X, Fisher TS, Hu H. Photoacoustic characterization of carbon nanotube array thermal interfaces. *J. Appl. Phys.* 2007; 101(5): 054313-054313.
- 368 Balandin AA, Ghosh S, Bao WZ, Calizo I, Teweldebrhan D, Miao F, et al. Superior thermal conductivity of single-layer graphene. *Nano Lett.* 2008; 8: 902-907.
- 369 Andrews R, Jacques D, Qian D, Rantell T. Multiwall carbon nanotubes: synthesis and application. *Acc. Chem. Res.* 2002; 35: 1008-1017.
- 370 Cai W, Moore AL, Zhu Y, Li, X, Chen S, Shi L, et al. Thermal transport in suspended and supported monolayer graphene grown by chemical vapor deposition. *Nano Lett.* 2010; 10(5): 1645-1651.
- 371 Kim D, Zhu L, Han CS, Kim JH, Baik S. Raman characterization of thermal conduction in transparent carbon nanotube films. *Langmuir* 2011; 27(23): 14532-14538.
- 372 Li Y, Chopra N. Fabrication of thermally-conductive carbon nanotubes-copper oxide heterostructures, *Mater. Res. Soc. Proc.*, Symposium V, 2013; 1543: mrss13-1543-v05-02.
- 373 Zhong Y, Jaidann M, Zhang Y, Zhang G, Liu H, Ioan MI, et al. Synthesis of high nitrogen doping of carbon nanotubes and modeling the stabilization of filled DAATO@ CNTs (10, 10) for nanoenergetic materials. *J. Phys. Chem. Solids* 2010; 71(2): 134-139.
- 374 Meier MS, Rodney A, David J, Kelby BC, Qian DL. Tearing open nitrogen-doped multiwalled carbon nanotubes. *J. Mater. Chem.* 2008; 18(35): 4143-4145.
- 375 Sumpter BG, Vincent M, José MR, Eduardo CS, David AC, Humberto T, et al. Nitrogen-mediated carbon nanotube growth: diameter reduction, metallicity, bundle dispersability, and bamboo-like structure formation. *ACS Nano* 2007; 1(4): 369-375.

- 376 Liu H, Zhang Y, Li R, Sun X, Abou-Rachid H. Thermal and chemical durability of nitrogen-doped carbon nanotubes. *J. Nanopart. Res.* 2012; 14(8): 1-8.
- 377 Ago H, Kugler T, Cacialli F, Salaneck WR, Shaffer MS, Windle AH, et al. Work functions and surface functional groups of multiwall carbon nanotubes. *J. Phys. Chem. B* 1999; 103(38): 8116-8121.
- 378 Wang Y, Shao Y, Matson DW, Li J, Lin Y. Nitrogen-doped graphene and its application in electrochemical biosensing. *Acs Nano* 2010; 4(4): 1790-1798.
- 379 Shin WH, Jeong HM, Kim BG, Kang JK, Choi JW. Nitrogen-doped multiwall carbon nanotubes for lithium storage with extremely high capacity. *Nano Lett.* 2012; 12: 2283-2288.
- 380 Dresselhaus MS, Jorio A, Hofmann M, Dresselhaus G, Saito R. Perspectives on carbon nanotubes and graphene Raman spectroscopy. *Nano Lett.* 2010; 10(3): 751-758.
- 381 Vinayan BP, Nagar R, Raman V, Rajalakshmi N, Dhathathreyan KS, Ramaprabhu S. Synthesis of graphene-multiwalled carbon nanotubes hybrid nanostructure by strengthened electrostatic interaction and its lithium ion battery application. *J. Mater. Chem.* 2012; 22(19): 9949-9956.
- 382 Calizo I, Balandin AA, Bao W, Miao F, Lau CN. Temperature dependence of the Raman spectra of graphene and graphene multilayers. *Nano Lett.* 2007; 7(9): 2645-2649.
- 383 Ayala P, Arenal R, Rummeli M, Rubio A, Pichler T. The doping of carbon nanotubes with nitrogen and their potential applications. *Carbon* 2010; 48(3): 575-586.
- 384 Klemens PG. Theory of the a-plane thermal conductivity of graphite. *J Wide Bandgap Mater* 2000; 7(4): 332-339.
- 385 Ayala P, Arenal R, Rummeli M, Rubio A, Pichler T. The doping of carbon nanotubes with nitrogen and their potential applications. *Carbon* 2010; 48(3): 575-586.
- 386 Park J, Bifano MF, Prakash V. Sensitivity of thermal conductivity of carbon nanotubes to defect concentrations and heat-treatment. *J. Appl. Phys.* 2013; 113(3): 034312-034312.
- 387 Bullen AJ, OHara KE, Cahill DG, Monteiro O, von Keudell A. Thermal conductivity of amorphous carbon thin films. *J. Appl. Phys.* 2000; 88(11): 6317-6320.
- 388 Yamane T, Nagai N, Katayama SI, Todoki M. Measurement of thermal conductivity of silicon dioxide thin films using a 3ω method. *J. Appl. Phys.* 2002; 91(12): 9772-9776.
- 389 Chopra N, Shi WW, Bansal A. Structural evolution and stability studies of heterostructures comprised of carbon nanotubes decorated with nickel/nickel oxide core/shell nanoparticles. *Carbon* 2011; 49(11): 3645-3662.
- 390 Lee YP, Kong MG. Heat generation and temperature distribution in DC metallized polymer film capacitors. *Ann. Rep. Con. Elec. Insul. Dielect. Phen.*, 2001; 669-672.

- 391 Duda JC, Hopkins PE, Shen Y, Gupta MC. Thermal transport in organic semiconducting polymers. *Appl. Phys. Lett* 2013; 102(25): 251912.
- 392 Incropera FP, Lavine AS, DeWitt DP. Fundamentals of heat and mass transfer. John Wiley and Sons Inc. 2011.
- 393 Chu K, Li WS, Jia CC, Tang FL. Thermal conductivity of composites with hybrid carbon nanotubes and graphene nanoplatelets. *Appl. Phys. Lett.* 2012; 101: 211903.